TRANSACTIONS
OF THE ASME
Series D

Journal of BASIC ENGINEERING

December 1960

Divisions: LUBRICATION • HYDRAULIC • INSTRUMENTS AND REGULATORS • METALS ENGINEERING • **Research Committees:** AUTOMATIC REGULATION THEORY • EFFECT OF TEMPERATURE ON THE PROPERTIES OF METALS • FLUID METERS • PREVENTION OF FRACTURE IN METALS • MECHANICAL PRESSURE ELEMENTS • LUBRICATION • PLASTIC FLOW OF METALS

Published Quarterly by
THE AMERICAN SOCIETY OF MECHANICAL ENGINEERS

TRANSACTIONS OF THE ASME
Series D

Journal of
BASIC ENGINEERING

VOLUME 82 • SERIES D • NUMBER 4

December 1960

CONTENTS

759 **Viscous Dispersion in Water Hammer** (59—A-12)
M. L. Walker, Jr., E. T. Kirkpatrick, and W. T. Rouleau

765 **A Review of Surge-Tank Stability Criteria** (59—A-270)
Charles Jaeger

784 **The Selection of Length and Head Scales for Cavitation Tests** (59—A-40)
Pierre Danel and Jacques Duport

795 **Some Corrosion Effects in Accelerated Cavitation Damage** (59—A-52)
W. C. Leith and A. L. Thompson

808 **On Cathodic Protection in Cavitation Damage** (59—A-170)
M. S. Plesset

821 **Correlation of Cavitation Inception Data for a Centrifugal Pump Operating in Water and in Sodium-Potassium Alloy (NaK)** (59—A-156)
A. G. Grindell

829 **The Creep-Rupture Properties of 80 Ni-20 Cr Alloys** (59—A-119)
Robert Widmer and N. J. Grant

839 **The Extrapolation of Families of Curves by Recurrence Relations, With Application to Creep-Rupture Data** (59—A-155)
A. Mendelson and S. S. Manson

848 **Some Observations on the Extrapolation of High-Temperature Ferritic Steel Data** (59—A-133)
R. M. Goldhoff

855 **Fabrication and Annealing Factors Affecting Grain Size of 18Cr8Ni-Ti Superheater Materials in Steam Boilers** (59—A-311)
F. Eberle and J. S. Makris

867 **Survey of Various Special Tests Used to Determine Elastic, Plastic, and Rupture Properties of Metals at Elevated Temperatures** (59—A-112)
F. Garofalo

882 **The Role of Atmosphere in the Creep-Rupture Behavior of 80 Ni-20 Cr Alloys** (59—A-122)
Robert Widmer and N. J. Grant

887 **Bourdon Tube Deflection Characteristics**
P. G. Exline

894 **Control of Oil Whip Frequency Ratio** (60—LubS-1)
E. H. Hull

899 **A Note on the Influence of Elastic Compliance on Sliding Friction in Ball Bearings** (60—LubS-2)
K. L. Johnson

901 **Pressure Oscillations in a Water-Cooled Nuclear Reactor Induced by Water-Hammer Waves** (60—Hyd-2)
P. Lieberman and E. A. Brown

912 **Pressure Surges in Pipelines Carrying Viscous Liquids** (60—Hyd-5)
W. T. Rouleau

921 **Two-Dimensional Flow With Standing Vortexes in Ducts and Diffusers** (60—Hyd-16)
F. O. Ringleb

929 **An Experimental Study of Cavitation in a Mixed Flow Pump Impeller** (60—Hyd-7)
G. M. Wood, J. S. Murphy, and J. Farquhar

941 **An Effect of Air Content on the Occurrence of Cavitation** (60—Hyd-8)
J. W. Holl

EDITORIAL DEPARTMENT

Editor, J. J. JAKLITSCH, JR.
Consulting Editor, LEO BLODGETT
Production, JEAN NORTH
Art Editor, HENRY BALFOUR

OFFICERS OF THE ASME

President, W. L. CISLER
Secretary, O. B. SCHIER, II
Treasurer, E. J. KATES
Assistant Treasurer, H. J. BAUER

PUBLICATIONS COMMITTEE

Chairman, B. G. A. SKROTZKI
HENDLEY N. BLACKMON
R. D. MINDLIN
MARTIN GOLAND
VITO L. SALERNO

Junior Representatives
A. S. GOLDSTEIN
J. W. FOLLANSBEE

REGIONAL ADVISORY BOARD

Region I, H. M. ROGERS, JR.
Region II, GLENN R. FRYLING
Region III, F. J. HEINZE
Region IV, FRANCIS C. SMITH
Region V, H. M. CATHER
Region VI, C. R. EARLE
Region VII, M. S. UMBENHAUER
Region VIII, CARL J. ECKHARDT

Published quarterly by The American Society of Mechanical Engineers. Publication office at 20th and Northampton Streets, Easton, Pa. The editorial department is located at the headquarters of the Society, 29 West Thirty-Ninth Street, New York 18, N. Y. Cable address, "Mechaneer," New York. Price $3.00 a copy, $10.00 annually; to members, $1.50 a copy, $5.00 annually. Add 50 cents for postage to all countries outside the United States and Canada. Changes of address must be received at Society headquarters seven weeks before they are to be effective on the mailing list. Please send old as well as new address. . . . By-Law: The Society shall not be responsible for, statements or opinions advanced in papers or . . . printed in its publications (B13, Par. 4). . . . Second-class mail privileges authorized at Easton, Penna. . . . This publication is authorized to be mailed at the special rates of postage prescribed by Section 132.122 . . . © Copyrighted, 1960, by The American Society of Mechanical Engineers. Reprints from this publication may be made on condition that full credit be given the Transactions of the ASME, Series D—Journal of Basic Engineering, and the author, and that date of publication be stated.

TRANSACTIONS OF THE ASME
is indexed by the Engineering Index, Inc.

CONTENTS

947 **A Jet Pump Design Theory** (60—Hyd-6)
T. W. van der Lingen

961 **Accelerations and Mean Trajectories in Turbulent Channel Flow** (60—Hyd-3)
S. Irmay

973 **Supersonic Diffuser for Radial and Mixed Flow Compressors** (60—Hyd-11)
F. Dallenbach and N. Van Le

TECHNICAL BRIEF

980 **Elastic Orifices for Gas Bearings**
J. H. Laub

TRANSACTIONS OF THE ASME Series A

Journal of
ENGINEERING FOR POWER
Volume 82 • Series A • Number 4

CONTENTS FOR OCTOBER, 1960

247 Throat Tap Nozzles Used for Accurate Flow Measurements, by K. C. Cotton and J. C. Westcott. (59—A-174)

264 Water-Treatment, Corrosion, and Internal-Deposit Studies for Eddystone, by R. C. Ulmer, H. A. Grabowski, and R. C. Patterson. (59—A-147)

275 The Selection of Materials and Fabricating Techniques for the Eddystone Boiler and Sulzer Control Valves, by E. C. Chapman and R. E. Lorentz, Jr. (59—A-318)

286 Development Associated With the Superpressure Turbine for Eddystone Station Unit No. 1, by W. E. Trumpler, Jr., A. F. LeBreton, E. A. Fox, and R. B. Williamson. (59—A-288)

293 Material Selection and Fabrication, Main Steam Piping for Eddystone No. 1, 1200-F and 5000-Psi Service, by R. H. Caughey and W. G. Benz, Jr. (59—A-327)

315 Solar Turbo Power-Plant Design, by D. B. Mackay and E. L. Leventhal. (59—A-74)

325 Analysis of Solar-Furnace Performance in Mechanical Testing at Extremely High Temperatures, by G. S. Leon and M. E. Shank. (59—A-79)

TRANSACTIONS OF THE ASME Series C

Journal of
HEAT TRANSFER
Vol. 82 • Series C • No. 4

CONTENTS FOR NOVEMBER, 1960

265 A Variable Density Single-Fluid Model for Two-Phase Flow With Particular Reference to Steam-Water Flow, by S. G. Bankoff. (59—HT-7)

273 Transient Temperatures and Thermal Stresses in Hollow Cylinders Due to Heat Generation, by John E. Schmidt and George Sonnemann. (59—A-144)

279 Thermal-Contact Resistance in Finned Tubing, by Karl A. Gardner and T. C. Carnavos. (59—A-135)

294 Mass Transfer, Flow, and Heat Transfer About a Rotating Disk, by E. M. Sparrow and J. L. Gregg. (59—A-107)

303 Heat Transfer and Effectiveness for a Turbulent Boundary Layer With Tangential Fluid Injection, by R. A. Seban. (59—A-177)

313 Sublimation Mass Transfer Through Compressible Boundary Layers on a Flat Plate, by T. K. Sherwood and Olev Trass. (59—A-137)

325 Laminar Skin Friction and Heat Transfer on Flat Plates With Wedge-Shaped Grooves in Flow Direction, by T. F. Irvine, Jr., and E. R. G. Eckert. (59—A-143)

333 Heat Transfer to Liquid Metals With Variable Properties, by R. Viskanta and Y. S. Touloukian. (59—A-148)

341 A Summary of Experiments on Turbulent Heat Transfer From a Nonisothermal Flat Plate, by W. C. Reynolds, W. M. Kays, and S. J. Kline. (59—A-157)

349 An Experimental Study of the Effects of Nonuniform Wall Temperature on Heat Transfer in Laminar and Turbulent Axisymmetric Flow Along a Cylinder, by R. Eichhorn, E. R. G. Eckert, and A. D. Anderson. (59—A-151)

360 Geometric Factors for Radiative Heat Transfer Through an Absorbing Medium in Cartesian Coordinates, by A. K. Oppenheim and J. T. Bevans. (59—A-206)

369 Thermal Radiation From a Cylindrical Enclosure With Specified Wall Heat Flux, by C. M. Usiskin and R. Siegel. (59—A-159)

375 Application of Variational Methods to Radiation Heat-Transfer Calculations, by E. M. Sparrow. (59—A-120)

381 Certain Thermodynamic and Transport Properties of the Atmospheres of Venus, Mars, and Jupiter, by W. E. Ibele and T. F. Irvine, Jr. (59—A-102)

TECHNICAL BRIEFS

387 Heat Transfer to Boiling Mercury, by F. E. Romie, S. W. Brovarney, and W. H. Giedt.

389 Temperature Distribution and Heat-Transfer Results for an Internally Cooled, Heat-Generating Solid, by E. M. Sparrow.

392 Effects of Initial Boundary-Layer Thickness on a Tangential Injection System, by R. A. Seban.

393 The Mechanism of Sound Field Effects on Heat Transfer, by J. P. Holman.

396 A Transducer for the Measurement of Heat-Flow Rate, by Robert Gardon.

TRANSACTIONS OF THE ASME Series B

Journal of
ENGINEERING FOR INDUSTRY
Volume 82 · Series B · Number 4

CONTENTS FOR NOVEMBER, 1960

283 Tensile and Short-Time Creep Properties of N-155 Alloy Sheet, by E. C. Bernett. (59—A-27)
303 A Photoelastic Analysis of Machining Stresses, by E. Usui and H. Takeyama. (59—A-37)
309 Correlation of Bendability of Materials With Their Tensile Properties, by J. Datsko and C. T. Yang. (59—A-110)
315 Comparisons Between the Shearing Properties of Alpha-Brass as Derived From the Cutting Process and From Static and Impact Torsion Tests, by S. S. Chang and W. B. Heginbotham. (59—A-38)
324 The Role of Friction in Metal Cutting, by S. Kobayashi and E. G. Thomsen. (59—A-132)
333 A Critical Comparison of Metal-Cutting Theories With New Experimental Data, by S. Kobayashi, R. P. Herzog, D. M. Eggleston, and E. G. Thomsen. (59—A-131)
348 New Developments in the Theory of the Metal-Cutting Process, Part I, by P. Albrecht. (59—A-243)
359 Structural Weight Approximation for a Bell-Nozzle Divergent Section, by G. D. Brewer and E. Levin. (59—A-69)
363 Optimum Tolerances of Sheet Materials for Flight Vehicles, by G. A. Hoffman. (59—A-70)
369 Mechanical Vibration Filters With Nonlinear Characteristics, by W. J. Worley. (59—A-42)
377 Refinement of Finite Difference Calculations in Kinematic Analysis, by B. W. Shaffer and I. Krause. (59—A-53)
382 The Measurement of Very Low Frictional Torques in Rotating Equipment, by M. Zaid and I. S. Tolins. (59—A-43)
387 Design by Quantitative Factor of Safety, by Hsuan-Loh Su. (59—A-48)
393 Study of Critical Velocity of Stick-Slip Sliding, by B. R. Singh. (59—A-146)
399 Inertial Effects in a Multiple-Ball Transmission, by W. S. Rouverol. (59—A-14)
407 Some Applications of the Cycloid in Machine Design, by E. P. Pollitt. (59—A-134)
415 A Discussion of the Vibration Characteristics of a Simple Mechanical Connection, by Arthur Sorensen, Jr. (59—A-41)
423 Deformation and Moments in Elastically Restrained Circular Plates Under Arbitrary Load or Linear Thermal Gradient, by M. Zaid and M. Forray. (59—A-39)
439 Dimensionless Parameters for Helical Compression Springs, by R. J. Erisman. (59—A-30)
444 Errata on previously published paper by R. C. Brewer.

TRANSACTIONS OF THE ASME Series E

Journal of
APPLIED MECHANICS
Volume 82 • Series E • No. 4

CONTENTS FOR DECEMBER, 1960

TECHNICAL PAPERS

603 Two-Dimensional Gas Jets, M. J. Cohen. (60—APM-27)
609 On the Compressibility Effects of the Lubricant for Two-Dimensional Slider Bearings, K. T. Yen. (60—WA-29)
613 Heat Transfer and Sublimation at a Stagnation Point in Potential Flow, W. W. Short. (60—WA-20)
617 Transient Heat Conduction in a Rod of Finite Length With Variable Thermal Properties, W. H. Chu and H. N. Abramson. (60—WA-25)
623 Transient Conduction in Coaxial Cylinders With Relative Motion and Heat Generation, V. S. Arpaci. (60—APM-24)
629 Thermal Stresses in an Elastic, Work-Hardening Sphere, Chintsun Hwang. (60—APMW-8)
635 Thermal Stresses Due to Disturbance of Uniform Heat Flow by an Insulated Ovaloid Hole, A. L. Florence and J. N. Goodier. (60—APMW-6)
640 Sinusoidal Excitation of a System With Bilinear Hysteresis, T. K. Caughey. (60—APM-8)
644 Forced Oscillations of a Semi-Infinite Rod Exhibiting Weak Bilinear Hysteresis, T. K. Caughey. (60—WA-28)
649 Random Excitation of a System With Bilinear Hysteresis, T. K. Caughey. (60—WA-27)
653 Vibrations of Elastic Sandwich Cylindrical Shells, Yi-Yuan Yu. (60—WA-21)
663 Free, Transverse Vibrations of a Solid Elastic Mass in an Infinitely Long, Rigid, Circular-Cylindrical Tank, J. H. Baltrukonis. (60—APMW-12)
669 Free Vibration of Continuous Skin-Stringer Panels, Y. K. Lin.
677 On a Class of Nonlinear Axisymmetric Plate Problems, F. Essenburg. (60—APMW-7)
681 Flexural Stress Waves in an Infinite Elastic Plate Due to a Suddenly Applied Concentrated Transverse Load, Julius Miklowitz. (60—APMW-11)
690 Propagation of Axisymmetric Waves in an Unlimited Elastic Shell, A. Kalnins and P. M. Naghdi. (60—WA-22)
696 Plastic Analysis of Circular Conical Shells, P. G. Hodge, Jr. (60—APM-31)
701 The Elastic Half Plane Subjected to Surface Tractions With Random Magnitude or Separation, A. C. Eringen and J. W. Dunkin. (60—APMW-10)
710 On the Response of an Elastic Half-Space to a Moving Blast Wave, J. W. Miles. (60—APMW-9)
717 The Penetration of Hard-Steel Spheres Into Plane Metal Surfaces, Werner Goldsmith and Peter T. Lyman. (60—WA-15)
726 Stress Distribution Analyzed in Bispherical Co-Ordinates, T. P. Mitchell and J. A. Weese. (60—APMW-4)

DESIGN DATA AND METHODS

733 Elastic-Plastic Bending of Curved Bars of Constant and Variable Thickness, H. D. Conway

M. L. WALKER, JR.[1]
E. T. KIRKPATRICK[2]
W. T. ROULEAU[3]

Viscous Dispersion in Water Hammer

When a column of fluid moving with uniform velocity is instantaneously stopped at the downstream end a pressure wave is propagated upstream. In an inviscid fluid the wave is a step discontinuity, and the pressure so calculated serves as an easily obtained upper bound for all practical "water-hammer" problems, the exact solution of which may be either difficult or impossible to obtain. This paper describes an analysis of viscous dispersion in relation to the upper bound. The conclusion is reached that in problems of practical interest the bound is not significantly changed by the dispersive effects of viscosity.

Introduction

STUDIES HAVE BEEN MADE of wall shear in water-hammer problems, and techniques have been devised which account for the resulting pressure drop [1, 2].[4] But comparatively little consideration has been given to the viscous effects which are related to velocity gradients in the direction of flow. As Lagerstrom, Cole, and Trilling [3] have pointed out, these effects are dispersive, rather than dissipative as in wall shear; disturbances are instantaneously propagated through the fluid, and steep wave fronts are "smoothed out."

In all practical water-hammer problems the exact solution may be difficult or impossible to obtain because of the combined effects of a complicated mode of valve closure, conduit elasticity, and wall friction. In these problems an easily obtained upper bound on pressure is found by assuming instantaneous valve closure, an inviscid fluid, and a rigid conduit. It may be obtained from the Joukowsky analysis [4] by letting the modulus of elasticity of the pipe approach infinity. In terms of the dimensionless pressure, $\frac{p - p_0}{U\sqrt{\beta\rho}}$, the value of this upper bound is unity. The purpose of this paper is to determine whether or not inclusion of viscous dispersion leads to a more conservative upper bound.

Lagerstrom, Cole, and Trilling have investigated the velocity distribution across one-dimensional longitudinal waves propagated in a viscous fluid. They have obtained asymptotic solutions for small time and large time for the problem in which one end of an initially motionless column of fluid is instantaneously accelerated to a constant velocity by a piston. This problem, of course, may be easily transformed by a change of co-ordinates to that of a moving column of fluid which is instantaneously stopped at one end. However, they do not have a solution for pressure. In this paper an expression for the pressure distribution is developed, in the form of an infinite series valid for all time.

Analysis

As a model for this study a compressible liquid is considered to

[1] Instructor, Mechanical Engineering Department, Howard University, Washington, D. C.; Graduate Student, Department of Mechanical Engineering, Carnegie Institute of Technology, Pittsburgh, Pa.
[2] Professor and Chairman, Department of Mechanical Engineering, University of Toledo, Toledo, Ohio. Assoc. Mem. ASME.
[3] Assistant Professor, Department of Mechanical Engineering, Carnegie Institute of Technology, Pittsburgh, Pa. Assoc. Mem. ASME.
[4] Numbers in brackets designate References at end of paper.
Contributed by the Water Hammer Subcommittee of the Hydraulic Division and presented at the Annual Meeting, Atlantic City, N. J., November 29–December 4, 1959, of THE AMERICAN SOCIETY OF MECHANICAL ENGINEERS.
NOTE: Statements and opinions advanced in papers are to be understood as individual expressions of their authors and not those of the Society. Manuscript received at ASME Headquarters, October 22, 1958. Paper No. 59—A-12.

Nomenclature

A_1, A_2 = constants
a, a_n = $\frac{\gamma^2 + \gamma\sqrt{\gamma^2 - 4}}{2}$, Equation (34)
B_1, B_2 = constants
b, b_n = $\frac{-\gamma^2 + \gamma\sqrt{\gamma^2 - 4}}{2}$, Equation (35)
c = $\sqrt{\beta/\rho}$, velocity of wave propagation in the fluid
$D_1, D_2, D_3, D_{3n}, D_4, D_{4n}, D_n$ = constants
k = index; assumes the values of all positive odd integers
L' = length of conduit
L = $\frac{3}{4}\frac{c}{\nu}L'$, dimensionless length of conduit
n = index; assumes the value of all positive odd integers
p = pressure
p_0 = initial pressure in conduit
s = condensation, Equation (8)
t' = time, measured from valve closure
t = $\frac{3}{4}\frac{c^2}{\nu}t'$, dimensionless time
u = velocity
U = initial velocity of fluid
x' = distance, measured positively upstream from valve
x = $\frac{3}{4}\frac{c}{\nu}x'$, dimensionless distance
β = bulk compression modulus
γ = $\frac{n\pi}{2L}$
δ = width of wave front
η' = displacement of a fluid particle from its initial position
η = $\frac{3}{4}\frac{c}{\nu}\eta'$, dimensionless displacement of a fluid particle
ν = kinematic viscosity
Ξ = function of x
ρ = density of fluid
ρ_0 = initial density of fluid
T = function of t

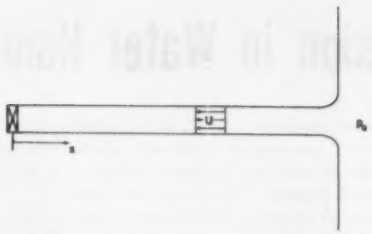

Fig. 1 Physical model and co-ordinate system

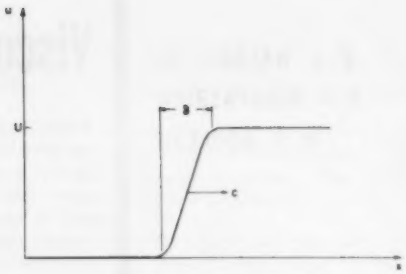

Fig. 2 Wave front in fluid

be flowing without wall shear in a rigid conduit of finite length at a constant and uniform velocity. At the downstream end of the conduit a valve is instantaneously closed, while at the upstream end the pressure remains at a constant value, Fig. 1. It is desired to find the pressure distribution as a function of time when the dispersive effects of viscosity are included.

There are three dependent variables, the pressure p, the density ρ, and the velocity u. These are related by the following three simultaneous differential equations:

(a) The Navier-Stokes equation for one-dimensional compressible flow [5],

$$\frac{\partial u}{\partial t'} + u\,\frac{\partial u}{\partial x'} = -\frac{1}{\rho}\,\frac{\partial p}{\partial x'} + \frac{4}{3}\,\nu\,\frac{\partial^2 u}{\partial x'^2}; \tag{1}$$

(b) the continuity equation [5],

$$\frac{\partial \rho}{\partial t'} + \frac{\partial(\rho u)}{\partial x'} = 0; \tag{2}$$

and

(c) the equation of state [6],

$$\frac{d\rho}{\rho} = \frac{dp}{\beta}. \tag{3}$$

As it stands, equation (1) is nonlinear because of the convective acceleration term, $u\partial u/\partial x'$. Fortunately, this term is negligible when compared with the local acceleration term, $\partial u/\partial t'$, which can be shown by the following argument: When the valve closes, successive layers of fluid are decelerated from the initial stream velocity U to zero velocity. Consider the interval of transition to be of length δ, Fig. 2. Now

$$\frac{\partial u}{\partial x'} \approx \frac{U}{\delta} \tag{4}$$

and

$$\frac{\partial u}{\partial t'} \approx \frac{U}{\frac{\delta}{c}}, \tag{5}$$

so that

$$\frac{u\,\dfrac{\partial u}{\partial x'}}{\dfrac{\partial u}{\partial t'}} \approx \frac{U}{c}. \tag{6}$$

A typical value for U is 50 ft/sec, whereas c is about 5000 ft/sec, which makes the magnitude of the convective acceleration one-one hundredth of the local acceleration. The Navier-Stokes equation (1) thus reduces to the linear form

$$\frac{\partial u}{\partial t'} = -\frac{1}{\rho}\,\frac{\partial p}{\partial x'} + \frac{4}{3}\,\nu\,\frac{\partial^2 u}{\partial x'^2}. \tag{7}$$

Since the bulk compression modulus β for liquids is very large, the variations of density are small. Employing the condensation s, where $s \ll 1$, the density can be expressed by

$$\rho = \rho_0(1 + s), \tag{8}$$

where ρ_0 is the initial density of the liquid. The continuity equation (2) and the equation of state (3) become, respectively:

$$\frac{\partial s}{\partial t'} + \frac{\partial u}{\partial x'} = 0, \tag{9}$$

$$ds = \frac{dp}{\beta}. \tag{10}$$

Substituting equation (10) into equation (9) gives

$$\frac{1}{\beta}\,\frac{\partial p}{\partial t'} + \frac{\partial u}{\partial x'} = 0. \tag{11}$$

If η' is the displacement of a fluid particle from its initial position, then

$$u = \frac{\partial \eta'}{\partial t'}. \tag{12}$$

Using equation (12), equation (11) becomes

$$\frac{1}{\beta}\,\frac{\partial p}{\partial t'} + \frac{\partial^2 \eta'}{\partial x' \partial t'} = 0. \tag{13}$$

Integrating equation (13) with respect to time gives

$$p(x', t') - p(x', 0) = -\beta\left[\frac{\partial \eta'}{\partial x'}(x', t') - \frac{\partial \eta'}{\partial x'}(x', 0)\right]. \tag{14}$$

Now $p(x', 0) = p_0$, the initial pressure in the conduit, which is constant and equal to the pressure at the open end. Also, $\partial\eta'/\partial x'(x', 0) = 0$ for $0 < x' \leq L'$; hence

$$p - p_0 = -\beta\,\frac{\partial \eta'}{\partial x'}. \tag{15}$$

Substituting equation (12) into equation (7) yields

$$\frac{\partial^2 \eta'}{\partial t'^2} = -\frac{1}{\rho}\,\frac{\partial p}{\partial x'} + \frac{4}{3}\,\nu\,\frac{\partial^3 \eta'}{\partial x'^2 \partial t'}. \tag{16}$$

When equation (15) is differentiated with respect to x' and substituted into equation (16) the result is

$$\frac{\partial^2 \eta'}{\partial t'^2} = \frac{\beta}{\rho}\,\frac{\partial^2 \eta'}{\partial x'^2} + \frac{4}{3}\,\nu\,\frac{\partial^3 \eta'}{\partial x'^2 \partial t'}. \tag{17}$$

It is convenient to introduce the following variables into equation (17):

$$c^2 = \frac{\beta}{\rho}, \tag{18}$$

$$t = \frac{3}{4}\frac{c^2}{\nu}t', \tag{19}$$

$$x = \frac{3}{4}\frac{c}{\nu}x', \tag{20}$$

and

$$\eta = \frac{3}{4}\frac{c}{\nu}\eta'. \tag{21}$$

Equation (17) becomes

$$\frac{\partial^2\eta}{\partial t^2} = \frac{\partial^2\eta}{\partial x^2} + \frac{\partial^3\eta}{\partial x^2\partial t}. \tag{22}$$

The solution of equation (22) must satisfy the following boundary and initial conditions:

$$\eta(0, t) = 0, \quad t \geq 0 \tag{23}$$

$$\frac{\partial\eta}{\partial x}(L, t) = 0, \quad t \geq 0 \tag{24}$$

$$\frac{\partial\eta}{\partial x}(x, 0) = 0, \quad 0 < x \leq L \tag{25}$$

$$\frac{\partial\eta}{\partial t}(x, 0) = -\frac{U}{c}, \quad 0 < x \leq L \tag{26}$$

Assuming a product solution for equation (22) of the form

$$\eta = \Xi(x)\mathrm{T}(t), \tag{27}$$

where Ξ is a function of x alone, and T is a function of t alone, gives

$$\Xi\mathrm{T}' = \Xi''\mathrm{T} + \Xi''\mathrm{T}' \tag{28}$$

which leads to

$$\frac{\Xi''}{\Xi} = \frac{\mathrm{T}''}{\mathrm{T} + \mathrm{T}'} = -\gamma^2, \tag{29}$$

where γ is a constant.

Thus, two total differential equations for the functions Ξ and T are obtained:

$$\Xi'' + \gamma^2\Xi = 0, \tag{30}$$

$$\mathrm{T}'' + \gamma^2\mathrm{T}' + \gamma^2\mathrm{T} = 0. \tag{31}$$

These have the solutions

$$\Xi = A_1\cos\gamma x + A_2\sin\gamma x, \tag{32}$$

$$\mathrm{T} = B_1e^{-at} + B_2e^{bt}, \tag{33}$$

where

$$a = \frac{\gamma^2 + \gamma\sqrt{\gamma^2 - 4}}{2} \tag{34}$$

$$b = \frac{-\gamma^2 + \gamma\sqrt{\gamma^2 - 4}}{2}. \tag{35}$$

Hence,

$$\eta = D_1e^{-at}\cos\gamma x + D_2e^{bt}\cos\gamma x + D_3e^{-at}\sin\gamma x + D_4e^{bt}\sin\gamma x. \tag{36}$$

Boundary condition (23) yields

$$0 = D_1e^{-at} + D_2e^{bt}. \tag{37}$$

Thus, $D_1 = D_2 = 0$.

Boundary condition (24) gives

$$0 = (D_3e^{-at} + D_4e^{bt})\gamma\cos\gamma L, \tag{38}$$

whence

$$\gamma L = \frac{n\pi}{2}, \tag{39}$$

where $n = 1, 3, 5, \ldots$.

Therefore,

$$\eta = \sum_{n=1,3,5,\ldots}^{\infty}(D_{3n}e^{-a_nt} + D_{4n}e^{b_nt})\sin\frac{n\pi x}{2L}. \tag{40}$$

Initial condition (25) gives

$$0 = \sum_{n=1,3,5,\ldots}^{\infty}(D_{3n} + D_{4n})\frac{n\pi}{2L}\cos\frac{n\pi x}{2L}. \tag{41}$$

Thus $D_{3n} = -D_{4n} = D_n$.

Initial condition (26) gives

$$\frac{U}{c} = \sum_{n=1,3,5,\ldots}^{\infty}D_n(a_n + b_n)\sin\frac{n\pi x}{2L}. \tag{42}$$

Multiplying equation (42) through by $\sin\frac{k\pi x}{2L}$ and integrating between $x = 0$ and $x = L$ gives

$$\frac{U}{c}\int_0^L\sin\frac{k\pi x}{2L}\,dx = D_k(a_k + b_k)\int_0^L\sin^2\frac{k\pi x}{2L}\,dx, \tag{43}$$

since all terms vanish except those in which $n = k$. Thus,

$$D_k = \frac{4U}{k\pi c(a_k + b_k)}, \tag{44}$$

and

$$\eta = \frac{4U}{\pi c}\sum_{n=1,3,5,\ldots}^{\infty}\frac{(e^{-a_nt} - e^{b_nt})}{n(a_n + b_n)}\sin\frac{n\pi x}{2L}. \tag{45}$$

Equations (34) and (35) are utilized to give

$$\frac{e^{-a_nt} - e^{b_nt}}{a_n + b_n} = e^{-\frac{\gamma^2}{2}t}\left[\frac{e^{-\frac{\gamma}{2}\sqrt{\gamma^2-4}\,t} - e^{\frac{\gamma}{2}\sqrt{\gamma^2-4}\,t}}{\gamma\sqrt{\gamma^2 - 4}}\right]. \tag{46}$$

For $\gamma > 2$, i.e., $n > 4L/\pi$,

$$\frac{e^{-\frac{\gamma}{2}\sqrt{\gamma^2-4}\,t} - e^{\frac{\gamma}{2}\sqrt{\gamma^2-4}\,t}}{\gamma\sqrt{\gamma^2 - 4}} = -\frac{2\sinh\frac{\gamma}{2}\sqrt{\gamma^2 - 4}\,t}{\gamma\sqrt{\gamma^2 - 4}}. \tag{47}$$

For $\gamma < 2$, i.e., $n < 4L/\pi$,

$$\frac{e^{-\frac{\gamma}{2}\sqrt{\gamma^2-4}\,t} - e^{\frac{\gamma}{2}\sqrt{\gamma^2-4}\,t}}{\gamma\sqrt{\gamma^2 - 4}} = -\frac{2\sin\frac{\gamma}{2}\sqrt{4 - \gamma^2}\,t}{\gamma\sqrt{4 - \gamma^2}}. \tag{48}$$

Thus, the displacement η is given by

$$\eta = -\frac{4U}{\pi c}\left[\sum_{n=1,3,5,\ldots}^{n<\frac{4L}{\pi}} \frac{e^{-\frac{1}{2}\left(\frac{n\pi}{2L}\right)^2 t}\sin\frac{1}{2}\left(\frac{n\pi}{2L}\right)\sqrt{4-\left(\frac{n\pi}{2L}\right)^2}\,t\sin\frac{n\pi x}{2L}}{\frac{1}{2}\left(\frac{n\pi}{2L}\right)\sqrt{4-\left(\frac{n\pi}{2L}\right)^2}\,n}\right.$$

$$\left. + \sum_{n>\frac{4L}{\pi}}^{\infty} \frac{e^{-\frac{1}{2}\left(\frac{n\pi}{2L}\right)^2 t}\sinh\frac{1}{2}\left(\frac{n\pi}{2L}\right)\sqrt{\left(\frac{n\pi}{2L}\right)^2-4}\,t\sin\frac{n\pi x}{2L}}{\frac{1}{2}\left(\frac{n\pi}{2L}\right)\sqrt{\left(\frac{n\pi}{2L}\right)^2-4}\,n}\right]. \quad (49)$$

Differentiating equation (49) with respect to x and using the result in equation (15) provides the following expression for the pressure:

$$\frac{p-p_0}{U\sqrt{\beta\rho}} = \frac{2}{L}\left[\sum_{n=1,3,5,\ldots}^{n<\frac{4L}{\pi}} \frac{e^{-\frac{1}{2}\left(\frac{n\pi}{2L}\right)^2 t}\sin\frac{1}{2}\left(\frac{n\pi}{2L}\right)\sqrt{4-\left(\frac{n\pi}{2L}\right)^2}\,t\cos\frac{n\pi x}{2L}}{\frac{1}{2}\left(\frac{n\pi}{2L}\right)\sqrt{4-\left(\frac{n\pi}{2L}\right)^2}}\right.$$

$$\left. + \sum_{n>\frac{4L}{\pi}}^{\infty} \frac{e^{-\frac{1}{2}\left(\frac{n\pi}{2L}\right)^2 t}\sinh\frac{1}{2}\left(\frac{n\pi}{2L}\right)\sqrt{\left(\frac{n\pi}{2L}\right)^2-4}\,t\cos\frac{n\pi x}{2L}}{\frac{1}{2}\left(\frac{n\pi}{2L}\right)\sqrt{\left(\frac{n\pi}{2L}\right)^2-4}}\right]. \quad (50)$$

Results

All of the numerical computations on which the following results and conclusions are based have been carried out by means of an IBM Type 650 Magnetic Drum Data Processing Machine.

The dispersive effect of viscosity is strikingly illustrated by Figs. 3 and 4 in which the pressure distribution at various times after valve closure is shown for $L = \pi/8$. If the fluid were inviscid then there would be a stepwise-discontinuous pressure wave which would move with the velocity c relative to the conduit, as shown in dimensionless form in Fig. 4. Of course, a dimensionless length of $\pi/8$ is infinitesimal when converted to dimensional units and is useful only for illustrative purposes. (The corresponding conduit length for water at 68 deg F is 1.187×10^{-9} ft.) For all lengths of practical importance viscous dispersion serves only to smooth out the discontinuity of a wave front, not to eliminate it entirely.

To answer the question of how viscous dispersion affects pres-

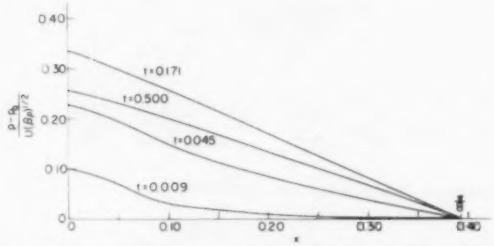

Fig. 3 Pressure distribution for a viscous fluid in a conduit of length $L = \frac{\pi}{8}$

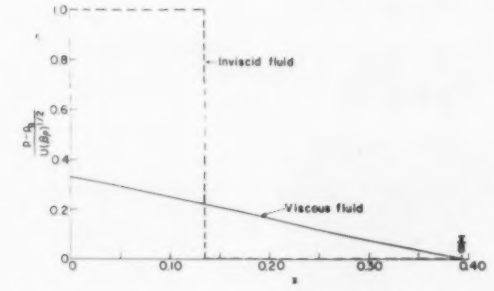

Fig. 4 Pressure distribution in a conduit of length $L = \frac{\pi}{8}$ for inviscid and viscous fluids at time $t = 0.135$

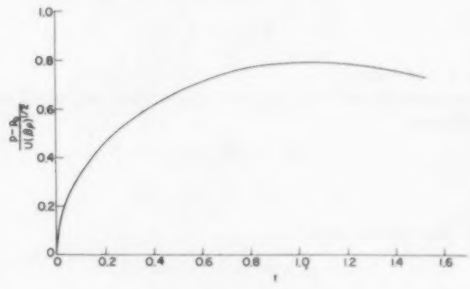

Fig. 5 Pressure variation at $x = 0$ in a conduit of length $L = \frac{\pi}{2}$

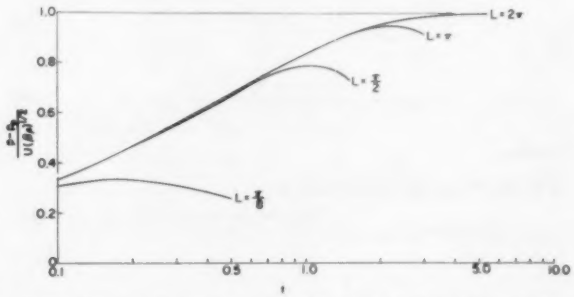

Fig. 6 Pressure variation at $x = 0$ in conduits of various lengths

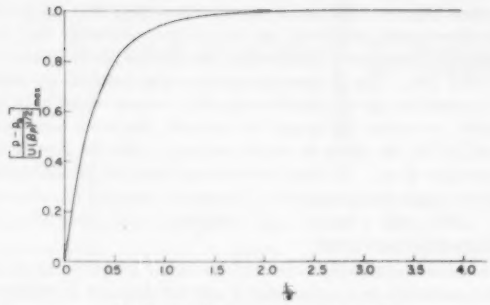

Fig. 7 Maximum pressure at $x = 0$

sure at the valve, the series has been evaluated for $x = 0$ and for various lengths up to and including $7\pi/2$. The pressure-time relations for some of these lengths are shown in Figs. 5 and 6. These figures show that the pressure rises gradually, and not instantaneously, as it would in an inviscid fluid. Also, it is evident that the maximum pressure depends on the length of the conduit, another departure from inviscid behavior.

Fig. 7 shows that, as L increases, the maximum value of $\dfrac{p - p_0}{U\sqrt{\beta\rho}}$ asymptotically increases to unity, which, of course, is the pressure rise calculated on the basis of an inviscid fluid and is the usual upper bound. For L smaller than 1.693π, $\left(\dfrac{p - p_0}{U\sqrt{\beta\rho}}\right)_{max}$ is more than 1 per cent lower than unity; while for larger L, $\left(\dfrac{p - p_0}{U\sqrt{\beta\rho}}\right)_{max}$ is less than 1 per cent lower. Using this 1 per cent as a criterion, it may be said that the consideration of viscous dispersion provides a more conservative upper bound than the inviscid analysis for $L < 1.693\pi$. However, for $L \geq 1.693\pi$, the improvement is negligible.

A typical dimensional length L' which corresponds to $L = 1.693\pi$ may be computed from the values of ν and c for water at 68 deg F: 1.088×10^{-5} ft²/sec and 4800 ft/sec; it is only 1.604×10^{-6} ft. Looking at $L = 1.693\pi$ another way, if the conduit were 25 ft long and c were 4800 ft/sec, then the corresponding kinematic viscosity would be 1.694×10^{4} ft²/sec. Since the kinematic viscosities of most liquids lie between 10^{-3} and 10^{-5} ft²/sec, pressure would be significantly lessened only if kinematic viscosity were on the order of 8 magnitudes greater than ordinarily encountered.

Thus, it may be concluded that in all practical water-hammer problems the consideration of viscous dispersion does not provide a significantly better upper bound than that computed on the assumption of an inviscid fluid.

References

1 J. Parmakian, "Waterhammer Analysis," Prentice-Hall, Inc., New York, N. Y., 1955, pp. 101–105.

2 R. W. Angus, "Waterhammer in Pipes, Including Those Supplied by Centrifugal Pumps: Graphical Treatment," Bulletin 152, University of Toronto Press, Toronto, Canada, 1938.

3 P. A. Lagerstrom, J. D. Cole, and L. Trilling, "Problems in the Theory of Viscous Compressible Fluids," Guggenheim Aeronautical Laboratory, California Institute of Technology, Pasadena, Calif., March, 1949, pp. 44–54.

4 N. Joukowsky, "Waterhammer," translated by Miss O. Simon, *Proceedings of the American Water Works Association*, vol. 24, 1904, pp. 365–368.

5 S. I. Pai, "Viscous Flow Theory: I—Laminar Flow," D. Van Nostrand Company, Inc., Princeton, N. J., 1956, pp. 35–37.

6 J. C. Hunsaker and B. G. Rightmire, "Engineering Applications of Fluid Mechanics," McGraw-Hill Book Company, Inc., New York, N. Y., 1947, p. 45.

DISCUSSION

W. Douglas Baines[5]

There is a real need for a fuller understanding of the fundamentals of water hammer. This paper provides a good introduction to the dispersive effects of viscosity and thereby should lead to other contributions. In particular, the demonstrated linearity of the differential equations should make it possible to analyze other cases.

Although the stated object of the paper is the evaluation of an upper bound for the pressure, many other flow characteristics should be obtainable from the solution because of its generality. In other words, equations (49) and (50) should provide full details of the shape and motions of the pressure wave under all conditions. The thickness of the wave δ (Fig. 2) is of particular interest in reflection problems. The authors do not discuss this further, nor is there any indication of it on the figures showing the solution obtained. The writer suspects that this is because the lengths of pipe which the authors analyze are short compared to this thickness. Thus one should examine solutions for very long pipes. Have these been obtained and, if so, is it possible to give the absolute size of δ for typical cases? Perhaps the solution given is not the best one for such a determination. It might be better to replace equation (24) with the boundary condition for infinitely long pipe. Has this been attempted? If so, is the solution more manageable than the one given?

The writer commends the authors on their analysis and urges them to continue further.

Henry M. Paynter[6]

The authors have here addressed themselves in fine style to the task of investigating *one* of the dispersive mechanisms in water-hammer phenomena. The writer and a colleague have recently discussed[7] a possibly more general situation and outlined a radically simpler and more widely useful method of approximate solution.

Using the methods of the cited reference, the present dispersion problem may be expressed as follows:

$$-\frac{\partial \rho}{\partial x'} \cong \left(\rho D\left[1 - \frac{4\nu}{3c^2} D\right]\right) u = Z(D)\cdot u$$

$$-\frac{\partial u}{\partial x'} \cong \left(\frac{1}{\beta} D\right) p \qquad = Y(D)\cdot p$$

Then in terms of the authors' notation (in so far as possible):

Finite Propagation Operator: $\Gamma = \gamma L' = \dfrac{L'}{c}\sqrt{1 - T_0 D}$

where

$$L_0 = \text{dispersion length} = \frac{4\nu}{3c}$$

and

$$T_0 = \text{dispersion time} = \frac{L_0}{c} = \frac{4\nu}{3c^2}$$

For a sufficiently long (i.e., semi-infinite) pipe, the operator $e^{-\Gamma}$ represents the pressure ratio between the pressure at distance

[5] Department of Mechanical Engineering, University of Toronto, Toronto, Canada.

[6] Associate Professor of Mechanical Engineering, Massachusetts Institute of Technology, Cambridge, Mass. Mem. ASME.

[7] F. D. Ezekiel and H. M. Paynter, "Firmoviscous and Anelastic Properties of Fluids and Their Effects on the Propagation of Compression Waves," ASME Paper No. 59—Hyd-19.

L' and that at the end. The writer has shown that when Γ is expanded in a power series

$$\Gamma(D) = T_m D - \frac{1}{2} T_s^2 D^2 + \dots$$

the time constants have the following significance:

T_m = mean delay

T_s = dispersion time

In the present case

Mean delay:	$T_m = L'/c$
Dispersion time:	$T_s = \sqrt{L'L_0/c}$
Relative dispersion:	$T_s/T_m = \sqrt{L_0/L'}$

These expressions lead to the authors' conclusions very directly, without the necessity of obtaining detailed solutions, yet also afford very rapid approximate solutions as indicated in the reference.

Authors' Closure

The authors wish to thank the discussers for their interesting comments and additional contributions to the subject of the paper.

Professor Baines is correct in stating that equations (49) and (50) contain much more information than has been presented in the form of curves and numerical results. The problem is that of extracting information from the infinite series. These series, equations (49) and (50), are so slowly convergent that the results which have been presented are about the maximum that can reasonably be obtained by summing the series with the relatively slow IBM 650. The original plans were to investigate the shape and thickness of the initial and reflected pressure waves in longer conduits; however, the longer the conduit, the more terms that are needed in the series to retain accuracy, and the greater the computation time. To have carried out these additional investigations would have required an exorbitant amount of computer time. Only with a much faster computer could more information have been presented.

The classical separation-of-variables method used in the paper is not applicable to a semi-infinite conduit because a boundary condition at infinity cannot be applied. For such a conduit an operational method of solution, such as that outlined by Professor Paynter, would appear to be appropriate.

The dispersion that Professor Paynter considers in his paper[7] is unrelated to viscous dispersion and is thus not a more general situation. Viscous dispersion results from the term $(4/3)\nu\partial^2 u/\partial x'^2$ in equation (1), but the dispersion analyzed by Professor Paynter is a consequence of a time-dependence of the bulk compression modulus. In certain situations this latter effect is probably important, as has been noted in the discussion and closure of a recent paper by one of the authors.[8] The more general situation would seem to be when both viscous dispersion and a time-dependent bulk compression modulus are considered.

[8] W. T. Rouleau, "Pressure Surges in Pipelines Carrying Viscous Liquids," published in this issue, pp. 912–920.

CHARLES JAEGER
English Electric Company,
Rugby, England

A Review of Surge-Tank Stability Criteria

The determination of surge-tank stability and the validity of the Thoma formula are currently demanding much attention from hydraulic engineers. The author believes that a useful contribution could now be made toward a better understanding of the problem by a comprehensive review of existing published works and by further comments on known facts and test results.

When Scimemi (Padua) published some critical remarks on the validity of the Stability Theory of Thoma, it was felt that a review of the whole problem of surges was desirable. A general discussion was introduced in 1953 at The Institution of Mechanical Engineers, London, England [24],[1] which brought forth much additional material in the form of further contributions.

The situation with regard to stability theories today is similar, and a review is desirable of the often widely divergent theories, facts, and opinions concerning surge-tank stability.

Theory of Thoma (See Appendix 1)

Thoma writes the dynamic equation of surges and the equation of continuity at the surge-tank junction to the tunnel for the case of a single surge tank. Assuming very small oscillations, the equations can be linearized and a discussion becomes possible. The so-called Routh-Hurwitz criterion leads to the formula (Ref. [40] and Fig. 1)

$$A_s = nA_{Th} = n\,\frac{v_0^2}{2g}\,\frac{LA_T}{Fv_0^2H_0} \qquad (1)$$

where n is the stability factor, and the controversy centers on its value.

Since it was first published, the Theory of Thoma has been extended to all types of tanks and systems of tanks, but it is well understood that the following assumptions on which it is based are not always fulfilled: (a) The turbine governor is governing for constant power,[2] (b) the surge-tank oscillations are small, (c) the turbine efficiency is constant, (d) pressure losses in the pipeline can be neglected, (e) velocity head in the tunnel can be neglected, (f) the governor is highly sensitive and reacts immediately, (g) the power station is isolated and not interconnected with another station.

It is with these assumptions in mind that any criticism must be made.

Criticism of Thoma

Recent criticism of the Formula of Thoma has been based on: (a) Mathematical analysis using Liapunoff's theorem, (b) tests on prototype and model surge tanks.

Surge-Stability Analysis Based on Liapunoff's Theorem [31]. Liapunoff's broad theorem shows that linearization of the equations is permissible near the points of instability and emphatically confirms the Routh-Hurwitz stability criteria. The two theories confirm the fact that unstable conditions may occur and make possible the calculation of these points. It can be suspected that the two approaches must lead finally to the same conclusions.

The Marris analysis [31] shows, like that of many authors before him, that there are two points where unstable conditions are likely to occur. His analysis is carried out in a plane s and $u = ds/dt$ (where $s = Z - Z_0$). The first point where $u = ds/dt = dZ/dt = 0$ and $s = 0$ (origin of co-ordinates) is obviously the same as that examined by Thoma, and Marris easily finds a condition identical to the Thoma condition. (See Appendix 1 for definitions.)

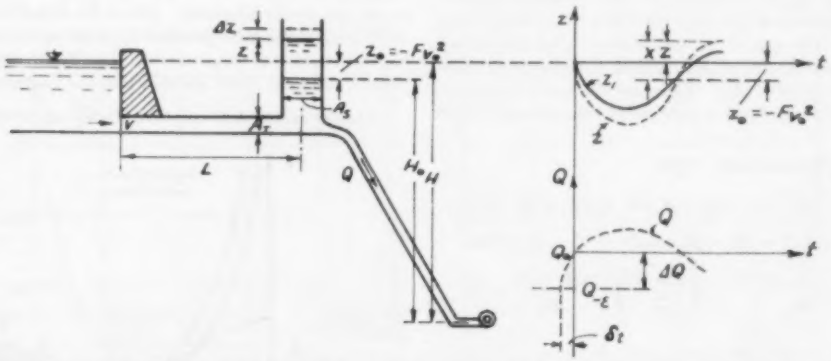

Fig. 1 Stability conditions for a single surge tank when governing for constant power output. $P = \gamma\eta Q(H + Z)$.

An additional condition is then introduced by Marris, who shows that, near the origin $u = 0$, $z = 0$, a surge can be repre-

[1] Numbers in brackets designate References at end of paper.

Contributed by the Hydraulic Division and presented at the Annual Meeting, Atlantic City, N. J., November 29–December 4, 1959, of The American Society of Mechanical Engineers.

Note: Statements and opinions advanced in papers are to be understood as individual expressions of their authors and not those of the Society. Manuscript received at ASME Headquarters, September 21, 1959. Paper No. 59—A-270.

[2] Very recently N. L. Barbarossa (*Proc. ASCE*, Paper HY.4, April, 1959) used a digital computer for problems where "governing with constant power" was assumed. The computed surges showed marked and partly unexplained differences with conventional results. Full gate opening was reached. These findings require further investigation.

sented by a function $u = u(z)$, u being a function of z, on a (z, u) diagram. This function is a spiral and Marris shows that for stability this spiral must lie within a circle having a diameter ρ where ρ can be calculated using the method of Kryloff-Bogolioubboff

$$\rho = 2\left[2\left(\frac{Fv_0^2}{Z_*}\right)^2 - \frac{Fv_0^2}{H_0}\right]^{1/2} \Big/ \left[\frac{3Fv_0^2}{H_0} - 2\left(\frac{Fv_0^2}{Z^*}\right)^2\right]^{1/2}$$

When the Thoma condition is fulfilled,

$$2\left(\frac{Fv_0^2}{Z_*}\right)^2 - \frac{Fv_0^2}{H_0} > 0,$$

and, for such a circle to exist, ρ must be real, hence

$$\frac{3Fv_0^2}{H_0} - 2\left(\frac{Fv_0^2}{Z_*}\right)^2 > 0,$$

giving a new condition

$$\frac{Z_*}{H_0} > 2/3\,\frac{Fv_0^2}{Z_*}.$$

Probable values of Z_*/H_0 are from 0.05 to 0.15 (since higher values are rarely acceptable because of governing conditions), giving $Fv_0^2/Z_* < 0.075$ to 0.025, corresponding to short pressure tunnels with low water velocities—an unlikely design.

In many cases there will be no such circle as shown by the theory and no additional condition for stability. Nevertheless, this additional condition shows that special care should be given to surge systems with relatively short tunnels. It is well known that they cause surges to originate which are slow to die out, and a substantial majoration factor is required which would automatically maintain the spiral curve well inside the stability circle.

The second point of the plane s, $u = ds/dt$ where instability may occur has the co-ordinates

$$u = 0$$

$$s = \alpha H_0 = -H_0 + \frac{Fv_0^2}{2} + \frac{Fv_0^2}{2}\left(1 + 4\,\frac{H_0}{Fv_0^2}\right)^{1/2} \qquad (2)$$

The Liapunoff theorem which shows the existence of such a point of instability is rather involved. The classical approach [25][3] shows the existence of this same point in a much simpler way in a plane (v, z). The axis of the oscillations is the intersection point of the loss curve $-Z = Fv^2$, and of the governing curve $Q(H + Z) = C = Q_0(H + Z_0)$. There are obviously two points of intersection (or, at the limit, a point where the two curves are tangent), Fig. 2.

Combining the two equations yields

$$A_T(H + Z)\sqrt{Z/(-F)} = C = A_T(H + Z_0)\sqrt{Z_0/(-F)}$$

or, with $H = H_0 + Fv_0^2 = H_0 - Z_0$; and $s = Z - Z_0$; then

$$\left(\frac{Z}{Z_0}\right)^{1/2}\frac{(H - Z_0 + Z)}{H_0} = \left(\frac{s + Z_0}{Z_0}\right)^{1/2}\frac{(H_0 + s)}{H_0} = 1$$

or,

$$(s + Z_0)(H_0 + s)^2 = H_0^2 Z_0$$

A first root of this equation is $s = 0$, $Z = Z_0 = -Fv_0^2$ which corresponds to the first solution indicated by Marris ($s = 0$, $ds/dt = u = 0$).

The second solution is the positive root of the equation

$$s^2 + (2H_0 + Z_0)s + H_0^2 + 2Z_0H_0 = 0,$$

which is

$$s = -H_0 + \frac{Fv_0^2}{2} \pm \sqrt{\left(\frac{-Fv_0^2}{H_0}\right)^2 + 4\,\frac{Fv_0^2}{H_0}} \qquad (3)$$

which is identical with the second solution given by Marris.

Direct calculations carried out by the analytical method or with the graphical method have already shown that the second axis of oscillations represents a highly critical position of equilibrium and that drainage of the tank is likely to occur.[4] It is most interesting to read that Marris' theory confirms this danger of drainage, well known to tank designers.

Although no actual design where the oscillations would take place around the second axis of oscillations is known to the writer—such a system would be highly uneconomical—it is excellent to be warned again against such a danger.

A further development of Marris' analysis may be mentioned here. Following some previous work by Paynter, Marris deals with the problem of the stability of large oscillations as opposed to the small oscillations considered by the classical approach. His final formula is

$$\left(\frac{Fv_0^2}{Z_*}\right)^2 = \frac{Fv_0^2}{H_0}\left[\frac{(2 - Fv_0^2/H_0) + \{(2 - Fv_0^2/H_0)^2 + 24Fv_0^2/H_0\}^{1/2}}{8}\right] \qquad (4)$$

whereas Paynter's development yields

$$\frac{Fv_0^2}{H_0} = 2\left[\frac{Fv_0^2}{Z_*}\left(1 - \frac{Fv_0^2}{H_0}\right)\right]^2 \qquad (5)$$

For comparison the two curves ② and ③ are drawn on Fig. 3, together with the curve ① of Thoma (see Appendix 1),

$$\frac{Fv_0^2}{H_0} = 2\left(\frac{Fv_0^2}{Z_*}\right)^2, \quad \text{or} \quad a = 0$$

and the curve ④

$$A_s = \frac{v_0^2}{2g}\,\frac{LA_T}{Fv_0^2H_0}\left(1 + 0.482\,\frac{Z_*}{H_0}\right) \cong A_{Th}\left(1 + 0.5\,\frac{Z_*}{H_0}\right) \qquad (6)$$

developed by the writer in 1943 [21]. Curves ③ and ④ are found to be practically identical. About the same time, J. Frank [15] had checked the same problem by direct graphical calculations of a great number of surge curves. The Frank curve, 1942, and the writer's findings, 1943, are shown in one diagram, Fig. 4.

[4] Charles Jaeger, *Schweizerische Bauzeitung*, 1943.

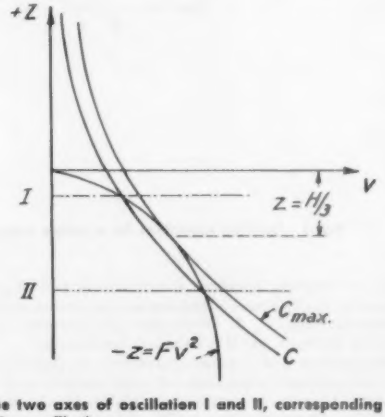

Fig. 2 The two axes of oscillation I and II, corresponding to singular points in Liapunoff's theorem

[3] C. Jaeger, "Engineering Fluid Mechanics," 1956, pp. 234–235, and Fig. 132.

There is, therefore, excellent agreement of the theories developed by Paynter [34], Marris [31], and the writer [21] with the curve of Frank and some results by others. To allow for the danger of large oscillations, the surge-tank area must be enlarged and formula (6) is the simplest and most direct one which can be used.

A final remark must be inserted here. When the surges are large, additional losses occur at the base of the surge shaft where the water is diverted from the pressure tunnel into the shaft, or from the shaft into the pipeline or tunnel. These losses have a stabilizing effect. These were considered by Escande [12, 13] and Gardel [18] in some of their developments.

Marris' work has yielded quite valuable results. In fact, there is nothing in his findings which contradicts the classical results of Thoma and of Calame and Gaden. On the contrary, they are confirmed and several other points are confirmed too.

Test Results. Scimemi's tests, 1947 and 1948, at Pelos, Fadalto, and Partidor showed that these surge tanks produced damped oscillations, even though the stability factors were 0.71, 0.66, and 0.49, respectively. These findings cast some doubts on the validity of Thoma's formula, but they may be explained by investigating the conditions prevailing during the tests.

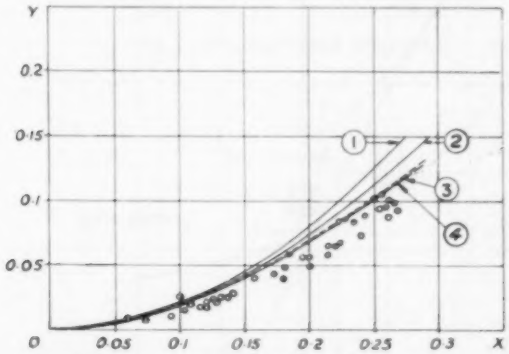

Fig. 3 Conditions for perpetual oscillations of large surges:
1. **Curve of Thoma**
2. **Curve of Marris**
3. **Curve of Paynter**
4. **Curve of Jaeger (1943)**

$x = Fv_0^2/Z_s = F_{r_0}$

$y = Fv_0^2/Z_s \cdot Z_s/H_0 = F_{r_0}/H_{r_0}$

(Diagram taken from Marris' paper, 1958, completed with curve 4, 1943.)

In Thoma's analysis, the efficiency factor η, in the expression for power: $P = \eta Q(H + Z)$, is assumed to be constant. However, Calame and Gaden, in a more advanced paper, have assumed that η varies with P. Where $\partial\eta/\partial P > 0$, the variation of η contributes substantially to the stability of the surges, but where $\partial\eta/\partial P < 0$ (usually for $P > 75$ per cent of the maximum capacity), variation of η causes the surges to be less stable.

The tests carried out by Scimemi were definitely in a region where $\partial\eta/\partial P > 0$, and the surge stability was substantially increased by the variation of efficiency[5] but his papers make no mention of possible variations of η with P and their effect on stability. Fig. 5 shows how Fig. 2 is to be modified when the efficiency is not constant, or when the turbine is provided with a gate limit.

A second factor concerns the governor characteristics. J. Chevalier and M. Hug have carried out most interesting tests on the Cordéac surge tank, showing that, when the surges can be represented by a function

$$s = Me^{-\sigma t} \sin 2\pi t/T,$$

the governor usually follows with a delay ϕ, the guide-vane displacement being given by a function

$$\xi = M'e^{-\sigma t} \sin 2\pi(t + \phi)/T.$$

This delay, estimated to be about 20 sec, causes a marked increase in the surge stability. The two authors think that this fact partly explains the results obtained by Scimemi. In addition, governors do not react to very small variations of turbine discharge.

To contradict Scimemi's conclusions, it is possible to enumerate a series of test results and measurements confirming the validity of the Thoma formula and the theory on which it is based:

1 The Heimbach surge tank showed unstable surges for $n = 0.92$. This marked instability was the starting point of Thoma's research.

2 A surge-tank model at the Ecole Polytechnique de l'Université de Lausanne tested by Gardel and Bonnard in 1954 [24].

[5] See C. Jaeger, *Proceedings, I. Mech. E.*, vol. 168, 1954, pp. 100–101. See also *La Houille Blanche*, December, 1957, p. 902—remark by Ransford.

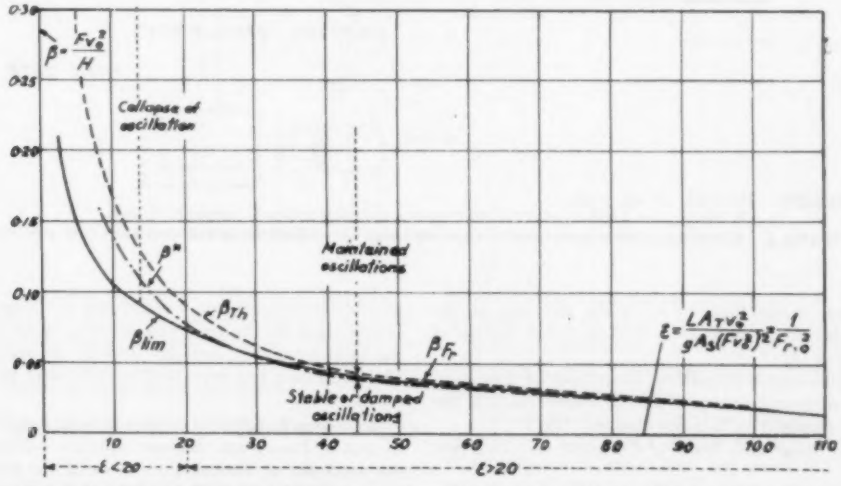

Fig. 4 Stability of surges according to Thoma, Jaeger (β''), and Frank (β_{lim}). Diagram from Jaeger, "Engineering Fluid Mechanics," 1956.

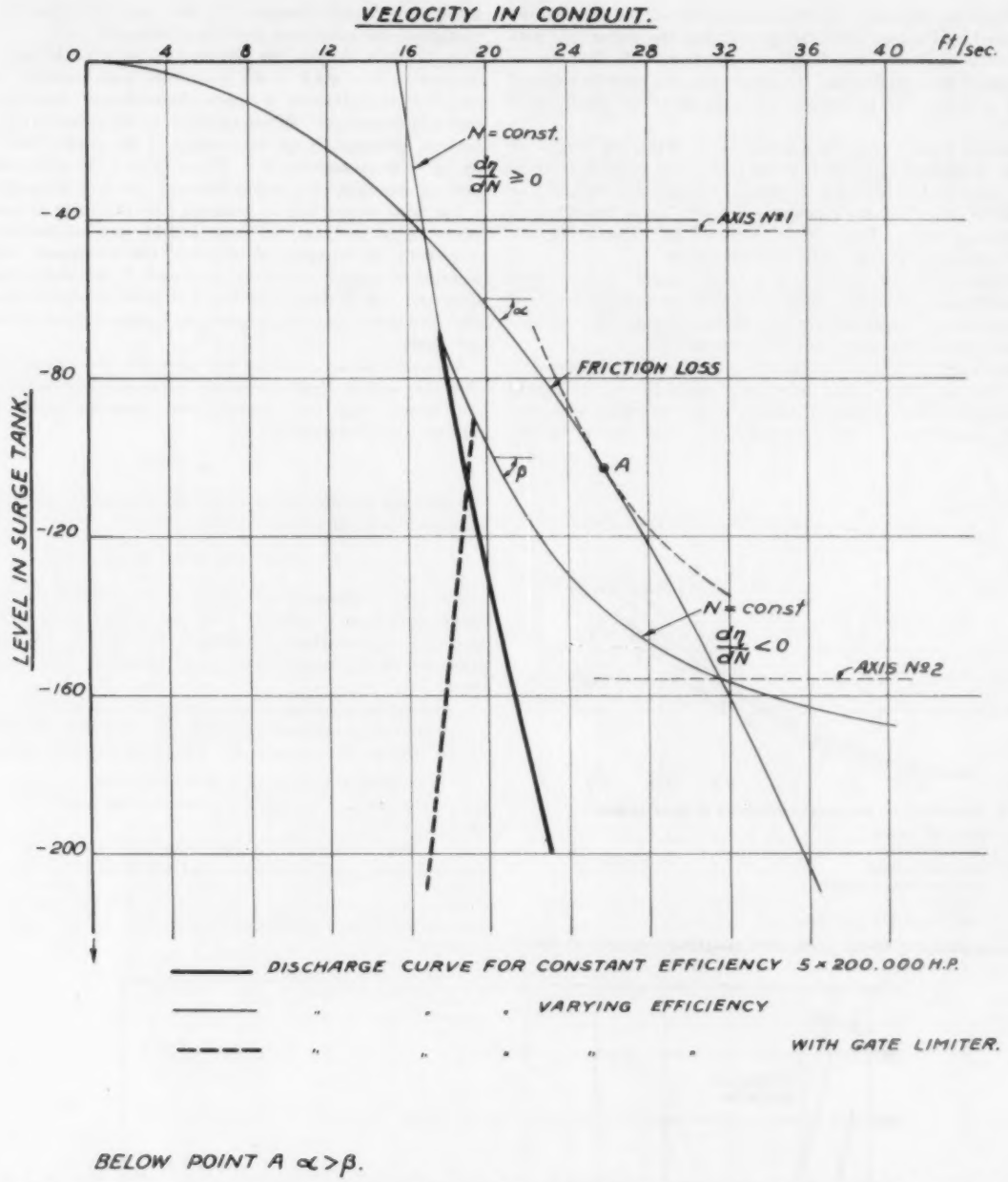

Fig. 5 Modified Fig. 2. Curves for constant power and constant efficiency, varying efficiency and conditions with gate limit, for a large surge tank.

3 A surge-tank model with an electronic governor at the Niagara Falls Laboratory tested by I. McCaig and F. Jonker of Messrs. H. G. Acres [32].

4 Direct step-by-step calculations (analytical or graphical method or by use of digital computer) permit a direct check of the Thoma formula (corrected for large oscillations) [15, 21].

5 The Cordéac surge-tank tests by Chevalier and Hug (see Appendix 2).

Calame and Gaden have shown that any surges are stable or damped whatever the surge-tank area, provided the power station under consideration is connected to a large electrical supply system, and the station's own capacity is less than one third of the total generating capacity directly connected to the system. This argument has been further developed by Evangelisti and others.

According to Ailleret, an electricity generating system similar to that in France can dispense with the necessity of abiding by the condition of Thoma, since most of the French hydropower stations are directly and permanently interconnected with large systems.

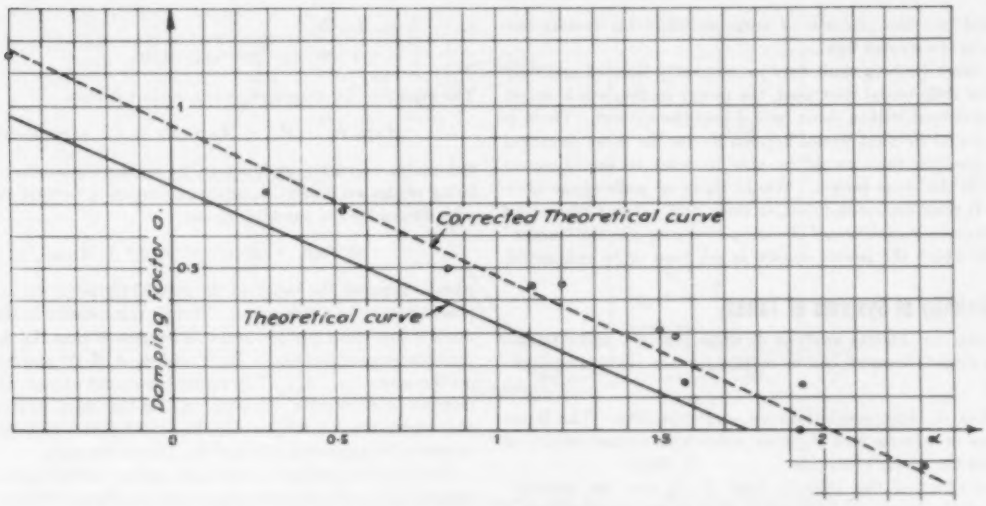

Fig. 6 Damping factor σ versus factor α. Theoretical curves and test results from Chevalier and Hug.

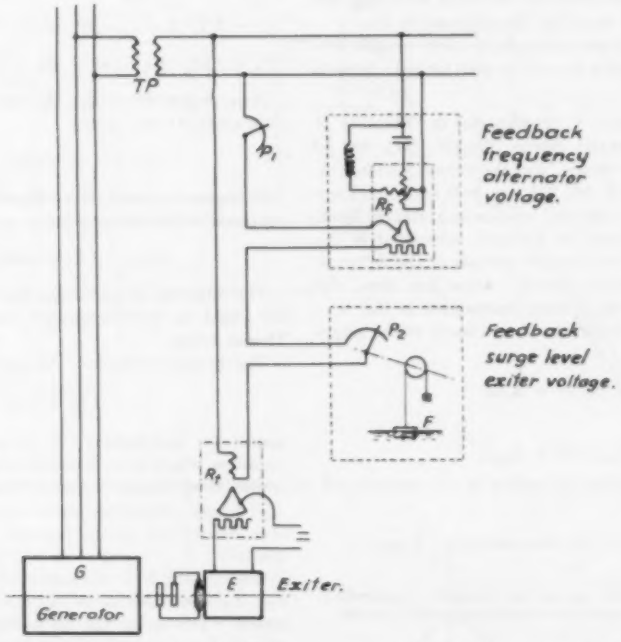

Fig. 7 Diagram showing feedback arrangement used by Cuénod and Gardel at Oelberg (1953). P_1 and P_2 are potentiometers, R_f and R_f are voltage regulators.

Two recently designed French surge tanks at La Rhue (n = 0.25) and Jouques (n = 0.077) take advantage of this approach (see Appendix 3), but "Ailleret" surge tanks do not prove the theory of Thoma to be at fault, they show that under certain conditions, the Thoma formula can be disregarded.

Methods for Improving Stability in "Sub-Thoma" Surge Tanks

It is always possible to get stability by severely limiting the up and down surges. This can be achieved by: (a) Heavily damping or eliminating the governor, (b) introducing restricted orifices in the surge tank, or, (c) proper electric feedbacks.

These conditions are now vastly different from the ones that were started with. The basic Thoma assumption that power is constant no longer applies.

Tests carried out by Cuénod and Gardel at the Oelberg Power Station (see Appendix 4), during which the main tank reservoir of the differential surge tank was closed off, and only the riser was used to give a widely unstable narrow cylindrical tank, showed that stability could be achieved by using electrical feed-

backs, and put the problem of surge stability for factors less than one in the correct light.

If the large Oelberg tank were permanently isolated and only the narrow differential riser used, the power station would inject a varying output with a short period into the system. There is some doubt as to what would happen if—on the same electrical system—another tank would be able to react to forced power surges with the same period. Would there be some surge resonance? It must be stressed that, in their 1927 paper, Calame and Gaden do exclude such forced electric power surges in the "larger" system to which the power station is assumed to be connected.

Surge Stability of Systems of Tanks

Assuming the Thoma analysis of surge stability to be fundamentally sound, research can be carried further along the following lines:

1 Effect of large oscillations on surge stability. The latest researches of Marris and Paynter agree with former results of Frank and the writer's formula.

2 The effect of the velocity head $V^2/2g$ and the influence of losses at the junction of the surge shaft to the pressure tunnel have been exhaustively analyzed by Gardel [18].[6] Similarly, the effect of the variations of η have been thoroughly studied and classical text books give formulas and methods including the effect of $V^2/2g$ and of η and $\partial\eta/\partial P$ in the estimate of A_{Th}.

3 The Thoma analysis has been extended to more complicated surge-tank systems, as they often have to be used for large modern hydropower systems.

The theories developed by O. C. Zienkiewicz in "Stability of Parallel-Branch and Differential Surge Tanks" [41], by L. Escande on "restricted-orifice tanks," and the writer's research on "systems of surge tanks" [21, 26, 27], are well known. They show that, depending on the type and location of the surge tank, its area can be reduced or must be enlarged, compared to the Thoma value, depending on the proper periods of the different interconnected systems. More recently there has been the analysis by L. Sideriades of the system represented in Fig. 8.

The author uses the usual equations of continuity at the surge-tank junction

$$A_{T_1}v_1 = A_{s_1}dz_1/dt + A_{P_1}u_1$$

and

$$A_{T_2}v_2 = A_{s_2}dz_2/dt + A_{P_2}u_2$$

and the dynamic equations

$$\frac{L_1}{g}\frac{dv_1}{dt} + Z_1 + Fv_1^2 = 0 \text{ for pressure tunnel I, and}$$

$$\frac{L_2}{g}\frac{dv_2}{dt} + Z_2 + Fv_2^2 = 0 \text{ for tunnel II.}$$

The equation for constant power output is then

$$A_{P_1}u_1(H_1 + Z_1) + A_{P_2}u_2(H_2 + Z_2) = \text{constant.}$$

Sideriades correctly includes $v^2/2g$ in the equations (they are being neglected here). A further equation is needed and Sideriades writes for the tunnel junction

$$u(A_{P_1}u_1 + A_{P_2}u_2) = A_{P_1}u_1^2 + A_{P_2}u_2^2,$$

which expresses the losses at the pressure-pipe junction and supposes them to be a minimum. There is some doubt in the writer's mind about this equation and it is suggested that the flow at the junction depends on $(h_1 + Z_1)^{1/2}$ and $(h_2 + Z_2)^{1/2}$ and not merely on the areas A_{P_1}, A_{P_2}. The remark does not change the fundamentals of Sideriades' analysis. Using the classical Routh-Hurwitz conditions, formulas can be developed which finally are shown to be a generalization of the Thoma formula.

The following numerical example applies to the Valabres power station which has the following essential characteristics:

$H_{0_1} = 199$ m; $A_{T_1} = 15$ m^2; $A_{P_1} = 3.8$ m$^2 = A_P$; $L_1 = 6592$ m.

$H_{0_2} = 203$ m; $A_{T_2} = 4.52$ m^2; $A_{P_2} = 1.32$ m^2; $L_2 = 1248$ m.

$F_1 = 5.3$; $A_{T_1}V_{1_0} = 16$; $\pi_{1_0} = F_1/L_1A_{T_1} = 4.7 \times 10^{-5}$.

$F_2 = 1.58$; $A_{T_2}V_{2_0} = 4$; $\pi_{2_0} = F_2/L_2A_{T_2} = 0$ or 1.88×10^{-4}.

According to Sideriades, the theory gives for the limiting surge-tank areas A^* the values

$$A_1^* = 1.74 \text{ m}^2 \text{ and } A_2^* = 0.43 \text{ m}^2.$$

It is easy to check the "Thoma areas" for the two systems, supposed to be independent

$$A_{Th_1} = 4.74 \text{ m}^2 \text{ and } A_{Th_2} = 0.89 \text{ m}^2.$$

The "stability-proof" surge-tank areas, according to Sideriades, are found to be substantially smaller than the corresponding Thoma areas.

The designer eventually adopted much larger areas

$$A_{s_1} = 136 \text{ m}^2 \text{ and } A_{s_2} = 6.10 \text{ m}^2,$$

mainly for maintaining the surges within reasonable limits, a condition which often overshadows the Thoma conditions, when applied to medium or high-head power stations.

The very exhaustive study of surge-tank systems, which has been carried out in the last few years, can be summarized as follows:

When there is a possibility of resonance between surges as with the system shown in Fig. 9, the surge-tank areas must be enlarged. This is all the more important when considering the greater danger of resonance when the periods T_1 and T_2 of the systems I and II are similar.

On the contrary, when it is not likely that the surges will enter into resonance as in Fig. 8 by Sideriades, the surge-tank areas can be reasonably reduced. The theoretical investigation of the case shown in Fig. 10 has proved that such an arrangement may require smaller or larger areas depending on the location of tank I.

Finally, the researches by Escande [12, 13] and Zienkiewicz [41] have proved the differential tank and the restricted-orifice tank to be reasonably stable.

[6] Model tests are being carried out at the Hawksley Laboratory, Imperial College, London, England, for checking Gardel's results.

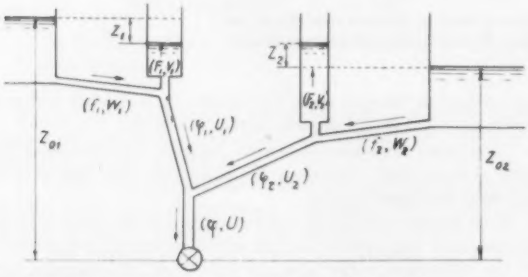

Fig. 8 Stability conditions for two surge tanks located upstream of a turbine with independent tunnels and pressure pipes. General case by Sideriades.

Selection of Value for Stability Factor

The discussion on surge-tank stability finally centers on the stability factor n to be adopted. The stability factor can be

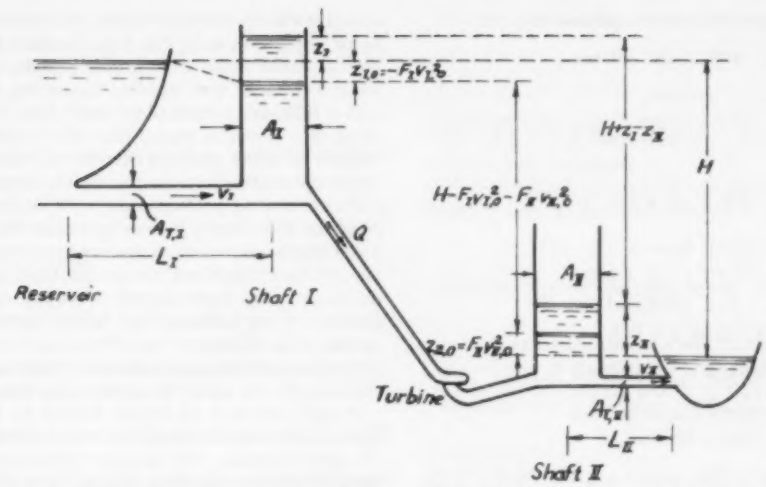

Fig. 9 Stability conditions for two surge tanks located one upstream, the other downstream of a reaction turbine

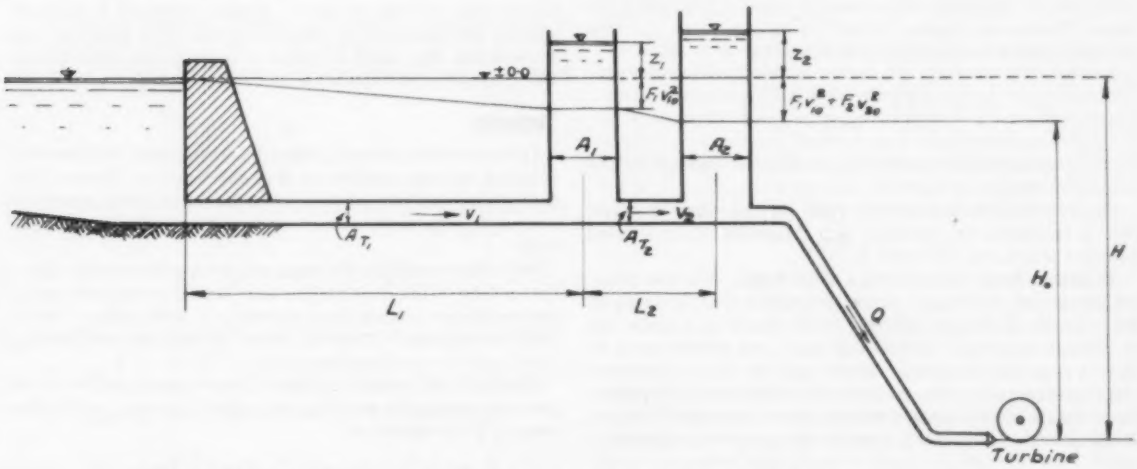

Fig. 10 Stability conditions for two surge tanks located on the upstream side of turbines, on one pressure system

analyzed from two different points of view: (*a*) A value required for reasonable damping of surges, (*b*) a safety factor against unforeseen causes not included in the classical approach.

Determination of the Stability to Cause Reasonable Damping of Surges. For a single tank and the classical Thoma approach to the problem, a damping factor Δ can be defined[7] (Fig. 11) as:

$$\Delta = \frac{Z_{i+T}}{Z_i} = e^{2\pi F_{r,0.1}(1/\sqrt{n}-\sqrt{n})T_r} \tag{7}$$

where (all values being relative)

$$F_{r,0.1} = n^{1/2}F_{r,0} = Fv_0^n/v_0(LA_T/gA_{Th})^{1/2}$$

$$T_r = \left\{1\Big/\left[1 - (F_{r,0.1})^2\,\frac{(1+n)^2}{n}\right]\right\}^{1/2}$$

[7] C. Jaeger, "Engineering Fluid Mechanics," 1956, pp. 253–255 and Formula (28). See also C. Jaeger, *Water Power*, August, 1957, pp. 303–305.

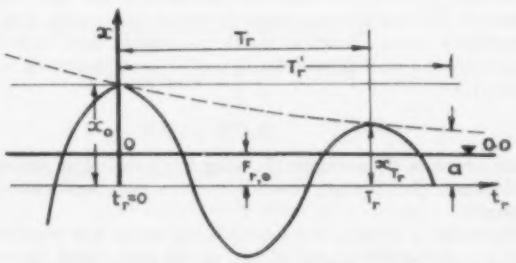

Fig. 11 Definition of damping of oscillations $\Delta = Z_{i+T}/Z_i$

The factor $n = A_s/A_{Th}$ can be determined so that after a time

$$T_r{}^*T = 2\pi T_r{}^* \left(\frac{LA_s}{gA_T}\right)^{1/2} = 1 \text{ hour, say;}$$

the damping of the surges Δ^* should be reduced to

$$\Delta^* = A/Z_{\max} \cong 1/10, \text{ say.}$$

Therefore

$$\Delta^* = A/Z_{\max} = e^{\pi(1/H_{r.0}-2F_{r.0})T_r^*} = e^{2\pi F_{r.0.1}(1/\sqrt{n}-\sqrt{n})T_r^*}$$

or

$$\log_e \Delta^* = 2\pi F_{r.0.1}(1/\sqrt{n} - \sqrt{n})T_r^*$$

or

$$\frac{\log_e \Delta^*}{\log_e \Delta} = \frac{T_r^*}{T_r} = \frac{1 \text{ hour}}{2\pi T_r (LA_s/gA_T)^{1/2}}$$

Let $T' = 2\pi(LA_{Th}/gA_T)^{1/2}$ be now introduced as the unit of time instead of $T = 2\pi(LA_s/gA_T)^{1/2}$.

A new relative value $T_r^{**} = T^*\sqrt{n}$ (longer than T_r^* if $n > 1$, as the unit time is now shorter) can be defined.

Introducing this new unit, a formula

$$\log_e \Delta^* = 2\pi F_{r.0.1}(1/\sqrt{n} - \sqrt{n})T_r^{**}/\sqrt{n}$$

or

$$\log_e \Delta^* = 2\pi F_{r.0.1}(1/n - 1)T_r^{**}$$

shows that all values can be expressed as implicit functions of the known Thoma area, instead of the still unknown area A_s. The stability factor n can now readily be calculated as

$$n = 1 \Big/ \left(1 + \frac{\log \Delta^*}{2\pi F_{r.0.1} T_r^{**}}\right)$$

and a damping Δ after a period T_r (or Δ^* after a period T_r^*) of the oscillations can be imposed.

The theory can be expanded to meet the case where stabilization is improved by feedback (see Appendix 4) or delayed governor action (see Appendix 2).

The Stability Factor Considered as a Safety Factor. The two previous paragraphs were based on the assumption that, knowing all the constants of the governor and the feedback[8] α, s and n can be calculated and the correct surge-tank area chosen so as to cause a prescribed damping. In the past the factor n has been long considered as a safety factor to be chosen in order to protect the hydraulic system against unforeseen or unthought-of causes of disturbance. Is it now possible to dispose of this attitude of mind?

There is still something unsatisfactory in the approach of most of the specialists who have dealt with the problem. All authors start their theories from the basic assumption that one brisk change in the load demand occurs on the electric system, which otherwise is stable. Nowhere has the assumption been made of a load demand varying periodically and a forced governing law of the type

$$\eta Q H_n^{\alpha} = P \sin(2\pi t/T_e + \delta)$$

being forced on the governor (T_e being the period of an electric load surge). Is there any reason for such a more sophisticated approach?

The study of systems of surge tanks has shown how sensitive they are on possible resonance but, on the other hand, figures shown by Sideriades and the author [26, 27][9] for systems where danger of resonance is not obvious prove that the Thoma areas can be reduced.

Typical of systems sensitive to resonance are those represented in Fig. 9 where majoration factors on the Thoma area have to be introduced, or in Fig. 8 as described by Sideriades where the two tanks would have similar periods, and also the system where two tanks with stability factors less than one (say, n = 0.25 to 0.70) and periods of the same order are linked by an electrical tie. It can be argued that such a system of two tanks is unlikely to be designed and that the two stations would be interconnected to other stations, thereby stabilizing the power output.

People dealing professionally with water-hammer resonance problems may wonder if these optimistic views are wise. When water hammer is concerned, systems have a curious habit of selecting just that upper and unexpected harmonic which will cause disaster.[10] The slower period of surges, as against the short period of water hammer, may protect tanks and tank systems against surge resonance, but this has not been proved.

The last possible cause for trouble which should be investigated concerns electric surges in transmission lines.

A recent article in *La Houille Blanche* by Eguiasaroff [11] describes scale models of major electrical networks with hydroelectric power stations. The purpose of this study is to check water-hammer effects on the whole system. In several cases, the turbine runner and the pressure pipeline are materially represented to scale and connected to an electrically analogous model of the new power system. The model turbine is calculated to represent all rotating masses, and the pipeline is distorted in order to bring elastic-wave velocities to scale. Similar models of hydropower stations with surge tanks connected to networks with very long transmission lines could be tested in order to determine if there is any danger of unbalance and of surge resonance.

Summary

Recent works by several authors have confirmed the theoretical approach to surge stability as first developed by Thoma. The theory has been extended to a number of different types and systems of surge tanks. Large surge oscillations have been dealt with.

Research on stability problems now reaches the second stage—the validity of the basic assumptions has to be checked against test results on existing surge systems. A more critical view of these assumptions is taken by several authors and tests have already yielded valuable information.

Based on our present knowledge, some recommendations are given concerning the so-called safe "stability factor" and further research is recommended.

APPENDIX 1

The Theory of Thoma

Referring to Fig. 1, the definitions are as follows:

L = length of tunnel
H = gross head
$\pm Fv^2$ = head losses in tunnel ($Z_0 = -Fv_0^2$)
H_0 = net head = $H - Fv_0^2$
A_T = area of cross section of tunnel
A_s = horizontal area of cross section of surge tank
Q = instantaneous flow through turbines
Q_0 = steady flow through turbines
v = velocity of instantaneous flow in tunnel = $\dfrac{Q}{A_T}$
v_0 = velocity of steady flow in tunnel = $\dfrac{Q_0}{A_T}$
u = vertical velocity of flow in surge tank = dZ/dt (positive direction = upward)

[8] See Appendix 2.

[9] See also C. Jaeger, TRANS. ASME, vol. 80, 1958, pp. 1574–1584, Fig. 8; and *Water Power*, vol. 9, July, 1957, p. 257, Fig. 5.

[10] C. Jaeger, "Engineering Fluid Mechanics," 1956, pp. 318–323, particularly Fig. 188 where the eleventh harmonic was involved. See also *Civil Engineering*, London, February to May, 1948.

Z = water level in surge tank above reservoir level
Z_* = maximum surge (neglecting friction) = $v_0\sqrt{LA_T/gA_s}$
γ = specific weight of water
η = turbine efficiency

The basic equations to be used are:

The dynamic equation (water assumed to be incompressible)

$$\frac{L}{g}\frac{dv}{dt} + Z \pm Fv^2 = 0 \tag{8}$$

The equation of continuity

$$Q = vA_T - A_s u = vA_T - A_s\frac{dZ}{dt} \tag{9}$$

To these two equations, the governing equation must be added. When governing with constant power P

$$P = \gamma\eta Q(H + Z) = \gamma\eta_0 Q_0 H_0 = \text{constant} \tag{10}$$

These three equations yield a differential equation of the second order of the type

$$\frac{d^2Z}{dt^2} + \phi(t)\frac{dZ}{dt} + \psi(t)Z = 0 \tag{11}$$

Thoma considered only small oscillations and referred them to the steady flow level $Z_0 = -Fv_0^2$, taking $Z = Z_0 + s$, or $s = Z - Z_0$. For small oscillations (11) becomes a linear equation of the second order

$$\frac{d^2s}{dt^2} + 2a\frac{ds}{dt} + bs = 0,$$

where a and b are constants. The general integral of this equation can be written

$$s = A_0 e^{-at}\sin\left(\frac{2\pi t}{T} - \mu\right)$$

A_0 and μ are constants depending on boundary conditions.

$T = 2\pi\left(\frac{L}{g}\frac{A_S}{A_T}\right)^{1/2}$ is the period of the surge oscillation.

The values of these coefficients a and b can be calculated

$$a = -\pi\left(\frac{Z_*}{H_0} - 2\frac{Fv_0^2}{Z_*}\right) = -\pi\left(\frac{1}{H_{r_0}} - 2F_{r_0}\right)$$

$$b = 4\pi^2\left(1 - 2\frac{Fv_0^2}{H_0}\right) = 4\pi^2\left(1 - 2\frac{F_{r_0}}{H_{r_0}}\right)$$

where $H_{r_0} = H_0/Z_*$ and $F_{r_0} = Fv_0^2/Z_*$ are dimensionless or relative values introduced by Calame and Gaden. They have proved to be very useful in the general treatment of many surge problems.

The discussion of a linear differential equation of the second order is a classical problem, which is a special case of the more general theory worked out by Routh and Hurwitz for linear differential equations of higher order.

It is known that for $a^2 < b$ the oscillations are periodic. They are damped if

$$a > 0 \quad \text{and} \quad b > 0.$$

The first condition $a > 0$ yields

$$A_s > \frac{v_0^2}{2g}\frac{LA_T}{Fv_0^2H_0} = A_{Th}$$

The second condition $b > 0$ is fulfilled if

$$H_0 > 2Fv_0^2$$

which is always true with practical designs of surge tanks, as the opposite case would lead to uneconomic designs.

For $a^2 > b$ the oscillations are aperiodic and the condition $a > 0$ remains unchanged.

A_{Th} is, then, the Thoma area. The surge-tank area A_s must be larger than A_{Th} for the surges to be damped or

$$A_s = nA_{Th}, \text{ with } n > 1,$$

n being known as the stability factor.

APPENDIX 2

Tests at Cordéac by J. Chevalier and M. Hug

Dimensions of the Cordéac hydraulic system are as follows:

Tunnel length	L	= 4600 m (15,050 ft)
Tunnel diameter	D	= 5.8 m (19.0 ft)
Gross head	H	= 95 m (311 ft)
Maximum discharge	Q_{max}	= 81 m³/sec (2860 cfs)
Number of pipelines		= 2
Pipeline length	L'	= 153 m (502 ft)
Surge-tank area	A_S	= 176 m² (1890 ft²)
Thoma area	A_{Th}	= 136 m² (1460 ft²)
Stability factor	n	= 1.29

During the tests, the Cordéac Power Station was not disconnected from the electrical system, but the power output was maintained constant (ηQH_n = constant) by hand regulation. The damping factor of the surge waves was recorded. The way the tests were carried out makes it clear that variations of efficiency and all pipeline losses were implicitly included in the test results.

For the analysis of the test results, the authors introduce a more general condition than the constant-power condition

$$QH_n^{\alpha} = \text{constant}$$

or

$$\frac{\Delta Q}{Q} + \alpha\frac{\Delta H_n}{H_n} = 0,$$

where H_n = variable net head

The Thoma analysis is based on the assumption that $\alpha = 1$. Where the governor is locked and the discharge passes through gates at constant opening, $\alpha = -0.5$, and the net head is

$$H_n = H + s + \left(\frac{v_1^2}{2g} - \frac{v_1^2}{2g}\right) - \lambda Q^2$$

including velocity heads and pipeline losses.

$$\Delta H_n = \Delta s + \Delta\left(\frac{v_1^2}{2g} - \frac{v_2^2}{2g}\right) - 2\lambda Q\Delta Q$$

$$= \Delta s - 2\lambda' Q\Delta Q$$

If x measures the governor stroke, then

$$\Delta s + A\Delta x = 0 \text{ (where } A = \text{constant)}$$

$$\Delta Q = \frac{\Delta x}{k} + \frac{Q}{2}\frac{\Delta H_n}{H_n}$$

where $1/k$ is the tangent to the curve of x against Q (x is a function of Q).

It can be shown that

$$\alpha = \frac{H_n/Q - Ak/2}{Ak + 2\lambda' Q}$$

The classical analysis of Thoma can be translated in relative values [5]. The linearized equation becomes

$$\frac{d^2s}{dt^2} + 2a\frac{ds}{dt} + bs = 0$$

where

$$a = -\pi\left(\frac{Z_*}{H_0} - 2\frac{Fv_0^2}{Z_*}\right)$$

$$= -\pi\left(\frac{1}{H_{r,0}} - 2F_{r,0}\right) \text{ in relative values}$$

Repeating this analysis for $\alpha \pm 1$, it can be shown that now

$$a = -\pi\left(\frac{\alpha Z_*}{H_0} - 2\frac{Fv_0^2}{Z_*}\right)$$

Hence[11] $$a = \pi\left(2F_{r,0} - \frac{\alpha}{H_{r,0}}\right)$$

which correlates α and a.

For $\alpha < 1$, a is larger than for $\alpha = 1$, and stability is improved.

One of the most interesting points of the two authors' analysis concerns the delay between the surges,

$$s = Me^{-at}\sin\frac{2\pi t}{T}$$

and the governor reaction

$$\xi = M'e^{-at}\sin\frac{2\pi}{T}(t + \phi) \qquad (\phi > 0)$$

It can be shown that this delay ϕ causes a reduction of a to $(a - \delta a)$ where

$$\delta a = \frac{2\phi Q_0}{A_s H_0}\,\frac{(s_1/s_2) + 1}{2}$$

This analysis was proved to be right by the Cordéac tests as shown in Fig. 6, where it can be seen that the theoretical curve obtained for $\phi = 0$ is displaced by δa and stability conditions improved when $\phi > 0$.

The limit value of ΔQ to which the governor reacted was 11 m³/sec.

APPENDIX 3[12]

Surge Tank at La Rhue (Bort-les-Orgues)

Water from the La Rhue river is diverted to the large reservoir of the Bort-les-Orgues dam, passing first through a Kaplan turbine located at the toe of the dam and working under high back pressure. Details are:

Static head	
Maximum	85.0 m (279 ft)
Minimum	22.5 m (73.6 ft)
Maximum discharge	40 m³/sec (1410 cfs)
Pressure losses in tunnel	14.3 m (40.4 ft)
Turbine output	
at H_n = 36.35 m	16,000 m.hp (15,500 hp)
at H_n = 70.0 m	32,000 m.hp (31,000 hp)
Length of pressure tunnel	L = 12,350 m (40,500 ft)
Area of pressure tunnel	A_T = 15.9 m² (170.5 ft²)
Area of surge tank	A_s = 31.0 m² (333.0 ft²)
Stability factor	
for H_n = 36.35[13] m	n = 0.25
for H_n = 70.0[14] m	n = 0.48

Remarks. The turbine gates open very slowly. In the case of large positive surges, water spilling over a spillway is discharged directly into the reservoir. Hence up-surges and down-surges are limited in extent.

The main object is the diversion of the Rhue water into the reservoir. Generation of electricity is of secondary importance and surge stability is not a primary requirement. In addition, La Rhue surge tank is part of a large generating system which makes power surges acceptable.[15]

Surge Tank at Jouques on the Lower Durance

One pressure tunnel feeds three Kaplan turbines, each having its own penstock and surge tank. The general surge-tank arrangement is similar to the surge tank at La Rhue, but the three tanks are interconnected. Details are:

Length of pressure tunnel	2000 m (6560 ft)
Area of pressure tunnel	78 m² (837 ft²)
Area of surge tank	50 m² (each) (536 ft²)
Total pressure losses in system when Q_0 = 250 m³/sec	4.5 m (14.7 ft)
Net head	H_n = 27.5 m (90.0 ft)
Turbine output for H_n = 28.4 m	28,600 P.S. (27,800 hp)
Thoma area	A_{Th} = 666 m² (7100 ft²)
Stability factor	n = 0.077
Stability factor for interconnected tanks	n = 0.23

Remarks. There are no indications as to how this power station will be run. The large station of Serre-Ponçon is under construction on the Upper Durance not far away, and Jouques will be interconnected to the same system.

APPENDIX 4

Tests at Oelberg by Cuénod and Gardel

Details of the Oelberg Power Station of the Entreprises Electriques, Fribourgeoises, are as follows:

Rated turbine capacity	P_0	= 7500 m.hp (7300 hp)
Maximum discharge	Q_0	= 32 m³/sec (1130 cfs)
Maximum head	H	= 20.8 m (68.0 ft)
Length of pressure tunnel	L	= 270 m (884 ft)
Area of pressure tunnel	A_T	= 18.3 m² (196.5 ft²)
Length of penstock	L'	= 47 m (154 ft)
Area of penstock	A_p	= 10.2 m² (109.5 ft²)
Turbine speed		250 rpm
Total flywheel effect	PD^2	= 170 t.m² (WR² = 1,000,000 lb ft²)
Differential surge tank		
Area of reservoir	A_s	= 300 m² (3220 ft²)
Area of riser	A_s'	= 7 m² (75.1 ft²)
	A_{Th}	= 40 m² (429 ft²)

Tests were made on a water resistance (P_0 = 2000 kw) using only the surge-tank riser, the ports to the main-surge-tank reservoir being closed to give a narrow cylindrical tank which was bound to be widely unstable.

A first feedback was introduced by connecting a float located in the surge tank to a potentiometer controlling the generator exciter voltage. Cuénod and Gardel had previously proved that such a feedback has a powerful stabilizing effect on surges. In

[11] Chevalier and Hug, *La Houille Blanche*, December, 1957, pp. 891–892.

[12] According to a letter from Mr. M. Hug, Electricité de France, dated 20th March, 1959.

[13] 119 ft.

[14] 229 ft.

[15] See discussion of the Cordéac paper in *La Houille Blanche*, vol. 13, August/September, 1958.

the particular case of Oelberg, this effect was not sufficient. A second feedback system was introduced by frequency line-voltage regulation, as shown in Fig. 7, to achieve stability.

During a discussion of the Cordéac tests at the Société Hydrotechnique de France [6] the method used by Cuénod and Gardel at Oelberg was mentioned. Tests by Chevalier and Hug, with feedback from the surge-tank level confirm the findings by Cuénod and Gardel. It is well known [25] that unstable surge oscillations are caused only by conditions equal to or similar to those defined by Thoma (constant power output P = constant). If there is no governor and the turbine works with constant gate opening, there is no surge instability.[16] If the governor action is damped by a feedback, better stability is obviously to be expected and it is not unusual for feedback conditions—not maintaining constant power output, and tending to reduce the surges—to cause the surges to be quickly stabilized.

The difficulties encountered at Oelberg during the tests are due to the exceptionally short period T of the surge oscillations (with A_s = 7 m² only)[17] which, in addition, coincides with the proper period of the speed governing. For conditions less stringent than Oelberg the stabilization system is bound to work.

References

1 Ailleret, Société Hydrotechnique de France, Discussion; *La Houille Blanche*, vol. 12, December, 1957, pp. 900–902.

2 F. Arredi, Convegno di Idraulica, Padova, Italy, October 13, 1947.

3 E. Balint, W. R. Flower, and F. Frueh, "Analysis of a Complex Surge-Tank System," *Journal, Institution of Engineers of Australia*, vol. 27, June, 1955.

4 J. Calame and D. Gaden, "Théorie des Chambres d'Equilibre," Paris, France, 1926.

5 J. Calame and D. Gaden, "De la Stabilité des Installations Hydrauliques," *Schweizerische Bauzeitung*, no. 5 and 6, 1927.

6 J. Chevalier and M. Hug, "Tests on the Cordéac Surge Tank, Concerning Thoma's Condition," *La Houille Blanche*, vol. 12, December, 1957.

7 M. Cuénod, "Influence des Phénomènes de Coup de Bélier sur le Réglage de la Vitesse des Turbines Hydrauliques," *La Houille Blanche*, no. 2, 1949.

8 M. Cuénod and A. Gardel, "Stabilisation des Oscillations du Plan d'Eau des Chambres d'Equilibre par Asservissement Temporaire de la Puissance Electrique à la Pression Hydraulique," *Bulletin Technique de la Suisse Romande*, no. 16, August 12, 1950 and July 26, 1952. See also Communication du Laboratoire d'Hydraulique, École Polytechnique de l'Université de Lausanne, 1953.

9 M. Cuénod and A. Gardel, "New Method for Stabilising the Operation of Hydroelectric Power Stations Having Surge Tanks," *La Houille Blanche*, no. 3, June, 1954.

10 M. Cuénod and A. Terrisse, "Le Réglage des Centrales Hydro-Electrique Disposées on Cascade," *Schweizerische Bauzeitung*, vol. 72, July 31, 1954.

11 I. V. Eguiasaroff, "Scale Models of Major Networks With Hydroelectric Power Stations. Study of Water Hammer Effects," *La Houille Blanche*, vol. 13, August/September, 1958, pp. 454–455.

12 L. Escande, "The Stability of Throttled Surge Chambers," *Water Power*, vol. 4, 1952, p. 221, and numerous other publications.

13 L. Escande and R. Houron, "Stability of Two Surge Tanks," *La Houille Blanche*, October, 1953, and *Water Power*, vol. 5, no. 9, 1953, p. 338.

14 G. Evangelisti, "Pozzi Piezometrici e Stabilita di Regolazione," *Energia Elettrica*, vol. 27, nos. 5 and 6, 1950; and vol. 28, no. 6, 1951, p. 12; vol. 30, no. 3, 1953; and Accademia delle Scienze, Bologna, Nov. 23, 1952.

15 J. Frank, "Zur Stabilität der Schwingungen in Schacht Wasserschlössern," *Bauingenieur*, 1942, p. 149. See also *Proceedings, The Institution of Mechanical Engineers*, London, vol. 168, no. 2, 1954.

16 D. Gaden, see Davis, "Handbook of Applied Hydraulics," 2nd ed., section 15 by Rich; and "Considérations sur le Problème de la Stabilité des Régulateurs de Vitesse," Lausanne, 1945, and *Bulletin Technique de la Suisse Romande*, 1951.

17 D. Gaden and L. Bozel, "Influence de la Loi de Variation de la Puissance sur la Condition de la Stabilité de Thoma," *Bulletin Technique de la Suisse Romande*, no. 9, 1951.

18 A. Gardel, "Chambres d'Equilibre," Lausanne, Switzerland, 1956.

19 A. Ghetti, "Ricerche Sperimentali Sulla Stabilita di Regolazione dei Gruppi Idroelettrici con Pozzo Piezometrico," *Energia Elettrica*, 1951.

20 C. Jaeger, "Théorie Générale du Coup de Bélier," Paris, France, 1933.

21 C. Jaeger, "De la Stabilité des Chambres d'Equilibre et des Systèmes de Chambres d'Equilibre," *Schweizerische Bauzeitung*, vol. 122, nos. 21, 24, 25, 26, Nov./Dec., 1943.

22 C. Jaeger, *Civil Engineering*, London, vol. 23, no. 500-3, February-May, 1948.

23 C. Jaeger, "Surge-Tank Stability," *Water Power*, vol. 4, no. 9, 1952.

24 C. Jaeger, "Present Trend in Surge-Tank Design," *Proceedings, The Institution of Mechanical Engineers*, vol. 168, no. 2, 1954.

25 C. Jaeger, "Engineering Fluid Mechanics," Glasgow, Scotland, 1956, New York, N. Y., 1957.

26 C. Jaeger, "The Double-Surge-Tank System," *Water Power*, vol. 9, July/August, 1957; and *La Houille Blanche*, no. 4, September, 1957.

27 C. Jaeger, "Contribution to the Stability Theory of Systems of Surge Tanks," TRANS. ASME, vol. 80, 1958, pp. 1574–1584.

28 C. Jaeger, "The Economics of Large Surge Tanks," *Water Power*, vol. 10, no. 5, 1958.

29 N. N. Krasovskii, "Application of the Second Method of A. M. Liapunov to Equations With Time Lag" (Russian), *Prikl. Math. Mekh.*, no. 3, May-June, 1956, pp. 315–327.

30 A. M. Liapunoff, "The General Problem of Stability," Princeton University Press, Princeton, N. J., 1947. (Reprint from *Annales de la Faculté des Sciences de Toulouse*, 1907.)

31 A. W. Marris, "Large Water-Level Displacements in Simple Surge Tanks," TRANS. ASME, Series D, JOURNAL OF BASIC ENGINEERING, vol. 81, 1959, p. 446.

32 I. W. McCaig and F. Jonker, "Applications of Computer and Model Studies to Problems Involving Hydraulic Transients," TRANS. ASME, Series D, JOURNAL OF BASIC ENGINEERING, vol. 81, 1959, p. 433.

33 N. Minorski, "Introduction to Nonlinear Mechanics," Ann Arbor, Mich., 1947.

34 H. M. Paynter, "Surge and Water-Hammer Problems. Electrical Analogies and Electronic Computer Symposium," *Trans. ASCE*, vol. 118, 1953, pp. 962–1009. See also TRANS. ASME, vol. 80, 1958, pp. 1580–1583.

35 G. A. Rich, "Hydraulic Transients," New York, N. Y., 1951.

36 E. Scimemi, "Sulla Validita Della Regola di Thoma," *Energia Elettrica*, November, 1947, pp. 537–541.

37 E. Scimemi and L. Ghetti, *Energia Elettrica*, vol. 28, September, 1951.

38 L. Sideriades, "The Stability of Two Parallel-Connected Surge Tanks," *La Houille Blanche*, vol. 13, August/September, 1958, pp. 442–449; and *Comptes Rendus, Société Française de Physique*, 1958.

39 A. Stucky, "Chambres d'Equilibre," Lausanne, Switzerland, 1958.

40 D. Thoma, "Zur Theorie des Wasserschlosses bei selbstätig geregelten Turbinen," Oldenburg, München, Germany, 1910.

41 I. C. Zienkiewicz, "Stability of Parallel-Branch and Differential Surge Tanks," *Proceedings, I.Mech.E.*, vol. 170, 1956, pp. 265–280.

DISCUSSION

M. Hug[18]

Following the publication quoted by Dr. Jaeger[19] we have undertaken, with Mr. B. Favez, the frequency analysis of the model of a hydroplant.

The model consists of a differential analyzer representing the transfer functions of hydraulic characteristics of the system together with those of the governor (gate opening and voltage); the generator and network are represented by a system of small scale generators and loads specially designed for that purpose, suitably interconnected with the differential analyzer.

[16] C. Jaeger, "Engineering Fluid Mechanics," 1956/57, p. 233, Fig 131.

[17] 75.1 ft².

[18] Service des Laboratoires et Essais Hydrauliques, Electricité de France, Chatou, France.

[19] Reference [6] of the paper.

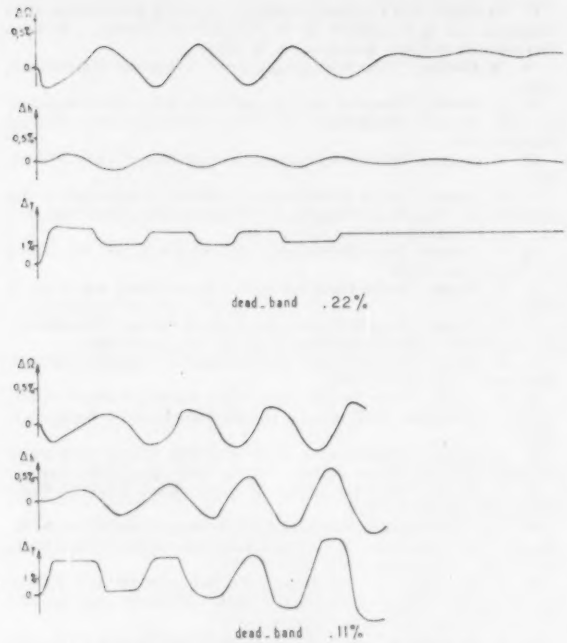

Fig. 12 Influence of the dead-band; load reject of 1.6 per cent

The results of this work have been published in French.[20] In particular, the influence of a short delay, quoted from the Cordéac tests by Dr. Jaeger on page 767) led us to study the influence of the governor dead-band, since we were able to represent such a nonlinear element in our differential analyzer. The following illustrations give the frequency, surge tank water level, and gate opening oscillations following the same load reject of 1.6 per cent in two cases where the dead-band is, respectively, 0.22 and 0.11 per cent. In the second case operation is definitely unstable (the surge tank cross section is half that of Thoma) where as in the first case oscillations decrease rapidly. Even though the dead-band values chosen here are rather large, they still may be met in some cases and show the important stabilizing effect of the dead-band. The drawback of such an operation as illustrated by the 0.22 per cent dead-band is that, after the gate has stopped moving, the frequency and surge tank level records still show slight oscillations. Practically acceptable values of frequency oscillations are difficult to quote and depend on the type of consumers and probable duration each year of such operation where the plant is disconnected from the general network.

A. W. Marris[21]

Dr. Jaeger is to be complimented on this exhaustive and authoritative survey.

The general equation for the simple surge tank operating under the condition of constant hydraulic power acceptance by the turbine, is

$$(1+w)^2\frac{d^2w}{dt^2}+\left(2X(1+w)-\frac{Y}{X}\right)\frac{dw}{dt}+(1-2Y)w+(2-Y)w^2+w^3+\frac{X^2}{Y}(1+w)^2\left(\frac{dw}{dt}\right)^2=0 \quad (12)$$

where X and Y, the co-ordinate axes of Fig. 3, are, respectively, the author's quantities Fv_0^2/Z_* and Fv_0^2/H_0, and $w = Z/H_0$ and t is a dimensionless time defined by $t = \left(\frac{gA_T}{LA_*}\right)t'$ where t' is time.

It is emphasized that the author's equations (4) and (5) refer to the stability of oscillations given by equation (12) only for the particular cases of instantaneous full load acceptance from an initial zero-flow condition. Further, the equations are derived on the assumption that the initial demand of the turbine is met entirely by water from the surge tank. Equation (4) is obtained by setting the initial point $w_0 = Y$, $u_0 = -Y/X$ on the circle

$$\rho = 2\left(\frac{2X^2-Y}{3Y-2X^2}\right)^{1/2}$$

With other initial conditions, such as would arise in the case of changing from one load to another, a different point would have to be set on the circle and a new stability criterion would result.

As the author points out, the method fails if ρ becomes imaginary due to $2X^2$ exceeding $3Y$.

It fails also for large load changes. The circle must always be considered as a small circle surrounding the node at the origin ($w = 0$, $u = 0$). The method of Kryloff and Bogoliuboff as applied by Evangelisti [14] to determine the circle, represents a method of determining a first approximation to the effect of the nonlinear terms of equation (12). It applies specifically to equations of the form

$$\frac{d^2w}{dw^2}+n^2w+mF\left(w,\frac{dw}{dt}\right)=0 \quad (13)$$

where m is small [33].

When $Y = 1/2$, representing the case of static instability due to inordinately high conduit friction, the unstable saddle point singularity given by

$$w=\alpha=-1+\frac{Y}{2}+\frac{Y}{2}\left(1+\frac{4}{Y}\right)^{1/2}, \text{ author's equation (3),} \quad (14)$$

coalesces with the singularity at the origin. For $Y < 1/2$ the phase plane topology comprises the node at the origin, *small* motions about which are oscillatory and may be stable or unstable; and next to it the unstable saddle point at ($w = \alpha$, $u = 0$). It may be shown from general energy considerations [33] that such a configuration requires the existence of a separatrix, a critical boundary in the phase plane separating the motions of different types centered on the singularities. Paynter has pointed out [31][22] that the separatrix governs the drainage criteria. Provided the trajectory remains on an "island" centered at the origin and does not touch the separatrix, the motion will be stable; but if the trajectory becomes tangent to separatrix the representative point will slide down it and critical drainage will result. Established drainage will result from all the trajectories crossing the separatrix.

The phase plane trajectories in the immediate neighborhood of a saddle point are hyperbolas. The separatrix emanates from an asymptote of the saddle point [33]. For critical drainage, in which the trajectory coincides with the separatrix, the surge tank water level passes through the point $w = \alpha$ with zero velocity. In the case of established drainage the velocity of the water level is minimum but not zero at $w = \alpha$. Then the phase plane saddle

[20] B. Favez and M. Hug, "A Contribution to the Study of the Speed Governing System for a Surge Tank Equipped Hydro Electric Plant," 5èmes Journées d' Hydraulique de la Société Hydrotechnique de France, June, 1958.

[21] Assistant Professor, Department of Civil Engineering, University of British Columbia, Vancouver, B. C., Canada. At present, Visiting Professor, The University of Texas, Austin, Texas. Mem. ASME.

[22] See discussion by H. M. Paynter.

point ($w = \alpha$, $u = 0$) is approached and missed. This effect was qualitatively observed with the writer's plexiglas model [31].

Physically, drainage results from the water in the conduit from the reservoir being unable to accelerate fast enough to meet the turbine demand. This acceleration is prohibited by the inertia of the water in the conduit. Drainage will occur at low friction, and, as shown by Paynter [31], such drainage is sensibly independent of the pipe friction. He asserts that critical drainage under these circumstances corresponds to a condition in which the curve relating conduit flow to surge tank water level is momentarily parallel to the curve between demand flow and surge tank water level. On the basis that the velocity of the surge tank water level is momentarily zero, this is in effect a statement that the acceleration of the water in the conduit just matches the acceleration of the demand flow. Paynter derives the result

$$X = 2.60\ Y \tag{15}$$

for the critical drainage line, which agrees admirably with both his analog computer data [34] and the experimental work of the writer [31].

The saddle point singularity ($w = \alpha$, $u = 0$) only exists because of the existence of the loss curve. It is eminently dependent on the pipe friction loss. Drainage at low friction has been shown to be independent of pipe friction. How then can one assert that the singularity is responsible for the drainage? Only because without the saddle point ($w = \alpha$, $u = 0$) the separatrix would not exist.

What has been established is that, while the separatrix must pass through the saddle point ($w = \alpha$, $u = 0$), its *shape* in the vicinity of the origin is only slightly influenced by the saddle point at low friction. This is borne out by the fact that $|\alpha|$ increases, i.e., the singularities get farther apart, as Y becomes small.

The separatrix and indeed all the other phase plane trajectories would of course be determined if the general energy integral of equation (1) could be obtained. The separatrix is the particular energy integral passing through the point ($w = \alpha$, $u = 0$). This would seem to be the best approach for those employing computers.

The writer experimentally assimilated a condition of constant hydraulic power input to the turbine by use of a specially shaped plunger valve connected by a lever to a slider with which the surge tank water level could be followed manually [31]. It was very apparent that stability in respect to both oscillatory motion and drainage was markedly increased by having the slider lag behind the water level. On the other hand, instability was increased if the slider was moved ahead of the water level. This would seem to endorse the results of Chevalier and Hug referred to by the author.

I. W. McCaig[23]

Dr. Jaeger's review of surge tank stability criteria is very useful in tying together the work of numerous workers in this field of research. His account of the tests at Cordéac by Messrs. Chevalier and Hug are of particular interest, as they indicate quantitatively the effect which governor lag has on surge tank stability.

In the electronically controlled model of the Bersimis No. 2 surge tank, which Dr. Jaeger referred to,[24] the model outlet gate control mechanism was designed to react immediately to any change of pressure sensed by a transducer attached to the model conduit. During the initial tests, however, it was found that with the pressure transducer installed at the end of the model penstock, immediate reaction of the outlet gate made stable operation impossible. The model could only be made stable by installing a capillary tube between the penstock and the pressure transducer. This capillary tube caused a delay corresponding to the action of the dashpot in the prototype governor. A comparison of simultaneous records of penstock pressure and control gate movement showed this delay corresponded to approximately six seconds in the prototype.

To find the effect of placing the capillary tube between the conduit and the pressure transducer, the pressure transducer was moved from its position at the downstream end of the model penstock to a position in the surge tank riser immediately below the base of the surge tank. With the pressure transducer in this position, tests could be made with and without the capillary tube inserted in front of the pressure transducer. These tests showed that the surge tank diameter required to give positive damping after a load increase was reduced 22 per cent, from 96 to 75 ft by the action of the capillary tube.

If the delay time of six seconds, for the Bersimis No. 2 development, is entered in the last equation of Appendix 2 in this paper, S_o will equal 0.086 for the condition of zero damping (S_1 equal to S_2). If, to find the minimum stable diameter with a six-second delay between the surge cycle and gate movement, the quantity $a = -\pi\left(\frac{Z_*}{H_0} - 2\frac{F_{v_0}^2}{Z_*}\right)$ of Appendix 2 is equated to 0.086 instead of zero, it will be found that the stable diameter is reduced by 8.4 per cent. The reduction which theory would allow is, therefore, for this case, less than that found by experiment.

H. Netsch[25]

The author has presented in concise form his recent accomplishments in the development of surge tank designs for hydroelectric stations.

The differential equation which is characteristic for the water oscillations in surge tanks of hydroelectric stations is composed of the simultaneous dynamic equation, the condition of continuity, and the equation, characteristic for the power supplied to the turbine. This differential equation is nonlinear of the second order, because of the head-losses in the pressure tunnel. These losses are proportional to the square of the velocity. The actual system, idealized to a linear one performs a damped motion only, if the damping constant is $\geqq 0$. This criterion yields a characteristic area, known as the "Thoma" value. The increase in this required area will decrease the time-varying amplitude of the motion, and, simultaneously, the frequency of the oscillations is smaller than the natural one. This transient condition will be different, whether the turbine efficiency increases or decreases during regulation. A decrease in efficiency tends toward the more unfavorable situation. The influence of the head-loss element will result in a further reduction of the oscillations in the surge tank. But this can only be guessed at or, with experience, be estimated.

To Dr. Jaeger, the credit is due for having solved the simultaneous differential equations for water oscillations in surge tank systems of hydroelectric stations. As a result, the smallest necessary value of the area for each surge tank can be computed; this also for stations which have a surge tank in front and behind each turbine, an arrangement frequently necessary in underground power stations.

Under certain conditions, it is also possible to find a solution of the nonlinear differential equation for the water surface motion in a surge tank. For this purpose, we assume, that the water supply Q to the turbine changes instantaneously and then remains constant. This implies, that the new value of Q does not depend on water oscillations in the tank, thus $z \ll H$. The efficiency of

[23] Hydraulic Engineer, H. G. Acres & Company Limited, Niagara Falls, Canada.

[24] Reference [32] in the paper.

[25] Professor of Applied Mathematics, Hydro- and Gasdynamics, University of Kansas City, Kansas City, Mo.

the turbine can change or remain constant, since only the flow is regulated and not the turbine output. The surge tank must be cylindrical in shape. The solution can be given graphically by applying the isokline method. We have stable oscillations only, if the $dz/dt - z$ curve spirals toward its singularity, the steady-state point. The degree of damping is determined by the slope of this spiral.

As to this nonlinear differential equation of the surge tank oscillations, the following basic statements can be made; the frequency (or spectrum of frequencies) depends on the initial condition of the change in water flow; this is also true of periodical oscillations of the water requirement.

The oscillations in a surge tank can be followed with graphical methods; their advantage is this, that the influence of the shape of the surge tank on the oscillations can be investigated.

The best and most suitable method for investigating a surge tank or a surge tank system of a power station is the recourse to model tests. The calculated surge tanks and their improved form, based on graphical investigations are to be used as a guide value for initial planning and station layout. The final layout agreed upon is the result of these model tests. The load fluctuations can be imitated closely and all possibilities should be considered; this besides the severe condition of separation of the station from the grid. The influence of other stations can be stated.

The final layout agreed upon is to be investigated with the same, preferably improved, mathematical tools.

A very close co-operation between large electricity companies in the development of surge tanks is necessary and the publication of model tests and actual oscillations is suggested; these should also include data of failures as a result of undersized tanks or detailed description of oversized layouts.

From my own experience with a large Hydro-Electric Authority abroad, a station design is only possible in close co-operation with the turbine manufacturer, so that data, concerning the machines, the shape of their efficiency curves, and cavitation behavior, are known. Despite the fact that, speaking from the viewpoint of hydraulics, waterhammer and surge-tank oscillations are treated separately, the layout of surge tanks must be undertaken with the characteristics of the turbine governor kept in mind.

H. M. Paynter[26]

Dr. Jaeger has here continued his superb tradition of periodic review of the state of the art in surge-tank analysis and design. This paper is again distinguished by its accuracy and completeness.

The writer would like to use this opportunity to point out that extensive researches at M.I.T. in this field from 1947 to 1952 culminated in the preparation of the writer's masters and doctoral theses [42, 43],[27] but, perhaps unfortunately, were not published sufficiently extensively [44, 45, 46]. The best testimonials to the importance of some of these results may be inferred from Fig. 9 of the closing discussion of the recent paper of Professor Marris [47], together with the statement that the writer had already studied in 1952 the forced oscillation problem in systems of surge tanks, under interconnected power system operation, using analog and digital computers, followed up by field experimentation and confirmation of results.

Some hope now may be held out for ultimate publication of these findings, with the reinauguration of power system studies at M.I.T., both in the Civil Engineering and in the Mechanical Engineering Departments. This Mechanical Engineering Department program, under the writer's supervision, commenced in 1959 and is sponsored by the Woodward Governor Company. The new studies are directed toward a complete investigation of the system governing problem, including transient regulation, supervisory control, and operational dispatching. Interim reports and other results will be published as rapidly as possible.

[26] Associate Professor of Mechanical Engineering, Massachusetts Institute of Technology, Cambridge, Mass. Mem. ASME.

[27] Numbers from 42 to 47 in brackets designate References at the end of this discussion.

References

42 H. M. Paynter, "Stability of Surge Tanks," SM thesis (unpublished), Massachusetts Institute of Technology, Cambridge, Mass., 1949.

43 H. M. Paynter, "Transient Analysis of Certain Nonlinear Systems in Hydroelectric Plants," ScD thesis (unpublished), Massachusetts Institute of Technology, Cambridge, Mass., 1951.

44 A. T. Gifford and H. M. Paynter, "New Relationships for the Analysis of Surge Tank Transients," Proceedings, The M.I.T. Hydrodynamics Symposium, Massachusetts Institute of Technology, Cambridge, Mass., June, 1951.

45 H. M. Paynter, "Methods and Results From M.I.T. Studies in Unsteady Flow," *Journal, Boston Society of Civil Engineers*, Boston, Mass., vol. 39, no. 2, April, 1952.

46 H. M. Paynter, "Surge and Water-Hammer Problems," Electrical Analogies and Electronic Computer Symposium, *Trans. ASCE*, vol. 118, 1953, pp. 962–1009. See also TRANS. ASME, vol. 80, 1958, pp. 1580–1583.

47 A. W. Marris, "Large Water-Level Displacements in the Simple Surge Tank," TRANS. ASME, Series D, JOURNAL OF BASIC ENGINEERING, vol. 81, 1959, pp. 446–454.

Lefteri Sideriades[28]

1 Writing of Fundamental Equations

While the equations expressing continuity at the hydraulic junction (intake tunnel + pressure pipe + surge tank) and the law of preservation of kinetic energy applied to the mass of water in the intake tunnel present no difficulty, the same cannot be said for the constant-output governing equation. In our article, *Comptes Rendus*, Académie des Sciences, vol. 245, pp. 1884–1887, we suggest defining an "effective" power at which the system is operating as the product at time t of the flow Q by the head h:

h = actual head $(Z_0 + Z)$ + loss head $P_0'W^2$

Z_0 = difference in level between elevation of turbine and that of water mass in reservoir

The loss head represents additional energy localized in the pressure pipe.

2 Stability Factor

The nonlinear terms of the differential equation should not interfere with the definition of "stability factor." This definition has meaning only if we stay near the singular point of the differential equation, where the stability conditions, by Liapunoff's theorem, are the same as those of the linearized system. Happily, the singular point of the oscillations may be isolated (the other points being in general very remote). The language of topology (cf. Minorsky) is best suited to handling this situation.

The linear equation

$$\ddot{x} + 2a\dot{x} + b = 0$$

is equivalent to the system

$$\frac{dx}{y} = -\frac{dy}{2ay + bx} = dt \qquad (\dot{x} = y)$$

The integral curves in the phase plane x, y have a singular point the nature of which characterizes the oscillations. The quality of stability sought requires that this point be a focus of attraction. Hence a two-fold condition:

Attraction (first Routh-Hurwitz criterion). Expressed by $a > 0$, or (using the notation of Appendix 1):

[28] Research Officer, National Ministry of Education, National Center of Scientific Research, Marseilles, France.

$$\frac{Z^*}{H_0} < \frac{2Fv_0^2}{Z^*} \rightarrow 2H_{r0}F_{r0} > 1 \qquad (16)$$

This is the classical Thoma criterion. It serves to define a theoretical area F_{th} for which, independently of operating conditions (governing, in particular), oscillations of water level would be self-sustained with constant amplitude. Topologically, the singular point would then be a *center*.

Focal character (again, second Routh-Hurwitz criterion). Expressed by $a^2 < b$, or in the other notation:

$$\left(\frac{Z^*}{H_0} - \frac{2Fv_0^2}{Z^*}\right)^2 < 4\left(1 - \frac{2Fv_0^2}{H_0}\right) \rightarrow \frac{1}{H_{r0}} + 2F_{r0} < 2 \qquad (17)$$

The relations connecting the two notations, by the way, are:

$$\begin{cases} a = -\pi\left(\dfrac{1}{H_{r0}} - 2F_{r0}\right) \\ b = 4\pi^2\left(1 - \dfrac{2F_{r0}}{H_{r0}}\right) \end{cases}$$

It seems natural to us to define the *damping* of the oscillations by the value of the *decrement*. The logarithmic decrement, then, is:

$$\delta = 2\pi \frac{(2F_{r0} - H_{r0} - 1)}{\sqrt{4H_{r0}^2 - (1 + 2F_{r0}H_{r0})^2}}$$

$$\left(\delta = L_s \frac{Z_{Mt}}{Z_{n(t+T)}} = \frac{2\pi a}{\sqrt{b - a^2}}\right)$$

Or, using the connection with the theoretical Thoma area:

$$\begin{cases} F_{r01} = \dfrac{Fv_0^2}{v_0}\sqrt{gA_{Th}/LA_T} = F_{r0}/\sqrt{n} \\ \qquad\qquad \rightarrow \delta = 2\pi \dfrac{(2nF_{r01}H_{r01} - 1)}{\sqrt{4nH_{r01}^2 - (1 + 2F_{r01}H_{r01}n)^2}} \\ H_{r01} = \dfrac{H_0}{v_0}\sqrt{gA_{Th}/LA_T} = H_{r0}/\sqrt{n} \end{cases}$$

Now $F_{r01}H_{r01} = \frac{1}{2}$. Putting $\dfrac{F_{r01}}{H_{r01}} = \dfrac{Fv_0^2}{H_0} = \epsilon$, or $\begin{cases} F_{r01} = \epsilon/2 \\ H_{r01} = 1/2\epsilon, \end{cases}$

we get the following general relation:

$$\left[n - \epsilon^2(1 + n^2)\right]\delta^2 - 4\pi^2\epsilon^2(n - 1)^2 = 0$$

In the n, δ-plane, this relation represents a pencil of curves whose parameter is none other than $2F_{r01} = \epsilon$ (cf. Fig. 13).

This pencil of curves shows that the damping is greater:

—The greater n is for given ϵ (meaning for given F and H_0). There is a critical value of n for which the damping is infinite. This is what is commonly referred to in electricity as "critical damping." It is to be noted that in this case, oscillations cease to be possible; the singular point is a *node*. When ϵ is small (which is, practically, the general case), $n_c = (H_0/2F) - 2$.

—The greater ϵ is for given n. The other values being fixed, the damping is greater, the greater the loss of head F or the smaller the net head H_0.

The "stability factor" may accordingly be defined by n. However, this definition seems to us to be ultimately improper, because it does not express the liability of the system to stability or instability. In actuality, there are other factors which are disregarded in the present theory (constriction at foot of surge tank and its consequences, pressure pipe, etc.) and which, if taken into account, would determine a practical area F_p, larger or smaller than the Thoma area according to the case. To be valid, the idea of stability factor reflected by the decrement ought to be defined in relation to that unknown practical value. This presents obstacles to a simple definition.

On the other hand, it is to be observed that this area F_p is close to the theoretical area F_{th} even in the case of interconnected surge tanks, as will be shown below. So we propose to define stability factor by the amplitude of the logarithmic decrement. Such a definition of course implies theoretical stability for $\delta > 0$, but has the further advantage of raising some doubt about very small values (positive as well as negative) of δ, which correspond likewise to very small values of ϵ.

3 Stability Factor in General Case of Coupled Systems

(a) *Parallel Case.*

This is the most general case where the systems are on the same side, upstream of the turbines.

In our article, *La Houille Blanche*, vol. 13, no. 4 (Aug./Sept. 1958), in the case of two surge tanks on the hypothesis of maximum stability ($\phi = \phi_1 + \phi_2$), we gave the following relationship for the minimum area values to be adopted (our notation):

$$\sum\left(\frac{P_{0i}\phi_i F_i}{W_{0i}^2 f_i^2}\right) = \sum\left(\frac{L_i}{f_i}\right)\left\{2g\sum\left(\frac{Z_{0i}}{\phi_i}\right)\right\}^{-1} \qquad (18)$$

If the two component systems are identical, it comes to exactly the same thing to imagine that we have a single system with surge tank divided into two like areas, observing all continuities, namely:

Same flow $\phi u = \Sigma(\phi_i u_i)$, $fW = \Sigma(f_i W_i)$ etc.

Same quantity of motion $\phi u^2 = \Sigma(\phi_i u_i^2)$ etc.

Same areas $\phi = \Sigma\phi_i$ etc.

It is easily shown that these hypotheses involve preservation of the flow velocity.

More generally, then, we can disconnect a given system into n identical partial systems, completely or incompletely, and the disconnection may be confined to the surge tanks. But, if all areas are thus divided by n, is there still preservation of stability? Or, in more practical terms, to what extent can the surge tank areas be diminished without changing the stability?

It is possible to answer this question in the case of two surge tanks. If, in the relationship (18), we disconnect into two identical systems, we get the following result: Calling F_e the area of the equivalent single system, we can take the value $F_e/4$ for the area of each surge tank without changing the stability. The rule of disconnection has the form $1/n^2$ in the case of two surge tanks.

If this holds good for the Jouques example (which is uncertain pending general analysis of the case of three surge tanks), where the area of a single surge tank should be 656 m², the area could be diminished to only 73 m², or even 61 m² (using the effective

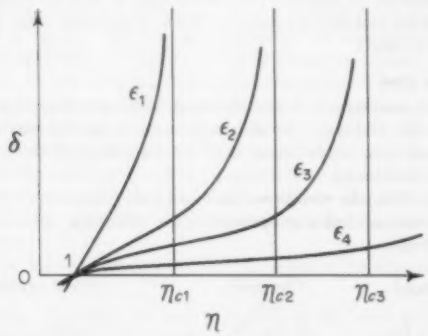

Fig. 13

output governing equation). So the excessively small stability factor 0.077 would be raised to 0.82, or still in the neighborhood of unity. This would seem to be an acceptable result. But we must have some hesitation about extending the $1/n^2$ rule to $n > 2$, as it seems unlikely to hold for very large n. A more plausible rule would be of the form $1/n(n)^{1/(n-1)}$. This problem calls for close study and analysis.

Now let us consider the Valabres example. Taken singly, the Thoma areas are (again in terms of our governing equation):

$$F_{1c} = 5.43 \text{ m}^2 \qquad F_{2c} = 0.79 \text{ m}^2 \qquad \text{(cf. Fig. 14)}$$

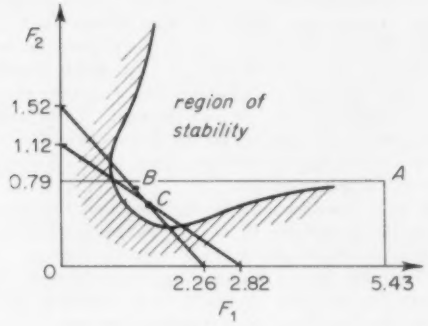

Fig. 14

There is a corresponding point A in the F_1, F_2-plane that ensures stability of the system. But these areas can be further diminished by taking account of the coupling at the hydraulic junction formed by the pressure pipes and of the relationship $R(\phi_1, \phi_2, \phi) = 0$, which is not involved—for good reason—in the independent operation of two partial systems. By way of illustration, let us examine the following two hypotheses:

(*a*) $\phi = \phi_1 + \phi_2$ (*ideal case*). This is the hypothesis where there is no loss of head at the branching of the pressure pipes. The available areas are distributed along a straight line intersecting the axes at the points $F_1' = 2.26$ and $F_2' = 1.52$ m². We can take the mid-point B of the segment so determined: $F_{1c}' = 1.13$, $F_{2c}' = 0.76$ m². This lies within the region of stability bounded by the equilateral hyperbola of the third Routh-Hurwitz condition. Note that, in the general case, we should find:

$$F_1' = \frac{(1 + f_1L_2/f_2L_1)}{(1 + \phi_1Z_{02}/\phi_2Z_{01})} F_{1c} \quad \text{and}$$

$$F_2' = \frac{(1 + f_2L_1/f_1L_2)}{(1 + \phi_2Z_{01}/\phi_1/\phi_1Z_{02})} F_{2c}$$

(*b*) $\phi = \phi_1$ or ϕ_2 (*real case*). If ϕ is the larger of the two areas there is a loss of head at the branch, but the loss is minimal. The possible areas are distributed along a straight line intersecting the axes at the points $F_1'' = 2.82$, $F_2'' = 1.12$ m.² Thus we can choose $F_{1c}'' = 1.41$ and $F_{2c}'' = 0.56$ m² if we take the mid-point, or $F_{1c}'' = 1.74$ and $F_{2c}'' = 0.43$ m² if we take one of the points of intersection with the hyperbola.

Conclusions. (1) When surge tanks are arranged in parallel, the areas to be adopted are generally smaller than the Thoma areas. The coefficient of diminution is determined by the coupling, that is to say by the values ϕ, ϕ_1, ϕ_2, which do not become involved in independent operation. We cannot say, in the general case, that the areas to be adopted are half the Thoma areas, though stability is approximately realized. But if the disconnection is into two identical systems, then the area of each surge tank may be made equal to $F_c/4$. This follows from the relationship (18), which is then written: $F_{ci} = \frac{1}{2} \cdot \frac{Lf}{4gP_0'Z_0} = \frac{F_c}{4}$

(2) Analogy with coupled electrical systems. In general, when losses of head are minimal ($\phi = \Sigma\phi_i$), we can take $F_1'/2 < F_{1c}$ and $F_2'/2 < F_{2c}$. In other words, the point B representing the areas adopted is within the rectangle determined by the Thoma areas. This result can be illustrated in another way so as to set up an analogy with electrical systems. If the F_2-axis is rotated forward by $+\pi/2$, we get the arrangement $a''b''ba$ (cf. Fig. 15): The coupling brings the critical areas together. Now it is well known that coupling takes the natural frequencies apart.

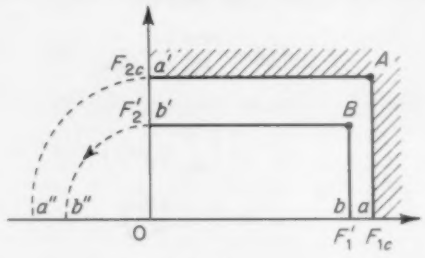

Fig. 15

This result was predictable because, if we make an analogy between the two types of systems (in the differential equations themselves), we find that the square of the frequency ω varies as $1/F$. This is not so when, by way of exception, $F_1' > 2F_{1c}$ and $F_2' > 2F_{2c}$. Letting $\alpha = f_1L_2/f_2L_1$, $\beta = \phi_1Z_{02}/\phi_2Z_{01}$, these inequalities are equivalent to:

$$1 + \alpha > 2(1 + \beta)$$
$$\beta(1 + \alpha) > 2\alpha(1 + \beta)$$

They cannot both be true at the same time, and the prohibited regions in the α, β-plane are indicated by (1) and (2) in Fig. 16.

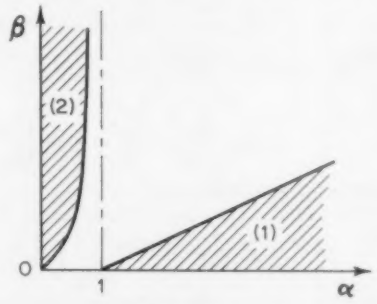

Fig. 16

In conclusion, we may say that, in the case of parallel coupling of surge tanks, stability is preserved when at least one of the Thoma areas is reduced.

(b) *Series Case.*

Here is another case where the surge tanks are located on either side of the turbines. It also represents a special case of the parallel system in the sense that the branching of the pressure pipes is eliminated.

We go from the results we have obtained for parallel coupling to the case of series coupling by the following table of correspondences:

Unchanged sign	Changed sign	Peculiarities
$f_1, F_1, F_2, L_1, P_{01}', Z_{01}, Z_{02}$	f_2, L_2, P_{02}'	$\phi_1 = -\phi_2$ and $\phi = 0$ $\rightarrow \lambda = -1$

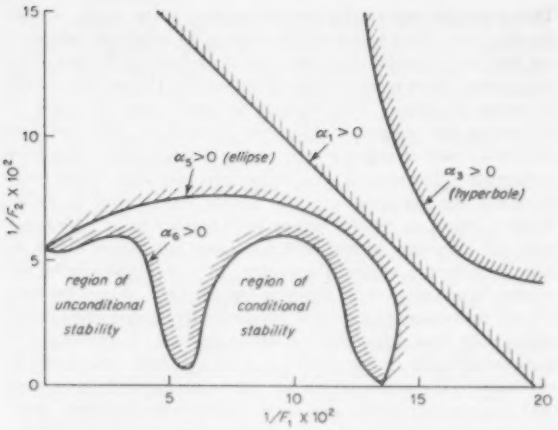

Fig. 17 Example of plant at Kiewa, Australia. Determination of region of stability in $1/F_1$, $1/F_2$-plane by application of the six Routh-Hurwitz conditions. α_2, α_4 not restrictive.

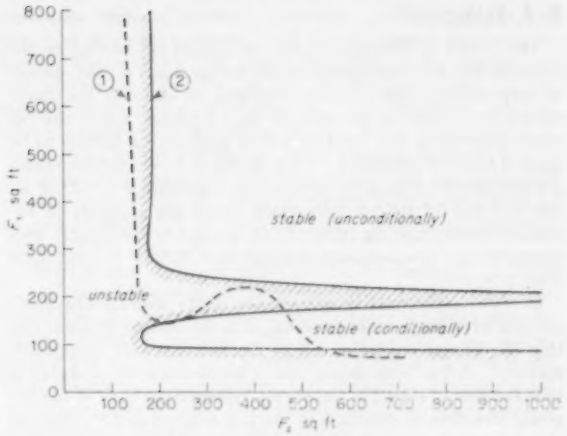

Fig. 18 Example of plant at Kiewa, Australia
Curve (1): Approximate calculation (Balint, Flower, and Frueh)
Curve (2): Approximate calculation (Sideriades)

We have made a complete study, by way of example, of the Kiewa plant in Australia, with the following values of the parameters:

$L_1 = 4.648$ m	$L_2 = 2.234$ m	$H = 166$ m
$f_1 = 26.477$ m²	$f_2 = 31.58$ m²	$K = 7.4 \times 10^3$
$W_{10} = 1.68$ m	$W_{20} = 1.42$ m	$F_{th1} = 6.92$ m² (or 74.3 ft²)
$P_{10} = 15.4$ m	$P_{20} = 2.74$ m	
$P_{01}' = 5.45$	$\phi_{02}' = 1.37$	$F_{th2} = 15.80$ m² (or 169.5 ft²)

The stability regions are blocked up step-by-step according to the Routh-Hurwitz conditions as direct functions of the several parameters. Only the sixth condition $\alpha_6 > 0$ is restrictive, and it appears as shown in Fig. 17. The transformation of the F_2', F_1' plane is shown in Fig. 18, where Balint, Flower, and Frueh's curve has also been drawn in for comparison of results. On the whole, the stability regions are similar. But our calculations show a clear division of the stability region into two species, conditional and unconditional. Such a result is familiar in electronic systems of servomechanisms when stability conditions are analyzed by Nyquist's criterion.

General Conclusion

It appears in this second study that the areas to be adopted are greater than the Thoma areas. If we idealize matters so as to get them into a simple form, we can submit the following result.

In all cases, we can define the Thoma areas of the independent partial systems. These areas determine the co-ordinates of a point A in the F_2', F_1' plane. If two straight lines parallel to the axes are drawn through this point, the straight lines may be thought of as the asymptotes of a curve of high degree (as representing the juxtaposition of the stability curves for the six Routh-Hurwitz conditions). The idealization consists in approximating this curve with a simpler one of *hyperbolic* form (cf. Fig. 19; e.g., mean values). The result is then as follows:

In the case of parallel coupling, the areas to be adopted lie in region (1).

In the case of series coupling, the areas to be adopted lie in region (2).

Remark. It would be rash to decide on the basis of the first condition $\alpha_1 > 0$ alone, despite its advantage of simplicity. For a better estimate, one should at least take in the fifth condition

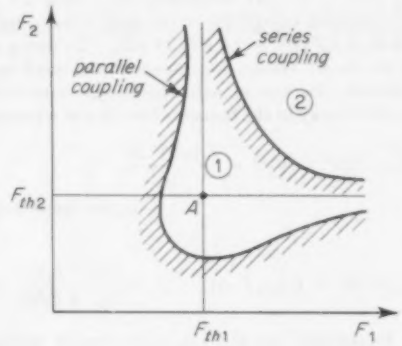

Fig. 19

$\alpha_5 > 0$, which in our method represents an ellipse, a curve whose geometrical properties are sufficiently familiar.

Remark on an Objection to the Writing of the Equation for the Pressure Pipe Junction

In our general preliminary analysis, we take account of the losses due to the change in velocity u as well as to the difference in the forces A and B. Upon the hypothesis (practical value) where this loss of head is minimal, the pipe branch conditions are localized at the hydraulic junction, and hence independent of the operating conditions upstream and downstream of that point. These latter conditions affect the presence of outside forces A, B, which cancel when we confine attention to the *loss of head* (a differential quantity and hence not absolute but relative) due to the function.

The only objection amounting to a valid restriction is that the relationship $u\Sigma(\phi_i u_i) = \Sigma(\phi_i u_i^2)$ adopted assumes that the change in quantity of motion is nil, or that $A = B$. This is a condition imposed by the construction of the lines, which implies $d\pi/du = 0$ where π is the total loss of head due to mixing. A and B certainly depend on $(h + Z)^{1/2}$ individually. But the quasi-differential situation at the junction cannot reflect this, especially since A is closer to B, the shorter the mixing distance, and the lines are so constructed that it shall be short.

R. A. Sutherland[29]

The author in this presentation has added yet another to the valuable list of contributions which he has made on the subject of surge tanks. The Thoma condition for stability has maintained its position as the basis of later analyses, which have in effect resulted in the development of multiplying factors to be applied to the Thoma area. Thus in Fig. 3, in which presumably y represents FV_0^2/H_0 and x presumably represents FV_0^2/Z^*, if we take a value 0.1 for FV_0^2/H_0 which would not generally be exceeded, the multiplying factors to be applied to the Thoma area appear to vary to a maximum of about $(0.25/0.223)^2 = 1.26$ (curve 4 for $y = 0.1$).

In view of the relative infrequency of the average engineer's contact with surge-tank problems, it is interesting to point out that the Thoma condition can be derived in a very elementary manner. It has been shown that a requirement for stability is that the energy stored in the supply system must vary in the opposite direction to variation in the power developed.[30] Assume that a small change in load takes place from the steady load condition shown in Fig. 1. For the sake of example assume a small increase of load, which will increase the tunnel velocity from V_0 to $V_0 + \Delta V$ and will at the same time drop the water level in the surge tank by a small amount Δz which is given by $\Delta Z = F\left(\overline{V_0 + \Delta V}^2 - V_0^2\right) = 2FV_0\Delta V$ discarding $(\Delta V)^2$ since ΔV is small. The loss in potential energy due to the drop of water level in the surge tank is $A_s\Delta Z\gamma H_0 = 2A_sFV_0\Delta V\gamma H_0$. To insure that the energy in the supply system decreases with the small increase of load considered, this loss of potential energy must exceed the gain in kinetic energy in the tunnel, which gain is represented by:

$$\frac{LA_T\gamma}{2g}\left(\overline{V_0 + \Delta V}^2 - V_0^2\right) = \frac{LA_T\gamma V_0\Delta V}{g}$$

[again discarding $(\Delta V)^2$]

Hence

$$2A_sFV_0\Delta V\gamma H_0 > LA_T\gamma V_0\Delta V \therefore A_s > \frac{V_0^2}{2g}\cdot\frac{LA_T}{FV_0^2H_0} = A_{Th}$$

Professor Evangelisti has given a more elegant mathematical derivation on p. 195 of the cited work.

If in this elementary discussion we add the increase in kinetic energy in the penstock to that in the tunnel, it readily appears that a multiplying factor to be applied to the Thoma area to take account of the penstock condition is $1 + \dfrac{lA_T}{LA_p}$ where l and A_p are length and area, respectively, of the penstock, assumed to be of constant area. This factor is always greater than unity and could be considerably greater.

The effect of turbine efficiency has been touched on by the author, but has been discussed more extensively by others.[31] It is readily apparent that an increase of efficiency with power will have a stabilizing influence, while a drooping efficiency curve will tend to promote or aggrevate instability. Hence an important multiplying factor to be applied to the Thoma area would take account of the variation in efficiency near full load. According to the late Mr. R. D. Johnson, in his discussion of the above-cited paper, the multiplier is $1 + 3/2 \cdot P/E \cdot dE/dP$ where E and P are, respectively, efficiency and power at the point considered.[32] This multiplier can readily have a value of 1.3 or more. Consequently, for a plant which will be required to supply an independent load, or to regulate frequency in a system of which it is a major component, there is no question but that the Thoma area should be largely increased. This warning has been repeatedly given by writers on the subject.[33] However it must be admitted that conditions have changed greatly since the days of the Heimbach occurrence. Power systems have become very large which tends to reduce the importance of the Thoma requirement at an individual plant, as several writers have pointed out. Also many units are operating at virtually fixed load conditions under instructions from a central dispatcher, with regulation being entrusted to one plant most suited to the purpose. There has been a trend to storage projects and, consequently, to restricted orifice tanks, with their surge limiting characteristics. Even large systems occasionally "come apart" and may require some hours to reconnect. The consequences for a given plant which has a surge tank may or may not be such as to require consideration. Summing up, it is evident that each surge tank installation constitutes a problem of its own, in which good engineering judgment must be exercised. This is probably the feature which has attracted so many eminent engineers to study and write on the subject.

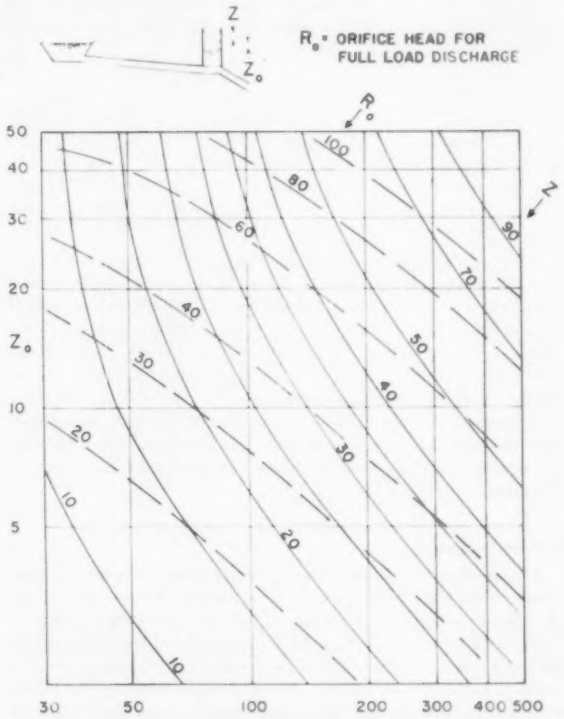

Fig. 20 Orifice surge tank; surge rise for "full load off"

In closing, the writer wishes to offer a typical chart (Fig. 20) which he has found useful in preliminary dimensioning of restricted orifice tanks. This diagram is based on Calame and Gaden's Fig. 27[34] but by using head/stability factor as an abscissa it has been possible to express the data in a very convenient form, to find surge rise for "full load off" with an orifice tank.

[29] Principal Engineer, Ebasco Services Incorporated, New York, N. Y.

[30] G. Evangelisti, "La Regolozione delle Turbine Idrauliche," Nicola Zanichelli, Editore, Bologna, Italy, 1947, p. 13.

[31] For example, A. W. F. McQueen, "Hydraulic Stability," *The Engineering Journal*, January, 1933, p. 13.

[32] Although not so stated by Mr. Johnson, he evidently intended dE/dP to be taken as positive on the drooping part of the efficiency curve.

[33] For example, George P. Rich, "Hydraulic Transients," McGraw-Hill Book Company, Inc., New York, N. Y., 1951.

[34] Author's reference [4].

Author's Closure

The problem of surge stability proves once more to be of interest to many engineers, mainly because of its practical implications. Furthermore, the discussion of surge stability attracts research workers and mathematicians because of the considerable interest of the mathematical analysis involved. The steady development of more elaborate theories justifies periodical surveys leading to a general discussion.

Mr. Hug uses a differential analyzer to check frequency variations and surge stability of surge tanks connected to an electric grid under different conditions of governor time lag, dead band, and system interconnection. Fig. 12 shows two convincing curves out of many more he has recently published in an important paper. To appreciate Mr. Hug's contribution to the subject, reference should be made to this paper.[35]

Results obtained by Mr. McCaig on a surge-tank model provided with an electronic governing system confirm Mr. Hug's theoretical research on the influence of the governor time lag.

Checking results obtained by different methods for surge stability problems is a must. This is the view of Mr. Netsch with whom the author entirely agrees.

Mr. Sutherland's simplified proof of Thoma's formula using the equation of energy recalls the publications of Evangelisti and some earlier work by Frank and Schüller[36] which yielded some important results at an early stage of the theoretical research.

The three contributions of Messrs. Paynter, Marris, and Sideriades form a coherent discussion based mainly on the theory of nonlinear systems. Now that we possess this most important mathematical tool, we are astonished at the precision of the information which has, in the past, been obtained with far simpler mathematical developments. On the whole, the new theory confirms what was found earlier. Surge tanks working in series on a pressure system have been examined exhaustively in the past. Sideriades now examines surge tanks put in parallel on the same hydraulic pressure system and shows them to be mainly stable. This particular point requires experimental confirmation.

There is one important point still to be clarified. It refers to the damping action of the energy head $V^2/2g$. For tanks located on the upstream side of the turbines the work done by Gardel should be checked. The mode of action of the energy head $V^2/2g$ when the tank is located on a tailrace tunnel is still most obscure and many authors think there is no damping at all. This point must be made clear as more and more power stations are provided with tailrace pressure sysems.

It is real good news that Professor Paynter is in a position to announce an extensive research program on power systems studies at the M.I.T. under his supervision sponsored by the Woodward Governor Company, the results of which will interest all specialists.

[35] B. Faves and M. Hug, 5èmes Journées d'Hydraulique de la Société Hydrotechnique de France, June, 1958.

[36] Frank and Schüller, "Schwingungen in Zuleitungs Kanälen," Berlin, 1938, and C. Jaeger, "Engineering Fluid Mechanics," London, 1956, p. 238.

PIERRE DANEL
Assoc. Mem. ASME

JACQUES DUPORT
SOGREAH,
Grenoble, France

The Selection of Length and Head Scales for Cavitation Tests

SOME OF THE "Aspects of Cavitation Similitude in Hydraulic Turbines," presented at the Seventh Congress of the International Association for Hydraulic Research at Lisbon, Portugal, in 1957, are included here with fuller treatment of certain points.

The most important problems to be solved in investigating cavitation on scale models concern choice of length and velocity scales and determination if there are lower limits beyond which these characteristics can be scaled down. In dealing with turbomachines, or more generally flow under pressure, it is also necessary to know whether the head (or velocity) scale and length scale can be chosen independently of each other as is done where cavitation does not occur.

These problems are by no means new. To the authors' knowledge they were first considered by Thoma more than 30 years ago. Professor Thoma stated that the cavitation factor, which he defined on that occasion, and the Froude number have to be equal on the model and on the prototype, and the length scale has to be the same as that of the head driving the machine or the head generated by the machine.

This law does not consider the amount of scaling down that can be done without causing exaggerated distortion of the phenomena being studied. In building models of large turbines (or structures) operating under low heads, Froude similitude requirements result in low flow velocities on the model. Would it not then be preferable to abandon Froude's law and choose heads which are scaled down less or which are the same as the prototype head, as done by some manufacturers?[1]

Much research on the similitude of cavitation phenomena has been done since Thoma's days, but it would appear that little is concerned with the possible influence of the Froude number. The authors have always considered that, for certain cavitation tests, the Froude number should be the same on both the model and the prototype, an opinion which differs from that held most frequently in other laboratories.

Recent research on cavitation, of which the most important has been done in American universities, has not shown that the Froude number has a particularly great effect, and this would, at first sight, seem to justify the frequently accepted practice of abandoning Froude's law.

The great variety of opinions on this subject results partly from the fact that no similitude rule can be said to be rigorous, and from the fact that a model can only claim to represent certain aspects of actual phenomena.

[1] Indeed it would seem that the use of heads higher than the "Froude" heads was originally motivated not by the desire to avoid a scale effect linked with velocity, but by experimental difficulties resulting from the expulsion of air from the water.

Contributed by the Hydraulic Division and presented at the Annual Meeting, Atlantic City, N. J., November 29–December 4, 1959, of THE AMERICAN SOCIETY OF MECHANICAL ENGINEERS.

NOTE: Statements and opinions advanced in papers are to be considered as individual expressions of their authors and not those of the Society. Manuscript received at ASME Headquarters, June 11, 1959. Paper No. 59—A-40.

The choice of similitude laws, and more generally of experimental techniques, depends upon the objective. One should concentrate on reproducing as accurately as possible the phenomena which have the most direct effect on achieving the objective, and at the same time accept the necessity, if it arises, of distorting other phenomena to a varying extent.

Thus, before considering the laws of similitude to be used in an experiment, it is advisable to recall to mind the reasons for carrying out the experiment and its objectives.

With hydraulic turbines or pumps the fundamental consideration is to avoid cavitation. Indeed, when cavitation occurs, it is always accompanied by effects which are injurious to a varying extent.

The deterioration of operating conditions beyond the limit at which cavitation occurs, generally produces effects which become disastrous very rapidly, e.g., strong vibrations, a serious reduction of output and efficiency, and erosion of the rotor or nonrotating parts of the machine, occurring with varying rapidity. Whatever may be done, the limits, beyond which cavitation effects become unacceptable, cannot be determined a priori with great accuracy.

In view of the serious results of cavitation, and because it is possible to be certain of moderating its effects, hydraulic turbine manufacturers and operators have mainly been concerned with avoiding cavitation as completely as possible.

Of course, such efforts deal mainly with normal operating conditions, since in nearly all practical instances it is necessary to accept a varying degree of cavitation during certain transient operating conditions, or even during certain rarely encountered steady operating conditions.

It can therefore be said that the similitude property, which is of prime interest to turbine manufacturers and operators, is that which applies to the no-cavitation limit conditions.

Scale model determination of the cavitation threshold really has the following objectives:

1 To make it possible to calculate the setting of the turbine which will avoid cavitation under normal operating conditions.

2 To improve turbine design so as to reduce the critical sigma as much as possible.

In connection with the first point it is assumed that the operating conditions can be varied to the point where cavitation starts and that the criteria with which cavitation is detected have been defined, i.e., visual or aural observation, or the deterioration of operating characteristics.

The second point implies that the location and appearance of incipient cavitation can be observed accurately.

Froude Similitude

The Justification for Using Froude's Similitude When Determining the Cavitation Threshold. Whatever criterion has been decided upon to define incipient cavitation, it is always linked with the appearance at a given point in the machine, and in this point's im-

mediate vicinity, of localized pressure which attains a certain critical value p_{cr}. Most frequently this pressure is considered to be the vapor pressure of water. This problem, which is one of the most tricky arising from scale-model experiments on cavitation, will be dealt with again later. It will now be shown that where hydraulic turbines are concerned, it is desirable to use the Froude and Thoma similitude conditions simultaneously, whatever the value alloted to the critical pressure may be.

The pressure at a given point in a turbine is given simply by Bernoulli's equation

$$h = h_a - h_s - z - \sigma H \tag{1}$$

where

h is the absolute pressure at the point under consideration in meters of water

h_a is atmospheric pressure in meters of water

h_s is the suction head[2]

z is the elevation of the point under consideration above a reference point in the turbine[2]

H is the total net head

σ is a factor which depends upon the operating conditions of the turbine and upon the location of the point under consideration

Let h_{cr} be the critical pressure given in meters of water.

Cavitation starts when h at a given point is equal to h_{cr}; since the pressure in the turbine is unknown, the elevation z of the point of incipient cavitation cannot be determined a priori.

When comparing two geometrically similar turbines operating under homologous conditions, it is convenient to divide height of water columns by the head H, and elevations by the diameter of the runner.

Equation (1) then becomes

$$\frac{h}{H} = \frac{h_a - h_s}{H} - Z\frac{D}{H} - \sigma \tag{2}$$

where $Z = z/D$ is the relative elevation of the point under consideration.

It is interesting to bring out the difference between the local pressure and the critical pressure

$$\frac{h - h_{cr}}{H} = \frac{h_a - h_s - h_{cr}}{H} - Z\frac{D}{H} - \sigma \tag{3}$$

For given operating conditions, the factor σ depends upon the location of the point being considered and therefore upon Z. For each value of Z there is a point at which σ is a maximum and takes the value σ_m which is dependent only on Z. It is obvious that cavitation is incipient at points where σ_m is a maximum.

Let $\left(\frac{h - h_{cr}}{H}\right)_m$ be the value of the left-hand side of (3) at such points.

Then

$$\left(\frac{h - h_{cr}}{H}\right)_m = \sigma_i - Z\frac{D}{H} - \sigma_m(Z) \tag{4}$$

where $\frac{h_a - h_s - h_{cr}}{H}$ is written as σ_i, the "plant sigma." $\left(\frac{h - h_{cr}}{H}\right)_m$ is a function of Z only. It can be expressed as the difference between the ordinates of the straight line Δ with equation $y = \sigma_i - Z\frac{D}{H}$, which only depends upon σ_i and $\frac{D}{H}$, and the ordinates of the curve $y = \sigma_m(Z)$, which only depends upon the design of the turbine and the conditions under which it operates, Fig. 1.

[2] Turbine manufacturers' practice is to take this as being the height above tailwater of a characteristic point in the turbine such as the axis of the vane trunions in Kaplan turbines or the center line of the distributor in Francis turbines.

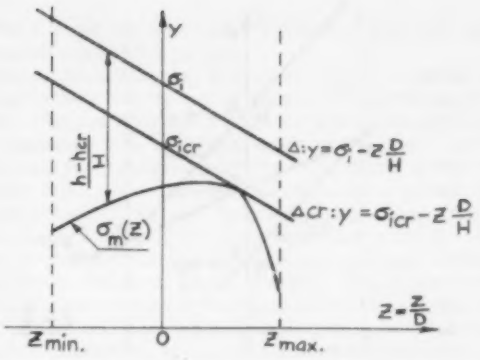

Fig. 1 Computation of $\frac{h - h_{cr}}{H}$

The limiting value of σ_i at which cavitation is incipient, i.e., σ_{icr}, is the value for which Δ is a tangent to the curve σ_m. It can be seen immediately that, for turbines having the same design and operating under homologous conditions, σ_{icr} will only be the same if the values of H/D are equal. Similarly, the location of incipient cavitation also depends upon H/D.

It is therefore necessary to conform to the Froude similitude conditions; i.e., make the values of H/D equal, to determine both the critical setting of the turbine and the location of regions which will cavitate.

The Effect of Distorting the Head and Length Scales. The preceding discussion has shown that it is mainly uncertainty as to the location of the point at which the critical pressure first appears which makes it necessary to conform to the Froude similitude conditions.

Naturally, if for various reasons it is possible to predict with certainty the location of this point and to be certain that it does not depend upon H/D,[3] it would seem permissible to distort the latter factor to some extent. Certain turbine manufacturers apparently have this in mind when they consider it possible to work with test heads nearly the same as the prototype heads rather than use scaled-down heads. However, this procedure can, in certain cases, result in a certain amount of uncertainty concerning the determination of the critical setting.

Starting with the simple hypotheses formulated earlier, it is possible, by running a test in which the ratio H'/D' is not the same as H/D in the prototype, to calculate the maximum error one is likely to make in determining the critical σ.

Assume that $H'/D' > H/D$. This inequality will be true if, for example, a test head is used which is nearly the same as the prototype head instead of scaling it down with the model.

Let σ_{icr}' be the critical value obtained on the model, Fig. 2. The only conclusion that can be drawn concerning the σ_m curve defined earlier is that it lies below the straight line Δ_{cr}' with coordinate σ_{icr}' and gradient $-D'/H'$, which cuts the lines with abscissas Z min and Z max, corresponding to the points on the runner having extreme elevations, at points A and B.

The gradient of the line Δ_{cr} which indicates incipient cavitation in the prototype will be $-D/H$ and the line will certainly:

(a) Lie below line Δ_1 with gradient $-D/H$ which passes through point B and cuts the axis $Z = 0$ at the point M, the ordinate of which is σ_{cr} max,

(b) Lie above the line Δ_2 with gradient $-D/H$ which passes through the point A and cuts the axis $Z = 0$ in the point N, the ordinate of which is σ_{cr} min.

[3] That is to say if the region likely to cavitate is not very deep, which is not generally the case in well-designed turbines where one tries to spread out the low-pressure regions over the greatest possible area on the runner vanes.

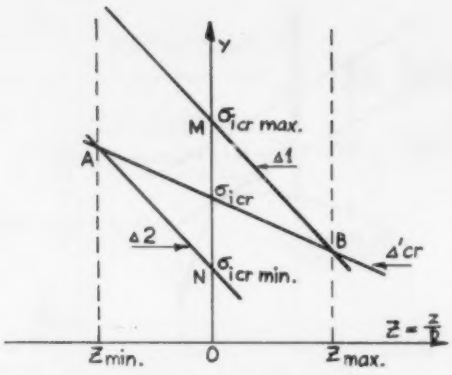

Fig. 2 Computation of $\sigma_{cr\ min}$ and $\sigma_{cr\ max}$

The only conclusion that can be drawn with certainty concerning the prototype turbine (H/D) from a test run on a model for which the characteristic value is H'/D', is that the σ_{cr} of the prototype certainly lies between the values σ min and σ max which can be calculated from the critical σ of the model (σ_{cr}') and from the values H/D and H'/D'. Indeed, the scatter which results from this may be rather wide.

The scatter of the critical sigmas is

$$\sigma_{max} - \sigma_{min} = L/D(D/H - D'/H')$$

where L is the height of the runner.

The corresponding uncertainty concerning the suction head is

$$h_S = L(1 - D'/H'\,H/D)$$

It can be seen that, if a cavitation test is run on a $^1/_{20}$ scale model with the test head the same as the prototype head, the degree of uncertainty concerning the setting of the prototype is $0.95L$. Now the total height L of a large Kaplan turbine may be as much as 1.5 to 2 meters (with the blades fully open). Scatter of this order is very much higher than that which results from experimental errors and any scale effects, and the ways in which it affects the cost of plant or the danger of cavitation, are far from negligible.

Scale Effects

However, the simultaneous application of Thoma's parameter and the Froude law is not sufficient in all circumstances if one wishes to reproduce the cavitation threshold absolutely accurately. As has already been stated, and this is true for all physical laws, the similitude laws are only approximations and the matters for concern are the differences between reality and what is expressed by these laws. These differences, which are usually referred to as "scale effects," will not be analyzed fully in this paper. Certain precautions will be described that have to be taken to reduce their magnitude and means suggested by which approximate corrections can be obtained.

Since the cavitation threshold occurs under conditions for which the localized pressure at a certain point is equal to the critical pressure, it may be expected that the differences between the model test results and the behavior of the prototype originate from: (*a*) Either the reproduction of the local pressure field, (*b*) or the magnitude allotted to the critical pressure, (*c*) or the evaluation of the moment at which both these pressures become equal; i.e., the sensitivity of the method used to detect incipient cavitation.

Magnitude of the Critical Pressure. Whether Froude's law is conformed to or not, it is essential that the critical pressure be known if it is to be possible to transpose the results of a cavitation test. Now this critical pressure, as will be seen later, can only be determined approximately and this results in uncertainty concerning the suction heads of the machines being studied. If the Froude similitude conditions are observed the error, to which the critical pressure (expressed in meters of water) is subjected, is scaled up (for instance an error of 0.10 m concerning the critical pressure in a test on a $^1/_{10}$ scale model becomes an error of 1 m), whereas, if the test head is the same as the prototype head, the error concerning the suction head is equal to the error concerning the critical pressure and can often be neglected.

In the authors' opinion this is not a reason for not using the Froude similitude conditions in cases where, because of the reasons stated in the section on the justification for Froude's similitude, they have to be used. What should be done is to try to reduce the uncertainty concerning the critical pressure as much as possible.

This leads to a brief discussion of the factors which affect the critical pressure.

The Critical Pressure for Gaseous Diffusion. If the water passing through the turbine contains both dissolved air and nuclei of undissolved air, bubbles form in the regions of lowest pressure and gaseous diffusion occurs. This is the reverse of what takes place when air is dissolved.

How does gaseous diffusion, the effects of which are likely to be confused with those of cavitation, take place when the Froude similitude conditions are being used, or when the head is nearly the same as the prototype head? This question will be considered with reference to a low head turbine.

A preliminary comment has to be made. If, whatever test method is used, it is assumed that, at the point where cavitation is incipient, the pressure is nearly the same as the vapor pressure of water, the critical pressure for gaseous diffusion will have been exceeded in both cases, but it must be noticed that there is nevertheless a great difference between operation with or without a scaled-down head for:

1 When the test head is nearly the same as the prototype head, the region, in which the localized pressure is less than the critical pressure, is very small. Since, in addition, flow velocities are very high and the models may be small, the time taken by water to pass through such regions is very small with the result that gaseous diffusion has hardly enough time to occur. This means that air bubbles form only in moderate quantities and affect neither the performance of the turbine nor any visual observation that may take place.

2 If the Froude similitude conditions are used, the very low pressure regions are much more extensive, especially upstream of the critical-cavitation region, and the models are relatively large with low flow speeds. Gaseous diffusion has time to take place, if only partially, so that when no precautions are taken the turbine no longer operates with water but with an emulsion, which both changes the nature of the phenomena and makes them difficult to observe. Such are the difficulties encountered by those who tried to run cavitation tests under Froude similitude conditions and who, for example, used natural-water supplies.

However there are methods of eliminating air bubbles and emulsions. For instance, large open surfaces and an adequately dimensioned air-absorber can be incorporated in the circuit of the test stand.

It would seem advisable to discuss the effect of such arrangements on the critical pressure for gaseous diffusion a little more fully.

The critical pressure for gaseous diffusion depends both upon the pressure of the air dissolved in the water and upon the dimensions of the nuclei of undissolved air. If one wanted to reproduce gaseous diffusion accurately in the model it would be necessary to

control both these factors. In any case, the rate of growth of bubbles from dissolved air or the rate of redissolving is low and it would probably be necessary to work with flow velocities (and therefore heads) which are still lower than those made necessary by the Froude similitude conditions. This brief consideration of the problem shows that it is certainly very difficult to investigate gaseous diffusion with scale models. Besides, this phenomenon is not of interest when running cavitation tests and its elimination can be considered, since it is only stray effect. To do this, it would be necessary to remove all dissolved air and all air nuclei from the water, but this cannot be done since the critical vaporization pressure would be reduced to very small negative values, which it would be difficult to determine and which, in any case, have no connection with the critical pressure encountered in the water used in prototype turbines.

In practice it has been noticed that it is sufficient to reduce appreciably the amount of air dissolved in the water and to eliminate the largest air nuclei. It is thus possible to reduce gaseous diffusion adequately without any likelihood of delaying the onset of vaporization.

Critical Vaporization Pressure. Unlike the critical pressure for gaseous diffusion, this does not appear to depend upon the amount of air dissolved in the water but only upon the temperature of the water and upon the dimensions of the nuclei of gas which are already present in the water. This is what is shown by an investigation of the static equilibrium of a nucleus in terms of the initial mass of gas which it contains, of the surface tension, and of the vapor pressure. Thus, for a bubble of given dimensions, there is a critical pressure, under which the bubble is unstable and grows larger indefinitely.

An investigation of dynamic equilibrium shows that, if the pressure in the liquid varies very rapidly, the critical pressure may be different from the critical static pressure. However, for this to be true it is necessary that the duration of the pressure variations be of the same order of magnitude as the oscillation periods of the nuclei.

In prototype turbines, as well as in sufficiently large models, the time taken to pass through a low-pressure region is always large compared with the natural period of the nuclei and it can always be assumed that they actually pass through a series of static states of equilibrium as they traverse the pressure field.

As an example, consider the case of a Kaplan turbine with a 6-m-diam runner operating under an 18-m head together with two scale models of the same turbine, one of them being designed for tests under the Froude similitude conditions with, for example, a 500-mm-diam runner and consequently operating under a 1.50-m head, and the other designed for tests under the prototype head with a runner having a diameter of only 200 mm.

The times that a liquid particle takes to pass through the runner are as follows:

—in the prototype	12×10^{-2} sec
—in the 500-mm model	3.5×10^{-2} sec
—in the 200-mm model	0.4×10^{-2} sec

Furthermore, the natural periods of the nuclei are of the order of 10^{-4} sec (at least for nuclei having a critical pressure near the vapor pressure). It is thus seen that, both in the prototype and in the models, the time taken to traverse cavitation-sensitive regions is much greater than the natural period of the nuclei.

It is only in very small models, operated with a high test head, that the time taken to pass through the runner might be of the same order of magnitude as the natural period of the nuclei. In the authors' opinion this suggests that it is preferable to use sufficiently large models operated with heads that are not too high. Observing the Froude similitude conditions, often leads to low testing head.

Thus it would not seem that flow velocities themselves affect the critical vaporization pressure.

However, the selection of velocities for a cavitation test also sets the general level and the form of the pressure distribution in the model. Can such a pressure distribution affect the concentration and dimensions of the cavitation nuclei? It would seem that the answer is in the affirmative, and furthermore there is no difference between this problem and the one raised in connection with gaseous diffusion. Indeed, it can be assumed that if velocities and pressures are sufficiently low in the model and in the test stand it will be possible to increase the mass of air originally contained in the nuclei because of gaseous diffusion. In this way certain nuclei, which were originally very small and which would have had a critical pressure much less than the vapor pressure (or even a negative value), can be brought up to the mass at which the critical pressure is almost the same as the vapor pressure. On the other hand, nuclei containing gas, the mass of which was already rather large, will come into the field of gaseous diffusion and this is the problem that was raised in considering the critical pressure for gaseous diffusion.

It would seem that the following conclusions can be drawn in this connection:

1 Inadequate removal of gas from the water during cavitation tests with very low heads resulting from the application of Froude similitude conditions, might lead to a critical pressure which is too high linked with the fact that gaseous diffusion rather than vaporization then exists.

2 On the other hand, too intensive removal of gas is likely to delay cavitation and this illustrates the importance of suitably adjusting the concentration of dissolved air in the test stand; however, this is a problem which is obviously less acute when work is being done with test heads which have not been scaled down from those of the prototype.

Critical Pressure for Deterioration of Performance. Very often the cavitation threshold is defined by the point at which performance begins to deteriorate. In particular, with tests involving turbines or pumps, the critical sigma which is considered is the sigma at which the efficiency, output, or delivery begin to be affected for better or for worse by pressure reductions. At the moment when the performance characteristics are modified in this way, cavitation has already developed to a certain extent and generally takes the form of a pocket clinging to the vanes. The authors believe that it is essential to conform to the Froude similitude conditions if phenomena are to be reproduced correctly, since a section of the pressure distribution, which is not a point, is affected by cavitation, or in other words, the dimensions and shape of the pocket are not the same when Froude's number is varied. Unfortunately, the critical pressure at this stage is no longer the critical pressure of the free nuclei but rather the pressure in the cavitation pocket. Experiments have proved that the latter pressure is appreciably higher than the vapor pressure and this has lead certain people[4] to consider that the critical pressure must be particularly high in this instance. The authors are of the opinion that the pressure in the bubble, and consequently the critical pressure for the phenomenon, must be affected by the concentration of dissolved air.

The Effect of Scale on Local Pressure. ***The Effect of Pressure Fluctuations.*** It is not only the mean pressure which governs the onset of cavitation, but also fluctuations about this mean value.

Pressure fluctuations originate in:

1 Local turbulence. This cannot be properly scaled down and only Reynolds numbers in the model that are as high as possible should be used.

[4] Particularly Mr. Michel Hug, Ingénieur à la Direction des Etudes et Recherches d'E.D.F., to whom the authors are indebted for the comments made here.

2 Turbulence on a much greater scale such as that set up by vortexes released at draft-tube and diffuser outlets or by unstable-flow separation effects on fixed or rotating vanes in the machine. Such large-scale pressure fluctuations affect the whole pressure distribution in the machine. They should not be neglected, and the problem arises of reproducing them as well as possible in scale-model experiments. This necessitates exact geometrical reproduction of turbine draft tubes and pump diffusers as well as any open surfaces at the outlets of such machines. Similarly, in the case of small-scale turbulence there is a minimum Reynolds number below which phenomena of this kind are reproduced badly.

The Effect of Geometrical Discrepancies. However carefully models and prototypes are made, it is impossible to assert that one is an accurate geometrical reproduction of the other. This is particularly true where surface roughness and waviness are concerned. A localized defect can set up a region of low pressure which is proportional to the kinetic head there.

The objective that has to be attained as far as the prototype is concerned, is not only to be certain that the localized pressure at all points is greater than the critical pressure, but also to maintain a "pressure margin" which is proportional to the kinetic head, in the region likely to experience cavitation. This safety margin is often characterized by a coefficient ϵ which expresses the ratio between the local kinetic head and the local static head. The critical value of ϵ, below which values should not go, obviously depends upon the nature of the surface and its finish.

When transposing from the model to the prototype, allowance should be made for the critical values of ϵ which are generally not the same. This should be a reason for prohibiting the use of very small models on which it is very difficult to reproduce relative roughness satisfactorily.

The Effect of Fluid Friction. The fact that one cannot reproduce hydraulic frictional forces exactly on the model under similitude conditions causes efficiency to be subjected to a scale effect which is corrected by partially or totally empirical formulas. The scale effect mentioned here also acts on all velocities and pressures in the machine and thus affects the cavitation threshold.

One might consider establishing a relationship between the efficiency discrepancy using the formulas referred to earlier, for instance, and the sigma discrepancy which is to be expected in the full-scale machine. In fact, knowing the discrepancy between the efficiencies is not enough, one must also know how it is distributed over the various parts of the machine. Information on this subject is given in certain theories which have been advanced in connection with the efficiency transposition formulas, but the assumptions on which they are based have not yet been adequately tested by experiments. The resulting uncertainty concerning the correction that has to be made to the critical sigma is often rather great as is shown by the following example.

Let us consider a Kaplan turbine operated under a 16-m head whose efficiency for the nominal rating is 88 per cent on the model and 92.5 per cent on the prototype.

If it is desired to determine the critical sigma by means of model tests, it is necessary, before determining the co-ordinates on the hill chart for the model, to increase the prototype head nominally by multiplying it by 92.5/88, since, as a first approximation, it can be assumed that the increase in efficiency in the prototype may be represented by a corresponding increase of the net head on the runner.

In the extreme case when only the losses in the scroll case and the distributor are involved in the scale effect, the suction head on the runner would be the actual geometrical suction height in the prototype. In the opposite extreme case, when the scale effect is only explainable by the energy-loss difference in the draft tube, the geometrical suction head would have to be increased by the nominal increase in head. The following figures are obtained by applying these considerations to actual laboratory results:

Suction head calculated without allowing for scale effects: (−2.80 m).

Suction head calculated making the first assumption (gain at inlet only): −1.70 m.

Suction head calculated making the second assumption (gain in draft tube only): −2.50 m.

These figures, which refer to a case that is by no means exceptional, show the extent to which the localization of the scale effects causes great uncertainty as to the critical suction heads. Of course, cavitation can always be avoided by making the most unfavorable assumption; i.e., that there is a gain only in the draft tube.

In order to be able to draw sufficiently accurate conclusions from a cavitation test, it is essential that it be carried out with such length and head scales that the effect of scale on efficiency remains reasonably small. Furthermore, corrections, as defined earlier, are only valid if the effect that scale has on tangential forces, does not result in complete deformation of the velocity and pressure fields.

Likewise it is felt that it is preferable not to use models which are too small, even with adequate Reynolds numbers, since the effect of scale on efficiency is then probably affected by roughness and is therefore harder to determine.

Conclusion

In the foregoing discussion some of the precautions have been described that have to be taken to obtain a correct representation of the pressure field in a cavitation model and to be certain of the critical pressure that has to be used.

It has been seen that, where the total height of the prototype cannot be neglected, the length and head scales ought to be connected by the Froude similitude conditions. It has also been seen that, for various reasons which agree with each other, it is necessary not to go below a minimum Reynolds number and also not to use a model of which the absolute dimensions are too small. Likewise the reasons have been shown why special precautions have to be taken concerning the concentration of air dissolved in the water, especially when one is working with low heads and pressures.

A practical result of these rules when considering large low-head turbines is that setting minimum Reynolds numbers makes for much larger models than operating with less scaled-down test heads. This, by the way, is one of the practical drawbacks of the Froude similitude conditions which, in most instances, make it necessary to build more expensive models.

Returning now to the general considerations at the beginning, it must be asked what cavitation effects can be suitably reproduced using the Froude similitude conditions and the Thoma criterion.

The threshold of incipient cavitation, which is detected by the visual or acoustic effects of cavitation bubbles, can be satisfactorily represented provided the pressure field is reproduced suitably and provided the corresponding critical pressure can be determined sufficiently accurately.

The point at which performance begins to deteriorate can be reproduced on the model as long as suitable similitude conditions are also used here for the pressure field and as long as the critical pressure at which performance begins to deteriorate is known. There is no reason why the latter pressure should not be different from the vapor pressure.

However, it would seem that, at the present stage in research, the idea of suitably representing the first onset of pitting should be abandoned. Research on this point, especially work done in the United States, shows that the absolute velocity has a very de-

cided effect, and various authors recommend that prototype velocities be used for tests concerning the onset of pitting. Obviously in certain instances this is incompatible with being able to reproduce the pressure field correctly and it is for this reason that it will probably be necessary to give up the idea of investigating erosion directly on scale models of machines or hydraulic structures.

If, as has been said, a model cannot provide data on the intensity or rapidity of pitting, it can at least, so long as the precautions described in this paper have been taken, give complete information on the location and extent of regions likely to be affected by cavitation and can, for example, thus indicate regions which ought to be protected by prewelding with stainless steel.

It may be asked why it is not enough to simulate the pressure field and the critical pressures exactly when attempting to formulate pitting similitude conditions. In the authors' opinion this is simply due to the fact that, when pitting begins, the cavitation threshold has already been passed. Strictly speaking it is practically impossible to create the similitude conditions for developed cavitation. Surface tension, the thermodynamic properties of gases, water, and water vapor have to be taken into account, and that is practically impossible. The rate of pitting is connected both with the energy involved in the collapse of the cavitation nuclei and with the frequency at which they collapse near the walls. A much clearer explanation of the preponderating influence of absolute velocities, as observed in the experiments mentioned earlier, would probably result from analyzing both these factors.

Bibliography

P. Eisenberg, "Modern Developments in the Mechanics of Cavitation," *Applied Mechanics Reviews*, vol. 10, March, 1957, pp. 85–89.

"Cavitation in Hydrodynamics," Proceedings of the First International Symposium on Cavitation in Hydrodynamics, Teddington, England, 1955, particularly the following papers:

P. Eisenberg, "A Critical Review of Recent Progress in Cavitation Research."

J. W. Daily and V. E. Johnson, Jr., "Turbulence and Boundary-Layer Effects on Cavitation Inception From Gas Nuclei," TRANS. ASME, vol. 78, 1956, pp. 1695–1706.

M. Strasberg, "Undissolved-Air Cavities as Cavitation Nuclei."

H. Gerber, "Some Reflections on Modern Scale Formulas for Cavitation Phenomena."

R. N. Cox and W. A. Clayden, "Air Entrainment at the Rear of a Steady Cavity."

F. Numachi, "Effect of Static Pressure Differences on the Cavitation Characteristics of Hydrofoil Profiles."

R. T. Knapp, "Further Studies of the Mechanics and Damage Potential of Fixed-Type Cavities."

R. T. Knapp, "Cavitation Scale Effect," Proceedings of the Seventh General Meeting, 1957, of the International Association for Hydraulic Research, Section I. (See also: Section II, papers on subject "B" and section III: Cavitation discussion.)

R. T. Knapp, "Cavitation and Nuclei," TRANS. ASME, vol. 80, 1958, pp. 1315–1324.

R. T. Knapp, "Accelerated Field Tests of Cavitation Intensity," TRANS. ASME, vol. 80, 1958, pp. 91–102.

A. T. Ellis, "Observations on Cavitation Bubble Collapse," California Institute of Technology, Hydrodynamics Laboratory, Report No. 21–12.

R. W. Kermeen, J. T. McGraw, and B. R. Parkin, "Mechanism of Cavitation Inception and the Related Scale-Effects Problem," TRANS. ASME, vol. 77, 1955, pp. 533–541.

J. W. Daily and V. E. Johnson, Jr., "Turbulence and Boundary-Layer Effects on the Inception of Cavitation From Gas Nuclei," Massachusetts Institute of Technology, Hydrodynamics Laboratory, Technical Report No. 21, July, 1955.

F. A. L. Winternits, "Cavitation in Turbomachines," *Water Power*, September, October, November, 1957.

K. S. Iyengar and E. G. Richardson, "The Role of Cavitation Nuclei," Mechanical Engineering Research Laboratory, East Kilbride, Glasgow, Scotland, Fluid Report No. 57.

DISCUSSION

David B. Benson[5]

Current hydraulic turbine practice is to avoid the presence of cavitation as completely as economics permits. As a result, the industry should be concerned with similitude laws for the inception of cavitation as well as similitude laws for advanced stages of cavitation.

The authors discuss briefly the fact that time affects the inception of cavitation, but they do not develop any scaling laws for the effect. The rate at which a nucleus can grow to a finite size is controlled not only by its initial physical size and shape but also by the thermodynamic properties of the liquid and by the magnitude and duration of the reduced pressure to which it is exposed. It may be assumed that a nucleus must be subjected to an average pressure $\overline{\Delta p}$ below the critical pressure for an interval of time t to grow and become unstable. If it is supposed that the liquid for the model and prototype has the same properties, and the nuclei present are the same size and shape, then we have

$$\overline{\Delta p}_p t_p = \overline{\Delta p}_m t_m$$

where the subscripts p and m denote prototype and model, respectively.

Ignoring Froude and Reynolds similitude, the usual model scaling laws are based on equal Euler numbers for prototype and model. Equal Euler numbers result from kinematic and geometric similarity and similarity of pressure and inertia forces only. From the condition of equal Euler numbers,

$$\frac{t_p \sqrt{\Delta p_p}}{L_p} = \frac{t_m \sqrt{\Delta p_m}}{L_m}$$

where L is a characteristic length. Letting

$$\frac{\overline{\Delta p}_p}{\overline{\Delta p}_m} = \frac{\Delta p_p}{\Delta p_m} = \Delta p_r = H_r$$

where H_r is the head ratio, and letting

$$\frac{L_p}{L_m} = L_r$$

where L_r is the scale ratio, then, from the preceding equations,

$$L_r \sqrt{H_r} = 1$$

If Froude similitude and time effects on inception are ignored, and only Euler and Reynolds similitude are considered, the relation between head and length ratios using water as the model fluid can also be shown to be

$$L_r \sqrt{H_r} = 1$$

From this, it is seen that the scaling law for Euler similitude and an assumed similarity of time effects on cavitation inception are the same as those for Reynolds and Euler similitude. However, when using water as a model fluid, it is not generally feasible to apply Reynolds similitude to the testing of hydraulic turbine models, and equally impractical to apply the derived time similitude on cavitation inception, due to the high model heads involved.

It is possible, at least in theory, to satisfy Reynolds, Froude, and Euler similarity requirements together by the use of a model

[5] Engineer, Hydraulic Department, Industrial Products Division, Newport News Shipbuilding and Dry Dock Company, Newport News, Va.

fluid other than water. Then the length and head ratios can be shown to be related by

$$L_r = H_r = \nu_r^{2/3}$$

with the previously assumed time similitude for cavitation inception adding the requirement

$$\rho_r \nu_r^2 = 1$$

where ρ_r is the density ratio and ν_r is the ratio of kinematic viscosities.

In view of the impracticability of applying Reynolds and Euler similitude when water is used as a model fluid, and the fact that the point of cavitation inception may be located, thereby satisfying Froude requirements, the selection of length and head ratios remains merely an opinion based on convenience of testing. Thus while researchers are debating the merits of their opinions, the attention of industry might well be directed to the search for a liquid to satisfy all the requirements of testing hydraulic turbine models.

G. Dugan Johnson[6]

The writer deeply appreciates this opportunity to present a prepared discussion on the authors' most unusual conception of the importance of adhering to Froude similitude in the cavitation testing of hydraulic turbine models. The cavitation phase of laboratory model tests was not included in our 1956 ASME Symposium,[7] but it appears that a session devoted specifically to this subject would prove also to be extremely interesting and valuable for users as well as for manufacturers of hydraulic turbines.

The writer is employed by a manufacturing company that has spent (and is continuing to spend) large sums of money to build and remodel laboratory facilities to permit testing turbine models under heads equal to (or closely approximating) those under which the prototype machines will operate. Obviously, we are in almost complete disagreement with most of the authors' major hypotheses and conclusions . . . . for reasons which we will now proceed to outline.

Actually, the authors themselves have admitted many of the practical disadvantages of applying the Froude similitude criterion to scale model tests of hydraulic turbines, including the very low test heads requiring high vacua at low sigma values and the resulting diffusion of air from the water throughout the model, which interferes with both the performance and the cavitation phenomena. This makes it necessary to attempt to regulate the air content of the water in such a way as to minimize diffusion without affecting either the normal performance or the cavitation "fluid mechanics." However, they insist that Froude similitude is sufficiently important to justify the seemingly unconquerable inherent difficulties and the potential inaccuracies resulting therefrom.

The authors credit Dr. Dieter Thoma with the original statement that the Froude number as well as the sigma value must be equal for the model and the prototype. But it certainly is interesting to note that Thoma, in his own tests, used prototype heads and completely disregarded Froude's law. . . . according to Dr. Hans Gerber.[8] Apparently, Thoma himself realized the impracticability of attempting to adhere to Froude similitude. . . . even if it is theoretically desirable.

This deviation was justified by the fact that, as Dr. Robert T. Knapp[9] pointed out, the only way to eliminate completely all scale effects is to test the full-size prototype itself under actual field conditions. Consequently, as the authors state, the choice of model similitude laws and experimental techniques should be such as to reproduce with a reasonable degree of accuracy the particular phenomena being investigated.

On this basis, our company has elected[10] to test models (with a runner discharge diameter of 12 in.) completely homologous to their respective prototypes under conditions duplicating or approximating those under which the prototype units will operate, including pressure and suction heads, water temperature, and natural air content. By the authors' own admission, this approach has the significant advantages that the air content problem is "obviously less acute" and any "error concerning the critical pressure . . . . can often be neglected."

It is our opinion, based upon almost thirty years of cavitation testing experience, that Froude similitude is not required for satisfactory model cavitation tests and that it should be disregarded completely. Theoretical potential errors can be minimized to the point where they may be classified as minor scale effects, smaller in magnitude than customary commercial "safety" margins. Since flow conditions through the larger prototype runners must be better than with prototype water velocities in the 12-in. diameter model runners, our prototype application margins automatically contain indeterminate "extra" amounts of safety.

We also take issue with the authors' statement that "the fundamental consideration is to *avoid* cavitation." We agree that, when plant sigma drops below the *critical* sigma for any head and load, cavitation, vibration, and loss of output may result. However, we determine *critical* sigma for the model as the value corresponding to a loss in output of 1 per cent, well within the margin between the "expected" and "guaranteed" performance of prototype units.

In our opinion, the authors' "threshold of incipient cavitation, which is detected by the visual or acoustic effects of cavitation bubbles" has little, if any, practical significance, especially since it "has already been passed . . . . when pitting begins." Our experience indicates that limited amounts of localized pitting will occur in prototype turbines during the first year of operation even though they are operated above *critical* sigma values 100 per cent of the time. Reasonable quantities of metal removal are allowed in the various contracts and the areas to be protected with stainless steel prewelding or inserts are determined with sufficient accuracy from previous prototype experience on similar designs. Consequently, we do agree with the authors' conclusion that "it will probably be necessary to give up the idea of investigating erosion (pitting) directly on scale models."

Fig. 3 of this discussion is an illustration of the accuracy and control attainable during cavitation tests under relatively high test heads, even at very low sigma values. Note the smooth curves obtained for unit output, discharge, and efficiency versus sigma. Although a critical sigma of 0.050 is indicated, operation at the very low sigma of 0.007 resulted in a total loss in output of only 7 per cent and an efficiency drop of only 4 per cent.

Now, let us examine the authors' attempted proof of the theoretical significance of maintaining Froude similitude between model and prototype. Although their equations (1) to (4) and Figs. 1 and 2 are essentially correct, they are misleading and con-

[6] Chief Hydraulic Engineer, Hydraulic Division, Allis-Chalmer Mfg. Co., York, Pa. Mem. ASME.

[7] "Symposium on Laboratory Testing of Hydraulic Turbine Models in Relation to Field Performance," TRANS. ASME, 1958, pp. 1525–1543.

[8] H. Gerber, "Some Reflections on Model Scale Formulae for Cavitation Phenomena," Proceedings of a Symposium on Cavitation in Hydrodynamics published in 1956 by the National Physical Laboratory, Teddington (Middlesex), England (11 p. 1–11 p. 13).

[9] R. T. Knapp, "Cavitation Scale Effect," Proceedings of the Seventh General Meeting (1957) of The International Association for Hydraulic Research.

[10] W. G. Whippen and G. D. Johnson, "A High Head Cavitation Test Stand for Hydraulic Turbines," *Journal of the Hydraulics Division*, ASCE Proc. Paper 1201.

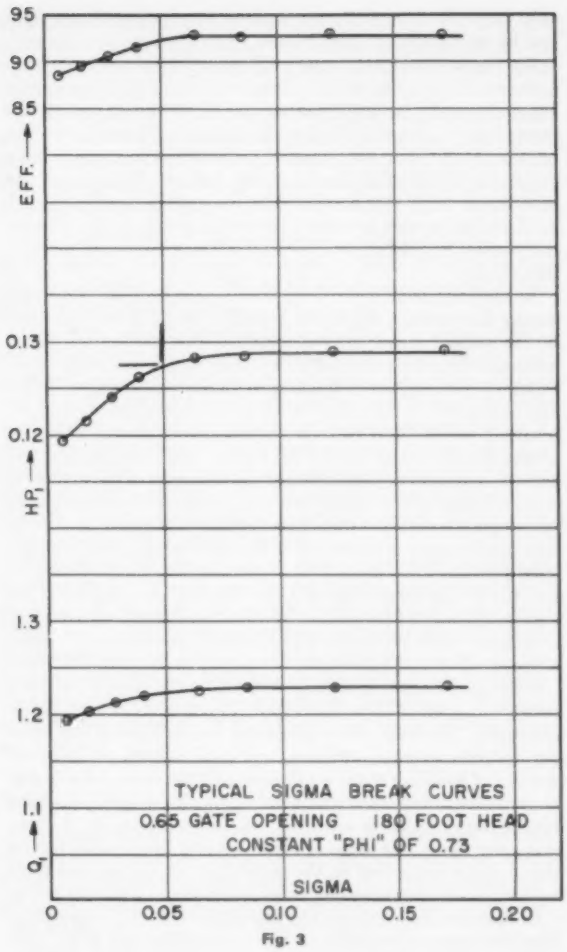

Fig. 3

fusing. We agree that "it is convenient to divide height of water columns by the head" but we can see neither convenience nor justification for dividing "elevations by the diameter of the runner." This results merely in the substitution for z of $Z = z/D$, a ratio which is more confusing than convenient . . . . but does serve the authors' purpose of introducing the Froude similitude ratio of D/H (or H/D).

Figs. 1 and 2 can be redrawn to demonstrate more clearly the discrepancy in elevation between the reference used for H, and sigma and the location where cavitation first becomes critical (as sigma decreases) by using z as the *vertical* (elevation) ordinate in place of $Z = z/D$ for the authors' *horizontal* ordinate. Moreover, this obvious discrepancy is not as significant as stated by the authors. For example, using the elevation of the axes of the blade trunnions in a large Kaplan turbine as the reference elevation for H, results in a maximum possible "unsafe" discrepancy of only about 2.5 ft (instead of the 6.5 ft given by the authors for the total blade height) and this is less than the margin of safety applied to the model test results in establishing prototype operating limits.

We trust that these comments will help to clarify the authors' presentation of the Froude similitude problem. In view of the obvious difficulties and uncertainties associated with Froude similitude testing of hydraulic turbine models, it is difficult to understand why the authors persist in this impractical approach to the cavitation problem. To our knowledge, the new Electricité de France laboratory at Chatou near Paris is the only organization in the world that shares their approach to this problem. The high vacuum required for a low sigma value causes air to come out of solution even on the "high-pressure" side of the model, and the only way to combat this effectively is to reduce the air content almost to zero, thereby introducing potential inaccuracies of major magnitude in relation to the very low test heads utilized.

Even Thoma dispensed with Froude similitude in his classic work, presumably because the resulting inaccuracies would have voided its significance. It appears that we agree with Thoma in this respect and also with the authors, who have pointed out the almost insurmountable difficulties of Froude similitude testing whereas prototype head tests are straightforward, accurate, and conservative. However, we are unable to understand the authors' persistence in the face of the unreasonable difficulties involved, especially since there is no practical necessity for maintaining Froude similitude in model tests of this type of equipment.

F. Numachi[11]

The paper is very timely, for it focuses attention on a problem that is relatively new in the cavitation tests and offers many fundamental factors which are to be investigated in the future concerning the length and head scale for cavitation tests.

The authors' justification for using Froude's similitude when determining the cavitation inception is based upon the following hypothesis:

$$\sigma_m = f(Z \text{ only}) \text{ i.e. } \left(\frac{h - h_r}{H}\right)_m = f(Z \text{ only}) \qquad (5)$$

But it is considered that the cavitation number at inception depends also on the head H,[12] the cavitation nuclei grow up in the boundary layer[13] and, consequently, the cavitation number at inception naturally depends upon Reynolds number.[14] So it is desirable that the ground for assuming the relation expressed in Equation (5) should be explained.

The authors' opinion concerning the critical pressure for deterioration of performance is also open to the same question. It is experimentally known that the deterioration of hydrofoil characteristics vary more or less according to the head H.[11]

Generally speaking, conditions for cavitation-inception and performance-deterioration ought to be considered to depend on the laws given by Thoma, Reynolds, Froude, and Weber. But, since it is practically impossible to have model tests that satisfy all those laws, it is understood that importance is attached to Thoma coefficient alone.

It is desirable that experimental or theoretical ground should be represented to make the opinion acceptable that, contrary to the above, attaches special importance to Froude's law alone excluding all others.

The authors state in their conclusion: "It is necessary not to go below a minimum Reynolds number (let us call it as $R_{min.}$ say) and also not to use a model of too small dimension ($Z_{min.}$ say), and to take precaution concerning the concentration ($C_{min.}$ say) of air dissolved in the water." But what designers of hydraulic machinery want to know seems to lie in the results of series-experiments concerning the concrete values of R_{min}, Z_{min}, and C_{min}.

[11] Director, Institute of High Speed Mechanics, Tōhoku University, Sendai, Japan. Mem. ASME.

[12] F. Numachi, "Effect of Static Pressure Differences on Cavitation Characteristics of Hydrofoil Profile (Report 2)," Proc. of Symposium on Cavitation in Hydrodynamics, N. P. L., 1955, p. 17–1/14.

[13] J. W. Daily and V. E. Johnson, "Turbulence and Boundary-Layer Effects on Cavitation Inception From Gas Nuclei," TRANS. ASME, vol. 78, 1956, p. 1695.

[14] R. W. Kermeen, J. T. McGraw, and B. R. Parkin, "Mechanism of Cavitation Inception and the Related Scale-Effects Problem," TRANS. ASME, vol. 77, 1955, p. 533.

Wm. J. Rheingans[15]

The authors have presented an interesting theoretical analysis of scale effects on model cavitation testing. The subject of Froude scaling is somewhat controversial and requires further study.

One method of determining the effect of a disregard of Froude similitude conditions on incipient cavitation, and on the point at which performance begins to deteriorate, would be by model testing. Many of the present-day model test laboratories are so arranged and equipped that cavitation tests can be made under heads varying from 10 to 100 ft or more without changing the dimensions of the model.

Tests of this nature were conducted in the test laboratory with which the writer is connected. They showed that there was very little variation of the point at which performance begins to deteriorate as the head was varied over wide limits. This is an indication that Froude scaling has very little influence on this phenomenon. However, no observations on incipient cavitation were made under these conditions.

It would not be very difficult or costly to make a careful series of tests to determine the actual effect of Froude scaling on the incipient cavitation, its location, and on the point at which performance begins to deteriorate. Such tests would go a long way toward settling the controversy regarding Froude scaling, which up to now has been based upon theoretical considerations combined with suppositions and assumptions.

The author is, I believe, correct in his statement that, as far as actual pitting damage is concerned, actual velocity and, as a consequence, the head under which the model is tested, is of importance. However, this also involves the type of material used in the model. It is generally accepted that a model test of this type is not a very satisfactory means for measuring actual pitting damage, where the model would have to be operated for 6 months to a year or even more to obtain results comparable to field performance.

R. B. Willi[16]

Unquestionably the variation in conditions under which a prototype turbine operates, as compared to those under which a model test must be run, does have an effect on the pattern of cavitation. From a scientific standpoint the ability to evaluate these variables accurately represents a desirable goal. This paper may leave a question in many minds, however, as to the adequacy and dependability of present day model testing. Primarily the question resolves as to the magnitude of error introduced by variation in Froude number, air content, friction head, etc. Since it could not be resolved theoretically, an empirical approach was necessary, which involved the comparison of model and field performance. We cannot take the position that such comparisons, made with a particular laboratory, are equally applicable to all other laboratories operating with different model sizes and heads. The pooling of such information from various laboratories could very well establish a trend, however, that might in a reverse manner assist in developing the theory.

With this thought in mind, the experience with one laboratory over a twenty-year period may be of interest. In all cases model runner throat diameter has been 11 inches. Each model, as installed in the test flume, is homologous to the prototype including casing and draft tube. With such an installation, efficiency versus horsepower and sigma tests are run off consecutively in a single setup. Sigma tests have been run under heads from 25 to 60 ft on both Francis and propeller turbines. Cavitation has been determined both by observation under stroboscopic light and by impairment of performance, sigma being varied by control of the pressure level in a closed flume. Critical sigma has been assumed as that value where a sharp reduction in power occurs or the similar point in the efficiency curve if this should precede the power break. These have been selected as a reference in preference to the break in the quantity curve which frequently lacks the sharp definition of the other two values. No attempt has been made to provide a sufficiently low setting to eliminate all local cavitation such as might exist at the periphery of a Kaplan wheel when at a steep pitch, such areas being protected by stainless overlay.

In applying critical sigma to the prototype at the start, not having any background on the effects of the variables discussed in the subject paper, it was reasoned that draft tube regain represented a relatively small proportion of total head on medium to high head turbines of the Francis type. Sigmas were, therefore, compared at the elevation of the bottom of the buckets, allowing a margin of 3 to 5 ft. In propeller turbines involving greater kinetic energy in the draft tube, additional margin was provided. Sigma was compared at the centerline of the blades for a given horsepower stepped from model to prototype rather than the stepped quantity. On a large turbine this would provide an additional margin of 5 to 6 ft over the nominal margin allowance. This would be made up to 3 ft in elevation from the blade centerline to the discharge edge and another 3 ft resulting from the higher efficiency of the prototype with the consequent reduction in quantity when producing a given stepped horsepower at which a measured critical sigma had been obtained on the model test.

Some one-hundred installations and 20 years later we are in a reasonably good position to evaluate the adequacy of our original approach. Allowing, in our judgment, for variables in loading of the turbines, average tailwater, and such factors, we find our method of handling sigma on Francis turbines to be reliable and on propeller turbines the additional margin is evident in the local pitting pattern that is observed. In other words, for a given operating sigma, the relative area, showing local cavitation on the model, exceeds that on the prototype. In no case has more severe pitting been noted on either a Francis or propeller prototype than would be indicated by model observation. Oppositely, those few cases, where units are operated deliberately at full gate and maximum head, exceeding guarantees for reasons peculiar to their particular installations, show appreciable pitting.

No effect has been noted in critical sigma from head variations within the limits of the test flume. Moderate admission of fine air bubbles makes no change nor does the deaerating of the test water through days of use without replacement. Variations in temperature and barometer cause no scattering when resolved to a standard temperature, pressure, and density. We can only conclude in our particular case that remaining variations, uncorrected for, are of a low order of magnitude.

George F. Wislicenus[17]

The authors have presented a valuable discussion of various considerations applying to model testing of large hydrodynamic machinery. They arrive at the conclusion that Froude's law of similarity should be observed in addition to other pertinent similarity considerations, particularly those with respect to cavitation. Their reasons for this conclusion are the following:

1 The vertical variations of the point of minimum pressure within the machine are a significant percentage of the total suction head of the machine.

2 With Froude scaling, characteristic times during which

[15] Assistant General Manager, Hydraulic Division, Allis-Chalmers Manufacturing Co., York, Pa. Mem. ASME.

[16] Manager of Engineering, Eddystone Division, Baldwin-Lima-Hamilton Corporation, Philadelphia, Pa. Mem. ASME.

[17] Director, Garfield Thomas Water Tunnel, Ordnance Research Laboratory, Pennsylvania State University, University Park, Pa. Fellow ASME.

fluid particles are in the low pressure zone change only with the square root of the scale ratio of linear dimensions, in contrast to the first power in cases where the model operates under full head and velocity conditions.

3 In order to avoid interference with other scale effects such as Reynolds' number effects, it is necessary to use fairly large model dimensions for Froude scaling, thereby minimizing problems arising from the lack of geometric similarity between the prototype and the model.

The reasons quoted before appear to be quite convincing. Yet there appears to exist some controversy as to whether or not Froude scaling for large hydrodynamic machines is really the best way to relate model to full scale performance.

This writer cannot quite understand this controversy. Obviously a laboratory or company is fortunate if it can build and test models of sufficient dimensions to permit Froude scaling without undue sacrifices in Reynolds number or other less definable aspects of similarity. At the same time, testing with smaller models is certainly preferable to no model testing at all. In addition, the laboratory with which this writer is connected has found it possible to produce models of hydrodynamic machines which are sufficiently accurate for precision cavitation testing with runner diameters between six and ten inches.

Furthermore, it seems strange that a laboratory capable of handling models of sufficient size for Froude scaling would not want to test the influence of other elements not included in Froude scaling by changing the head or linear velocities from those prescribed by Froude's law of similarity. After all, the authors recognize that much is as yet unknown about the scaling laws for cavitation, so that an opportunity should never be missed to check the validity of any model cavitation test in as many ways as possible.

Authors' Closure

Mr. David B. Benson states that a nucleus must be subjected to an average pressure Δp below the critical pressure for an interval of time t to grow and become unstable. He assumes that for a given liquid and for a given size of nucleus the under-pressure Δp is proportional to the reciprocal of time t.

This is not in contradiction with the authors' opinion. However, the "under pressure" Δp is certainly very small when the time t is large if compared with the "natural period" of the nucleus.

Mr. Benson has shown that if it was wanted to reduce Δp in the same ratio as the head, it would be necessary to increase the head, according to the relation $Lr\sqrt{Hr} = 1$, and this is generally not feasible.

The authors' opinion is that Δp is small on the prototype, and should be maintained as small as possible on the model, then being neglected; if Mr. Benson's relation were followed, i.e., if Δp were enlarged in the same ratio as the head, Δp_m would be high while its value would be rather uncertain.

The idea of searching for a liquid which would satisfy all the requirements of similitude is very attractive. Unfortunately, it has not yet led to any practical applications.

Not only the physical and thermodynamic properties should be adjusted, but also the "granulometry" of nuclei.

Mr. G. Dugan Johnson agrees with the authors' opinion that Dr. Thoma himself did not use Froude's similarity because of the practical difficulties it involves and in spite of its theoretical interest. However, since the time when Thoma and others started with cavitation research, some practical progress has been made. The inherent difficulties, even if "seemingly unconquerable," have been conquered and the potential inaccuracies avoided.

Mr. Johnson is of the opinion that Froude similitude should be disregarded completely. The authors on their side do not consider that Froude similitude has to be used in any case. For instance, when the total height of the prototype runner is rather small, Froude's number can be disregarded. Mr. Johnson would probably agree that it is questionable to neglect the influence of static pressure gradient in a horizontal shaft Kaplan turbine when the prototype runner diameter is about 18 ft, as is the case for the Rance tidal plant.

From Mr. Johnson's experience, localized pitting occurs in prototype turbines during the first years of operations, even if they are operated all the time above critical σ. This seems to be rather pessimistic, if compared with the authors' experience.

The amount of metal that will be removed by pitting in a given period of time could not be predicted by means of model tests only. On the other side, field experience may be insufficient when the project considered is new either from the point of view of hydraulic design, or size, or operating head. In those cases reference should be made to prototype experience as well as to model experience. For that purpose it may be useful to determine on the models not only the critical σ for loss of efficiency or output, but also the "incipient cavitation" critical σ. The authors' opinion is that Froude's similarity is helpful in that case, chiefly when the location of expected pitted areas has to be determined.

We do not agree with Mr. Johnson's suggestion of redrawing Figs. 1 and 2 with z instead of Z, since in that case the σ curve would not be unique: There would be one such curve for each particular value of H/D. A more complete explanation of the authors' computation is given in the answer to Professor Numachi's discussion.

To Mr. Johnson's knowledge the new Electricité de France laboratory at Chatou is the only organisation that is using Froude's law of similarity. This is not true: *Several* European manufacturers have recently built new laboratories where it is possible to run model tests in accordance with Froude's similarity, and are actually using them in that way in some cases.

Mr. Johnson writes that it is difficult for him to understand why the authors persist in their impractical approach to the cavitation problem. As a conclusion he repeats that he is unable to understand the authors' persistence in the face of the unreasonable difficulties involved. We are sure that Mr. Johnson would have been able to understand the authors' opinion, if they had insisted enough on the fact that the practical difficulties involved in Froude's similarity have been solved for many years in their own laboratories, as well as in some other European ones.

Prof. F. Numachi points out that σ_m and $\left(\frac{h - h_r}{H}\right)_m$ depend not only on reduced elevation but also on H, Reynolds number, and Weber number. We are in agreement with this opinion, which leads us to clarify and complete our discussion of scale effects in cavitation tests:

(a) The parameter σ in equation (2) can be considered as the "velocity pressure coefficient." As a result, from dimensional analysis it can be considered as a function of:

—The position of the point on the blade surface, then of the "reduced co-ordinates" Z (as defined in the paper) and $x = r/D$, r being the radial distance to the center line of the machine.

—Reynolds number R.

—Rugosity of the model.

For given Z, R, and rugosity, there exists a value of $x = r/D$ for which σ is a maximum (σ_m). It is practically impossible to run model tests with Reynolds numbers as high as they are on the prototype. Then the pressure field on the model is affected by some scale effect, as has been mentioned by the authors. As high as possible Reynolds numbers should be adhered to on the model, in order to reduce this scale effect. When comparing models of equal Reynolds numbers, but of different sizes, preference should be given to the larger model, because the distortion

of rugosity can be less in that case. However, it can be thought of using "large" models with high testing heads (then disregarding Froude's law) in order to reach the highest possible Reynolds number: This is discussed in the authors' answer to Mr. Rheingans.

(*b*) The critical pressure h_{cr} depends chiefly on Weber numbers, as well as on some other physical properties of the fluid. Weber numbers are to be expressed in terms of nuclei. Since the same fluid is used on both model and prototype, the critical pressure depends chiefly on the size of nuclei. As a matter of fact, there may exist, in natural water as well as in laboratory water, nuclei of different sizes. The larger ones do not result in cavitation, but in gaseous diffusion, which should as far as possible be avoided. The very small ones can produce actual cavitation, but their critical pressure is much smaller than vapor pressure. Let us call "mean size" nuclei the nuclei for which cavitation critical pressure is close to the value of vapor tension. Such mean size nuclei normally exist in both natural and laboratory water. There are at least two possible origins of them in laboratory water:

(i) Smaller nuclei can be grown up to the required size, due to pressure reduction.
(ii) Gas nuclei adsorbed at solid boundaries.

Reducing the pressure of laboratory water could then result in increased gaseous diffusion,[18] but not in altered critical pressure for incipient cavitation, which is never far from vapor tension.

Professor Numachi wishes to know the minimum Reynolds number, minimum dimension, and minimum air-content which should be recommended.

A precise answer concerning the minimum Reynolds number can be given for Kaplan turbines; tests have been run with models of 150, 300, and 500-mm runner diameter, and varying testing heads. From the results of those tests, it appears that when the Reynolds number is less than about 2,500,000,[19] turbine operation becomes unstable, while efficiency, instead of varying slowly and progressively, drops rather suddenly with decreasing Reynolds number.

No such effect has been observed with Francis turbines, maybe because low enough Reynolds numbers have not been reached.

Minimum size for a Kaplan model normally results from the Reynolds condition when Froude's similarity is to be applied. When Froude's similarity is disregarded the model can be smaller since the testing head can be larger. However, it has been observed that it is very difficult to obtain accurate results from 150-mm diameter models; this is probably due to the influence of surface rugosity and, above all, to the influence of the clearance between runner tip and runner ring. For the same reasons (rugosity and tip clearance influences), the authors are of the opinion that the size of Francis models should not be less than about 200-mm runner diameter.

With respect to the air content C_{min}, the authors can give the following information; the amount of air dissolved in water of their own cavitation circuits is normally reduced to about $^1/_{10}$ of the saturation content under atmospheric pressure. With such conditions gaseous diffusion is limited enough in the models, while no delay in cavitation is observed. It is not known whether a smaller air content could result in reduced critical pressure, i.e., in "delayed cavitation." Anyway the critical minimum air content must depend on many factors such as the amount of solid impurities and surface roughness.

Mr. Wm. J. Rheingans' suggestion of varying testing heads to study the influence of Froude's parameter is of primary interest. This has been done by the authors as well as by other investigators.

Mr. Beaufrère, an engineer of Electricité de France, has observed on a model of a horizontal shaft bulk unit that the influence of testing head, i.e., of the Froude parameter, is quite significant.[20] Same results were obtained by the authors in their own laboratory; with vertical shaft machines the influence of the Froude parameter is small when there exists a small, localized zone of low pressure along the blades, which is sometimes the case. Anyway, to observe the influence of testing head, or of the Froude number, it is necessary to make it vary over a wide range seeing that, as can be deduced from the authors' computations, σ_{cr} does not vary with the ratio H/D when it is either very large or very small.

The authors agree with Mr. Rheingans' opinion about the interest of systematic tests on the influence of testing head. The possible range of heads in their Grenoble Laboratory extends from 0 to 65 ft, while it is large in the Electricité de France laboratory. However, to run really systematic experiments it is necessary to test many runners of different design since, as explained previously, these may affect very much the influence of Froude number.

Mr. R. B. Willi suggests that information concerning the comparison of laboratory results with prototype performance should be pooled in order to help in developing the theory. He starts at once to apply this very good idea of giving an interesting "digest" of the valuable experience gained in his own laboratory. The authors would like to mention that pooling field and laboratories comparisons has been started for some years in France under the leadership of the "Société Hydrotechnique de France." We must be grateful to Mr. Willi not only for his contribution, but also for the opportunity he gives of suggesting some exchange of experimental results between American and French specialists. In spite of the rather theoretical aspect of their contribution, the authors were thinking of such co-operation when writing the paper.

Mr. George F. Wislicenus writes that a small model is better than no model at all. The authors agree with him: Froude similarity and large models must not be a religion. Many of the tests which are run in the authors' laboratory do not conform to Froude's law of similarity. It is the case when the size of available models is not large enough, or when it is wanted to increase the Reynolds number, or where it can be predicted that the height of the cavitation zone is small.

Mr. Wislicenus, as Mr. Rheingans did, suggested that the testing head should be varied, in order to study the influence of it. An answer to this has already been given.

Conclusion

The authors are very grateful to the contributors of discussions. It appears from these discussions that the paper was perhaps written in too dogmatic a manner; it has never been our opinion that Froude similarity would be a kind of a "panacea," the use of which would solve all the problems involved. However, the Froude law seems to have been rather generally forgotten for a long time. Our aim was to call attention to it again, while showing that in some cases it leads to the proper way of scaling down the pressure field in a hydraulic machine.

[18] This can be at least partially avoided by removing or redissolving the largest nuclei, as has been mentioned in the paper.

[19] Reynolds number is expressed in terms of diameter D and peripheral velocity V of the runner: $R = \frac{\pi D^2 n}{60}$ (n = rotational speed, rpm).

[20] A thesis has been prepared by Mr. Beaufrère and will be published in the near future.

W. C. LEITH
Mechanical Research Engineer, Dominion Engineering Works, Montreal, Quebec, Canada. Mem. ASME

A. LLOYD THOMPSON
Associate Professor, Department of Mechanical Engineering, McGill University, Montreal, Quebec, Canada

Some Corrosion Effects in Accelerated Cavitation Damage[1]

The conjoint mechanical-chemical destruction of metals by accelerated cavitation in a magnetostriction apparatus indicates relative effects of the metal properties (hardness, metallurgical structure, corrosion-fatigue limit) and of the liquid characteristics (temperature, pressure, wettability) which have been confirmed by field experience in hydraulic turbines and in water-cooled diesel cylinder liners.

Cavitation can be described as a hydrodynamic phenomenon which relates to the formation and collapse of vapor bubbles in a flowing liquid. These bubbles form in regions where the local pressure is reduced below the vapor pressure at that temperature; and conversely, these bubbles start to collapse as soon as the local pressure increases above the vapor pressure.

Objective of Study

Additional experimental evidence will be presented on the role of corrosion attack in accelerated cavitation damage, with particular emphasis on the effects of the metal properties and the liquid characteristics which can be correlated to field experience in hydraulic turbines and diesel engines. In the past, most investigators have taken a test liquid of water at room temperature. This has been suitable for the usual hydraulic turbine However, recent studies related to diesel engines have confirmed the need for testing at operating conditions of temperature and pressure, as proposed by References [1][2] and [2]. The ASME standardized test as outlined in 1958 by Robinson, Holmes, and Leith [3], has been followed in this paper.

Ramsay [4] in 1912 first suggested that cavitation erosion was not mechanical erosion but electrolytic corrosion occurring at the strain-hardened indentations where cavitation bubbles had collapsed on the metal surface Fottinger [5] proposed in 1926 that the mechanical-destruction process in cavitation was predominant and any electrochemical effects were minor. Kerr [6] first reported in 1937 comparative results for most common metals in tap water and sea water. Poulter [7] reported that, when iron was eroded by cavitation in alcohol, particles of pure iron were produced, whereas in water, particles of iron hydroxide were produced. Novotny [8] published a comprehensive report in 1942 which gives much information on the general effects of surface tension, viscosity, gas content, and chemical solutions. Beeching [9] reported the definite occurrence of corrosion during accelerated cavitation and concluded that the corrosion attack accelerates the mechanical erosion. Evans [10] suggested that cavitation erosion is a conjoint action of mechanical-chemical effects. The film of oxide which would ordinarily stifle the initial rapid rate of corrosion is continually torn off by collapsing bubbles, and the chemical corrosion attack continues at the initial rapid rate instead of decreasing. Thus cavitation erosion is mechanical in the sense that oxidized material is being continually torn away but chemical in the sense that oxide continually re-forms. Frenkel [11] first suggested that the gases present in cavitation bubbles can have a chemical influence on the deformed metal after a collapsing bubble has indented the metal surface. Krenn [12] has proposed that cavitation erosion was an electrolytic action resulting from temperature gradients or flow of heat between metal parts submerged in an electrolyte. Various test liquids such as alkalis, acids, and oils were reported by Rheingans [13].

The formation of reactive unstable ions due to the dissociation of water by cavitation was proposed by Weyl and Marboe [14], and the formation of reactive free radicals at the instant of bubble collapse was proposed by Taylor [15]. The separation of the eroded and corroded materials in an accelerated cavitation test was reported by Wheeler [16], who concluded that the weight loss due to the chemical attack is numerically additive to the weight loss due to accelerated cavitation.

Accelerated Cavitation Apparatus

A schematic diagram of the magnetostriction apparatus for producing accelerated cavitation is shown in Fig. 1, for details see Reference [3]. The bubble pattern on the vibrating test button is shown in Fig. 2, which is a Fastax photo taken at 8000 frames per second. The star-shaped pattern of bubble formation confirms the presence of radial vibrations of the test button in addition to the forced resonant longitudinal vibrations of the nickel tube. The magnetostriction machine consists of a high-frequency oscillator which produces a resonant longitudinal vibration of a nickel tube by subjecting it to an alternating magnetic field. The nickel tube vibrates at 6500 cps and the test button has a total amplitude of 0.0034 in., peak to peak. The high-speed photographs were taken with a pyrex liquid container, but the diesel-engine tests had to be run in a stainless-steel pot of standard dimensions which could be pressurized safely.

Intensity of Cavitation Attack

Cavitation inception under measurable and reproducible conditions suitable for observation has been studied most successfully by Knapp [17], who correlated the measured history of an actual vapor bubble to the classical analysis of Rayleigh [18]. The collapse of a spherical bubble in an incompressible liquid was considered, assuming isothermal compression and neglecting viscosity and surface tension. The excellent agreement of the experimental results with the theoretical postulates confirmed that the kinetic energy of bubble collapse was absorbed elastically in the water and given back largely undiminished in the rebound effects. The intensity of cavitation attack at various flow velocities has been reported by Knapp [19]. Fig. 3 illustrates that the vibration amplitude in this study has an effect similar to flow velocity, since both vibration amplitude and flow velocity show a threshold value for the metal resistance, below which no metal is removed

[1] This paper is based on the PhD thesis of W. C. Leith, to be submitted to McGill University, in 1960. The experimental work was conducted at Dominion Engineering Works under the guidance of Dr. H. S. Van Patter, vice-president.

[2] Numbers in brackets designate References at end of paper.

Contributed by the Cavitation Subcommittee of the Hydraulic Division and presented at the Annual Meeting, Atlantic City, N. J., November 29–December 4, 1959, of The American Society of Mechanical Engineers.

Note: Statements and opinions advanced in papers are to be understood as individual expressions of their authors and not those of the Society. Manuscript received at ASME Headquarters, July 2, 1959. ASME Paper No. 59—A-52.

despite some plastic deformation, but above which the rate of metal removal increases rapidly with increased cavitation intensity.

Effect of Metal Properties

Many attempts have been made to correlate the resistance of a metal to cavitation erosion with some physical property such as tensile strength. One of the most useful results, which applies only to rolled metals, is the determination of the incubation period or the time interval at the beginning of each test during which considerable plastic deformation of the test surface takes place without any apparent loss of weight. Fig. 4 suggests that the incubation time for rolled metals is proportional to the corrosion-fatigue limit, and therefore, that the incubation time can be converted into the number of cycles of accelerated cavitation attack necessary to develop corrosion fatigue in the central pitted area of the test button.

For a homogeneous metallike rolled stainless Type 420 and for similar types of bronzes, the weight loss is inversely proportional to the hardness, as shown in Fig. 5. It is well-known that ferritic metals have inferior mechanical properties, and Figs. 6 and 7 confirm their low resistance to cavitation damage, both for carbon and stainless steels.

Cathodic Protection and Cavitation in Tap Water

It was found that the weight loss of cast steel as a result of erosion by cavitation is greater in tap water than in distilled water, as shown in Fig. 8, and cathodic protection increases slightly the incubation time and decreases slightly the weight loss. However, an increase in the impressed current up to 0.060 amp did not increase the protection. These results agree with Petracchi [20] that, at small cavitation intensities, cathodic protection can suppress cavitation erosion. Electrolytic anodic corrosion applied in addition to accelerated cavitation eliminates the incubation period and increases the weight loss, as has been reported by Wheeler [16], who studied ferrous materials in chloride solutions.

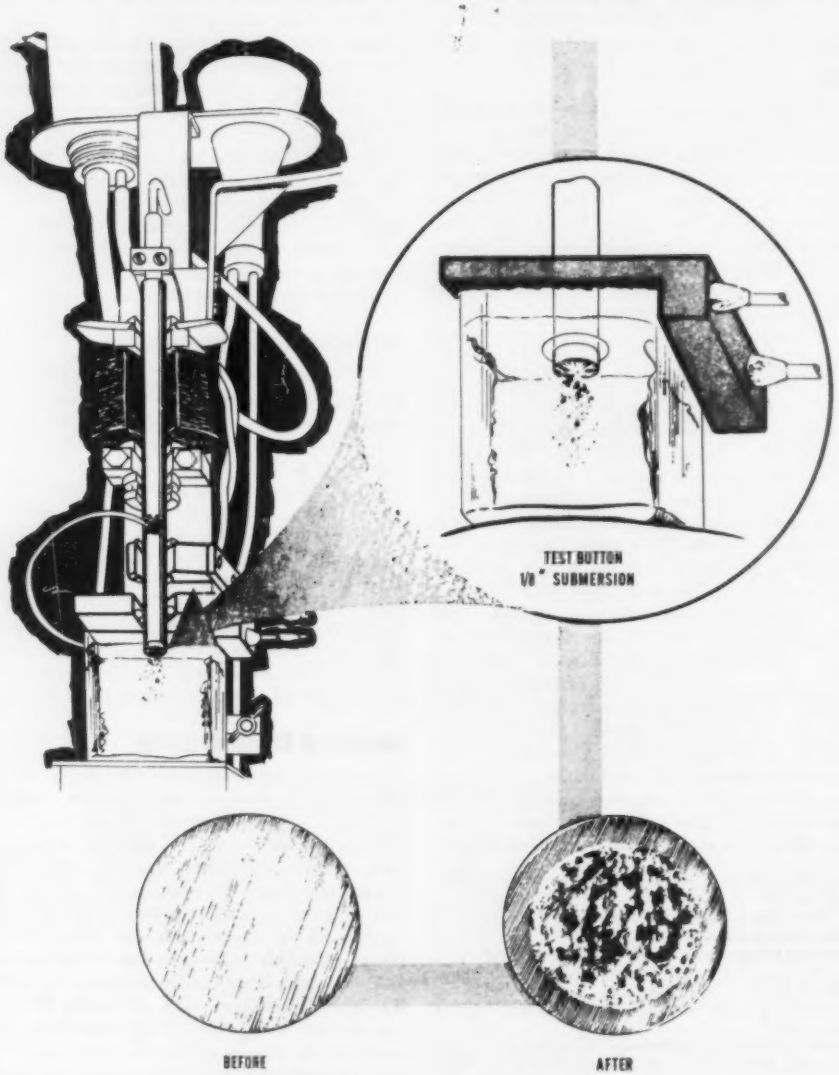

Fig. 1 Accelerated cavitation apparatus

Fig. 2 Bubble pattern on vibrating test button

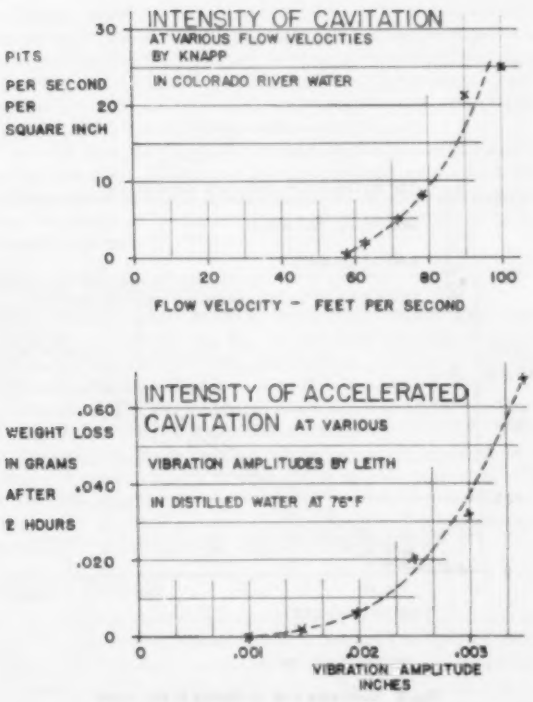

Fig. 3 Flow velocity and vibration amplitude

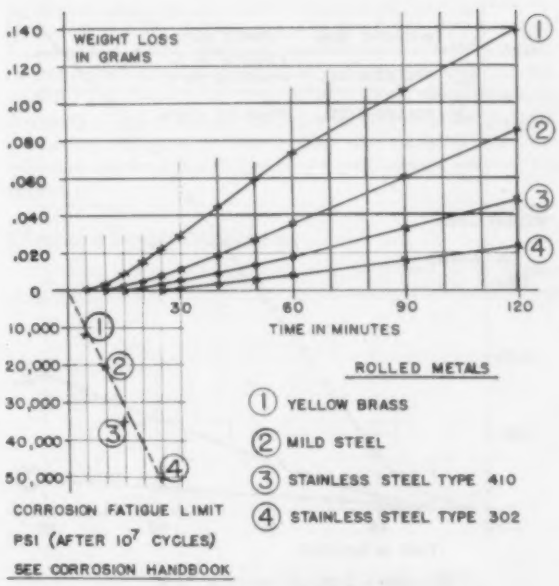

Fig. 4 Effect of corrosion-fatigue limit

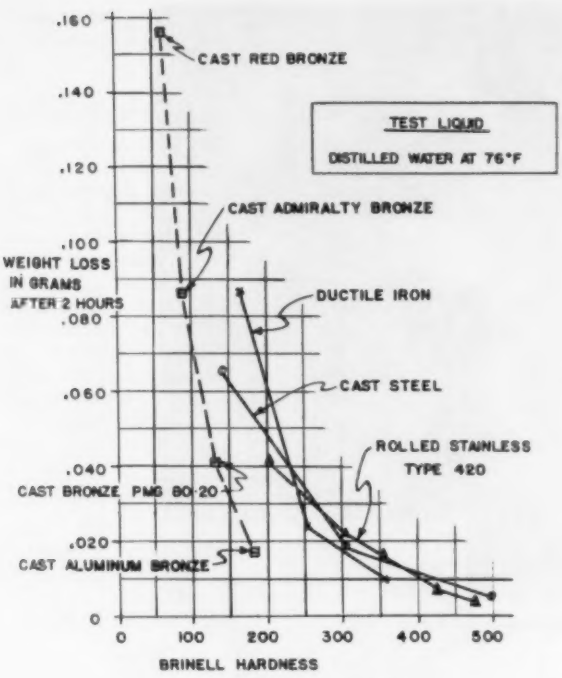

Fig. 5 Effect of metal hardness

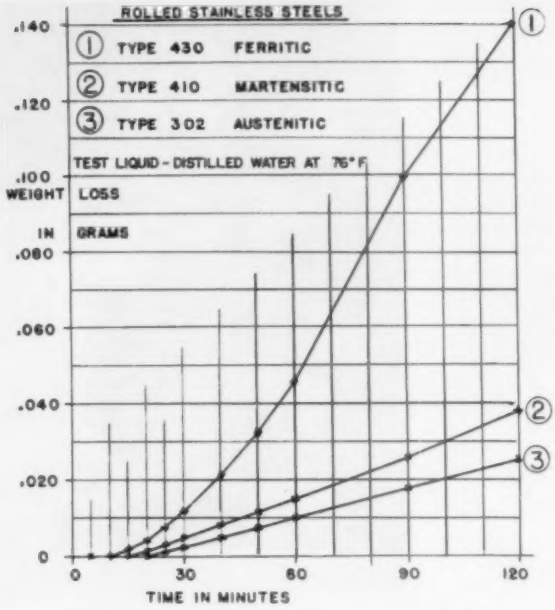

Fig. 7 Effect of metallurgical structure of stainless steels

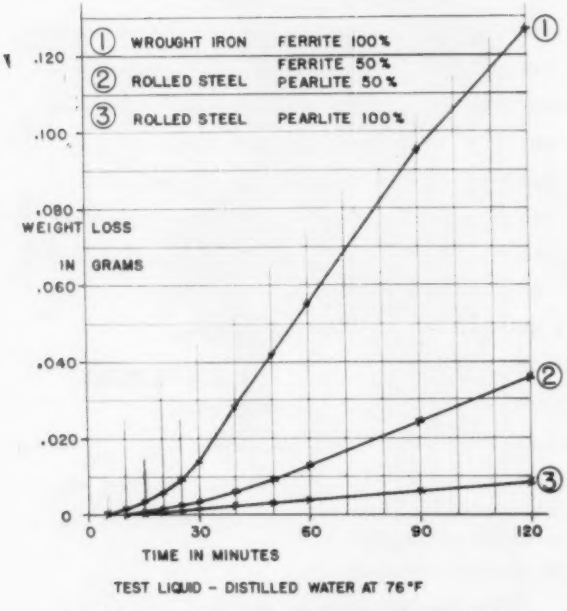

Fig. 6 Effect of metallurgical structure of carbon steels

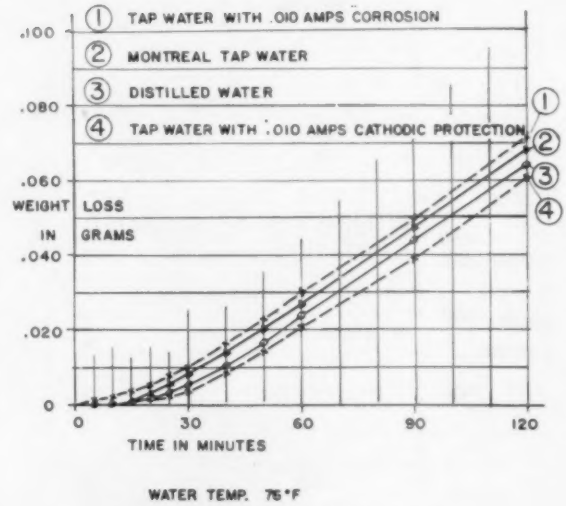

Fig. 8 Corrosion and cavitation in tap water

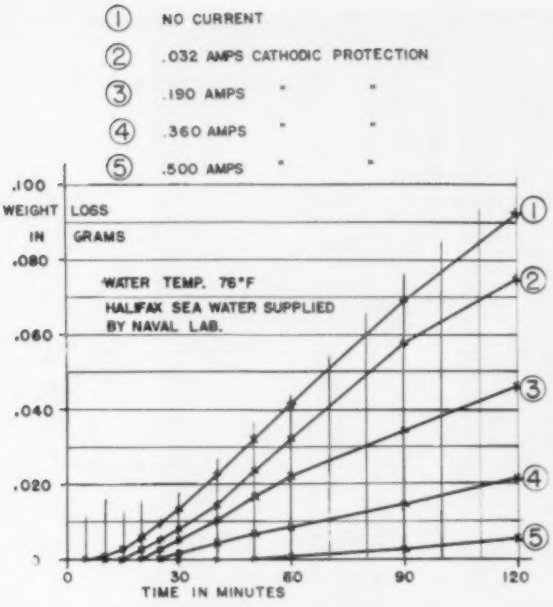

Fig. 9 Corrosion and cavitation in sea water

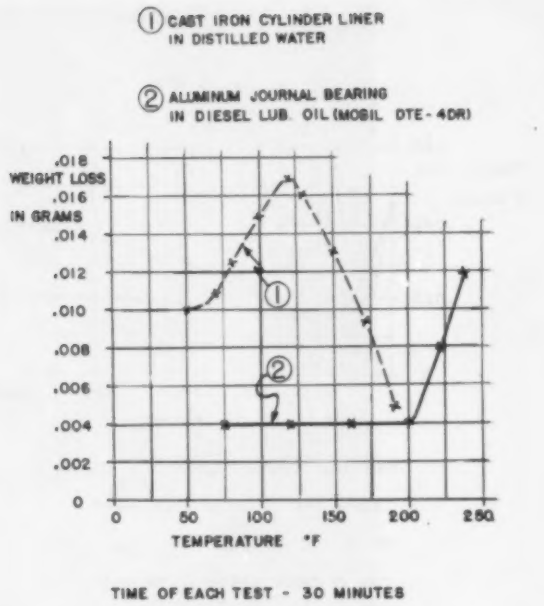

Fig. 10 Effect of liquid temperature

Cathodic Protection and Cavitation in Sea Water

The suppression of accelerated cavitation effects of cast steel in sea water by cathodic protection has caused some investigators to conclude that cavitation attack is of an electrochemical nature. However, Fig. 9 shows that the current density necessary to protect cast steel in sea water is about 3 amp per sq in., which puts the equipment into a hydrogen-generator category.

It is felt that the suppression of cavitation effects is due mainly to the formation of hydrogen bubbles cushioning the cavitation-bubble collapses. This cushioning effect of hydrogen bubbles may be compared to the cushioning effect of injected air in hydraulic turbines.

Effect of Temperature

Cavitation problems in diesel engines are concerned with water-cooled cylinder liners and the oil-lubricated crankpin bearings, where the operating temperature is about 170 F in both cases. However, Fig. 10 shows that, for the water-cooling system, the maximum weight loss occurs at about 120 F while for the lubricating oil, the weight loss increases sharply above 200 F. Thus, laboratory tests must be made at the operating temperature so that the results will be applicable for specific examples. The effect of the liquid temperature should be related to the test pressure, since the vapor pressure increases with higher temperatures while the viscosity and the surface tension decrease.

Effect of Pressure

The modern diesel engine suitable for a mainline locomotive has a water-cooling system which is designed to operate at increased but stabilized cavitation levels. Diesel engines operating in the Rocky Mountains were among the first to report severe cavitation damage at the cylinder liners and the nozzle tubes. Laboratory tests showed that a reduction of pressure from 10 to 5 psig can nearly double the cavitation damage, as shown in Fig. 11. A pressure-relief valve now maintains the back pressure in all engines at 20 psig where the cavitation damage is nominal, and the useful life of these cylinder liners depends on the usual wear of the bore.

Effect of Chemical Additives

Stationary diesel engines operating in areas with hard water have presented several cavitation problems which are illustrated in Fig. 12. Chromate-type additives at 2000 ppm have proven satisfactory, but diesel operators often increase the chromate concentration to 5000 or 8000 ppm, in the belief that increased concentration gives increased protection. Nevertheless, field results confirm laboratory data that the chromate concentration should be maintained at 1500 to 2000 parts, since additional chromate above this level will increase the cavitation damage. A new chemical additive Nalco D-1595 shows a better characteristic than the chromate, in that the concentration is not nearly so critical.

Effect of Nitrogen Atmosphere

An inert gas such as nitrogen was considered as a possible atmosphere above water, which might reduce any chemical cor-

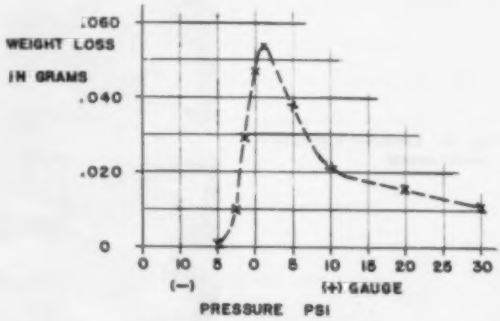

Fig. 11 Effect of liquid pressure

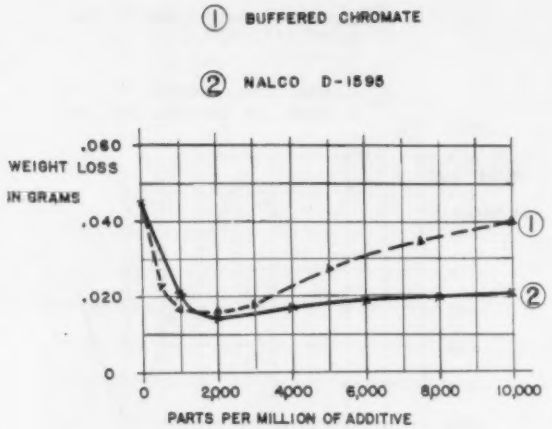

Fig. 12 Effect of chemical additives

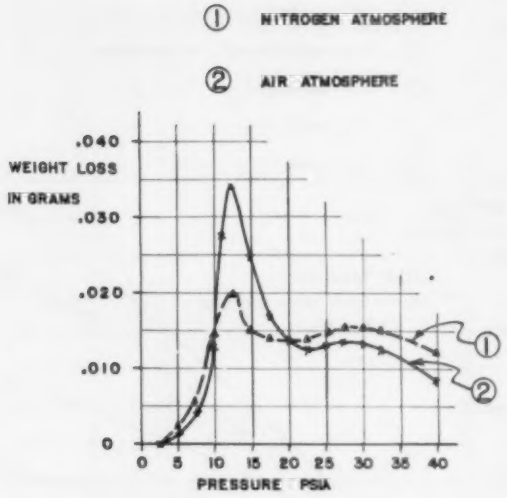

Fig. 13 Effect of nitrogen atmosphere

rosion attack and thus decrease the cavitation damage. A nitrogen atmosphere above water decreases the maximum cavitation-damage level by about half that for air near atmospheric pressure as shown in Fig. 13. However, below 10 psia and above 20 psia, the weight loss was slightly greater in nitrogen than in air.

Validity of Accelerated Cavitation Tests

The magnetostriction apparatus has provided means for a rapid evaluation of a metals resistance and a comparative scale for selecting more resistant alloys for severe cavitation conditions in hydraulic turbines as illustrated in Fig. 14. The validity of accelerated cavitation tests of 2-hr duration has been questioned by Speller and LaQue [21], as regards cavitated diesel liners such as shown in Fig. 15, since their tests at 76 F did not show the beneficial effects of (*a*) chemical additives, or (*b*) austenitic cast iron, that have been observed in the field. However, accelerated cavitation tests at the operating conditions of 170 F and 20 psig have confirmed the optimum concentration of chemical additives shown in Fig. 12. The advantage of austenitic cast iron at 356 Bhn compared to ferritic iron at 162 Bhn is shown in Fig. 16; and Fig. 17 confirms field experience that Ni-resist cast iron at 145 Bhn is superior to the typical liner iron at 180 Bhn.

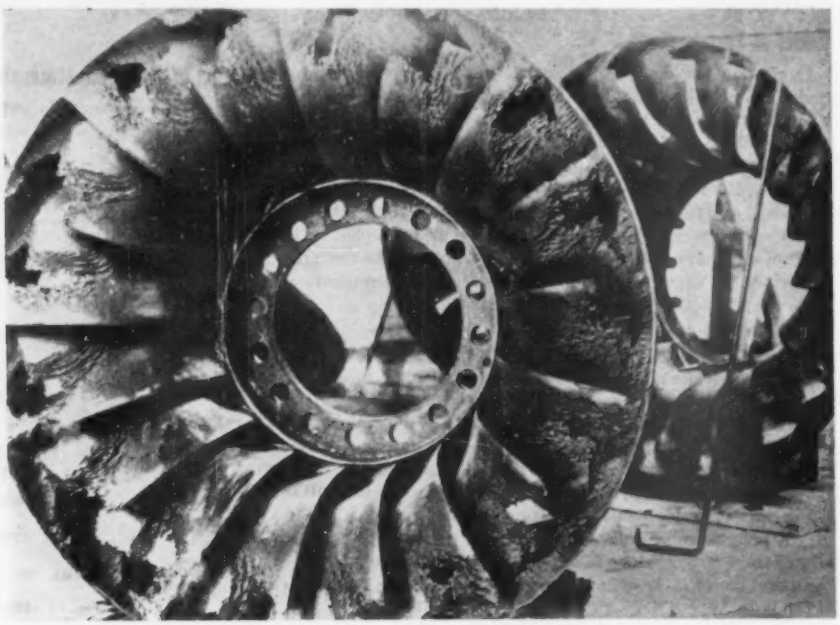

Fig. 14 Cavitated hydraulic turbine runner

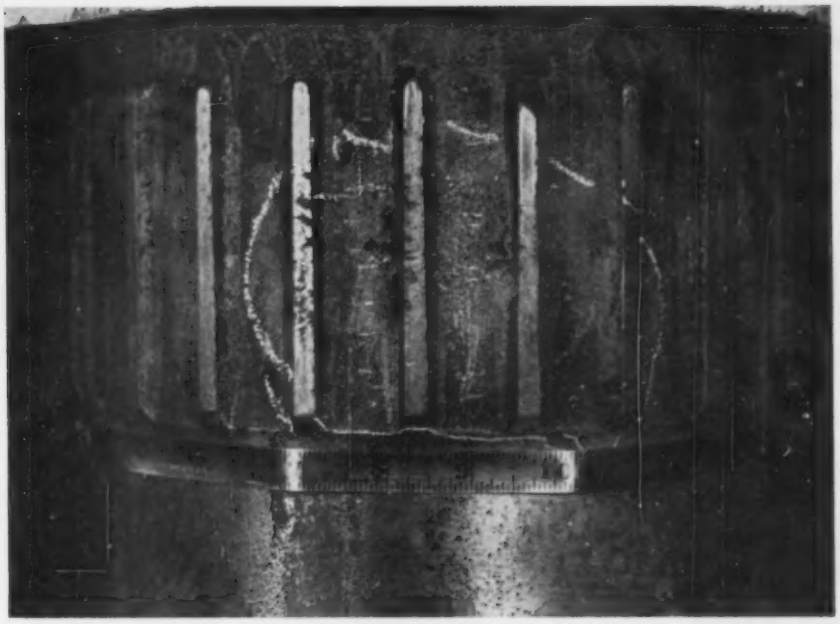

Fig. 15 Cavitated diesel cylinder liner

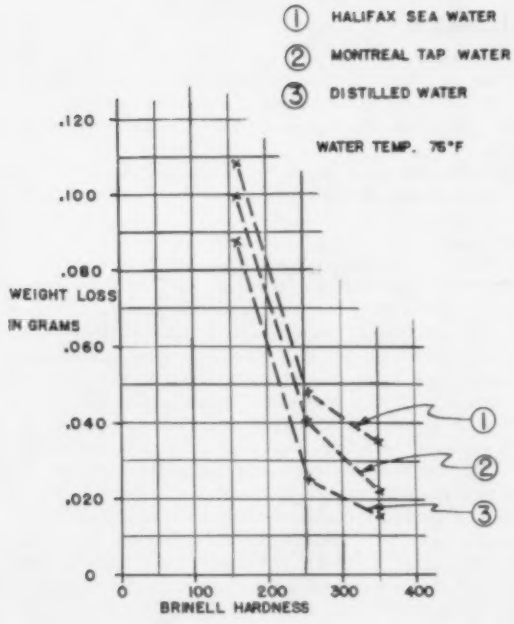

Fig. 16 Ductile iron in corrosive liquids

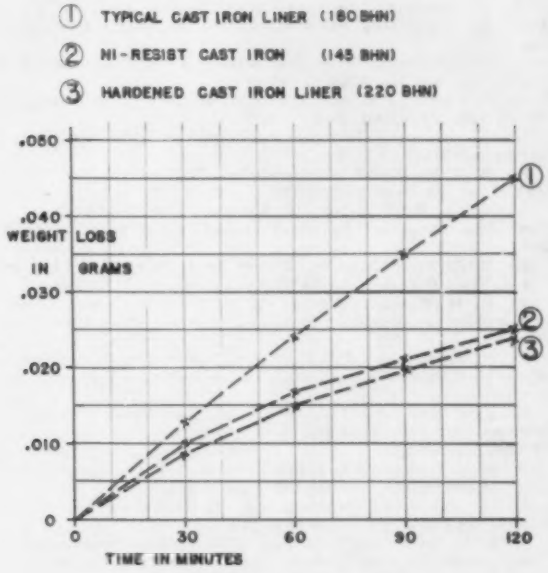

Fig. 17 Ductile iron diesel liners

Conclusions

The accelerated cavitation machine has indicated *relative* effects of metal properties (corrosion-fatigue limit, hardness, and metallurgical structure) and of the liquid characteristics (temperature, pressure, and wettability) which have been confirmed by field experience in hydraulic turbines and diesel engines.

The ASME standardized test is applicable to hydraulic turbines, but the operating conditions of 170 F and 20 psig are important for tests simulating the water-cooling system in a diesel engine.

References

1 W. Margulis, J. A. McGowan, and W. C. Leith, "Cavitation Control Through Diesel-Engine Water Treatment," *Trans. SAE*, 1957, pp. 331–336.

2 W. C. Leith, "Cavitation Damage of Metals," *Engineering Journal of Canada*, March, 1959, pp. 43–49.

3 L. E. Robinson, B. A. Holmes, and W. C. Leith, "Progress Report on Standardisation of the Vibratory-Cavitation Test," TRANS. ASME, vol. 809, 1958, pp. 103–107.

4 W. Ramsay, "Corrosion of Bronze Propeller Blades," *Engineering*, vol. 93, 1912, pp. 687–690.

5 H. Fottinger, "Studies of Cavitation and Erosion in Turbines," Hydraulic Problems, Berlin, Germany, 1926, pp. 14–64.

6 S. L. Kerr, "Determination of the Relative Resistance to Cavitation Erosion by the Vibratory Method," TRANS. ASME, vol. 59, 1937, pp. 373–397.

7 T. C. Poulter, "The Mechanism of Cavitation Erosion," *Journal of Applied Mechanics*, vol. 9, TRANS. ASME, vol. 64, 1942, pp. A-31–37.

8 H. Novotny, "Destruction of Materials by Cavitation," VDI Verlag, Berlin, Germany, 1942, 84 pages, reprinted by Edwards Brothers, Ann Arbor, Mich., 1946.

9 R. Beeching, "Resistance to Cavitation Erosion," *Trans. Institution of Engineers and Shipbuilders in Scotland*, vol. 85, 1942, pp. 210–238.

10 U. R. Evans, "Stress Due to Collapse of Vapor Bubbles," *Engineering*, vol. 155, 1943, p. 454.

11 J. Frenkel, "Kinetic Theory of Liquids," The Clarendon Press, Oxford, England, 1946.

12 H. Krenn, "Thermoelectric Corrosion," *Electric Review*, 1949, pp. 545–548.

13 W. J. Rheingans, "Accelerated-Cavitation Research," TRANS. ASME, vol. 72, 1950, pp. 705–724.

14 W. A. Weyl and E. C. Marboe, "Mechano-Chemistry in Cavitation Corrosion," *Journal of Applied Physics*, vol. 21, 1950, p. 937.

15 I. Taylor, "Cavitation Pitting by Instantaneous Chemical Action From Impacts," ASME Paper No. 54—A-109, 11 pages.

16 W. H. Wheeler, "Mechanism of Cavitation Erosion," Dept. of Scientific and Industrial Research, Glasgow, June, 1954, Fluid Note 18.

17 R. T. Knapp and A. Hollander, "Laboratory Investigations of the Mechanism of Cavitation," TRANS. ASME, vol. 70, 1948, pp. 419–435.

18 Lord Rayleigh, "On the Pressure Developed in a Liquid During Collapse of a Spherical Cavity," *Philosophical Magazine*, vol. 34, 1917, pp. 94–98.

19 R. T. Knapp, "Accelerated Field Tests of Cavitation Intensity," TRANS. ASME, vol. 80, 1958, pp. 91–102.

20 G. Petracchi, "Investigation of Cavitation Corrosion," *Engineering Digest*, vol. 10, 1949, p. 314.

21 F. N. Speller and F. L. LaQue, "Water-Side Deterioration of Diesel-Engine Cylinder Liners," *Corrosion*, vol. 6, 1950, pp. 209–215.

DISCUSSION

A. V. Beloborodov[3,4]

The work convincingly shows that cavitational damage accompanies corrosion to a significant degree and a corrosion resistance factor must be taken into account in the selection of material which can withstand cavitational damage.

This work also permits one to suggest that experiments carried out with accelerated methods on a magnetostriction apparatus with correct methods (methodology) can furnish hopeful data for the selection of cavitation resistance materials.

Of special interest are the experiments in which the investigation shows the influence of cathodic protection, the influence of gas medium on surface liquid, and the influence of temperature and pressure in the liquid.

The results of these experiments, apparently, succeeded in explaining the influence of corrosion factors and the pressure change of vapor formation. It is fully possible that, in these circumstances, the quantity of gases dispersed in the fluid plays an important role, and this influence must be connected with the magnitude of pressure of vapor formation. Experiments in this direction ought to show to advantage the effect of the medium on the surface of both inert and also active gases, particularly of those which are well dispersed in the liquid. Perhaps, in this way it will be possible to find the inert gas, whose dispersal in a liquid-cooled diesel system reduces the cavitational damage.

Unfortunately, there is no detailed information about correlation between cavitation damage on the magnetostriction apparatus and in the actual hydroturbine. It is possible that the same presentation of conditions of damage in the actual state and on the magnetostriction apparatus would provide the method for repeating the experiment, and would permit certain new physical factors, acting on cavitation damage, to be shown.

J. I. Bregman[5]

Congratulations are due to the authors for the clear concise manner in which they have presented their data. This paper can be considered to make a significant contribution to the literature concerning the relationship of corrosion and cavitation erosion.

The relationship of chemical corrosion and cavitation erosion is a complex one. It is generally agreed that cavitation erosion is a mechanical effect. As a result of the erosion, however, the metal surface is left quite susceptible to corrosion. There are many possible reasons for this. Those most regularly cited are that stresses and weak points are set up at the metal surface, while the protective oxide film (in the case of iron) is ineffective since it is constantly being removed. The resulting corrosion further weakens the metal and makes it even more susceptible to cavitation erosion, thus setting up a corrosion-erosion cycle.

The ideal role of a corrosion inhibitor in a system subject to cavitation erosion would appear to be that of minimizing the contribution of chemical corrosion to the erosion and also of interfering with the erosive action of the collapse of large bubbles. The new inhibitor mentioned in this paper, Nalco D-1595, is a mixture of organic materials and is believed to function in a twofold manner: (*a*) It reduces the surface tension of the liquid. This results in a reduction in cavitation erosion probably due to a combination of several mechanisms, one of which being that more and smaller bubbles will be formed due to the lower energy required for nucleation with reduced surface tension. (*b*) The inhibitor protects by means of tough organic film formation. This means that it is relatively easy to keep the protective film in good repair after it has been formed initially. It might also be postulated that the resilient nature of the film might "cushion" the attack on the surface from the shock waves due to the collapse of the bubbles.

[3] Engineer of the Leningrad Metallurgical Factory Named for Stalin, Leningrad, Russia.

[4] Translated by C. A. Sebastianowitch, Dominion Engineering Works.

[5] Supervisor, Physical Chemistry Research, Armour Research Foundation of Illinois Institute of Technology, Chicago, Ill.

J. M. Hobbs[6]

This paper proved not only interesting, but also gratifying, as a number of the observations are in agreement with some made at Manchester University using a drop-impact test. This, and related work, is described in an article under the joint authorship of Mathieson and Hobbs.[7]

In this the specimens were subjected to a succession of practically uniform impacts with the working fluid, and hence the effect of time and impact velocity on the damage produced could

[6] Scientific Officer, Fluids Division, National Engineering Laboratory, East Kilbride, Scotland.

[7] "Cavitation Erosion—Comparative Tests," *Engineering*, vol. 189, 1960, pp. 136–137.

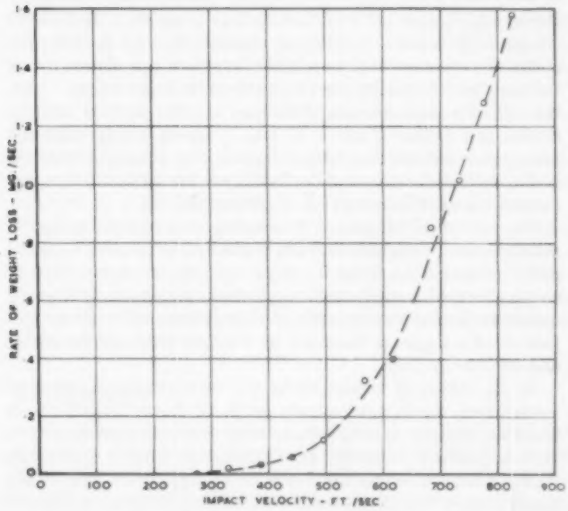

Fig. 18 Erosion at different impact velocities

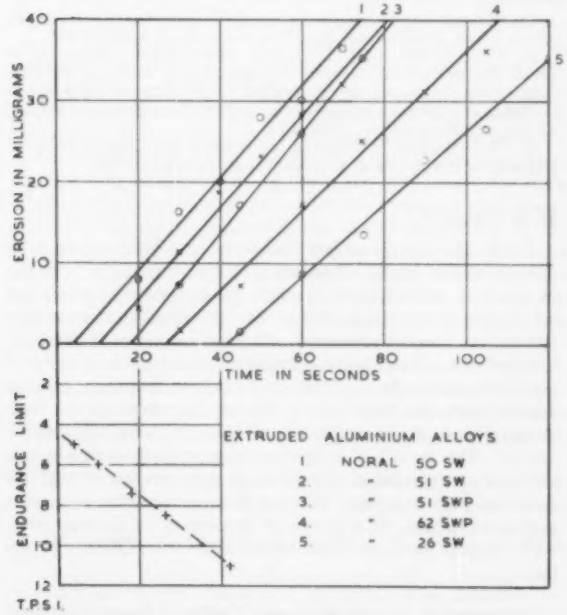

Fig. 19 Effect of endurance limit

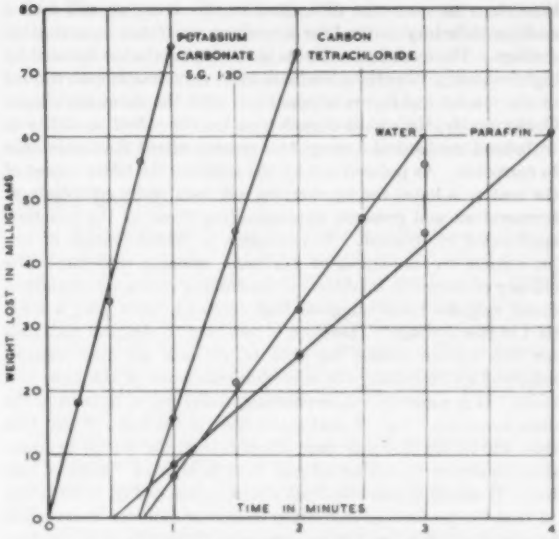

Fig. 20 Erosion with different test fluids

be investigated meaningfully. The specimens were not immersed in the working fluid as in other forms of test, but although the stress pattern was different from that due to true cavitation, similar effects were obtained.

As in the vibratory test, a period of time elapsed before any material was removed. This was found to increase with speed, as did also the rate of erosion when once begun (Fig. 18). It was generally observed that harder materials of high tensile strength were the more resistant to damage, but this was by no means without exception. A correlation of the "incubation period" with the endurance limit showed a distinct relation, although it was only possible for a range of several aluminum alloys (Fig. 19).

An investigation into the effect of the chemical nature of the test fluid gave rise to some quite spectacular results. With a strong solution of potassium carbonate, for example, a weight loss of over three times that caused by water was obtained. Estimations based on a study of density effects indicated an increase of only 70 per cent. (Fig. 20 shows typical results.)

Experiments carried out using a solution of similar composition to that of sea water gave differing results according to the material under test. In general it was found that the rate of erosion of ferrous materials increased and the onset was hastened, but little measurable change was detected with bronzes.

Admittedly much of the work described only serves to indicate possible lines of further and more detailed investigation, some of which are, in fact, being followed at NEL by the discusser. However, it is encouraging to find that consistent results are obtained in somewhat different approaches to the solution of fundamentally the same problem.

F. L. LaQue[8]

The authors have provided in this paper a useful review of data developed by many investigators of cavitation phenomena and of the extent to which corrosion may contribute to total damage. The results of their own experiments have served very well to facilitate the interpretation of data provided by many of the earlier investigations.

While such accumulations of data have extended our knowledge of cavitation erosion and have served as useful guides to prac-

[8] Vice President and Manager, Development & Research Division, The International Nickel Company, Inc., New York, N. Y.

tical steps to overcome difficulties in this area, we still lack a really satisfactory method for appraising resistance to cavitation damage. The most favored tests involving cavitation induced by high frequency vibrations tend still to be very drastic with respect to the mechanical forces as compared with the corrosive effects. Consequently, the results of such tests tend to reflect an ability to withstand mechanical damage to a greater extent than resistance to corrosion. As pointed out by the authors, the latter aspect of the matter is improved by carrying out tests under conditions of temperature and pressure approximating those of the practical application of interest. Nevertheless, a demonstration of improvement by reduction of corrosion remains difficult. The efficacy of chromate inhibition in controlling cavitation-erosion of diesel cylinder liners suggests that corrosion must play a large part in this damage. Therefore, a test used to compare materials for this service should be able to indicate an improvement achieved by increasing the corrosion resistance of the liner material. It is somewhat disappointing, therefore, to note from the data covered by Fig. 17 that an increase in hardness of cast iron from 180 to 220 Bhn was more effective than the change in corrosion resistance from that of cast iron to that of Ni-Resist cast iron. It would appear also from a comparison of Fig. 17 with Fig. 12 that the problem of cavitation erosion of cylinder liners might be solved about as readily by increasing the hardness of the liner material, as by the use of an appropriate inhibitor. Practical experience has shown that this is not the case.

It is hoped, therefore, that those concerned with the study of resistance to cavitation erosion will continue their efforts to develop a more reliable means of appraising this quality of material, and especially one that will more readily reflect the advantages of reducing the corrosion factor in the over-all result.

The authors' conclusion, that the hydrogen bubbles released on surfaces made strongly cathodic by applied currents play a principal role in the reduction of cavitation erosion by cathodic protection, is supported by results of recent investigations by Dr. M. S. Plesset at the California Institute of Technology to be dealt with in more detail directly by him on the occasion of the presentation of this paper.

The point raised by reference to an earlier paper by this author with Dr. F. N. Speller has already been dealt with here. With further reference to this earlier paper, the author cannot resist expressing his satisfaction with the acceptance now accorded his original suggestion that deterioration of diesel engine cylinder liners is often the result of cavitation erosion. At the time of presentation of the 1950 paper, this explanation of what was happening was considered by some engineers as being too far fetched to be acceptable.

J. Z. Lichtman[9]

The authors have made a valuable contribution to the understanding of erosion of metals in cavitating fluids. In addition to the importance of establishing relationships between numerous experimental factors and the degree of metallic erosion, this paper is valuable also because it recognizes and is concerned with the importance of simulating actual service conditions in evaluating the resistance of a material to erosion.

In regard to the studies of the effects of inhibited coolants at elevated temperatures and pressures in controlling erosion of the outer walls of diesel cylinder liners the writer suggests that further experiments be carried out at metal temperatures up to 400 F and mean coolant temperatures of 170 F. Although the mean coolant temperature may be only 170 F, liner temperatures on the water side may be at the higher temperature in some areas [22].[10] The coolant temperature adjacent to the cylinder liner would be lower than the outer liner temperature but probably higher than the mean coolant temperature. It is suggested that these experiments be made at a range of vibration amplitudes to determine the relative significance of corrosion alone and the increased effect of cavitation turbulence and erosion as the vibration amplitude is increased. These proposed experiments may provide information as to the erosion rates of liner materials under conditions more closely approximating actual operating conditions. Liner damage may be predominantly electrochemical and stress corrosion at the high temperature; mechanical cavitation erosion may contribute to only a minor degree as shown by the pressure and temperature relationships of Figs. 10 and 11. This would also account for the effectiveness of inhibitors in service and the general lack of effect of inhibitors in the magnetostriction tests made by Speller and LaQue [23]. Although they observed a decrease in erosion with increase in inhibitor concentration for heat-treated nickel chrome cast iron, no significant effect was shown by an "as-cast" nickel chrome cast iron or three Ni-Resist alloys. Also, the cylinder liner damage illustrated by the authors and by Speller and LaQue (Figs. 1, 2, and 3) shows widely scattered pitting and undercutting resembling corrosion damage in contrast to the continuous nature of cavitation erosion as shown by magnetostriction and rotating disk specimens [23, 24].

The nature of the erosion mechanism in a cavitating fluid is shown to be a complex one being dependent on inherent material and environmental factors. Also, the relative significance of electrochemical or mechanical mechanisms is apparently dependent on the level of impact stress on a surface caused by the cavitation cloud collapse as discussed by Godfrey [25] and the writer and co-authors [24].

At low levels of impact stress the electrochemical corrosion mechanisms would predominate while at higher impact stress levels the mechanical fatigue processes would tend to predominate. It is important, therefore, that accelerated erosion studies be made under environmental conditions which do not distort the significance of the physical and chemical properties of a material as related to its normal operating conditions.

References

22 "Diesel Engineering Handbook," 1955 edition, A. N. Newell, editor, Diesel Publications, Inc., New York, N. Y., 1955, p. 268.

23 F. N. Speller and F. L. LaQue, "Water Side Deterioration of Diesel Engine Cylinder Liners," *Corrosion*, vol. 6, 1950, pp. 209–215.

24 J. Z. Lichtman, D. H. Kallas, C. K. Chatten, and E. P. Cochran, Jr., "Study of Corrosion and Cavitation-Erosion," TRANS. ASME, vol. 80, 1958, pp. 1325–1341.

25 D. J. Godfrey, "Technical Information and Library Service," Ministry of Supply S and T Memo 17/57, September, 1957.

M. S. Plesset[11]

The authors have ascribed the star-shaped bubble pattern to the presence of radial vibrations of the test specimen. In the experiments which I have reported, the star-shaped pattern did not appear to have this origin. My observations showed that this pattern was not connected with the diameter or thickness of the specimen. I also found a random element in the number of rays in the star pattern. It must be admitted that the apparatus used by Leith and Thompson is different from mine so that their interpretation of the mechanism of the star formation may be correct. This point is of some importance since these star bubble patterns are associated with lines of deep erosion of the test specimen. My experience has been that the formation of uneven cavitation damage is a source of inaccuracy in damage data. Such damage patterns make reproducible data difficult to obtain.

[9] Supervisory Technologist, Materials Development Branch, Naval Material Laboratory, New York Naval Shipyard, Brooklyn, N. Y.

[10] Numbers from [22 to 25] designate References at end of this discussion.

[11] Professor of Applied Mechanics, California Institute of Technology, Pasadena, Calif. Mem. ASME.

In the authors' discussion of the *effect of metal properties* they attach significance to the so-called incubation time. This time is considered by the authors to be a period during which there is no loss of weight. I believe that it is incorrect to describe the "incubation period" as a period in which there is no loss of weight. In our experiments we observe a weight loss immediately following exposure to cavitation. The initial rate of weight loss is less than that found after some exposure. The small initial rate increases with exposure until a characteristic constant rate is obtained. The smaller initial rates of weight loss require greater accuracy for their observation. When the characteristic constant rate of weight loss is obtained, further damage can eventually lead again to a nonlinear region of weight loss. This excessive damage is often a cause of inaccuracy in measurements.

A question may be raised regarding the data presented on cathodic protection. Fig. 8 of the paper shows a greater weight loss when anodic currents were applied to the specimen. The authors do not state whether these weight losses for the anodic case were corrected for loss of material due to anodic current flow alone. Unless such a correction is made this curve is meaningless.

In their consideration of temperature effects on cavitation damage the authors have found a result which has already been reported by A. S. Bebchuk.[13] It appears further in the authors' consideration of temperature and pressure effects that the authors have attempted to consider these separately. From a fundamental point of view this approach is very likely not possible. There is certainly an important effect in cavitation damage of the amount of dissolved gas, and this amount is related both to temperature and pressure.

V. Salemann[12]

The authors, judging by the title of the paper, attributed the difference of cavitation damage in, for example, distilled water and tap water largely to chemical effects. They do stress the necessity of repeating the pressure and temperature conditions of the liquid as found in the application. Since the threshold sound pressure and the type of cavitation (gaseous versus vaporous) depend on air content and bubble-size distribution, it may well be expected that such factors may also influence mechanical damage. According to Strasberg,[14] the threshold pressure of tap water increases from $1^1/_2$ to $2^1/_2$ atm if it is allowed to stand for several days after being drawn. In both cases the water was slightly supersaturated with air and the same absolute air content was measured. Just as there is a hysteresis effect on the threshold pressure when the static pressure is varied, there may be a hysteresis in damage produced, such that the results shown in Figs. 11 and 13 may depend on direction of pressure variation.

It is interesting to speculate on the reasons why, in Fig. 11, the weight loss approaches zero at −5 psig, and in Fig. 10, drops sharply after 120 F. What is the reason for the maximum of approximately 1 psig on Fig. 11? Is it possible to correlate this maximum weight loss with the maximum on Fig. 10, which occurs at a different pressure and temperature?

Fig. 11 shows that operating at −5 psig is more effective in reducing damage than operating at 20 psig. Is this so because of the low absolute pressure per se or because air content was reduced by applying vacuum? Did the weight loss on Fig. 10 also go down due to air being driven off?

The intensity of magnetostrictive pressure field depends on frequency and amplitude. It is conceivable that the maxima and minima exhibited by Figs. 10 and 11 will also shift with frequency and amplitude. Thus, maximum damage to a cylinder liner may occur at different pressures and temperature. While on the subject of cylinder liners, this discusser would expect the water temperature at the surface of the liner to be above the average cooling system temperature which seems to be 170 F. Thus, tests should be conducted at a higher temperature.

[13] *Soviet Physics—Acoustics*, vol. 3, 1957, p. 97, and vol. 3, 1957, p. 395.

[12] Research Engineer, Worthington Corporation, Research and Development Section, Harrison, N. J. Assoc. Mem. ASME.

[14] M. Strasberg, "The Onset of Ultrasonic Cavitation in Tap Water," The Catholic University of America Press, 1956.

Authors' Closure

The authors appreciate the thoughtful contributions of the discussers and are gratified at the agreement on this rather controversial subject. Accelerated cavitation test results have shown good correlation with field experience in hydraulic turbines, as reported at the ASME 1956 Cavitation Symposium. The authors apologize to Mr. Beloborodov for the omission of this reference.

The ideal role of a corrosion inhibitor in water cooling systems has been explained very clearly by Dr. Bregman. The authors appreciate this contribution.

The authors gratefully acknowledge the drop-impact test data presented by Dr. Hobbs confirming the correlation between the incubation period and the corrosion-fatigue limit, as shown in Fig. 4.

The magnetostriction test may emphasize the mechanical rather than the chemical action of cavitation attack, as suggested by Mr. LaQue, but laboratory tests at the operating conditions have evaluated chemical additives whose relative effects have been confirmed by field experience in many diesel engines. Our experience indicates that an increase in hardness improves the cavitation resistance at a reasonable cost, while a more corrosion-resistant liner of Ni-resist iron is too expensive for our customers. Cavitation attack becomes more pronounced in older engines. Harder liners and chemical additives are helpful.

The pioneer work of Speller and LaQue, who identified the deterioration of diesel cylinder liners as cavitation damage, should have been acknowledged more fully, but the authors suggest that the operating conditions of 170 deg F and 20 psig are very important for related laboratory tests.

The authors agree with Mr. Lichtman that a metal temperature of 400 F would be more realistic. Further tests are contemplated with various vibration amplitudes.

Dr. Plesset's discussion emphasizes the divergence of opinion that exists between investigators who study different aspects of the same phenomenon. His most recent paper[15] describes a novel experimental procedure to study the effect of cathodic protection in cavitation damage.

Dr. Plesset's apparatus has a solid exponential horn transducer operating at a frequency of 14,200 cps with an amplitude of 0.0020 in., while the standardized ASME apparatus has a nickel tube transducer operating at a frequency of 6,500 cps with an amplitude of 0.0034 in. It would be interesting if Dr. Plesset could correlate his test results to the standardized ASME test.

Dr. Plesset has proposed that a rimmed test button will eliminate the star-shaped damage pattern by reducing the radial flow. Following this proposal, standard flat buttons and rimmed buttons of rolled aluminum with the same surface roughness were tested. The Plesset rimmed button has a similar damage pattern to that shown in Fig. 21, but the total weight loss for a rimmed button is about 10 per cent less than for a flat button, as shown in Fig. 22. These buttons were tested with the ASME standard procedure, and the weight loss curves are definitely in the characteristic linear region, where accuracy and reproducibility are easily attained. It is suggested that the modulus of elasticity of the test button may have some influence on the damage pattern, since a soft metal with a low modulus, such as cast aluminum, shows a distinct star-shaped damage pattern, while a harder metal with

[15] Published in this issue, pp. 808–820.

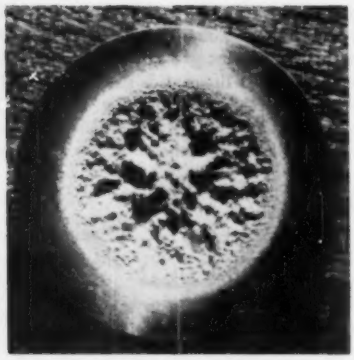

ASME standard flat button (rolled aluminum)

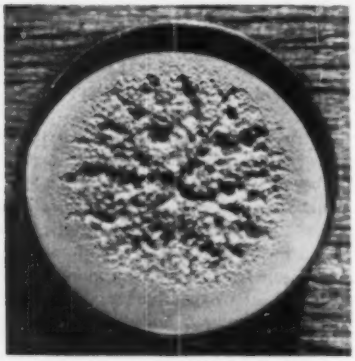

Plesset rimmed button (rolled aluminum)

Fig. 21 Effect of a Plesset rimmed button

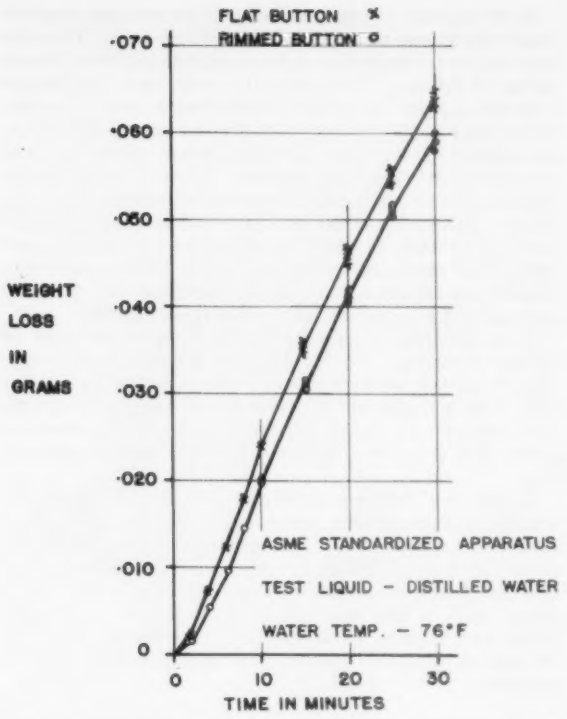

Fig. 22 Characteristic weight loss curves (rolled aluminum 6068-0)

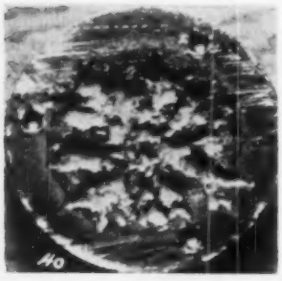

CAST ALUMINUM

MODULUS $E = 10 \times 10^6$ PSI

CAST IRON

MODULUS $E = 16 \times 10^6$ PSI

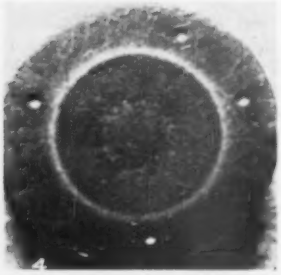

CAST ALUMINUM BRONZE

MODULUS $E = 22 \times 10^6$ PSI

Fig. 23 Effect of modulus of elasticity

a higher modulus, such as cast aluminum bronze, shows a more uniform damage pattern as shown in Fig. 23.

As stated on page 796 in the paper, the incubation period is found for rolled metals only. The surface roughness for standard buttons is about 3 microinches. It is encouraging to note that Fig. 29 in Dr. Plesset's paper[15] shows an incubation period for stainless 17/7 steel.

The larger weight loss with an anodic current as shown in Fig. 8 has been corrected for the static corrosion loss, and these data agree with the published works of Beeching.

The general effects of temperature were reported first by Kerr in 1937, but Fig. 10 refers to the specific case of a diesel engine. The separate curves of temperature and pressure may not satisfy Dr. Plesset's fundamental point of view, but they can be adjusted separately, both in the laboratory and the engine, to show the desired relative effects.

A cavitation parameter of water for temperature has been established empirically which combines the effects of vapor pressure, viscosity, and surface tension, as shown in Fig. 24. This cavitation parameter is extremely useful for cavitation problems in water cooling systems.

The literature on cavitation contains many conflicting observa-

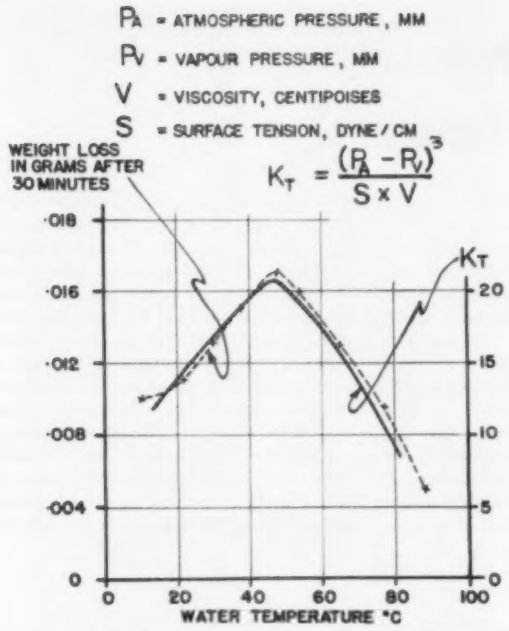

Fig. 24 Cavitation parameter K_T of water for temperature

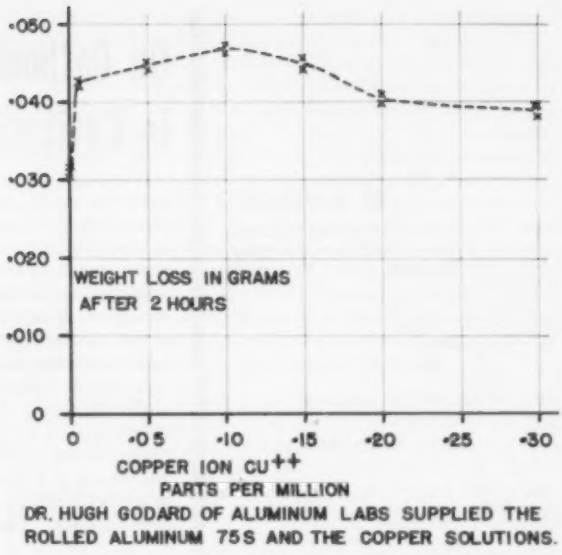

Fig. 25 Effect of copper ions on cavitation erosion of rolled aluminum 75.S

tions on the effects of dissolved air. It certainly has an important effect. However, a complete series of temperature and pressure curves show relative effects, which include the amount of dissolved air.

The authors agree with Mr. Salemann that the air content is important, but the ASME standardized procedure specifies a pre-test boiling, which should stabilize the air content. The maximum weight loss with temperature may be connected with a critical number and size of cavitation bubbles, as suggested in Fig. 24. We expect to investigate the effects of frequency and vibration amplitude on the maxima exhibited by Figs. 10 and 11.

The chemical effects related to cavitation attack are illustrated conclusively by Fig. 25, which indicates the increase of cavitation damage on rolled aluminum 75.S in the presence of copper ions.

On Cathodic Protection in Cavitation Damage

M. S. PLESSET
Professor of Applied Mechanics, California Institute of Technology, Pasadena, Calif. Mem. ASME

An experimental procedure has been developed which makes possible accurate and reproducible determinations of cavitation damage. This procedure has been applied to a study of the effect of cathodic currents on cavitation damage. A series of experiments, in which the test liquid was a solution of salt in water, showed a reduction in cavitation weight loss for all of the materials examined when the test specimen was made the cathode of an electrolytic cell and when the conditions were such that gas was evolved at the specimen surface. This protective effect against cavitation damage increased with increasing magnitude of the cathodic current. These observations support the view that the protective effect was due to the layer of hydrogen gas evolved on the surface of the specimen. A similar protective effect was observed when the specimen was made the anode in a test liquid which was buffered distilled water; in this situation the gas evolved at the specimen surface is oxygen. Additional evidence for this protective mechanism of a gas layer on the specimen surface was found in a series of experiments in which the voltage applied to the cell was reduced to a level at which no gas was evolved on the surface. There was then no protective effect with the specimen cathodic or anodic.

LARGE mechanical stresses are known to be produced [1][1] in a solid when cavitation bubbles collapse near the surface and the importance of this physical effect has been emphasized in studies described elsewhere [2]. Some investigators [3, 4], on the other hand, have emphasized the possibility of chemical effects in cavitation damage and have found a protective effect for a metal specimen when it is made the cathode of an electrolytic cell while it is being exposed to cavitation. The value of cathodic protection for a metal exposed to corrosion in an active liquid with no cavitation is well known. In such cathodic protection, the current flow in the cell reduces any galvanic action between possible anodic and cathodic areas on the surface of the metal. There is also the possibility of hydrogen liberation at the surface of the metal. The question which is to be considered here is whether making a metal the cathode of an electrolytic cell has any specific effect in protecting against cavitation damage. The series of experiments to be described was designed to give some information on this question.

Experimental Apparatus and Procedure

The apparatus used in the experiments is shown in Figs. 1–3 and a block diagram is given in Fig. 4. Alternating current is supplied at an adjustable frequency by an audio oscillator, Fig. 4, and is amplified in a power amplifier so that a nickel transducer stack may be excited into mechanical oscillation. The amplitude of these mechanical oscillations of the transducer stack is increased by means of a solid steel exponential horn soldered to the end of the stack. This horn tapers to a cylindrical section in the end of which the specimen is screwed, Fig. 2. The specimens have a threaded portion and a cylindrical portion; the cylindrical section is $^5/_8$ in. in diameter and about $^3/_{16}$ in. thick. The specimens were immersed to approximately half this cylindrical depth in the test liquid. The oscillations generated in the horn are such that the motion is almost totally confined to the axial direction; an account of this use of such a horn, together with the theory, may be found elsewhere [5, 6]. The vibration of the specimen was observed with a microscope and the amplitude was determined from a scale. A much more accurate way of following the relative amplitude of oscillation was furnished by the displacement pickup coil. This displacement detector consisted of a coil of wire wound on an annular magnet through which the horn passed. The oscillations of the horn generated an alternating current which was read on a vacuum-tube voltmeter, Fig. 4. The vacuum-tube-voltmeter reading made it very easy to hold the specimen oscillation amplitude constant during an experiment. The double amplitude of the oscillation was kept at 0.0020 in. for most of the test runs. The oscillation frequency was determined by the resonant frequency of the system which was approximately 14.2 kilocycles.

During a test run not only could the amplitude be held constant

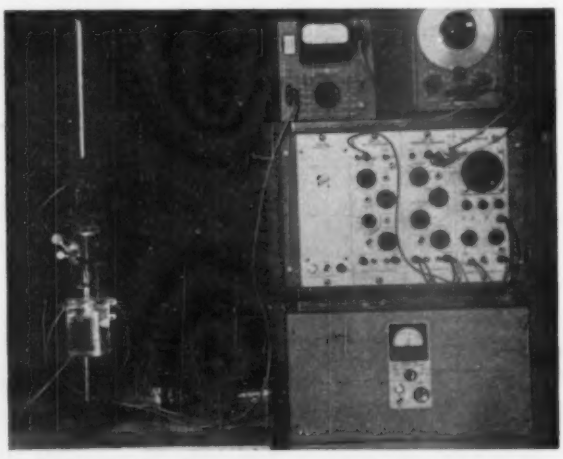

Fig. 1 Apparatus used to generate cavitation including oscillator amplifier, nickel stack, stainless-steel horn, and pickup coil

[1] Numbers in brackets designate References at end of paper.

Contributed by the Cavitation Subcommittee of the Hydraulic Division and presented at the Annual Meeting, Atlantic City, N. J., November 29–December 4, 1959, of THE AMERICAN SOCIETY OF MECHANICAL ENGINEERS.

Note: Statements and opinions advanced in papers are to be understood as individual expressions of their authors and not those of the Society. Manuscript received at ASME Headquarters, August 11, 1959. Paper No. 59—A-170.

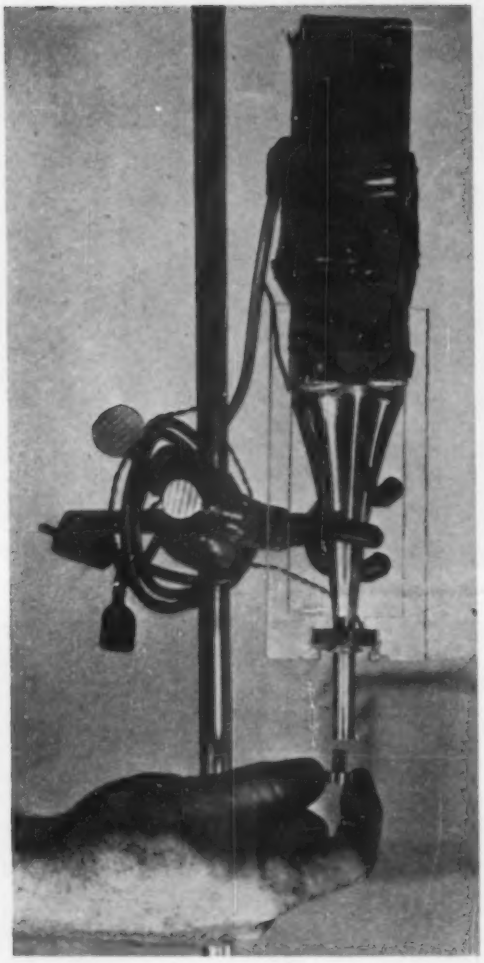

Fig. 2 Specimen being attached to end of horn

but the cooling requirement for holding the test liquid temperature constant was easily met. The specimens were weighed accurately before each run. After a run, the specimen was washed in distilled water, then in ethyl alcohol, and dried in a vacuum desiccator before being weighed.

When the specimen was made one electrode of an electrolytic cell, the second electrode was in every case a platinum wire insulated from the liquid except at its end, Fig. 3, which was mounted in a plastic tripod. The exposed end was a disk, also of platinum. During these runs the current was held constant although the voltage also was measured. The current and voltage readings were relatively insensitive to the distance between the electrodes but this distance was kept at the constant value of 1.5 cm.

Modification in the Shape of Specimens

The specimens which were used initially for the tests had flat surfaces exposed to cavitation. With specimens of this shape it was found that there was a serious lack of reproducibility in experimental results in spite of every effort to control the experimental conditions. This lack of reproducibility in the data was connected with the nonuniform nature of the cavitation damage on the specimen surfaces. This nonuniformity of the damage was evident in the formation of deep radial ruts, examples of which are shown in Fig. 5. The number and depth of these ruts varied from one specimen to another even when the test conditions were kept the same. There was some correlation of larger weight losses with a larger number of these radial ruts, and smaller weight losses with a smaller number. It may be remarked that the damage patterns found in the experiments described here are fairly uniform compared to other damage patterns observed with magnetostrictive devices [7]. These radial ruts or "stars" were investigated also for specimens of smaller diameter and were found to occur in the same way as for specimens of larger diameter. The formation of the star pattern appeared to be unconnected with any vibration mode of the specimen surface, as is also indicated by the observations elsewhere [7] that these star patterns are independent of the specimen thickness.

The explanation of these star patterns in the cavitation damage with these flat specimens has hydrodynamic basis. As the specimen oscillates, the cavitation bubbles are formed in the half-cycle during which it moves away from the liquid. This motion of the specimen away from the liquid is accompanied by a flow which has a radially inward component over the specimen face. The cavitation bubble cloud is consequently somewhat concentrated toward the center of the face during this interval of growth of the bubbles. In the subsequent half-cycle, during which the specimen moves into the liquid, the cavitation bubbles are collapsed. It is, of course, the bubble collapse that produces the cavitation damage. This motion, during this collapse portion of the cycle, must be accompanied by a liquid flow which has a component directed radially outward over the specimen surface. The bubble cloud consequently experiences some radial outward acceleration so that a flow region containing a mixture of bubbles and liquid is being accelerated into a flow region containing only liquid. In this collapse portion of the cycle, one has, therefore, a situation in which a lighter fluid medium is being accelerated into a heavier one. This situation produces a Taylor instability [8]. The cavitation cloud should therefore develop fingers, or rays, of bubbles. This type of behavior is observed and is shown in Fig. 6, which is a short exposure photograph of the face of a specimen while undergoing high-frequency vibrations in water. Once damage has been initiated in some radial directions, there would be a definite tendency for the instability to persist in these directions so that the more intense damage should appear in a star pattern. A mechanism of this kind with an element of randomness arising from an instability would clearly lead to difficulty in obtaining reproducibility of weight loss in damage tests.

This explanation of the lack of reproducibility in cavitation weight losses suggests a modification in the shape of the specimen, and the success of this modification, in turn, supports the explanation. On the basis of the mechanism just described, it follows that a reduction in the magnitude of the radial accelerations over the face of the specimen would make the damage patterns more uniform and at the same time would make the damage determinations more reproducible. Specimens were therefore tried which did not have completely flat surfaces but which, instead, were "dished" so that they consisted of a flat surface surrounded at the edge by a wall approximately 0.030 in. high and 0.010 in. thick, Fig. 7. The damage pattern obtained with such a dished-specimen face is shown in Fig. 8. It is extremely uniform, and it is clear that the reduction in the radial flow by providing a stagnation rim has eliminated any kind of preferential damage which took place previously. As might be expected, this type of specimen gave much more consistent results than the flat specimens, and it was adopted for all the experiments reported here. It is estimated that the error in cavitation weight-loss determinations to follow is within $\pm 2 \times 10^{-4}$ gram.

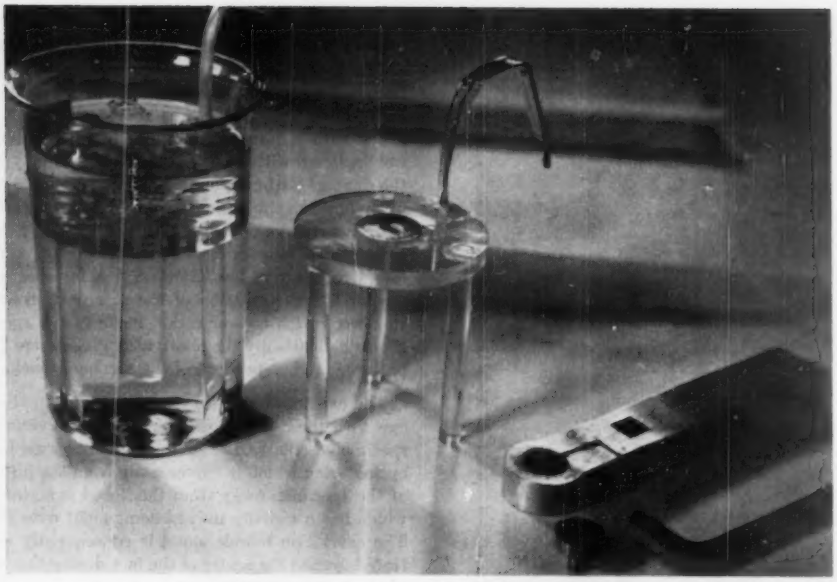

Fig. 3 Platinum anodes used for cathodic-protection tests

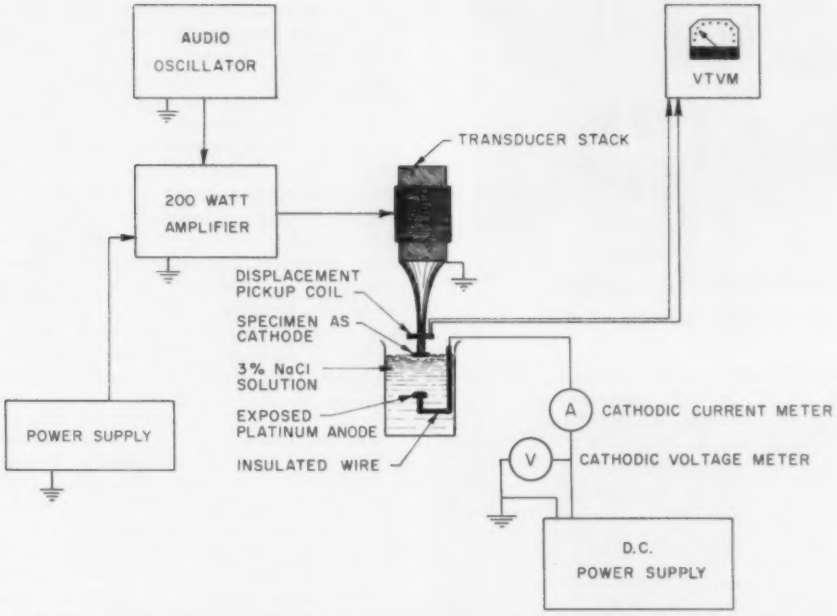

Fig. 4 Block diagram showing the circuit used to generate cavitation on the specimen, and the circuit for cathodic protection

The Current Field in Test Cell

Some studies were made of the electric current field between the platinum electrode and the test specimen which was of the dished-face type. The purpose of this investigation was to make certain that a significant fraction of the current flowed to the face of the specimen. The findings are illustrated for a specimen of mild steel (1018) made cathodic relative to the platinum electrode in a 3 per cent solution of NaCl in distilled water. The circuit had an inherent back emf resulting from electrolytic action which always had to be subtracted from the external voltage readings. For a given current, the voltage between the electrodes was observed to decrease noticeably with the onset of cavitation vibrations. This observed reduction in the cell resistance is presumably due to the agitation and partial removal of poorly conducting layers of hydrogen gas at the cathode. The voltage as a function of cathodic current to the test specimen in the noncavitating

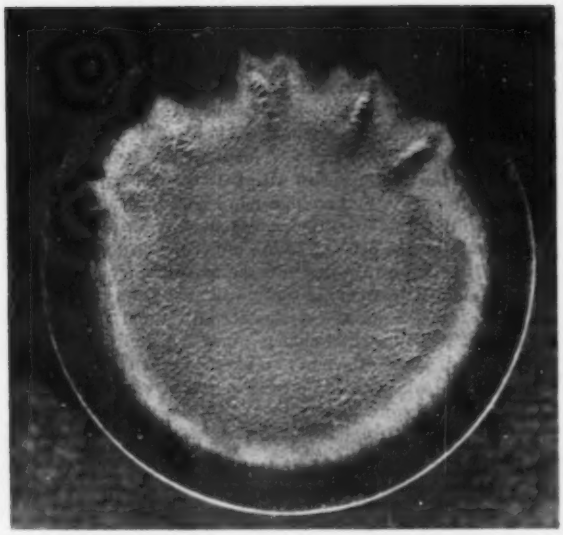

Fig. 5 Cavitation damage on a flat specimen with no cathodic protection

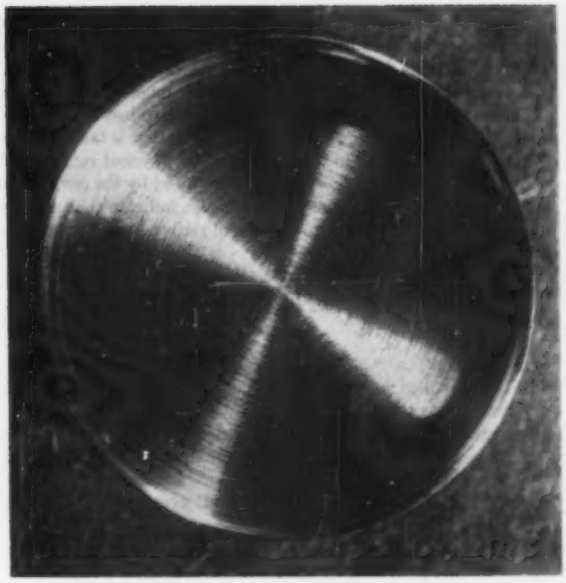

Fig. 7 Photograph of a dished specimen

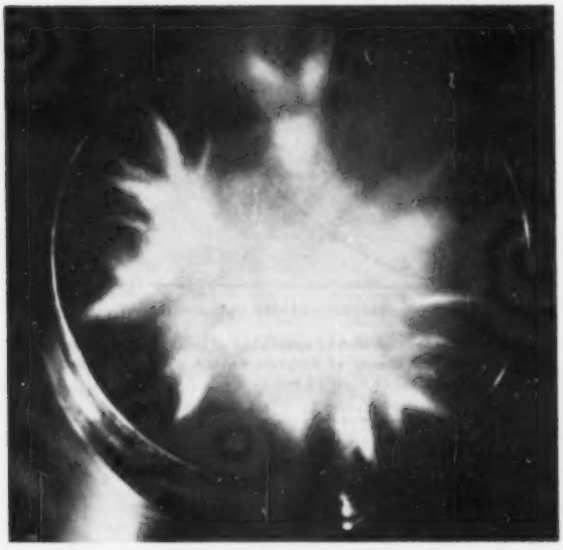

Fig. 6 Cavitation cloud shown on the face of the oscillating specimen

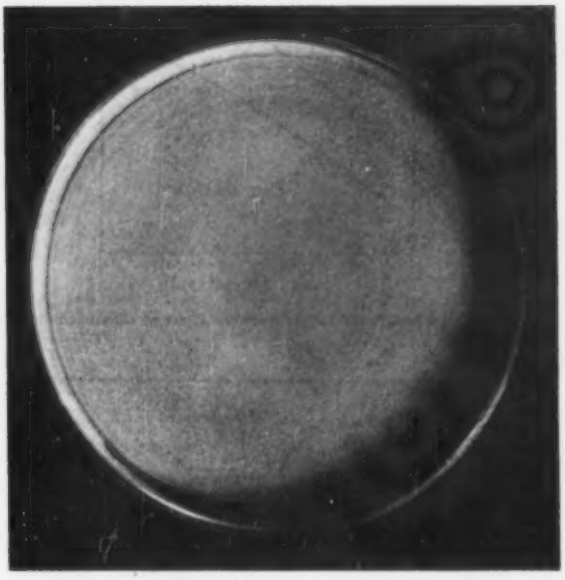

Fig. 8 Damage pattern obtained with a dished specimen. The damage pattern has this uniform appearance with or without cathodic current.

(stationary) condition and in the cavitating condition is shown in Fig. 9.

To determine the proportion of the total current which passed through the cavitating part of the cathode surface, two dished specimens were prepared. The flat surface exposed to cavitation of one of these specimens was coated with insulating enamel while the sides and edge of the other dish were so coated. The enamel used was "Formvar."[2] The current readings for the salt solution are shown in Table 1 for a total impressed voltage of 3 volts. Since all the current measurements given in Table 1 were at the same voltage, they are inversely proportional to the cell resistance. As has been remarked, the cell resistance in all three configurations shows a marked decrease when cavitation is taking

Table 1 Test specimen cathode and platinum anode; impressed voltage 3 volts

		milliamp
Bare specimen	No cavitation	2.3
	With cavitation	6.2
Specimen with sides insulated	No cavitation	1.6
	With cavitation	4.4
Face-insulated specimen	No cavitation	1.5
	With cavitation	2.8

[2] Material used by General Electric Company for wire insulation.

place. With no cavitation, there is only a small difference in the cell resistance between a specimen with its sides insulated and a specimen with its face insulated. In the cavitating condition, however, the cell resistance is found to be much lower for the specimen with insulated sides than for the face-insulated specimen. This "depolarizing" effect when cavitation is taking place over the specimen face indicates that some physical removal of hydrogen from the specimen surface is produced by the cavitation bubbles. These current measurements also indicate that a large fraction of the current flows to the face of the specimen while cavitation occurs.

Cavitation Damage Results in Salt Solution With Cathodic Currents

A series of experiments was carried out in a 3 per cent solution of NaCl in distilled water with specimens made of several different materials.

The results with mild steel (1018) are summarized in Fig. 10. The composition of this material is as follows: C 0.17, Mn 0.73, P 0.007, and S 0.024 per cent. The Brinell hardness number (on the scale of a 10-mm ball with 500 kg load) averaged 160 and was found to vary only slightly with each specimen. Each curve shown in Fig. 10 is the average of the weight loss values which were measured with three different specimens. Examples of the data, and the average curve, are shown in Figs. 11 and 12.

The results with 4340 steel, of Brinell hardness number 210 (on the 3000-kg scale), are summarized in Fig. 13. Each of these curves is the average of the data for three different specimens. Examples of the data, together with the average curve, for a few values of cathodic current are shown in Figs. 14, 15, and 16.

The results with 17–7 PH stainless steel, of Brinell hardness number 235 (on the 3000-kg scale), are shown in Fig. 17. Examples of the data, together with the average curve, for a few values of cathodic current are shown in Figs. 18, 19, and 20.

The preceding series of experiments all showed very similar trends, but it seemed desirable to study a material of a quite different kind. It was thought of interest to examine a relatively inactive metal which could be easily obtained with high purity. Copper was therefore investigated with the results shown in Fig. 21. Figs. 22, 23, and 24 show examples of the data obtained together with the averaged curves.

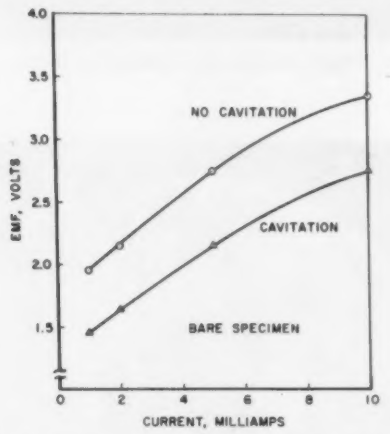

Fig. 9 Emf as a function of cathodic current with and without cavitation on the cathode

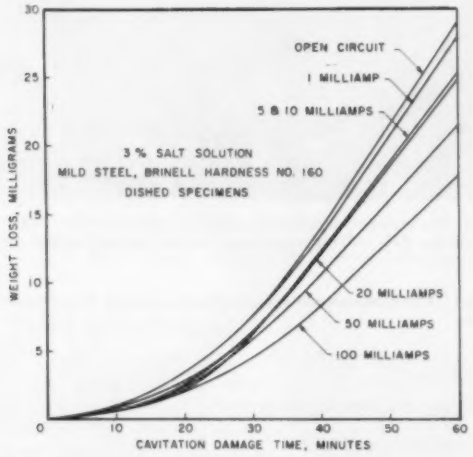

Fig. 10 Weight loss for dished specimens as a function of damage time; different levels of cathodic current

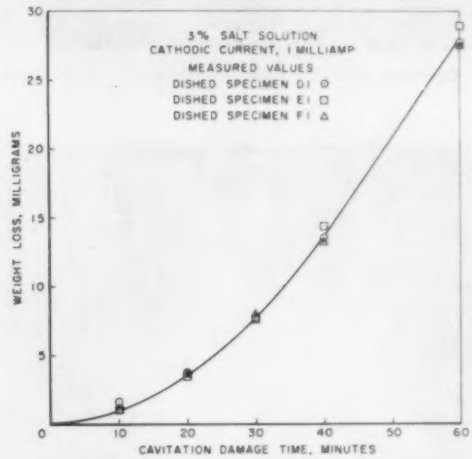

Fig. 11 Weight loss for dished specimens of mild steel as a function of damage time; 1 milliamp of cathodic current. Test liquid was 3 per cent solution of NaCl in distilled water.

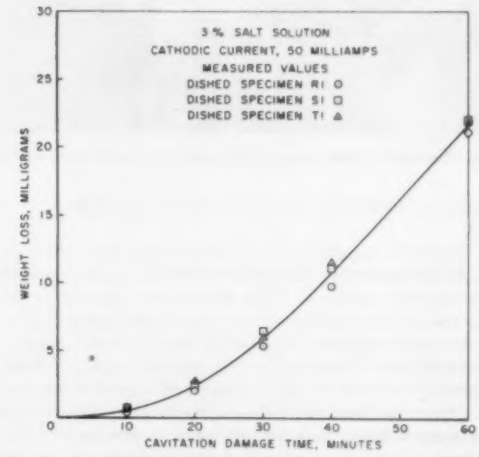

Fig. 12 Weight loss for dished specimens of mild steel as a function of damage time; 50 milliamp of cathodic current. Test liquid was 3 per cent of NaCl in distilled water.

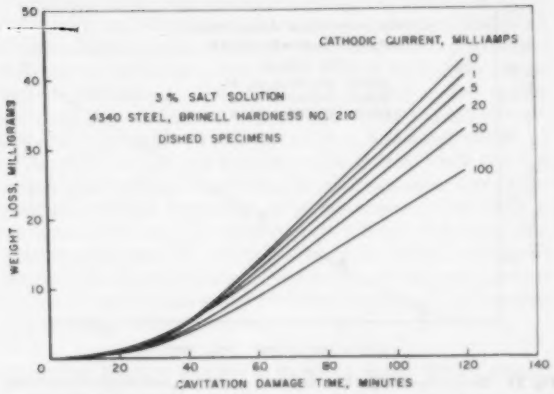

Fig. 13 Summary curves of cavitation weight losses in 4340 steel for several values of cathodic current. Each of these curves is the average of the data for three different specimens.

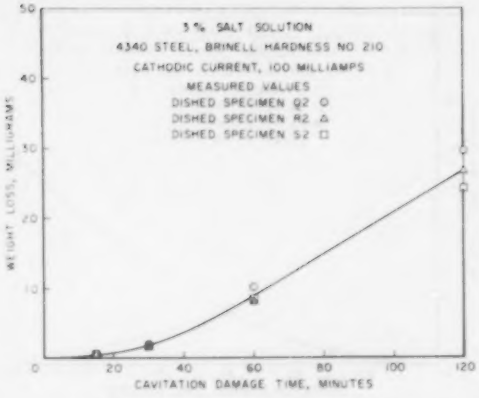

Fig. 16 Cavitation weight loss for 4340 steel specimens in 3 per cent salt solution with cathodic current of 100 milliamp

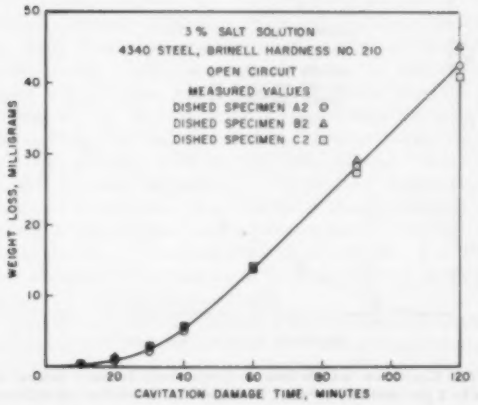

Fig. 14 Cavitation weight loss determinations for 4340 steel specimens in 3 per cent solution of NaCl in distilled water with no cathodic current

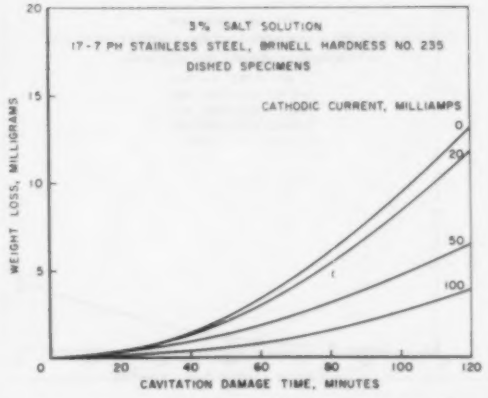

Fig. 17 Summary curves of cavitation weight losses in 17–7 PH stainless steel for several values of cathodic currents. Each curve is the average of data for three different specimens.

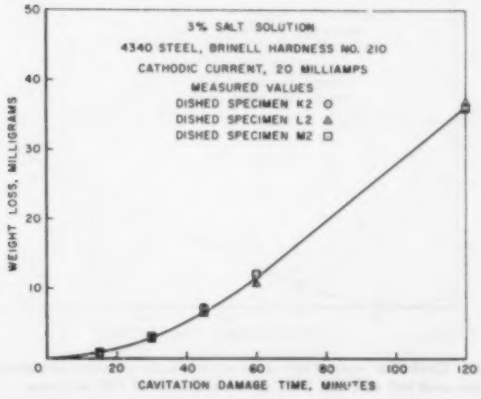

Fig. 15 Cavitation weight loss for 4340 steel specimens in 3 per cent salt solution with cathodic current of 20 milliamp

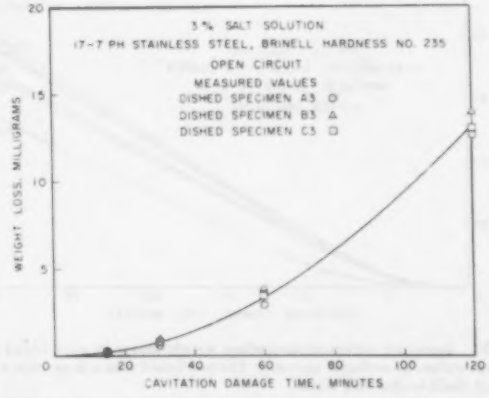

Fig. 18 Cavitation weight loss for 17–7 PH stainless steel in 3 per cent salt solution with no cathodic current

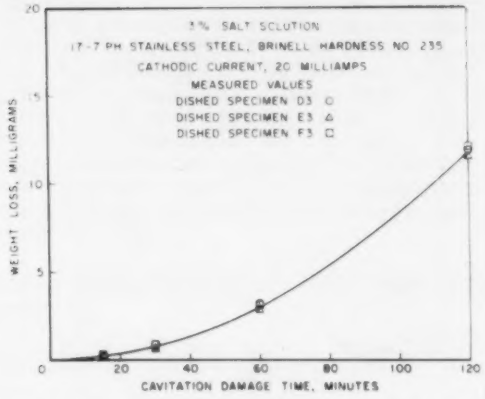
3% SALT SOLUTION
17-7 PH STAINLESS STEEL, BRINELL HARDNESS NO. 235
CATHODIC CURRENT, 20 MILLIAMPS
MEASURED VALUES
DISHED SPECIMEN D3 ○
DISHED SPECIMEN E3 △
DISHED SPECIMEN F3 □
WEIGHT LOSS, MILLIGRAMS
CAVITATION DAMAGE TIME, MINUTES

Fig. 19 Cavitation weight loss for 17–7 PH stainless steel in 3 per cent salt solution with cathodic current of 20 milliamp

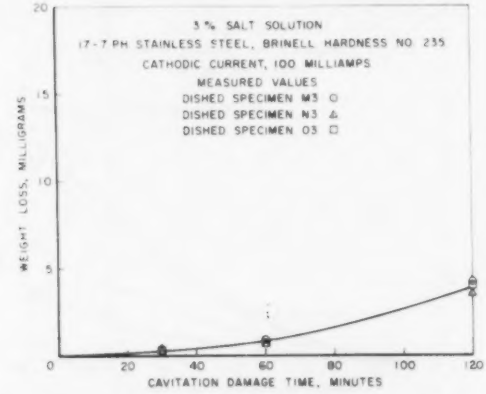
3% SALT SOLUTION
17-7 PH STAINLESS STEEL, BRINELL HARDNESS NO. 235
CATHODIC CURRENT, 100 MILLIAMPS
MEASURED VALUES
DISHED SPECIMEN M3 ○
DISHED SPECIMEN N3 △
DISHED SPECIMEN O3 □
WEIGHT LOSS, MILLIGRAMS
CAVITATION DAMAGE TIME, MINUTES

Fig. 20 Cavitation weight loss for 17–7 PH stainless steel in 3 per cent salt solution with cathodic current of 100 milliamp

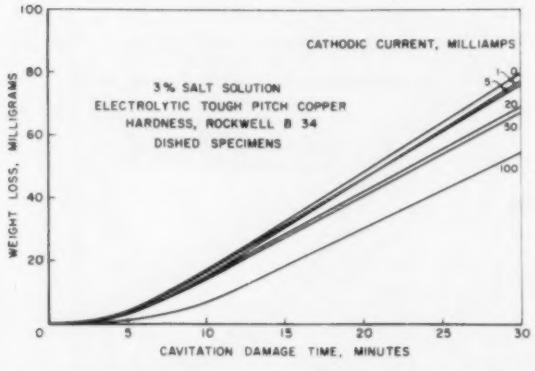

Fig. 21 Summary curves of cavitation weight losses in pure copper for several values of cathodic current. The test liquid was a 3 per cent solution of NaCl in distilled water.

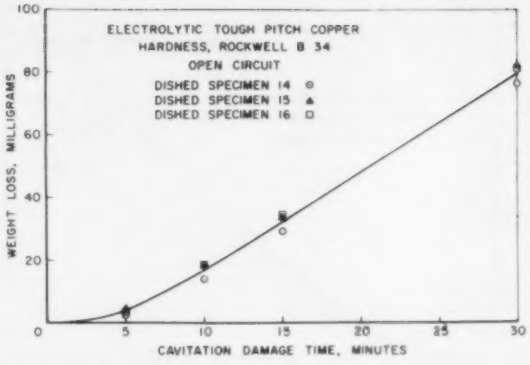

Fig. 22 Cavitation weight loss determinations for pure copper specimens in 3 per cent solution of NaCl in distilled water with no cathodic current

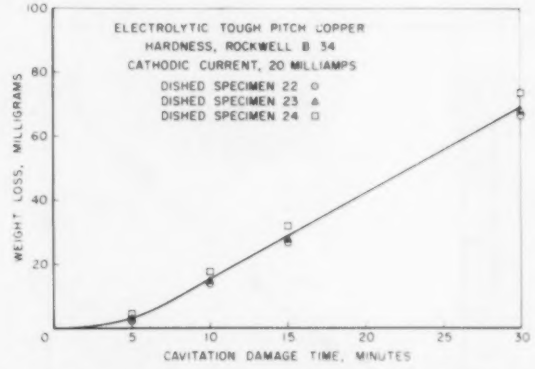

Fig. 23 Cavitation weight loss determinations for pure copper specimens in 3 per cent salt solution with cathodic current of 20 milliamp

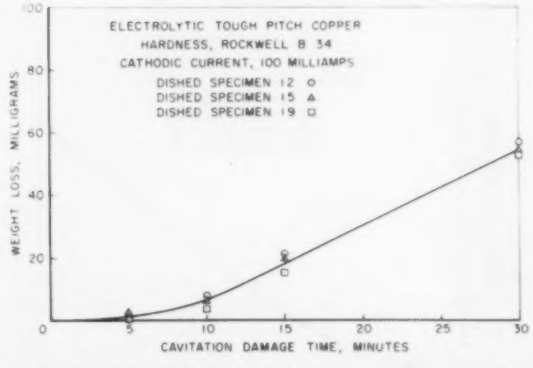

Fig. 24 Cavitation weight loss determinations for pure copper specimens in 3 per cent salt solution with cathodic current of 100 milliamp

The trend found with specimens made of the various steels continued with the pure copper. It must be emphasized that in all of these experiments in the salt solution, the evolution of hydrogen was observed on the specimen surface even at the lowest cathodic current (1 milliamp). This finding of a protective effect against cavitation damage for such a range of materials suggests that the observed hydrogen evolution provided a cushioning effect. A further indication in this direction is the general result that the weight loss decreased monotonically with increasing rate of gas evolution, or with increasing cathodic current. This result is reasonable since the study of the current-voltage relation with and without cavitation indicated that some of the hydrogen layer was removed by the cavitation. Presumably, if the hydrogen gas layer was complete and undisturbed by the cavitation, the cavitation damage would disappear.

Cavitation Damage Results in Buffered Water With Cathodic and Anodic Currents

To give further indication that gas evolution is the significant effect in so-called cathodic protection, it would be most desirable to be able to perform cavitation tests while the specimen was the anode of a cell and at the same time had gas evolved at its surface. It was suggested to the author by Mr. F. L. LaQue, of the International Nickel Company, that such experiments could be done quite readily in buffered distilled water with stainless-steel specimens. Such a series of experiments was performed in distilled water buffered to pH 8. One electrode of the cell was platinum as before and the other was the specimen which was 17–7 PH stainless steel. In the first series of experiments, the specimen was the cathode of the cell, and cavitation damage was determined for cathodic currents of 20, 50 and 100 milliamp. For all of these current values, hydrogen gas was visually observed to be evolved at the specimen. The results of the measurements of cavitation damage weight losses are summarized in Fig. 25. Examples of the data are shown in Figs. 26, 27, and 28. The reduction in cavitation weight loss which increases with the magnitude of the current is clearly demonstrated.

In a second series of experiments, the stainless-steel specimen was made the anode of the cell and cavitation damage was measured for anodic currents of 40, 100, and 200 milliamp. For all of these currents, gas could be observed visually to be evolved at the specimen. The gas evolved at the anode is oxygen and, in order to compare the anodic and cathodic values for the same volume rate of gas evolution, the anodic current must be double that of the cathodic current since the valence of oxygen is twice that of

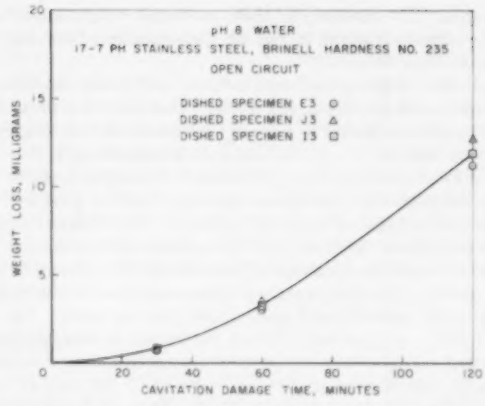
pH 8 WATER
17-7 PH STAINLESS STEEL, BRINELL HARDNESS NO. 235
OPEN CIRCUIT
DISHED SPECIMEN E3 ○
DISHED SPECIMEN J3 △
DISHED SPECIMEN I3 □
WEIGHT LOSS, MILLIGRAMS
CAVITATION DAMAGE TIME, MINUTES

Fig. 26 Cavitation weight loss determinations for 17–7 PH stainless steel in buffered distilled water with no current

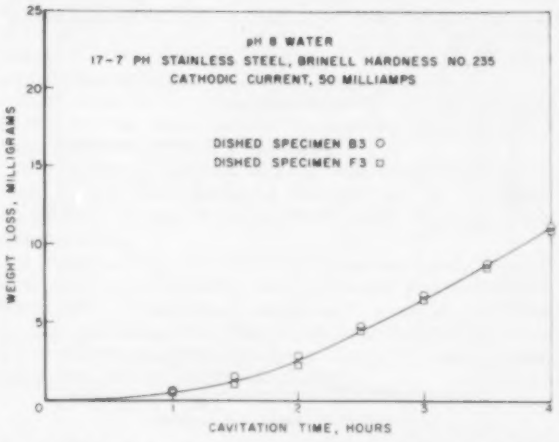
pH 8 WATER
17-7 PH STAINLESS STEEL, BRINELL HARDNESS NO 235
CATHODIC CURRENT, 50 MILLIAMPS
DISHED SPECIMEN B3 ○
DISHED SPECIMEN F3 □
WEIGHT LOSS, MILLIGRAMS
CAVITATION TIME, HOURS

Fig. 27 Cavitation weight loss determinations for 17–7 PH stainless steel in buffered distilled water with cathodic current of 50 milliamp

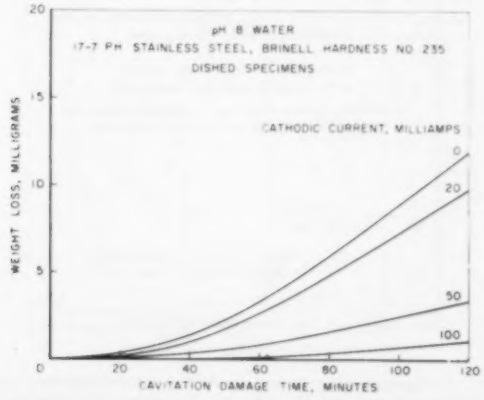

Fig. 25 Summary of cavitation weight loss observations with 17–7 PH stainless-steel specimens as cathodes in buffered distilled water

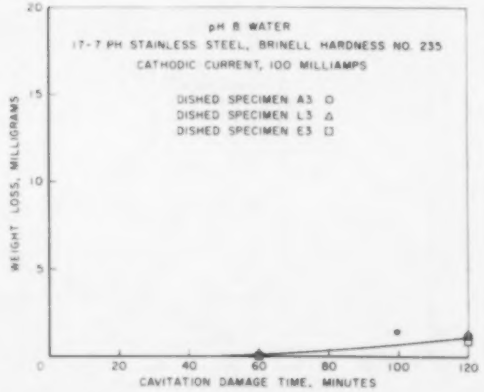
pH 8 WATER
17-7 PH STAINLESS STEEL, BRINELL HARDNESS NO. 235
CATHODIC CURRENT, 100 MILLIAMPS
DISHED SPECIMEN A3 ○
DISHED SPECIMEN L3 △
DISHED SPECIMEN E3 □
WEIGHT LOSS, MILLIGRAMS
CAVITATION DAMAGE TIME, MINUTES

Fig. 28 Cavitation weight loss determinations for 17–7 PH stainless steel in buffered distilled water with cathodic current of 100 milliamp

hydrogen. The summary of these cavitation weight losses with anodic currents is shown in Fig. 29, and examples of the data are shown in Figs. 30 and 31.

From the comparison of these cathodic and anodic experiments at corresponding currents, it is evident that there is a protective effect against cavitation damage in both cases which is roughly of the same magnitude. In making such a comparison it must be kept in mind that there is a weight loss in an anodic specimen entirely independent of cavitation damage which is produced by electrolytic solution of the anode material. The weight loss in a specimen exposed to cavitation damage should be corrected for this effect when the specimen is the anode of the electrolytic cell. After such a correction, a more precise comparison of the weight losses in the cathodic and anodic cases may be made. Fig. 32 shows such a comparison. When the curves of this figure are compared with the open-circuit weight losses, it is clear that there is a large protective effect which is very nearly the same in both cases. There is, however, an indication that the weight losses are slightly higher in the anodic case. This difference is so small that it might appear to be subject to question. In order to get additional information on this point, rather sensitive measurements are required. The following type of experiment was undertaken for this purpose. It may be noted in the experimental data that the initial values of the cavitation weight losses as a function of exposure time correspond to slower rates than the later values. This initial behavior has been described as being due to an "incubation period." It is probably a result of incomplete roughening of the surface in the early stages of the cavitation damage. In the latter stages of cavitation exposure, the weight losses become linear functions of exposure time, at least until the surface becomes severely damaged. This behavior of the weight loss has been used to get additional information on the relative effects in the cathodic and anodic cases. The results of these determinations of weight losses in the postincubation, or linear, region are shown in Fig. 33. The anodic curve is shown after correction for weight loss due to electrolytic solution as a result of the current flow alone. Even after this correction is made, there is an indication that the rate of anodic cavitation weight loss is slightly greater than the corresponding cathodic weight loss.

It is clear that there is a protective effect both for the cathodic and anodic cases which is associated with gas evolution and which is to be ascribed to a cushioning effect of the gas being evolved. One may say, further, that the amount of the protective effect is roughly the same in the two cases. There is evidence, however, that the weight losses for corresponding values of the currents are somewhat greater in the anodic case than in the cathodic case. Such a result is not surprising since, in the anodic situation, anode material is going into solution by the electrolytic action of

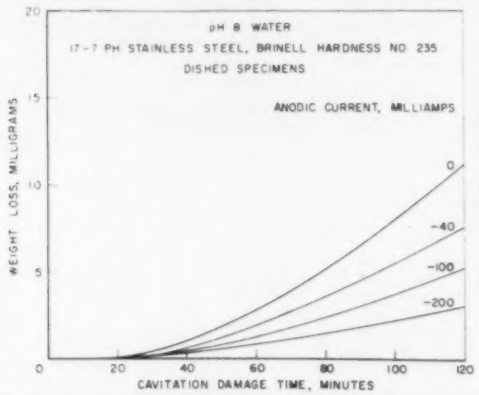

Fig. 29 Summary of cavitation weight loss observations with 17-7 PH stainless-steel specimens as anodes in buffered distilled water. The anodic current values are double the cathodic current values so as to give corresponding rates of gas evolution in the two cases: Oxygen with valence two for the anodic case, hydrogen with valence one for the cathodic case.

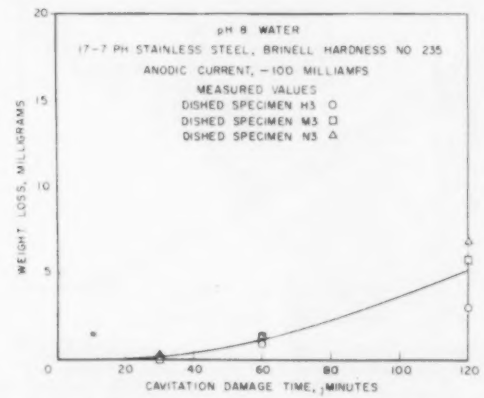
pH 8 WATER
17-7 PH STAINLESS STEEL, BRINELL HARDNESS NO. 235
ANODIC CURRENT, -100 MILLIAMPS
MEASURED VALUES
DISHED SPECIMEN H3 ○
DISHED SPECIMEN M3 □
DISHED SPECIMEN N3 △
WEIGHT LOSS, MILLIGRAMS
CAVITATION DAMAGE TIME, MINUTES

Fig. 30 Cavitation weight loss determinations for 17-7 PH stainless steel in buffered distilled water with anodic current of 100 milliamp

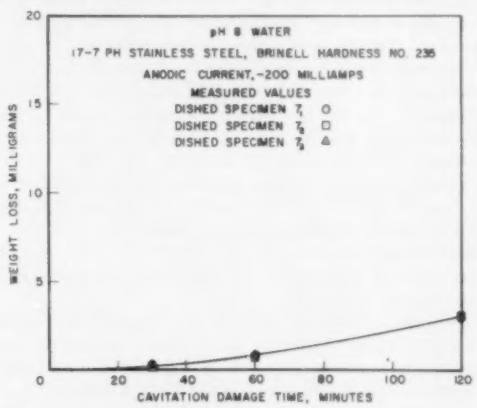
pH 8 WATER
17-7 PH STAINLESS STEEL, BRINELL HARDNESS NO. 235
ANODIC CURRENT, -200 MILLIAMPS
MEASURED VALUES
DISHED SPECIMEN 7₁ ○
DISHED SPECIMEN 7₂ □
DISHED SPECIMEN 7₃ △
WEIGHT LOSS, MILLIGRAMS
CAVITATION DAMAGE TIME, MINUTES

Fig. 31 Cavitation weight loss determinations for 17-7 PH stainless steel in buffered distilled water with anodic current of 200 milliamp

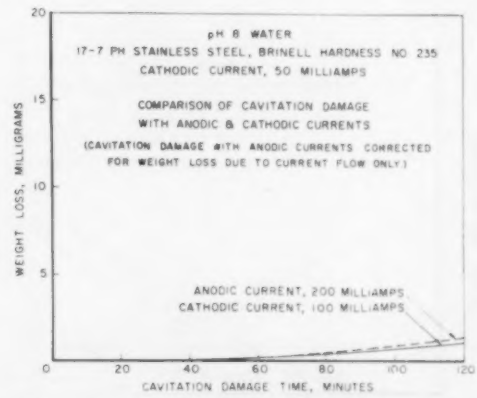
pH 8 WATER
17-7 PH STAINLESS STEEL, BRINELL HARDNESS NO. 235
CATHODIC CURRENT, 50 MILLIAMPS
COMPARISON OF CAVITATION DAMAGE
WITH ANODIC & CATHODIC CURRENTS
(CAVITATION DAMAGE WITH ANODIC CURRENTS CORRECTED
FOR WEIGHT LOSS DUE TO CURRENT FLOW ONLY)
ANODIC CURRENT, 200 MILLIAMPS
CATHODIC CURRENT, 100 MILLIAMPS
WEIGHT LOSS, MILLIGRAMS
CAVITATION DAMAGE TIME, MINUTES

Fig. 32 Comparison of cavitation weight loss for stainless-steel specimens with anodic and cathodic currents. The observed weight loss for the case in which the specimen is the anode of the cell is corrected for the weight loss due to current flow only.

the current. That the weight loss after exposure to cavitation should be slightly enhanced under such conditions could very well be expected. This nonadditive, interaction effect of the anodic current erosion and the cavitation erosion is under continued investigation.

A final type of experiment which is readily performed with a cathodic or anodic specimen in buffered distilled water is the reduction of the current level to so low a value that no visible gas evolution occurs. Such a reduction in current level for the cathodic experiments with the salt solution was not practicable since gas was observable at the cathode with currents as low as 1 milliamp. It was found that there was no observable gas evolution at a cathodic or at an anodic specimen in the buffered water at a current of 2 milliamp. Under such conditions, no protective effect in cavitation damage should be detected. In order to obtain high experimental sensitivity, the specimens used were in the postincubation, or linear, stage of cavitation weight loss. Further, each specimen was run alternately as a cathode with 2-milliamp current and then at zero current. Similarly, a specimen was run alternately as an anode at 2-milliamp current and then at zero current. The successive values of the cavitation weight losses were measured and they are shown in Fig. 34 for 4340 steel specimens and in Fig. 35 for 17-7 PH stainless-steel specimens. The arrows in these figures show the direction of the successive cavitation experiments. It should be remarked that any anodic electrolytic weight losses at the current levels used would be extremely small. Within the limits of experimental accuracy there was no protective effect for these cathodic or anodic currents.

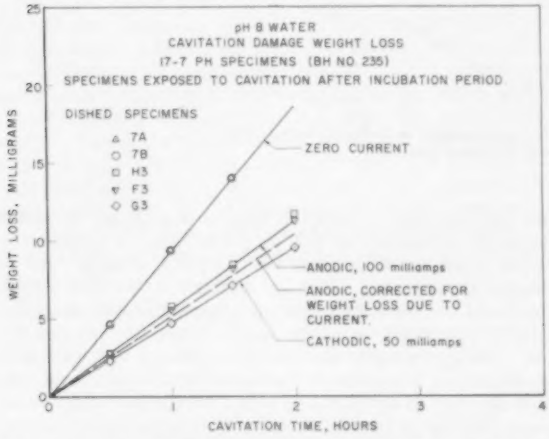

Fig. 33 Comparison of anodic (100 milliamp) cavitation weight losses with cathodic (50 milliamp) cavitation weight losses. The dashed anodic curve shows correction due to electrolytic solution by the current only and is to be compared with the cathodic curve.

Conclusions

1 Experiments in a 3 per cent solution of salt in water showed a protective effect in cavitation damage for a wide variety of materials when the test specimens were made the cathodes of an electrolytic cell. The reduction of the cavitation weight loss is associated with the evolution of gas (hydrogen) at the surface of the specimen.

2 Experiments in buffered distilled water showed a protective effect in cavitation damage both when the specimen was an anode and when it was the cathode of an electrolytic cell, provided the voltage or current was high enough so that gas would be liberated at the specimen surface.

3 Experiments in buffered distilled water at voltages or currents so low that no gas was evolved, showed no protective effect either for cathodic or anodic specimens.

4 It is strongly indicated that a cathodic or anodic protective effect in cavitation damage is primarily due to a cushioning effect of the gas which is electrolytically liberated at the material surface.

5 An interesting, nonadditive or incremental, weight loss of small magnitude is indicated when a specimen is simultaneously losing mass by electrolytic-current transfer and by cavitation damage. There is no indication as yet of any reverse effect due to any corrosion protection when a specimen is the cathode while being exposed to cavitation weight loss.

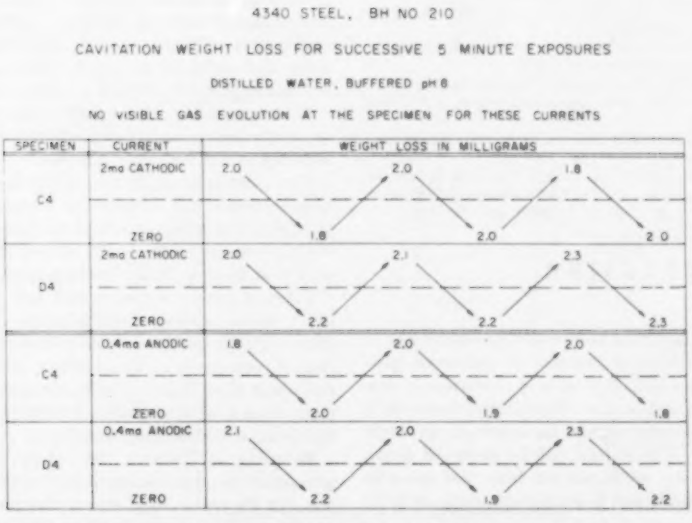

Fig. 34 Cavitation weight losses for 4340 steel in buffered water. The arrows show the sequence of successive runs with the same specimens.

17-7 PH STAINLESS, BH NO 235

CAVITATION WEIGHT LOSS FOR SUCCESSIVE 15 MINUTE EXPOSURES

DISTILLED WATER, BUFFERED pH 8

NO VISIBLE GAS EVOLUTION AT THE SPECIMEN FOR THESE CURRENTS

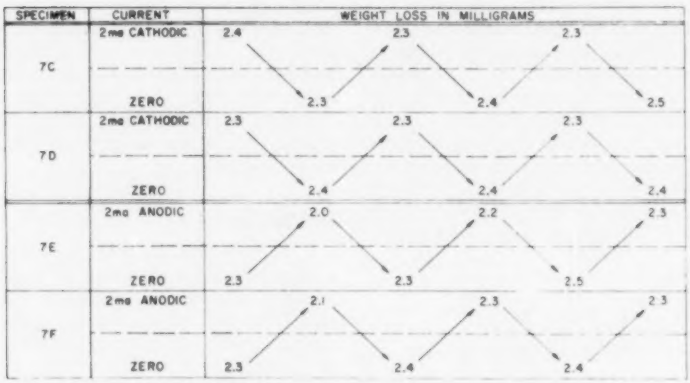

Fig. 35 Cavitation weight losses for 17–7 PH stainless steel in buffered water. The arrows show the sequence of successive runs with the same specimen.

Acknowledgments

This study was supported by the U. S. Navy Office of Naval Research, Mechanics Branch. The author wishes to thank Mr. Barry Bass for valuable assistance with the measurements. He is indebted to Mr. F. L. LaQue of International Nickel Company, Inc., for his suggestion of the anodic experiments in buffered water which proved to be most informative.

References

1 M. S. Plesset, "On Physical Effects in Cavitation," "Deformation and Flow of Solids," R. Grammel, editor, Springer, Berlin, Germany, 1956, pp. 218–235.

2 M. S. Plesset and A. T. Ellis, "On the Mechanism of Cavitation Damage," TRANS. ASME, vol. 77, 1955, pp. 1055–1064.

3 G. Petracchi, "Intorno all' interpretazione del processo di corrosione per cavitazione," *La Metallurgica Italiana*, 1949, pp. 1–6.

4 W. H. Wheeler, "Mechanism of Cavitation Erosion," Proceedings of the Symposium on Cavitation in Hydrodynamics, National Physical Laboratory, Paper No. 21, 1956, pp. 1-31 (Her Majesty's Stationery Office, London, England).

5 O. K. Mawardi, Technical Memorandum No. 4, Acoustics Research Laboratory, Harvard University, 1949.

6 W. P. Mason, "Internal Friction and Fatigue in Metals at Large Strain Amplitudes," *Journal of the Acoustical Society of America*, vol. 28, 1956, pp. 1207–1218.

7 R. W. Wood, "Supersonics, The Science of Inaudible Sounds," Colve Lecture, Brown University, 1937, pp. 103–116.

8 G. I. Taylor, "The Instability of Liquid Surfaces When Accelerated in a Direction Perpendicular to Their Planes, I," *Proceedings of The Royal Society*, vol. 201, series A, 1950, pp. 192–196.

DISCUSSION

R. M. Henry[3]

I wish to complement the author on a well presented paper in which he contributes valuable information on cavitation phenomena and a comprehensive analysis of how cavitation is produced in oscillatory type of equipment. Especially noteworthy is his addition of a wall around the edge of the specimen to obtain more uniform test results. This feature will be discussed later.

We use a magnetostrictive cavitation machine that operates at approximately 1.2 kilocycles and a double amplitude of 0.018 in. This results in a maximum velocity of 5.7 ft per sec and a maximum acceleration of 1330 g's. The vibrating element is a hollow nickel rod 60 in. long and 1.5 in. in diameter and is clamped at the center. The two driving coils are mounted one above and one below the rod clamp. Cooling is accomplished by blowing air through the annular space between the coils and the rod. The test specimens are 1.5 in. in diameter by $^1/_8$ in. thick and are secured, by two screws, to a plug brazed in the end of the rod. Specimens are immersed 0.5 in. with 6 in. depth of water under them. Plexiglas is used for the water container to cut down noise.

Although our equipment and the Cal. Tech. equipment operate at quite different frequencies the results we have obtained in a limited number of tests tend to substantiate the results published in this paper.

We think of cathodic protection in terms of current density in milliampere per sq ft of wetted surface. Based on the dimensions of the submerged part of Professor Plesset's specimen and 1 milliamp of current, his lowest current density was approximately 295 milliamps per sq ft. With 100 milliamps he was using 29.5 amperes per sq ft, which adds up to a prodigious amount of power if applied to a large surface.

We have used from 25 to 300 milliamps per sq ft and observed no cavitation protection except with 300 milliamps. Our tests were run in city water at 78 to 80 F.

The most interesting part of these experiments to us is the modification of the shape of the test specimens to provide a wall at edge of the specimen, resulting in a uniform damage pattern. We have observed the "star" pattern in the bubbles and have experienced uneven damage pattern in our experiments.

There is one consequence that may have resulted from use of the "dished" specimen which is not mentioned by the author. The wall may have served to collect the hydrogen or prevent it from dispersing as it would with a perfectly flat specimen, with the result that this probably increased the effectiveness of the cushioning to a considerable extent. The author's comment on this point would be appreciated.

Referring to Table 1, the current when cavitating is much greater for the side-insulated specimen than for the face-insulated one, but the uninsulated area is also greater for the side-insulated condition. The current in these two cases is very nearly proportional to the uninsulated surface area. Also, since cavitation

[3] Engineering Research Laboratory, Newport News Shipbuilding and Dry Dock Company, Newport News, Va.

bubbles do not act on the sides of the specimen perhaps some phenomenon other than the action of the cavitation bubbles is responsible for the decrease in resistance. It seems possible that the layer of hydrogen formed on the sides is removed by the scrubbing action of the water. This detail concerning why the resistance is less when cavitating does not invalidate the results and conclusions given by the author.

Martin Friedman, Jr.[4]

As a welding contractor who specializes in cavitation damage repair of turbines, I have been doing some research in cathodic protection of turbine runners. One of the largest manufacturers of cathodic protection equipment for ships has been working with me; also one of the larger turbine builders has made some magnetic stricture tests, up to 300 milliamp, and the results parallel Professor Plesset's findings.

The testing equipment used to simulate cavitation conditions in these tests reproduces in two hours the cavitation that would occur in approximately three months; so in effect, it is increasing the cavitation rate by approximately 1000 times. In the standard use of cathodic protection on ships' propellers, an impressed current of not over 60 milliamp per sq ft is used, with success, in salt water. Raising the rate of damage in the test specimens by a factor of better than 1000 to 1 and not being able to raise the impressed current by the same ratio makes the accuracy of the graphs open to question. I believe the cathodic protection effect would be even better than that shown by the author's results.

Fig. 36 shows the prepared location of anodes in a typical turbine installation.

[4] Job and Contract Welding, So. Norfolk, Va.

S. A. Tatum[5]

Professor Plesset has done an admirable job of supporting the theory that cathodic protection of cavitating parts can only be expected to take place when there is enough hydrogen evolved at the specimen to cushion the effect of the collapsing bubbles. The data and curves displayed might lead to some incorrect interpretations however.

The ampere densities used in this experiment are extremely large. While the 100 milliamperes that gave a large amount of protection may seem to be a small number, it corresponds to 29.5 amp per sq ft which, for large specimens, would make it prohibitive. This is likely to be the low extreme of the current density needed for protection. Since the amount of protection is in some manner proportional to the number of hydrogen atoms on the surface of the plate, the per cent retention of the evolved gas would be a very important factor in determining the ampere density necessary for a given amount of protection. When Professor Plesset dished the specimen to reduce the radial flow, he probably increased severalfold the retention of evolved gas.

If we calculate the number of amperes necessary to keep a layer of hydrogen 10^{-4} cm thick on the surface of the specimen with zero retention from cycle to cycle, we get 2.41 amperes or 324 amperes per square foot. The actual current density necessary for a given application would depend on the per cent retention and the intensity of cavitation. It is apparent, however, that except for small areas of metal that can be electrically isolated the power requirements for cathodic protection of cavitating parts would be prohibitive.

[5] Engineering Research Laboratory, Newport News Shipbuilding and Dry Dock Company, Newport News, Va.

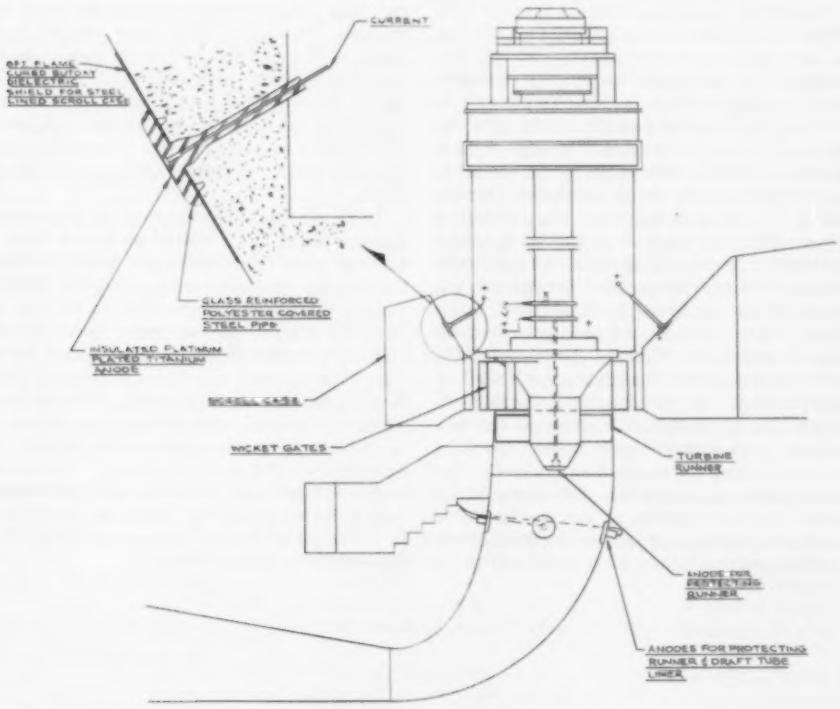

Fig. 36 Proposed cathodic protection equipment turbine

Appendix

A Area of specimen

(1) $A_{face} = \pi r^2 = \pi/4\ (^5/_8)^2 = 0.305$ sq in. $= 1.98$ cm^2

(2) $A_{wall} = \pi \cdot d \cdot t = \pi \times {}^5/_8 \times {}^1/_{32} = 0.184$ sq in.

(3) Max current used in experiment

$$\frac{0.100 \text{ amps} \times 144}{0.489} = 29.5 \text{ amps/ft}^2$$

B Current density needed to deposit film of hydrogen on 1.98 cm^2

(1) There are 0.268×10^{20} molecules/cm^3 at STP
For one square cm area 10^{-4} cm thick
No. molecules $= 0.268 \times 10^{20} \times 10^{-4} = 0.268 \times 10^{16}$
No. atoms $= 2 \times 0.268 \times 10^{16} = 0.536 \times 10^{16}$

(2) Total charge to deposit this number of atoms on specimen

$$Q = 1.6 \times 10^{-19} \times 0.526 \times 10^{16} \times 1.98 = 0.000172 \text{ coul}$$

(3) Total current if atoms must be replaced at 14200 times a second

$$I = 0.000172 \text{ coul/cycle} \times 14.2 \times 10^3 \text{ cycle} = 2.41 \text{ amps}$$

Author's Closure

It was of particular interest to me to learn from the comments of Mr. Henry that he has also observed the "star" pattern of the cavitation as well as the uneven damage associated with it. This uneven damage with flat specimens is of significance, I believe, for the behavior of the damage with high cathodic currents. I shall return to this point below.

Mr. Henry has suggested that the dished specimens might keep the evolved gas from dispersing so that the cushioning effect might thereby be enhanced in comparison with the behavior with flat specimens. While such an effect is a possibility I believe that it does not play an important role in the experiments. To support this view I shall briefly summarize the relative protective effects of gas evolution which we have observed on flat and on dished specimens. Aside from greater scatter in the data, we find essentially the same decrease in cavitation damage with flat and with dished specimens for the same values of the current in the range from zero to approximately 10 milliamperes. One can say, therefore, that in the corresponding range of gas evolution there is no "retention" effect as a result of dishing the specimen face. The relative behavior of the damage with flat and dished specimens for high currents is also of interest. For high currents the protective effect with the dished specimens is always larger the larger the current. This monotonic behavior is very reasonable and is what one would expect. With flat specimens, on the other hand, a rise in current above 10 milliamperes leads to a *decrease* in the protective effect. At the same time it was observed that there is a wider area of cavitation damage on the face of these flat specimens at the higher current levels. We have explained this behavior as being the result of an interaction between the cavitation bubble cloud and the evolved gas which spreads the cavitation cloud over a greater area of specimen face. With the dished specimens, the damage pattern is quite uniform and well spread over the specimen face for all currents. It seems to me unlikely that "retention" is a significant item for the difference between flat and dished specimens. It would appear that a much more important factor is the interaction of the evolved gas with the cavitation bubble cloud and the resultant effect on the region of damage. To conclude the discussion of this point, it should be remarked that it is incorrect to think of the evolved gas as giving some kind of uniform coverage of the specimen face when cavitation is taking place. The resistance measurements showed a significant increase in current flow to the face of the specimen when it was exposed to cavitation. This behavior is to be interpreted as being a consequence of greater rate of removal of the gas by the violent flow patterns produced by the collapse of the cavitation bubbles near the specimen face.

The resistance measurements have been discussed by Mr. Henry, and some clarifying remarks regarding them appear to be required. These measurements had the primary purpose of making certain that an appreciable fraction of the current flowed to the face of the specimen where cavitation damage would take place. One should be concerned with this point because the electric field has its largest value at the edge of the specimen and in its immediate neighborhood. A disproportionately large fraction of the current can therefore be expected to flow to this region. This behavior is observed, as expected, when there is no cavitation. When the sides of the specimen are insulated so that the current flows only to the face, the current flowing to the face was 1.6 milliamperes. When the face of the specimen was insulated so that the current flowed only to the sides, the current is nearly the same, i.e., 1.5 milliamperes. This approximate equality of current is observed in spite of the fact that the area of the sides is only 0.6 of the area of the face. The current flow distribution, however, alters appreciably with the onset of cavitation. With cavitation, the current flow to the face with the sides insulated rose to 4.4 milliamperes, while the current flow to the sides with the face insulated increased only to 2.8 milliamperes. In other words, there was relatively a *greater* decrease in the resistance for current flow to the face than for current flow to the sides in spite of the presence of the cavitation bubble cloud which appears only over the face of the specimen and not on the sides. One concludes, therefore, that the cavitation bubbles are more effective in removing adsorbed gas on the face than the noncavitating acceleration of the sides through the liquid.

There was general discussion of the large currents, expressed in amperes per sq ft, for marked protective effect. Once it is clear that the protective effect is the result of a cushioning effect of the evolved gas and when the protective effect is being provided under conditions of strong cavitation with noticeable removal of the evolved gas by the cavitation, then it should be obvious that high rates of gas evolution will be required for significant protection. The original suggestion of cathodic protection was presumably based on the well-known reduction in ordinary corrosion which it produces. Any reduction in ordinary corrosive action by cathodic protection appears to be negligible in most laboratory experiments with cavitation damage. It is conceivable, however, that low rates of gas evolution might give some effective protection under conditions in which the cavitation takes place in such a way that there is less removal of the protective evolving gas cushion by the cavitation.

Correlation of Cavitation Inception Data for a Centrifugal Pump Operating in Water and in Sodium-Potassium Alloy (NaK)

A. G. GRINDELL
Oak Ridge National Laboratory,[1] Oak Ridge, Tenn. Assoc. Mem. ASME

The static head at pump suction at the time of cavitation inception was correlated for water and for 1500 F NaK on the basis of the differences of the vapor pressures of the two liquids. The difference between the vapor pressures, for the same conditions of pump speed and liquid flow, was added to the water-test cavitation inception value; this proved to be a good approximation to the experimental value found for cavitation inception with NaK.

In view of the expanding use of nonaqueous heat-transfer media, it would be desirable, from the viewpoint of economy and convenience, to be able to predict the inception of pump cavitation for nonaqueous systems by using the information which has been obtained for aqueous systems. (Cavitation in a flowing liquid is described as the vaporization of the liquid when the static pressure is reduced to or below the vapor pressure equivalent to the local temperature of the flowing liquid.) The operation of a centrifugal pump under cavitation conditions can lead to reduction of pump performance and to impeller and casing damage. The working pressure of components of high-temperature heat-exchanger circuits, and consequently their design, will depend to some extent upon the pressure necessary to suppress pump cavitation.

Some work has been reported on cavitation in liquid metals, but no data are available that are correlated with data on cavitation in water. Hall and Crofts [1][2] and Trummel [2] have reported data on cavitation in liquid metals. Both reports concerned cavitation in a venturi; Hall and Crofts worked with eutectic sodium-potassium alloy at 250 C, and Trummel worked with sodium at 1215 to 1475 F. Stepanoff [3] has reported on the density dependence of cavitation suppression for propeller pumps in a molten salt of sp gr 1.75 at 850 F. Stepanoff, in a further publication [4], writes, "Vapor pressure should not be overlooked with liquids other than water." Allis-Chalmers Manufacturing Company [5] has reported on a study of cavitation damage to specimens of various materials of construction in 70 F water, 350 F sodium, and 350 F eutectic sodium-potassium alloy.

In order to determine whether a useful relationship exists between centrifugal-pump cavitation inception in water and in a molten metal, a centrifugal pump was operated, first in water, and then in 1500 F NaK (56-wt per cent Na, 44 wt per cent K). Five test points of pump operation were chosen; three runs were made at 300 gpm for pump speeds of 2600, 3000, and 3375 rpm, and two runs were made at 430 gpm for pump speeds of 3000 and 3375 rpm. One run was made at each of the five test points for water and for NaK. Two additional runs were made with NaK for each of the two flow conditions at 3000 rpm.

Test Procedure

Equipment A centrifugal pump was installed in a closed loop of Inconel pipe, sched 40, 4-in. IPS. The loop was equipped with thermocouples, a venturi flowmeter, a throttling valve, pressure-measuring devices, heaters and coolers to provide for isothermal operation, an oxide-removal cold trap, thermal insulation, a drain valve, a drain tank, pump-speed measuring devices, and devices for measuring the level of the liquid in the pump tank. A sketch of the test equipment is presented in Fig. 1, and Fig. 2 is a sketch of the wetted portions of the pump. Fig 3 presents the test pump characteristics with NaK alloy.

Test Method. The methods for obtaining cavitation data and the types of data obtained were, in general, identical for tests with both water and high-temperature NaK. The pump was operated in a noncavitating manner at the speed, flow, and temperature requirements of a selected test point. Data were obtained on pump speed, liquid flow rate, pump head, static head at pump suction, and temperature of the liquid after each of

[1] Operated by Union Carbide Corporation for the U. S. Atomic Energy Commission.

[2] Numbers in brackets designate References at end of paper.

Contributed by the Cavitation Subcommittee of the Hydraulic Division and presented at the Annual Meeting, Atlantic City, N. J., November 29–December 4, 1959, of The American Society of Mechanical Engineers.

Note: Statements and opinions advanced in papers are to be understood as individual expressions of their authors and not those of the Society. Manuscript received at ASME Headquarters, July 14, 1959. Paper No. 59—A-156.

Nomenclature

N	= pump speed, rpm	ΔP_v	= venturi differential pressure, psi	$Bar.$	= barometric pressure, ft
Q	= pump flow, gpm	ΔP_{vc}	= corrected venturi differential pressure, psi	$sp\ gr$	= specific gravity of flowing liquid
T	= temperature of flowing liquid, deg F	H_t	= pump total head, ft	TM	= venturi temperature multiplier
P_d	= pump discharge pressure, psig	H_{ss}	= static head at pump suction, ft abs	C	= venturi coefficient-of-discharge
P_{dc}	= corrected pump discharge pressure, psig	H_{vp}	= vapor pressure of liquid, ft	g	= acceleration of gravity, 32.2 ft/sec^2
P_{pt}	= pump suction static pressure, psig	H_{ci}	= static head at pump suction at cavitation inception, ft abs	A	= venturi throat area, ft^2
P_p	= venturi upstream pressure, psig	c	= pump discharge pressure gage correction, ft	D	= venturi throat diameter, ft
P_t	= venturi throat pressure, psig			β	= ratio of venturi throat to pipe diameters
				V	= velocity in the suction pipe

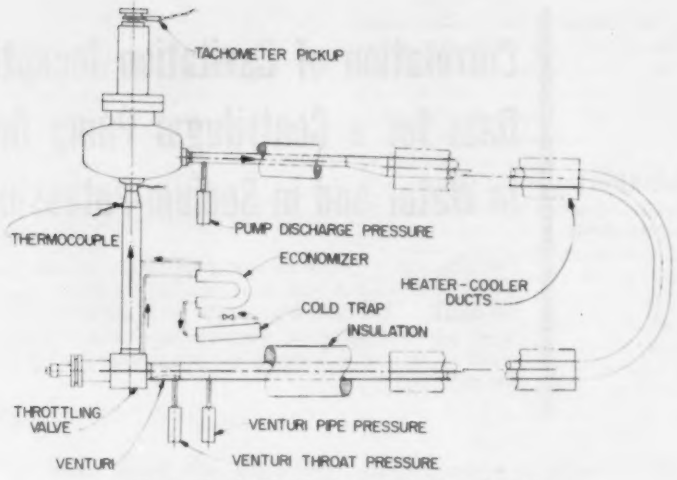

Fig. 1 Sketch of facility for cavitation inception tests

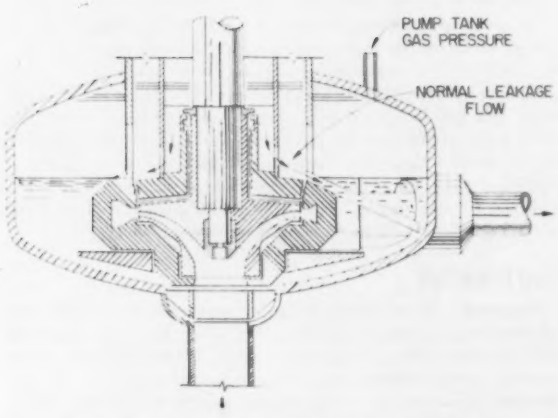

Fig. 2 Sketch of test centrifugal pump and expansion tank

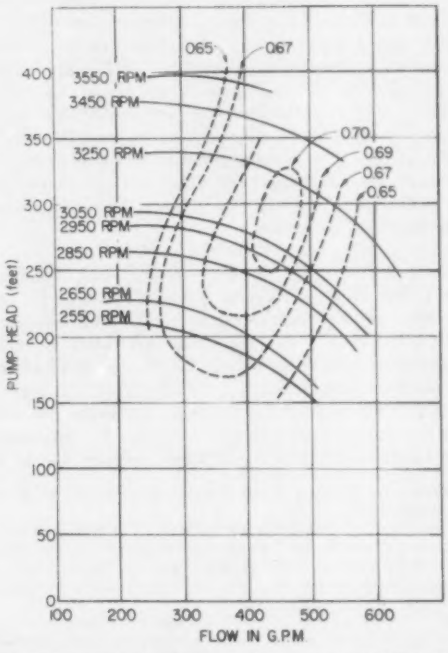

Fig. 3 Performance characteristics of test pump with 1250 F NaK

several successive reductions in pump-tank gas pressure (static head at pump suction). Air was the pump-tank cover gas for the water tests, and helium was used as a protective cover for the NaK.

A sufficient number of reductions in pump-tank gas pressure were made in order to identify the cavitation inception point, H_{ci}, on a plot of H_t versus H_{ss}, where H_t is pump total head measured in feet and H_{ss} is static head at pump suction measured in feet absolute. The data were adjusted by using the appropriate calibration corrections, and graphs (Figs. 4 through 8) were plotted of pump head (measured in feet) versus static head at pump suction (measured in feet absolute) for each run. The absolute static head at pump suction at the inception of cavitation was determined for each run from the corresponding graph. The difference between the vapor pressure of water and of NaK was added to the water-test cavitation-inception value, and this calculated value was compared with the corresponding NaK-test cavitation-inception value.

The flow rates of both water and NaK were measured with the same flowmeter, a 4-in. IPS, 1.53-in-throat nozzle-type venturi tube. The flow rate of NaK was based on the product of the water venturi-meter differential pressure multiplied by the square of the temperature multiplier (TM). Appendix 1 presents a derivation of the temperature multiplier from the standard flowmeter equation for a venturi. The underlying assumption for this particular application of the temperature-multiplier method is that the venturi coefficient-of-discharge (C) varies insignificantly in value between the water and the alloy tests. The discharge coefficient varies from approximately 0.9915 for water flow-rate measurements to approximately 0.9940 for NaK flow-rate measurements [6]. The purpose of setting the flow rates of the alloy in this manner was to duplicate as closely as practicable the flow rates of the water and to permit the absolute flow rates to approach the nominal values of 300 and 430 gpm.

Test Variables. The principal test variables of interest were pump-shaft speed, liquid flow rate, pump tank gas pressure,

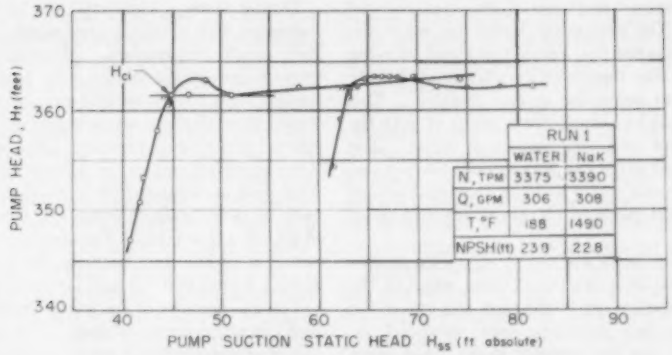

Fig. 4 Cavitation inception for water and for NaK, run 1

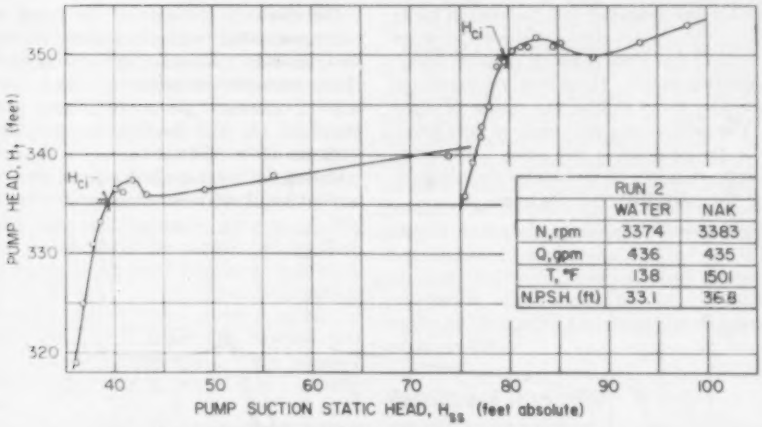

Fig. 5 Cavitation inception for water and for NaK, run 2

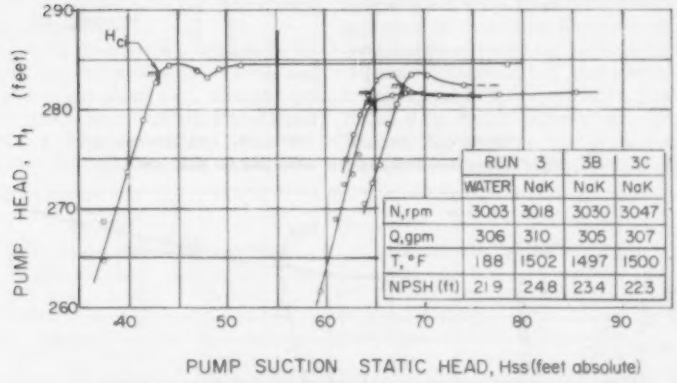

Fig. 6 Cavitation inception for water and for NaK, run 3

pump discharge pressure, and liquid temperature. The method of measuring each of these quantities for water and for high-temperature NaK will be discussed here.

The pump-shaft speed for the water test was measured by two methods. A Strobotac adjusted to line frequency at 3600 rpm was used to stop an image of the pump-shaft coupling at the desired speed. In addition, a count-rate meter was used to integrate, for a selected period of time, the voltage pulses of the pump drive-motor tachometer generator. The integrated number of pulses was then reduced to pump-shaft speed by use of a multiplier which reflected the number of pulses per revolution of the shaft and the selected time period.

Pump-shaft speed for the NaK tests was measured by various methods. For the 3000-rpm run, a Strobotac operating on line frequency was used to obtain a particular image from a pattern of marks which had been painted on the periphery of the pump-shaft coupling. This speed was checked by two methods, one being the count-rate meter method. A second check was performed by using a Hewlett-Packard counter, Model 522B. The three types of measurements agreed to within 5 rpm. Other

pump-shaft speeds which were not multiples of 300 were measured in the following manner: The pump-shaft speed was set at the speed multiple of 300 rpm nearest the desired test speed by using the Strobotac operating on line frequency in order to obtain the shaft-coupling pattern image particular to that multiple. This particular speed was then used to check the readings of both the Hewlett-Packard instrument and the count-rate meter. The shaft speed was then adjusted to the desired speed for the test and was checked by the count-rater meter and the Hewlett-Packard instrument. A measurement range of 10 rpm at the test speed was observed.

The flow rate for the water tests was measured with a nozzle-type venturi meter that had been calibrated using water as the system liquid. A single pressure tap in the pipe and one in the throat were used. These two pressures were measured individually with laboratory-type test pressure gages. The gages were checked at least twice during the water tests and had a maximum error of 0.3 psig at the maximum gage reading.

The flow rate of the alloy was measured with the venturi meter used for the water tests. The venturi pipe and throat pressures were measured with bellows-actuated balanced pressure transmitters connected to receiving gages. These pressure measuring devices were calibrated four times during the course of high-temperature testing. The calibrations were made at zero pump speed by increasing the gas pressure in the pump (expansion) tank in increments of approximately 10 psi and by recording for each step the reading of the individual receiving gage.

During these calibrations, the pump-tank gas pressure was measured with a master gage which had been calibrated by the dead-weight test method. The receiving-gage readings for each pressure measuring device were corrected to the master-gage reading, and the corrections were plotted. A smooth curve was drawn through the correction points, and the measured values of venturi differential pressure, ΔP_v, were corrected accordingly. The corrected values of venturi differential pressure, ΔP_{vc}, were used to compute flow of NaK alloy. An analysis, based on each of three pressure measuring device calibrations, was made of the alloy flow rates. The maximum deviations of the probable actual alloy flow rate from the desired flow rate were calculated to be +5 gpm and −5 gpm for alloy runs 3A and 5, respectively.

The gas pressure of the pump tank was measured with a 0–30 psig laboratory-type test gage. The gage was calibrated against the dead-weight-tested master gage, and the maximum error in the range of interest was 0.10 psig. The pump-tank gas pressure data were not corrected.

The discharge pressure of the pump was measured with a bellows-actuated balanced pressure transmitter connected to a receiving gage. An analysis, based on three separate calibrations of this pressure transmitter was made of the pump head. The largest deviation in pump head, based on the three calibrations, was +1.1 ft. The discharge pressure data were corrected by using one of the calibrations.

During the water cavitation tests, the system temperature was measured with a Taylor dial-type thermometer inserted into the

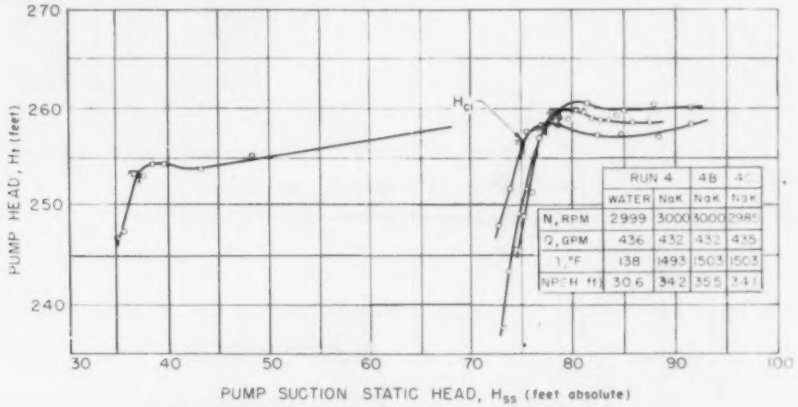

Fig. 7 Cavitation inception for water and for NaK, run 4

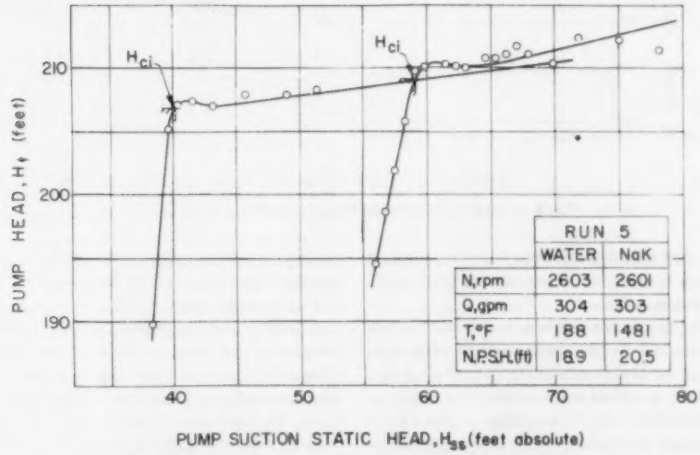

Fig. 8 Cavitation inception for water and for NaK, run 5

flowing liquid. The thermometer was calibrated [7] after the conclusion of the water tests and was found to be reading 2 F high. The water-temperature data were corrected to this calibration.

The temperature of the NaK entering the pump suction was measured during high-temperature testing by means of a Chromel-Alumel thermocouple attached to the outside of the suction pipe (Fig. 1). Subsequently, the thermocouple was calibrated in place against a Pt-Pt-10 per cent Rh thermocouple which had been calibrated against an NBS thermocouple [8]. The calibration indicated that the Chromel-Alumel temperature data were 7 F high, and this correction was applied to the NaK test temperatures. The suction pipe was thermally insulated with 3 in. of Superex (Johns-Manville Co.) pipe insulation. The temperature gradient through the wall of the pipe was estimated to be about 0.9 deg F and was not used to correct the temperature reading of the alloy which entered the pump inlet.

The Experiment

The water tests proceeded smoothly except that attempts to induce cavitation at 2600 rpm and 430 gpm caused oscillations in the system pressure levels, and ingassing of the water occurred. The ingassing apparently resulted from a disturbance to the normal liquid leakage (Fig. 2), which flows from the discharge region of the impeller inward across the top side of the impeller and into the free liquid surface in the pump tank. The direction of the leakage could be reversed when the head developed by the top side of the impeller exceeded the static pressure at the periphery of the impeller. Reversal of the normal leakage flow leads to the pumping of gas from the pump tank into the system liquid by the top side of the impeller. A remedy for this situation might possibly be found in a change in the head-producing ability of the top side of the impeller in order to forestall the flow reversal. In water cavitation run No. 4, some ingassing may have occurred coincidental to cavitation. There was no evidence of ingassing in the other water tests.

The water test temperatures were selected after preliminary testing to provide a positive pressure of air in the pump tank during cavitation inception in the approximate range of from 5 to 10 ft, measured in water at temperature.

During initial testing with NaK, nearly every attempt to induce cavitation led to oscillations in the system pressure levels and to flooding of the upper region of the pump tank with the hot NaK. The difficulty was thought to arise from the introduction of helium into the impeller inlet, and the source of the helium was thought to be the cold trap used for oxide removal. In this device, a small portion, about 1.5 gpm, of the circulating 1500 F NaK is cooled to a relatively low temperature, 250–350 F, in order to remove sodium oxide and is then returned to the system in the pump suction line (Fig. 1).

It was postulated by Watson [9], that the temperature dependence of helium solubility in NaK accounted for the presence of helium as a gas in the oxide trap. That is, helium may be more soluble in 1500 F NaK in the pump tank than in the 250–350 F NaK in the cold trap. Accordingly, valving the cold trap out of the system was sufficient to prevent gassing the pump from that source during subsequent high-temperature operation.

Attempts to induce pump cavitation during a high-temperature run at 2600 rpm and 430 gpm with NaK produced oscillations in the system pressure level and a rapid rise in the liquid level in the pump tank in a manner very similar to the water ingassing incident described in the foregoing. The oxide level in the circulating NaK increased from approximately 30 ppm, the value at the time the cold trap was isolated from the system, to approximately 225 ppm at the conclusion of the test.

Vapor Pressure and Specific Gravity of Water and of NaK. Values for the vapor pressure and specific gravity of water were taken from the standard reference [10]. The specific gravity of the alloy and the vapor pressure of NaK, as predicted by Raoult's law, are presented in Figs. 9 and 10. Experimental work by Miller, et al. [11] indicated that the vapor pressure of the alloy might be slightly higher at a given temperature than would be predicted by Raoult's law. Therefore the vapor pressures of the alloy in the temperature range of interest, as predicted by Raoult's law, and as experimentally checked by Miller and Ewing [11], are presented in Fig. 10. For the purpose of this correlation experiment, the average of the two values was used. The values for the specific gravity of the alloy were taken from p. 34 of reference [12].

Results and Discussion

Determination of Cavitation Inception, H_{si}. For all tests, the average pump speed for each run was set as the speed of that run, and the average flow from the noncavitation region to just beyond the inception of cavitation was used as the flow. The corrected temperature was used as the temperature of the run. Equations (6) and (8) (Appendix 2) were used to compute pump head, H_s, for water and NaK, respectively. Equations (7) and (9) (Appendix 2) were used to compute the absolute static head at pump suction, H_{ss}, for water and NaK, respectively. The flow rates were obtained by using Equation (4) (Appendix 1).

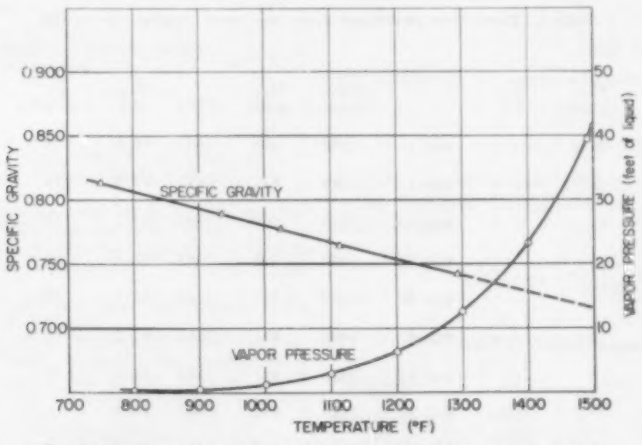

Fig. 9 Vapor pressure and specific gravity of NaK (56 wt per cent Na)

Stepanoff (p. 266, [4]) and Church (p. 83, [13]) have outlined several methods of displaying cavitation inception data in graphical form. The conventional methods consist in plotting pump efficiency versus Thoma's cavitation factor or absolute static head at pump suction, and pump head versus Thoma's cavitation factor or absolute static head at pump suction. The data obtained in these tests were plotted in terms of pump head versus absolute static head at pump suction. Pump head versus absolute static head at pump suction was plotted for each run and is presented in Figs. 4 through 8. A smooth curve was drawn in order to utilize as many of the data points of each test as practicable.

Several criteria for the determination of cavitation inception, H_{ci}, are outlined by Stepanoff (p. 264, [4]). The criterion used here involved identifying the value of the static head at pump suction at which a continued drop in pump head occurred. Three methods for determining that value were investigated:

1 The intersection of the tangent to the nearly horizontal portion of the curve with the tangent to the sloping portion of the curve was found.

2 The intersection of a horizontal line drawn through the lowest noncavitating pump-head data point with the sloping portion of the curve was found

3 The intersection of a horizontal line drawn 2 ft below the lowest noncavitating pump-head data point with the sloping portion of the curve was found.

The maximum deviation of the three methods was 0.6 ft for run No. 1. The second method was chosen to determine the cavitation inception point for each run (Fig. 4).

Correlation of Data for Water and NaK. The cavitation-inception data obtained with high-temperature NaK were compared with an estimated value for NaK cavitation inception that was obtained by adding the difference in the vapor pressures of the two liquids (water and NaK) to the cavitation inception value obtained with water at the same conditions of pump speed and liquid flow. Table 1 gives the pump operating conditions for each run and presents a comparison of the estimated value for cavitation inception with the experimental values for cavitation inception for each NaK run.

For run 1 (Table 1), the estimated cavitation-inception value for NaK, 64.3 ft, was obtained by adding 19.2 ft (the difference between the vapor pressure of water and NaK for this run) to 45.1 ft (the cavitation inception value for water for this run) The experimentally determined cavitation-inception value for NaK is 63.3 ft, and thus is 1 ft lower than the 64.3 ft estimated.

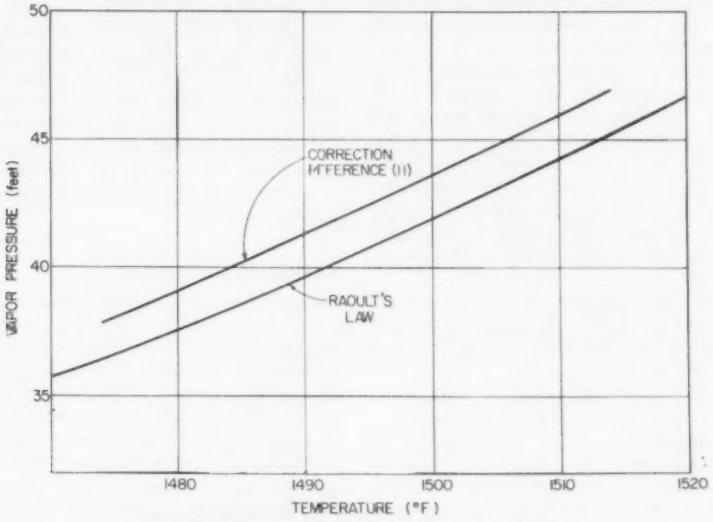

Fig. 10 Vapor pressure of NaK (56 wt per cent Na)

Table 1 Comparison centrifugal pump cavitation inception test results

	Water Tests					Sodium-Potassium Tests							
	N_{av} (rpm)	Q_{av} (gpm)	T (°F)	H_{ci} (ft abs)	H_{vp} (ft)		N_{av} (rpm)	Q_{av} (gpm)	T (°F)	H_{vp} (ft)	Estimated H_{ci} (ft abs)	Alloy Test H_{ci} (ft abs)	Difference (ft)	Difference (%)
Run 1	3375	306	188	45.1	21.3	Run 1	3390	308	1490	40.5	64.3	63.3	+1.0	+1.6
Run 2	3374	436	138	39.5	6.4	Run 2	3383	435	1501	43.0	76.1	79.8	-3.7	-4.7
Run 3	3003	306	188	43.2	21.3	Run 3A	3018	310	1502	43.2	65.1	68.0	-2.9	-4.3
						Run 3B	3030	305	1497	42.1	64.0	65.5	-1.5	-2.3
						Run 3C	3047	307	1500	42.7	64.6	65.0	-0.4	-0.6
Run 4	2999	436	138	37.0	6.4	Run 4A	3000	432	1493	41.2	71.8	75.4	-3.6	-4.8
						Run 4B	3000	432	1503	43.5	74.1	79.0	-4.9	-6.2
						Run 4C	2985	435	1503	43.5	74.1	77.6	-3.5	-4.5
Run 5	2603	304	188	40.2	21.3	Run 5	2601	303	1481	38.5	57.4	59.0	-1.6	-2.7

Discussion. A temperature change of 2 F changes the vapor pressure of 188 F water by 1 ft, and from Fig. 10 it may be seen that a temperature change of 4.4 F effects a change of 1 ft in the vapor pressure of 1500 F NaK. The necessity for precise temperature measurement is readily apparent, and although much effort was expended to obtain satisfactory measurements, the precision required for identifying a change of 1 ft in vapor pressure (particularly for 1500 F NaK) could not be guaranteed in these tests. The test equipment was quite large; there were about 35 gal of alloy in about 1500 lb of Inconel, and a safety-shielded volume of about 1200 ft³ was required.

In his text, Stepanoff [4] presents a thermal cavitation criterion, B, based on certain physical properties of the system liquid and its vapor. The curves presented by Stepanoff were apparently obtained at constant pump speed and available NPSH by varying the flow (resistance to flow). These data were obtained at constant pump speed and flow conditions by varying the available NPSH. The difference in test methods and an apparent lack of information regarding the specific volume of the vapor and the latent heat of vaporization of NaK alloys combine to make analyses of these data by the thermal-cavitation criterion difficult. Resolution of these two difficulties should make the analysis feasible.

Conclusions and Recommendations

The nine estimated values for cavitation inception by 1500 F NaK differ from the experimental values over a range of +1 ft to −4.9 ft. The differences yield a maximum average difference of 4.1 ft, which may be expressed as an average of 5 per cent of the pump-suction static-head values at cavitation inception for the nine NaK runs.

It is suggested that, for the pump studied, cavitation inception with other liquid metals may be estimated on the basis of water-test cavitation inception and vapor pressure data. However, it would be very helpful to obtain similar experimental correlations for other pumps and other liquids.

It is recommended that the temperature of the flowing liquid be accurately determined in future attempts to correlate cavitation inception for a centrifugal pump, particularly if the liquid exhibits a steep slope of vapor pressure versus temperature.

Acknowledgment

The author wishes to express his appreciation to Dr. George F. Wislicenus for suggesting the problem, and to H. W. Savage and E. R. Dytko for encouragement. Thanks are extended to L. V. Wilson for constructive criticism, and to H. C. Young, D. L. Gray, and J. N. Simpson for assistance in obtaining test data. Permission from ORNL to use these data is gratefully acknowledged.

References

1 W. B. Hall and T. I. M. Crofts, "The Use of Sodium and Sodium-Potassium Alloy as a Heat Transfer Media," *Atomics*, vol. 7, No. 8, pp. 273, 290, 1956.

2 J. M. Trummel, "Some Observations Made of Cavitating Sodium Flow in a Venturi," ORNL CF 54-8-225, Aug. 31, 1954.

3 A. J. Stepanoff, "Propeller Pumps for Circulation of Molten Salt," *Refiner and Natural Gasoline Manufacturer*, vol. 19, no. 12, pp. 74–76.

4 A. J. Stepanoff, "Centrifugal and Axial Flow Pumps," John Wiley & Sons, Inc., New York, N. Y., 1948.

5 Final Report, "Development of Hermetically Sealed Centrifugal Pump Units for Liquid Metals," Nuclear Power Section, Allis-Chalmers Manufacturing Company, Milwaukee, Wis., pp. 59–63 (June 30, 1953). Subcontract No. 56, under Contract No. W-31-109-ENG-52.

6 H. J. Metz, ORNL, personal communication.

7 J. N. Simpson, personal communication.

8 A. L. Southern, ORNL, personal communication.

9 G. M. Watson, ORNL, personal communication.

10 J. H. Keenan and F. G. Keyes, "Thermodynamic Properties of Steam," John Wiley & Sons, Inc., New York, N. Y., 1936.

11 R. R. Miller, C. T. Ewing, R. S. Hartman, and H. B. Atkinson, Jr., "Quarterly Progress Report No. 3 in the Measurement of the Physical and Chemical Properties of the Sodium-Potassium Alloy," Naval Research Laboratory Report No. C-3105, pp. 9–12, April, 1947.

12 "Liquid Metals Handbook," third edition, Sodium-NaK Supplement, Atomic Energy Commission and The Department of the Navy, GPO, Washington, D. C., 1955.

13 A. H. Church, "Centrifugal Pumps and Blowers," John Wiley & Sons, Inc., New York, N. Y., 1944.

14 A. J. Stepanoff, "Centrifugal and Axial Flow Pumps," John Wiley & Sons, Inc., New York, N. Y., second edition, 1957.

APPENDIX 1

Venturi Meter Temperature-Multiplier

The standard venturi-meter flow-rate equation for flow rate at temperature t may be written as

$$Q_t = k \frac{A_t}{\sqrt{sp\ gr_t}} \sqrt{\Delta P_w}, \tag{1}$$

where

$$k = \frac{450\ C}{\sqrt{1-\beta^4}} \sqrt{\frac{2g(144)}{62.37}}.$$

Also the flow rate at a base temperature bt may be written

$$Q_{bt} = \frac{kA_{bt}}{\sqrt{sp\ gr_{bt}}} \sqrt{\Delta P_w}. \tag{2}$$

Multiplication of Equation (1) by $\left(\frac{A_{bt}}{A_{bt}}\right) \frac{\sqrt{sp\ gr_{bt}}}{\sqrt{sp\ gr_{bt}}}$, and regrouping to obtain

$$Q_t = \frac{A_t}{A_{bt}} \frac{\sqrt{sp\ gr_{bt}}}{\sqrt{sp\ gr_t}} k \frac{A_{bt}}{\sqrt{sp\ gr_{bt}}} \sqrt{\Delta P_w}. \tag{3}$$

from which

$$Q_t = K(TM) \sqrt{\Delta P_w}, \tag{4}$$

where

$$K = \frac{kA_{bt}}{\sqrt{sp\ gr_{bt}}}, \quad \text{and}$$

$$TM = \left(\frac{D_t}{D_{bt}}\right)^2 \frac{\sqrt{sp\ gr_{bt}}}{\sqrt{sp\ gr_t}}.$$

From reference [6], and for a base temperature of 1400 F,

$$K = 84.18,$$
$$TM = 1.000.$$

Table 2 presents several temperature multipliers of interest.

The NaK flow rate should equal a previously established water flow rate when

$$(\Delta P_w)_{NaK} = \left(\frac{TM_w}{TM_{NaK}}\right)^2 (\Delta P_w)_w, \tag{5}$$

Table 2 Venturi temperature multiplier

Temperature, t (°F)	TM	$(TM_t/TM_{1500°F})$	$(TM_t/TM_{1500°F})^2$
140	0.8414	0.832	0.6922
190	0.849	0.8397	0.7051
1400	1.000		
1500	1.011		

where subscript w refers to water and subscript NaK refers to the sodium-potassium alloy.

APPENDIX 2

Pump Head Equations

The pump head and the static head at pump suction for water and for NaK were calculated by using the following equations. In the pump head equation for water, the constant 3 represents an elevation correction to the discharge pressure gage. The symbol c represents a flow rate dependent correction to the measured value of pump discharge pressure. The location of the discharge pressure tap for water and NaK alloy testing differed. Data for both taps were taken during water testing from which the values of c were deduced.

For water,

$$H_t = \frac{2.31}{sp\ gr}(P_{dw} - P_{sl}) - 3 + (1.127 \times 10^{-4})\,Q^2, \text{ and} \quad (6)$$

$$H_{sw} = \frac{2.31}{sp\ gr}P_{sl} + Bar. \quad (7)$$

For NaK,

$$H_t = \frac{2.31}{sp\ gr}(P_{dw} - P_{sl}) + c + (1.127 \times 10^{-4})\,Q^2, \text{ and} \quad (8)$$

$$H_{sw} = \frac{2.31}{sp\ gr}P_{sl} + Bar. \quad (9)$$

DISCUSSION

V. Salemann[3]

The author and his associates have performed the difficult task of measuring cavitating performance of a centrifugal pump on NaK at 1500 F. Having worked with water at 400 deg, this discusser can appreciate the difficulties in handling a fluid at 1500 F, and a dangerous one at that. It is almost lamentable that the paper was not made more interesting by some unexpected results which are not entirely due to experimental accuracy.

Theoretically, cavitation inception is independent of fluid properties. The point used by the author, however, is really "performance drop inception" and could be expected to be retarded if certain thermodynamic effects are strong. I do not know of a theory that would advance either point of inception in any fluid. The results obtained in this paper, that NaK, on the average, needs more NPSH than water, are therefore either experimental errors or results of poor vapor pressure and specific gravity data. It may be significant that whenever the NPSH values differed, the noncavitating head also differed for the two fluids.

It is questionable whether extensive testing on other pumps would be useful. In the absence of thermodynamic suppression cavitating performance may be predicted for any fluid. These tests show that up to 1500 F there is no thermodynamic suppression on NaK. Future tests are advisable at higher temperatures or with other liquids. In practice, however, temperature-dependent suppression cannot be fully utilized if dependable operation is required, and transient temperature changes are possible.

Author's Closure

Mr. Salemann's comments are very illuminating; however, it is mildly confusing to note in one comment that "theoretically, cavitation inception is independent of fluid properties," and in another comment that "future tests are advisible at higher temperatures or with other liquids." The author agrees to the advisability of further testing.

---

[3] Research Engineer, Worthington Corporation, Research and Development Section, Harrison, N. J. Assoc. Mem. ASME.

The Creep-Rupture Properties of 80 Ni-20 Cr Alloys

ROBERT WIDMER
Formerly, Research Staff Member, M.I.T.; now, Technical Director, New England Materials Laboratory, Inc., Medford, Mass.

NICHOLAS J. GRANT
Professor, Department of Metallurgy, Massachusetts Institute of Technology, Cambridge, Mass.

The creep-rupture properties and the creep behavior of a series of 80 Ni-20 Cr alloys were investigated over the 1200 to 1800-F range. In the group were two vacuum-melted and three air-melted alloys. Among these five heats there were small but important differences in minor constituents such as silicon, manganese, sulfur, and possible tramp elements, primarily as a result of the melting practice in each case. Of particular interest in this study was the variation in ductility which the various alloys exhibited in creep-rupture tests which lasted from a few minutes to more than 1000 hr. A close examination of ductility behavior was undertaken by breaking down the creep curve into primary, secondary, and third-stage creep as a function of stress and temperature. It is shown that the stress-rupture properties are not affected over a wide temperature and stress range by a change in minor constituents, whereas the ductility behavior can vary considerably.

THE TERM "DUCTILITY" as it is commonly used is seldom accurately defined. Ductility may be the product of a tensile test or a bend test; it can be an evaluation of elongation over a variable gage length or reduction of area for different diameters; or it can be a measurement from creep-rupture tests where temperature and strain rate should be specified. In low-temperature testing, ductile materials generally fail after some measurable necking, leading to a discontinuous rate of change of cross section; at high temperatures, high-strain-rate tests show necking in ductile materials, but complete absence of necking in low-strain-rate tests, accompanied by intercrystalline cracking. Intercrystalline cracking has a greater effect on the measured elongation values and a small effect on the reduction-of-area values. Since a material has lost essentially all of its usefulness as soon as intercrystalline cracking has become a significant factor, it is quite important to know when such intercrystalline cracking takes place and at what rate the cracks progress. Equally important are the distribution of these cracks and their rate of propagation.

It is now well known that creep behavior, in terms of strength or ductility, can be markedly influenced by minor constituents and impurity elements. Small amounts of lead, bismuth, sulfur, and so forth, markedly affect the grain-boundary behavior of many metals, resulting in poorer properties. Small additions of boron and zirconium, on the other hand, have been shown to influence favorably the strength and ductility of the nickel-chromium high-temperature alloys hardened with titanium and aluminum, especially if vacuum-melted [1].[1] The ability of vacuum melting to remove low-melting-point, high-vapor-pressure tramp elements is of considerable importance in determining the ductility behavior of high-temperature materials. Along with the usual minor constituents or tramp elements from the raw materials are phases or constituents which come about from deoxidation practice during the melting of these alloys. These, too, play an important role in the creep-rupture behavior.

[1] Numbers in brackets designate References at end of paper.

Contributed by the Metals Engineering Division and presented at the Annual Meeting, Atlantic City, N. J., November 29–December 4, 1959, of THE AMERICAN SOCIETY OF MECHANICAL ENGINEERS.

NOTE: Statements and opinions advanced in papers are to be understood as individual expressions of their authors and not those of the Society. Manuscript received at ASME Headquarters, July 17, 1959. Paper No. 59—A-119.

Experimental Procedure

The compositions of the five nickel-chromium alloys are listed in Table 1. It will be noted that three of these are air-melted and two are vacuum-melted. The residual elements which were determined by chemical analysis are also noted in Table 1 and are shown to be quite consistent and at very low levels with one or two exceptions. The carbon content is of the order of 0.02 per cent, the phosphorus content is less than 0.003 per cent, the sulfur content is less than 0.004 per cent with the exception of one heat, alloy No. 7V, which showed 0.011 per cent sulfur. On the other hand, the ratio Mn/S is low in all cases except in alloy 2V (Table 1). Iron and manganese are also low in all instances, as are the H_2S-group metals. Silicon was the major compositional variable, having been added as a major alloying constituent in three of the alloys.

Alloys 1, 2, and 3 were received in the solution-treated condition (2050 F, 1 hr, water quench) and alloys 4 and 5 were hot-rolled. Table 1 shows the final heat-treatments used to attain a grain size of ASTM 3 to 4 for all of the alloys. Following the final solution treatment, all of the alloys were held at 1500 F for 24 hr in order to precipitate any carbides or nitrides present in the alloys to prevent an aging effect.

Constant-load creep-rupture tests were carried out on test bars with a 0.25-in-diameter × 1-in-gage section, at temperatures from 1000 to 2000 F, although in most instances the bulk of the tests were run at 1200, 1500, and 1800 F in air. Stresses were selected to produce failure in times from a few seconds to several thousand hours.

The elongation values of the specimens were measured by means of a dial gage attached at the outside of the furnace. From prior knowledge of the stress-strain curves for each of these different alloys at each different temperature, where plastic strain was expected on the full application of load, the specimens were first preloaded to about 50 per cent of full load in order to take out all of the slack in the holder system, and were then fully loaded with the dial gage in position. A significant number of checks indicated that this method of loading permitted a fairly accurate determination of the primary creep portion of the creep curve.

Elongation and reduction-of-area values at fracture were determined for all specimens. In every case the ruptured specimens were carefully examined metallographically to determine what types of structural changes had occurred in order to assist in the

Table 1 Composition, melting process, and heat-treatment of alloys

Alloy no.	Element, weight per cent: Ni	Cr	C	S	P	Si	Fe	Mn	H_2S group metals	Mn/S ratio	Heat-treatment
1V[a]	bal.	19.17	0.02	0.011	<0.003	0.12	0.07	0.11	≪0.05	10	2050 F 1 hr water, 1500 F 24 hr air
2V	bal.	19.59	0.03	0.003	<0.003	1.33	0.10	0.27	≪0.05	90	2050 F, 1 hr water, 1500 F 24 hr air
3A	bal.	19.45	0.02	0.003	<0.003	1.38	0.12	0.01	≪0.05	3.3	2350 F 1 hr water, 1500 F 24 hr air
4A[b]	bal.	19.98	0.02	0.002	<0.003	1.22	0.34	<0.01	≪0.05	<5	2200 F 1 hr water, 1500 F 24 hr air
5A[b]	bal.	19.96	0.02	0.004	<0.003	0.30	0.60	<0.01	≪0.05	<2.5	2200 F 1 hr water, 1500 F 24 hr air

[a] V means vacuum-melt; A means air-melt.
[b] Alloys 4A and 5A were deoxidized by the addition of Al, Ti, B, and Mg; whereas alloys 1V, 2V, and 3A were deoxidized with Ca.

drawing of the log stress versus log rupture time or log minimum creep-rate curves. In other instances, creep-rupture tests were interrupted prior to fracture in order to study the initiation and progress of intercrystalline cracks, to determine the effect of nitrogen, and oxygen contamination from the atmosphere, and so forth.

Results

Creep-Rupture Properties. Fig. 1 illustrates the behavior of three of the alloys on a log stress log rupture time plot at temperatures of 1200, 1500, and 1800 F. Based on the actual points and supported by metallographic examination of the fractured specimens, the convention of drawing the best straight line through various portions of the points was followed. The breaks shown in the curve are associated with distinct changes in the behavior of the material, for example, a transition from ductile transcrystalline fracture to intercrystalline fracture. In this way, emphasis can be laid on material instabilities which result in a marked change in the rate of load-carrying capacity or creep resistance [2].

Examination of Fig. 1 indicates that these curves are made up of three distinct sections, namely:

1 At high stresses (short rupture-life tests) the curves are quite flat, high ductility values were recorded, and there is a complete absence of intercrystalline fractures or failure.

2 Following the first break in these curves, at intermediate stress levels, the material undergoes progressively more severe intercrystalline cracking, and failure is by means of an intercrystalline mechanism. The longer the rupture time, the more severe the intercrystalline cracking. Through this temperature-stress region there is a distinct decrease in the ductility of the alloys, showing a minimum in ductility at the end of this intermediate-stress region.

3 At the lowest stresses (the longest rupture-life tests) the slopes of these log-log curves show a break in the upward direction, indicating a strengthening effect instead of the usual weakening effect which is normally associated with long-time tests and structural instabilities. This type of behavior has been noted in other materials and is associated with any one or several of the following changes: (*a*) Grain growth (but not classical recrystallization), (*b*) nitrogen solution from the atmosphere and nitride formation, (*c*) internal oxidation, (*d*) oxidation of the surface of the specimen and of the intercrystalline cracks.

Because of the involved and lengthy discussion necessary to describe this phase of the material behavior, the results will appear in a separate technical paper [6].

Fig. 1, more specifically, shows the variation of rupture life as a function of stress for two vacuum-melted alloys, one low-silicon and the other high-silicon, and for an air-melted alloy of high-silicon content.[1] It will be noted at 1200 F that the high-silicon

[1] In all illustrations, the alloys are identified as 1V, 2V, 3A, and so forth, for convenience. Please refer to Table 1.

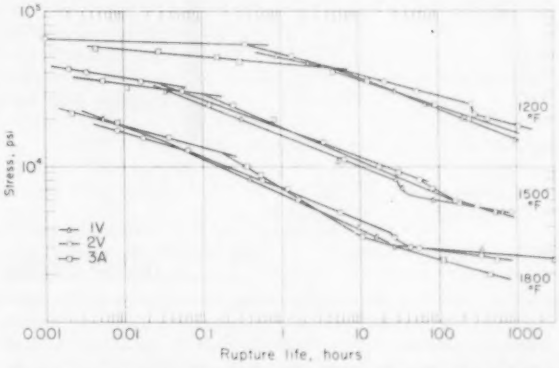

Fig. 1 Log stress versus log rupture life plot of alloys 1V, 2V, and 3A at 1200, 1500, and 1800 F

vacuum-melted alloys show superior strength over the entire stress range, although the degree of superiority changes as a function of the stress. At 1500 F, the vacuum-melted product is superior at high stresses, inferior at intermediate stresses, and approximately equivalent at low stresses. The behavior pattern at 1800 F is also variable, with the air-melted material first superior and ultimately inferior to the vacuum-melted material. The low-silicon alloy, vacuum-melted, also goes through the same type of variation of showing superiority at certain stresses and inferior properties at other temperatures and stresses. On this basis, it would be exceedingly difficult to try to establish superiority among these alloys and for these test conditions either on the basis of the higher-silicon content or on the basis of the vacuum-melting procedure.

When comparisons were made among the alloys on the basis of minimum creep rate, a comparable disposition of curves was noted as in Fig. 1. The creep-rupture properties of alloys 4A and 5A are listed in Table 3 and in the Appendix. The values indicate that both these materials have a lower creep strength at all temperatures and stress levels.

Characteristics of Creep Curves. Of particular interest was the change in the nature of the creep curve, both as a function of the stress at any one temperature and as a function of the test temperature. Without attempting to classify in an absolute sense or to oversimplify the problem, there were several types of curves observed which were related to the test stress and temperature. These several different types of curves are:

1 The classical type of creep curve in which there is significant primary creep, which varies from less than one per cent to as much as 30 per cent for some of the high-stress tests, with a well-defined secondary or steady-state creep portion, followed by an accelerating creep rate in the third stage. This type of curve was obtained for all of the alloys at the high stresses and was

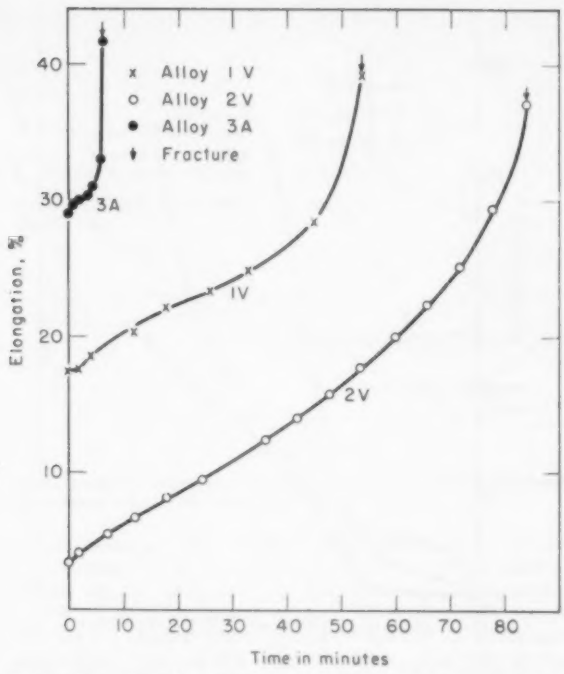

Fig. 2 Creep curves for alloys 1V, 2V, and 3A tested at 1200 F and 50,000 psi

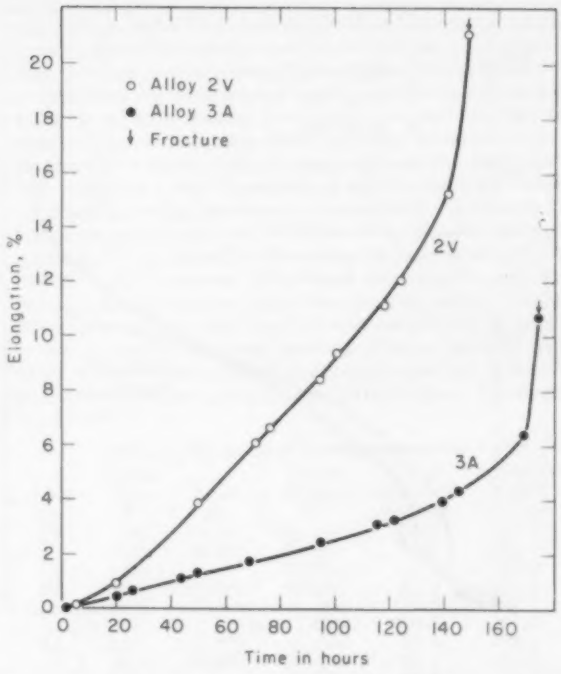

Fig. 3 Creep curves for alloys 2V and 3A tested at 1500 F and 6000 psi

observed more extensively at the lower temperatures. Associated with this type of creep curve was a tendency for transcrystalline fracture, with distinct necking of the specimen at fracture. The third stage of creep was associated with necking of the specimen. Typical curves are shown in Fig. 2 for each of the three different alloys which are summarized in Fig. 1.

2 Creep curves with essentially no observable primary creep. These curves appear to start at the origin with a constantly accelerating creep rate, the acceleration being quite slow at first, but then going into a rapidly accelerating third-stage region leading to fracture. In curves of this sort, it is exceedingly difficult to find a steady-state creep portion or to measure a minimum creep rate. It is frequently easier to measure the creep rate at some fixed amount of plastic strain, such as 0.5 to 1 per cent. This type of creep curve was obtained predominantly at intermediate stresses at all test temperatures. For these alloys, these curves are associated with intercrystalline fracture in the creep-rupture tests. Typical curves of this type are shown in Fig. 3.

3 Creep curves with two minimum creep-rate regions. A complex creep curve was obtained where a strengthening effect took place due to reaction with the atmosphere at 1800 F and for longer periods of time at 1500 F. The first portion of these creep curves is similar to that already described under item 2. As the creep curve begins to enter third-stage creep, which undoubtedly indicates some significant amount of intercrystalline cracking, there is apparently a reaction with the atmosphere which brings about a decreasing rate of creep and the re-establishment of another minimum creep-rate period [3]. When the curve re-enters third-stage creep for the second time, it goes on to rupture, thereby giving essentially two creep curves in sequence. It is interesting to note that the second part of the curve shows a longer period of decreasing creep than does the first part. Typical curves of this sort are shown in Fig. 4(*a*), and with enlargement of the first portion of the creep curves in Fig. 4(*b*).

If one now examines the different alloys with respect to the creep curves at different stress levels, the following observations can be made:

1 At high stresses—alloy 4, vacuum-melted, high-silicon, shows the smallest amount of primary creep and the largest amount of second-stage creep.

2 At intermediate stresses—here the differences in the shape of the curves for the different materials are almost insignificant.

3 Low stresses—the anomaly of two minimum creep-rate periods is noted for all of the alloys; however, it is strongest in alloy 3 (vacuum-melted, low-silicon).

Ductility Observations. If one were to follow the usual convention of looking at the total elongation or the reduction of area at fracture, useful and interesting information would be gained, as is indicated by a close examination of Fig. 5.

(a) Total Elongation. Fig. 5 summarizes the change in total elongation as a function of the rupture time at 1200, 1500, and 1800 F for the high-silicon alloys, one in the vacuum-melted condition, and the other in the air-melted condition. It is fairly obvious that the total ductility values for the vacuum-melted material are of the order of two to three times those shown by the air-melted material.

Except for the 1200-F tests, both materials show a distinct minimum in ductility between 10 and 1000-hr rupture life at 1500 and 1800 F.

The change in ductility in going from the short-time stress-rupture tests to those which yield the minimum values in ductility is much more pronounced in the vacuum-melted alloys than in the air-melted materials.

At 1200 F the total elongation for the vacuum-melted as well as for the air-melted material changes but slightly. There is evidence of a slight tendency for the ductility to be decreasing in the longer time tests, but this is a small trend, and slightly more marked in the case of the air-melted alloy.

At 1500 F, the vacuum-melted alloy shows a minimum in duc-

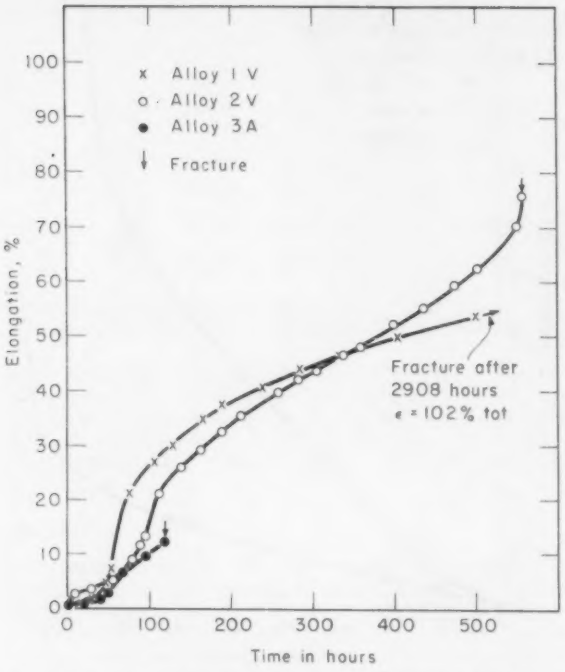

Fig. 4(a) Creep curves for alloys 1V, 2V, and 3A tested at 1800 F and 2500 psi

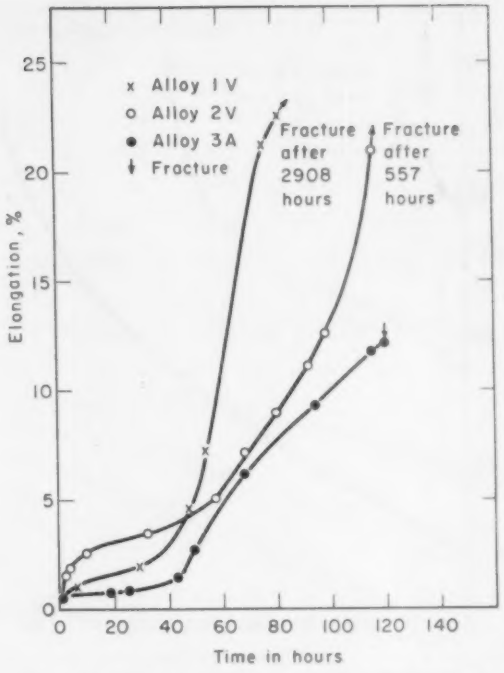

Fig. 4(b) Enlargement of first position of creep curves in Fig. 4(a)

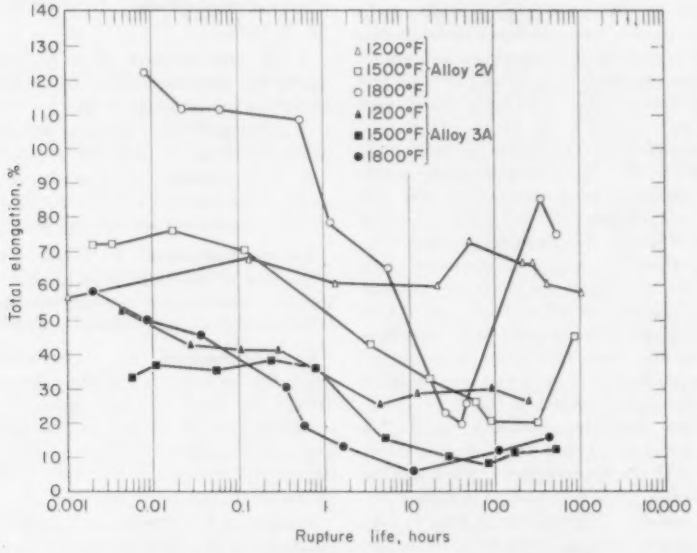

Fig. 5 Total elongation as a function of log rupture life for alloys 2V and 3A tested at 1200, 1500, and 1800 F

tility at about 400 hr, but shows a sharp recovery in a test lasting about 1000 hr. There is an equal drop for the air-melted material, but there seems to be no recovery in the ductility in the longer-time tests.

At 1800 F, the short-rupture-time ductilities are extremely high, but fall very sharply to a minimum in tests lasting about 40 hr, followed by a sharp recovery in ductility in a fashion similar to that noted for the vacuum-melted material at 1500 F, except that the recovery is considerably greater at 1800 F. In the air-melted materials, there is also a drop to a minimum in the vicinity of about 10-hr with a slight recovery in the longer time tests.

(b) Reduction of Area. Fig. 6 is similar to Fig. 5 except that values of the reduction of area are plotted against rupture life. The general observations which were made regarding total ductility seem to be substantiated in kind by the reduction of area. There are several exceptions to this, but the exceptions are primarily in degree of change rather than in the direction of the change. For example, at both 1500 and 1800 F the recovery of the reduction-

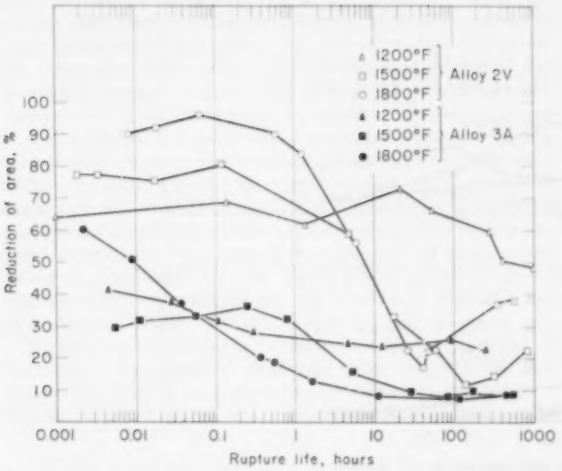

Fig. 6 Reduction of area as a function of log rupture life for alloys 2V and 3A tested at 1200, 1500, and 1800 F

of-area values after the minimum values had been reached are considerably smaller than was noted in the case of the elongation values. In the air-melted materials, there is no evidence of a recovery of reduction-of-area values in the longer time tests. A minimum is reached which appears to level off in this region without any evidence of a return to higher values such as was noted at 1800 F in terms of total ductility.

As in the case with elongation, the reduction-of-area values for the vacuum-melted high-silicon alloy are generally two to three times as high as for the air-melted alloy.

(c) Primary and Second-Stage Creep Values. From a design point of view, it is of prime interest to know the amount of plastic deformation which a material undergoes in primary and second-stage creep. Because of the marked changes which were noted in Figs. 3 and 4 in primary creep, it appeared desirable to determine whether primary and secondary creep were functions of the applied stress and the test temperature. While difficulties were encountered in accurately defining first-stage and second-stage creep, nevertheless approximate limits could be placed on both these quantities to determine the direction of the effect, even though absolute values could not be determined.

Fig. 7 is a plot of primary creep as a function of the rupture time for the high-silicon vacuum-melted and air-melted alloys. It will be noted that primary creep tends to be relatively large in short-time tests, generally being higher the lower the temperature. In most instances, those stresses which would give a rupture life of 100 hr or more resulted in no primary creep. This would mean that in tests exceeding 100 hr, the creep curves start from the origin at an accelerated rate practically from the very beginning. Comparing the vacuum-melted with the air-melted alloy, differences in primary creep can be observed with tests at 1200 F. This is not unexpected if the yield stress of the different materials is considered (see Table 2). Since alloy 3A has a lower yield at 1200 F, a larger amount of first-stage creep can be expected when the applied stress is higher than the yield stress. Such a difference in primary creep has been reported recently [3] based on studies made of the creep behavior of some nichrome-type alloys. They further observed that the grain size had an important effect on the amount of primary creep for given test conditions.

Table 2 Tensile tests at elevated temperatures

Alloy no.	Temp, deg F	Yield, psi	Tensile strength, psi	Total elongation per cent	Reduction of area per cent
1V	1200	15,300	58,000	34.3	37.7
	1500	10,000	28,900	38.5	35.2
	1800	...	10,900	60.6	44.0
2V	1200	17,300	58,100	62.2	63.6
	1500	10,600	31,400	110.0	87.0
	1800	...	11,000	148.7	94.0
3A	1200	13,700	60,000	35.5	32.1
	1500	10,600	28,400	49.7	42.7
	1800	...	12,000	58.2	36.6

Fig. 8 is a plot of the amount of second-stage creep as a function of rupture life for the same two alloys at 1200, 1500, and 1800 F. Again, it was exceedingly difficult to define the limits of second-stage creep; nevertheless, Fig. 8 shows the direction of this effect. The most that can be said is that the amount of second-stage creep appears to be a relatively constant quantity which is not particularly dependent either on the test temperature or on the stress. Because of the lack of a trend with temperature or with stress for either alloy, at best it might be said that the change in the amount of second-stage creep is relatively insensitive to temperature and to stress.

Accordingly, to explain the large difference in total elongation which exists between the vacuum and the air-melted products,

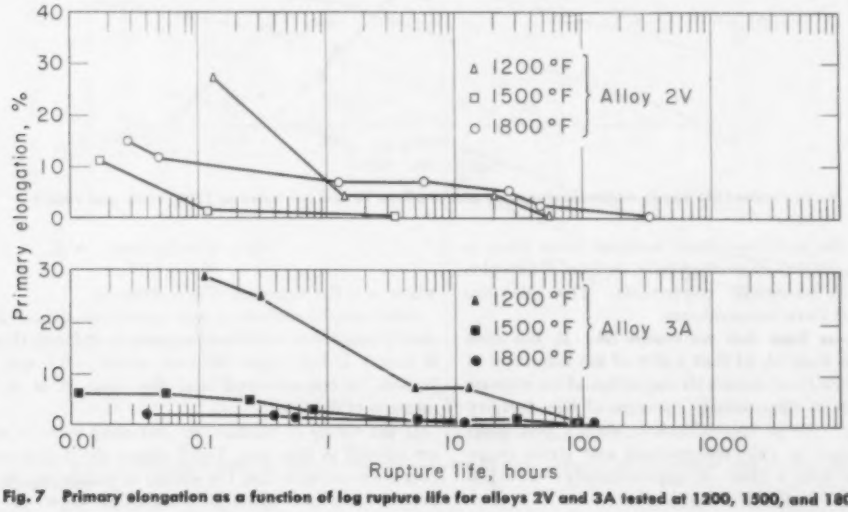

Fig. 7 Primary elongation as a function of log rupture life for alloys 2V and 3A tested at 1200, 1500, and 1800 F

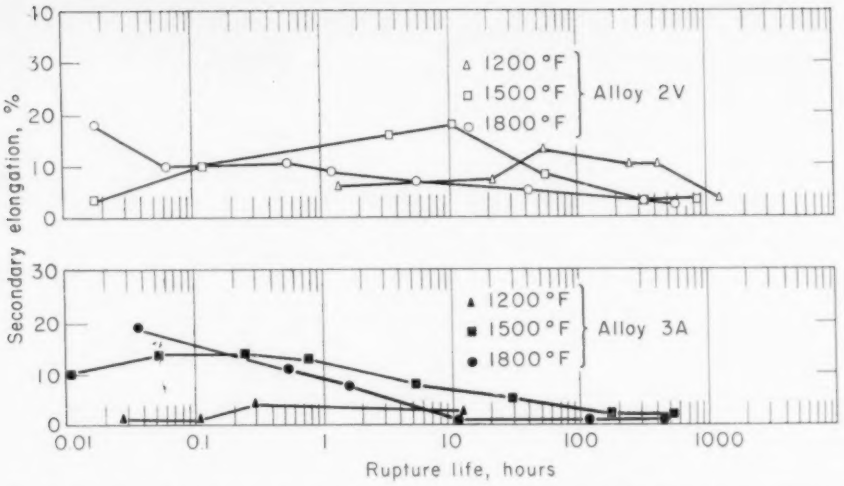

Fig. 8 Secondary elongation as a function of log rupture life for alloys 2V and 3A at 1200, 1500, and 1800 F

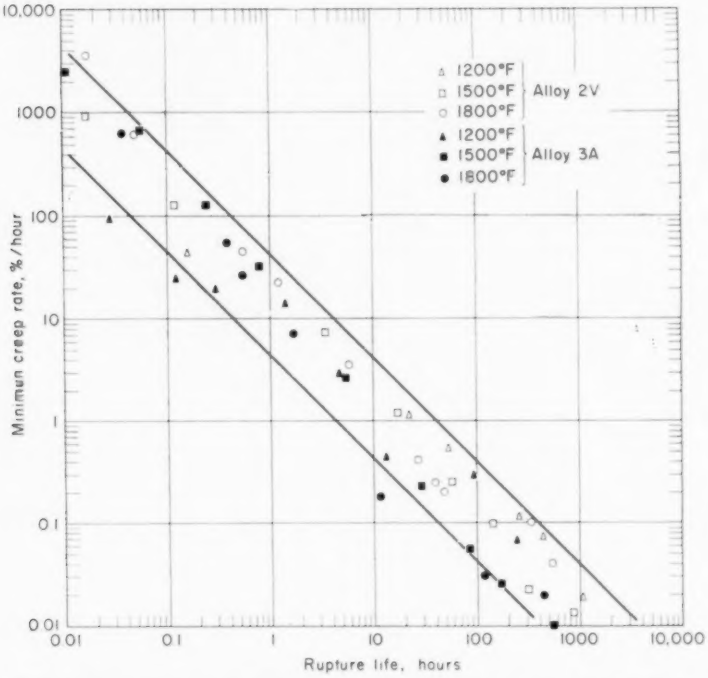

Fig. 9 Log rupture life versus minimum creep-rate plot of alloys 2V and 3A tested at 1200, 1500, and 1800 F

it is obvious that the vacuum-melted material must show a vastly larger amount of third-stage creep since the total of first plus second-stage creep is essentially comparable. This situation appears to hold at all three temperatures.

(d) Relationship Between Creep Rate and Rupture Life. It has been indicated in previous work [4, 5] that a plot of the logarithm of the minimum creep rate (mcr) versus the logarithm of the rupture life t_r appears to be an approximate measure of the ductility behavior of an alloy. As an approximation, such a plot when summarizing data over a wide temperature and stress range gives a straight line with a slope of approximately -1. The equation which applied in this instance is

$$\log t_r + m \log (\text{mcr}) = K$$

where m is the slope and K is a constant.

More careful analysis of large quantities of data obtained under closely controlled conditions appears to indicate that the value of m is not 1, but varies between about -0.7 and about -1.2. It was further observed that the value K is an approximate measure of ductility

If the values of rupture life and creep rate for alloys 4 and 5 are plotted in this way, Fig. 9 shows the distribution of points. It is quite obvious that the scatter of points can be encompassed between two lines which yield a band of slope -1. However, if

one examines the individual sets of points for each alloy, one notices that there is a distinct difference in the distribution of these points within the scatter band based on ductility values. One notes that at short rupture times the vacuum-melted and air-melted alloys yield points which are approximately equally distributed; on the other hand, for rupture-life values in excess of 1 to 10 hours, it is quite obvious that the points for the air-melted alloy are on the lower side of the scatter band (indication of low ductility), whereas the vacuum-melted points are on the upper side of the band (indication of high ductility). If individual curves were drawn through these two sets of points for each alloy, the constants from the foregoing equation, at each temperature, would be such as to indicate higher ductility values for the vacuum-melted material than for the air-melted material, in line with observed values.

Because reduction-of-area values give a better indication of ductility in creep-rupture behavior, these values have been plotted for alloy 2V in a log stress versus log rupture time plot, Fig. 10. Dashed curves have been utilized to separate zones of about 60, 40, and 20 per cent reduction-of-area regions to show the effect of stress, temperature, and rupture time on ductility. It will be noted that:

1 The minimum ductility falls at an intermediate stress or rupture-life region (based on actually encountering such areas at the four higher temperatures), rather than necessarily at the very lowest stresses. Such a minimum in ductility might not be achieved at 1000 to 1200 F except in long periods of time. Such a minimum is indicated to exist in the vicinity of a 10,000-hr rupture life at 1200 F, based on extrapolation.

2 The stress interval over which the minimum ductility occurs becomes relatively small at higher temperatures.

3 The minimum value noted was at 1500 F (9 per cent) and was higher at both 1650 and 1800 F. It would not be unexpected if the minimum at 1350 F were lower than at 1500 F.

The ductility values of alloys 1V, 4A, and 5A are not included in the plots discussed in this paragraph; they are listed in the Appendix and partially in Table 3. Alloy 1V has much lower

Table 3 Stress and reduction of area of designated rupture life

	1 hr		10 hr		100 hr		1000 hr	
Alloy no.	Stress, psi	Reduction of area, per cent	Stress, psi	Reduction of area, per cent	Stress, psi	Reduction of area, per cent	Stress, psi	Reduction of area, per cent
1200 F								
1V	50,000	30	35,000	25	21,000	16	13,000	9
2V	51,000	65	38,000	65	27,000	64	16,000	48
3A	43,000	27	34,000	24	22,000	25	14,000	20
4A	43,000	25	30,000	20	20,000	13	...	...
5A	34,000	8	23,000	6	14,000	5	...	...
1500 F								
1V	13,500	15	10,000	8	6,000	6	5,000	8
2V	15,500	70	10,500	45	6,800	15	5,000	25
3A	18,000	30	10,500	15	6,500	8	4,600	8
4A	11,000	9	7,000	9	5,000	8	...	...
5A	9,500	3	6,500	3	5,200	2	...	...
1800 F								
1V	7,000	15	4,000	13	2,800	8	2,400	12
2V	7,000	85	4,500	40	2,800	25	2,200	40
3A	6,500	15	3,300	6	2,200	8	1,700	9
4A	4,500	6	3,100	6	2,100	8	...	...
5A	3,500	6	2,300	6	2,000	6	...	...

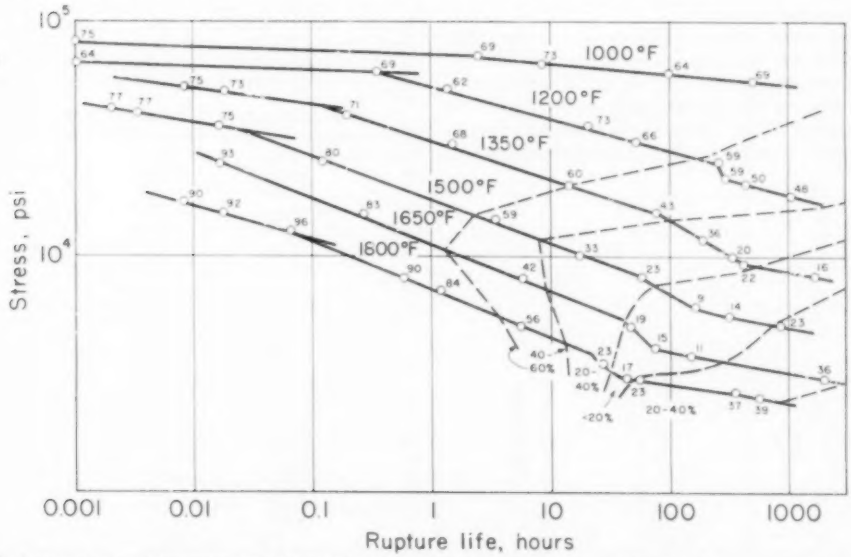

Fig. 10 Log stress versus log rupture life plot of alloy 2V showing ductility in terms of reduction of area as a function of stress and temperature

ductility than the vacuum-melted alloy 2V. (Values are about comparable to those of alloy 3A.) Total elongation and reduction of area of both alloys 4A and 5A are even lower at all temperatures and stresses.

Discussion and Conclusions

Processing variables and minor constituents would certainly appear to play a significant role in the over-all stress-rupture properties of 80-Ni 20-Cr type alloys. The effect of melting variables and minor constituents and tramp elements appears to affect different properties both as a function of temperature and stress.

In terms of rupture life or a stress for a given rupture time, the results are not entirely predictable; the vacuum-melted high-silicon alloy shows, for example, superiority at 1200 F at high and very low stresses, but not at intermediate stresses. The same effect would hold in the case of the measurements of the minimum creep rate. Even the presence of a significant amount of silicon as an alloying element does not play a predictable role in affecting either the rupture life or the minimum creep rate over a wide temperature or stress range.

Perhaps a much more interesting effect of vacuum melting versus air melting is noted in the ductility behavior of these alloys when tested in air. Observations of first-stage and second-stage creep indicate that the variation between air-melted and vacuum-melted material is small. Furthermore, the addition of silicon does not appear to change this observation significantly. On the other hand, comparison of the two alloys in terms of total elongation or reduction of area at fracture shows a large difference, amounting to two or three times greater ductility values for the vacuum-melted material than for the air-melted material. This superiority appears to be maintained at all three test temperatures and at all rupture times from a few seconds to well over a thousand hours.

Under these circumstances, it would appear that strength based on a maximum permissible deformation of the order of only $^1/_2$ or 1 per cent, would indicate no superiority for the vacuum-melted product. On the other hand, as a safety factor, or in terms of the nature of intercrystalline crack formation and propagation, there are significant differences between the vacuum-melted and the air-melted product.

Reduction-of-area values, while comparable to total-elongation values in terms of amount and direction of change, are preferred and give more reproducible values than do the total-elongation values, which are affected to a greater degree by the amount of intercrystalline cracking which occurs during third-stage creep. Intercrystalline crack propagation, being approximately normal to the stress direction, affects the reduction-of-area values to a smaller extent.

In comparing the various alloys in terms of ductility, it is noted that the high-silicon vacuum-melted alloy 2V shows significantly higher ductilities. A close examination of the creep curves shows that the difference is due primarily to the amount of elongation which takes place during the third stage of creep.

Because of the superior ductility of the vacuum-melted alloy, it is obvious that improvement in ductility must be associated with the elimination of tramp elements, or in a diminution of the amount of contaminating constituents normally present in this class of air-melted alloys.

On the other hand, the ductility of vacuum-melted alloys can still be relatively poor if the chemical composition is slightly changed in terms of the Mn/S ratio and/or the silicon content. This is illustrated by the behavior of alloy 1V, which has a Mn/S ratio that is much lower than that of alloy 2V and a silicon content of only 0.12 per cent (compared with 1.33 per cent of alloy 2V). The explanation of the poor ductility values of this alloy can possibly be made in terms of the decreased cohesion between the grains due to low-melting-point sulfides being present in the grain boundaries. In addition to that, it seems that the silicon content influences crack propagation. This is also demonstrated by the behavior of alloys 4A and 5A: A lower silicon content (5A), but otherwise the same composition, results in lower elongation and reduction-of-area values.

Acknowledgment

The authors wish to express their thanks to the International Nickel Company, sponsors of this research program.

References

1 R. F. Decker, J. P. Rowe, and J. W. Freeman, "Relations of High-Temperature Properties of Titanium-Plus-Aluminum Hardened Nickel-Base Alloy to Contamination by Crucibles," *Trans. AIME*, vol. 212, 1958, p. 686.

2 N. J. Grant and A. G. Bucklin, "On the Extrapolation of Short-Time Stress-Rupture Data," *Trans. ASM*, vol. 42, 1950, p. 720.

3 G. Ya. Kozyrskii, V. A. Kononenko, and P. N. Okrainets, "Study of Structural Changes in Nickel-Chromium Alloys During Creep," *Izvestiya Akademii Nauk SSSR, Otdelenie Tekhnicheskikh, Nauk*, August, 1958, no. 8, pp. 90–92.

4 F. C. Monkman and N. J. Grant, "An Empirical Relationship Between Rupture Life and Minimum Creep Rate in Creep-Rupture Tests," *Trans. ASTM*, 1956.

5 G. D. Gemmell and N. J. Grant, "Effects of Solid-Solution Alloying on Creep Deformation of Aluminum," *Trans. AIME*, vol. 209, 1957, p. 417.

6 R. Widmer and N. J. Grant, "The Role of Atmosphere in the Creep-Rupture Behavior of 80 Ni-20 Cr Alloys," published in this issue, pp. 882–886.

APPENDIX

Summary of the Stress-Rupture Data

Temp, deg F	Stress, psi	Rupture life, hr	Total elongation, per cent	Reduction of area, per cent	mcr, % per hr	Type of fracture[a]
Alloy 1V						
1200	50,000	0.90	39.1	29.5	13.0	T + I
	45,000	2.3	32.0	26.7	4.0	T + I
	30,000	28.1	31.1	18.9	0.35	I
	25,000	69.0	18.25	16.9	0.17	I
	20,000	203.0	13.8	13.8	0.037	I
	14,000	967.0	10.2	9.35	0.001	I
1500	35,000	0.036	45.6	36.0	375.0	I
	20,000	0.317	26.0	20.0	63.0	I
	11,000	5.26	13.8	10.2	1.1	I
	8,000	29.3	5.5	9.6	0.025	I
	7,000	32.2	6.3	6.3	0.025	I
	6,000	87.0	11.6	6.3	0.031	I
	5,000	659.0	21.2	8.15	0.0012	I
1800	20,000	0.0056	74.5	63.9	13,000	I
	8,000	0.40	27.6	19.1	36.0	I
	4,000	9.48	15.1	12.6	0.75	I
	3,500	16.5	12.4	10.2	0.35	I
	3,000	27.9	13.3	7.9	0.24	I
	2,750	358.0	70.5	9.35	0.115	I
	2,500	2908.0	102.0	13.2	0.10	I
Alloy 2V						
1000	75,000	0.001	61.0	66.5	56,000	T
	70,000	2.5	66.8	68.5	0.50	T
	65,000	8.7	64.5	73.0	1.25	T + I
	60,000	67.1	67.1	64.0	0.21	T + I
	55,000	504.0	70.2	68.0	0.05	T + I
1200	65,000	0.001	56.0	64.0	5600.0	T
	60,000	0.136	68.0	68.6	42.5	T
	50,000	1.4	61.0	61.5	13.5	T + I
	35,000	21.6	59.5	73.0	1.1	T + I
	30,000	53.0	73.5	66.0	0.53	T + I
	25,000	260.0	59.3	59.0	0.11	T + I
	22,000	294.0	67.0	59 3	0.090	I
	20,000	428.0	61.0	50.5	0.070	I
	18,000	1032.0	57.8	48.0	0.018	I
1350	52,000	0.0089	59.0	75.0	1300.0	T
	50,000	0.018	62.6	73.0	650.0	T
	40,000	0.20	77.8	71.0	85.0	T + I
	30,000	1.55	86.0	68.3	21.0	T + I
	20,000	14.0	81.8	59.5	2.3	T + I
	15,000	79.2	67.0	43.0	0.15	I
	12,000	202.0	39.6	36.0	0.044	I
	10,000	322.9	29.3	26.0	0.045	I
	9,000	419.7	23.8	21.5	0.034	I
	8,000	1660.0	27.1	15.5	0.0014	I
1500	42,500	0.0020	72.0	77.0	35,000	T
	40,000	0.0033	60.5	77.0	18,000	T
	35,000	0.017	75.6	75.0	900.0	T
	25,000	0.12	70.6	80.5	125.0	T + I
	14,000	3.47	43.0	59.0	7.2	I
	10,000	17.3	38.2	32.8	1.22	I
	8,000	58.6	26.2	22.6	0.26	I
	6,000	143.8	22.2	9.4	0.10	I
	5,500	315.0	20.0	13.8	0.0225	I
	5,000	870.0	45.3	22.6	0.013	I
1650	24,000	0.017	105.5	93.2	2200.0	T
	15,000	0.25	72.0	83.0	132.0	T + I
	8,000	5.9	52.5	42.0	4.2	I
	5,000	50.9	22.7	19.2	0 21	I
	4,000	77 0	13.8	15.5	0.11	I
	3,500	169.8	15.0	11.0	0.04	I
	3,000	2050.0	84.0	36.0	0.029	I
1800	17,000	0.0083	122.0	90.0	15,000	T
	15,000	0.018	110 0	92.0	3,300	T
	12,000	0.064	111.0	96.0	550.0	T
	8,000	0.55	108.0	90.0	44.0	T + I
	7,000	1.23	78.2	84.0	22.0	I
	5,000	5.85	65.5	56.5	3.5	I
	3,500	27.0	22.7	22.8	0.4	I
	3,000	42.3	20.9	16 9	0.22	I
	2,900	48.1	26.6	22.6	0.20	I
	2,750	348.0	85.2	37.3	0.10	I
	2,500	557.0	75.5	38.5	0.04	I

(Continued on next page)

Temp, deg F	Stress, psi	Rupture life, hr	Total elongation, per cent	Reduction of area, per cent	mcr, % per hr	Type of fracture*
Alloy 3A						
1200	55,000	0.0044	52.9	41.0	104.0	T + I
	52,000	0.028	43.2	37.3	90.0	T + I
	50,000	0.11	41.6	31.5	23.0	T + I
	45,000	0.30	41.5	28.1	19.0	T + I
	40,000	4.7	25.6	24.6	2.8	T + I
	35,000	12.35	18.3	23.2	0.47	I
	25,000	92 4	30.2	25.8	0.29	I
	20,000	251.0	26.5	22.6	0.065	I
1500	35,000	0.0055	33.4	29.5	4000 0	T + I
	32,000	0.011	36.8	31.5	2300.0	T + I
	30,000	0.055	35.6	32.8	660.0	T + I
	25,000	0.25	38.5	36.0	125.0	T + I
	20,000	0.806	36.5	32.1	32.0	I
	11,000	5.28	15.55	16.2	2.6	I
	9,000	30.3	9.95	9.35	0.23	I
	7,000	83.9	8 45	8 10	0.055	I
	6,000	175.0	11.30	9.35	0.025	I
	5,000	524.0	12.40	8.15	0.009	I
1800	23,000	0.0022	56.8	60.6	30,000	T + I
	18,250	0.0086	50.0	51.0	4000.0	T + I
	15,000	0.0383	45.7	37.3	600.0	T + I
	10,000	0.372	30.2	20.4	52.0	I
	8,000	0.555	18.9	19.0	26.0	I
	6,000	1.67	15.4	13.1	7.0	I
	3,500	11.5	8.45	6.3	0.18	I
	2,500	119.0	12.0	7.9	0.030	I
	2,000	445.0	16.0	8.95	0.019	I
Alloy 4A						
1200	30,000	11.4	22.3	19.7	1.0	I
	20,000	112.1	16.2	13.1	0.1	I
1500	10,000	2.5	5.8	9.3	1.5	I
	5,000	39.4	4.4	7.9	0.05	I
1800	3,500	6.5	9.3	5.5	0.60	I
	2,500	78.0	22.2	7.9	0.20	I
Alloy 5A						
1200	30,000	2.7	4.1	6.3	1.5	I
	20,000	28.2	5.1	4.7	0.09	I
1500	10,000	0.7	3.3	3.2	2.0	I
	5,000	43.7	3.4	2.4	0.04	I
1800	3,500	1.5	6.6	5.5	1.0	I
	2,500	9.5	11.7	6.3	0.35	I

* T-Transcrystalline; I-Intercrystalline.

A. MENDELSON
S. S. MANSON
Lewis Research Center,
NASA, Cleveland, Ohio

The Extrapolation of Families of Curves by Recurrence Relations, With Application to Creep-Rupture Data

A method using finite-difference recurrence relations is presented for direct extrapolation of families of curves. The method is illustrated by applications to creep-rupture data for several materials and it is shown that good results can be obtained without the necessity for any of the usual parameter concepts.

Introduction

THE PROBLEM of extrapolating sets of data finds many applications in engineering practice. An example which will be treated in detail in this report is the extrapolation of short-time creep-rupture data to predict long time life.

The present day techniques for the extrapolation of creep-rupture data are based primarily on the time-temperature parameter concept. It is generally assumed that all creep-rupture data for a given material can be correlated to produce a single master curve using as one of the co-ordinates a parameter involving a combination of time and temperature. This master curve which can be obtained using primarily short time data could then be used for extrapolation to long times. The three best known parameter methods are the Larson-Miller, Manson-Haferd, and Dorn parameters [1 to 3].[1]

These parameter methods have the great advantage that, at least in theory, they require only a relatively small number of data to establish the required master curve. In particular, the development of the objective least squares method in reference [4] makes it possible to obtain the optimum constants contained in the parameters described in references [1 to 3] without plotting and crossplotting the data and with the use of a minimum of judgment on the part of the analyst.

On the other hand, an alternative to the parameter methods would be advantageous for several reasons. First, these parameter methods presuppose a knowledge of the existence of some form of functional relationship between the variables. Thus it is assumed that, at a constant nominal (initial) stress, the logarithm of rupture time is linearly related to the temperature, for the Manson-Haferd parameter, and to the reciprocal of the absolute temperature for the Larson-Miller and Dorn parameters. For most materials it has been found that such relationships are valid in the range of variables investigated. In particular, the Manson-Haferd parameter has been shown [5 and 6] to give best results in the majority of cases. However, occasionally materials are encountered for which none of the parameters are valid. For example, plots of the logarithm of rupture time against temperature or reciprocal of absolute temperature at constant nominal stress will not result in straight lines for crucible 422 steel [7]. In these cases, modification of the parameter methods is necessary [7].

Secondly, the parameter methods in their usual form give equal weight to all the data, whether they be low time or high time data. For extrapolating to long times more weight should be given long time data. The method to be presented attempts to overcome these objections as well as providing an independent check on the parameter methods.

The method presented in this paper enables one to extrapolate directly a family of curves such as creep-rupture curves without assuming any particular parametric form. The method is based on the assumption that a family of curves such as a set of isothermal curves can be represented approximately by a finite-difference recurrence relation. Once the coefficients of this recurrence relation are determined, it is a simple matter to extrapolate each member of the family individually. The method has the advantage that it does not require an explicit knowledge or assumption as to the analytic character of the curves or as to what parametric form to use to correlate the data, although implicitly it assumes any of the broad class of functions which satisfy linear finite-difference equations. It is thus much more general in nature than the parametric methods previously discussed and can be used by itself to extrapolate creep-rupture data or as an independent check on any of the parameter methods. In addition, the method treats the data in such a way as to give more weight to the higher time data than to the lower time data.

Several examples of the use of the method are described in detail in the body of the paper, and the results of this type of extrapolation on the creep-rupture curves of several materials are presented. The use of this method is, of course, not restricted to creep-rupture data, and several examples of other type curves such as Bessel functions, Legendre polynomials, and power functions, are presented.

Method

The usual method for extrapolating a curve is to assume some explicit functional relation between the ordinate y and the abscissa x. The present method assumes instead a linear relation between successive equally spaced ordinates without directly introducing the abscissa x. Thus consider a section of a curve such as the solid line from 0 to 60 deg in Fig. 1. This section is actually part of a sine curve; however, assume that this is not known and that it is desired to extrapolate the curve. This can be done in several ways and, as previously mentioned, the one that is generally used is to fit the known curve by some assumed function and to then use this function for extrapolation. For example, a polynomial such as a parabola or cubic can be fitted to the curve. While assumptions of this type usually yield very good values when interpolating they are usually poor in extrapolating more than a short distance beyond the end of the curve.

[1] Numbers in brackets designate References at end of paper.

Contributed by the Metals Engineering Division and presented at the Annual Meeting, Atlantic City, N. J., November 29–December 4, 1959, of THE AMERICAN SOCIETY OF MECHANICAL ENGINEERS.

NOTE: Statements and opinions advanced in papers are to be understood as individual expressions of their authors and not those of the Society. Manuscript received at ASME Headquarters, August 7, 1959. Paper No. 59—A-155.

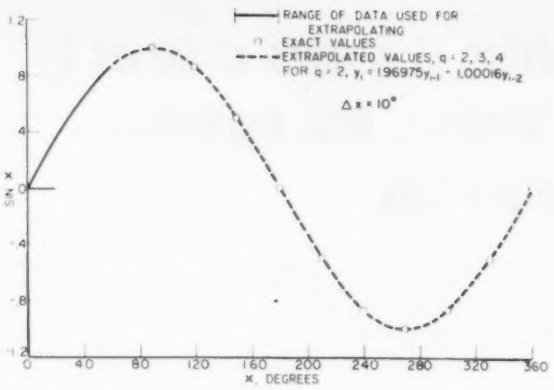
RANGE OF DATA USED FOR EXTRAPOLATING
EXACT VALUES
EXTRAPOLATED VALUES, q = 2, 3, 4
FOR q = 2, $y_i = 1.96975y_{i-1} - 1.00016y_{i-2}$
Δx = 10°
sin x
x, DEGREES

Fig. 1 Extrapolation of sin x

Table 1 Extrapolation of sin x

x, deg	sin x, extrapolated	sin x, exact
0		0
10		0.1736
20		0.3420
30		0.5000
40		0.6428
50		0.7660
60		0.8660
70	0.9397	0.9397
80	0.9840	0.9848
90	1.000	1.000
100	0.9848	0.9848
110	0.9396	0.9397
120	0.8658	0.8660
130	0.7657	0.7660
140	0.6423	0.6428
150	0.4993	0.5000
160	0.3411	0.3420
170	0.1725	0.1736
180	−0.0014	0
200	−0.3439	−0.3420
220	−0.6451	−0.6428
240	−0.8685	−0.8660
260	−0.9871	−0.9848
280	−0.9864	−0.9848
300	−0.8666	−0.8660
320	−0.6421	−0.6428
340	−0.3401	−0.3420
360	0.0031	0

If, however, the sine function were chosen to fit this curve, then in the foregoing case it would obviously give excellent results. Thus, although for interpolating purposes it is possible to fit a curve by many different functions, the extrapolated values will, in general, be very sensitive to the function used.

The present method avoids this difficulty by working directly with successive values of the ordinates of the curve rather than assuming any functional relation between the co-ordinates. A linear relation is sought between successive ordinates on the curve of the following form

$$y_i = A_1 y_{i-1} + A_2 y_{i-2} + \ldots + A_q y_{i-q} \qquad (1)$$

where y_i represents the value of the dependent variable at the end of the ith interval, and the A_j are constants to be determined. Equation (1) gives the value of the ordinate at the ith station in terms of the values at the q previous stations. Once the value at the ith station is computed, this value is used together with the $q - 1$ values preceding it, to calculate the value at the $(i + 1)$st station. In this way successive ordinates can be computed in terms of the previous ordinates.

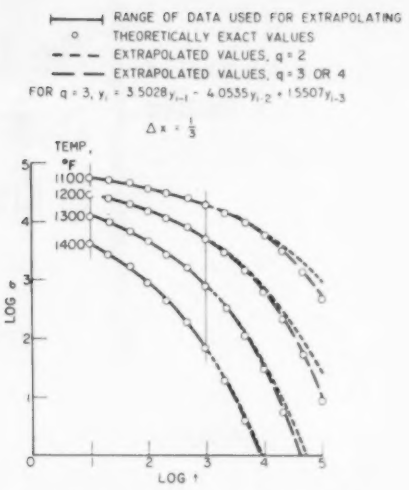

Fig. 2 Results for theoretical stress-rupture curves given by

$$\log \sigma = 5.131 - \left[\frac{T - 600}{81.8(9.5 - \log t)}\right]^{2.9216}$$

Equation (1) can, for example, be obtained from a differential equation. Thus, consider the differential equation associated with the sine function

$$\frac{d^2y}{dx^2} + y = 0 \qquad (2)$$

writing (2) in finite difference form gives

$$\frac{y_{i+1} - 2y_i + y_{i-1}}{(\Delta x)^2} + y_i = 0$$

or

$$y_{i+1} = [2 - (\Delta x)^2]y_i - y_{i-1} \qquad (3)$$

which is an equation of the form of (1) relating the ordinates of the sine curve to each other. In the general case, of course, the differential equation for the curve is not known. The coefficients A_j appearing in (1) can, however, be obtained from the ordinates of the curve by least squares as will be subsequently described.

One additional assumption is necessary in order to apply the present method to a family of curves. Just as equation (3) is valid for any one of an infinite family of sine curves of the same frequency (the members of the family can have different amplitudes or different phase angles), so it will be assumed in general that all the members of the family of curves to be extrapolated are represented by the same recurrence relation of the form of (1). A more extensive discussion of the origin and validity of equation (1) is given in the Appendix.

In order to determine the coefficients A_j of equation (1) use is made of least squares. Consider a family of curves to be extrapolated as for example in Fig. 2. In general, these will be obtained by fairing by eye the best curves through the data points. Choose n equally spaced stations for each member of the family. (These stations need not be chosen at the same values of the abscissas for every member of the family, but the spacing must be the same.) Choose the order q of the recurrence relation to be used (usually, $q = 3$ or 4). For each member of the family write a recurrence relation of the form of (1), as follows

$$
\left.
\begin{aligned}
y_k^{(1)} &= A_1 y_{k-1}^{(1)} + A_2 y_{k-2}^{(1)} + A_3 y_{k-3}^{(1)} + \ldots + A_q y_{k-q}^{(1)} \\
y_k^{(2)} &= A_1 y_{k-1}^{(2)} + A_2 y_{k-2}^{(2)} + A_3 y_{k-3}^{(2)} + \ldots + A_q y_{k-q}^{(2)} \\
&\cdots \\
y_k^{(m)} &= A_1 y_{k-1}^{(m)} + A_2 y_{k-2}^{(m)} + \ldots + A_q y_{k-q}^{(m)}
\end{aligned}
\right\} \quad (4)
$$

where $y_k^{(p)}$ represents the value of the dependent variable at the end of the kth interval and the superscript represents the member of the family under consideration. It should be noted that q cannot be greater than the number of intervals chosen.

The A_j are now chosen so that the recurrence relation (4) will best represent the data in the given range. To do this the usual least squares method of minimizing the sum of the squares of the residuals is used. Thus, the following sum is here minimized

$$
S = \sum_{p=1}^{m} \sum_{k=q+1}^{n} (y_k^{(p)} - A_1 y_{k-1}^{(p)} - A_2 y_{k-2}^{(p)} - \ldots - A_q y_{k-q}^{(p)})^2 \quad (5)
$$

Differentiating S with respect to each of the A_j and setting the results equal to zero, to find the optimum values of the A_j results in the following set of simultaneous equations for the coefficients.

$$
\begin{aligned}
r_{11}A_1 + r_{12}A_2 + \ldots + r_{1q}A_q &= r_{10} \\
r_{21}A_1 + r_{22}A_2 + \ldots + r_{2q}A_q &= r_{20} \\
&\cdots \\
r_{q1}A_1 + r_{q2}A_2 + \ldots + r_{qq}A_q &= r_{q0}
\end{aligned}
\quad (6)
$$

where the coefficients r_{ij} are given by

$$
r_{ij} = \sum_{p=1}^{m} \sum_{k=q+1}^{n} y_{k-i}^{(p)} y_{k-j}^{(p)} = r_{ji} \quad (7)
$$

Once the A_j are determined from (6), each member of the family can be extrapolated using (4), as previously explained.

Examples

As a first illustration consider the simple case of extrapolating a single sine curve as shown in Fig. 1. The values of the sine function are assumed to be given between 0 and 60 deg and it is desired to extrapolate by the method presented herein. Choose seven equally spaced stations so that

$y_1 = \sin 0° = 0$ $\quad$ $y_5 = \sin 40° = 0.6428$
$y_2 = \sin 10° = 0.1736$ $\quad$ $y_6 = \sin 50° = 0.7660$
$y_3 = \sin 20° = 0.3420$ $\quad$ $y_7 = \sin 60° = 0.8660$
$y_4 = \sin 30° = 0.5000$

Let $q = 2$ then from (1)

$$
y_i = A_1 y_{i-1} + A_2 y_{i-2}
$$

and from (7)

$$
r_{11} = \sum_{k=3}^{7} y_{k-1}^2 = y_2^2 + y_3^2 + y_4^2 + y_5^2 + y_6^2
$$

$$
r_{12} = r_{21} = \sum_{k=3}^{7} y_{k-1} y_{k-2} = y_2 y_1 + y_3 y_2 + y_4 y_3 + y_5 y_4 + y_6 y_5
$$

$$
r_{22} = \sum_{k=3}^{7} y_{k-2}^2 = y_1^2 + y_2^2 + y_3^2 + y_4^2 + y_5^2
$$

$$
r_{10} = \sum_{k=3}^{7} y_{k-1} y_k = y_2 y_3 + y_3 y_4 + y_4 y_5 + y_5 y_6 + y_6 y_7
$$

$$
r_{20} = \sum_{k=3}^{7} y_{k-2} y_k = y_1 y_3 + y_2 y_4 + y_3 y_5 + y_4 y_6 + y_5 y_7
$$

Substituting the values for y_1 through y_7 gives

$$
r_{11} = 1.3970488
$$

$$
r_{12} = r_{21} = 1.0441560
$$

$$
r_{22} = 0.81029280
$$

$$
r_{10} = 1.7075120
$$

$$
r_{20} = 1.2463024
$$

Substituting into equation (6) and solving gives

$$
A_1 = 1.96975
$$

$$
A_2 = -1.00016
$$

Therefore

$$
y_i = 1.96975 y_{i-1} - 1.00016 y_{i-2}
$$

Thus at 70 deg

$$
\begin{aligned}
y_8 &= 1.96975 y_7 - 1.00016 y_6 \\
&= 1.96975(0.8660) - 1.00016(0.7660) \\
&= 0.9397
\end{aligned}
$$

continuing this way the values of $y = \sin x$ have been computed up to 360 deg and compared with the exact values in Table 1 and Fig. 1.

As a second example, a family of curves was chosen simulating a set of stress-rupture data. It was assumed that an equation can be written for this family similar in form to those proposed in reference [7].

$$
y \equiv \log \sigma = 5.131 - \left[\frac{T - 600}{81.8(9.5 - \log t)}\right]^{2.9236} \quad (8)
$$

The curves represented by equation (8) are plotted in Fig. 2 for four temperatures. Again take seven stations ($n = 7$) equally spaced from $\log t = 1$ to $\log t = 3$ as shown. The values of $y_j^{(p)}$ for these stations as computed from equation (8) are shown in Table 2. The r_{ij} are now computed from equation (7). In this case we have a double summation. The products for all four curves ($m = 4$) must be added together. Thus, for example, taking $q = 2$:

$$
\begin{aligned}
r_{12} = {} & y_2^{(1)} y_1^{(1)} + y_3^{(1)} y_2^{(1)} + y_4^{(1)} y_3^{(1)} + y_5^{(1)} y_4^{(1)} + y_6^{(1)} y_5^{(1)} + \\
& y_2^{(2)} y_1^{(2)} + y_3^{(2)} y_2^{(2)} + y_4^{(2)} y_3^{(2)} + y_5^{(2)} y_4^{(2)} + y_6^{(2)} y_5^{(2)} + \\
& y_2^{(3)} y_1^{(3)} + y_3^{(3)} y_2^{(3)} + y_4^{(3)} y_3^{(3)} + y_5^{(3)} y_4^{(3)} + y_6^{(3)} y_5^{(3)} + \\
& y_2^{(4)} y_1^{(4)} + y_3^{(4)} y_2^{(4)} + y_4^{(4)} y_3^{(4)} + y_5^{(4)} y_4^{(4)} + y_6^{(4)} y_5^{(4)}
\end{aligned}
$$

Table 2 Values of $\log \sigma = 5.131 - \left[\frac{T - 600}{81.8(9.5 - \log t)}\right]^{2.9236}$

$\log t$ \ T	1100°	1200°	1300°	1400°
1.0	4.751	4.482	4.111	3.622
1.333	4.703	4.401	3.984	3.434
1.667	4.648	4.306	3.835	3.214
2.000	4.582	4.194	3.659	2.953
2.333	4.504	4.061	3.449	2.642
2.667	4.410	3.900	3.197	2.269
3.000	4.296	3.706	2.891	1.817

Once the r_{ij} are computed, equation (6) is solved for the A_j and the extrapolation is then carried out for each curve from the relations

$$y_i^{(1)} = A_1 y_{i-1}^{(1)} + A_2 y_{i-2}^{(1)}$$

$$y_i^{(2)} = A_1 y_{i-1}^{(2)} + A_2 y_{i-2}^{(2)}$$

$$y_i^{(3)} = A_1 y_{i-1}^{(3)} + A_2 y_{i-2}^{(3)}$$

$$y_i^{(4)} = A_1 y_{i-1}^{(4)} + A_2 y_{i-2}^{(4)}$$

The values obtained for this case were: $A_1 = 2.2052$, $A_2 = -1.2048$. The results for this calculation are shown in Fig. 2.

Results and Discussion

Fig. 1 and Table 1 show the results of extrapolating $\sin x$ by the method presented herein. It is seen that excellent results are obtained using only a second-order recurrence relation ($q = 2$). As a matter of fact, little or no improvement can be obtained by going to higher values. However, this is to be expected since the governing differential equation is of the second order. It is seen from equations (2) and (3) that a recurrence relation with q equal to 2 is sufficient to describe the sine function. As a matter of fact, taking Δx equal to 10 deg or 0.174533 radians gives from equation (3)

$$y_{i+1} = 1.96954 y_i - y_{i-1}$$

which is seen to be very close to the values previously obtained by the method presented herein.

Fig. 2 shows the results obtained for the theoretical set of

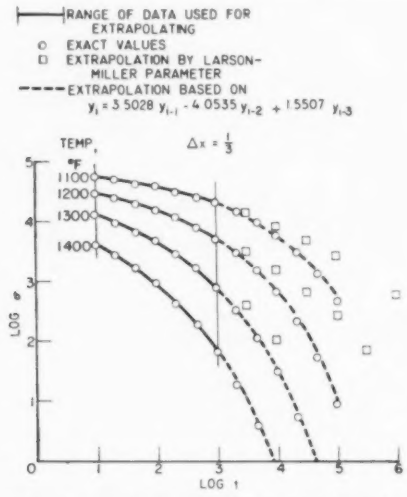

Fig. 3 Results of extrapolating stress-rupture curves based on Manson-Haferd parameter by recurrence relation and Larson-Miller parameter

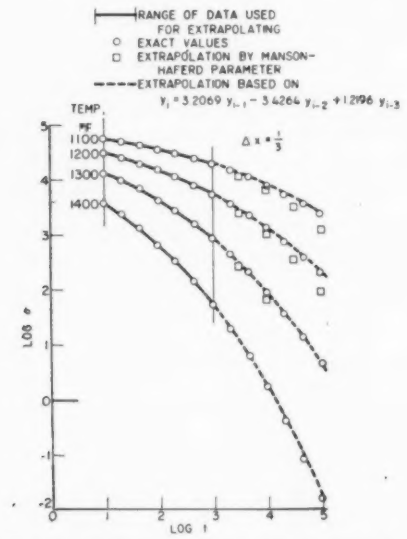

Fig. 4 Results of extrapolating stress-rupture curves based on Larson-Miller parameter by recurrence relation and Manson-Haferd parameter

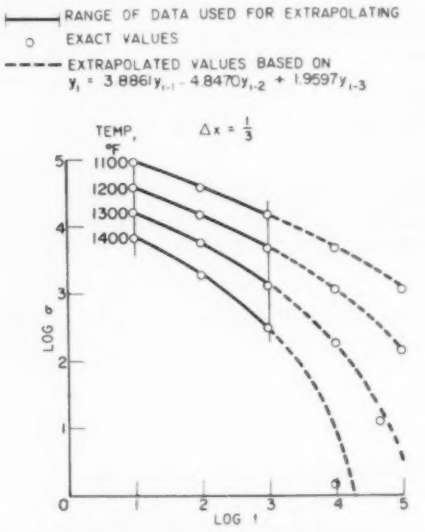

Fig. 5 Extrapolation of curves based on Dorn equation

$$e^{0.34(\log \sigma)^{2.5}} = 10^{-10}\, \frac{e^{\frac{60{,}000}{T+460}}}{t}$$

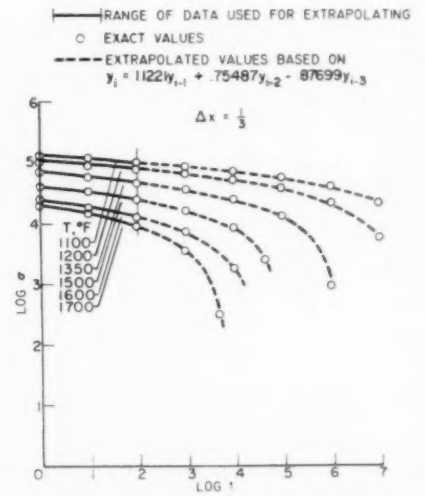

Fig. 6 Extrapolation of curves based on Conrad equation

$$t = 3.24 \times 10^{-9}\, e^{\frac{60{,}600}{T+460}}\, e^{-\frac{\sigma}{\sigma\sqrt{(T)}}}$$

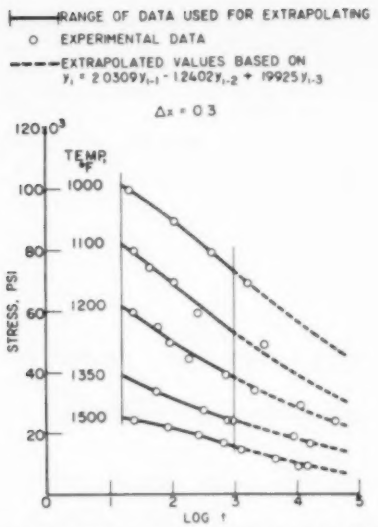

Fig. 7 Results of extrapolating alloy S-590. Data from reference [6].

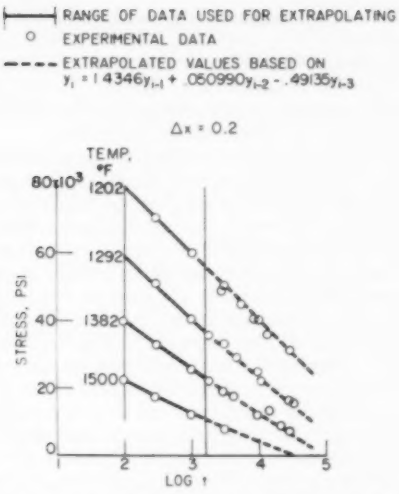

Fig. 8 Results of extrapolating alloy Nimonic 80A. Data from reference [6].

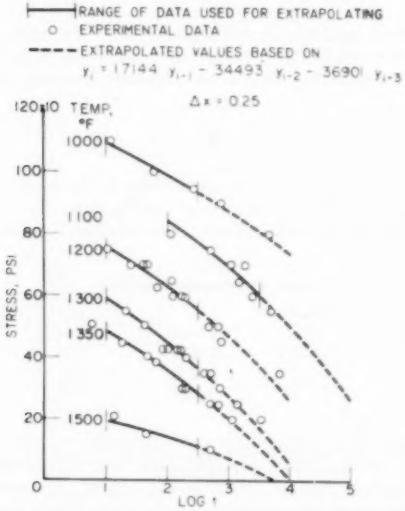

Fig. 9 Results of extrapolating alloy A-286. Data from reference [6].

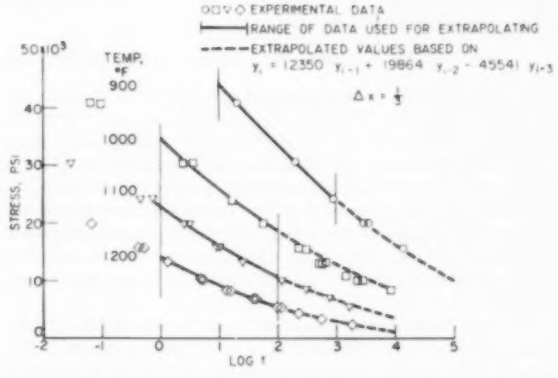

Fig. 10 Results of extrapolation for killed carbon steel. Data from reference [10].

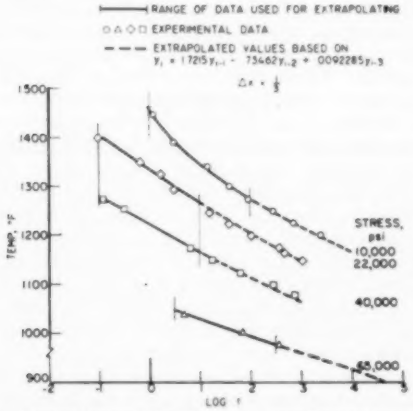

Fig. 11 Results for crucible 422 steel. Data from reference [7].

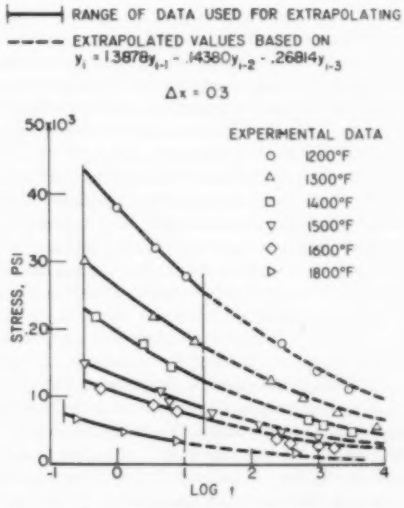

Fig. 12 Results of 18-8 stainless. Data from reference [2].

creep-rupture curves as given by equation (8). The extrapolations were made with q equal to 2, 3, and 4, and it is seen that there is no significant difference between the results obtained for q equal 3 and those obtained for q equal 4. In both cases the extrapolated values up to a hundred thousand hours shows excellent agreement with the theoretically exact values.

The generality of the present method for creep-rupture application was tested by trying it for several cases where one or another of the parameter methods could not be expected to give good results. Thus if one took a set of data given exactly by the Manson-Haferd parameter equation (8) and tried to correlate and extrapolate these data by the Larson-Miller parameter, one would not expect to obtain good results. This was done as shown in Fig. 3. Using the data exactly satisfying the Manson-Haferd parameter equation (8) in 10–1000 hour range, the best value of the Larson-Miller parameter C was computed by the method of reference [4]. The value of C was determined as 18, and a master curve was then constructed and the isothermals extrapolated as shown in Fig. 3. It is seen that as expected the extrapolation is very poor. However, using the same data between 10 and 1000 hours, the extrapolation obtained by the recurrence relation method gives excellent results as previously shown in Fig. 2 and repeated in Fig. 3.

A second calculation was then made using the reverse procedure. A set of data exactly satisfying the Larson-Miller parameter was generated by the equation

$$(\log t + 18)(T + 460) = 33{,}500(5.13 - \log \sigma)^{0.128} \quad (9)$$

The data obtained by this equation are very close to those obtained from equation (8) in the range between 10 and 1000 hours. These data were then used to obtain the best values of the constants for the Manson-Haferd parameter and to construct a master curve which was then used to extrapolate the original isothermals. The results are shown in Fig. 4 and as expected the extrapolation by the Manson-Haferd parameter for this case was not very good. However, again as can be seen the extrapolation obtained by the recurrence relation, using the same data, is excellent.

The calculations shown in Figs. 3 and 4 indicate the greater generality of the proposed method. The recurrence relation technique can be used whether the data are best fitted by the Larson-Miller parameter or the Manson-Haferd parameter. As a further test the method was applied to sets of data generated by use of the Dorn parameter and the recently proposed equation by Conrad [8]. The results are shown in Figs. 5 and 6, and it is seen that the agreement is very good.

In the previous examples the values of the ordinates required to calculate the r_{ij} by equation (7) were precisely known, since they were obtained from exact mathematical expressions such as equations (8) and (9). It might be expected therefore that these input data would reflect implicitly the shape of the curves even at a distance relatively far from the initial range of the data used. In practice, however, the data are given experimentally, and the input data for equation (7) are therefore much cruder than in the examples given. The extrapolation in this case might therefore not be quite so good as previously indicated, particularly if the curves have a large amount of curvature in the extrapolated range.

The method was therefore tried out using the actual creep-rupture data for six different materials. The actual data were plotted in the range to be used for extrapolating, and curves drawn by eye through these data. The values of the ordinates at seven equally spaced values of the abscissa were then read from these curves, and the coefficients of the finite difference recurrence relations obtained. The curves were then extrapolated and the results are shown in Figs. 7 through 12. It is seen that good extrapolation is obtained for all six materials.

The materials in Figs. 7, 8, and 9 were analyzed in reference [6], where a comparison was made between the Larson-Miller, Manson-Haferd, and Dorn parameters. In evaluating the various parameters, reference [6] uses the standard deviation defined by

$$D = \sqrt{\frac{1}{N}\Sigma d^2}$$

where D is the standard deviation, d is the deviation of each data point, and N is the total number of data points. Part of the results comparing the various parameters are reproduced in Table 3.

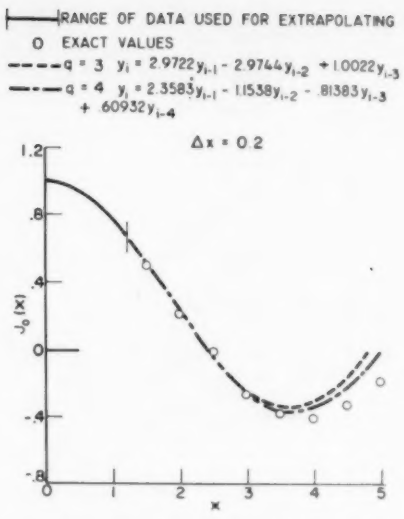

Fig. 13 Extrapolation of Bessel function, $J_0(x)$

Table 3 Standard deviations

Material	Larson-Miller	Dorn	Manson-Haferd	Recurrence relation
S-590	0.351	0.430	0.324	0.133
Nimonic 80A	0.385	0.235	0.091	0.045
A-286	0.207	0.172	0.134	0.148

In addition, the standard deviations using the method presented herein for extrapolation were also computed and added to the table. It is seen that the present method gives better results than any of the parameters shown.

Inspection of Figs. 7 through 12 shows that this method generally gives good results. However, a note of caution is in order. In order to use this method a sufficient number of low time data are needed for adequate definition of the basic curves to permit proper fairing. If such data are not available then the present method cannot be used. It should also be noted that the value of q or the number of terms appearing in the recurrence relation should not be made too large since it has been found that the larger the number of simultaneous equations to be solved the greater is the loss in significant figures in carrying out the calculations. However, the results for the examples and materials shown indicate that in general using a value of q equal to 3 is adequate and that very little can be gained by going to higher values of q.

It is obvious from the foregoing that this method is not restricted to families of creep-rupture curves. The sine function used as an example illustrates that other type curves can be extrapolated with equal ease. For example, Fig. 13 shows the results of applying this method to a Bessel function, Fig. 14 shows the results for a Legendre polynomial, and Fig. 15 shows a family given by $y = x^n$ with n equal to $1/2$, $1/3$, and $1/4$. In all these

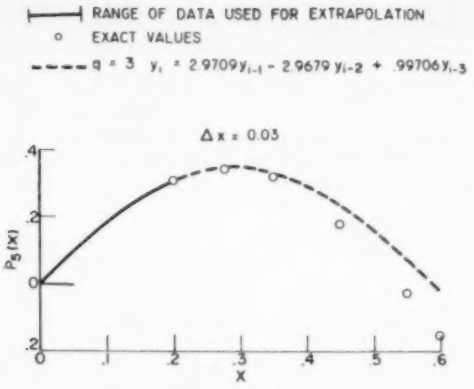

Fig. 14 Extrapolation of Legendre polynomial, $P_5(x)$

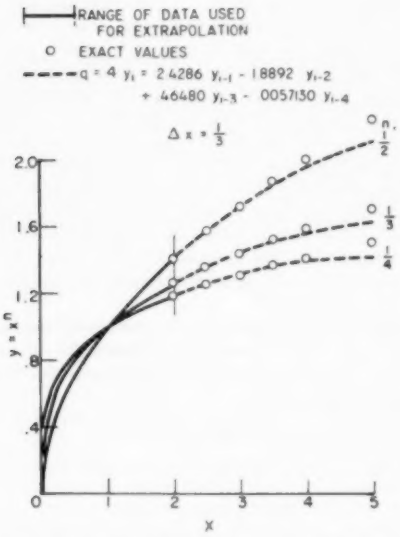

Fig. 15 Extrapolation of family of curves given by $y = x^n$

cases good results are obtained, even though as indicated in the Appendix one would not expect that these functions could be represented by finite-difference recurrence relations with constant coefficients. It is evident, therefore, that the applications of this method can be manifold.

APPENDIX

Origins of Finite-Difference Recurrence Relations

Consider any nth-order ordinary linear differential equation with constant coefficients. It is apparent that if each of the derivatives appearing in the differential equation is replaced by its finite difference equivalence, a finite difference recurrence relation is obtained relating $(n + 1)$ stations to each other. This has already been illustrated by the sine function discussed earlier. As another simple example consider the differential equation

$$\frac{d^3y}{dx^3} = 0 \tag{10}$$

in finite difference form this becomes

$$\frac{y_{i+1} - 3y_i + 3y_{i-1} - y_{i-2}}{(\Delta x)^3} = 0$$

or

$$y_{i+1} = 3y_i - 3y_{i-1} + y_{i-2} \tag{11}$$

which is the recurrence relation for a family of parabolas, the particular member of the family being determined by the starting values. In this particular case the relation (11) is exact since it is independent of the step size Δx.

It is apparent that, for every family of curves which are derivable as the solution of a linear differential equation with constant coefficients, there exists a corresponding recurrence relation. In the general case the recurrence relation can be said to approximate the actual function by a function which satisfies a linear differential equation with constant coefficients. Moreover, since the solution of an ordinary linear differential equation with constant coefficients or of the corresponding difference equation is generally given in terms of exponentials, it can be said that the actual function is being approximated by a sum of exponentials.

There is, however, a great difference between the use of the finite difference recurrence relation proposed herein and trying to fit the curves by a sum of exponentials. Thus consider this recurrence relation

$$y_i = A_1y_{i-1} + A_2y_{i-2} \tag{12}$$

and the corresponding exponential solution

$$y = B_1e^{\alpha_1 x} + B_2e^{\alpha_2 x} \tag{13}$$

Equations such as (13) have been used for interpolating purposes as, for example, in the Prony method [11]. Equation (12) contains two unknown constants which can be evaluated from four successive ordinates by writing down two such equations as (12) for two successive values of i. Equation (13), however, requires the evaluation of four constants: B_1, B_2, α_1, and α_2. Moreover, these constants will in general be complex numbers. The generation of the curve represented by (12) of course requires four values, A_1, A_2, y_{i-1}, and y_{i-2}, just as for (13).

This advantage of the use of (12) over (13) becomes even more evident if a family of curves is considered. Equation (12) remains the same with just two constants required, each member of the family being generated from its two starting values. The use of (13), however, requires the evaluation of a different set of constants B_1 and B_2 for each member of the family.

The major advantage of (12) over (13), however, lies in the ease with which least squares can be used to determine the unknown coefficients. Using (12) one can find the best values of the constants to fit all the data by conventional application of least squares procedures. This case is brought about by the fact that the least squares equations are linear in the unknown constants. An attempt to find the best fit for all the data using (13) leads to a set of nonlinear equations in the constants to be determined which are difficult to solve. Furthermore, it has been shown [12] that the unknown constants in (13) are extremely sensitive to the accuracy of the input data.

Another way of looking at these recurrence relations is in terms of weighting functions rather than as difference equations. Consider, for example, the problem of automatic fire control where it is necessary to point a gun not at where the target is, but where it is likely to be by the time the shell arrives. On the basis of the knowledge of the past path of the target, it is necessary to predict or extrapolate its future path. This problem has been handled in a very sophisticated way by Wiener [9] making use of autocorrelation functions and the modern techniques of operational calculus. Basically what is involved, however, is to obtain the approximate output of a given time series from a linear combination of the

input and a number of its past values. The output, thus, is given approximately by a weighted sum of a number of past values of the input. The coefficients in the recurrence relation can then be considered as weighting coefficients.

To put it another way, in the linear theory of prediction an attempt is made to express $f(t + h)$ as a linear combination of values of $f(t - \tau)$ where $f(t)$ is the function one wishes to predict, h is an interval of time in the future, t is the present time, and $\tau \geq 0$. One way of doing this would be to select several values of τ, $\tau_i \geq 0$ and choose coefficients A_i, so that

$$\sum_0^n A_i f(t - \tau_i)$$

gives an optimum prediction. This is precisely what has been done here.

References

1 F. R. Larson and J. Miller, "A Time Temperature Relationship for Rupture and Creep Stress," TRANS. ASME, vol. 74, 1952, pp. 765–771.

2 S. S. Manson and A. M. Haferd, "A Linear Time Temperature Relation for Extrapolation of Creep and Stress Rupture Data," NACA TN 2890, March, 1953.

3 R. L. Orr, O. D. Sherby, and J. E. Dorn, "Correlations of Rupture Data for Metals at Elevated Temperatures," *Trans. ASM*, vol. 46, 1954, pp. 113–128.

4 S. S. Manson and A. Mendelson, "Optimization of Parametric Constants for Creep-Rupture Data by Means of Least Squares," NASA MEMO 3-1059E, 1959.

5 W. Betteridge, "The Extrapolation of the Stress-Rupture Properties of the Nimonic Alloys," *Journal, Institute of Metals*, vol. 86, no. 5, 1958.

6 R. M. Goldhoff, "Comparison of Parameter Methods for Extrapolating High Temperature Data," TRANS, ASME, Series D, JOURNAL OF BASIC ENGINEERING, vol. 81, 1959, p. 629.

7 S. S. Manson and W. F. Brown, Jr., "Time-Temperature Relations for the Correlation and Extrapolation of Stress-Rupture Data," *Proceedings, ASTM*, vol. 53, 1953, pp. 693–719.

8 Hans Conrad, "Correlation of High Temperature Creep and Rupture Data," TRANS. ASME, Series D, JOURNAL OF BASIC ENGINEERING, vol. 81, 1959, p. 617.

9 Norbert Wiener, "Extrapolation, Interpolation, and Smoothing of Stationary Time Series," The Technical Press and John Wiley & Sons, Inc., New York, N. Y., 1949.

10 P. N. Randall, "Constant Stress, Creep-Rupture Tests of a Milled Carbon Steel," *Proceedings, ASTM*, vol. 57, 1957, p. 854.

11 R. A. Buckingham, "Numerical Methods," Sir Isaac Pitman & Sons, Ltd., London, England, 1957.

12 Cornelius Lanczos, "Applied Analysis," Prentice-Hall, Inc., Englewood Cliffs, N. J., 1956.

DISCUSSION

Burt M. Rosenbaum[2]

The authors are to be commended for devising a method of extrapolation which is both simple and widely applicable. As pointed out by the authors in comparing equations (12) and (13), this ease of application stems from the fact that the resulting equations for the unknown constants A_1 and A_2 are linear in these constants whereas the Prony method of approximating the curve by a sum of exponentials gives rise to nonlinear equations. It is evident that the recurrence relation gives exactly the same extrapolated curve as would be obtained if the exponential solution, as determined by the more complicated Prony method, were used for extrapolation.

However, the Prony method does yield additional information in that it gives the entire curve over the range of the independent variable and not just points at intervals along the range. The Prony method actually determines the constants entering into the differential equation best fitting the data points. As an illustration, the curve given by equation (13) satisfies the second-order linear differential equation

$$\frac{d^2y}{dx^2} - (\alpha_1 + \alpha_2)\frac{dy}{dx} + \alpha_1\alpha_2 = 0$$

For a second-order recurrence relation, the coefficients of the corresponding differential equation may be found from the values of A_1 and A_2 by the equations

$$\left.\begin{aligned} \alpha_1 + \alpha_2 &= \frac{\ln(-A_2)}{(\Delta x)} \\ \alpha_1\alpha_2 &= \frac{1}{(\Delta x)^2}\left[\ln\left(\frac{A_1 + \sqrt{A_1^2 + 4A_2}}{2}\right)\right. \\ &\qquad \left.\ln\left(\frac{A_1 - \sqrt{A_1^2 + 4A_2}}{2}\right)\right] \end{aligned}\right\}$$

The determination of the constant-coefficient differential equation corresponding to the recurrence relation is desirable in some cases. Because the data are to be physically significant, one of the requirements of the differential equation in order that it can properly represent the data is that it possess a real solution throughout the range of the independent variable. This requirement implies that the coefficients of the differential equation must be real. As far as the recurrence relation is concerned, the A_i's always are real. However, the differential equation corresponding to these real A_i's may possess complex coefficients so that the solution of the differential equation is complex in general, turning real only at the stations originally chosen. A recurrence relation that corresponds to a complex-coefficient differential equation has only questionable physical significance and extrapolation by the use of such a recurrence relation must be viewed with suspicion.

It is possible to determine the recurrence coefficients for half-intervals from a knowledge of the coefficients for the original intervals. Let the order of the recurrence relation be two and let the relation be given by

$$y_i = A_1 y_{i-1} + A_2 y_{i-2} \tag{14}$$

Similarly, the half-interval recurrence relation is given by

$$\begin{aligned} y_i &= a_1 y_{i-1/2} + a_2 y_{i-1} \\ &= a_1 (a_1 y_{i-1} + a_2 y_{i-3/2}) + a_2 y_{i-1} \end{aligned} \tag{15}$$

Solving for $y_{i-3/2}$ by means of

$$y_{i-1} = a_1 y_{i-3/2} + a_2 y_{i-2}$$

and substituting in equation (15), one obtains the desired result

$$y_i = (a_1^2 + 2a_2) y_{i-1} - a_2^2 y_{i-2} \tag{16}$$

A comparison of equations (14) and (16) yields

$$\left.\begin{aligned} A_1 &= a_1^2 + 2a_2 \\ A_2 &= -a_2^2 \end{aligned}\right\} \tag{17}$$

The above process can be continued indefinitely, each step giving the recurrence coefficients for double the number of stations. If either $A_2 > 0$ or $A_1 + 2\sqrt{-A_2} < 0$, the new recurrence coefficients are complex indicating that the interpolated values of the ordinate, that is, the values of the ordinate at the new stations, are not real. In order to insure that the recurrence coefficients stay real at each step, which is equivalent to requiring that the differential equation possess a real solution, the inequalities $A_2 < 0$ and $A_1 + 2\sqrt{-A_2} > 0$ must be satisfied. Thus, conditions on the recurrence coefficients may be found which are

[2] Nuclear Reactor Division, National Aeronautics and Space Administration, Lewis Research Center, Cleveland, Ohio.

equivalent to requiring that the coefficients of the corresponding differential equation be real without actually finding these latter coefficients.

The full-interval recurrence coefficients are given in terms of the half-interval coefficients by

$$\left.\begin{aligned} A_1 &= a_1^2 + 2a_2 \\ A_2 &= 2a_1a_2 - a_2^2 \\ A_3 &= a_2^2 \end{aligned}\right\}$$

for a three-term recurrence relation and

$$\left.\begin{aligned} A_1 &= a_1^2 + 2a_2 \\ A_2 &= 2a_1a_2 + 2a_4 - a_2^2 \\ A_3 &= a_2^2 - 2a_2a_4 \\ A_4 &= -a_4^2 \end{aligned}\right\}$$

for a four-term relation. Note that a necessary condition for an nth order recurrence formula to yield a real curve is apparently

$$(-1)^n A_n < 0.$$

As a final observation, data points are inaccurate to some degree and in addition the recurrence relation that is established does not fit the data points exactly. But in order to extrapolate to the next station by the use of a recurrence relation of order q, it is necessary to know the values of the ordinates at the last q stations of the curve which as mentioned are somewhat in error. Would the authors care to discuss more fully how the extrapolated curve may be obtained once the recurrence coefficients have been determined?

Authors' Closure

The authors wish to thank Dr. Rosenbaum for his illuminating comments. In particular, the equation relating the coefficients of the finite-difference recurrence relation to those of the corresponding differential equation and the conditions for the latter coefficients to be real are of great interest.

The significance of the fact that the coefficients of the differential equation may turn out to be complex is not very clear. In any recurrence relation, values of the desired function can only be obtained at discrete points. Nothing at all can be said about the function in the region between successive points. The reason for replacing the continuous solution by one which is valid at only discrete points is to simplify the solution. The fact that the corresponding differential equation would give nonreal solutions between stations does not seem to be relevant. Thus, for example, examination of Figs. 6, 8, 9, 10, and 12 indicates that, although one of the conditions given by Dr. Rosenbaum for the coefficients of the differential equation to be real, namely, $(-1)^n A_n < 0$, is violated in these cases, the extrapolations obtained were very good.

For a qth order recurrence relation, the extrapolated curves will in general be sensitive to the last q ordinates of the original data curves. This is due to the fact that once the A_i are determined, the last q values of the ordinates are used directly to begin the extrapolation. It is therefore important that these last q values be obtained in the best possible manner.

If there is a sufficient number of data points in this region, with little scatter, then one can have confidence in the originally faired curve. If, however, such is not the case, it might be wise to investigate further the validity of the extrapolation. Thus, one could extrapolate to the desired point using the last q values as described. One could then successively repeat the extrapolation each time beginning at one station earlier. In this way a set of extrapolated values can be obtained. If all these values agree with each other fairly well, one could have some confidence in the final result. If, however, widely differing values are obtained for the extrapolated point, care must be taken in deciding which value to use. One could, for example, average the different values obtained, using an appropriate weighting factor for each one.

In deciding on appropriate weighting constants, at least three important factors should be considered: (1) the number of stations between the extrapolated point and the starting values on which they are based, (2) how well the faired curve fits the data in the region where the extrapolation is started, and (3) the number of actual data points in this region. Thus it is obvious that the closer the extrapolated point is to the region where the extrapolation is started, the greater the number of data points in this region and the closer the faired curve fits the data in this region, the more weight should be attached to the resultant extrapolated value. Thus one could tentatively assume the weighting factor to be approximately inversely proportional to the number of intervals extrapolated, directly proportional to the number of data points in the region one is extrapolating from, and proportional to some function of the inverse of the deviation of these data from the faired curve. (A direct inverse proportion cannot be used for the deviation from the curve since this would lead to infinite weight for a data point right on the curve.) A detailed analysis of the type of weighting factors to be used could form an interesting future investigation.

ROBERT M. GOLDHOFF
Applied Research Metallurgist,
Materials and Processes Laboratory,
Large Steam Turbine-Generator Department,
General Electric Company,
Schenectady, N. Y.

Some Observations on the Extrapolation of High-Temperature Ferritic Steel Data

When calculating long-time working stresses for machine components, the starting point must necessarily be some value of material strength and ductility. Normally such figures involve specific times and service temperatures. Usually tests to determine long-time material properties can be carried out at ultimate service temperatures, but testing times corresponding to design criteria can be prohibitive. In the present case, these values are the 100,000-hr rupture strength and limiting creep stresses for deformation up to 0.5 per cent in the same time period. Obviously, such strength values must be extrapolated from short-time data.

A favorite technique among designers has been the use of one or another time-temperature parameter. Such a technique substitutes higher temperatures for longer times in obtaining data, and the eventual correlation of data permits the long-time strength, but not ductility, extrapolation. The pros and cons of these methods are adequately covered in the literature.

Recently some proposals for the use of combined creep and rupture data have been published which could have an interesting bearing on the long-time design problem [1–9].[1] It is the purpose of this paper to discuss these proposals and analyze some extensive creep and rupture data obtained on several ferritic steels in the light of one of them, the Monkman-Grant relationship [7]. In addition, comparisons are drawn with results obtained using the Larson-Miller and Manson-Haferd parameter methods.

Recent Proposals

Several recent publications are of special interest in the study of presenting and using high-temperature data, and these will be examined briefly.

Ivanova and Oding [1–3] have proposed a design criterion of plasticity for metals to be used in long-time service. This criterion purports to describe approximately the amount of deformation which can occur before the third stage of creep is reached. It is defined as the product of the minimum or second-stage creep rate[2] and the rupture time and is termed "usable elongation." This expression can be determined analytically by assuming empirical relationships between minimum creep rate and stress as well as between rupture time and stress. The authors assume the following

$$\text{mcr} = P\sigma^{-p} \text{ and } t_r = D\sigma^{-d} \qquad (1) \text{ and } (2)$$

and from these derive

$$\epsilon_r = \text{mcr} \times t_r \qquad (3)$$

where

mcr = minimum creep rate
t_r = time to rupture
ϵ_r = usable elongation
σ = stress
P, p, D, d = constants

From this the three-quadrant "generalized creep diagram" is derived and can be conveniently used to extrapolate long-time values of ϵ_r. These values are then used as limiting factors in the applicability of a given steel for a desired use. The basic fallacy in this approach is the assumption that ϵ_r is closely associated with the total creep up to the third stage. Both Nikitina [5] and Borzdyka [6] point this out. Logically, the total creep up to the third stage must be associated with the form of the creep curve, and this can vary appreciably. Actually, the primary or first-stage creep is highly important, and it is not determined by the Russian proposal. In particular, for steels with low values of elongation (1–3 per cent), the differences between ϵ_r and measured creep to the start of the third stage are substantial and tend to underestimate the plasticity of the steel. Aside from the obvious limitations of the quantity ϵ_r, the liberty which is taken in extrapolating short-time log-log or semilog data by a graphic straight-line method over two log cycles (from 10^3 to 10^5 hr) is highly questionable. Indeed it is almost certain that such a procedure is incorrect for the type of alloy considered. Thus, even if the concept of ϵ_r were justifiable, the inability to extrapolate reliably would still invalidate its use.

Nevertheless, the idea of combining creep and rupture data has been carried further. If equations (1) and (2) are combined the relation

$$t_r = (DP)^{\frac{d}{p}} \times (\text{mcr})^{\frac{-d}{p}} \qquad (4)$$

is obtained, where the symbols mean the same as before. This relationship, where the exponent d/p is constant, is the Monkman-Grant [7] formulation commonly given as

$$\log t_r = C + m \log (\text{mcr}) \qquad (5)$$

where C and m are constants.

In the form of equation (5) this relation says that there is a linear correlation between time to rupture and minimum creep rate when the data are plotted on logarithmic co-ordinates. Furthermore, the relation as shown does not rule out independence from stress and temperature. If this were true, the potential of this relationship for strength and some form of ductility extrapolation would be enormous. These advantages have been discussed thoroughly in the original paper [7].

The recent proposal by Glen [8, 9] for the extrapolation of creep data should be seriously considered. In essence, this method is based on the observation that creep curves, for commercial alloys in particular, are highly structure dependent, and numerous transitions in creep rate during test may be expected. The

[1] Numbers in brackets designate References at end of paper.

[2] Wherever "minimum creep rate" is used in this report, it will be understood that the context is "second-stage creep rate" as generally recognized.

Contributed by the Metals Engineering Division and presented at the Annual Meeting, Atlantic City, N. J., November 29–December 4, 1959, of The American Society of Mechanical Engineers.

Note: Statements and opinions advanced in papers are to be understood as individual expressions of their authors and not those of the Society. Manuscript received at ASME Headquarters, July 8, 1959. Paper No. 59—A-133.

course of this behavior is followed by plots of creep rate versus strain which eventually allow for the extrapolation of time by integration. The crux of the method is the interpolation and extrapolation of regular curve patterns established by test over a relatively small range of stress or temperature to obtain a complete family of "strain/rate" curves. Having assumed such a family of curves, a simple graphic integration method allows the calculation and consequent extrapolation of times for iso-strain conditions at lower temperatures or stresses. Glen points out that the extrapolation of rupture times by this method is not infallible. If the materials are highly ductile, so that the final stages of elongation are accomplished in a small fraction of the total time, the approximation is good. If, however, the fracture is intercrystalline and therefore usually at extremely low elongations, the terminal elongation must be known before good approximations can be made. It will be recognized that, unfortunately, the latter is the case with many of our most usable steels. Obviously, the greatest importance must be attached to the determination of creep-rate transitions in this method. Analysis by this technique in light of contemporary needs is difficult because the amount, type, and precision of data needed almost certainly preclude this. Thus, the method appears basically sound, but at the same time too complex for practical use.

Because of the unusual availability of combined creep and rupture data plus some very long time (30,000-hr) creep data, it was decided to thoroughly exploit the simple Monkman-Grant relationship. At the time of its presentation several objections were raised, and these are treated in this report.

The method was not originally intended for extrapolative use, and the reasons for this will be apparent as objections are raised and discussed. It should be kept in mind, however, that the interest here is in application to very limited alloy systems over limited ranges of service conditions, and interest centers chiefly around how reliable the approximate extrapolations are with reference to methods currently in use.

Let it further be emphasized that the extrapolations to which reference is made concern only values derived from test bars stressed in uniaxial tension, and the values predicted can therefore only refer to material strengths in this stress state. In combination with these data the design engineer must use his judgment and experience to choose safety factors which will ultimately determine the allowable stresses on a working component.

Experimental Procedure

In the original Monkman-Grant presentation [7] data for a given class of alloys, e.g., stainless ferritic, stainless austenitic, and so forth, over fairly wide ranges of stress and temperature were lumped together and the relationship along with the statistical 2σ scatter limits was determined. It was subsequently shown that structural variations within a group or system of alloys might affect the relationship. Hence, in the present analysis, individual equations have been derived for the data available within a specific alloy type of ferritic forging or casting steel. Table 1 shows the materials chosen according to type, significant properties, and composition.

In general, the creep-rupture data analyzed to determine the equations were not of the highest accuracy because the tests were run in rupture stations with creep readings being taken externally by means of a transfer gage. The importance of this fact will be reflected in the width of the calculated scatter bands and should therefore be kept in mind. On the other hand, the very-long-time creep tests which did not fail and which were used in the extrapolations discussed later were taken under more accurate test conditions.

The number of tests considered in each category ranged from 16 to 64 with some 239 tests being considered over-all. In order to extend the analysis to alloy compositions other than Cr–Mo–V and 12-Cr types, several low-alloy ferritics with sufficient creep-rupture and long-time creep data were also studied. Tabular data on these alloys are included in the lower portion of Table 1. This separation is made because data from these latter alloys were not used in deriving the t_r versus (mcr) equations employed in their subsequent extrapolation analysis.

The individual sets of rupture data and corresponding minimum-creep-rate data were plotted on log-log graph paper. Later the best straight lines describing each set of data and accompanying predicted scatter limits were plotted. A machine program for least-squares analysis was used for this determination. The t_r versus (mcr) curves thus obtained were extrapolated graphically by merely extending the straight lines sufficiently far into the region necessary to accommodate creep-test conditions. Note, however, that the machine-predicted scatter limits tend to fan out giving wider scatter bands in the region of extrapolation.

Next, long-time creep data ranging from 10,000 to 30,000 hr were carefully studied and, where possible, final rates which appeared to be in the second stage were ascertained. In certain instances, actual third-stage creep had been attained and selection is more certain in these cases. From these rates and the appropriately extended t_r versus (mcr) curves, predicted rupture times for the stress and temperature conditions of the creep test are obtained. Obviously, the effect is to obtain a long-time extrapolation of a given stress-rupture curve.

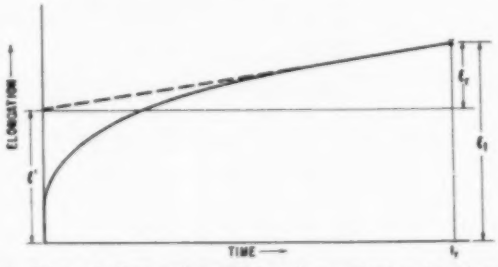

Fig. 1 Schematic diagram for prediction of approximate value of rupture elongation

By combining the partial creep curve with the predicted value of rupture time, as shown schematically in Fig. 1, an approximate value of elongation, ϵ_t, can be obtained. This same value can be determined simply by adding ϵ' and ϵ_r as shown. ϵ_r is the product of minimum creep rate and predicted rupture time and is the same value the Russians call "usable elongation." ϵ' is determined by an extension of the minimum-creep-rate line to its intersection with the elongation axis. For very long time rupture tests on brittle steels where little third-stage creep is expected, the value ϵ_t should be quite close to the combined total of primary and secondary extensions and in fact very close to the total elongation.

Attention is given to the factors which previously caused objections to this method of data presentation. These include structural instability in the alloys, possible effects of stress and temperature, and the mechanics of determining minimum creep rates.

Experimental Results

A typical log-log plot of the data described is shown in Fig. 2. For clearer presentation, the actual data points have not been shown in the curve. Instead the scatter band derived statistically from the least-squares analysis is shown. In Table 2, the test values, equation constants, and scatter limits for the alloys studied are compiled. In each case, the correlations were highly significant being well within the one per cent level as determined by machine computation.

The results of the extrapolative application of the t_r versus (mcr) equations to obtain approximate strength values at long times are given in Table 3. For illustrative purposes, the extrapolations at 1000 F for a forged and a cast Cr-Mo-V steel are shown in the graph of Fig. 3. Where sufficient data were available comparisons with useful parameter methods are shown both tabularly and graphically. The extrapolations and comparisons are limited to the particular alloys shown because long-time creep data useful in this method were available only to this extent. The Larson-Miller parameter method with constant equal 20 is included in each analysis. Since it appears that a better correlation of data, and possibly therefore a more realistic extrapolation (although this is not proved) can be obtained with the Manson-Haferd parameter, such comparisons are included where data permit the necessary calculation of constants. For steel 1(*a*) in Fig. 3, the situation is developed one step further. Here both the rupture data and minimum-creep-rate data have been subjected to parameter correlation and a combination of the two evolved (see Manson's discussion to reference [7] for extrapolative purposes.) This method is discussed later in the paper. Figs. 4 and 5 show the necessary plots for this evaluation of steel 1(*a*) data.

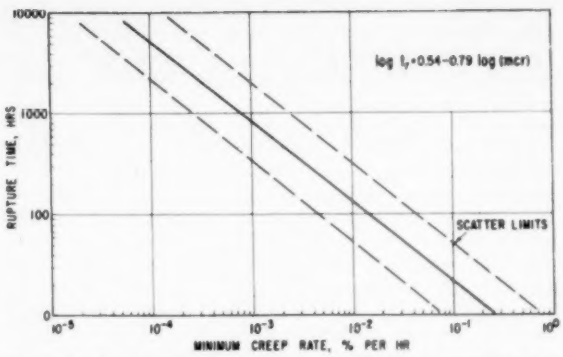

Fig. 2 Log-log plot of rupture time versus minimum creep rate for steel 1(a)

In Figs. 6 through 9, data are plotted to assist in the determination of stress and temperature dependency as well as the effect of material instability on the rupture-time minimum-creep-rate equation.

Table 1 Composition and properties of alloys

Steel No.	Chemical Composition, % C	Cr	Mo	V	Mn	Si	Ni	P	S	Others	Mech. Props. TS, psi	Elong. %	Heat Treatment Temp, °F
1(a)	.33	.90	1.40	.28	.87	.31	.14	—	—	—	142,900	13.5	1830–AC; 1150 for 135 hrs.–FC
1(b)	.32	1.01	1.23	.22	.79	.26	.15	—	—	—	138,900	10.0	1850 for 45 hrs.–AC; 1225 for 60 hrs.–FC
2(a)	.33	1.13	1.28	.26	.89	.28	.11	.019	.024	—	113,000	17.5	1750–AC; 1250 for 20 hrs.–FC
2(b)	.33	1.02	1.23	.23	.83	.20	.23	.011	.010	—	122,000	15.5	1750 for 26 hrs.–AC; 1140 for 33 hrs.–FC
2(c)	.34	1.13	1.20	.21	.89	.35	.11	.024	.024	—	120,500	14.5	1750–AC; 1250–FC
3(a)	.28	.96	1.25	.25	.80	.31	.23	.015	.009	—	120,000	20.0	
3(b)	.28	.96	1.25	.25	.80	.31	.23	.015	.009	—	122,000	20.0	
4(a)	.17	.99	.99	.23	.63	.50	.17	—	—	Cu-.13	104,900	22.5	1970 for 24 hrs.–AC; 1290 for 40 hrs.–FC; 1200 for 8 hrs.–FC
4(b)	.18	1.00	.94	.24	.66	.41	.19	—	—	Cu-.20	112,700	24.0	1920 for 11 hrs.–AC; 1275 for 32 hrs.–FC
5(a)	.08	.97	.87	.21	.51	.24	—	—	—	—	83,900	27.0	1920 for 2 hrs.–AC; 1300 for 12 hrs.–FC
5(b)	.12	.99	.93	.21	.53	.18	—	—	—	—	86,400	28.0	1920 for 2 hrs.–AC; 1300 for 12 hrs.–FC
6(a)	.18	11.6	.07	.27	1.15	.38	.23	—	—	W-3.35; Co-5.13	163,000	17.5	1750 for 5 hrs.–AC; 1200 for 8 hrs.–AC
6(b)	.18	12.3	.12	.25	.35	.24	.16	—	—	W-4.7; Co-4.5	149,000	15.7	1750 for 6 hrs.–AC; 1200 for 12 hrs.–AC
7	.23	12.3	.92	.21	.78	.28	.82	—	—	W-.82	149,000	—	1875–OQ; 1150–AC
8	.19	13.8	.03	.26	1.20	.22	.10	—	—	W-3.17; Co-5.30	148,000	13.5	1750 for 10 hrs.–FC; 1200 for 24 hrs.–FC
9	.09	12.0	1.5	.20	.70	.60	—	—	—	Cu-1.5; N_2-.1; W-2.0	180,000	12.0	2010 for 4 hrs.–AC; 1200 for 2 hrs.–FC
10	.09	13.4	—	.42	—	.42	.47	—	—	Cb-.32	140,000	16.5	2010 for 2 hrs.–AC; 1200 for 2 hrs.–FC; 1250 for 4 hrs.–FC
11	.17	—	1.10	.22	.57	.50	—	—	—	—	83,000	28.5	1920 for 8 hrs.–FC; 1200 for 4 hrs.–FC
12	.11	—	0.99	.17	.49	.30	—	—	—	—	115,400	21.0	1920 for 4 hrs.–AC; 1200 for 4 hrs.–FC
13	.19	1.00	1.00	—	.76	.29	—	—	—	—	88,000	21.5	1920 for 12 hrs.–FC; 1275 for 13 hrs.–FC
14	.09	.98	.52	—	.43	.30	—	—	—	—	65,000	56.0	1750 for 2 hrs.–AC; 1275 for 4 hrs.–FC

Table 2 Summary of equation constants and scatter limits

Steel No.	Time Range, Hrs.	Temp. Range, °F	Stress Range psi x 10^{-3}	No. of Tests	Slope* m	Intercept* C	Scatter Limits, Log Cycles of Rupture Life
1	4-16,400	900 to 1200	80 to 20	28	0.79	0.54	±0.4
2	12-12,900	900 to 1100	70 to 15	34	0.90	0.61	±0.4
3	5- 2,076	850 to 1050	75 to 35	18	0.98	0.51	±0.25
4	4-22,900	900 to 1100	74 to 16	27	0.92	0.29	±0.90
5	14-11,000	900 to 1100	56 to 21	32	0.67	1.05	±0.30
6	8- 3,400	1000 to 1200	70 to 21	25	0.80	0.78	±0.40
7	9- 3,100	1000 to 1200	70 to 12.5	16	0.84	0.75	±0.40
6 - 10 Inclusive	2- 5,000	1000 to 1200	70 to 12.5	64	0.83	0.76	±0.40
All Alloys Studied		850 to 1200	80 to 12.5	239	0.78	0.77	±0.55

* In the equation log (time to rupture) = $C - m$ log (minimum creep rate).

Table 3 Long-time material strengths predicted by several extrapolation methods (in psi)

Steel No.	Predicted Stresses For 100,000 Hrs. @ 1000°F			Predicted Stresses For 30,000 Hrs. @ 1100°F		
	Larson-Miller	Manson-Haferd	Monkman-Grant	Larson-Miller	Manson-Haferd	Monkman-Grant
1 (a)	27,500	23,500	13,000	14,000	-	6,700
4 (b)	26,500	23,500	17,000	19,000	(13,000)	11,000
5 (a)	22,000	19,000	10,000	15,000	-	7,400
8	24,000	-	15,000	13,000	-	6,800
9	35,000	-	26,000	-	-	-
10	23,000*	-	14,000*	-	-	-
11	13,000	-	9,000	-	-	-
12	25,000	-	16,000	(13,000)	-	5,000
13	24,000	-	21,000	(18,000)	-	13,000
14	15,000*	13,000	12,000*	-	-	-

† Based on long-time creep data to 30,000 hr (see Table 4).
* 50,000 hr extrapolations.
() Obtained from extrapolation of master curve.

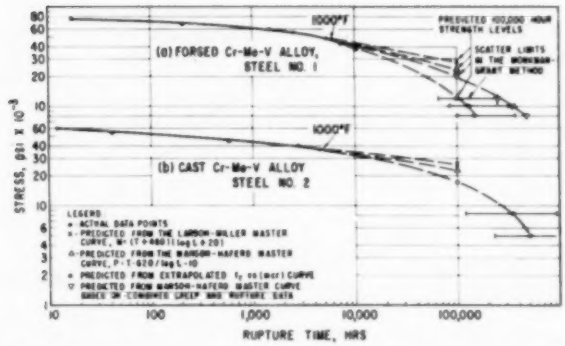

Fig. 3 Extrapolated stress rupture curves for forged and cast Cr-Mo-V steels

Discussion

That the data evaluated for each of the steels chosen conform to a linear equation of the type presented is evident from the high degree of significance obtained in machine computation. From Table 2, it is further to be noted that the scatter limits obtained are somewhat less than Grant and Monkman observed using a wider diversity of classification in their alloy grouping (the one exception is steel no. 4). The values of slope and intercept in the equation for stainless ferritic steels as originally derived were 0.85 and 0.56. From the present work as shown in Table 2, the values are 0.83 and 0.76. These values when plotted graphically are seen to be quite close. However, the variations observed over the entire class of ferritic alloys leave little doubt that each must be treated individually.

Passing to the extrapolations based on the plots already discussed and the long-time creep data (Fig. 3 and Tables 3 and 4), it is quite evident that extremely conservative predictions of 100,000-hr strength are obtained in each case, particularly when compared to the Larson-Miller extrapolations shown on each plot. Obviously these, as well as other methods for extrapolation of data, need to be examined.

Perhaps the most common technique is the simple graphical projection of a straight isothermal line from existing data out to the 100,000-hr point on the time axis. The very recently published German high-temperature data [10] with long-time points in the range 30,000–40,000 hr indicate that, at least for the low-

Table 4 Stability of low alloy steels judged by room temperature tensile strength before and after creep

Steel No.	Temp., °F	Creep Time, Hrs.	Stress psi	Tensile Strength, psi x 10^{-3} Before Creep	Tensile Strength, psi x 10^{-3} After Creep
1 (a)	1000	12,900	10,000	142.9	134
4 (b)	1000	30,600	6,000	112.7	100
	1000	31,100	8,500	112.7	101
	1000	31,500	3,000	112.7	83.5
5 (a)	1000	31,100	6,800	83.9	64.4
	1000	31,100	9,600	83.9	83.1
	1100	31,550	3,000	83.9	70.0
	1100	31,550	4,000	83.9	66.4
8	1000	11,600	12,000	148.0	152.0
	1100	3,515	-	148.0	132.0
9	1000	16,760	15,000	180.0	166.0
10	1000	16,900	15,000	138.0	109.0
11	1000	29,900	10,000	83.0	52.0
12	1000	11,600	8,000	115.4	75.0
14	900	35,400	11,000	65.5	64.5

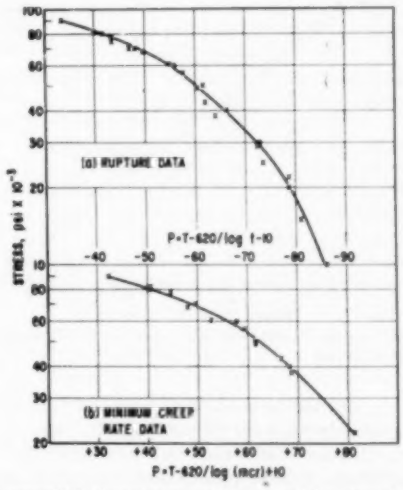

Fig. 4 Manson-Haferd master curves based on (a) rupture data and (b) creep data for steel 1(a)

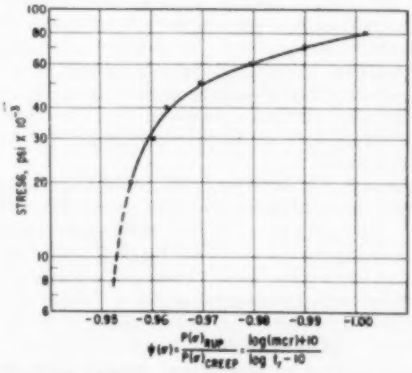

Fig. 5 Manson-Haferd master curve combining both rupture and minimum creep rate data; steel 1(a)

alloy steels studied, the 100,000-hr strength obtained by straight-line extrapolation of log-stress log-time plots drawn from short-time data is too liberal. Further, in the recent work by Glen [8], extrapolations to 100,000 hr based on his proposed method definitely show the same trend. These again are for low-alloy

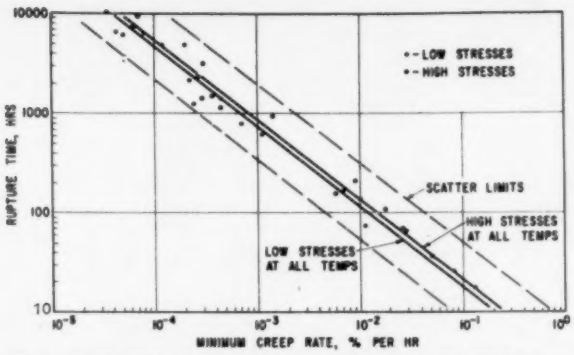

Fig. 6 Time to rupture versus minimum creep rate as a function of stress; range for steel 1(a)

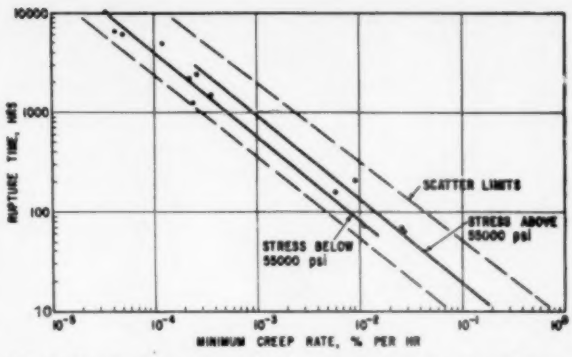

Fig. 7 Time to rupture versus minimum creep rate as a function of stress; range at 1000-deg F for steel 1(a)

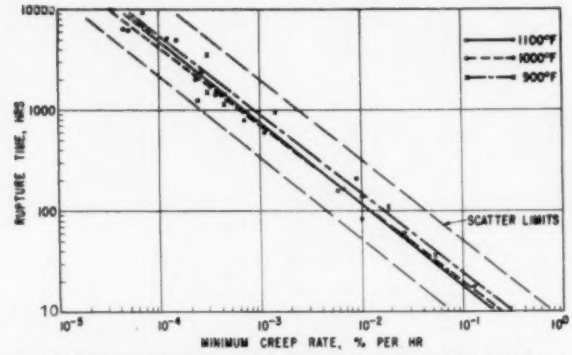

Fig. 8 Time to rupture versus minimum creep rate as a function of temperature for steel 1(a)

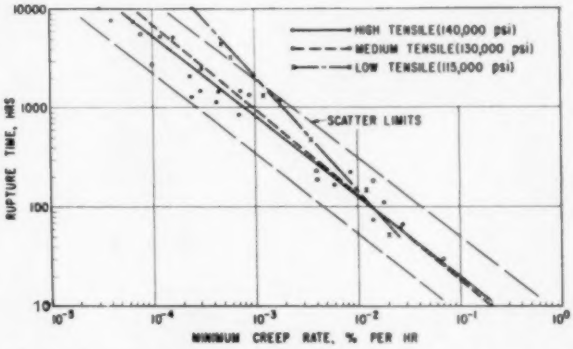

Fig. 9 Time to rupture versus minimum creep rate as a function of stability (heat-treated tensile strength) for steel 1(a)

steels. It should also be noted that for the instances cited, the data lend themselves to a curvilinear rather than straight-line (or lines) plot. On the other hand, very long time data for alloy S-590 would seem to indicate that the straight-line extrapolation from log-log data will be correct. The fact that the circumstance will alter the case seems evident. The Larson-Miller technique has been preferred, at least for low-alloy turbine steels, because it will generally give somewhat more conservative predictions than graphical straight-line extrapolation. However, it is widely recognized that no single value of constant in the Larson-Miller equation will satisfactorily correlate data taken over any appreciable range of stress or temperature. Thus, the need for compromising accuracy and the inevitable question of the validity of the extrapolation.

The extremely low 100,000-hr strength levels obtained by the Monkman-Grant method are also open to question. It is to be noted that the extrapolation of the scatter limits accompanying the best straight line allows a wide range of time prediction at very low minimum creep rates. These scatter limits accompany each predicted point on the graph of Fig. 3. Under these conditions the actual choosing of a representative stress is difficult. In addition to this, it is necessary to consider whether the proposed relation is truly independent of stress and temperature effects as well as material instabilities. This again is difficult to show with the limited data on hand, but an attempt has been made using the accumulated data from steel no. 1. In Fig. 6, the data taken at all temperatures have been divided into two stress ranges representing low and high values. The low stresses are in the range from 10,000 to 50,000 psi while the high stresses encompass the 50,000 to 90,000-psi range. Linear relations are developed for each of these ranges, and the evaluation shows them to be quite close together considering the few points available. In Fig. 7, a further step is taken by limiting the data to one temperature and then proceeding to again divide the stresses into two ranges. The results are not very different and it would be difficult to say that the relation is stress dependent at least for this set of data. In Fig. 8, the same data are treated with reference to temperature dependency and again little effect is evident. When, however, the effects of instability are considered, some definite trends are evident. If the measure of tensile strength at room temperature prior to testing is the criterion of stability (the lower the tensile strength for a given material the more stable it can be considered) then the differences shown in Fig. 9 appear. A steel of the type studied here is, of course, subject to secondary hardening on tempering after austenitizing. This means that a large range of hardness values (or tensile strengths) is attainable depending on the degree of tempering. The particular steel of Fig. 9 varies from 140,000 to 115,000 psi and the corresponding curves of t_r versus (mcr) deviate accordingly. When consideration is given to the fact that the extrapolated portion of these curves is some 90 per cent of the service time, the question naturally arises as to the possible tempering effects taking place in this interval. The data of Table 4 shed considerable light on this matter. Basing the instability criterion on drop of tensile strength after high-temperature exposure, it is evident that all the low-alloy steels examined here tend to be unstable. The diminution of strength after 1100-F exposure is drastic but less pronounced at 1000 F. This, of course, depends on the original level of strength. The behavior indicated would tend to impart curvature to the Monkman-Grant plot and the extrapolations shown would necessarily be conservative. Thus, for the steels

considered, this relationship should not be used for extrapolative purposes.

Finally, predictions based on the Manson-Haferd parameter need to be considered. Such predictions are meager because the number of isothermal data needed to evaluate the constants in this method are seldom available. However, a few comparisons are shown in Table 3. The trend is for a somewhat lesser value of extrapolated strength than that produced by the Larson-Miller method. Fig. 3 also contains the graphical Manson-Haferd predictions. It has been shown in several prior publications that this method is more accurate at least in correlating the data at hand. One might infer then that a method which gives the best correlation of known data stands the best chance of producing the most reasonable extrapolation. This deduction is not inconsistent with the results shown in Table 3, and the previous discussion which has pointed out that our limited experience with these alloys tends to justify some intermediate prediction between the extremes shown. Again, however, this is not proved.

One possible advantage inherent in the Monkman-Grant relation is the use of relatively short-time creep data to predict long-time rupture. However, the parameter techniques can also be extended to include the concept of combined creep and rupture data (see Manson's discussion to Ref. [7]). This is illustrated for the Manson-Haferd parameter with the aid of Figs. 4 and 5 using again the data from steel no. 1. Both creep and rupture data taken simultaneously are treated by this parameter technique to establish master curves as shown in Fig. 4(a) and (b). The constants derived on the basis of creep and rupture individually are equal in this case. Combining these relations leads to

$$\Psi(\sigma) = \frac{P(\sigma)\ \text{rupture}}{P(\sigma)\ \text{creep}} = \frac{\log(\text{mcr}) + 10}{\log t_r - 10} \qquad (6)$$

The master curve derived from (6) is shown in Fig. 5. It is now evident that long-time creep data at a known stress can be made to yield long-time-rupture-strength extrapolations using Equation (6) providing the master curve is fully developed. Also, the derivation of ductility from the long-time creep test will be applicable. The apparent advantage of this latter method is that the effect of stress, temperature, and material instabilities on both creep and rupture can best be taken into account. In Fig. 3 the 100,000-hr strength at 1000 F for steel no. 1 has been predicted by this method (a short extropolation of the master curve being necessary), and it is seen to be slightly less than that of the Manson-Haferd prediction based on rupture data alone. Of course, the use of this method depends on the validity of obtaining and using minimum-creep-rate data.

Glen's recent findings of numerous creep-rate deviations during the course of testing low-alloy steels certainly invalidates a "true" minimum rate. There is also a good deal of doubt as to the significance of this stage of creep especially as it is derived from constant-load tests. Nevertheless, in our present state of knowledge, this concept seems usable in providing better approximations of long-time materials strengths.

Next, the question of obtaining a reliable value for minimum creep rate without actually proceeding into the third stage of creep needs to be considered. It has been pointed out that to obtain the deviations noted by Glen requires extreme care in testing and highly expanded plotting facilities. Under the creep-test conditions generally in use, such trends could easily pass unnoticed. This does not mean they are unimportant, but it would seem that their incorporation in workable extrapolation procedure is impractical.

Again it is difficult to stipulate just how long one has to test under given conditions before being assured that second-stage creep is reached. About the best procedure is to watch each curve as it develops and use judgment for each separate case. Of course, experience with the material in question is invaluable in this operation. In general, it would appear that where reasonably carefully taken creep data are available second-stage rates can be estimated which, though admittedly approximate, are quite adequate for use in parameter techniques to estimate long-time material strengths.

Summary and Conclusions

In summary, better estimates of long-time high-temperature material properties can probably be achieved by the use of some form of the Manson-Haferd parameter method as opposed to other simple methods currently in use. However, until reliable data to times of 50,000–100,000 hr are produced for numerous alloys, none of the speculation accompanying the attempts to produce a much needed answer to an important design problem can be checked. A program designed to provide the necessary answers would seem mandatory for the responsible organizations which exist to further such needs.

The conclusions derived from the work are:

1 The Russian proposal to incorporate the concept of "usable elongation" into design procedure is based on fictitious assumptions and therefore open to doubt.

2 Glen's proposal for the extrapolation of creep data and the interrelation of ductility and creep-rate deviations appears quite sound but too complex to be of practical use.

3 The Monkman-Grant relationship between rupture time and minimum creep rate appears valid for several low-alloy turbine steels over short time ranges (up to 10,000 hr) of exposure. Extrapolations to 100,000 hr using this method are invalidated by the possible dependence of the relationship on stress and temperature and the probable dependence on material instability.

4 The use of the Manson-Haferd method based on either rupture data or combined creep and rupture data seems to give the most reliable prediction of long-time properties. This conclusion is inferred and not based on actual data.

5 Actual long-time data to check speculative attempts at extrapolation are a dire necessity.

Acknowledgment

The interest shown and aid given by Messrs. R. F. Gill and B. M. Wundt of the Large Steam Turbine-Generator Department of the General Electric Company in furthering this work are duly acknowledged.

References

1 V. S. Ivanova, "Creep Ductility Criterion for Metals," *Zavodskaya Laboratoriya*, vol. 21, 1955, no. 2, pp. 212–216; Brutcher Translation #4210.

2 I. A. Oding and V. S. Ivanova, "Analysis and Application of Certain Creep Criteria," *Vestnik Mashinostroeniya*, vol. 35, 1955, no. 5, pp. 62–66; Brutcher Translation #4211.

3 I. A. Oding and V. S. Ivanova, "Generalized Creep-Criteria Diagram," *Issledovaniya Po Zharoprochnym Splavam*, vol. 1, pp. 52–59; Brutcher Translation #4235.

4 A. V. Stanyukovick, "Estimation of Ductility of Creep-Resisting Alloys," *Zavodskaya Laboratoriya*, vol. 23, 1957, no. 4, pp. 476–484; Brutcher Translation #4232.

5 L. P. Nikitina, "On Criteria for the Plasticity of Metals During Creep," *Zavodskaya Laboratoriya*, vol. 22, 1956, no. 2, pp. 230–237.

6 A. M. Borzdyka, "On the Problem of the Evaluation of the Long-Term Plasticity of Steel and Other Alloys at High Temperatures", *Zavodskaya Laboratoriya*, vol. 22, 1956, no. 2, pp. 225–229.

7 F. C. Monkman and N. J. Grant, "An Empirical Relationship Between Rupture Life and Minimum Creep Rate in Creep-Rupture Tests," *Proceedings, ASTM*, vol. 56, 1956, pp. 593–620 (including discussion).

8 J. Glen, "A New Approach to the Problem of Creep," *Journal of the Iron and Steel Institute*, August, 1958, pp. 333–343.

9 J. Glen, "Ductility in High Temperature Rupture Tests," *Journal of the Iron and Steel Institute*, September, 1958, pp. 30–39.

10 *Archiv für das Eisenhüttenwesen*, Articles 1 through 10, May/June, 1957.

DISCUSSION

M. J. Manjoine[3]

Extrapolation of rupture data using creep-rate data assumes that fracture is controlled by the same factors and in the same degree as those for flow. The work of Jones, Newman, and Brown[4] indicates that creep-rupture damage results from two independent mechanisms. The first is related to strain, strain-hardening, and other structural changes which occur in the grain and grain boundaries. This is a nonpermanent damage which in many cases can be completely removed by reheat-treatment. The second mechanism is that of crack initiation and growth. When crack growth has proceeded to a critical level, then the damage becomes permanent and cannot be removed by reheat treatment.

This work shows that fracture can be initiated by other mechanisms which are different from that of flow and, therefore, the time-temperature characteristics may be different from that of flow. The extrapolation of stress-rupture curves based on the parameters derived from creep-rate relationships may thus lead to serious error.

[3] Westinghouse Electric Corporation, Research Laboratories, Pittsburgh, Pa. Mem. ASME.

[4] TRANS. ASME, vol. 79, 1957, p. 117.

Author's Closure

Mr. Manjoine's remarks are appreciated. Since it appears that efforts to combine high-temperature flow and fracture data will not aid in data extrapolation because of their independent mechanisms, the last conclusion of the paper should be emphasized. Programs to actually obtain long-time rupture data for various materials are essential.

F. EBERLE
Chief Metallurgical Engineer

J. S. MAKRIS
Associate Metallurgist

The Babcock & Wilcox Company,
Research Center, Alliance, Ohio

Fabrication and Annealing Factors Affecting Grain Size of 18Cr8Ni-Ti Superheater Materials in Steam Boilers

The effect of cold deformations as encountered in tube and superheater fabrication and of temperature and time of annealing on the grain-size characteristics of 18Cr8Ni-Ti is demonstrated by laboratory experiments with material from six heats of steel. It is shown that cold-drawn tubing retains a relatively uniform small grain size at annealing temperatures up to about 1900 F to 1950 F and that above this temperature individual grains begin to grow at an accelerated rate, leading to a mixed grain-size structure. Annealing times between 5 and 15 minutes caused only insignificant differences in the over all grain size, but extension of exposure to 30 minutes produced a noticeably larger grain structure. Small cold deformations as may be introduced into the material by tube straightening can, when followed by a final anneal, cause excessive localized grain enlargements. Observations pointed to the possibility that materials with high Ti/C ratios may retain a predominantly small grain size at annealing temperatures as high as 2050 F.

Introduction

THE GRAIN-SIZE characteristics of 18Cr8Ni-Ti (SA-213, TP321H) superheater material have become a matter of general interest in the power-boiler industry because of the premature swelling in service of some fine-grained tubing. The grain-size characteristics of the material have therefore been associated with its creep-rupture strength and performance expectancy, and a grain-size requirement has been written into the material specification of SA-213 in order to give the user assurance that the tubes have been suitably heat-treated. However, metallurgists familiar with the 18Cr8Ni-Ti steel have pointed out that a grain-size stipulation would not be feasible because of the difficulty of evaluating microstructures of irregular mixed grain sizes and the generally recognized personal errors involved in grain-size determinations of such materials. It is the purpose of this paper to create a better understanding of this important superheater material by showing its recrystallization and grain-growth pattern and by demonstrating some of the important factors which influence the latter and thereby also the high-temperature-strength properties.

Fundamentals of Recrystallization and Grain Growth

The fundamentals of recrystallization and grain growth of metals are well established. Thus, it is known that they are influenced by the composition and purity of the material, by plastic deformation preceding heat-treatment, and by the temperature and time of annealing.

The composition and purity of the material affect the recrystallization and grain-growth process very strongly. In pure metals, minute additions of other elements or traces of contaminants have been found to have a marked influence in this respect. It is also known that submicroscopically dispersed nonmetallic inclusions in steel such as oxides, nitrides, and difficultly soluble carbides may act not only as recrystallization nuclei, but also as grain-growth inhibitors. The element titanium in TP321H steel is apt to form such nucleating and grain-growth-inhibiting agents because it reacts strongly with oxygen, nitrogen, sulfur, and carbon, forming stable oxides, nitrides, sulfides, and carbides. Titanium furthermore has a large atom which diffuses relatively sluggishly. It is therefore to be expected that the TP321H steel tends to contain this element and its reaction products in a nonhomogeneous and sometimes even segregated distribution. In their role as nucleating agents and grain-growth inhibitors, they are therefore apt to cause irregular grain-size patterns. These chemistry effects are experimentally difficult to evaluate and, in the present study, have been investigated only in so far as materials with varying Ti/C ratios were used.

The effects of plastic deformation preceding annealing are of importance because 18Cr8Ni-Ti superheater tubing is cold-worked to final dimensions. The amount of cold-work varies for different tube sizes. In the present study, these effects have been investigated for deformations of 25 and 50 per cent. The effects of very small deformations which may be expected as a result of tube-straightening or operations in superheater fabrication have been studied for tension strains of 1, 3, and 5 per cent. So-called critical strains have been explored with cold-bent tube strips.

The effects of temperature and time of annealing which are of practical importance in commercial heat-treatment have been determined at temperature intervals of 100 deg up to 2200 F for exposure durations ranging from 5 to 30 min.

Experimental Materials

The experimental materials used are listed in Table 1. They include cold-drawn tubing 2-in. diameter × 0.125-in. wall, 2.5-in. diameter × 0.313-in. wall, 4-in. diameter × 0.337-in. wall, and $^1/_2$-in. diameter hot-finished bar stock with a fine-grained (ASTM No. 7), plastically deformed microstructure. The Ti/C ratios represented in these materials were 6.7, 7.0, 7.29, 7.65, 7.74, and 8.2. The chemistry was normal for all materials. One steel was higher in silicon and lower in nickel than the other materials, but all were within the specification range.

Contributed by the Joint ASTM-ASME Committee on Effect of Temperature on the Properties of Metals and presented at a joint session with the Metal Engineering Division at the Annual Meeting, Atlantic City, N. J., November 30-December 4, 1959, of THE AMERICAN SOCIETY OF MECHANICAL ENGINEERS. Manuscript received at ASME Headquarters, October 8, 1959. Paper No. 59—A-311.

Table 1 Experimental materials

Identification	Dimensions	C	Mn	Si	P	S	Cr	Ni	Ti	Ti/C	Mo	Cu
A	2-in.-dia. x 0.125-in.-wall	0.059	1.80	0.58	0.015	0.009	18.06	11.08	0.43	7.29	0.26	0.36
B	"	0.064	1.86	0.73	0.015	0.007	17.80	10.52	0.49	7.65	0.23	0.48
C	"	0.062	1.62	0.52	0.014	0.007	17.76	11.14	0.48	7.74	0.32	0.26
D	2.5-in.-dia. x 0.313-in.-wall	0.067	1.69	0.56	0.014	0.009	17.96	10.50	0.55	8.2		
E	4.0-in.-dia. x 0.337-in.-wall	0.055	1.61	0.44	0.012	0.007	17.84	12.54	0.37	6.7		
F	0.75-in.-dia. bar stock	0.06	1.77	0.50			17.88	12.28	0.42	7.0		0.12

Note: (a) Materials A to E were standard cold-worked tubing.
(b) Tubing A, B, and C were subjected to the experimental anneals without further processing.
(c) Tubing D and E were further processed as follows before experimental anneals:
Annealed 20 min. at 2000 F/W.Q. - cold-flattened - annealed 20 min. at 2000 F/W.Q. - 0.050 in. milled off each surface - cold-rolled 25% and 50%, respectively.
(d) Material F was obtained as hot-finished bar stock with plastically deformed, fine-grain structure (A.S.T.M. No. 7). It was then annealed 20 min. at 1950 F/W.Q., machined into standard 0.505 tensile specimens which were strained 1%, 3%, and 5%, respectively, before recrystallization anneals.

Experimental Program

The experimental program consisted of the following phases:

1 Determination of the time-temperature relationship for the beginning and end of recrystallization of:

a Material F (Ti/C = 7.0) in the 1, 3, and 5 per cent tension-strained condition.

b Material D (Ti/C = 8.2) in the 25 and 50 per cent cold-worked (cold-rolled) condition.

c Materials A (Ti/C = 7.29), B (Ti/C = 7.65), and C (Ti/C = 7.74) in the form of 2.0-in. diameter × 0.125-in. wall cold-worked tubing.

2 Determination of the recrystallization and grain-growth patterns of:

a Solution-annealed and subsequently 25 and 50 per cent cold-worked (cold-rolled) materials E (Ti/C = 6.7) and D (Ti/C = 8.2).

b Cold-worked 2.0-in. diameter × 0.125-in. wall tubing of materials A (Ti/C = 7.29), B (Ti/C = 7.65), and C (Ti/C = 7.74).

c 1, 3, and 5 per cent tension-strained 0.505-in. tensile specimens of material F (Ti/C = 7.0) which had previously been annealed at 1950 F to obtain a predominantly uniform grain-size pattern.

3 Determination of the effect of very small critical strains upon the grain-growth characteristics of materials E (Ti/C = 6.7) and D (Ti/C = 8.2) by microscopic examination of zones adjacent to the neutral axis of tube-strip specimens, cold-bent 50 deg around a 1.5-in. diameter mandrel and subsequently annealed 30 min at 1900 F, 2000 F, and 2100 F, respectively.

4 Determination of the exaggerated grain-growth characteristics of individual grains (duplexing) in material A (Ti/C = 7.29) at annealing temperatures of 1900 F, 2000 F, and 2100 F by planimetrically determining the percentage area occupied by the coarse grains in an otherwise more or less fine-grained matrix.

Experimental Techniques

The most satisfactory method of studying recrystallization and grain-growth phenomena consists of microscopically observing the size, shape, and distribution of the crystals. Determination of changes in material properties which accompany the recrystallization-annealing process are also useful for this purpose. In the present investigation, only the microscopic method and changes in hardness were employed as criteria. In general, the prestrained specimens were heated to temperatures between 1400 and 2200 F, at 100-deg intervals, and exposed at each temperature for periods of 5, 10, 15, 20, 25, and 30 min. In the determination of the beginning and end of recrystallization and in the study of the effect of small strains, shorter as well as longer exposure periods have been employed.

Metallographic grain-size determination, consisting of comparing the observed grain structure with the standard ASTM grain-size charts, presents well-recognized difficulties when the material displays an irregular mixed grain size as the 18Cr8Ni-Ti steel is apt to do. In such cases, different observers frequently disagree on grain-size ratings. The results presented in this paper are based on the interpretations of one experienced observer, and, for the reason given, must be considered as subjective interpretations. However, this fact does not affect the validity of the observations nor the conclusions derived from them; it merely means that other observers may, in some instances, rate a given grain size somewhat smaller or somewhat larger.

Recrystallization Behavior of TP321H Steel

When steel is cold-worked, energy is stored in it, but the stored energy is not uniformly distributed because of chemical and microstructural nonhomogeneities of the material. When the latter is then heated to a temperature at which the displaced atoms acquire sufficient mobility to rearrange themselves toward equilibrium positions, new crystals are nucleated at points of greatest energy concentration such as at grain boundaries, slip

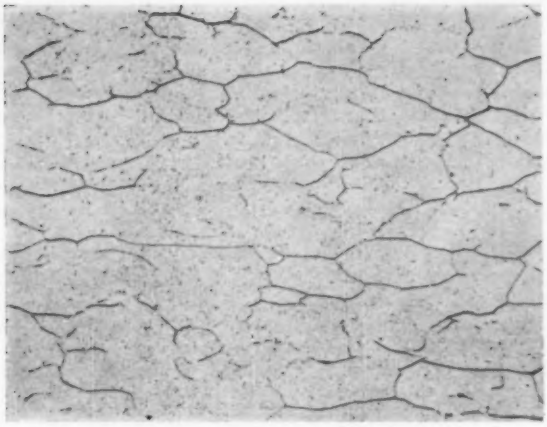

Fig. 1 Elongated cold-deformed crystals; X500

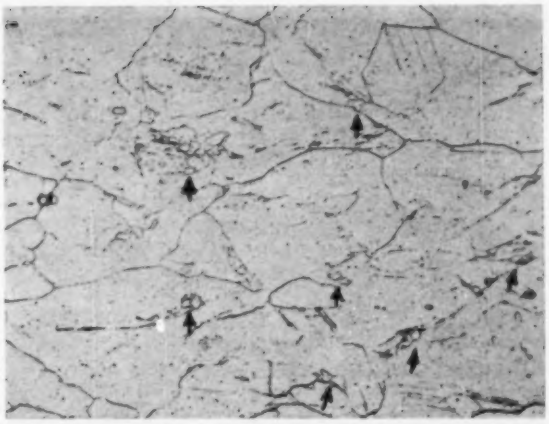

Fig. 2 Formation of new crystals in reheated cold-worked metal; X500

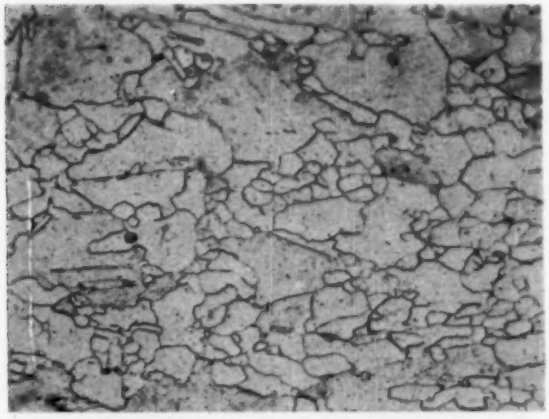

Fig. 3 Recrystallization process half completed; X500

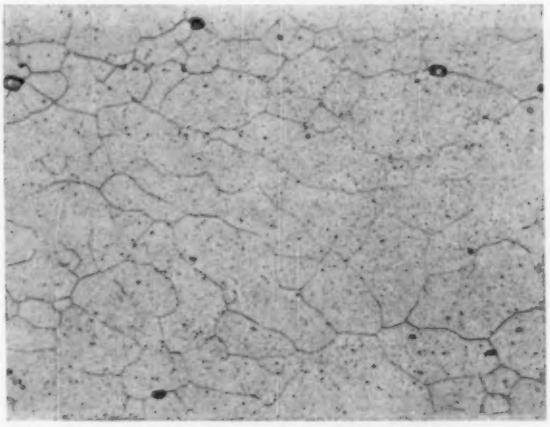

Fig. 4 Recrystallization completed; X500

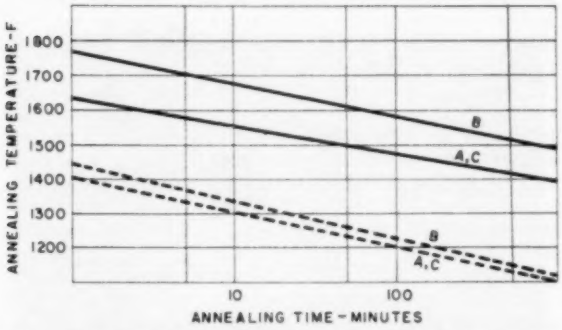

Fig. 5 Time-temperature relationship for the beginning and end of recrystallization of cold-finished superheater tubing from three heats of steel (A, Ti/C = 7.29; B, Ti/C = 7.65; C, Ti/C = 7.74)

– – – – – Beginning of recrystallization
——— End of recrystallization

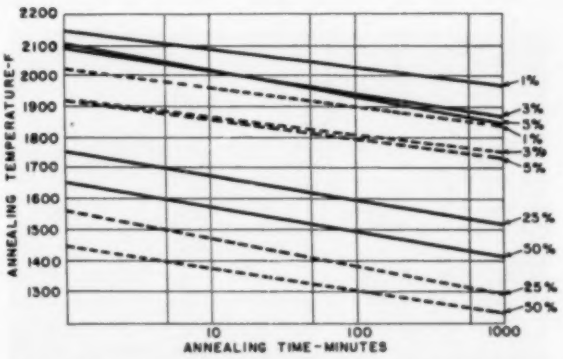

Fig. 6 Time-temperature relationship for the beginning and end of recrystallization of 1 per cent, 3 per cent, 5 per cent tension-strained material F (Ti/C = 7.0) and of 25 per cent and 50 per cent cold-reduced (cold-rolled) material D (Ti/C = 8.2)

– – – – – Beginning of recrystallization
——— End of recrystallization

planes, submicroscopic precipitates, and crystal discontinuities. These tiny new crystals grow rapidly at the expense of the original crystals which thereby become smaller. When recrystallization is completed, the microstructure is of fairly uniform small-grain size. This process is illustrated by the photomicrographs in Figs. 1 to 4. Fig. 1 shows plastically deformed, elongated grains before annealing; Fig. 2 depicts clusters of newly formed, very small crystals in the cold-worked matrix; Fig. 3 shows the process of recrystallization half completed; and Fig. 4 depicts the completely recrystallized structure.

It may be assumed that the recrystallization process itself has a significant influence upon the final grain size obtained with a given heat-treatment. The recrystallization characteristics have therefore been studied for four materials and for various degrees

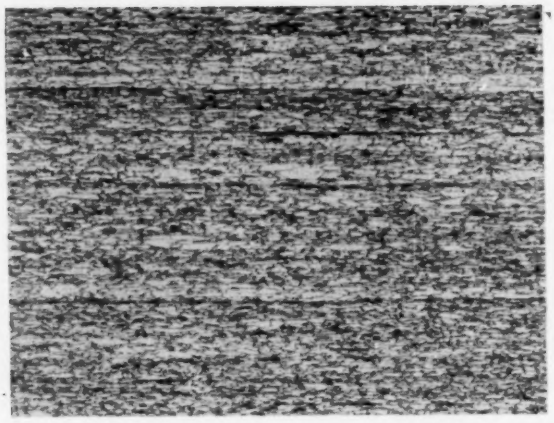

Fig. 7 Cold-finished tubing; material C; ×100

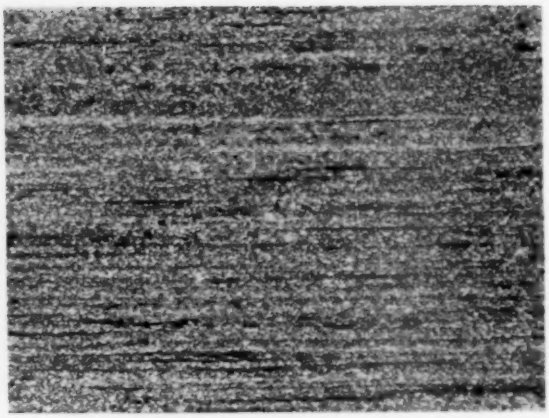

Fig. 8 Material C; reheated 15 min at 1600 F/WQ; ×100

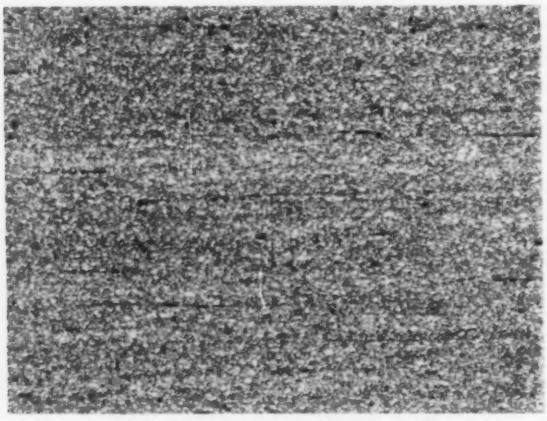

Fig. 9 Material C; reheated 15 min at 1700 F/WQ; ×100

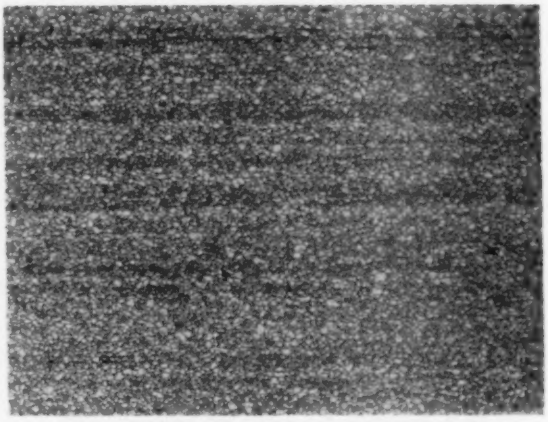

Fig. 10 Material C; reheated 15 min at 1800 F/WQ; ×100

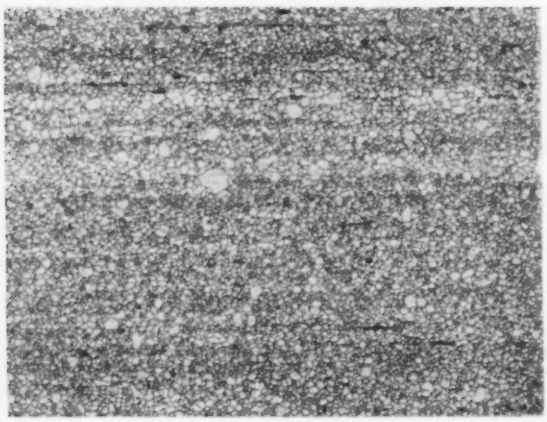

Fig. 11 Material C; reheated 15 min at 1900 F/WQ; ×100

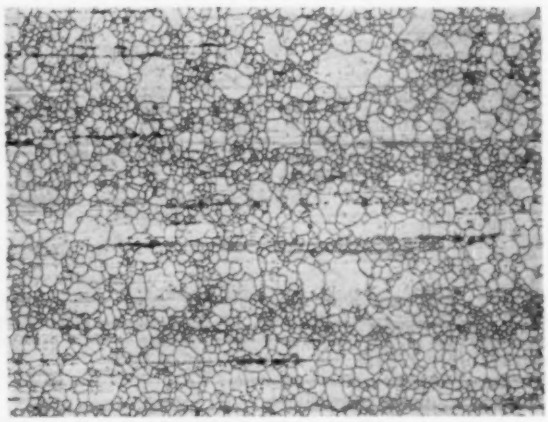

Fig. 12 Material C; reheated 15 min at 2000 F/WQ; ×100

of prestraining. The results are plotted in Figs. 5 and 6 in the form of diagrams indicating the time-temperature relationship for the beginning and end of recrystallization. Fig. 5 shows the recrystallization features of three cold-worked tubes of materials A, B, and C. Heats A and C are seen to behave identically, whereas material B recrystallizes at a higher temperature and also requires more time for the completion of the process. Since the three tubes were of the same initial grain size, of the same dimensions, and have identical mechanical histories, the difference in their recrystallization behavior must be explained by composition differences. Conventional analysis reveals only that tube B has a somewhat higher silicon and a somewhat lower

nickel content than tubes A and C, and that the Ti/C ratios of the three materials do not seem to be significantly different. However, it is possible that submicroscopic composition differences which are not revealed by conventional analysis may also have been influential. The question of what caused material B to recrystallize more slowly and at higher temperatures, must therefore remain unanswered. When the three tubes were annealed at 2050 F, all three materials developed the same range of grain size, but the microstructure of material B contained a greater proportion of small crystals.

The grain size at the completion of the recrystallization process was, in all cases, very small. There were, however, some distinguishable differences, but their effect was not consistent and their significance could not be established within the scope of this investigation.

Fig. 6 illustrates the effect of various degrees of prestraining upon beginning and end of recrystallization and demonstrates that the process shifts to lower temperature as prior strain or deformation is increased.

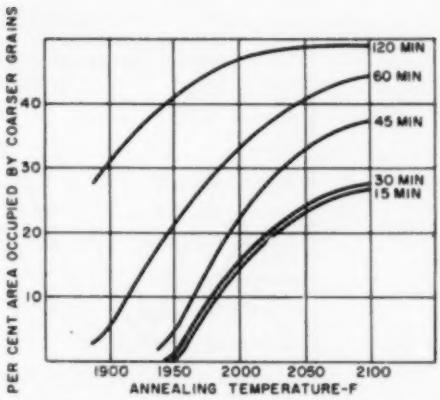

Fig. 13 Exaggerated grain growth by individual crystals (duplexing) as influenced by temperature and time of annealing. Cold finished tubing; material A (Ti/C = 7.29).

Grain-Growth Behavior of TP321H Steel

When the recrystallized material is heated to progressively higher temperatures, the grain size increases at first very slowly and generally uniformly until about 1900 F. In the vicinity of this temperature, individual scattered crystals begins to grow at an accelerated rate; that is, the process of "duplexing" begins, which leads to a mixed grain size. This is illustrated by the photomicrographs in Figs. 7 to 12.

It is important to keep in mind that, at annealing temperatures above 1900 F, TP321H material may develop a mixed nonuniform grain size and that it is the relative proportions of the small and larger crystals which determine the relevant material properties. To what extent this relative proportion of small and larger grains changes at various annealing temperatures and exposure times is indicated in Fig. 13 which shows the percentage area of the larger grains in the microstructure, determined with a metallographic planimeter.

The pattern of recrystallization and grain growth can be shown graphically by plotting grain size versus annealing temperature for fixed exposure periods. Such pattern diagrams have been used in Figs. 14 to 18 to illustrate the grain-growth characteristics and the effects of composition differences, prior deformation, and annealing temperature upon the final grain size of the investigated materials.

The recrystallization and grain-growth pattern as revealed by the change in hardness, Fig. 19, has the disadvantage of not clearly indicating the end of recrystallization and the beginning of duplexing, and is useful only in so far as it supplements the microscopic observations.

Figs. 14 and 15 show the grain size-temperature diagrams of two materials with what is believed to be significant differences in the Ti/C ratios. Material E, with a Ti/C ratio of 6.7, had prior to cold-working (cold-rolling) a larger grain size (ASTM No. 5-6), finished recrystallization at about 1700 to 1800 F, and coarsened rapidly above 1900 F. Material D, with a Ti/C ratio of 8.2, displayed an initially small grain size (ASTM No. 6-7), finished recrystallization at a lower temperature, that is, at about 1550 to 1700 F, and coarsened less rapidly above 1900 F. For a chosen annealing treatment above 1900 F, material E, with the lower Ti/C ratio, will therefore give a generally coarser grain structure as is verified by the photomicrographs in Figs. 20 and 21.

The two materials E and D were investigated in the 25 and 50 per cent cold-worked (cold-rolled) conditions. It has been shown previously that increasing prior cold deformation lowers the recrystallization temperature. This is also demonstrated by the diagrams in Figs. 14 and 15. The effect of increased prior deformation upon the grain-size characteristics is, however, not revealed because the diagrams give only the range of the resulting grain size, but do not indicate the relative proportions of small and large crystals. It becomes therefore necessary to examine the microstructures for this purpose. These are shown in Fig. 20. The materials with the greater amount of prior cold-work are seen to have obtained a generally larger grain size.

The grain-growth behavior of the three cold-worked tubes of materials A (Ti/C = 7.29), B (Ti/C = 7.65), and C (Ti/C = 7.74) is illustrated by the diagrams in Figs. 16, 17, and 18. These diagrams look remarkably similar and indicate no noticeable differences. The range of grain sizes obtained at the various annealing temperatures appears to be the same for all three materials. However, when their microstructures are compared, as has been done in Fig. 22, it can be recognized upon closer examination that material B—which had been found to recrystallize at a higher temperature than materials A and C—has a larger proportion of small crystals than the two other steels. The reason for this is not apparent unless one feels inclined to ascribe the deviating recrystallization and grain-growth behavior of material B to its higher silicon and lower nickel content.

Effect of Annealing Time on Grain-Size Characteristics

The effect of annealing time on the microstructural properties is a matter of practical importance and has been investigated for exposure periods of 5 to 30 min and temperatures up to 2100 F. The results are illustrated by the photomicrographs in Figs. 21 and 22 for five materials. Extending the annealing time from 5 to 15 min is seen to cause only a very slight increase in the general grain size, but prolonging the exposure to 30 min produced a noticeable grain enlargement.

Effect of Annealing Temperature on Grain Size

The ASME Code stipulates for TP321H material an annealing temperature of not less than 2000 F. In this connection, it is of interest to examine what differences in grain size might be obtained with a material of a high Ti/C ratio at the straddling temperatures of 2000 F and 2100 F. The results are shown in Figs. 20(*c*) and (*d*) for material D (Ti/C = 8.2). At 2000 F, this material is seen to have a predominantly very fine-grain structure with an exposure period as long as 30 min. In contrast, material

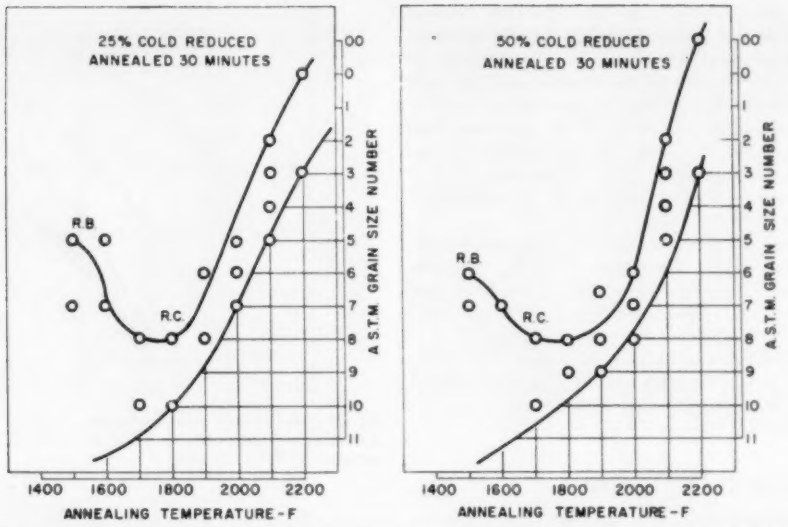

Fig. 14 Recrystallization and grain growth pattern of material E (Ti/C = 6.7) (R.B. = recrystallization begun; R.C. = recrystallization completed)

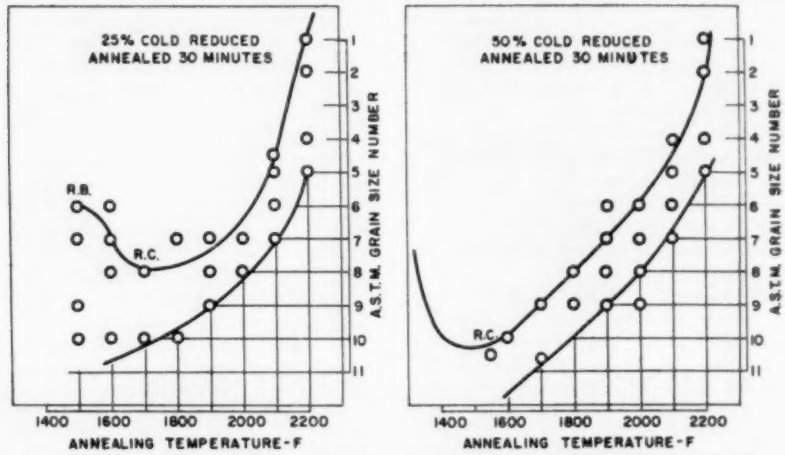

Fig. 15 Recrystallization and grain growth pattern of material D (Ti/C = 8.2) (R.B. = recrystallization begun; R.C. = recrystallization completed)

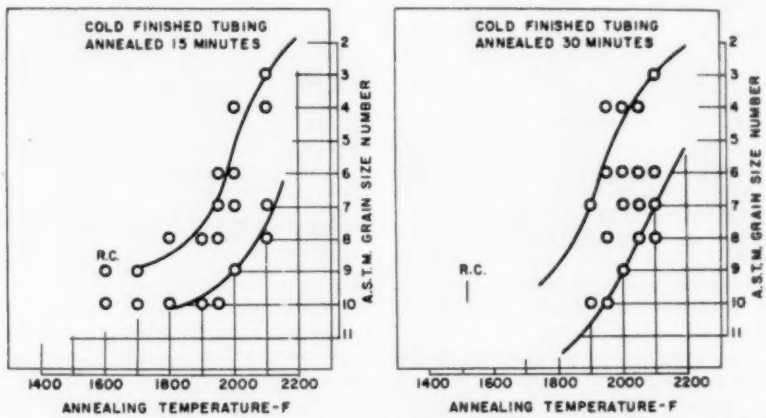

Fig. 16 Grain-growth characteristics of material A (Ti/C = 7.29) (R.C. = recrystallization completed)

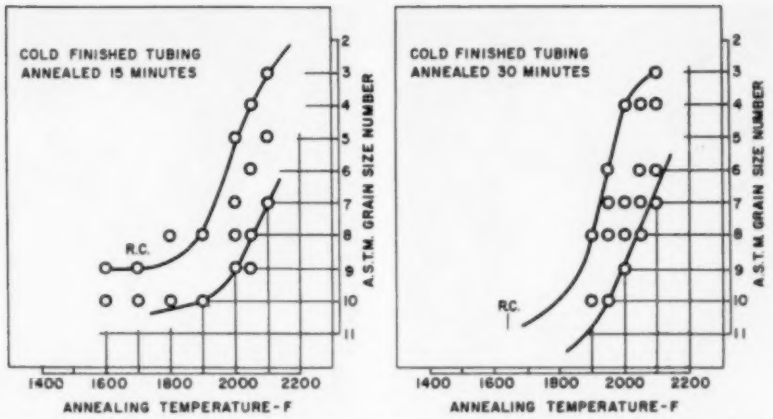

Fig. 17 Grain-growth characteristics of material B (Ti/C = 7.65) (R.C. = recrystallization completed)

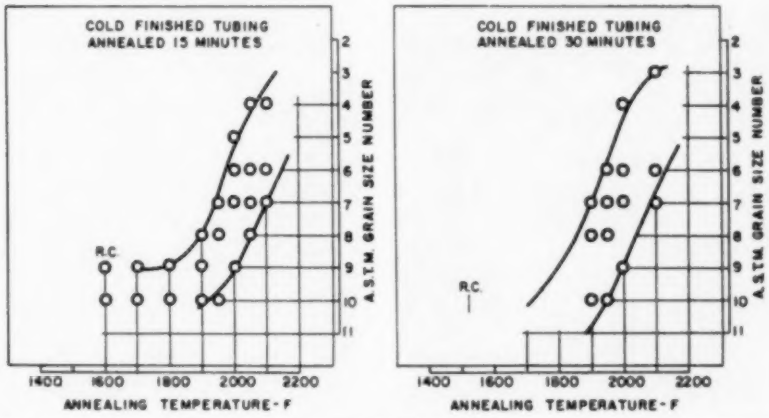

Fig. 18 Grain-growth characteristics of material C (Ti/C = 7.74) (R.C. = recrystallization completed)

E, with a Ti/C ratio of 6.7, displayed at 2000 F an essentially medium-to-fine grain size. These examples suggest the possibility that materials with a high Ti/C ratio may be predominantly fine-grained at annealing temperatures as high as 2050 F.

Effect of Small Prior Strains

It is a matter of established knowledge that very small deformations produce a larger grain size upon subsequent annealing than large deformations. The very coarse, localized grain structure which is sometimes observed in superheater tubing has been suspected to be the result of such small strains. Such grain-coarsening may possibly be caused by tube-straightening or bending and subsequent annealing in superheater fabrication. In order to verify this assumption, tensile-test specimens were prepared from material F (Ti/C = 7.0) and strained 1, 3, and 5 per cent, respectively, before subjecting them to a 30-min recrystallization anneal at 2000 F. Prior to the straining, the material had been annealed at 1950 F. This relatively low temperature had been chosen in order to keep the initial grain size small and

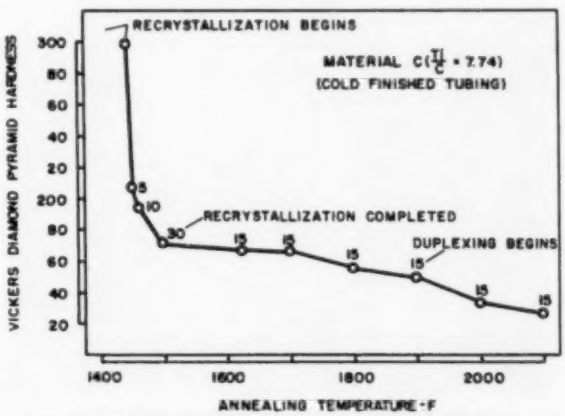

Fig. 19 Recrystallization and grain-growth trend as indicated by hardness changes accompanying annealing. (Figures at curves represent annealing time in minutes.)

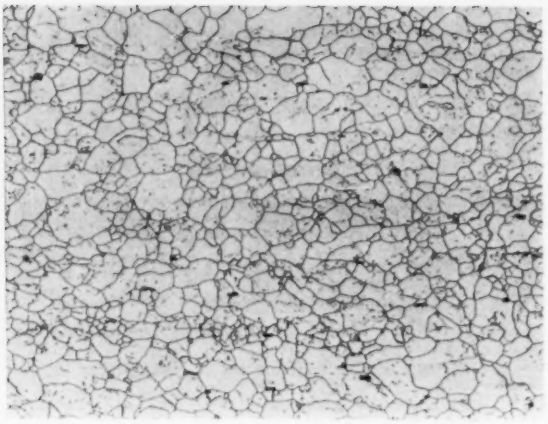

(a) Material E, 25 per cent cold-reduced; 2000 F/WQ

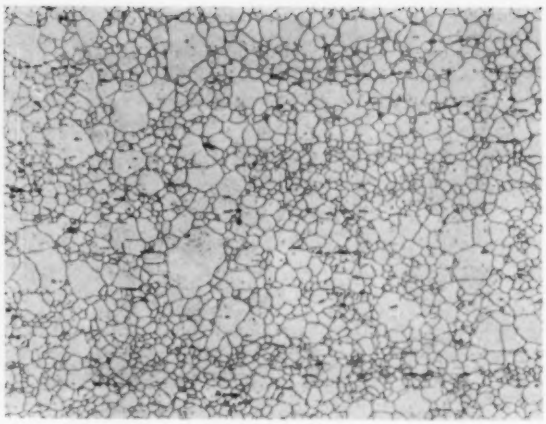

(d) Material D, 50 per cent cold-reduced; 2000 F/WQ

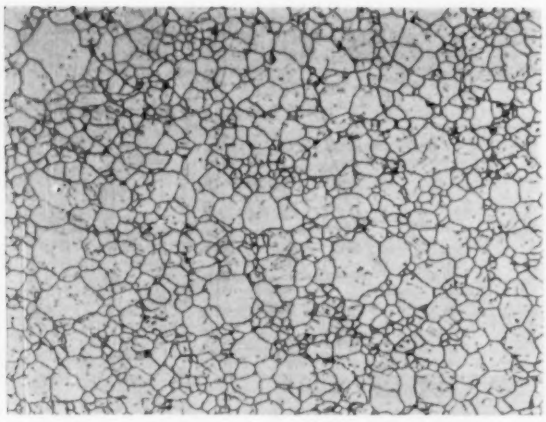

(b) Material E, 50 per cent cold-reduced; 2000 F/WQ

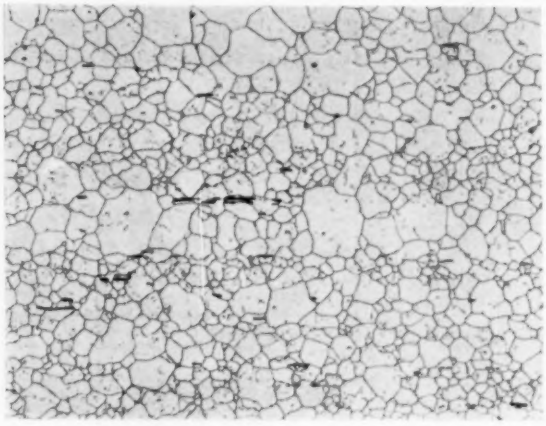

(e) Material D, 25 per cent cold-reduced; 2100 F/WQ

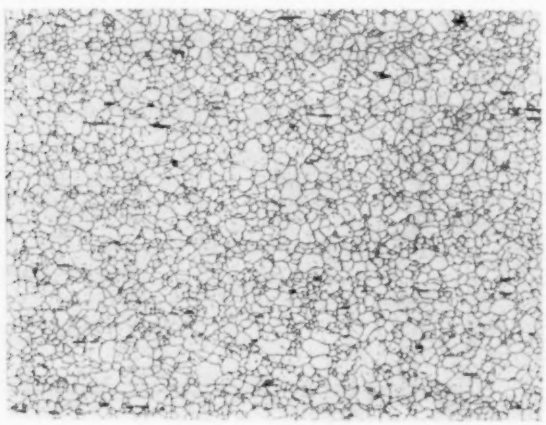

(c) Material D, 25 per cent cold-reduced; 2000 F/WQ

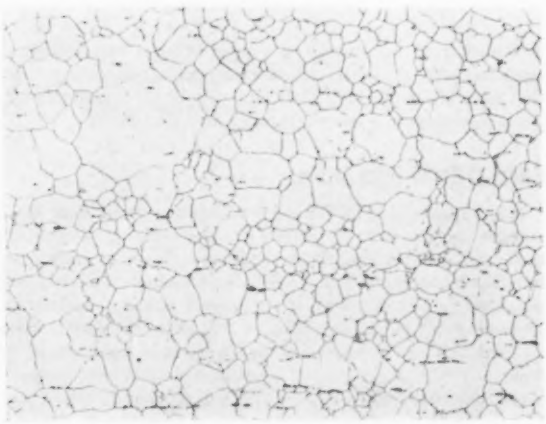

(f) Material D, 50 per cent cold-reduced; 2100 F/WQ

Fig. 20 Effect of prior cold deformation on grain size of materials E (Ti/C = 6.7) and D (Ti/C = 8.2) annealed 30 min at 2000 F and 2100 F, respectively; ×100

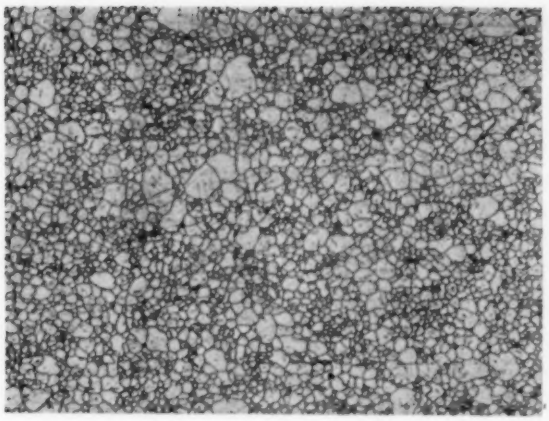

(a) Material D, 5 min at 2000 F/WQ

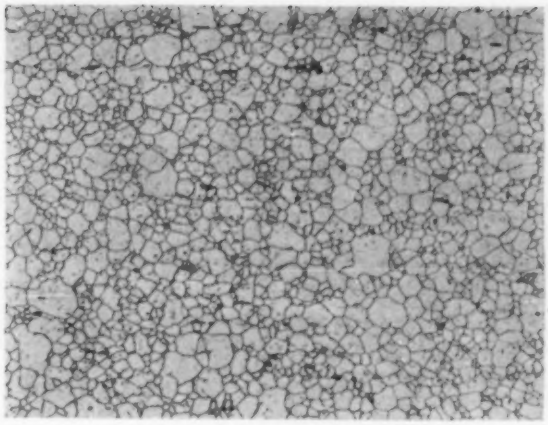

(d) Material E, 5 min at 2000 F/WQ

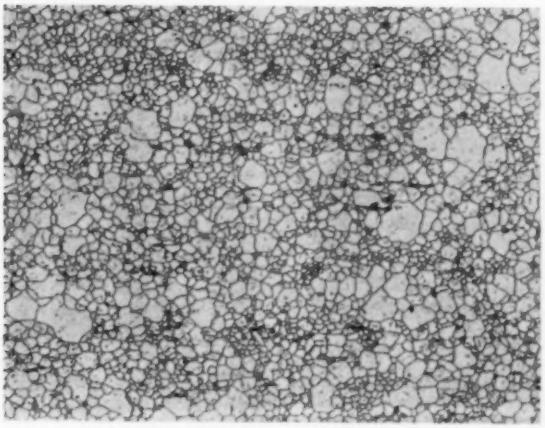

(b) Material D, 15 min at 2000 F/WQ

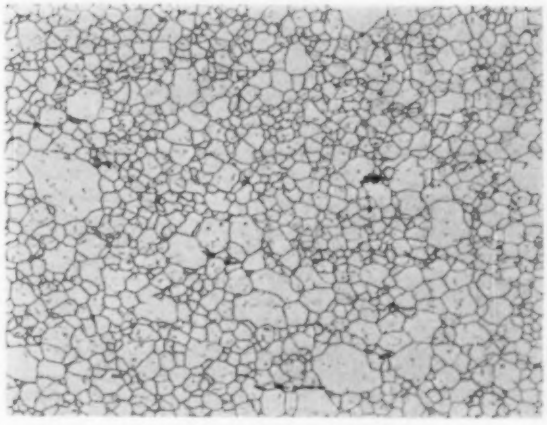

(e) Material E, 15 min at 2000 F/WQ

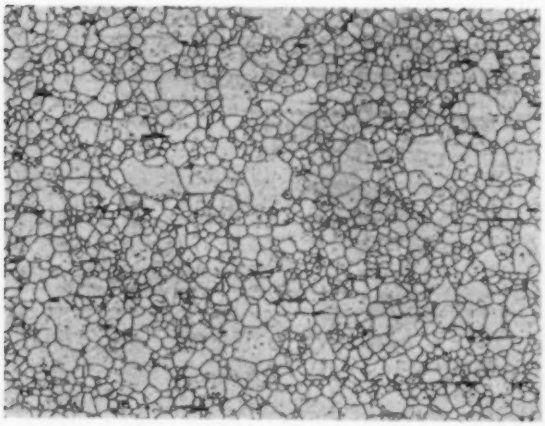

(c) Material D, 30 min at 2000 F/WQ

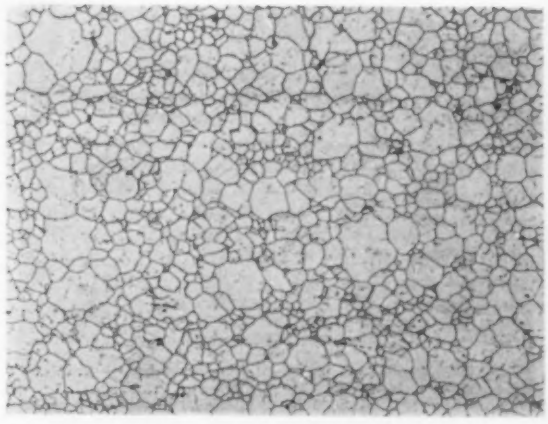

(f) Material E, 30 min at 2000 F/WQ

Fig. 21 Effect of increasing annealing time on 50 per cent cold-reduced materials D (Ti/C = 8.2) and E (Ti/C = 6.7); ×100

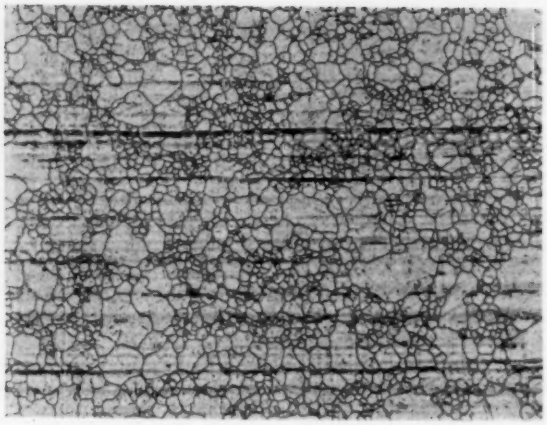

(a) Material A, 15 min at 2050 F/WQ

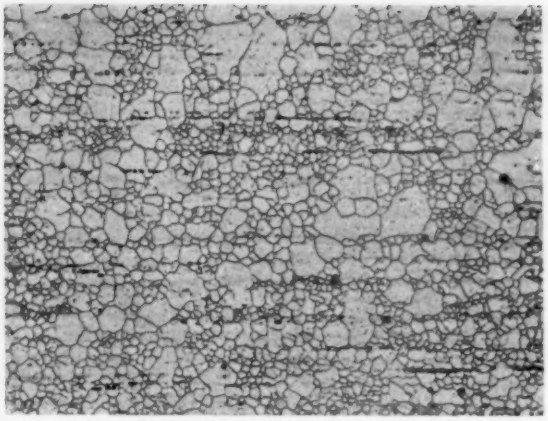

(d) Material B, 30 min at 2050 F/WQ

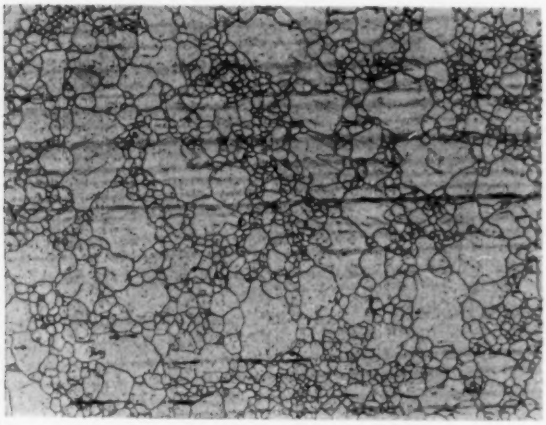

(b) Material A, 30 min at 2050 F/WQ

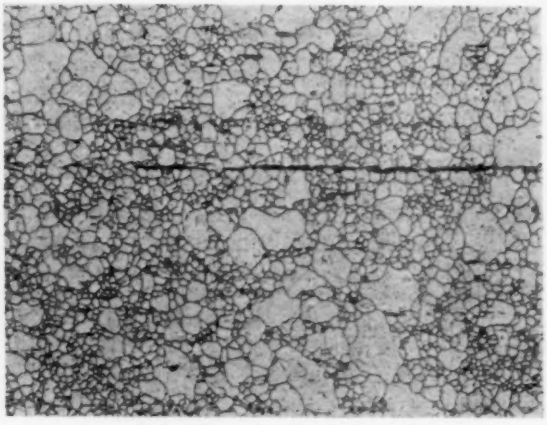

(e) Material C, 15 min at 2050 F/WQ

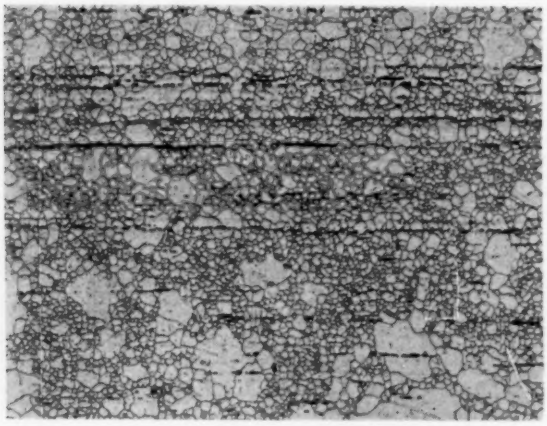

(c) Material B, 15 min at 2050 F/WQ

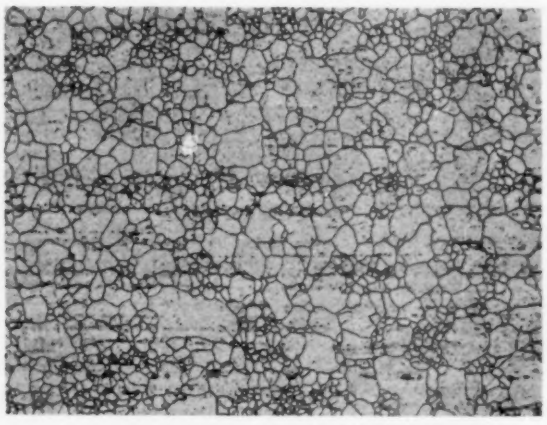

(f) Material C, 30 min at 2050 F/WQ

Fig. 22 Effect of increasing annealing time on cold-finished tubing of materials A (Ti/C = 7.29), B (Ti/C = 7.65), and C (Ti/C = 7.74); ×100

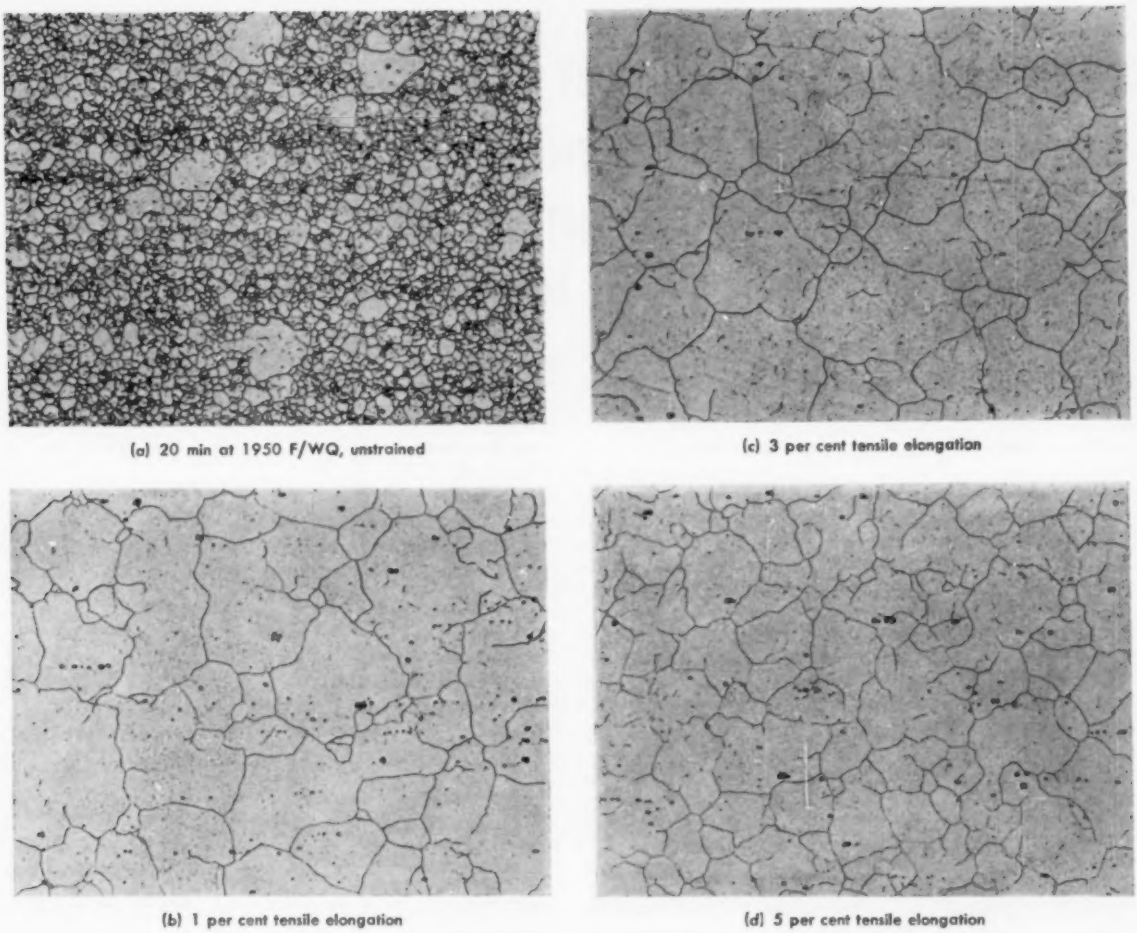

(a) 20 min at 1950 F/WQ, unstrained

(c) 3 per cent tensile elongation

(b) 1 per cent tensile elongation

(d) 5 per cent tensile elongation

Fig. 23 Effect of small strains on grain size of material F (Ti/C = 7.0), annealed 30 min at 2000 F/WQ; ×1000

to avoid undue duplexing. The exaggerated grain growth which occurred in these specimens at the only slightly higher annealing temperature of 2000 F is shown in the photomicrographs, Fig. 23. These pictures also demonstrate that the smaller strains produced the larger grain size.

Sometimes, even larger grains than those shown in Fig. 23 are observed in superheater tubing. These are believed to be the result of so-called "critical strains"; i.e., very small strains which produce abnormal grain growth. Their effect has been verified by bending a strip of annealed tubing around a mandrel, reannealing it at 2000 and 2100 F, and microscopically examining the zones adjacent to the so-called "neutral fiber." The grain size obtained in some of these zones was truly enormous, as is illustrated in Fig. 24.

Summary and Conclusions

The presented investigation and the conclusions drawn from it are summarized as follows:

1 The recrystallization process of cold-worked 18CrNi-Ti steel may occur at low or at high temperatures, depending on the magnitude of prior strain or deformation. Large deformations shift the process to lower temperatures and small strains to high temperatures. Cold-worked tubing has been found to begin to recrystallize at temperatures as low as 1450 F. On the other hand, annealed material containing strains of 5 per cent or less may, upon reannealing, not begin to recrystallize until temperatures as high as 1900 F are reached and then cause excessive grain coarsening.

2 For heavily cold-worked material (25 to 50 per cent reductions), no correlation has been found between the temperature level of recrystallization and the 2000–2100 F annealing grain size. General observations suggested that the most heavily cold-worked material gave a somewhat more uniform grain size than less heavily worked material.

3 No correlation could be determined between the temperature level of recrystallization and chemistry variations within specification limits. Under comparative conditions, one material with higher silicon and lower nickel content has recrystallized at a higher temperature and given a smaller 2000–2100 F annealing grain size, whereas a second material with relatively high silicon and low nickel content recrystallized at a lower temperature but also gave a smaller 2000–2100 F annealing grain size than the corresponding comparison materials. The Ti/C ratios likewise could not be correlated with the temperature level of recrystal-

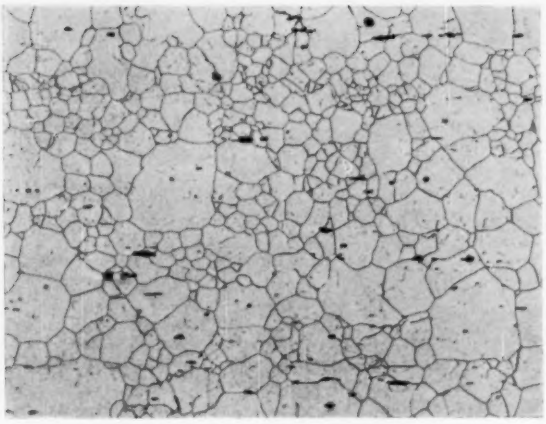

(a) Microstructure prior to bending; ×100

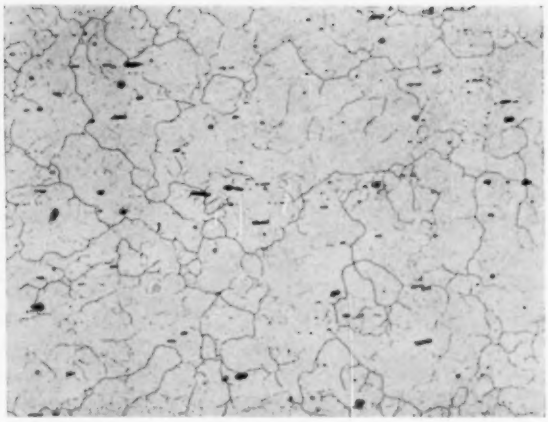

(c) Microstructure after reheating 30 min at 2000 F/WQ; zone adjacent to neutral fiber; ×100

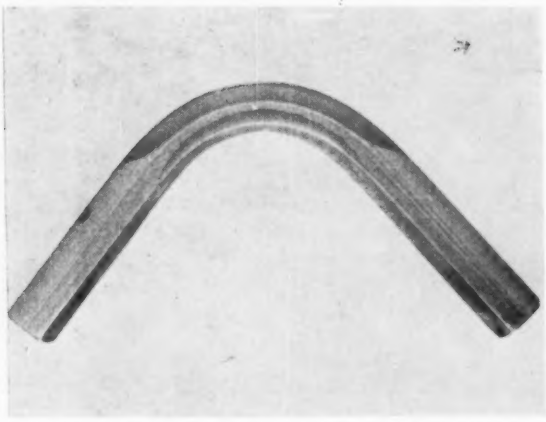

(b) Strip of tubing (material D) annealed 30 min at 2100 F/WQ, cold-bent around 1.5-in. diam mandrel, and reannealed at 2000 F

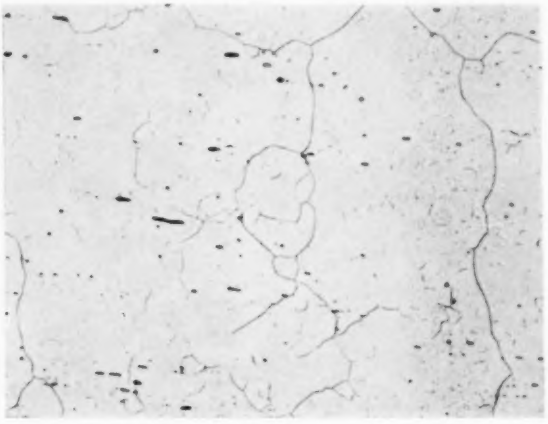

(d) Microstructure after reheating 30 min at 2100 F/WQ; zone adjacent to neutral fiber; ×100

Fig. 24 Effect of critical strains on annealing grain size

lization. However, the material with the lowest Ti/C ratio has consistently displayed a somewhat larger grain size after recrystallization and has also given a larger 2000–2100 F annealing grain size than the materials with relatively high Ti/C ratios.

4 At the completion of recrystallization of heavily cold-worked material, the grain size was uniformly small. Upon further heating to higher temperatures, the grain size increased very slowly and uniformly until a temperature of about 1900–1950 F was reached. At this approximate temperature level, individual randomly scattered grains began to grow at an accelerated rate, leading to a structure consisting of a range or mixture of grain sizes ("duplex structure").

5 The grain-size characteristics of tubing annealed at duplexing temperatures cannot be adequately defined by ASTM grain-size numbers alone, since the latter give no information on the relative proportions of smaller and larger grains.

6 Material with high Ti/C ratios has given a predominantly small grain size at annealing temperatures up to 2000 F. It seems to be reasonable to expect that some heats with high Ti/C ratios may remain fine-grained at temperatures as high as 2050 F.

7 Annealing times between 5 and 15 min have not produced marked differences in grain size, but extending the annealing time to 30 min has caused a noticeable general increase in grain size.

Survey of Various Special Tests Used to Determine Elastic, Plastic, and Rupture Properties of Metals at Elevated Temperatures

F. GAROFALO
Associated with the
Edgar C. Bain Laboratory
for Fundamental Research,
U. S. Steel Corporation Research
Center, Monroeville, Pa.

Testing techniques employed in determining the elastic moduli, that is, Young's modulus, shear modulus, and Poisson's ratio, at room and elevated temperatures are described. These techniques depend on static or dynamic measurements. A comparison and an analysis of test results determined by these two methods are presented. The effect of composition, grain size, and various transformations on the elastic moduli or their temperature dependence is discussed.

A review of techniques and experimental data on the effect of high strain rates on plastic and rupture behavior of metals, and alloys at elevated temperatures is presented. It is shown that recovery effects explain qualitatively the results obtained. A brief description of the various stages of recovery is also presented.

The variation of hardness with temperature is discussed for pure metals and alloys, including a description of a typical hot-hardness tester. The relationship between hardness and tensile strength, creep, and creep-rupture behavior is briefly summarized. The use of the hot-hardness tester as a research tool for following solid-state reactions at elevated temperatures is discussed. These reactions may depend on temperature, time, or plastic strain or a combination of these.

As SERVICE CONDITIONS have become more demanding, high-temperature alloys have had to meet more stringent specifications, and a better understanding of their mechanical behavior is necessary.

This is often evaluated from results determined in routine, control-type tensile, creep, creep-rupture, and in some cases fatigue tests. But a great deal of information on the elastic, plastic, and rupture behavior of metals at elevated temperatures cannot easily be obtained from such tests. A variety of elevated-temperature tests employing special techniques are available at present to study more completely these properties in metals and alloys.

Three special high-temperature-test methods for determining the elastic moduli, tensile behavior at high strain rates, and hot hardness will be described, and experimental data will be presented and analyzed.

Determination of Elastic Moduli at Elevated Temperatures

Under certain conditions of design at room or somewhat higher temperature the permissible strain is of the order of magnitude of the elastic strain and it is necessary to compute design stresses on the basis of the elastic constants of the material. In most engineering work it is assumed that metals and alloys exhibit elastic behavior whereby the strain on loading is directly proportional to the stress and upon unloading the strain is completely recovered. By assuming that all polycrystalline metals and alloys are essentially isotropic, it is necessary then to define only two elastic constants. Two of these are the proportionality constants between stress and strain in tension or compression and in simple shear. The elastic constant in tension or compression E is usually referred to as Young's modulus. The shear modulus G is usually referred to as the modulus of rigidity. A third constant, Poisson's ratio μ, is also required in many cases. However, as shown later it can be computed if both E and G are known. Poisson's ratio can also be measured directly from a simple tension test and is defined as the ratio of the transverse to the longitudinal strain. One important use of all three elastic constants is the computing of thermal stresses developed at elevated temperatures. Certain phenomena occurring in the solid state can also be studied from determinations of the elastic moduli.

Elastic-moduli measurement falls into two broad categories—testing under static-loading conditions and under dynamic-loading conditions. Under static loading, Young's modulus can be determined from a simple tension or a bend test and the shear modulus can be determined from a torsion test. In such tests fairly high stress levels are reached. Under dynamic loading, low or high-frequency cyclic tests of relatively low stress amplitude are generally used. Young's modulus and the shear modulus can be determined from such a test by measuring the natural frequency of a pendulum, the resonance frequency in oscillatory systems, or the velocity of longitudinal and transverse waves produced by high-frequency pulses.

Elastic Moduli Determination Under Static Load. The most convenient method for measuring Young's modulus and the shear modulus at room or elevated temperatures under static loading conditions is one which will yield both moduli from a single test. Various modifications have been employed to determine the elastic moduli in tension and torsion [1, 2].[1] By subjecting a canti-

Contributed by the Metals Engineering Division and presented at the Annual Meeting, Atlantic City, N. J., November 29–December 4, 1959, of THE AMERICAN SOCIETY OF MECHANICAL ENGINEERS.

NOTE: Statements and opinions advanced in papers are to be understood as individual expressions of their authors and not those of the Society. Manuscript received at ASME Headquarters, August 13, 1959. Paper No. 59—A-112.

[1] Numbers in brackets designate References at end of paper.

ever beam to simultaneous bending and twisting moments both Young's modulus and the shear modulus can be determined, Fig. 1. The specimen is held rigidly at one end and loaded by application of small weights at A, which is displaced from the axis of the specimen by a fixed distance along torque arm B. The angular rotations in both bending and twisting upon applying a small weight at A are amplified by an optical-lever system also shown in Fig. 1 and are measured over a 4-in. gage length. Two small mirrors rigidly attached to the sample by means of extension arms translate the small rotations in the beam to measurable displacements on the recording platform after amplification by the optical-lever system. The angular displacements are measured from a reference axis which is determined before each test by loading the sample under only a bending movement; that is, by applying weights at C. The dashpots at A and C check vibrations which occur upon application or removal of each weight. The specimen assembly, Fig. 1, is surrounded by a furnace, Fig. 2. When making determinations above room temperature it is important to obtain constant temperature within the gage length. Between 200 and 1500 F the temperature variation along the gage length was ±4 F from the mean temperature. The actual temperature at the ends or center of the gage length can be controlled to within ±1 F for several hours. Three determinations, each requiring about 15 min, are usually made at each temperature. The maximum tensile fiber stress imposed on the specimen did not exceed 5000 psi and the maximum stress was decreased as the temperature was increased. In calculating the elastic moduli, results on unloading were employed to minimize the effect of creep, and only the linear range in the load-displacement graph was employed. Young's modulus E is then calculated from the relation

$$E = \left[\frac{(l + 2l_1)d}{I}\right]\frac{\Delta P}{\Delta B} \tag{1}$$

where

l = gage length
l_1 = forelength (see Fig. 1)
d = distance from mirrors to recording platform
I = moment of inertia
ΔP = load increment
ΔB = average bending displacement within the gage length

The shear modulus G is computed from

$$G = \left[\frac{2tld}{J}\right]\frac{\Delta P}{\Delta T} \tag{2}$$

where

t = length of torque arm
J = polar moment of inertia
ΔT = average torsional displacement within the gage length

Poisson's ratio μ is computed from the relation

$$\mu = \frac{E}{2G} - 1 \tag{3}$$

Values of E and G have been determined in this way for a large number of commercial steels between room temperature and 1500 F, Fig. 3. The steels tested have been divided into three groups. The first two include ferritic steels and the third group includes austenitic stainless steels. The high-chromium steels of the second group have been separated because they exhibit significantly different elastic moduli; this is true in particular for the shear modulus. It has been suggested by Zener [3] that E and G for metals should vary linearly with temperature up to nearly the melting point. However, in polycrystalline metals various types of discontinuities or deviation from linearity are found beyond certain critical temperatures. The factors which cause these deviations will be discussed in detail later. It will be sufficient to merely point out at this time that for the results shown in Fig. 3 both E and G initially vary linearly with temperature but a deviation from linearity is found at higher temperatures. Although

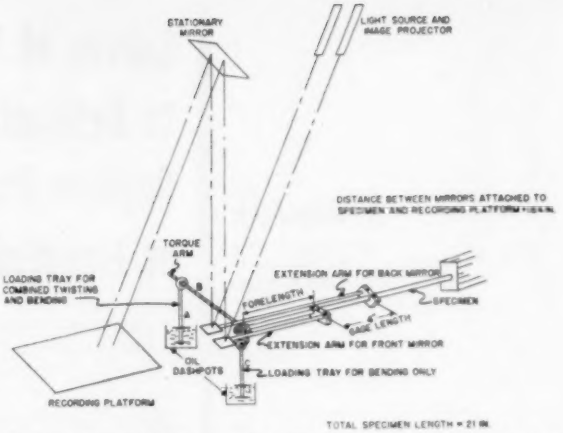

Fig. 1 Schematic diagram of test apparatus for determining E and G statically at elevated temperatures (Garofalo, et al. [2])

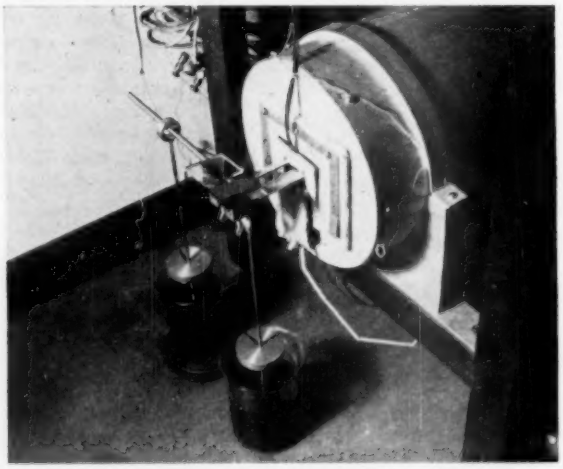

Fig. 2 Photograph of apparatus for determining E and G statically at elevated temperatures (Garofalo, et al. [2])

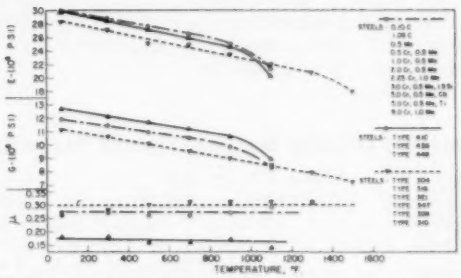

Fig. 3 Variation of E, G, and Poisson's ratio with temperature for various ferritic and austenitic stainless steels—determined statically (Garofalo, et al. [2])

some scatter is found in Poisson's ratio, there is essentially no change with temperature.

Elastic-Moduli Determination Under Dynamic Load. Test methods for measuring the elastic moduli of metals and alloys under dynamic-loading conditions have become very popular [4–8] and can be made with high accuracy. Oscillating stresses in some cases can be applied very rapidly at low stress amplitudes, minimizing creep effects at elevated temperatures.

With the simplest type of apparatus for measuring the elastic moduli under dynamic loading, Fig. 4, either E or G can be measured by determining the natural vibration of a pendulum which consists of a long wire of the test metal rigidly clamped at one end with a known mass attached to the other end. Assuming frictional losses to be small, E and G can be calculated from the natural frequency of the pendulum as shown in the relations in Fig. 4. In Fig. 4(*a*) the oscillations are vertical and therefore this type of apparatus permits determinations of E. A torsion pendulum, Fig. 4(*b*), commonly employed to study internal friction, is useful for determining the shear modulus G of low-damping metals. Low frequencies, up to about 20 cps, are employed.

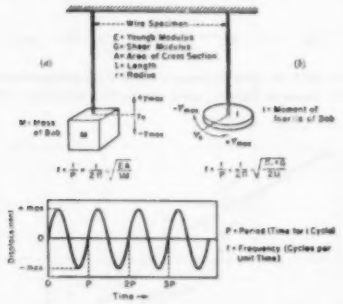

Fig. 4 Schematic diagram of pendulums for determining E and G dynamically (Fine [4])

A second method of determining E and G under dynamic-loading conditions at room or elevated temperatures employs an externally supplied, sinusoidally varying force for stressing the specimen. Apparatus is readily available for producing forced vibrations over a wide range of frequencies. In systems of forced vibrations in the range of kilocycles per second it is most convenient to increase the driving frequency until the resonant frequency is reached This means that frequency of the external force equals the natural frequency of the system and the vibration amplitude reaches a maximum. By measuring the resonant frequency, E and G can be measured as in the case of the pendulum [4]. Thus

$$E = \frac{4l^2}{\eta^2}\rho f_L^2 \tag{4}$$

and

$$G = \frac{4l^2}{\eta^2}\rho f_T^2 \tag{5}$$

where l is the length of the specimen, ρ is the density, η is an integer,[3] and f is the frequency at resonance. Both relations apply to materials in which internal friction is low. For relation (4) the cross section of the specimen must be uniform and the cross-sectional dimensions small in comparison with the wave length ($\lambda = 2l/\eta$). In relation (5) it is assumed that the cross section is circular.

Three techniques have been employed for exciting longitudinal and torsional vibrations—the electromagnetic, electrostatic, and the piezoelectric-crystal methods, shown schematically for longitudinal vibrations in Fig. 5. For the electromagnetic method the specimen must be ferromagnetic, or disks which are ferromagnetic must be cemented to the ends of the sample. Alternate tension and compression are applied to the sample. The receiver is similar to the driver and detection is accomplished by measuring the voltage generated by the specimen moving in the magnetic field of the receiver. The input frequency is increased until resonance is reached.

In the electrostatic and piezoelectric-crystal (usually a quartz crystal) methods the specimen which need not be ferromagnetic is also subjected to alternate tension and compression, in one by an alternate electrostatic force between a condenser plate and the specimen and in the other by the deformation in the crystal [4]. In the electrostatic method the detector is similar to the driver. In the piezoelectric-crystal method the resonant frequency of the system is detected from the crystal itself. In both methods the input frequency is increased until resonance is reached.

A third method of determining the elastic constants under dynamic-loading conditions involves the propagation and measurement of the velocity of acoustic waves of ultrasonic frequencies in the megacycles per second range [4, 5, 6]. The elastic constants are calculated from the velocity of the propagating waves through the sample. Very small specimens, including crystals, can be employed and it is possible to determine both E and G simultaneously.

Acoustic-pulse waves of short duration are delivered from a pulse generator to a piezoelectric crystal, such as quarts or barium-titanate, attached to one end of the specimen and a similar crystal may be attached to the other end of the specimen to detect the propagating elastic wave, Fig. 6. Several types of pulse generators may be employed [5]. The generator is triggered by the oscilloscope and the pulse traverses the sample. Because of the reflection of the elastic waves by the receiver surface and

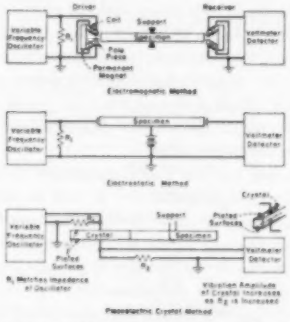

Fig. 5 Schematic representation of apparatus for determining E dynamically from resonance measurements under forced vibrations (Fine [4])

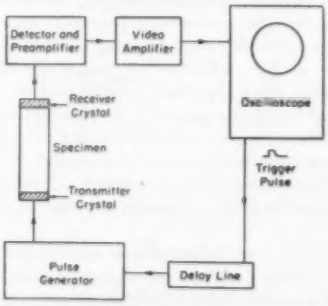

Fig. 6 Schematic diagram of ultrasonic pulse apparatus for determining E and G dynamically (Reynolds [5])

[3] If E or G are known approximately, η can be readily computed.

surfaces parallel to the specimen axis, one pulse will result in a number of waves reverberating back and forth through the sample. However, since attenuation occurs rapidly the number of reverberations is finite. The signals detected at the receiver crystal are amplified and observed on the oscilloscope. A schematic representation of oscilloscope traces [5] is shown in Fig. 7; t_0 represents the initial pulse; t_1, t_5, and t_8 are longitudinal pulses, t_1 being the initial transmitted pulse, t_5 transmitted and reflected back once, and t_8 transmitted and reflected back twice; t_2, t_3, t_4, t_6, t_7, and t_9 are shear waves reflected by two longitudinal surfaces. Because of the reflection of the elastic waves by the receiver end surface and by longitudinal surfaces it is possible to determine E, G, and Poisson's ratio on one specimen using one or more crystals for transmitting and receiving [5, 6].

Determinations of this nature have been made on a variety of ferritic and austenitic steels [7]. In these experiments E, G, and μ can be computed from the following relations

$$E = 2V_s^2\rho\left[\frac{1 - 1/2\left(\frac{V_L}{V_T}\right)^2}{1 - \left(\frac{V_L}{V_T}\right)^2}\right] \tag{6}$$

$$G = V_T^2\rho \tag{7}$$

and

$$\mu = \frac{1 - 1/2\left(\frac{V_L}{V_T}\right)^2}{1 - \left(\frac{V_L}{V_T}\right)^2} \tag{8}$$

where ρ is the density of the material, V_L the velocity of the longitudinal wave, and V_T the velocity of the transverse wave.

The experimental results, Fig. 8, have been separated into three groups as with statically determined moduli on steels. The first two include ferritic steels and the third includes austenitic stainless steels. Again it is found that initially E and G decrease linearly with temperature, but a temperature is reached for the ferritic steels beyond which the moduli decrease more rapidly. For the austenitic steels a linear relation is found between the elastic constants and temperature. Poisson's ratio seems to increase slightly with temperature.

Before comparing the statically determined elastic constants with those determined dynamically, it will be necessary to discuss certain factors which cause deviations from linearity as the temperature is increased. This is of importance because good agreement is found between the two types of determinations for temperatures where linear variation occurs. Beyond the temperature of deviation the statically determined values of the elastic constants are always lower than those determined dynamically.

Deviations of Elastic Moduli From Linearity. As mentioned previously the ideal variation of the elastic moduli with temperature should be linear up to almost the melting point [3]. However, in polycrystalline metals and alloys a number of solid-state reactions occur which affect the elastic moduli and therefore change the variation of the elastic moduli with temperature. A number of factors have been found to affect the elastic moduli: (*a*) Transformations from one crystal structure to another [4, 8], (*b*) order-disorder transformations [4, 8], (*c*) magnetic transformation [4, 8, 9], and (*d*) relaxation of shear stresses at grain boundaries [3, 10, 11].

The effect of two types of transformations on the temperature dependence of Young's modulus determined under dynamic-loading conditions is shown in Fig. 9. The discontinuity in linearity found for cobalt results from a change in crystal structure which does not seem to occur at a critical temperature, but is known to

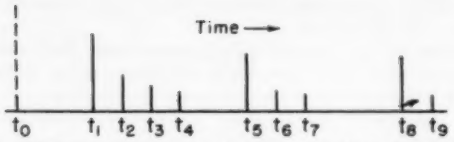

Fig. 7 Schematic presentation of ultrasonic pulses (Reynolds [5])

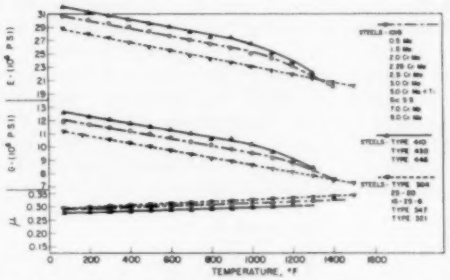

Fig. 8 Variation of *E*, *G*, and Poisson's ratio with temperature determined dynamically for various ferritic and austenitic stainless steels (Timken résumé [7])

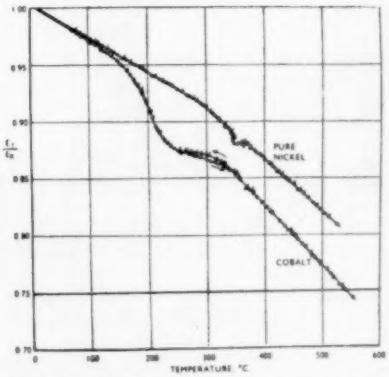

Fig. 9 Variation in ratio of *E* at temperature to *E* at room temperature for Ni and Co (Bennett and Davies [8])

be rather sluggish. The discontinuity for nickel occurs at the Curie temperature. It is found, however, that the deviation from linearity for nickel begins at least 100 C below the Curie temperature. As will be indicated later such an effect may also occur in ferritic steels. The effect of viscous flow or shear-stress relaxation at grain boundaries on the shear modulus of aluminum is shown in Fig. 10. These results were obtained from a low-frequency dynamic test, which consisted of a torsion pendulum. Between room temperature and 200 C the shear modulus decreases linearly with temperature for a single crystal and a polycrystalline specimen. Beyond 200 C the shear modulus for the single crystals follows the same linear behavior. However, the polycrystalline specimen shows a rapid drop in G. A similar behavior has been observed for brass [12]. The behavior in the polycrystalline specimen has been attributed to viscous flow at the grain boundaries. The rate of shear, $d\gamma/dt$, at the grain boundaries has been shown to be of the form [11]

$$\frac{d\gamma}{dt} = k\lambda \exp\left(\frac{-Q}{RT}\right) \tag{9}$$

where k is in essence the coefficient of viscosity, λ the shear stress, Q is a constant which is found to be equal to the activation energy for self diffusion and R and T have the usual meaning. It may be seen from relation (9) that at constant temperature the total

shear depends on time of stress application. Thus at temperatures above 200 C for aluminum, increasing the frequency of testing should result in an increase in the shear modulus from the relation $G = \lambda/\gamma$. Such an effect has been confirmed experimentally [3, 14]. Thus the relaxed modulus, that is, E or G, determined under conditions where measurable amounts of grain-boundary shear occurs depends on frequency of loading. The unrelaxed moduli, that is, moduli determined in the absence of grain-boundary creep, should be independent of frequency of loading or such other variables as grain size. It has been shown experimentally by Kê [11–13] and others [14] that the following functional relation exists

$$\frac{G_R}{G_u} = F(AD^m\nu e^{Q/RT}) \tag{10}$$

where G_R is the relaxed shear modulus, G_u is the unrelaxed shear modulus, D is the grain diameter, A and m are constants, ν is the frequency, and Q, R, and T have the usual meaning. The functional relationship in relation (10) shows that as the frequency is increased the temperature beyond which the shear modulus is relaxed increases at constant grain size. A similar effect is found by increasing the grain diameter.

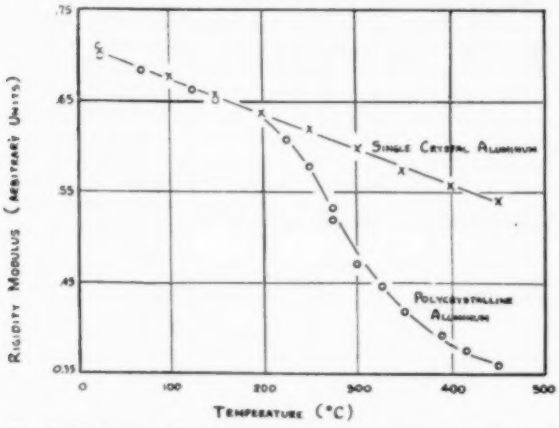

Fig. 10 Variation of G with temperature for a single crystal and polycrystalline aluminum (Kê [12])

In comparing the variation of Young's modulus with temperature for a variety of commercial steels under static and dynamic loading it is found from Fig. 11 that good agreement exists for the unrelaxed modulus. A constant difference seems to exist, however, for the high-chromium steels, types 410 and 430. For the ferritic steels the temperature at which the decrease of Young's modulus with temperature deviates from a linear relation is the same for both the static and dynamic results. Beyond the point where the deviation occurs for the ferritic steels the static results drop more rapidly than the dynamic results. The more rapid drop for the ferritic steels may be associated with grain-boundary shearing, because of the much higher stresses used in the static tests. However, the fact that the deviation from linearity begins at the same temperature may be related to the decrease in ferromagnetism as the Curie point is approached. In this respect it should be mentioned that the austenitic stainless materials which are paramagnetic exhibit linearity even up to 1800 F under dynamic loading. The deviation found for the static results is undoubtedly related to grain-boundary shearing. According to relation (10) deviation from linearity for the dynamic results should occur at a much higher temperature.

A similar observation is found in comparing values of the shear modulus on similar steels obtained statically and dynamically. Good agreement is found for the unrelaxed modulus, but for the relaxed modulus the static values are lower. Such a comparison is shown in Fig. 12. As shown in Fig. 13, good agreement, except again for the high-chromium steels, is found for Poisson's ratio.

Other investigations on polycrystalline metals other than steels also indicate that good agreement is found between the unrelaxed moduli determined statically and dynamically, but the statically determined relaxed moduli are lower than those determined dynamically. This is shown for titanium, aluminum, and

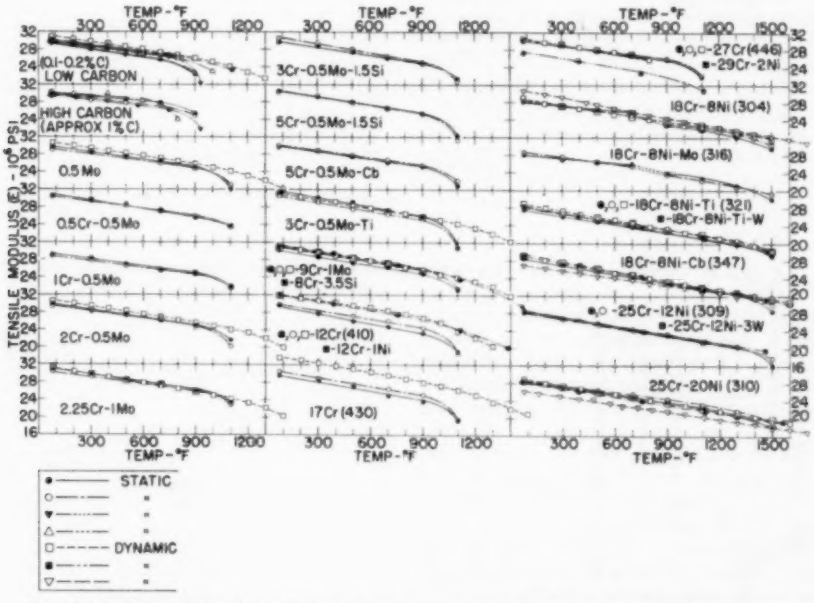

Fig. 11 Variation of E with temperature for various steels determined statically and dynamically (Garofalo, et al. [2])

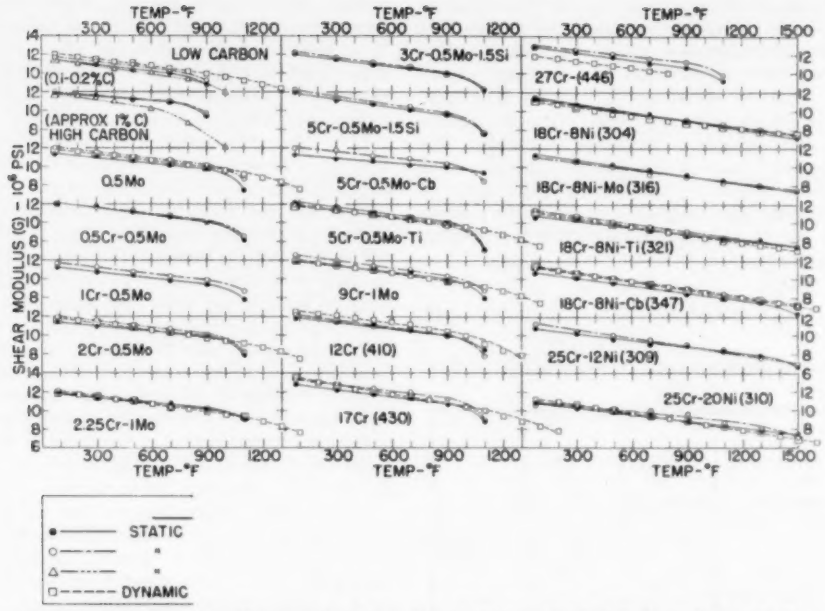

Fig. 12 Variation of G with temperature for various steels determined statically and dynamically (Garofalo, et al. [2])

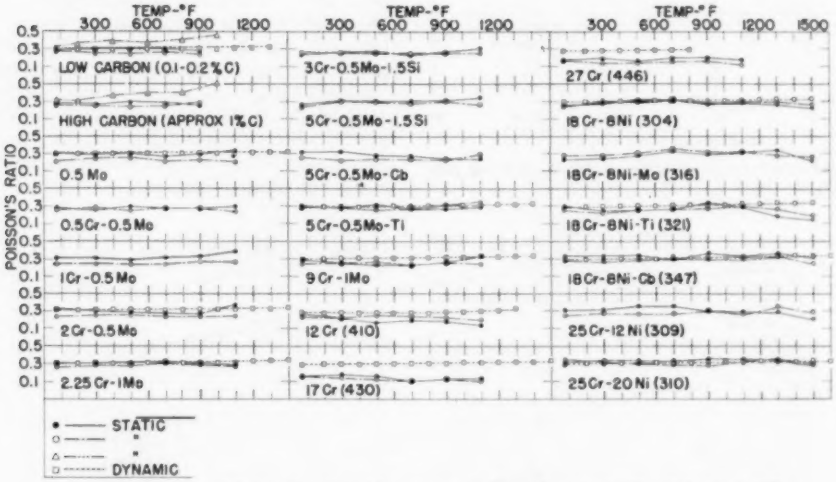

Fig. 13 Variation of Poisson's ratio with temperature for various steels (Garofalo, et al. [2])

magnesium [39] in Fig. 14. It is quite clear, thus, that in designing it is justifiable to use interchangeably values obtained statically or dynamically for the unrelaxed moduli. However, for the relaxed modulus which depends on the type of loading, the moduli employed should be determined in relation to the specific application.

An additional point of interest deals with the effect of composition on the elastic moduli. It is usually assumed that the elastic constants are structure insensitive. However, there is evidence which shows that composition has a measurable effect on the elastic constants [2, 15, 37]. As shown in Fig. 15, it is found that at room temperature, G and μ change systematically as the chromium content in ferritic steels is increased. As shown in Fig. 16, Young's modulus increases as carbon is added to titanium [15]. The increase seems to remain constant at all test

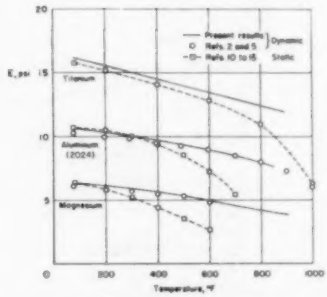

Fig. 14 Variation of E with temperature for Al, Ti, and Mg determined statically and dynamically (Vosteen [39])

temperatures. The elastic-modulus density ratio is also improved at all temperatures within the range covered.

The effect of composition can be predicted from the behavior of dislocation loops within the so-called elastic range. In determining the elastic constants, the strain produced may be made up of two parts. One part is truly elastic, resulting from a separation of the atoms. The second part is from the bulging of the dislocation loops which are properly oriented. Both parts of the strain are recoverable on unloading. The effect of length of dislocation loops on the elastic constants can be appreciable. The fractional change or, more correctly, decrease in Young's modulus depends on the square of the apparent loop length, $\Delta E/E = \alpha NL^3$, where α is a coefficient, N the length of dislocation line per unit volume, and L the loop length. If alloying decreases the loop length by pinning along the dislocation line, then it is seen that an increase in Young's modulus should result. Qualitatively this agrees with results in Fig. 16. A similar effect should be observed for the shear modulus and this agrees with results in Fig. 15. The reason for no apparent change in E in Fig. 15 is not known.

Tensile Behavior of Metals at Elevated Temperatures at High Strain Rates. In many applications at elevated temperatures the loads encountered are sufficiently high to develop stresses which are greater than the elastic limit of usable alloys. In these cases it is not possible to design on the basis of elastic behavior. It becomes necessary, then, to understand in greater detail the plastic behavior of alloys at elevated temperatures and to avoid catastrophic failure it is necessary to understand the rupture behavior of these alloys.

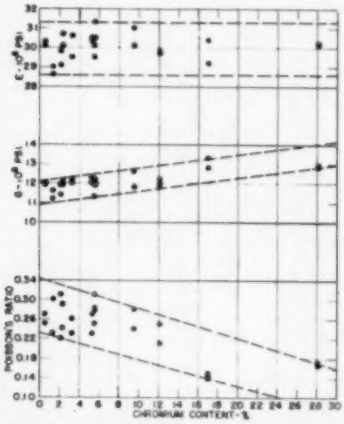

Fig. 15 Effect of chromium content on elastic moduli of various steels at room temperature (Garofalo, et al. [2])

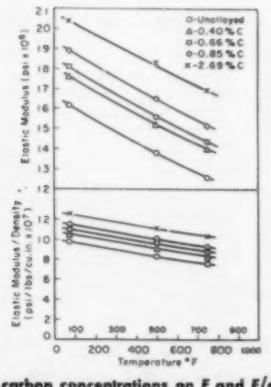

Fig. 16 Effect of carbon concentrations on E and E/density ratio for titanium at elevated temperatures (Graft, et al. [15])

A great deal of information on plastic and rupture behavior is continually being compiled on commercially available alloys and on newly developed alloys. Such information is obtained primarily from tensile, creep, and creep-rupture tests and in some cases from fatigue tests. The information obtained from these tests is in many cases directly applied in design; however, for certain special applications these tests must be modified to simulate service conditions.

One special application receiving a great deal of attention is the use of metals in missile components where service life may be very short, yet very high temperatures and stresses may be attained in structural members and power-plant components, increasing the need to know the effect of high rates of heating and high strain rates on mechanical behavior.

It is generally known that various solid-state reactions occur in metals and alloys which affect the mechanical properties profoundly. These reactions may depend on temperature, time, or strain, or a combination of these. Obviously, not only the effect of strain rate but the effect of rate of heating need to be studied. However, only the effect of strain rate on mechanical behavior will be dealt with in this discussion.

A number of methods for testing specimens in simple tension at elevated temperature at high strain rates have been developed [16–22]. The test method must permit a wide range of strain rates and it must be possible to measure load and strain values accurately, and at any time during the test the true strain rate. It should be possible of course to accomplish all of these measurements within a wide range of temperatures.

A recent test method developed at Battelle Memorial Institute [20, 23] under United States Steel Corporation sponsorship permits the accurate determination of stress-strain curves in tension over a wide range of strain rates. Although employed only up to 300 F, it can be used at much higher temperatures with slight modifications. The loading device consisted of a 10-ton-capacity hydraulic press with adjustable ram travel variable from 0.25 to 190 in. per min. Within a 4-in-gage section the rate of travel permitted strain rates between 0.001 and 0.8 in/in. sec^{-1}. The downward travel of ram was converted into a motion in the opposite direction by placing the subpress, Fig. 17, between the ram and the stationary base of the press. In the subpress the top plate A is rigidly attached to columns B which protrude through the lower plate. The upper grip F is attached to the dynamometer E which in turn is attached to the upper plate A. Plate C is attached to the columns D. These in turn protrude through upper plate A. Columns B rest on the lower plate of the press. The upper end of columns D rest against the ram and as the ram starts to move downward the specimen is subjected to a tensile load.

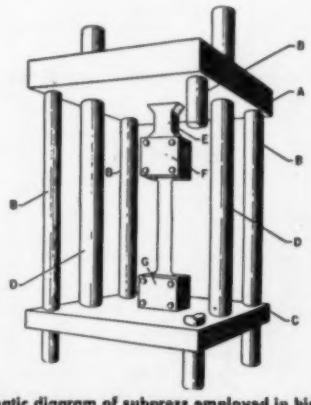

Fig. 17 Schematic diagram of subpress employed in high-speed tension testing (MacDonald, et al. [20])

The load is measured by the dynamometer E which utilizes SR-4 wire strain gages. The elastic strains in the dynamometer are recorded by a two-channel strain analyzer and oscillograph. A calibration curve is used to translate strain into load. Strain measurements are made by a clip gage which also utilizes SR-4 strain gages to translate longitudinal motion into elastic strains in the clip-gage beams. The extensometer is shown schematically in Fig. 18. The strains from the clip gage are also recorded on the oscillograph, Fig. 19. From such a record in conjunction with calibration results the load, extension, and strain rate can be readily determined. Nominal or time stress-strain diagrams can be obtained from load and extension values. Since the extension seems to vary linearly with time the nominal strain rate remains constant during the test. The true strain rate of course must decrease. However, at high strain rates it becomes extremely difficult to maintain a constant true strain rate even with very elaborate equipment by increasing the rate of head motion.

A set of experimental results obtained at Battelle, Fig. 20, shows the variation of the flow stress of a fully killed, temper-rolled steel sheet at maximum load with temperature and strain rate. For this essentially nonaging steel a decrease in the flow stress, even though slight, would be expected as with all materials which do not exhibit temperature and/or strain or time-induced reactions. A similar observation applies to the increase in flow stress with increasing strain rate. The behavior is unusual since the increase of the flow stress with strain rate is much greater at the lower temperatures. This effect is undoubtedly related to the appearance in this material of a discontinuous yield point, which is sensitive to strain rate, and which raises the level of the entire flow curve at the lower temperatures.

The effects of strain rate on tensile strength of various pure metals [16] show, as already stated, that the strength increases with strain rate. However, the effect is somewhat more pronounced at elevated temperatures. Two examples of the effect of strain rate on tensile strength of pure copper and aluminum are given in Figs. 21 and 22. The flow stress of mild steel, Fig. 23, shows a similar behavior at 600 C, a temperature at which no discontinuous yielding is observed. The effect of strain rate on the change in tensile strength as the temperature is increased for various ferrous and nonferrous materials [22] is shown in Fig. 24.

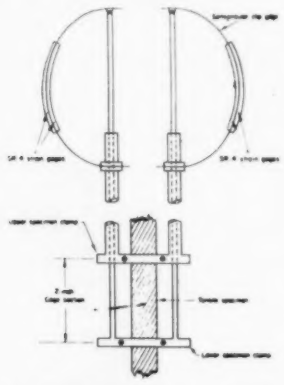

Fig. 18 Design of clip-gage extensometer for high-speed tension testing (MacDonald, et al. [20])

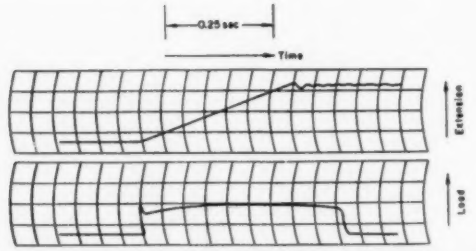

Fig. 19 Load and extension diagrams obtained during a high-speed test (MacDonald, et al. [20])

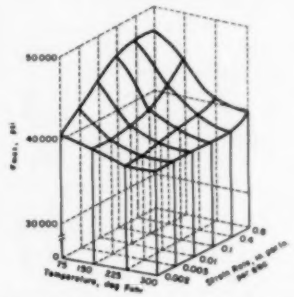

Fig. 20 Effect of strain rate and temperature on true tensile strength of a deep drawing steel sheet (MacDonald, et al. [20])

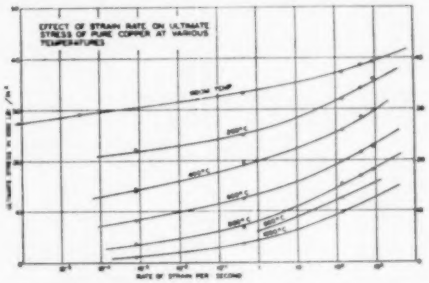

Fig. 21 Effect of strain rate and temperature on tensile strength of pure copper (Nadai, et al. [16])

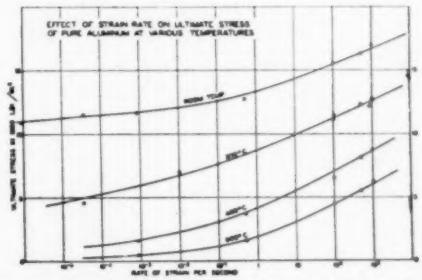

Fig. 22 Effect of strain rate and temperature on tensile strength of pure aluminum (Nadai, et al. [16])

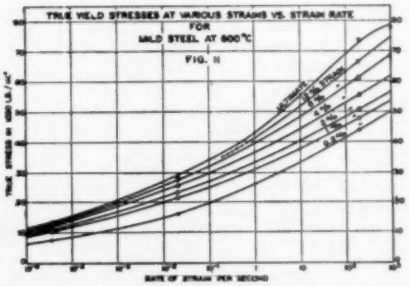

Fig. 23 Effect of strain rate at 600 C on true stress at various strains in mild steel (Manjoine [18])

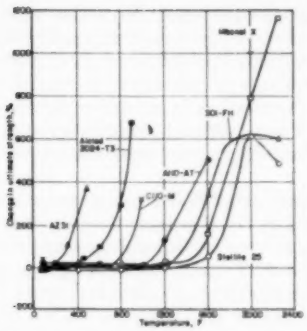

Fig. 24 Effect of temperature at two different strain rates, 0.00005 and 1.0 in/in/sec, on change in tensile strength for various ferrous and nonferrous alloys (Kattus [22])

It is shown here that, by changing the strain rate from 5×10^{-2} to 1.0 in./in. sec^{-1}, the tensile strength may be essentially unchanged over a certain temperature range until a temperature is reached where the tensile strength begins to increase very rapidly. The temperature at which an increase of 50 per cent is found for each alloy is noted:

Alloy	Temperature, deg F
A231 magnesium alloy	250
AlClad 2024-T3 aluminum alloy	450
C110-M titanium alloy	800
A110-AT titanium alloy	1100
Full-hard 301 stainless steel	1300
Inconel X	1450
Stellite 25	1600

The temperatures seem to be very close to the point for each of these alloys where recovery becomes extremely rapid. This may indicate that the rate-controlling process at the higher temperatures is one of recovery. In the absence of such reactions as order-disorder, strain-aging, precipitation of stable phases, phase transformations, or recrystallization, recovery does explain at least qualitatively the effect of strain rate on strength within the plastic range at sufficiently high temperatures. The degree of recovery for a constant amount of strain-hardening depends on time and temperature. Thus as the temperature or time or both are increased the greater becomes the amount of recovery. Increasing the strain rate diminishes the amount of time available for recovery and therefore should lead to high strengths. At the higher temperatures where recovery is more rapid, the effect of strain rate in increasing the strength should be more pronounced. This is in essential agreement with all the results which have been presented thus far.

Although very little is known of rate-governing processes during plastic deformation, there are indications that at high enough temperatures the rate-controlling process is one of dislocation climb [24]. Work of Dorn and co-workers [24], on the dependence of flow stress on temperature and strain rate shows that the activation energy for the rate-governing process is 35,000 calories per mole for aluminum. This is equivalent to the activation energy for self diffusion and therefore indicates that the process is one of dislocation climb which is one of the processes of recovery. These results are shown in Fig. 25, which is a plot of the logarithm of the strain rate $\dot{\epsilon}$ against the reciprocal of the absolute temperature $1/T$ for various flow stresses. At the higher temperatures the activation energy remains constant at 35,000 cal per mole. At intermediate stress levels or temperatures the activation energy decreases but is essentially constant again at very low temperatures or high stress levels. The rate-controlling process at the intermediate or high stress levels, that is, intermediate and low temperatures, is not known. Wiedersich in a discussion of Dorn's paper indicates that for the intermediate stress region the rate-controlling process is the cutting by edge dislocations in one glide plane of dislocations in an orthogonal glide plane and the motion may be controlled to a substantial degree by thermal activation as suggested by Seeger [38]. This means that dislocations do not glide through the lattice at high velocity but are momentarily arrested by other dislocations threading the glide plane. Such a behavior is observed in thin films in the electron microscope at reasonably low temperatures where the dislocations advance along the glide plane in finite steps. The results in Fig. 25 substantiate the Zener-Hollomon parametric relationship between the parameter Z temperature, and strain rate

$$Z = \dot{\epsilon} \exp\left(\frac{\Delta H}{RT}\right) \tag{11}$$

where $\dot{\epsilon}$ is the plastic-strain rate, ΔH the activation energy of the rate-controlling process, and R and T have the usual meaning. For constant values of Z within certain ranges in temperature and strain rate it is possible to predict strength values from limited data. However, Fig. 24 indicates that ΔH is not independent of stress, therefore extrapolation over wide ranges in stress is not permissible. Various limitations to the range of applicability of various other parametric procedures are also found [19, 25].

It is clear from the results discussed thus far that in general increasing the strain rate leads to higher strengths. However, under certain conditions as in the presence of stress raisers such as notches, certain materials may be embrittled. No results of this nature seem to be available in the literature. As a matter of fact, very little is known of the effect of strain rate on ductility and fracture behavior at elevated temperatures. One such study on the effect of strain rate, at various temperatures for a carbon-molybdenum steel, on ductility and mode of rupture is shown in Fig. 26. These results were obtained from tensile tests on unnotched specimens. The irregular variation of the elongation with strain rate may be related to the necking behavior in the tensile specimens. However, the reduction in area shows that the ductility is not adversely affected for the material tested by increasing the strain rate and in general an improvement is found. Of particular interest is the change in mode of fracture as the strain rate is increased. At low strain rates the rupture is intergranular; at intermediate strain rates it is both intergranular and transgranular and at high strain rates it is transgranular. The rate-controlling process in this case is undoubtedly shear-stress relaxation at the grain boundaries mentioned previously. At the low strain rates relaxation along grain boundaries oriented preferentially at or near 45 deg to the applied load will undergo

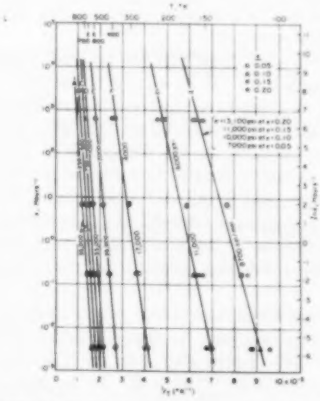

Fig. 25 Variation of strain rate with temperature at various flow stresses for pure aluminum (Trozera, et al. [24])

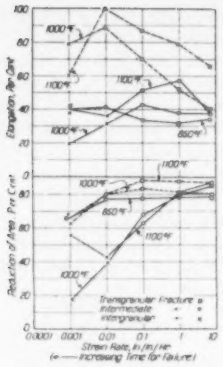

Fig. 26 Influence of strain rate on ductility and rupture behavior of a carbon-molybdenum steel at 850, 1000, and 1100 F (Miller, et al. [17])

extensive creep. A stress concentration thus develops at points where several grains meet and unless the strain energy can be relieved by boundary migration, which may be very difficult except in pure metals, a crack starts normal to the applied load [26]. Joining of numerous such cracks completes total rupture. At intermediate strain rates insufficient time is available for extensive creep at grain boundaries, thus diminishing the degree of intergranular rupture. At high strain rate the amount of creep should be insignificant as may be interpreted from relation (9), and no appreciable stress concentration is developed at points where several grains meet. Therefore the rupture is totally transgranular. The latter type of rupture may result from microcracks formed at the tip of pile-up groups of dislocations. At high strain rates dislocation climb is minimized by the short time of stress application, thus preventing any relief of the high normal stresses developed at the tip of the pile-up groups of dislocations.

Hardness Measurements at Elevated Temperatures

Although tensile, creep, and creep-rupture tests are necessary to evaluate the strength and ductility characteristics of high-temperature alloys, the hardness test has been employed to obtain an estimate of the tensile, creep, and creep-rupture strength up to 2000 F or higher. The advantages of the hardness test are several. Very little time is required for specimen preparation and the hardness can be determined at many different temperatures on one specimen within a period of a few hours. A linear relationship with little scatter is found between tensile strength and hardness. However, the relationship between hardness and creep or creep-rupture is at best approximate. Nevertheless, the hot-hardness test can be used as a screening tool in the development of high-temperature alloys.

In addition, it is also found that the hot-hardness test is well suited as a research tool. The measure of hardness at elevated temperatures is very sensitive to structural changes which may be time, temperature, or strain induced, or affected by a combination of all three. Because of the versatility of this test, these structural changes can be studied under various combinations of temperature, strain, and time; and some indication obtained of the controlling mechanisms. Briefly, the phenomena which have been studied by means of the hot-hardness test include strain-aging, precipitation hardening, recovery, and recrystallization and phase changes.

The test methods which have been used in measuring hardness at elevated temperatures may be classified into two types, static and dynamic [27–30]. In the static test the time of load application is at least of the order of seconds. In the dynamic test the load is applied by impact. Hardness is found to depend on rate of load application at elevated temperatures in a manner similar to that of tensile flow strength. For proper evaluation of hot hardness test results, it is necessary to report the time of load application. Little or no standardization has been achieved in methods for dynamic hot-hardness testing; however, some standardization has been achieved among hot hardness tests of the static-loading type. Because of better control and the greater degree of standardization, static hardness methods have proved more useful.

A hot-hardness tester [30] employing static loading is shown schematically in Fig. 27. The lower assembly shows the coarse-adjustment jack and the fine-adjustment screw which support a rotating stage and anvil stem. The specimen is positioned at the upper end of the anvil stem. As the lower assembly is raised the anvil stem enters the furnace chamber and a seal is formed at the bottom end of the furnace tube when it enters the seal cup which is attached to the bottom of the anvil stem. The seal is formed with a low-melting alloy which is kept molten by a small electric heater placed around the seal cup.

The load is applied directly onto the indenter stem which enters the furnace tube through a flexible bellows attached to the stem and furnace tube. The indenter, which is of the Vickers type, is positioned at the bottom end of the stem. The anvil stem is positioned so that its axis is offset from the axis of the indenter stem. By rotating the anvil stem after each indentation, a series of hardness impressions can be obtained in a circular path on the specimen surface. The distance between impression is controlled by the angle of rotation measured on the graduated stage. By the system of seals used the load can be applied and relieved and the specimen rotated without disturbing the atmosphere employed within the furnace tube. A purified atmosphere of 98 per cent He + 2 per cent H is employed. The 2 per cent H in the atmosphere and a titanium getter surrounding the specimen are used to minimize oxidation.

A cylindrical specimen up to $^3/_4$ inch in diameter or a square specimen up to $^1/_2$ inch on edge can be employed. The bottom and top surfaces of each specimen must be parallel. The surface on which the impressions are made is given a metallographic polish not only as an aid for more precise measurements of the diagonals of the indentations but also to eliminate the disturbed surface layer resulting from machining. Measurement of diagonals is performed after the specimen is cooled to room temperature. A

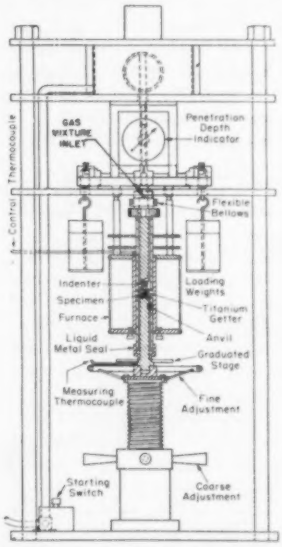

Fig. 27 Schematic diagram of a hot-hardness tester employing static loads (Garofalo, et al. [36])

thermocouple is spot welded onto the polished surface to measure surface temperature during testing.

A dead-weight load of 3 to 10 kg may be applied and relieved automatically or manually. When loading is done automatically the load is applied within 25 seconds and held on the indenter for an additional 1.25 minutes before being relieved. Manually the load can be applied within one second and relieved within a similar period of time.

Relation Between Hardness and Strength at Elevated Temperatures. The relationship between hot hardness and tensile strength at temperatures between 75 and 1500 F for ferritic and austenitic steels is shown in Fig. 28. The ratio of hardness to tensile strength is a constant and is independent of temperature as well as composition between the limits examined. The relationship between hardness H, in Kg/mm², and tensile strength T.S., in psi, may be written as

$$H = 1.9 \times 10^{-3}\,\text{T.S.} \tag{12}$$

However, if the units for the hardness are changed to psi the proportionality constant becomes 2.7, which is in good agreement with that predicted from theory of plasticity [31].

The relationship between hot hardness and creep strength for a number of steels at various temperatures is shown in Fig. 29. As might be expected the creep strength increases as the hardness increases. It should also be pointed out that a large amount of scatter is found, making the relationship between hardness and creep strength, at best, approximate. The relationship between hardness and creep-rupture strength, as shown in Fig. 30, is similar to that found for the creep strength.

In order to take into account the differences in strain rates during hardness, tensile, creep, and creep-rupture testing, attempts have been made to use time-temperature-compensated parameters, mentioned previously, to correlate results of these tests. The results in Fig. 31 show a so-called master curve [25] obtained from hardness, tensile, and creep results for an iron-chromium-beryllium alloy [32]. These results show again that the tensile strength or creep strength can be predicted from the hardness test at various temperatures. One objection to this type of plot is that the time-temperature-compensated parameter may have a limited range of usefulness. Until such range is established extrapolation over wide limits in time and temperature are not warranted.

A similar analysis, Fig. 32, shows the effect of grain size on the master curve [33]. The constants needed to define the master curves for the two different grain sizes differ appreciably. Grain size, as one might suspect, may have a measurable effect on hardness, and a fair dependence of hardness on time of load application is indicated. This effect is shown more directly [31] for

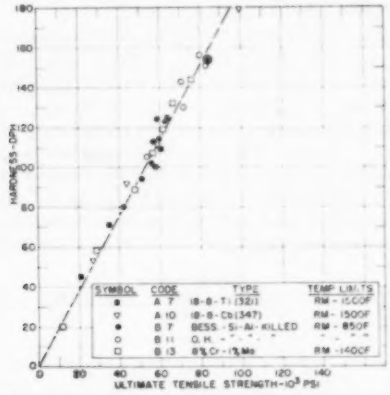
HARDNESS - DPH
ULTIMATE TENSILE STRENGTH-10³ PSI
SYMBOL CODE TYPE TEMP LIMITS
A 7 18-8-Ti (321) RM - 1500F
A 10 18-8-Cb (347) RM - 1500F
B 7 BESS - Si - Al - KILLED RM - 850F
B 11 O.H. RM - 1400F
B 13 8% Cr - 1% Mo

Fig. 28 Relationship between hardness and tensile strength for various steels at room and elevated temperatures (Garofalo, et al. [30])

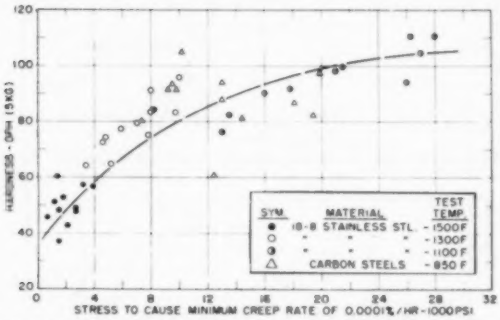
HARDNESS - DPH (5KG)
STRESS TO CAUSE MINIMUM CREEP RATE OF 0.0001%/HR-1000PSI
SYM MATERIAL TEST TEMP
18-8 STAINLESS STL - 1500F
" " - 1300F
" " - 1100F
CARBON STEELS - 850F

Fig. 29 Relationship between hardness and creep strength for various steels (Garofalo, et al. [30])

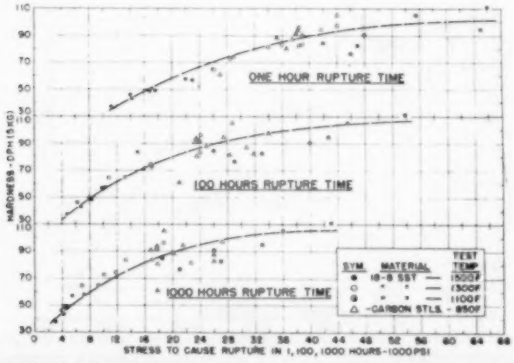
ONE HOUR RUPTURE TIME
100 HOURS RUPTURE TIME
1000 HOURS RUPTURE TIME
HARDNESS - DPH (5KG)
STRESS TO CAUSE RUPTURE IN 1, 100, 1000 HOURS-1000PSI
SYM MATERIAL TEST TEMP
18-8 SST - 1500F
" " - 1300F
" " - 1100F
CARBON STLS - 850F

Fig. 30 Relationship between hardness and creep-rupture strength for various steels (Garofalo, et al. [30])

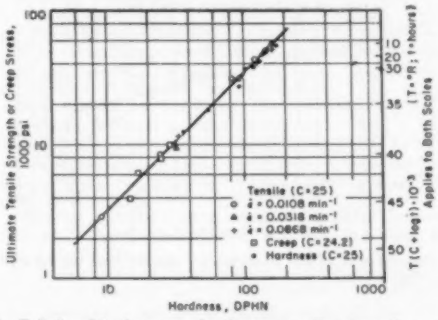
Ultimate Tensile Strength or Creep Stress, 1000 psi
Hardness, DPHN
T(C + log t) · 10⁻³ (T = °R; t = hours)
Applies to Both Scales
Tensile (C = 25)
ȧ = 0.0108 min⁻¹
ȧ = 0.0318 min⁻¹
ȧ = 0.0868 min⁻¹
Creep (C = 24.2)
Hardness (C = 25)

Fig. 31 Relationship between hardness, tensile strength, and creep-rupture strength of a Fe-Cr-Be alloy (Underwood [32])

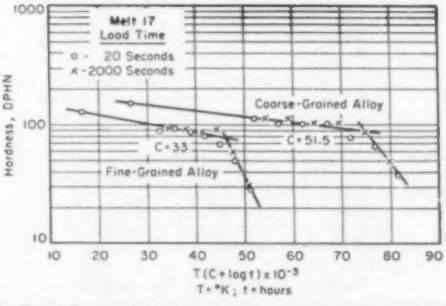

Fig. 32 Dependence of hardness on loading time for an Fe-Cr alloy (Douglass [33])

zirconium and a zirconium alloy in Fig. 33. As expected there is a drop in hardness as the time of load application is increased. It would seem that this behavior is related to the creep behavior.

Certain correlations between hardness and other mechanical properties have already been discussed. To take advantage of such correlations, extensive surveys over wide ranges in composition and temperature have been made to determine conditions for optimum high-temperature strength. One such study has been made on the zirconium-uranium system [34]. From the results obtained, Fig. 34, it is found that hardness maxima are observed at various temperatures and compositions. At 700 C it is shown that phase changes can affect the hardness markedly. Hardness results of this type may also be useful in determining appropriate temperature ranges for forging or hot rolling of promising compositions.

Use of Hot-Hardness Tester as a Research Tool. As a research tool the hot hardness test is useful for studying solid-state reactions which may be temperature, strain, or time dependent or a combination of these. At elevated temperatures it is first necessary to determine the temperature dependence of hardness for high-purity metals. In the absence of allotropic transformations and at temperatures below recrystallization, high-purity metals should not exhibit any solid-state reactions except for the rearrangements of crystal imperfections which are usually termed crystal recovery. These are produced during the hardness test and may play an important role in the temperature dependence of hardness. The typical behavior for the change in hardness with temperature for pure metals is similar to that of copper [35, 36], Fig. 35. The change in mechanism which accounts for the pronounced change in slope in the log H-temperature plot is not fully understood. The temperature at the intersection of the two straight-line segments falls between 0.4 and 0.6 of the absolute melting temperature of all high-purity metals tested [35, 36]. As will be discussed, at temperatures above 0.4 of the absolute melting temperature, the rate of plastic flow and crystal recovery may be controlled by a dislocation climb mechanism. This indicates that the strain-hardening effect of barriers blocking arrays of dislocations is diminished, leading to a more rapid decrease in hardness with temperature.

As shown in the lower part of Fig. 35, "high-purity" iron does not behave in a manner similar to that of other pure metals. The observed maximum in hardness is a typical strain-aging peak. This behavior is caused by residual amounts of C and N which effectively pin dislocations in ferrite, as proposed by Cottrell and eliminated by removing both C and N in a commercial low-carbon open-hearth steel, shown as Steel C. For this material the temperature at the point of intersection lies within the range established previously, 0.4 to 0.6.

Typical strain-aging peaks for a number of commercial carbon steels, Fig. 36, occur within the 350 to 400-F range. By adding molybdenum to a 1 per cent chromium steel the peak is moved to about 700 F, Fig. 37. This shift is undoubtedly due to the effective retarding of recovery by additions of molybdenum and to some extent chromium. Thus the strain-aging reaction is spread over a wider temperature range. It may also be observed in Fig. 37 that, in the presence of Cr and Ti or Cr and Si, the strain-aging reaction can be eliminated and two line segments obtained in log-hardness-temperature plot. In both of these steels the nitrogen

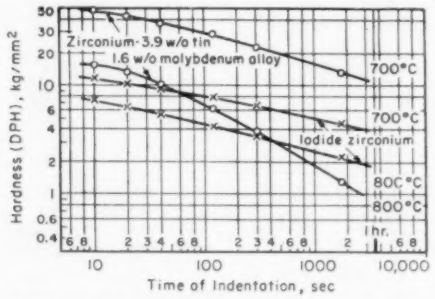

Fig. 33 Dependence of hot hardness on loading time for various alloys (Douglass [33])

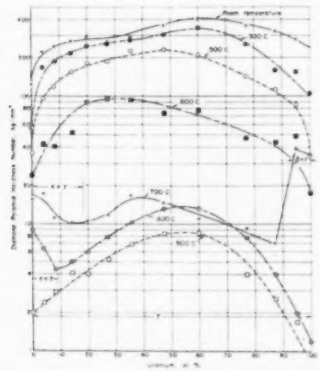

Fig. 34 Hot hardness isotherms in the Zr-U system (Chubb, et al. [34])

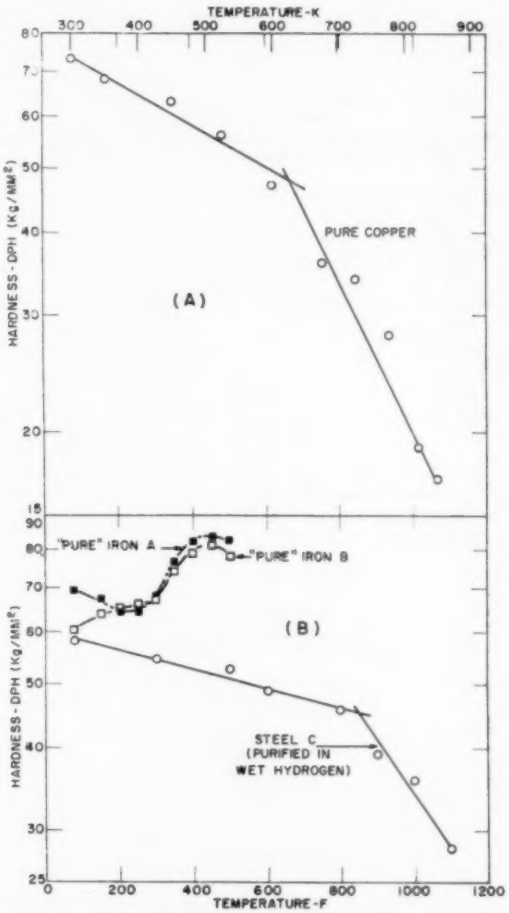

Fig. 35 Dependence of hardness on temperature for pure copper, pure iron, and a purified steel (Garofalo, et al. [36])

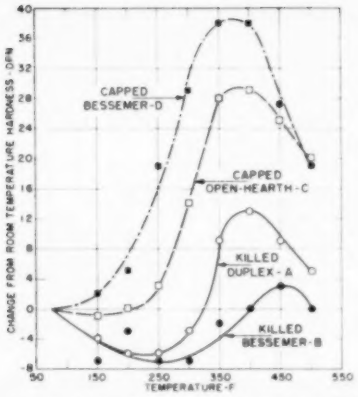

Fig. 36 Change in hardness from room temperature to 500 F for various normalized steels

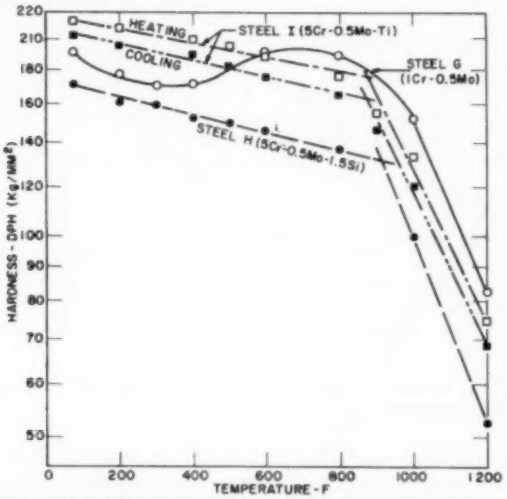

Fig. 37 Change in hardness with temperature for various low chromium steels (Garofalo [36])

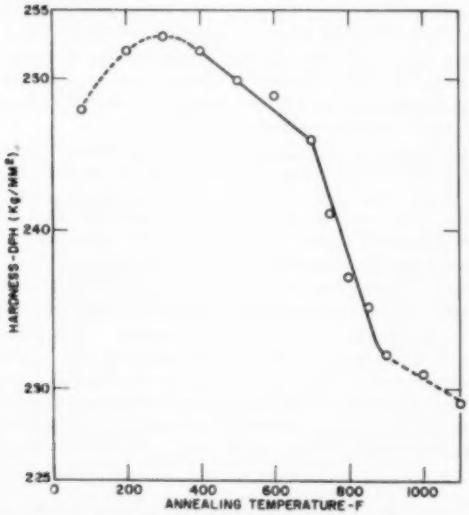

Fig. 38 Effect of annealing for 15 minutes at various temperatures on hardness at room temperature for a 5 Cr-0.5 Mo-Ti steel cold-rolled 11 per cent (Garofalo [36])

may be combined with Ti and Si and perhaps Cr and Mo. Carbon may be combined with Ti and perhaps Cr and Mo. In Fig. 38 the recovery characteristics of the 5 Cr-0.5 Mo-Ti steel are shown. This steel was cold-rolled 11 per cent at room temperature and sectioned into $^1/_8$-inch specimens. Each specimen was heated to a predetermined temperature for 15 minutes and the hardness determined upon cooling to room temperature. The results in Fig. 38 indicate four stages of recovery. The first stage indicates a strengthening reaction which cannot be ascribed to strain-aging because as shown in Fig. 37 this alloy does not show a strain-aging peak. It is very likely that the strengthening effect of the first stage is caused by migration of vacancies to dislocations causing jogs in the dislocation lines. The mechanism involved in the second stage is not understood although it may be associated with a thermally induced glide in areas of high internal stress leading to a more uniform distribution of dislocations along the glide planes. During the third stage the greater rate of softening may be due primarily to thermally-induced glide, dislocation climb, and the resulting annihilation of dislocations of opposite sign. During the fourth stage the reduced rate of softening may be related to early stages of polygonization and pinning of short-range boundary segments by solute atoms. Although the nature of the four stages, which are perhaps not distinct but may overlap from one to the other, is not known, it is believed that the change in slope in the log-hardness-temperature plot is related to the change from the second to the third stage.

As indicated by these few examples, the hot-hardness test is well suited to studying solid-state reactions. Other types of phenomena which have been studied with this test, in addition to those mentioned, include tempering reactions at the tempering temperature and 885-F embrittlement in high-chromium steels.

References

1 F. L. Everett and J. Miklowitz, "Poisson's Ratio at High Temperatures," *Journal of Applied Physics*, vol. 15, 1944, p. 592.

2 F. Garofalo, P. R. Malenock, and G. V. Smith, "The Influence of Temperature on the Elastic Constants of Some Commercial Steels," ASTM Special Technical Publication No. 129, 10, 1952.

3 C. Zener, "Elasticity and Anelasticity of Metals," University of Chicago Press, Chicago, Ill., 1948.

4 M. E. Fine, "Dynamic Methods for Determining the Elastic Constants and Their Temperature Variation in Metals," ASTM Special Technical Publication No. 129, 43, 1952.

5 M. B. Reynolds, "The Determination of the Elastic Constants of Metals by the Ultrasonic-Pulse Technique," *Trans. ASM*, vol. 45, 1953, p. 839.

6 J. R. Frederick, "A Study of the Elastic Properties of Various Solids by Means of Ultrasonic-Pulse Techniques," PhD thesis, University of Michigan, 1947.

7 "Résumé of High-Temperature Investigations Conducted During 1948–50," The Timken Roller Bearing Co., Steel and Tube Division, Canton, Ohio.

8 G. E. Bennett and R. M. Davies, "An Experimental Investigation by a Dynamical Method of the Variation of Young's Modulus With Temperature," *Journal Institute of Metals*, vol. 75, 1948–1949, p. 759.

9 P. Chevenard, "So-Called Secondary Mechanical Properties: Internal Friction, Viscous Relaxation, Reactivity, and Poisson's Ratio," *Revue de Metallurgie*, vol. 40, 1943, p. 289.

10 C. Zener, "Theory of Elasticity of Polycrystals With Viscous Grain Boundaries," *Physical Review*, vol. 60, 1941, p. 906.

11 T. S. Kê, "Experimental Evidence of the Viscous Behavior of Grain Boundaries in Metals," *Physical Review*, vol. 71, 1947, p. 533.

12 T. S. Kê, "Viscous Slip Along Grain Boundaries and Diffusion of Zinc in Alpha Brass," *Journal of Applied Physics*, vol. 19, 1948, p. 285.

13 T. S. Kê, "Stress Relaxation Across Grain Boundaries in Metals," *Physical Review*, vol. 71, 1947, p. 533.

14 C. D. Starr, E. C. Vicars, A. Goldberg, and J. E. Dorn, "Effect of Alloying Elements on Grain-Boundary Relaxation in Alpha Solid Solutions of Aluminum," *Trans. ASM*, vol. 45, 1953, p. 275.

15 W. H. Graft, D. W. Levinson, and W. Rostoker, "The Influence of Alloying on the Elastic Modulus of Titanium Alloys," *Trans. ASM*, vol. 49, 1957, p. 263.

16 A. Nadai and M. J. Manjoine, "High-Speed Tension Tests at

Elevated Temperatures—Parts II and III," *Journal of Applied Mechanics*, vol. 8, TRANS. ASME, vol. 63, 1941, p. A-77.

17 R. F. Miller, G. V. Smith, and G. L. Kehl, "Influence of Strain Rate on Strength and Type of Failure of Carbon-Molybdenum Steel at 850, 1000, and 1100 F," *Trans. ASM*, vol. 31, 1943, p. 817.

18 M. J. Manjoine, "Influence of Rate of Strain and Temperature on Yield Stresses of Mild Steel," *Journal of Applied Mechanics*, vol. 11, TRANS. ASME, vol. 66, 1944, p. A-211.

19 C. W. MacGregor and J. C. Fisher, "A Velocity-Modified Temperature for the Plastic Flow of Metals," *Journal of Applied Mechanics*, vol. 13, TRANS. ASME, vol. 68, 1946, p. A-11.

20 R. J. MacDonald, R. L. Carlson, and W. T. Lankford, "The Effects of Strain Rate and Temperature on the Stress-Strain Relations of Deep-Drawing Steel," *Trans. ASTM*, vol. 56, 1956, p. 704.

21 M. J. Manjoine, E. T. Wessel, and W. H. Pryle, "Constant-Head Rate-Testing Machine With Instantaneous Speed Change," *ASTM Bulletin*, no. 226, December, 1957.

22 J. R. Kattus, "Effect of Holding Time and Strain Rate on the Tensile Properties of Structural Metals," Short-Time High-Temperature Testing, Amer. Soc. for Metals, Cleveland, Ohio, 1958.

23 R. J. MacDonald, R. L. Carlson, and W. T. Lankford, "An Apparatus for the Determination of Stress-Strain Properties at High Rates of Strain," *Proceedings of SESA*, vol. 14, no. 1, 1956.

24 T. A. Trozera, D. D. Sherby, and J. E. Dorn, "Effect of Strain Rate and Temperature on the Plastic Deformation of High-Purity Aluminum," *Trans. ASM*, vol. 49, 1957, p. 173.

25 F. Garofalo, G. V. Smith, and B. W. Royle, "Validity of Time-Compensated Temperature Parameters for Correlating Creep and Creep-Rupture Data," TRANS. ASME, vol. 78, 1956, p. 1423.

26 C. Zener, "The Micro-Mechanism of Fracture," Fracturing of Metals, Amer. Soc. for Metals, Cleveland, Ohio, 1948.

27 E. Fetz, "Dynamic Hardness Testing of High-Speed Steel at High Temperatures," *Trans. ASM*, vol. 30, 1942, p. 1419.

28 E. C. Bishop and M. Cohen, "Hardness Testing of High-Speed Steel at High Temperatures," *Metal Progress*, vol. 413, March, 1953, p. 413.

29 F. P. Bens, "Hardness Testing of Metals and Alloys at Elevated Temperatures," *Trans. ASM*, vol. 38, 1947, p. 505.

30 F. Garofalo, P. R. Malenock, and G. V. Smith, "Hardness of Various Steels at Elevated Temperatures," *Trans. ASM*, vol. 45, 1953, p. 377.

31 O. Richmond, paper on "Theory of Plasticity" to be published.

32 E. E. Underwood, discussion to Reference [36].

33 D. L. Douglass, discussion to Reference [36].

34 W. Chubb, G. T. Muhlenkamp, and A. D. Schwope, "A Hot Hardness Survey of the Zirconium System," *Trans. ASM*, vol. 50, 1958, p. 298.

35 J. H. Westbrook, "Temperature Dependence of the Hardness of Pure Metals," *Trans. ASM*, vol. 45, 1953, p. 221.

36 F. Garofalo, G. V. Smith, and D. C. Marsden, "The Temperature Dependence of the Hardness of 'Pure' Iron and Various Ferritic Steels," *Trans. ASM*, vol. 49, 1957, p. 372.

37 J. E. Dorn and T. E. Tietz, "The Modulus of Elasticity—A Review of Metallurgical Factors," *Metal Progress*, vol. 81, July, 1950.

38 A. Seeger, *Philosophical Magazine*, vol. 46, 1955, p. 1194.

39 L. F. Vosteen, "The Effect of Temperature on Dynamic Modulus of Elasticity of Some Structural Alloys," NACA Tech. Note 4348, August, 1958.

DISCUSSION

M. J. Manjoine[3]

Hot-hardness data have been related to the elevated temperature strength of materials for the same range of loading or deformation rates, such as those encountered in forging, rolling, or extrusion. We have successfully utilized hot-hardness data to determine the optimum temperature for the rolling and extrusion of metals with cladding. However, the use of hot-hardness data to predict creep and rupture strength may be very misleading. The hot-hardness test measures the short-time resistance of the material under compressive loading. For some materials the tensile creep properties are different from those in compression. Fig. 39 shows that for a stainless iron at 1000 F the creep rate in compression is far less than that in tension. This is true even if both tests are run at constant true stress instead of constant load. This difference in creep strength may be corrected when dealing with materials of similar composition and structure However, Fig. 40 indicates that, although lead has a higher creep rate in tension than that in compression, woods metal has a lower creep rate in the tension direction.

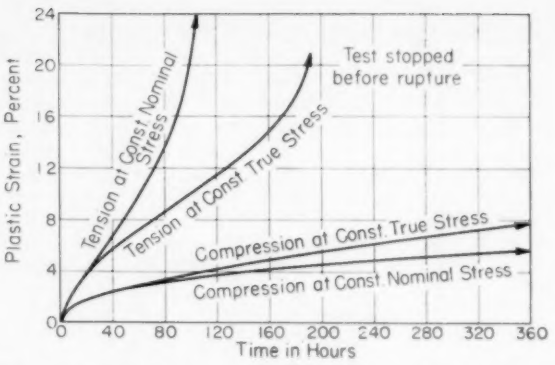
Plastic Strain, Percent
Time in Hours
Tension at Const Nominal Stress
Tension at Const True Stress
Test stopped before rupture
Compression at Const True Stress
Compression at Const Nominal Stress

Fig. 39 Creep tests in tension and compression of stainless iron at 34,000 psi and 1000 F

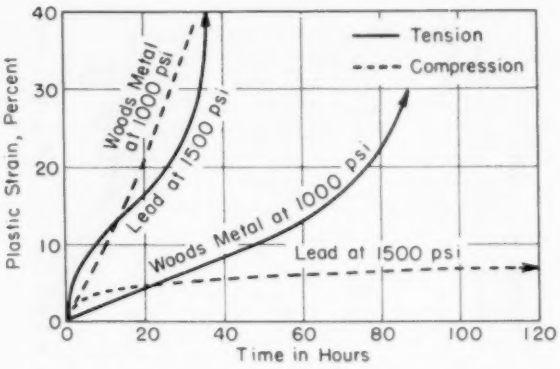

Fig. 40 Tension and compression creep tests on lead and woods metal at room temperature

Finally, the rate effect is much more important in the strength of metals at elevated temperatures. In Fig. 41 the creep strength of a Cr-Mo steel with several carbon contents is plotted as a function of a parameter which is a function of the creep rate and the absolute temperature.

For a constant temperature the log of the strength varies with the log of the creep rate as given by the curves. The curves show that at high creep rates, extreme right hand, the strength of the steel increases with increasing carbon content. This is same result that would be found from the hot-hardness test. At the low creep rates, such as those encountered in long-time tests, extreme left hand, the creep strength decreases with increasing carbon content or just the opposite to that which would be predicted by the hot-hardness or short-time tensile tests.

[3] Westinghouse Electric Corporation, Research Laboratories, Pittsburgh, Pa. Mem. ASME.

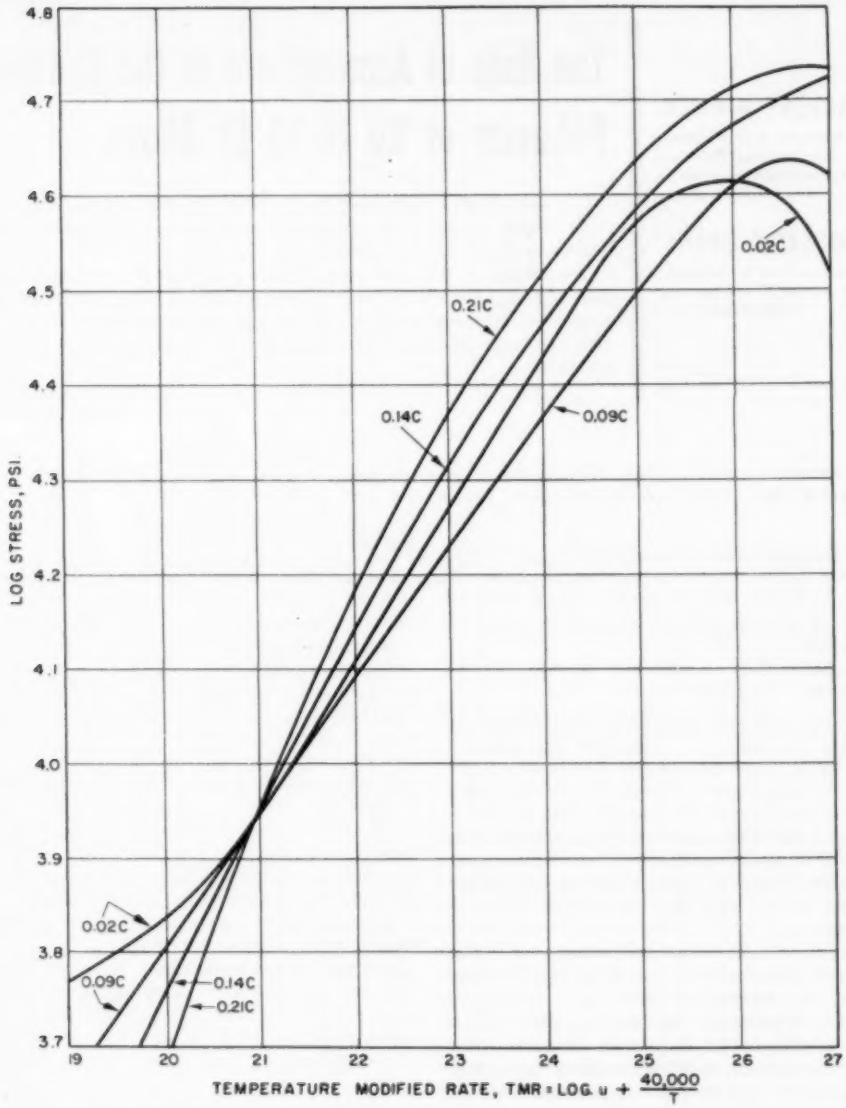

Fig. 41 Flow stress at ultimate versus temperature modified rate, $2^1/_4$ Cr-0.6 Mo steels

Author's Closure

The results presented by Mr. Manjoine are extremely interesting and indicate further that the relationship between hardness and creep strength in tension can only be at best approximate as stated in the paper. These results bring up a second point which is of fundamental importance. No present theory of creep can predict the behavior observed by Mr. Manjoine and it may well be that studies of this type will lead to a better understanding of the rate controlling processes in creep and relationships between mechanical properties.

The Role of Atmosphere in the Creep-Rupture Behavior of 80 Ni-20 Cr Alloys

ROBERT WIDMER
Formerly, Research Staff Member, M.I.T.; now, Technical Director, New England Materials Laboratory, Inc., Medford, Mass.

NICHOLAS J. GRANT
Professor, Department of Metallurgy, Massachusetts Institute of Technology, Cambridge, Mass.

The microstructure of several 80 Ni-20 Cr alloys was studied after creep at 1500 and 1800 F with respect to the influence of atmosphere. In particular the propagation of intercrystalline cracks was investigated.

By comparison with tests conducted in argon it can be shown that the atmosphere has a strengthening effect in all cases. The mechanism of this effect changes with the variation of minor constituents in the metals (such as silicon and Mn/S ratio). Crack propagation is strongly affected by the melting process, which influences the purity of the grain boundaries.

In a previous paper [1][1] the creep-rupture properties of five alloys of the 80 Ni-20 Cr type were reported. These alloys included:

1V—low-silicon (0.12 per cent) vacuum-melted, Mn/S ratio 10
2V—high-silicon (1.33 per cent) vacuum-melted, Mn/S ratio 90
3A—high-silicon (1.38 per cent) air-melted, Mn/S ratio 3.3
4A—low-silicon, air-melted, deoxidation practice varied, Mn/S ratio low
5A—low-silicon, air-melted, deoxidation practice varied, Mn/S ratio low

Aside from the silicon variation, small differences existed in the usual elements, Mn, C, and S. Grain size was adjusted through heat-treatment to be comparable in all five heats. Significant differences were noted in rupture life, or stress for a given life, over the test temperature range of 1000 to 1800 F (most tests were at 1200, 1500, and 1800 F); however, these differences were not consistent in that greater strengths were displayed by alloys 1V, 2V, and 3A over narrow temperature and rupture-time regions, shifting from one alloy to another even at only one temperature.

The differences among the alloys were most striking in terms of ductility values. The reasons for this must be sought in the minor constituents and in the structure of the grain boundaries. In this respect, it was of particular interest to compare the air-melted versus the vacuum-melted alloys. In connection with vacuum melting, a vast amount of literature clearly shows that many tramp elements and low-melting or volatile constituents are removed. These impurities would normally be found enriched at the grain boundaries and would exert an important influence on grain-boundary sliding, boundary migration, and cohesion between grains. Thus crack initiation and propagation would be affected. Such effects were indeed noted.

It was also expected that significant effects would be observed due to reaction of the atmosphere with the alloy. Profound effects have been noted in the case of titanium and several of its alloys [2] and recent publications have reported large effects for nickel-chromium alloys [3, 4]. It was the intent of this investigation to determine these atmospheric effects as a function of temperature, time, composition of the alloy (small variations), and alloy preparation (air versus vacuum-melted). For this purpose, alloys 1V, 2V, and 3A were studied. Test conditions are given in Reference [1].

Results

Fig. 1 shows a plot of log-stress versus log-rupture time for alloy 2V over the temperature range 1000 to 1800 F and for rupture times up to 1000 hr. This figure is reproduced in order to show the irregular behavior noted at certain temperatures and rupture times (or stress). Normally a break downward occurs at the equicohesive region, where intercrystalline cracking begins, and at any other region, where a weakening effect becomes operative. A break upward or a decrease in slope indicates a strengthening effect [2]. In Fig. 1, it will be noted that the equicohesive change is observed at the high-stress region for each temperature. Subsequently, however, there is a region of a sharp break downward (weakening) followed by a decrease of slope (strengthening). This change occurs at shorter times for increasing temperature. The question was this: Is the second break in the curves purely one of the initiation of recrystallization (weakening) followed by grain growth (strengthening) [5], or is there an effect of atmosphere, too?

Crack Initiation and Propagation. Tests were interrupted at 1200, 1500, and 1800 F (such interruptions being based on prior completed tests under comparable test conditions [1]) after various amounts of creep to try to establish the time for initiation of intercrystalline cracking. The following observations can be made:

1 During the second stage of creep small intercrystalline cracks can be seen, usually located at triple points, but also between grains. The number of these small cracks was considerably larger in the case of the vacuum-melted alloy (2V) than in the air-melted alloy (3A).

2 During the later period of second-stage creep the cracks of alloy 2V open up rather than propagate. These cracks are fairly uniformly distributed over the entire gage length of the specimen.

3 At a comparable elongation some of the cracks in alloy 3A have propagated much more rapidly.

4 During the last stage of creep, an increasing number of newly initiated cracks can be observed in alloy 3A. They are usually concentrated in the vicinity of the larger cracks, which have now spread through a rather large portion of the specimen cross section. These new cracks are a result of the stress concentrations and bending forces brought about by the propagation of the earlier cracks.

Table 1 shows, for comparable stress tests at 1500 and 1800 F, the amount of elongation contributed to total elongation by the crack thickness in axial direction, for the air and vacuum-melted

[1] Numbers in brackets indicate References at end of paper.

Contributed by the Metals Engineering Division and presented at the Annual Meeting, Atlantic City, N. J., November 29–December 4, 1959, of The American Society of Mechanical Engineers.

Note: Statements and opinions advanced in papers are to be understood as individual expressions of their authors and not those of the Society. Manuscript received at ASME Headquarters, July 17, 1959. Paper No. 59—A-122.

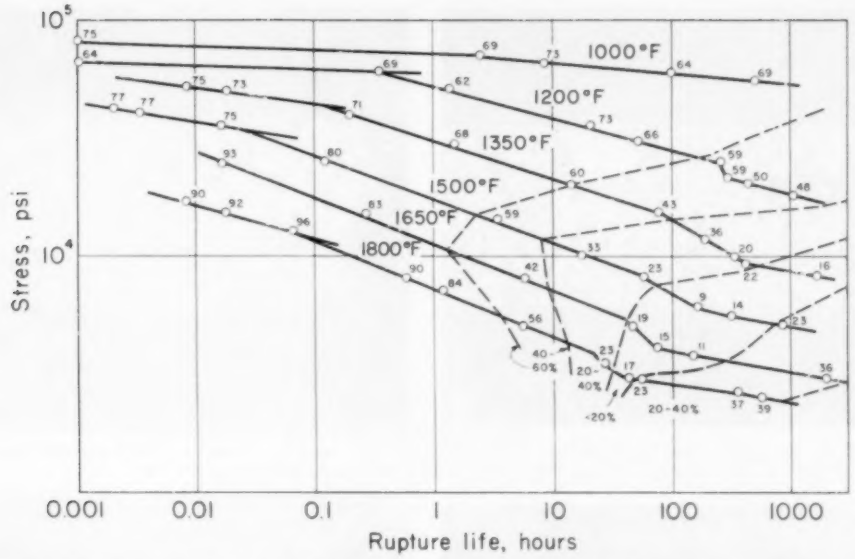

Fig. 1 Log-stress versus log-rupture life plot of alloy 2V (vacuum-melted, high Si) showing ductility in terms of reduction of area as a function of stress and temperature. All tests conducted in air.

high silicon heats (see Fig. 2). The thickness of the cracks was measured metallographically in longitudinal sections over a given gage length. From Fig. 2, it is obvious that this contribution is considerably larger for alloy 2V than for alloy 3A. Nevertheless, the amount of actual metallic elongation of the vacuum-melted alloy remains vastly larger than for the air-melted alloy (see Table 1). As was illustrated [1], the bulk of the difference in ductility occurs in the last stage of creep for both alloys, but the total elongation for the vacuum-melted alloy is 2 to 3 times that measured for the air-melted alloy.

Observations of alloys 2V and 3A indicate that the air-melted alloy, because of the greater concentration of impurities and constituents, undergoes less grain-boundary shear initially; the vacuum-melted alloy, with less to obstruct grain-boundary shear, undergoes more such deformation and thus suffers first from intercrystalline cracking. These cracks, usually at triple points, do not, however, propagate and merely seem to serve as stress-relaxation sources. Unfortunately, the air-melted alloy, once such intercrystalline cracking takes place, suffers from more rapid crack propagation than does the vacuum-melted alloy.

Influence of Atmosphere on Creep Strength and Ductility. A number of mechanisms have been proposed to explain the strengthening influence of atmospheric reaction with the test specimen [3, 4].

In the present study, those creep tests which were run in air at 1500 and 1800 F for long times (more than 50 hr) showed a deceleration of creep while in the last stage of creep, leading to a second region of steady-state creep and later a second period of last-stage creep (see Fig. 3). This is unusual because the second creep period comes about after major occurrence of intercrystalline cracking had initiated the normal third stage of creep. This behavior results in prolonging rupture life and brings about the slope decrease of the curves shown in Fig. 1.

Tests at 1800 F were repeated on alloy 2V in a highly purified argon atmosphere. For purification purposes, the gas (99.8 per cent Ar) had to pass through a train consisting of calcium-chloride and calcium-hydride drier tubes, a tube with titanium at 1500 F, and a tube with calcium at 1200 F. The specimen itself was surrounded by a small tube of pure tantalum. Before the furnace was brought up to test temperature, the system was flushed for 2 hr. Subsequently, a pressure slightly higher than

Table 1 Contribution of crack volume to total elongation

Alloy	Temp, deg F	Stress, psi	Total % E at fracture (E_t)	% E due to cracks (E_c)	$E_t - E_c$, per cent
2V	1500	5000	45	18	27
3A	1500	5000	12	3.5	8.5
2V	1800	5000	56	17	39
3A	1800	5000	16	9	7

1 atm was maintained. Fig. 4 compares the log-stress versus log-rupture-time curves for this alloy at 1800 F. The air tests show the decreased slope or strengthening effect referred to previously. The argon tests begin to show a deviation after about 10 hr from the air-tested values. More important however is the straight-line trend of the test points. At each stress, therefore, the air test values show the relative strengthening effect of the atmosphere. Fig. 3, which compares the argon-versus-air tests at 1800 F and 2500 psi, shows the double creep curve of the air test, the large increase in rupture life (11X), and a large increase in ductility. There is no strengthening effect in an argon atmosphere.

Fig. 5 compares the reduction-of-area values for alloy 2V at 1800 F for the air and argon tests. It will be noted that argon testing does not prevent the usual drop in ductility (reduction of area) with increasing test time—this drop is normal for high-temperature material behavior in the absence of significant recrystallization or other effects. However, in the longer-time tests, where the air atmosphere prolonged the rupture time, there is a sharp increase also in ductility as illustrated in Fig. 5. In the argon tests the ductility falls to a low minimum and remains there, showing no reversal.

Microstructural Changes by Influence of Atmosphere. The log-stress versus log-rupture-time plots of the three alloys suggest that the rate and amount of strengthening (therefore possibly the mechanism) are not the same (see Fig. 6, which is part of the stress-rupture plot reproduced in Reference [1]). Careful study of the microstructures of test specimens with approximately the same rupture life, coupled with x-ray analysis of the residues obtained by electrolytic separation, show that there are important differences. See Table 2 and Fig. 7.

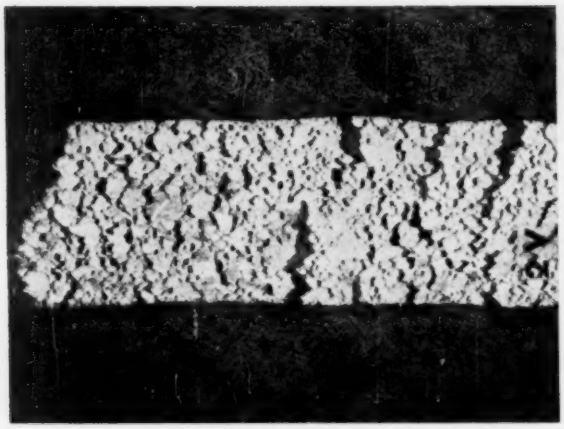

Fig. 2(a) Alloy 2V (vacuum-melted, high Si). Tested at 1500 F and 5000 psi. Rupture life, 870 hr, total elongation, 45 per cent. 10X

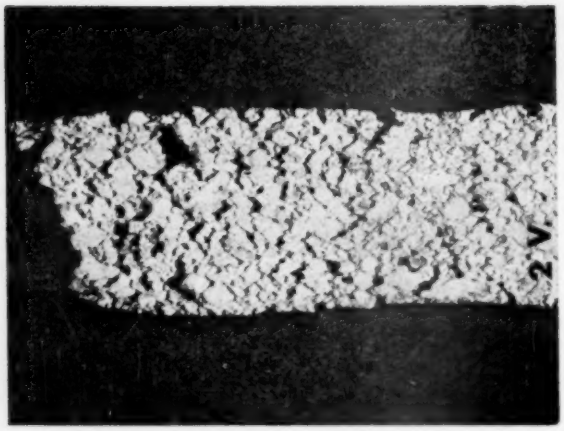

Fig. 2(c) Alloy 2V. Tested at 1800 F and 2750 psi. Rupture life, 347 hr, total elongation, 85 per cent. 10X

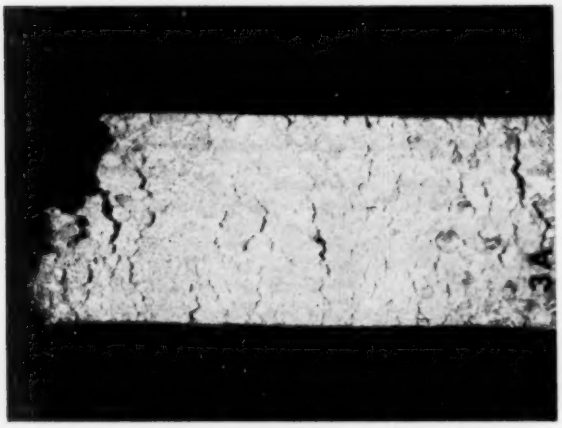

Fig. 2(b) Alloy 3A (air-melted, high Si). Tested at 1500 F and 5000 psi. Rupture life, 524 hr, total elongation, 12 per cent. 10X

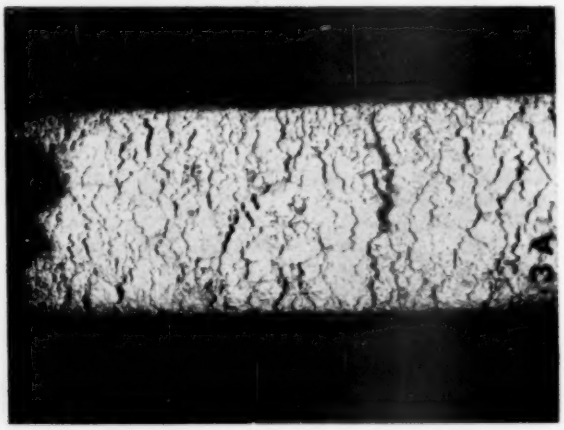

Fig. 2(d) Alloy 3A. Tested at 1800 F and 2000 psi. Rupture life, 445 hr, total elongation, 16 per cent. 10X

Fig. 2 Crack propagation. Vacuum-melted alloy compared with an air-melted alloy.

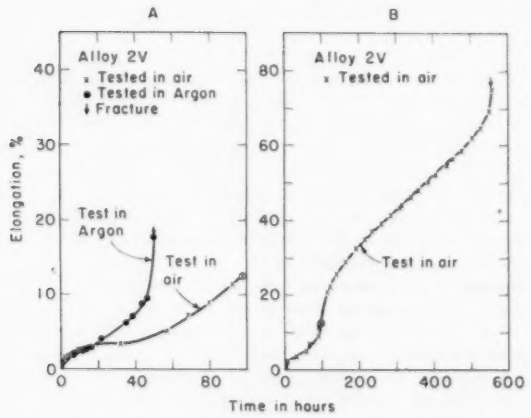

Fig. 3 Creep curves of alloy 2V tested at 1800 F and 2500 psi. Plot B shows entire curve of specimen tested in air. ⊗ on both graphs represents same point.

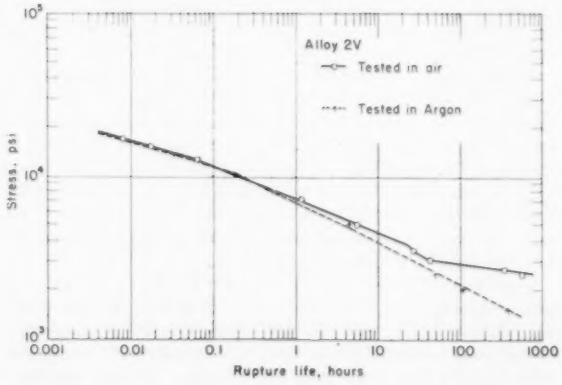

Fig. 4 Log-stress versus log-rupture life plot of alloy 2V tested at 1800 F in air and in argon

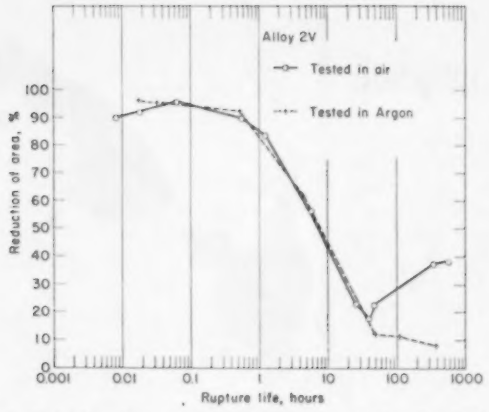

Fig. 5 Reduction of area as a function of rupture life for alloy 2V, tested at 1800 F in air and in argon

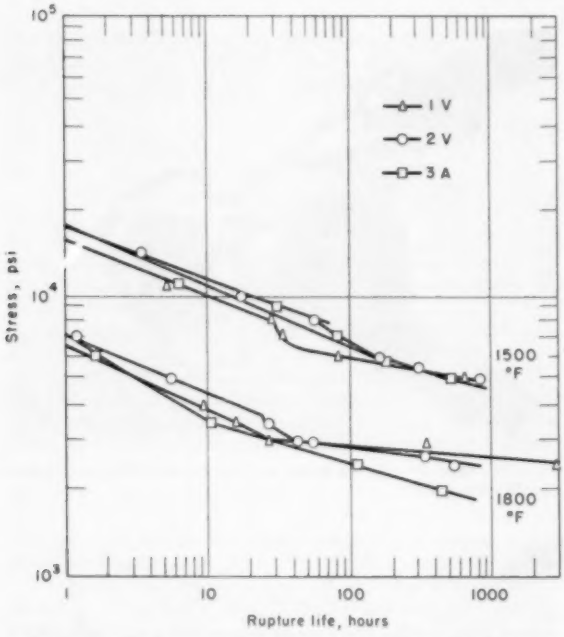

Fig. 6 Log-stress versus log-rupture life plot of alloys 1V, 2V, and 3A at 1500 and 1800 F. Taken from Reference [1], Fig. 1.

Fig. 7(*a*) shows the structure of alloy 2V tested in argon at 1800 F for 390 hr. The structure is quite clean, and shows normal intergranular cracks which are also free of other phases.

By comparison, Fig. 7(*b*) shows alloy 1V (low silicon), tested in air at 1800 F. In addition to an intergranular product, extensive internal oxidation has taken place, both reactions leading to strengthening, and the type of behavior noted in Fig. 3.

Figs. 7(*c*), (*d*), and (*e*) show alloy 2V (high silicon) tested at 1800 F. View (*c*) is near the surface and shows internal oxidation similar to that in Fig. 7(*b*); however, an internal examination, see view (*d*), showed vastly less internal oxidation than for alloy 1V. Intergranular phases were abundantly present, as in alloy 1V, the identity being shown in Table 2, with oxides and chromium nitride both present.

Fig. 7(*e*) illustrates how crack propagation is inhibited by the formation of nitrides at the crack tips. It seems that the cohesion between nitride and metal is better than between two metal crystals in the grain boundary.

Table 2 X-ray analysis of residues obtained by electrolytic separation[a]

Alloy 1V	Vacuum-melted, Si—0.12 per cent	NiO $NiO \cdot Cr_2O_3$ Cr_2O_3
Alloy 2V	Vacuum-melted, Si—1.33 per cent	NiO $NiO \cdot Cr_2O_3$ Cr_2O_3 Cr_2N
Alloy 3A	Air-melted, Si—1.38 per cent	NiO Cr_2O_3 Cr_2N

[a] In all cases a few additional reflections were obtained which cannot easily be identified. It is probable that they represent double oxides or chromium oxide with silicon or iron in solution. It was expected that SiO_2 would be identified; the absence of SiO_2 reflections might well be explained by too small amounts compared with the other compounds identified. It seems, for instance, reasonable that the oxide formed in alloy IV by internal oxidation is SiO_2.

Fig. 7(*f*) shows the structure of alloy 3A (internal view). Much less internal oxidation was noted in this alloy than in the others. Table 2 shows, however, the presence of oxides and chromium nitride which were formed extensively during test, and cover most of the intergranular cracked surfaces.

These studies clearly showed that much more internal oxidation takes place in the low-silicon alloy than in the high-silicon alloy. The mechanism of strengthening in the high-silicon alloy is that of crack oxidation and nitriding, and internal oxidation to a lesser extent. It is not quite clear why nitrides were not found in the structure of alloy 1V.

From these results it is clear that the intercrystalline cracks which form extensively during the last stage of creep expose metal to oxygen and nitrogen from the atmosphere.

Oxide and nitride formation on these surfaces, and especially at the radius of each crack obstruct and delay crack propagation. Simultaneously internal oxidation leads to further strengthening. The action of either or both mechanisms causes relative strengthening and results in the re-establishment of a second period of decreasing creep (see Fig. 3), followed by a second period of last-stage creep which brings about failure. Of especial interest is the apparent interconnection of the great bulk of the intercrystalline cracks.

Because of the difference in rate of crack formation and crack propagation, the vacuum-melted alloys (1 and 2V) and the air-melted alloy (3A) show different amounts of cracked boundary area to the atmosphere at any one time during the creep process. This would necessarily stipulate a difference in subsequent strengthening by reaction with the atmosphere, as evidenced by Fig. 6.

Acknowledgment

The authors wish to thank The International Nickel Company for their sponsorship of this program.

References

1 N. J. Grant and Robert Widmer, "The Creep and Rupture Properties of 80 Ni-20 Cr Alloys," published in this issue, pp. 829–838.

2 John Lunsford and N. J. Grant, "Relative High-Temperature Properties of the Hexagonal-Close-Packed and Body-Centered-Cubic Structure in Iodide Titanium," *Trans. ASM*, vol. 49, 1957, p. 328.

3 Paul Shahinian, "Effect of Environment on Creep-Rupture Properties of Some Commercial Alloys," *Trans. ASM*, vol. 49, 1957, p. 862.

4 Paul Shahinian and M. R. Achter, "The Effect of Atmosphere on Creep-Rupture Properties of a Nickel-Chromium-Aluminum Alloy," NRL Report 5133, 1958.

5 N. J. Grant and Albert G. Bucklin, "Creep Rupture and Recrystallization of Monel From 700 to 1700 F," *Trans. ASM*, vol. 45, 1953, p. 151.

Fig. 7(a) Alloy 2V (vacuum-melted, high Si). Tested in argon at 1800 F and 2000 psi. Rupture life, 390.6 hr. 500X

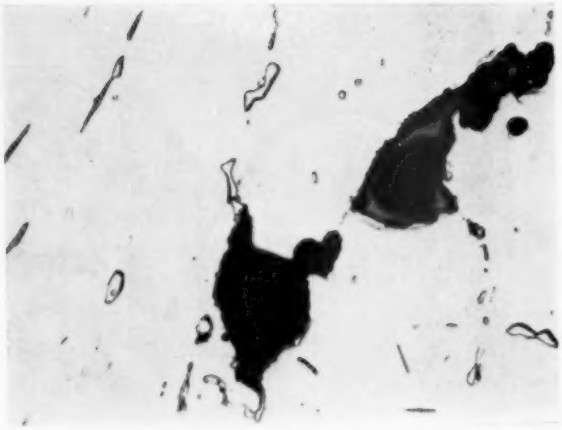

Fig. 7(d) Alloy 2V. Same specimen as Fig. 7(c), near center of specimen. 500X

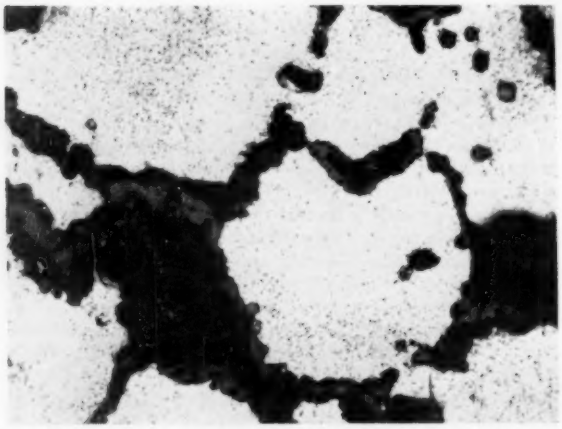

Fig. 7(b) Alloy 1V (vacuum-melted, low Si). Tested in air at 1800 F and 2750 psi. Rupture life, 358 hr. 500X

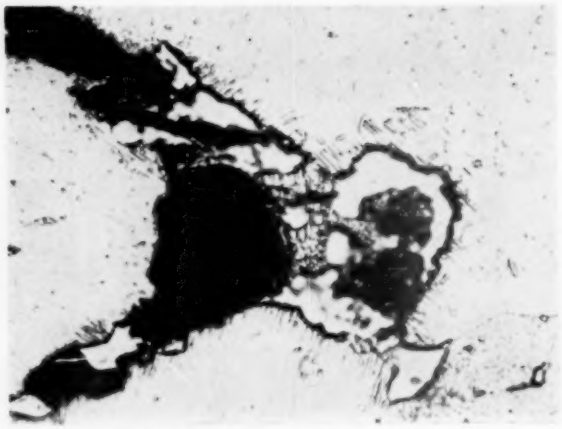

Fig. 7(e) Alloy 2V. Tested in air at 1800 F and 2500 psi. Rupture life, 557 hr. 1000X

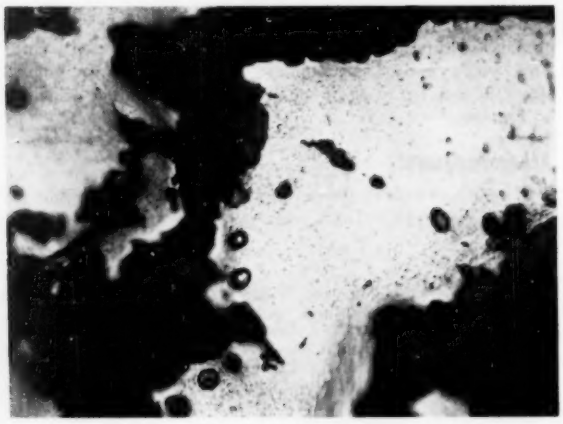

Fig. 7(c) Alloy 2V (vacuum-melted, high Si). Tested in air at 1800 F and 2500 psi. Shows area near edge of specimen. Rupture life, 557 hr. 500X

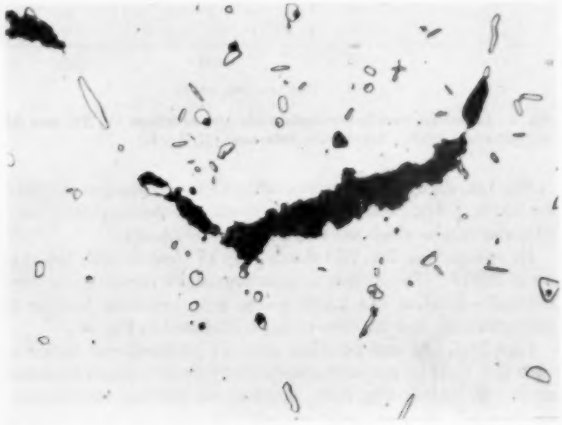

Fig. 7(f) Alloy 3A (air-melted, high Si). Tested in air at 1800 F and 2000 psi. Rupture life, 445 hr. 500X

Fig. 7 Microstructures of different alloys after creep at 1800 F. All specimens etched with 10 per cent chromic-acid solution, electrolytically.

Bourdon Tube Deflection Characteristics

PAUL G. EXLINE
President, Exline Engineering Company, Tulsa, Okla. Mem. ASME

This paper summarizes data obtained at Oklahoma State University under contract with ASME through RCMPE to measure the deflection characteristics of commercially produced Bourdon tubes. The method of measurement was designed to produce accurate results without including effects of end constraints. Reasonably good agreement with theory was shown. Deviation of the cross-sectional shape of the tube from ideal flat oval shape could not be shown to influence the behavior.

An outline of a method of preliminary design of a Bourdon tube is given.

Suggestions are made for additional research using stress free electroformed tubes of ideal shapes.

Introduction

This paper describes the results of measurements of the deflection characteristics of a group of 50 Bourdon tubes. The measurements were made at Oklahoma State University under contract with ASME as part of a program developed by the Research Committee on Mechanical Pressure Elements.

One of the first steps in the RCMPE program was an examination of existing theories of Bourdon tube performance which was conducted by F. B. Jennings [1].[1]

A second step was the collection of a large mass of data on tube performance by Dr. H. L. Mason [2]. His analysis of these data showed qualitative agreement with theoretical predictions. The scatter was quite large and there was reason to believe it was not wholly due to theoretical deficiencies. The data were received from a number of manufacturers without description of the measuring equipment used or of the procedures followed. Subsequently a group of tubes were sent successively to different manufacturers for performance tests in their own shops. Variations in the reported results demonstrated the need for a uniform method of measurement.

The project at OSU was expected to establish a measuring procedure which would yield performance data of high order of accuracy and to provide data which could more reliably be correlated with theoretical predictions. This work was reported by Prof. Gordon G. Smith [3] who was in charge of the project and who made most of the measurements himself. The data used in this paper were taken from his report.

Measuring Procedure

The measuring procedure followed in the OSU work was that proposed by the author to members of RCMPE during the preparation of the program. This consists of locating three points on the side of the tube, each point coinciding with the terminus of a major axis of the cross section. The co-ordinates of the three points were determined by measurement. From these six measurements, the co-ordinates of the center of the circle determined by the three points were computed. This led directly to calculation of the radius of the circle. By repeating the measurements at various pressures, the change of radius with pressure was determined.

Fig. 1 illustrates the placement of the three points on the tube. The co-ordinates of the center of curvature X, Y and the radius R are determined from the following equations:

$$X = \frac{(Y_2 - Y_1)[(Y_3 - Y_1)^2 + (X_3 - X_1)^2] - (Y_3 + Y_1)[(X_2 - X_1)^2 + (Y_2 - Y_1)^2]}{2[(Y_3 - Y_1)(X_2 - X_1) + (X_3 - X_1)(Y_2 - Y_1)]}$$

$$Y = \frac{(X_3 - X_1)[(X_2 - X_1)^2 + (Y_2 - Y_1)^2] + (X_2 - X_1)[(Y_3 - Y_1)^2 + (X_3 - X_1)^2]}{2[(Y_3 - Y_1)(X_2 - X_1) + (X_3 - X_1)(Y_2 - Y_1)]}$$

$$R = [(X - x_1)^2 + (Y - y_1)^2]^{1/2}$$

Measurements of the six co-ordinates were made at zero pressure and at increments of approximately 25 per cent of rated pressure for each of the 50 tubes. Without access to a high speed digital computer, the labor of reducing the data would have been prohibitive.

It had originally been planned to locate five points on each tube at approximately equal intervals, with the first and last points as close as practicable to the socket and tip, respectively. It was expected that determination of radii and their change from the center and the two outermost points and from three inner points would show the reduction in tip travel due to the constraint caused by the end closures. This plan was abandoned when examination of the tubes showed that most of them suffered major changes in both the radius of curvature and in shape of the cross section near the ends. Consequently, the three points were

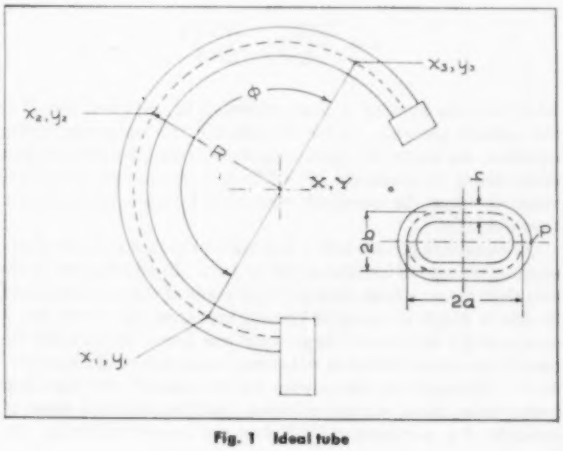

Fig. 1 Ideal tube

[1] Numbers in brackets designate References at end of paper.

Contributed by the Research Committee on Mechanical Pressure Elements and presented at the Annual Meeting, Atlantic City, N. J., November 30–December 4, 1959, of THE AMERICAN SOCIETY OF MECHANICAL ENGINEERS. Manuscript received at ASME Headquarters, December 1, 1959. This paper was not preprinted.

located to include only the most uniform portion of the arc in the hope that end effects would not be present in the results.

In the technique developed by Professor Smith for placing the points on the tube, it was first mounted in a vertical plane above a surface plate. The tube was rotated until a tangent to the arc at the location of the desired point was horizontal. The lower and upper surfaces of the tube at this point were accurately located by means of a height gage. A specially designed fixture was used to make a small 60-degree conical indentation midway between the two surfaces. The indentation was approximately 0.001 inch across at the top and afforded a good target on which to sight the cross hairs of the microscope during the measurements.

For the measurements, the tube was mounted in a vertical plane with the socket down (as shown in Fig. 1) on the table of a small toolmakers milling machine. The table could be moved in three co-ordinate directions by means of screws. A microscope was mounted on a bracket from the fixed column of the machine with its axis perpendicular to the plane of the tube arc. By using the vertical and lateral feed screws, the first point to be measured was centered in the field of view of the microscope.

The lead screws were not used for the measurements. Instead, the distance between a bracket attached to the table and a similar bracket attached to the machine frame was measured. A sensitive dial micrometer, reading to 0.0001 in., was mounted in one bracket with its spindle parallel to the co-ordinate axis being measured.

A stack of standard gage blocks was made up to fill the space between the dial indicator spindle and the other bracket. The length of the gage block stack which would cause the indicator needle to point to zero was taken as the co-ordinate value. All measurements were recorded to the nearest 0.0001 in.

Accuracy

The piston gage used in the investigation had been submitted to the Bureau of Standards for certification. It is estimated that the absolute error in the indicated pressures did not exceed 0.25 psi.

Considerable effort was expended in determining the accuracy of the co-ordinate measurements. For each tube there were six co-ordinates measured and each was measured at five pressures. An equation of the straight line representing the change of each variable as a function of the pressure was determined. If v represents any one of the six variables, the slope m and the intercept b of the line is given by

$$m = \frac{n\Sigma Pv - \Sigma P\Sigma v}{n\Sigma p^2 - (\Sigma P)^2}$$

$$b = \frac{\Sigma P^2\Sigma y - \Sigma P\Sigma Py}{n\Sigma p^2 - (\Sigma P)^2}$$

where n is the number of observations, 5 in this case, and P is the applied pressure. After determining the constants of the equation, the values of v were computed for the pressures used in determining the constants. The difference between the calculated value of v and the observed value of v for each pressure was then obtained.

On examining the 300 sets of 5 differences each, a number of unexpectedly large differences could be seen. In an effort to ascertain their cause, a large scale plot was made of the approximately 30 sets in which the large differences appeared. In nearly every case a single abnormally large error was found which could be ascribed to personal error in either reading or recording a measurement. Although the curves were not recomputed after rejecting such points, there is good evidence that the standard error of estimate of v as measured by P does not exceed 0.0003 in. In the OSU report the values of $\Delta R/R_0$ were rounded off to two significant figures. There is no reason to believe that the error in $\Delta R/R_0$ is greater than that introduced by the rounding off.

The values of $2a + h$ and $2b + h$ were measured with precision micrometers and should be good to ± 0.0001 in. for tubes having good uniformity.

The values of h on the tube sections were measured at four points, the terminals of the major and minor axes. The four values, some of which varied significantly, were averaged to produce the reported value.

Results

Because of the large volume of observed data tabulated during the investigation, it is not reported in this paper. Table 1 lists the characteristics of the tubes and Table 2 shows the results of the measurements and the derived parameters for the pressure change from zero to maximum only. Because of the linearity of the curves, nothing would be gained by including the results for the intermediate pressures.

Recent authors have used two dimensionless parameters to describe graphically the behavior of Bourdon tubes. These are the pressure sensitivity ratio, $\frac{\Delta R}{R_0}\frac{E}{P}\frac{bh^2}{a^4}$, and the geometric

Table 1 Physical and dimensional characteristics

Tube No.	Material	Max P psi	E x10^6	a	b	h
1	Steel	410	28.5	.3346	.0916	.0308
2	Steel	510	28.5	.3366	.0751	.0368
3	"	410	28.5	.3420	.0690	.0319
4	"	200	28.5	.3436	.0788	.0264
5	"	100	28.5	.4491	.0670	.0229
6	"	40	28.5	.5507	.0727	.0095
7	"	120	28.5	.4448	.0775	.0171
8	"	810	28.5	.3234	.0826	.0400
9	"	810	28.5	.3189	.0864	.0461
10	"	1000	28.5	.3156	.0806	.0498
11	Bronze	50	15.5	.4086	.1151	.0177
12	"	130	15.5	.4127	.1337	.0285
13	"	120	15.5	.4124	.1279	.0251
14	"	80	15.5	.4133	.1248	.0224
15	"	240	15.5	.4187	.1357	.0385
16	"	160	15.5	.4163	.1328	.0304
17	"	200	15.5	.4203	.1313	.0363
18	"	160	15.5	.4171	.1356	.0327
19	"	40	15.5	.4047	.1247	.0156
20	"	80	15.5	.4082	.1267	.0186
21	316 SS	800	28	.2971	.1251	.0397
22	"	1000	28	.2885	.1180	.0599
23	"	1000	28	.2973	.1133	.0523
24	"	200	28	.4055	.1290	.0370
25	"	80	28	.4103	.1263	.0243
26	"	120	15.5	.4196	.1136	.0308
27	"	200	15.5	.4253	.1278	.0464
28	"	800	15.5	.3633	.1093	.0673
29	"	40	15.5	.4129	.1129	.0242
30	"	400	15.5	.4391	.1116	.0648
31	Steel	120	28.5	.3875	.0490	.0159
32	"	120	28.5	.3879	.0479	.0162
33	"	200	28.5	.3949	.0269	.0182
34	"	200	28.5	.3948	.0298	.0174
35	"	240	28.5	.2475	.0500	.0189
36	"	240	28.5	.2480	.0490	.0189
37	"	320	28.5	.2547	.0297	.0196
38	"	320	28.5	.2546	.0291	.0198
39	BeCo	200	19.5	.3167	.0402	.0225
40	"	200	19.5	.3169	.0409	.0222
41	Steel	800	28.5	.3013	.0528	.0384
42	"	800	28.5	.3011	.0576	.0387
43	Bronze	520	15.5	.2981	.1001	.0347
44	"	520	15.5	.2986	.1001	.0348
45	"	520	15.5	.2986	.1001	.0348
46	"	520	15.5	.2986	.1001	.0347
47	"	520	15.5	.2986	.1001	.0348
48	"	520	15.5	.2985	.1000	.0349
49	"	520	15.5	.2986	.1001	.0347
50	"	520	15.5	.2985	.1000	.0349

parameter $\frac{R_0 h}{a^2}$. Fig. 3 shows all the data plotted against these parameters.

Fig. 4 shows a plot of the axis ratio of all tubes as a function of the related pressure of the tube.

Fig. 5 shows the wall thickness of all tubes as a function of the rated pressure of the tube. Examination of Fig. 3 shows considerable scatter of the points, a condition encountered by all investigators using this graph. Among various explanations for this scatter are inaccuracy of measurements, deviation of actual cross-sectional shape of the tube from the ideal shape, internal stresses in the tube resulting from the forming procedure, and variations in the wall thickness around the periphery of the tube.

In the present investigation any errors due to inaccuracies in the measurement of P and $\Delta R/R_0$ should not be perceptible on the graph.

The author has not been able to determine how to assess the effect of deviation of shape from the ideal. Fig. 2 shows the cross-section shapes of 6 of the tubes. The dotted lines are accurate drawings made on enlarged photographs of tube sections. The solid lines are ideal sections drawn to the same scale from the tabulated values of a, b, and h in Table 1. In these drawings, the arrow heads on the minor axes point toward the center of curvature of the arc.

Because the value of a enters the pressure sensitivity to the fourth power a small difference between its effective value and its ideal value would have a marked effect on this parameter. Trial efforts to reduce the scatter by arbitrary adjustments of a did not lead to a rational method of establishing the adjustments.

The effect of variations in wall thickness also are magnified in the pressure sensitivity. Measurements were made at four points on the section, and in some cases all four values were different. The values tabulated in Table 1 are arithmetic averages of the four measurements.

All but one or two of the points are within 25 per cent of a smooth curve drawn through them. It would be a simple matter to bring them all on this line by small adjustments of a and h.

All the theoretical work by Wolf [4], Wuest [5, 6], and Clark, et al. [7, 8] show that this type of plot should be a family of curves with the axis ratio b/a as the third parameter. Fig. 4 shows that the axis ratio of all tubes measured, varied from 0.068 to 0.420. The average value was 0.244 and the values above this are distinguished from those below in the plot of Fig. 3. This plot does not confirm the large effect of axis ratio on the pressure sensitivity predicted by theory.

Kardos [9] has suggested that the unit deflection $\frac{\Delta R}{R_0}\frac{E}{P}$ might be a more useful parameter in displaying tube performance. Some of his data plotted as $\log \frac{\Delta R}{R_0}\frac{E}{P}$ versus $\log R_0 h/a^2$ show a straight line relationship which could be expressed

$$\frac{\Delta R}{R_0}\frac{E}{P} = K\frac{(R_0 h)^N}{a^2}$$

where K and N are constants depending upon b/a. Fig. 6 shows the OSU data plotted in this manner.

One manufacturer was requested to submit a number of dupli-

Table 2 Performance data and derived constants

Tube	R_0 in.	ΔR in.	$\Delta R/R_0$ in.	ϕ_0 rad.	$-\Delta\phi$ rad.	$\frac{b}{a}$	$\frac{R_0 h}{a^2}$	$\frac{\Delta R}{R_0}\frac{E}{P}$	$\frac{E}{P}\frac{b^3}{a^2}$	$\frac{E}{P}\frac{\Delta R}{R_0}$
1	1.646	.034	.020	2.564	.050	.274	.453	.296		1390
2	1.625	.031	.019	2.517	.048	.223	.528	.308		1062
3	1.621	.041	.025	2.637	.065	.202	.442	.295		1738
4	1.619	.029	.018	2.373	.042	.229	.362	.265		2565
5	1.630	.035	.021	2.012	.042	.149	.185	.119		5990
6	1.684	.097	.057	1.815	.097	.132	.053	.027		40600
7	1.616	.063	.039	1.819	.066	.174	.140	.092		9260
8	1.636	.029	.018	2.719	.049	.255	.626	.308		633
9	1.648	.022	.013	2.676	.034	.271	.747	.374		458
10	1.621	.019	.012	2.709	.032	.255	.811	.341		343
11	2.513	.053	.021	3.256	.067	.282	.266	.149		6510
12	2.538	.048	.019	3.197	.060	.324	.425	.241		2190
13	2.547	.062	.024	3.169	.076	.310	.376	.217		3100
14	2.532	.052	.021	3.113	.063	.302	.332	.196		4070
15	2.523	.044	.017	3.145	.054	.324	.554	.276		1100
16	2.563	.056	.022	3.192	.067	.319	.450	.265		2130
17	2.540	.045	.018	3.154	.055	.312	.521	.282		1400
18	2.545	.045	.018	3.173	.055	.325	.478	.274		1740
19	2.539	.064	.025	3.146	.083	.308	.241	.171		9690
20	2.543	.078	.031	3.145	.096	.310	.282	.179		6160
21	2.445	.028	.012	2.993	.036	.421	1.098	.423		420
22	2.484	.010	.004	3.097	.012	.409	1.788	.407		112
23	2.492	.017	.004	3.137	.021	.381	1.475	.408		196
24	2.456	.024	.010	2.966	.028	.318	.553	.337		1400
25	2.465	.026	.010	2.951	.031	.308	.355	.225		3500
26	2.510	.045	.018	2.971	.050	.271	.439	.248		2330
27	2.515	.024	.010	3.232	.032	.300	.644	.303		775
28	2.485	.023	.009	3.041	.027	.300	1.275	.334		174
29	2.498	.022	.009	3.074	.026	.273	.355	.192		3490
30	2.514	.023	.009	3.084	.027	.254	.844	.285		349
31	1.552	.076	.049	2.942	.137	.126	.165	.092		11600
32	1.540	.074	.048	2.910	.133	.123	.165	.103		11400
33	1.035	.070	.068	3.129	.198	.068	.120	.065		9690
34	1.047	.074	.071	2.955	.194	.076	.117	.065		10100
35	1.495	.035	.023	3.189	.073	.202	.460	.244		2730
36	1.511	.039	.026	3.057	.077	.198	.464	.271		3090
37	1.098	.044	.040	2.636	.100	.117	.331	.189		3560
38	1.067	.041	.038	2.592	.094	.114	.327	.181		3380
39	1.000	.043	.043	2.553	.108	.127	.224	.190		4190
40	1.000	.034	.034			.129	.221	.143		3320
41	1.571	.034	.022	3.128	.059	.175	.663	.285		784
42	1.583	.031	.019	3.475	.066	.191	.681	.279		677
43	1.617	.029	.018	3.444	.061	.336	.632	.288		542
44	1.623	.030	.018	3.405	.062	.335	.633	.292		551
45	1.620	.030	.018	3.368	.060	.335	.632	.290		548
46	1.620	.030	.018	3.374	.060	.335	.630	.284		540
47	1.624	.030	.018	3.288	.059	.335	.633	.295		557
48	1.625	.030	.018	3.346	.061	.335	.637	.296		551
49	1.611	.030	.019	3.384	.060	.335	.627	.292		556
50	1.618	.029	.018	3.339	.059	.335	.634	.293		546

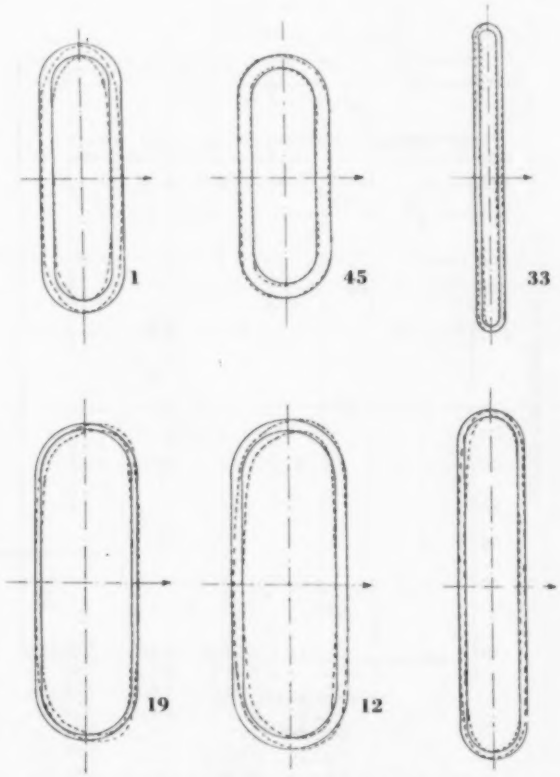

Fig. 2 Typical cross sections; dotted line, actual, solid line, ideal

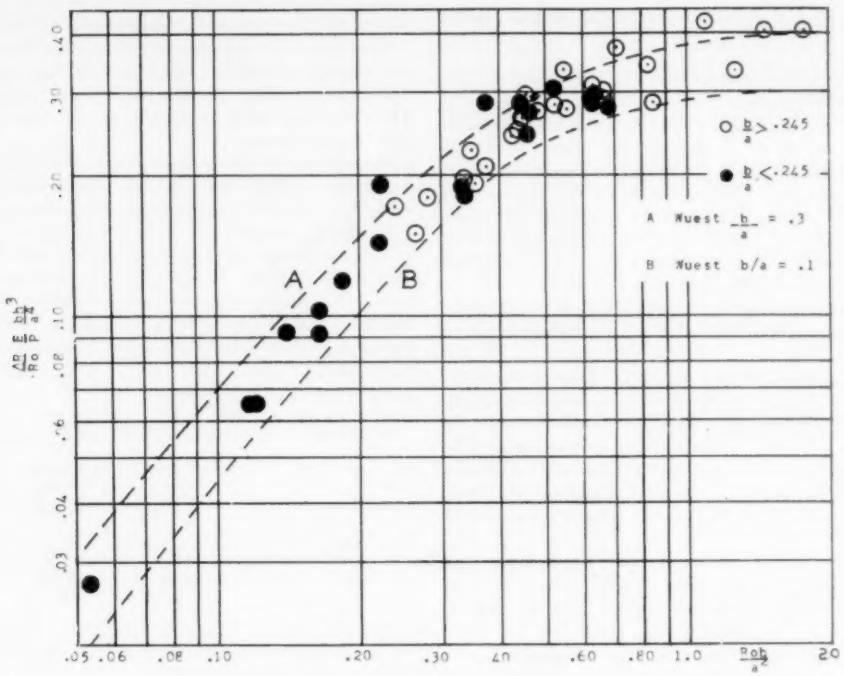

Fig. 3 Pressure sensitivity curve

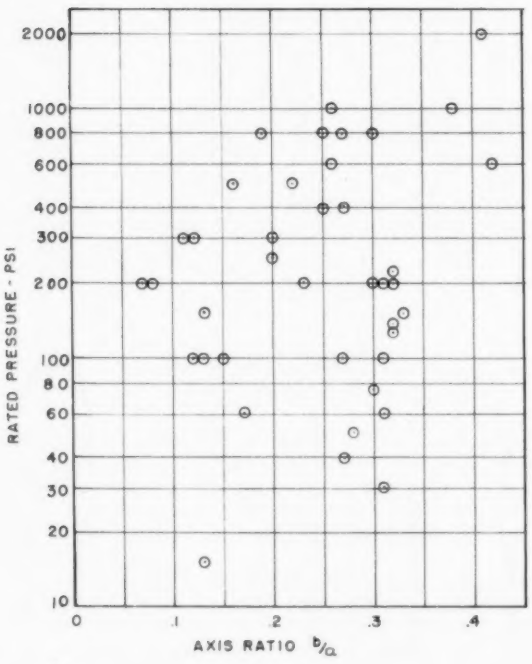

Fig. 4

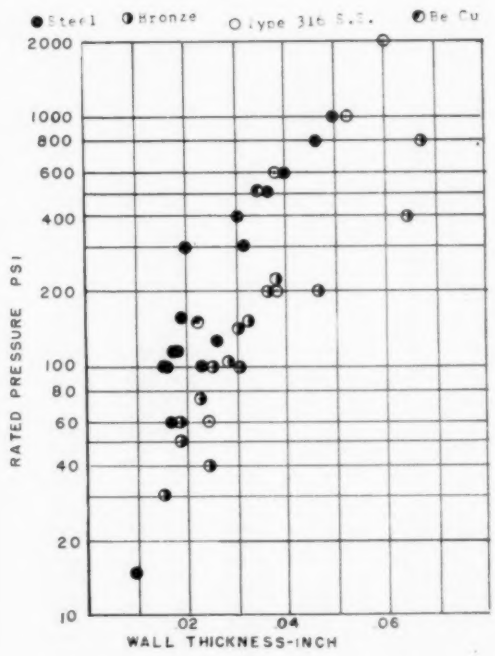

Fig. 5

cate tubes by Professor Smith. It was his thought that by making measurements on such a set he could determine the magnitude of the variations which could be expected in commercial practice. These tubes were numbered 43 to 50, inclusive, and inspection of Table 1 will show a high degree of uniformity from tube to tube. The performance data for these tubes are shown separately in Table 3 together with the per cent variation from the average of the eight tubes. These variations result from a combination of slight manufacturing variations and measurement errors. To the author this table provides justification for the attempt to make all measurements to 0.0001 in.

Of the 240 separate measurements of the point co-ordinates which were made on this group of tubes, one was in error by 0.0030 in., and was rejected as being an observer error. The root mean square of the remaining 239 differences obtained as previously described was 0.0002 inch.

The accuracy analysis of the data provided an opportunity to examine the results for linearity of response. In every case the response was linear with pressure within the accuracy of measurement.

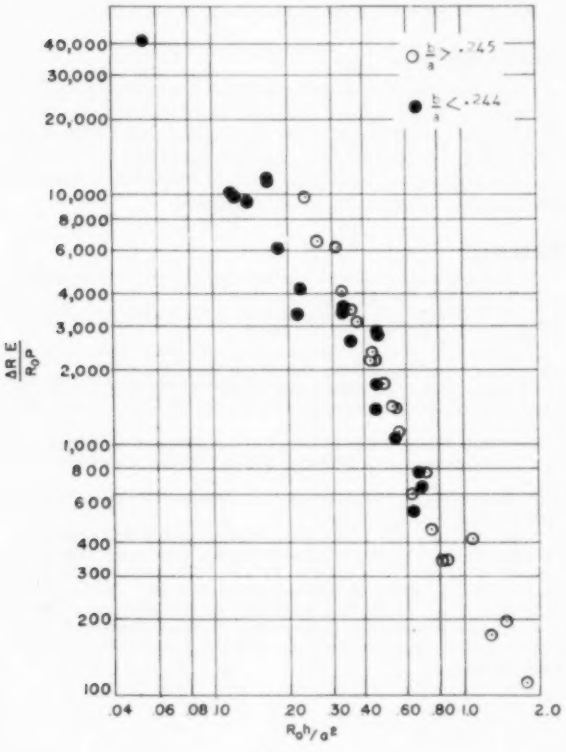

Fig. 6

Use of the Data as a Design Guide

While this investigation leaves many questions unanswered, the data offer a practical guide for at least the preliminary design of a Bourdon tube. The first step would be to select the wall thickness for the desired pressure range and material from Fig. 5. Unless the design is for a high production run it would be well to check available stock lists so that an easily obtainable wall thickness can be chosen.

The choice of a value of R_0 may be dictated by space considerations. If not, several tentative values may be chosen.

The curves give no guide for choice of a value for a; actually the range of a covered by the data is not large, from 0.24 to 0.55. After selecting what appears to be a suitable value, the geometric parameter $R_0 h/a^2$ can be calculated. The corresponding value of $\frac{\Delta R}{R_0} \frac{E}{P} \frac{bh^3}{a^4}$ can then be taken from Fig. 3 or from Table 4.

After making a final choice of b, the expected value of ΔR may be calculated.

Three factors of interest in the performance of a Bourdon tube are the tip travel T, the angular rotation of the tip $\Delta\phi$, and the angle θ between the direction of displacement of the tip and a reference axis. To compute these the included angle of the arc ϕ_0 must be established. The angle of rotation of the tip will then be given by

$$\Delta\phi = \frac{-\phi_0 \Delta R}{R_0 + \Delta R}$$

Let the reference axis be established by placing the fixed end of the tube at the origin of the co-ordinate system with the neutral axis tangent to the Y axis, as shown in Fig. 7. The two components of the tip travel will be

$$\Delta X = \Delta R(1 - \cos\phi - \phi \sin\phi)$$
$$\Delta y = \Delta R(\sin\phi - \phi\cos\phi)$$

The tip travel will then be

$$T = \sqrt{\Delta X^2 + \Delta y^2}$$

Table 4 Consistency in performance of duplicate tubes

$\frac{Poh}{a^2}$	$\frac{\Delta R}{Ro} \frac{E}{P} \frac{bh^3}{a^4}$	$\frac{Poh}{a^2}$	$\frac{\Delta R}{Ro} \frac{E}{P} \frac{bh^3}{a^4}$
.043	.020	.290	.180
.059	.030	.328	.200
.074	.040	.370	.220
.084	.050	.420	.240
.102	.060	.473	.260
.115	.070	.530	.280
.129	.080	.600	.300
.142	.090	.685	.320
.158	.100	.785	.340
.188	.120	.920	.360
.217	.140	1.10	.380
.253	.160	1.50	.400

Table 3 Pressure sensitivity data

Tube No.	Ro	% Var.	ΔR	% Var.	$\frac{\Delta R}{Ro}$	% Var.	$\frac{\Delta R}{R} \frac{E}{P} \frac{bh^3}{a^4}$	% Var.
43	1.61699	-.16	.02940	-1.40	.01818	-1.25	.2878	-1.16
44	1.62275	+.50	.02997	+ .51	.01847	+ .32	.2917	+ .18
45	1.61974	+.01	.02977	- .16	.01838	- .17	.2903	- .30
46	1.62000	+.02	.02936	-1.54	.01812	-1.58	.2839	-2.50
47	1.62373	+.25	.03035	+1.78	.01869	+1.52	.2952	+1.38
48	1.62494	+.33	.03002	+ .67	.01848	+ .37	.2955	+1.48
49	1.61115	-.52	.03004	+ .74	.01865	+1.30	.2922	+ .35
50	1.61775	-.12	.02964	- .60	.01832	- .49	.2929	+ .59

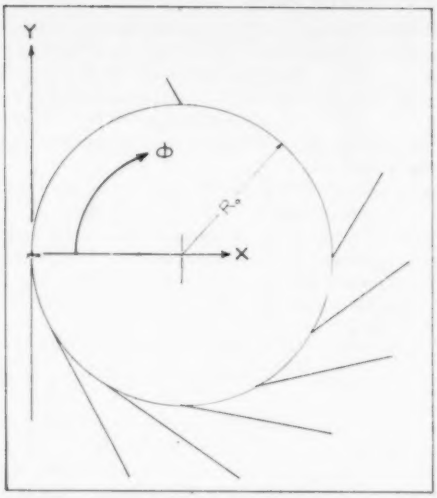

Fig. 7 Magnitude (exaggerated) and direction of displacement of points on an arc with increasing radius

The angle θ between the direction of tip travel and the X-axis will be

$$\theta = \text{arc sin } \frac{\Delta Y}{T}$$

Fig. 7 illustrates the relative magnitude and the direction of the tip travel for various values of ϕ up to 2π.

Suggestions for Additional Research

The author has suggested to the RCMPE that a group of special tubes be constructed which would be designed to provide an answer to some of the outstanding questions. The practice of electroforming enables complex shells to be formed by electroplating nickel on a properly shaped matrix to the desired thickness and then removing the matrix by melting or dissolving it. In this proposal a solid torus would be machined from plastic with a cross section shaped to produce the desired shape of the resulting Bourdon tube. The plastic ring would be given a conductive coating and plated to the desired wall thickness.

A plastic is suggested as the matrix rather than a low melting alloy to prevent contamination of the plating bath. It is reported that baths which have been developed to produce an electroformed object completely free from internal stresses is sensitive to contamination by the usual low melting alloys.

After completion of the plating, a small segment would be cut from the ring and the matrix removed by a suitable solvent. An accurate determination of the wall thickness could be determined at this time by weighing the ring. End fastenings would be attached by soldering and the tube would be ready for measurements.

It is believed that a series of tubes could be designed which would readily demonstrate the effect of the various parameters. It would be possible to duplicate such variations from ideal shape as shown in Fig. 2 and compare the results with a tube having the corresponding ideal shape. Even a tube of rectangular shape as considered by Jennings would offer no difficulty.

The tensile strength of the electroform would be of the order of 60 to 75,000 psi with a modulus of elasticity of approximately 20×10^6 psi. Since the tubes can be produced without residual stresses it should be possible to gain some information on the maximum stress in a Bourdon tube by applying pressure in successively increasing steps until permanent set occurs.

Preliminary correspondence with organizations specializing in high grade electroforming indicate that the total cost of producing a tube in this manner might not exceed 50 to 75 dollars.

Acknowledgments

The author wishes to acknowledge helpful suggestions made by members of RCMPE and particularly those of Mr. J. R. Keim. Much credit should also be given Mr. G. G. Smith for his painstaking efforts to produce data of such a high order of accuracy.

Those anonymous manufacturers who contributed tubes to OSU for their investigation are to be thanked.

References

1 F. B. Jennings, "Theories on Bourdon Tubes," TRANS. ASME, vol. 78, 1956, pp. 55–64.

2 H. L. Mason, "Sensitivity and Life Data on Bourdon Tubes," TRANS. ASME, vol. 78, 1956, pp. 65–77.

3 Gordon G. Smith, "Bourdon Tube Pressure Deflection Investigation," Oklahoma State University, August, 1958.

4 Alfred Wolf, "An Elementary Theory of the Bourdon Gage," *Journal of Applied Mechanics*, vol. 13, TRANS. ASME, vol. 68, 1946, p. A-207.

5 Walter Wuest, "The Influence of the Shape of the Cross Section on the Behavior of Bourdon Tubes," ASME Paper No. 54—A-165.

6 Walter Wuest, "Theory of High Pressure Bourdon Tubes," ASME Paper No. 58—A-119.

7 R. A. Clark and E. Reissner, "Deformations and Stresses in Bourdon Tubes," *Journal of Applied Physics*, vol. 21, pp. 1340–41.

8 R. A. Clark, Gilroy, and E. Reissner, "Stresses and Deformations of Toroidal Shells of Elliptical Cross Sections," *Journal of Applied Mechanics*, vol. 19, TRANS. ASME, vol. 74, 1952, pp. 37–48.

9 G. Kardoe, "Tests on Deflection of Flat Oval Bourdon Tubes," TRANS. ASME, Series D, JOURNAL OF BASIC ENGINEERING, vol. 81, 1959, p. 645.

DISCUSSION

G. Kardos[2]

The experiments and data presented in this paper do much to confirm and enlighten our knowledge of Bourdon tube deflection. These data, because of the excellent testing method employed, have virtually eliminated experimental error, any remaining error is due primarily to manufacturing variation.

In Fig. 6 Mr. Exline has plotted the OSU data as log $\frac{\Delta R}{R}\frac{E}{P}$ versus log $\frac{Rh}{a^2}$ in accordance with my original paper [9]. This curve shows considerable scatter and may lead to the erroneous conclusion that the technique is of little value. In my original paper I put the limitation on the method that all tubes plotted have the same major axis, the same axis ratio, and the same curvature. The data for OSU tubes 11 to 20 meet the original requirement and are plotted as Fig. 8. It can be seen that in this case test results differ less than 10 per cent from the mean line.

In Fig. 8 the chain line denotes the mean line for $\frac{\Delta R}{R}\frac{E}{P}$ from a set of data published in reference [9]. Examination indicates that the slope and origin are approximately equal. The data to produce the two curves show that their axis ratios b/a are approximately the same and although their major axes a and curvatures R_0 are different the ratio a/R is the same for both sets of data. Thus we can modify my original conclusions as follows:

$$\frac{\Delta RE}{RP} = K\left(\frac{R_0 h}{a^2}\right)^n$$

where K and n are functions of b/a and a/R_0.

Thus it seems that a curve such as given in Fig. 8 can apply to a much wider number of geometrically similar tubes than was envisioned in my original paper.

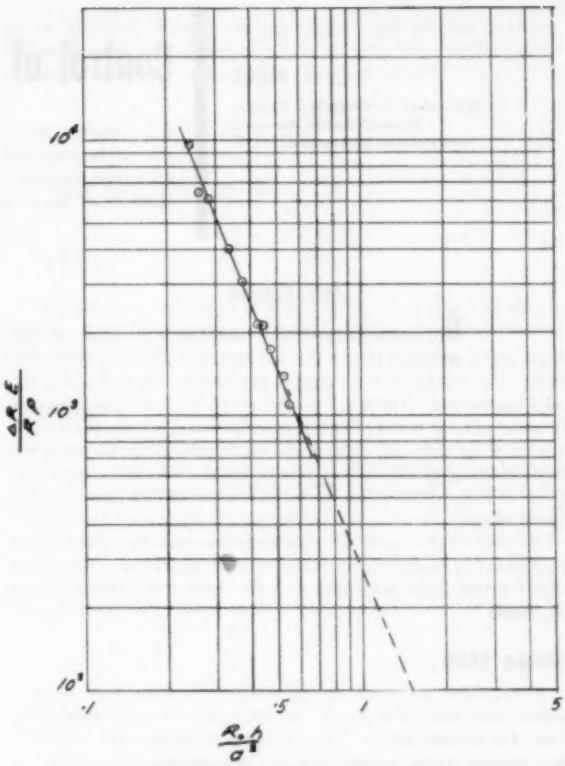

Fig. 8 OSU data for tubes 11 to 20

[2] Engineering Supervisor, Aviation Electric Limited, Montreal, Canada. Assoc. Mem. ASME.

E. H. HULL
Mechanical Investigations Section,
General Electric Research
Laboratory, Schenectady, N. Y.

Control of Oil Whip Frequency Ratio

Experiments described in this paper show that a rotatable intermediate sleeve in a journal bearing will change the average oil film velocity and hence can be made to control oil whip frequency. This device should allow oil whip frequency control of shafts running at two or more times their critical speed.

Introduction

Oil whip is generally considered to occur at half shaft speed although in practice the ratio is slightly less than one half. The resultant slip supplies the energy for sustaining the oil whip motion. There are exceptions to the half frequency rule in some critical speed oil whip experiments [1].[1] In these cases the oil whip will lock in with the shaft critical speed when the shaft running speed reaches twice critical. The shaft may continue to whip at its critical speed over a 2-to-1 or larger running-speed range.

We believe that some oil whip problems could be solved if one could control positively the ratio of oil whip frequency to shaft speed rather than accepting the one half value which nature provides.

Simple Theory

A simplified digest of the oil whip mechanism may be presented with the aid of Fig. 1. O' indicates the equilibrium position of a journal center. The journal is rotating at the speed N_j in a bearing whose center is at O. This position O' is chosen by the journal as a result of equilibrium between the fixed load W (represented by the force vector RW) applied to the bearing, and the integrated hydrodynamic oil film pressure reaction represented by the equal and opposite force vector WR.

If we assume that oil flow in the supporting oil film region is laminar and that its velocity varies linearly between the boundaries, the average angular velocity of the oil will be $N_j/2$ (see Fig. 1).

Conditions shown in Fig. 1 are for the steady-state running of a loaded bearing without oil whip. If we remove the load W and then strike the shaft in such a way that the journal center will return to its former position O', oil whip may be induced. The oil pressure reaction WR, no longer counterbalanced by RW, acts on O' pushing the journal around O with the torque $WR \times OB$. When O' moves to a new position, WR will change direction, continuing to rotate O' about O in the direction of shaft rotation N_j. This torque will be present for all positions of O' except O.

The maximum speed which the oil film may force O' around O is equal to the average velocity of the oil in the film or $N_j/2$. Actually the oil whip rotational frequency N_o will be slightly less than $N_j/2$. The slip will supply energy for maintaining the shaft in its oil whipping motion as slip in an induction motor provides output energy.

If now we add a rotatable sleeve to the bearing as shown in Fig. 2 we may control the average oil film velocity and the oil whip frequency. The sleeve is made with a small clearance between its outer diameter and the bearing, too small for oil whip. When the

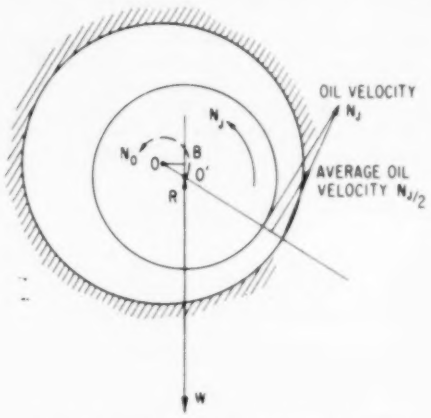

Fig. 1 Average oil velocity in a journal bearing

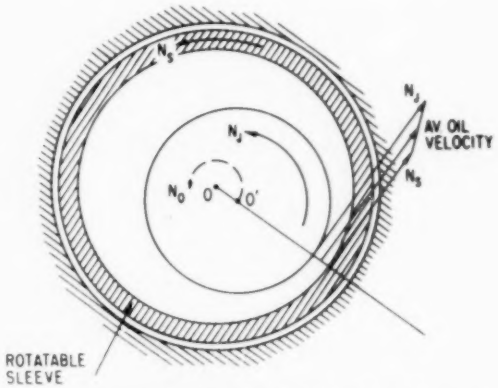

Fig. 2 Average oil velocity in a rotating sleeve bearing

[1] Numbers in brackets designate References at end of paper.

Contributed by the Lubrication Division and presented at the Lubrication Symposium, New York, N. Y., March 14–15, 1960, of The American Society of Mechanical Engineers.

Note: Statements and opinions advanced in papers are to be understood as individual expressions of their authors and not those of the Society. Manuscript received at ASME Headquarters, August 31, 1959. Paper No. 60—LubS-1.

Nomenclature

C_R = radial clearance, in.
n = eccentricity ratio, OO'/C_R, dimensionless
N_j = shaft speed, rpm
N_o = oil whip rotational frequency, rpm
N_s = sleeve speed, rpm
N_o/N_j = oil whip frequency ratio, dimensionless
O = bearing center
O' = journal center
OO' = eccentricity, in.
W = load, lb

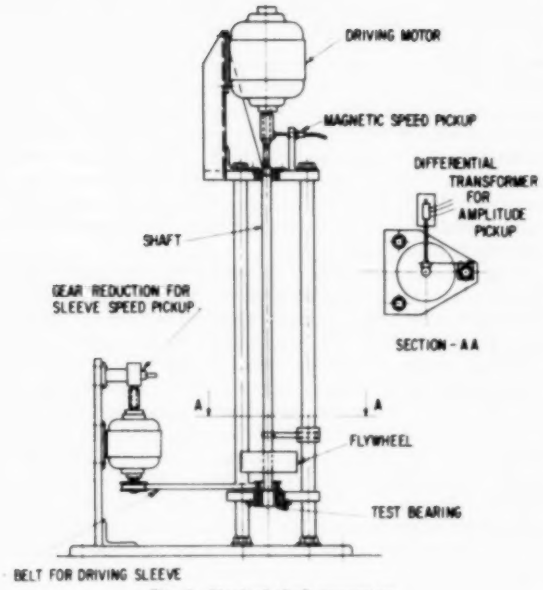

Fig. 3 Vertical shaft apparatus

sleeve speed is N_s the average angular oil velocity, between the sleeve and journal, will be $(N_j + N_s)/2$. Oil whip frequency should be equal to or slightly less than this value or

$$N_o \gtrsim \frac{N_j + N_s}{2} \tag{1}$$

and the oil whip frequency ratio will be

$$\frac{N_o}{N_j} \gtrsim \frac{N_j + N_s}{2N_j} \tag{2}$$

Sleeve rotation in the same direction as the journal is turning will increase the oil whip frequency ratio N_o/N_j; reverse rotation will decrease this ratio.

Apparatus

A simple vertical shaft apparatus was built as shown in Fig. 3. The main shaft is 1 in. in diameter and $36^{13}/_{16}$ in. between bearing centers. At the upper end the shaft is supported in a single-row ball bearing which may be considered as a pivot bearing for small radial displacements of the shaft's lower end. The shaft is driven by a 1-hp d-c motor through a pair of metal universal joints.

At its lower end the shaft is supported by the test bearing. Two bearing types were used in these experiments as shown in

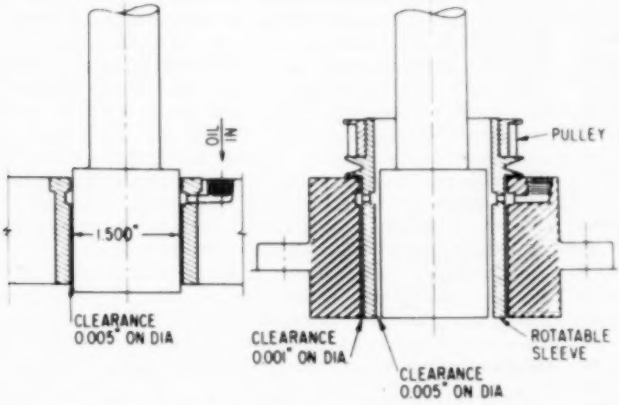

Fig. 4 Plain bearing and rotating sleeve bearing

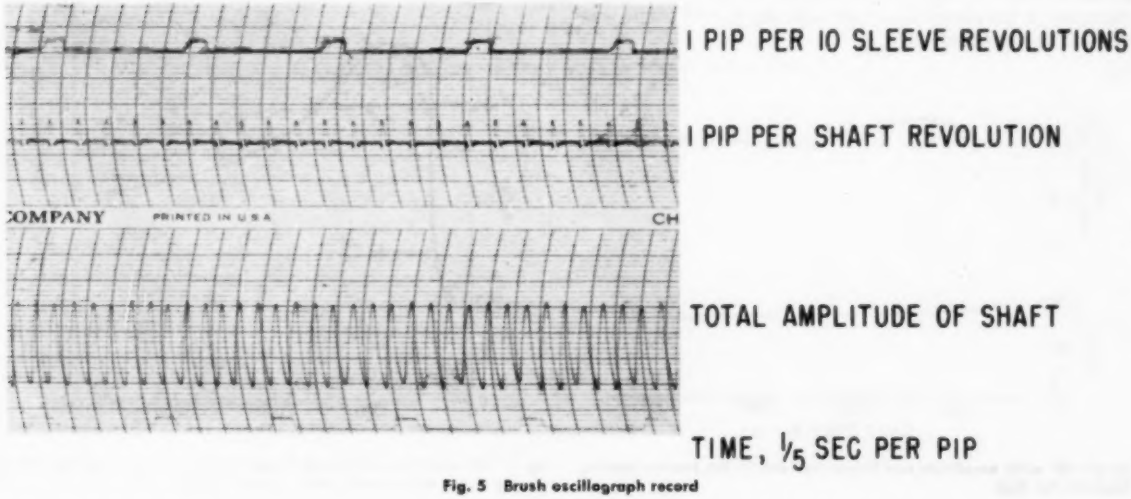

Fig. 5 Brush oscillograph record

Fig. 4. A normal bearing (Fig. 4*a*) is edge oiled from a groove near the top supplied by a gear pump at 5 psi. In Fig. 4(*b*) the same journal is shown surrounded by a rotatable sleeve running in a bearing similar to that shown in Fig. 4(*a*). The sleeve-journal surface is oiled via 8 holes passing through the sleeve. Diametral clearances between the bearing and sleeve are small, but large between sleeve and journal. In the simple bearing (Fig. 4*a*) the diametral clearance is 5.0 mils. The bearing with a sleeve shown in Fig. 4(*b*) has a diametral clearance between the bearing and sleeve of 1 mil, and between the sleeve and journal of 5.0 mils.

The sleeve may be rotated in either direction from an external variable speed motor and timing belt (no slippage).

Just above the test bearing a 23-lb flywheel is attached to the shaft. This weight was added to make the oil whip movements more regular and repeatable.

Instrumentation is relatively simple. Radial shaft displacements are picked up immediately above the bearing through contact with the shaft by a differential transformer excited at 10,000 cps. The resulting signal, after being electronically treated, appears as a trace on Brush oscillograph paper (see Fig. 5). Three other traces appear on this oscillograph record; a one-fifth-second time pip, a once-per-revolution shaft pip, and a pip at once-per-ten revolutions of the sleeve.

Results and Discussion

With the bearing arrangement shown in Fig. 4(*a*), data were taken which show the oil whip frequency ratio N_o/N_j and total amplitude of the oil whip motion versus shaft speed. As plotted in Fig. 6 we see that N_o/N_j varies from 0.49 at low speed to 0.46 at 4000 rpm. Presumably the energy requirements for maintaining whip at high speeds are greater than at lower speeds, hence the larger slip to supply this energy. Whip amplitude drops off rapidly at low speed where the whipping tendency of the shaft tends to disappear [2].

The bearing arrangement was changed to that shown in Fig. 4(*b*) incorporating the rotatable sleeve. With a sleeve speed of zero, data shown in Fig. 7 were taken. N_o/N_j results are about as shown in Fig. 6, although in the Fig. 7 case the shaft oil whipped at a lower shaft speed. Data shown in Figs. 6 and 7 have established the classical oil whip frequency ratio of 0.48 to 0.5 for this apparatus. Other investigators report a similar behavior in frequency ratio [2, 3].

When the bearing sleeve is rotated, the ratio N_o/N_j may be changed radically. Data for N_o/N_j versus sleeve speeds are plotted in Fig. 8 for several shaft speeds from 500 to 4000 rpm. The slope of the curves drawn through the plotted points is as required by expression (2)

$$\frac{N_o}{N_j} \gtrless \frac{N_j + N_s}{2N_j}$$

where these curves pass through the zero sleeve speed point. When the shaft and sleeve are rotating in the same direction, Equation (2) is satisfied for the entire tested range for shaft speeds of 500 and 1000 rpm. In the remainder of the conditions covered by Fig. 8, the values of N_o/N_j fall below the constant slope required by expression (2) for high sleeve speed in the same direction as shaft rotation and at all sleeve speeds for reverse direction. No explanation is offered for the departure from linearity in the regions mentioned.

This method of controlling oil whip frequency ratio appears effective over the speed ranges used in these experiments. N_o/N_j has been increased up to 8 times normal and reduced to $^1/_8$ normal, a variation of 24-fold. We see no reason why the range cannot be extended in the upward direction without limit. The upper limits shown in Fig. 8 are dictated by motor speed and power in our apparatus. When the sleeve rotates backward with respect to the shaft, oil whip amplitude becomes small ($^1/_4$ mil total amplitude). Fig. 9 shows the decrease in oil whip amplitude in terms of eccentricity ratio as the backward sleeve rotation is increased. For the conditions tested in this apparatus and at 4000 rpm CW shaft speed, the oil whip amplitude was reduced from 3 mils at zero sleeve speed to $^1/_2$ mil at 2000 rpm CCW sleeve speed.

It might be useful to speculate on the application of this device to a machine which we assume is limited by critical speed oil whip, in that the first shaft critical speed must be held to greater than one half the running speed in order to avoid critical speed oil whip. Assuming a shaft speed of 1000 rpm, Fig. 8 tells us that with no sleeve we must design the shaft with sufficient stiffness to keep the first shaft critical above 500 rpm in order to avoid critical speed oil whip at the ratio $N_o/N_j = 0.5$. However, if we install a sleeve and rotate it backward at 500 rpm then N_o/N_j will be less than 0.2, and we may run a shaft at 1000 rpm whose critical speed is 200 rpm without encountering critical-speed oil whip. Furthermore, at this sleeve speed the amplitude of oil whip will be reduced to $^1/_8$ normal as indicated in Fig. 9.

This oil whip control device as tested depends on a close clearance between the rotating sleeve and the outer fixed bearing to suppress any oil whip tendency in the oil film occupying this space. A close running clearance may be assured by making the sleeve expandable as in a very wide piston ring.

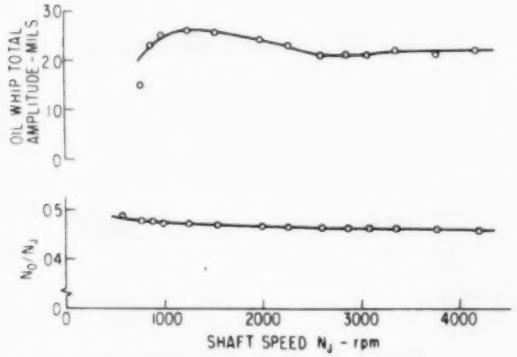

Fig. 6 Oil whip amplitude and frequency ratio in the journal bearing shown in Fig. 4(*a*)

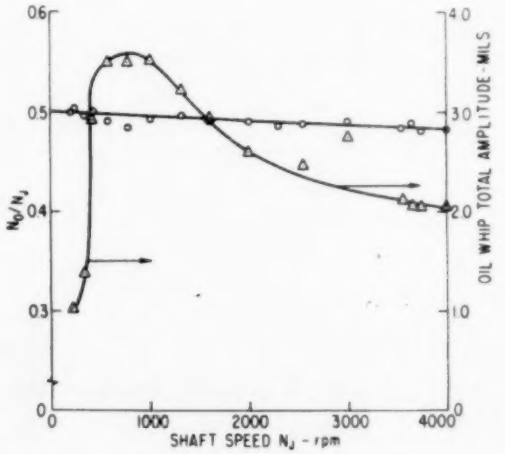

Fig. 7 Oil whip amplitude and frequency ratio for the bearing with a rotating sleeve shown in Fig. 4(*b*). Sleeve speed = 0.

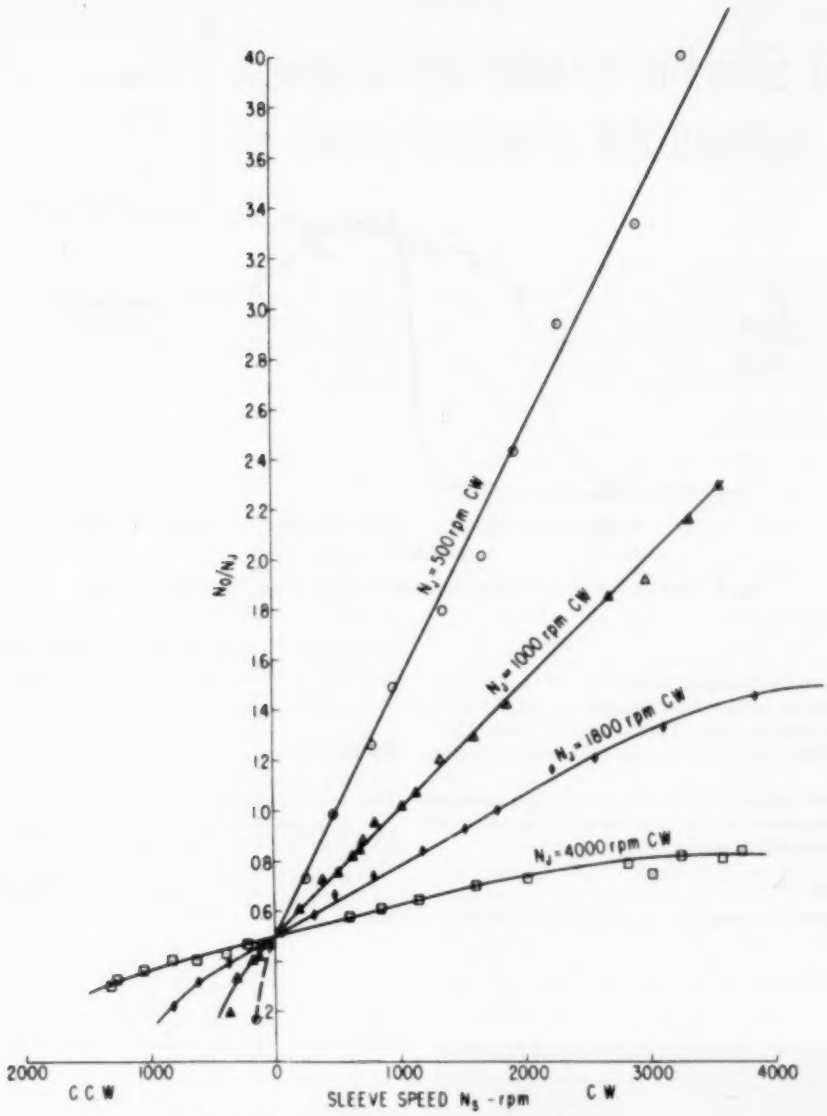

Fig. 8 N_o/N_j versus sleeve speed for several shaft speeds

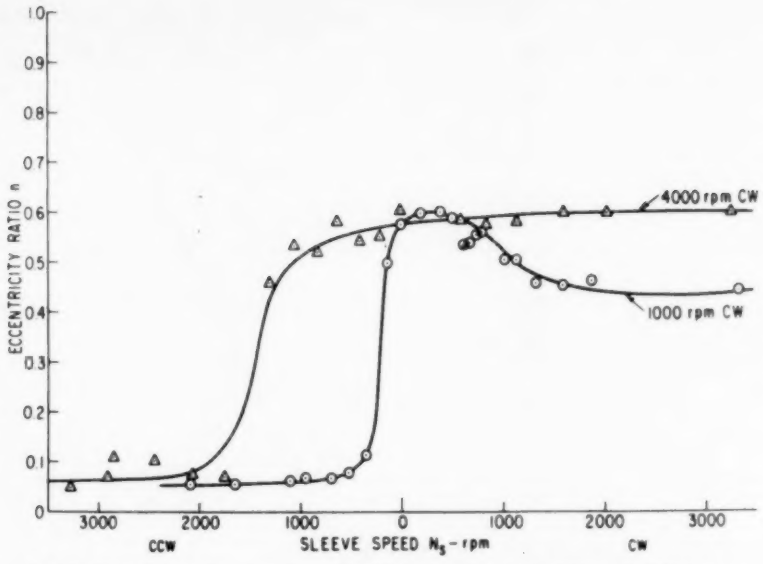

Fig. 9 Eccentricity ratio versus sleeve speed for two shaft speeds, 1000 and 4000 rpm

Conclusions

From the experimental results described we see that oil whip frequency ratio can be controlled by inserting a rotatable sleeve in an oil whipping bearing. In addition, the oil whip amplitude is much reduced when the sleeve is rotated backward with respect to the shaft.

We may infer that average oil film velocity is a simple average of the boundary velocities over the range shown in Fig. 8 in which the shaft-speed curves are straight lines.

Acknowledgments

The author wishes to express his appreciation for assistance from several members of the General Electric Research Laboratory staff, in particular A. J. Nerad, O. Brusdal, F. Dickey, and K. A. Darrow.

References

1 O. Pinkus, "Experimental Investigation of Resonant Whip," TRANS. ASME, vol. 78, 1956, pp. 965–983.

2 G. F. Boeker and B. Sternlicht, "Investigation of Translatory Fluid Whirl in Vertical Machines," TRANS. ASME, vol. 78, 1956, pp. 13–19.

3 D. L. Newkirk and H. D. Taylor, "Shaft Whipping Due to Oil Action in Journal Bearings," *General Electric Review*, vol. 28, 1925, pp. 559–568.

K. L. JOHNSON
Lecturer in Engineering,
Engineering Laboratory,
University of Cambridge,
Cambridge, England

A Note on the Influence of Elastic Compliance on Sliding Friction in Ball Bearings

In a recent paper A. B. Jones [1][1] analyzed the way in which the motion of a ball in a rolling bearing is controlled by friction forces developed in the zones of contact between the ball and the races. In that study the surfaces are permitted to compress elastically so that contact is established over an elliptical area defined by the Hertz theory. On the other hand, tangential compliance of the surfaces under the action of interfacial friction forces is explicitly excluded from consideration.

The present author has recently investigated several aspects of the effect of tangential elastic displacements in the contact zone on the rolling motion of a ball [2, 3]. In this note discussion will be restricted to effect of tangential compliance on the friction moment resisting the motion of a ball which is spinning whilst rolling (denoted by Q_s in reference [1]). The problem then concerns a ball of radius r, which has a forward rolling velocity U while having at the same time an angular velocity of spin ω_s about an axis perpendicular to the contact surface. It is required to determine the magnitude of the moment about this axis, Q_s, due to friction forces at the interface.

If tangential displacements in the contact area are ignored, the rolling motion does not contribute to the relative velocity between points in the surface of contact, so that the relative motion reduces to one of simple rigid-body spin about a normal axis through the center of the contact ellipse; as though the ball were pivoting about the axis without any forward roll. Assuming that the frictional force at any point in the contact area is equal to the product of a constant coefficient of friction μ and the normal pressure at that point, the friction moment is easily calculated to be given by

$$Q_s/Pa = \frac{3}{8}\,\mu E(\epsilon) \qquad (1)$$

where $E(\epsilon)$ is the complete elliptic integral of the second kind whose modulus depends upon the shape of the contact ellipse according to $\epsilon = (1 - b^2/a^2)^{1/2}$. This is equation (179) in reference [1] from which the notation is also taken.

The effect of tangential elastic displacements during rolling is to make the actual pattern of relative velocities between contacting points much more complex. Particularly for small angular velocities of spin, interfacial slip is eliminated from an appreciable fraction of the contact area. It is shown in reference [2] that slip initiates at the trailing edge of the contact surface and spreads over the contact area as the spin velocity is increased in relation to the rolling velocity. However, even at the large spin velocities normally encountered in angular contact bearings, an area of no slip still exists near to the leading edge of the contact. The pattern of slip for a circular contact area has been observed using a rubber ball rolling on a transparent plane onto which a screen of ink dots had been printed previously, Fig. 1. The ink has smeared where slip occurred, and it can be seen that the slip is restricted to the rearward quadrants of the contact area. The pattern is very different from the rotationally symmetrical one which would be expected for rigid-body spin. It is now clear that the frictional spinning moment exerted during rolling will be less than the value predicted by equation (1) for two reasons: (*a*) Since slip does not occur everywhere, the friction forces will not reach their limiting value everywhere, and (*b*) slip is not always in a circumferential direction so that the friction forces will not exert a maximum moment about the spin axis.

Experiments [3] with a ball in a very shallow groove (circular contact area) showed the frictional spinning moment to be a function of the parameter $\omega_s r/U$ and to have a *maximum* value about 60 per cent of the pivoting friction moment given by equation (1).

To cover the practically more important situation of close conformity between the ball and the groove in which it rolls, further experiments have been performed which are reported in this note.

The races of a commercial thrust bearing were used having a track of 1.46-in. radius and a groove of 0.231-in. radius. In all the experiments the surfaces were oiled and then lightly wiped dry of surplus oil to eliminate any hydrodynamic action. To simulate the conditions under which equation (1) might be expected to apply, balls of different size were pivoted about the spin axis (without rolling) under a wide range of load. The measurements showed that in each case the friction moment Q_s was directly proportional to (load $P)^{2/3}$ thereby indicating that the coefficient of friction was reasonably constant. The results for different ball sizes are given in Fig. 2, where it will be seen that they fit equation (1) very closely taking a value of $\mu = 0.125$. This value, although high compared with that quoted by Jones [1] is consistent with the author's previous work.

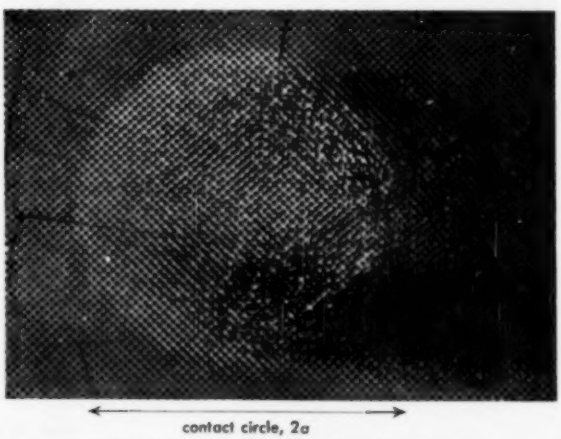

Fig. 1 Circle of contact of a rubber ball rolling with spin on a transparent plane showing pattern of slip
← Forward rolling direction of ball, U
↻ Spin direction of ball, ω_s

[1] Numbers in brackets designate References at end of paper.

Contributed by the Lubrication Division and presented at the Lubrication Symposium, New York, N. Y., March 14–15, 1960, of The American Society of Mechanical Engineers. Manuscript received at ASME Headquarters, August 27, 1958. Paper No. 60—LubS-2.

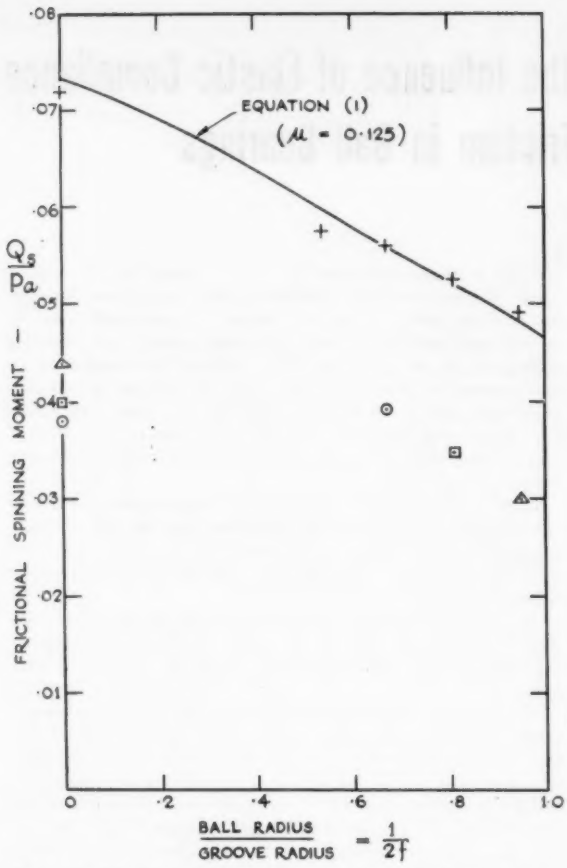

Fig. 2 Frictional spinning moment Q_s as a function of conformity between ball and groove

+ Pivoting without rolling
⊡ Rolling, r/e = 0.128
⊙ Rolling, r/e = 0.107
△ Rolling, r/e = 0.162

The frictional spinning moment was then measured during rolling for comparison with equation (1). In this experiment the bearing rotated freely about a vertical axis, containing three balls only and with no cage. In both this and the pivoting experiment, the friction moment was observed to be independent of speed, which supports the contention that the frictional behavior was not influenced by hydrodynamic action. It might be mentioned here that local contact deformation influences the observation of frictional spinning moments in a way which is perhaps not widely known. It has been shown in reference [3] that a ball in a thrust or angular contact bearing does not take up a position in the trough of the groove, but creeps outward from the bearing axis until the tangential planes at the points of contact are inclined to each other at an angle 2β. The positions of the balls in the groove were carefully observed from which the angle β was found in some cases to be as much as $4^1/_2$ deg. The spin-friction moment is then related to the moment about the bearing axis Q_s by the expression

$$Q_s = Q_s \left(\cos \beta + \frac{e}{r} \tan \beta \right) \tag{2}$$

where e is the radius of the track of the ball center. It is finally necessary to allow for the contribution of elastic hysteresis to the resistance to rotation of the bearing. Here the theory of Tabor [4] has been found satisfactory, by which

$$(Q_s)_{hy} = 0.0018 \frac{e}{r} Pb \tag{3}$$

where P is the normal load per ball.

The results of these measurements are also plotted in Fig. 2. It is evident that even with close conformity between the ball and groove the spin frictional moment during rolling is appreciably lower than the value calculated by equation (1).

It should be mentioned in conclusion that, although the angular velocities of spin in the pivoting experiments and the rolling experiments were the same so that direct comparison between them is valid, the actual magnitude of the spin velocities (1–4 radians/sec) was small compared with high-speed ball-bearing practice. At high speed it is likely that the behavior of the contact forces will be further complicated by hydrodynamic action.

References

1 A. B. Jones, "Ball Motion and Sliding Friction in Ball Bearings," TRANS. ASME, Series D, JOURNAL OF BASIC ENGINEERING, vol. 81, 1959, pp. 1–12.

2 K. L. Johnson, "The Effect of Spin Upon the Motion of an Elastic Sphere Rolling on a Plane," *Journal of Applied Mechanics*, vol. 25, TRANS. ASME, vol. 80, 1958, pp. 332–339.

3 K. L. Johnson, "The Influence of Elastic Deformation Upon the Motion of a Ball Rolling Between Two Surfaces," *Proceedings, I.Mech.E.*, vol. 173, 1959, p. 795.

4 D. Tabor, "The Mechanism of Rolling Friction—the Elastic Range," *Proceedings, Royal Society (London)*, vol. 229, series A, 1955, pp. 198–220.

Pressure Oscillations in a Water-Cooled Nuclear Reactor Induced by Water-Hammer Waves

P. LIEBERMAN

E. A. BROWN

Armour Research Foundation of Illinois Institute of Technology, Technology Center, Chicago, Ill.

Shutdown of the Babcock & Wilcox[1] nuclear reactor water coolant pumps will cause check valves to close which will induce the generation of water hammer in the system. The magnitude, frequency, and duration of possible pressure oscillations in the pipeline and the discharge of the pressure oscillations into the attached plenum chamber were evaluated. Although the plenum chamber contains a great number of suspended rods, it was possible to establish the upper bound for the pressure loading across the internal structure of the plenum chamber at various stations for determination of design criteria.

Introduction

A Origin of Problem. Shutdown of the reactor water pumps was expected to interrupt the steady flow of the water column in the pipe which would have resulted in sudden closure of a check valve. Sudden closure of the check valve would have then caused water-hammer pressure pulses to travel along the approximately 60 ft of pipeline between the check valve and plenum chamber. Thus, the water-hammer waves could have caused stress loads on the check valve at one end of the pipeline, and then the discharge of pressure pulses into the plenum chamber at the other end of the pipeline. The purpose of this report is to analyze the fluctuating pressure loads on the check valve and also on the components inside the plenum chamber.

B Description of the Water-Hammer Cycle in the Pipe. Qualitatively, the water-hammer cycle can be described as follows: The sudden closure of the check valve interrupts the steady flow of the water column in the pipe. The kinetic energy of the flowing water is converted into the elastic energy of the stretched pipe and compressed water. This condition of zero water velocity and stagnation pressure spreads from the check valve to the plenum chamber with acoustic velocity as is shown by the uppermost schematic of Fig. 1.

The second portion of the cycle begins after the entire line is filled with compressed stagnant water that is at a higher pressure than the water in the plenum chamber. Thus the pipe begins to discharge the high pressure water back into the plenum chamber. As shown in Fig. 1, the initial reservoir pressure is being propagated into the pipeline, and the initial magnitude of the velocity of the water is being restored except the direction of the velocity is opposite to the initial direction.

The third portion of the cycle begins after all the water in the pipe is at the initial pressure, but the water is flowing out of the pipe into the plenum chamber. The water column that moved into the plenum chamber in the previous cycle was moved by the regained elastic energy stored in the stretched pipe and compressed water and also by a force created by a pressure difference between the pipe and reservoir. However, in this cycle, the

[1] This program was sponsored by The Babcock & Wilcox Company, Atomic Energy Division, Lynchburg, Virginia.

Contributed by the Water-Hammer Subcommittee of the Hydraulic Division and presented at the Gas Turbine Power & Hydraulic Conference, Houston, Texas, March 6–9, 1960, of THE AMERICAN SOCIETY OF MECHANICAL ENGINEERS.

NOTE: Statements and opinions advanced in papers are to be understood as individual expressions of their authors and not those of the Society. Manuscript received at ASME Headquarters, July 10, 1959. Paper No. 60—Hyd-2.

Nomenclature

a = smaller cross-sectional area
A = larger cross-sectional area
b = wall thickness of pipe
c = speed of sound
D = diameter
E = modulus of elasticity of steel
f = pipe friction factor proportional to the water flow velocity squared
F = pipe friction factor proportional to the water flow velocity
g = gravitational constant and conversion factor $32.2 \frac{\text{lb}_M \text{ ft}}{\text{lb}_F \text{ sec}^2}$
G_n = a constant
H_n = a constant
K = bulk modulus of elasticity of water
L = length of pipe
n = an integer
N = number of pressure reversals
P = pressure
Q = effective modulus of elasticity of pipe and water
r = radius
t = time
T = time dependent function
U = velocity
W = weight density of water
X = space dependent function
β = frequency of water-hammer cycle defined by Equation (23) as $\sqrt{\lambda^2 c^2 - \left[\frac{F}{2\rho}\right]^2}$
η = area ratio factor, $1 - A/a$
$\lambda = \frac{2n-1}{2}\frac{\pi}{L}$
θ = dummy variable
ξ = area ratio factor, $1 + A/a$
ρ = mass density of water
σ = Poisson's ratio ($\sigma = 3.6$ for iron or steel)
τ = time
$\psi = 4\frac{\eta}{\xi}\frac{U_1}{c} + \left[\frac{\eta}{\xi - 1}\frac{U_2}{c}\right]^2 - \frac{2\eta^2 U_2}{\xi(\eta - 1)c}$

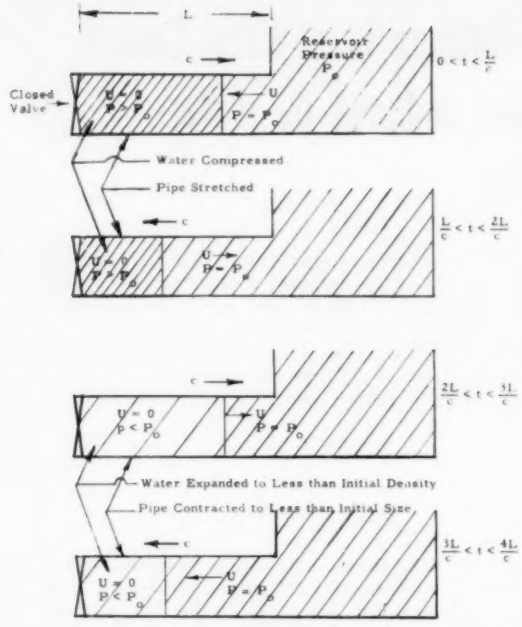

Fig. 1 Water-hammer wave cycle caused by instantaneous valve closure

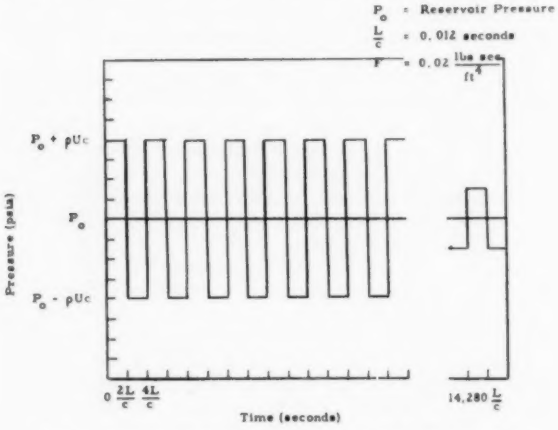

Fig. 2 Pressure oscillation in the pipeline at the closed valve

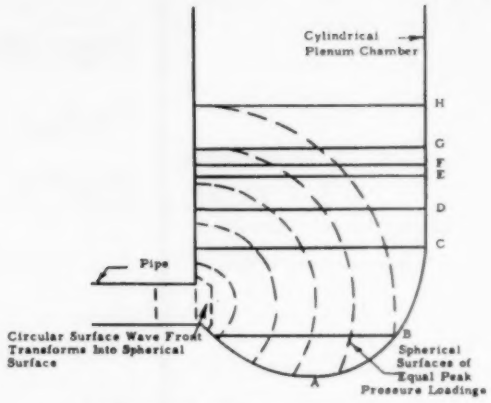

Cylindrical Section	Per Cent Cross-Sectional Area Available for Fluid Flow
A - B	25.0
B - C	83.8
C - D	80.4
D - E	64.8
E - F	21.0
F - G	29.8
G - H	18.2

Fig. 3 Contours of equal pressure loading in plenum chamber caused by water-hammer waves discharging from the pipe

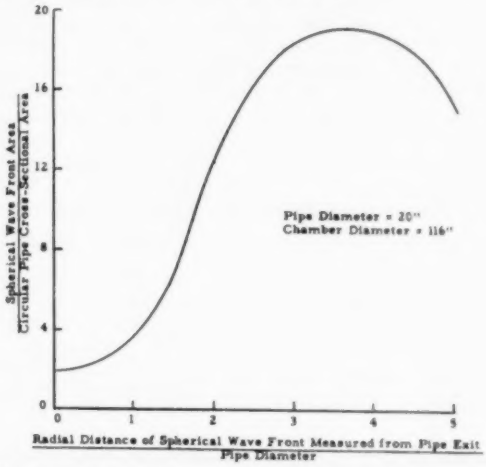

Fig. 4 Contour of two-dimensional duct for a plane wave which is hydraulically equivalent to the three-dimensional plenum chamber containing a spherical wave

water column in the pipe continues to discharge into the plenum chamber because of the momentum of the water column. The water column tends to empty the pipeline and thus the water pressure drops to below plenum chamber pressure. When the water pressure attains a sufficiently low level in the pipeline, the momentum of the water outflow is balanced by the adverse pressure gradient so the fluid comes to rest.

The fourth portion of the cycle begins after the entire fluid column is stagnated and at a pressure that is lower than the plenum chamber water pressure. This pressure differential causes plenum chamber water to flow into the pipe at the plenum chamber pressure and with the initial velocity magnitude and direction. The lower schematic of Fig. 1 shows this condition.

Fig. 2 portrays the pressure-time history of the water-hammer cycle at the check valve end of the pipe.

C Description of the Water-Hammer Cycle in the Plenum Chamber. The water-hammer wave discharges into the plenum chamber and induces pressure loads on the plenum chamber structure. The initial wave from the pipe exit is a steep fronted, flat topped compression wave. As the wave spreads into the large plenum chamber, the compression wave changes wave form and reduces in strength.

At the pipe exit the wave front is a planar disk, but at several pipe diameters downstream of the pipe exit the wave front becomes spherical, as shown in Fig. 3. Since the wave front propagating into the plenum chamber is obstructed by the internal structure and bounded by the cylindrical geometry of the plenum chamber, the surface area of the wave front is distorted from that of a simple spherical wave. The internal structure and the bounding cylindrical walls cause wave reflections to superimpose themselves upon the compression wave emanating from the pipe

exits. In addition, as shown in Fig. 4, the spherical wave moving biasly through an obstructed cylinder becomes equivalent to a plane wave moving through a duct of varying cross section which will cause only a portion of the incident compression wave to be transmitted and the rest to be reflected. Thus, the plenum chamber contains a complicated array of undulating pressure waves. These pressure oscillations cause dynamic loads on the reactor plenum chamber internal structure.

Explanation of Model Used in the Analysis

As a matter of convenience, the water-hammer pressure oscillations in the system are treated in two parts. First, the pipe will be considered independent of the plenum chamber by applying the usual open-ended pipe boundary conditions. Second, the transmitted and reflected pressure waves at the open-ended pipe is considered with particular emphasis on the wave transmitted into the plenum chamber.

A Pipe. The analysis of the pressure oscillations in the pipe follows the usual acoustic approximations that second order terms such as $U\partial\rho/\partial x$ and $U\partial U/\partial x$ are negligible. Since the decay of the oscillations is of primary concern, the frictional effects must be included.

One end of the pipe is terminated by a valve which is assumed to close instantaneously, thus providing a zero velocity boundary. The other end of the pipe is open providing a constant pressure boundary when entrance and exit losses are neglected.

B Plenum Chamber. Herein the assumption of a constant pressure between the pipe and plenum chamber is investigated. Rudinger [2][1] has shown that, for a pipe terminated by an infinite reservoir and for distances greater than a few pipe diameters from the open end, the pressure in the pipe is that given by a constant pressure boundary. Since the pipe is 36-pipe-diameters long, the constant pressure boundary condition is satisfactory for the analysis of the pipe. On the other hand, at distances of the order of a few pipe diameters into the plenum chamber, pressure-time histories are of interest.

The plenum chamber contains the reactor core and associated structure in a cylindrical shell. This is a complicated three-dimensional system. In order to obtain an estimate of the pressure-time history within the plenum chamber, the three-dimensional system was reduced to an equivalent one-dimensional system of varying cross section and analyzed by the acoustic approximation.

The interaction of the spherical wave fronts with the complex internal structure and cylindrical boundary of the plenum chamber causes wave reflections and viscous friction losses that lead to pressure wave shape distortion. Thus, neglecting these effects results in a conservative estimate of the average pressure loads at various stations in the plenum chamber. This, however, does not exclude the possibility of local high pressures that are characteristic of wave reinforcement. The extent of the wave shape distortion makes it unreasonable to carry the analysis beyond the point where the wave approaches the end of the reactor vessel.

Damage Potential

A Pipe. As shown in Equation (5), the pressure pulse associated with a water-hammer wave is given by

$$\Delta P = \rho c(\Delta U)$$

Thus, for example, velocity changes of only 3 ft per sec in a fluid having a density of 62 lb per cu ft and a sonic velocity of 5000 ft per sec, could cause a pressure pulse of approximately 200 psi. If the fluid were at an elevated temperature and pressure, then the density and sonic velocity could become 50 lb per cu ft and 3000 ft per sec, so that the 3 ft per sec fluid velocity would then only cause approximately 100 psi pressure pulses. The latter example more closely describes the condition anticipated in the coolant water of a reactor.

For the condition of 60 ft of pipe length, and a sonic velocity of 5000 ft per sec, the pressure pulse at the check valve would reverse itself every $2L/c = 24$ milliseconds. But when the sonic velocity is reduced to 3000 ft per sec, the pressure pulse at the check valve would reverse itself every 40 milliseconds.

The amplitude of the water-hammer cycle decays exponentially because of the pipe wall frictional effects [Equation (23), where $P - P_0$ is proportional to $e^{-\frac{F}{2\rho}t}$], although the periodicity of the water-hammer cycle can be considered constant, Equation (23). For exponential pressure decay it is usually assumed that the time for the pressure pulse to decay to 36.7 per cent of its initial value is significant. Thereafter, the pressure decays at a much slower rate. Hence, the pressure pulse will decay to 36.7 per cent of its initial value in the time, τ_D.

$$\tau_D = \frac{2\rho}{F} = \frac{4D}{fU}$$

Continuing with this hypothetical example, only the diameter of $D = 1.67$ ft and friction factor of $f = 0.013$ need be specified to determine $\tau_D = 171.5$ sec, i.e., 3570 cycles or 7140 pressure reversals at the check valve before the pressure amplitude-decays to within 36.7 per cent of its initial value. If entrance and exit losses at the junction between the pipe and plenum chamber is taken into account, then it can be shown that the decay time τ_D is shortened from 3 minutes to less than 1 minute.

The pressure and temperature level of the water within the pipe is significant from two aspects; (1) magnitude of pressure pulse; (2) mechanisms of pressure pulse decay. For the first consideration, suppose the pressure level is raised from P to P' and the temperature level is raised from T to T' then the magnitude of the new pressure pulse is P'.

$$P' = \rho' U c' = \rho U c \left(\frac{\rho' c'}{\rho c}\right) = \rho U c \left(\frac{\rho'}{\rho}\frac{K'}{K}\right)^{0.5}$$

For the second consideration, if the pressurization level is greater than the water-hammer pressure amplitude then wall friction and entrance-exit losses decay the pressure fluctuations. However, if the pressurization level is less than the water-hammer pressure amplitude then there is an additional decay mechanism as was shown by the experiments and analysis of Leconte [3]. Each time the water attempts to achieve pressure below the vapor pressure, the pressure is held constant at the vapor pressure or at a metastable pressure level lower than the vapor pressure until the next cycle begins. Thus the negative pressure fluctuations are chopped off. The irreversible losses of this condition cause a more rapid amplitude decay than in the conventional water-hammer condition. In addition, the time period between cycles becomes progressively shorter. Leconte [3] introduces the term "Coefficient of Restitution," which is used to evaluate the progressive amplitude decay and frequency increase of water-hammer waves which are driven by a reservoir of insufficient pressurization.

B Plenum Chamber. The peak pressure loading of the first incident compression wave as it progresses across the plenum chamber is shown in Fig. 6, and derived in Appendix C.

The pressure distribution at the pipe exit is almost the same as the pressure distribution in the pipe. The pressure distribution near the pipe exit exhibits the pressure decay with increasing distance as in the case of spherical wave propagation from a point source wherein the pressure varies inversely as the first power of the radius. The pressure further downstream from the pipe exit

[1] Numbers in brackets designate References at end of paper.

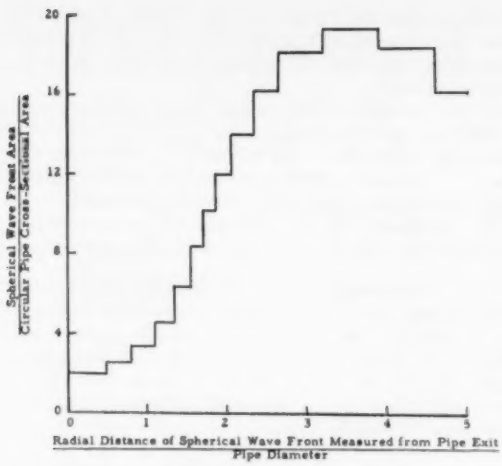
Spherical Wave Front Area
Circular Pipe Cross-Sectional Area
Radial Distance of Spherical Wave Front Measured from Pipe Exit
Pipe Diameter

Fig. 5 Contour of a one-dimensional duct which approximates the propagation of an acoustic wave through a duct of varying cross sections

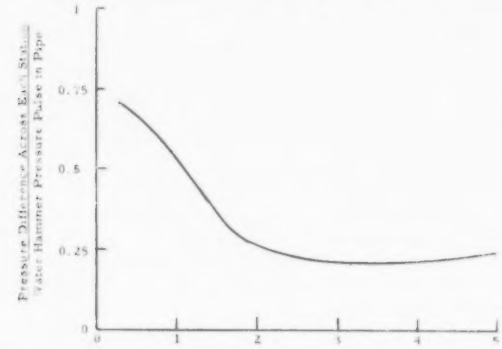

Fig. 6 Pressure loading across each station of the reactor plenum chamber caused by discharge of a water-hammer wave from a pipe

approaches a constant value as in the case of a plane wave moving through a constant area duct. As the wave progresses further into the narrowing cylindrical plenum chamber, the pressure begins to recover. These qualitative trends can be deduced from Figs. 3, 4, and 6.

Fig. 6 is based upon the absence of wave reflections from internal structure, therefore, the solution to the wave propagation characteristics beyond five pipe diameters (2 milliseconds) into the plenum chamber is not realistic. Also, the internal structures do reflect a portion of the compression wave emanating from the pipe exit. Thus, it can be expected that the pressure distribution close to the pipe exit is somewhat higher than that shown in Fig. 6, while further downstream of the pipe exit the pressure distribution is conservative. To compute the pressure loading across a particular structure it is necessary to multiply the pressures presented in Fig. 6 by a factor ranging between 1 and 2. For flat plate structures that are parallel to the incident wave front, the multiplication factor is 2. For structures that are not parallel to the incident wave front and that have other than flat plate shapes, the multiplication factor is greater than 1 but less than 2. After use of the multiplication factor, the resultant pressure loading represents the upper bound of the expected pressure loading because of the omission of viscous dissipation which in the actual case will cause loss of pressure head.

References

1 G. R. Lewitt, "Hydraulics and the Mechanics of Fluids," Sir Isaac Pitman and Sons, Ltd., London, England, 1946, pp. 561–569.
2 G. Rudinger, "The Reflection of Pressure Waves of Finite Amplitude From an Open End of a Duct," *Journal of Fluid Mechanics*, vol. 3, part 1, October, 1957, p. 48.
3 J. M. Leconte, "Experiments and Calculations on the Resurge Phase of Water Hammer," TRANS. ASME, vol. 59, 1937, pp. 691–694.
4 G. R. Rich, "Water Hammer Analysis by the Laplace-Mellin Transformation," TRANS. ASME, vol. 67, 1945, pp. 361–376.
5 A. H. Gibson, "Hydraulics and Its Applications," Constable and Company, Ltd., London, England, 1946, pp. 232–241.
6 G. R. Rich, "Hydraulic Transients," McGraw-Hill Book Company, Inc., New York, N. Y., 1951, pp. 1–7.
7 R. H. Cole, "Underwater Explosions," Princeton University Press, Princeton, N. J., 1948, pp. 18–23.
8 F. M. Wood, "Application of Heaviside's Operational Calculus to the Solution of Problems in Water Hammer," TRANS. ASME, vol. 59, 1937, pp. 707–713.

APPENDIX A

Pressure and Velocity Increase Across a Water Wave of Small Amplitude

The pressure and velocity variation across a small amplitude water wave in one dimension can be derived from the conservation of momentum

$$\frac{\partial U}{\partial t} + U\frac{\partial U}{\partial x} = -\frac{1}{\rho}\frac{\partial P}{\partial x} \tag{1}$$

Since the velocity and rate of change of velocity with distance are small quantities, the product of $U\partial U/\partial x$ is negligible. Hence, Equation (1) reduces to

$$\frac{\partial U}{\partial t} = -\frac{1}{\rho}\frac{\partial P}{\partial x} \tag{2}$$

The solution to Equation (2) can be accomplished by the use of the dummy variable θ

$$\theta = x \mp ct \tag{3}$$

where the minus sign is associated with a wave moving in the positive x-direction. Hence, Equation (3) reduces Equation (2) to

$$\mp c\frac{dU}{d\theta} = -\frac{1}{\rho}\frac{dP}{d\theta} \tag{4}$$

integrating Equation (4) produces the required result presented as

$$\left(\frac{P_2 - P_1}{U_2 - U_1}\right) = \pm\rho c \tag{5}$$

In Equation (5) the ratio of pressure difference to velocity difference is positive when the wave front is moving in the positive U-direction.

APPENDIX B

Decay of Water-Hammer Pressure Oscillations in a Pipe With Friction

The pressure pulse of a water-hammer wave can be described by the one-dimensional equations of conservation of mass, conservation of momentum, and the isentropic definition of the speed of sound in water (neglecting the effect of the pipe)

$$\frac{\partial \rho}{\partial t} + \frac{\partial(\rho U)}{\partial x} = 0 \tag{6}$$

$$\frac{\partial U}{\partial t} + U\frac{\partial U}{\partial x} = -\frac{1}{\rho}\frac{\partial P}{\partial x} - \frac{FU}{\rho} \tag{7}$$

$$\frac{\partial P}{\partial t} = c^2\frac{\partial \rho}{\partial t} \tag{8}$$

Solution of Equations (6), (7), and (8) necessitates the friction force to be proportional to the first power of the fluid velocity. Hence, the friction factor F of Equation (7) is related to the conventional friction factor f by

$$FUL = f\frac{L}{D}\rho\frac{U^2}{2} \tag{9}$$

The assumption of small amplitude water-hammer waves permits the terms $U\partial\rho/\partial x$ and $U\partial U/\partial x$ to be neglected. Hence, Equations (6), (7), and (8) reduce to

$$\frac{\partial \rho}{\partial t} = -\rho\frac{\partial U}{\partial x} \tag{10}$$

$$\frac{\partial U}{\partial t} = -\frac{1}{\rho}\frac{\partial P}{\partial x} - \frac{FU}{\rho} \tag{11}$$

$$\frac{\partial P}{\partial t} = c^2\frac{\partial \rho}{\partial t} \tag{12}$$

Using Equation (12), pressure and velocity relations are determined as per

$$\frac{1}{c^2}\frac{\partial P}{\partial t} = -\rho\frac{\partial U}{\partial x} \tag{13}$$

$$\frac{\partial U}{\partial t} = -\frac{1}{\rho}\frac{\partial P}{\partial x} - \frac{FU}{\rho} \tag{14}$$

To obtain a relationship for the spacial and time distribution of pressure; differentiate Equation (13) with respect to time, and differentiate Equation (14) with respect to space.

$$\frac{\partial^2 U}{\partial x\partial t} = -\frac{1}{\rho c^2}\frac{\partial^2 P}{\partial t^2} \tag{15}$$

$$\frac{\partial^2 U}{\partial t\partial x} = -\frac{1}{\rho}\frac{\partial^2 P}{\partial x^2} + \frac{F}{\rho}\frac{1}{\rho c^2}\frac{\partial P}{\partial t} \tag{16}$$

Equations (15) and (16) combine to form the required pressure relationship to time and space in

$$\frac{\partial^2 P}{\partial x^2} = \frac{1}{c^2}\frac{\partial^2 P}{\partial t^2} + \frac{F}{\rho c^2}\frac{\partial P}{\partial t} \tag{17}$$

The time distribution of pressure can be obtained by using the method of separation of variables in (17). Let

$$P = X(x)T(t) \tag{18}$$

Then

$$X''T = \frac{1}{c^2}XT'' + \frac{F}{\rho c^2}XT' \tag{19}$$

$$\frac{X''}{X} = \frac{1}{c^2}\frac{T''}{T} + \frac{F}{\rho c^2}\frac{T'}{T} \tag{20}$$

The left-hand side of (20) is independent of variations of the right-hand side of (20), and vice versa. Hence, (20) can be written as

$$\frac{X''}{X} = -\lambda^2 = \frac{1}{c^2}\frac{T''}{T} + \frac{F}{\rho c^2}\frac{T'}{T} \qquad \text{where } \lambda = \text{constant} \tag{21}$$

The time distribution of pressure is, therefore, represented by

$$T'' + \frac{F}{\rho}T' + \lambda^2 c^2 T = 0 \tag{22}$$

The characteristic Equation (22) indicates the pressure time history of the water-hammer wave is described by exponentials of the form e^{mt} where

$$m = -\frac{F}{2\rho} \pm i\sqrt{\lambda^2 c^2 - \left(\frac{F}{2\rho}\right)^2} = -\frac{F}{2\rho} \pm i\beta \tag{23}$$

or

$$T = e^{-\frac{F}{2\rho}t}\sum_{n=1}^{\infty}(G_n\cos\beta t + H_n\sin\beta t) \tag{24}$$

Equation (24) is the time-dependent portion of the solution of Equation (18). The time decay of the pressure wave is given by the term $e^{-\frac{F}{2\rho}t}$, and it is this factor that is used for the sample calculations in this report.

The complete solution of Equation (17) is given by Rich [4]:

$$P - P_0 = -\frac{U_0\pi^2 c^2}{4L^2 Q}\sum_{n=1}^{\infty}\frac{(-1)^{n-1}(2n-1)^2 e^{-\frac{F}{2\rho}t}\sin\left[\frac{(2n-1)\pi x}{2L}\right]\left\{\frac{2F\beta}{\rho}\cos\beta t + \frac{F^2}{2W^2}\sin\beta t - 2\beta^2\sin\beta t\right\}}{\beta\left\{\frac{F^2}{4\rho^2} + \beta^2\right\}^2} \tag{25}$$

where

$$\Delta P = 0 \qquad \text{at } x = 0$$

$$U = 0 \qquad \text{at } x = L$$

Note:

The equivalent speed of sound for wave travel, in the combined media of water and pipeline, is given by Gibson [5] and others in

$$c = \frac{1}{\sqrt{\rho Q}} = \frac{1}{\sqrt{\rho\left[\frac{1}{K} + \frac{D}{4bE}(5 - \sigma)\right]}} \tag{26}$$

Gibson developed this equation on the assumption that the pipeline experiences both longitudinal and circumferential stresses. If the longitudinal stress is neglected, then

$$c = \frac{1}{\sqrt{\rho\left(\frac{1}{K} + \frac{D}{bE}\right)}} \tag{27}$$

In this paper

$$c = \frac{1}{\sqrt{\frac{\rho}{K}\left(1 + \frac{KD}{Eb}\right)}} \approx \sqrt{\frac{K}{\rho}} \tag{28}$$

because

$$\frac{KD}{Eb} \approx 0.1$$

hence the definition of the speed of sound used in this appendix, neglecting the contribution of the pipe, is justified.

APPENDIX C

Transmitted and Reflected One-Dimensional Waves in a Duct of Varying Cross Section

When a small amplitude compression wave, propagating through a parallel wall duct, encounters an abrupt increase in cross-sectional area, then a portion of the wave is transmitted as a compression wave and the other portion is reflected as a rarefaction wave. This condition is shown in Fig. 7.

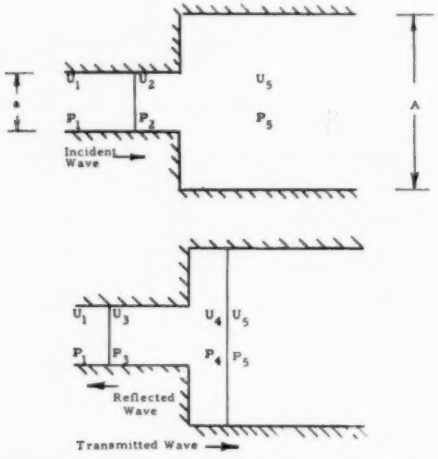

Fig. 7 Propagation of one-dimensional wave through a duct junction containing a change of cross-sectional area

The magnitude and direction of the acoustic waves are determined by the following seven equations:

Conservation of Energy:

$$P_3 - P_4 = -\frac{\rho}{2}(U_3^2 - U_4^2) \tag{29}$$

$$P_2 - P_5 = -\frac{\rho}{2}(U_2^2 - U_5^2) \tag{30}$$

Conservation of Mass:

$$AU_5 = aU_2 \tag{31}$$

$$AU_4 = aU_3 \tag{32}$$

Acoustic Impedance (See Equation 5):

$$\frac{P_2 - P_1}{U_2 - U_1} = +\rho c \tag{33}$$

$$\frac{P_3 - P_1}{U_3 - U_1} = -\rho c \tag{34}$$

$$\frac{P_5 - P_4}{U_5 - U_4} = +\rho c \tag{35}$$

Combining these seven equations according to identity (36) will determine the value of $(P_4 - P_5)$. It is successive evaluation of $(P_4 - P_5)$ at various stations in the reactor plenum chamber that permits thrust loads to be calculated for reactor components at each station between P_4 and P_5.

$$P_5 - P_4 = (P_5 - P_2) + (P_2 - P_1) + (P_1 - P_3) + (P_3 - P_4) \tag{36}$$

$$\rho c(U_5 - U_4) = -\frac{\rho}{2}(U_5^2 - U_2^2) + \rho c(U_2 - U_1) + \rho c(U_3 - U_1) + \frac{\rho}{2}(U_4^2 - U_3^2)$$

$$\rho c(U_5 - U_4) = \frac{\rho}{2}U_5^2\left[\left(\frac{A}{a}\right)^2 - 1\right] + \rho c\left[\frac{A}{a}U_5 - U_1\right] + \rho c\left(\frac{A}{a}U_4 - U_1\right) + \frac{\rho}{2}U_4^2\left[1 - \left(\frac{A}{a}\right)^2\right]$$

$$2c(U_5 - U_4) = U_5^2\left[\left(\frac{A}{a}\right)^2 - 1\right] + 2c\left[\frac{A}{a}U_5 - U_1\right] + 2c\left[\frac{A}{a}U_4 - U_1\right] + U_4^2\left[1 - \left(\frac{A}{a}\right)^2\right]$$

$$\left[1 - \left(\frac{A}{a}\right)^2\right]U_4^2 + 2c\left[\frac{A}{a} + 1\right]U_4 - 4cU_1 + \left[\left(\frac{A}{a}\right)^2 - 1\right]\left(\frac{a}{A}\right)^2 U_2^2 + 2c\left[\frac{A}{a} - 1\right]\frac{a}{A}U_2 = 0$$

let

$$\xi = 1 + \frac{A}{a} \tag{37}$$

$$\eta = 1 - \frac{A}{a} \tag{38}$$

$$\xi\eta U_4^2 + 2c\xi U_4 - 4cU_1 - \xi\eta\left(\frac{U_2}{\xi - 1}\right)^2 + 2c\left(\frac{\eta}{\eta - 1}\right)U_2 = 0$$

$$U_4 = -\frac{c}{\eta} \pm \sqrt{\frac{c^2}{\eta^2} + \frac{4cU_1}{\xi\eta} + \left(\frac{U_2}{\xi - 1}\right)^2 - \frac{2c}{\xi}\frac{U_2}{\eta - 1}}$$

$$U_4 = -\frac{c}{\eta} \pm \frac{c}{\eta}\left\{1 + \frac{4\eta}{\xi}\frac{U_1}{c} + \left[\frac{\eta}{\xi - 1}\frac{U_2}{c}\right]^2 - \frac{2\eta^2}{\xi(\eta - 1)}\frac{U_2}{c}\right\}^{1/2} \quad (39)$$

but

$$\frac{U_1}{c} \ll 1 \quad \text{and} \quad \frac{U_2}{c} \ll 1 \quad (40)$$

and by definition (see Nomenclature)

$$\psi = \frac{4\eta}{\xi}\frac{U_1}{c} + \left(\frac{\eta}{\xi - 1}\frac{U_2}{c}\right)^2 - \frac{2\eta^2}{\xi(\eta - 1)}\frac{U_2}{c} \quad (41)$$

so, by substituting (40) into (41)

$$\psi \ll 1$$

Consequently,

$$(1 + \psi)^{1/2} = 1 + \frac{1}{2}\psi$$

Then

$$U_4 = -\frac{c}{\eta} \pm \frac{c}{\eta}\left\{1 + \frac{1}{2}\psi\right\} \quad (42)$$

Taking the plus sign of the second term in (42)

$$U_4 = +\frac{1}{2}\frac{c\psi}{\eta} = \frac{2}{\xi}U_1 + \frac{\eta U_2}{(\xi - 1)^2}\frac{U_2}{c} - \frac{\eta}{(\eta - 1)}U_2 \quad (43)$$

Again, by substituting (40) into (43),

$$U_4 = \frac{2}{\xi}U_1 - \frac{\eta}{\xi(\eta - 1)}U_2 \quad (44)$$

also by (37) and (38) into (44)

$$U_4 = \left[\frac{1}{1 + \frac{A}{a}}\right]\left[2U_1 + \left(\frac{a}{A} - 1\right)U_2\right] \quad (45)$$

from (31)

$$U_5 = \frac{a}{A}U_2 \quad (46)$$

Thus the required expression for the transmitted pressure wave is

$$P_4 - P_5 = +\rho c(U_4 - U_5) = \rho c\left[\frac{2}{1 + \frac{A}{a}}\right][U_1 - U_2] \quad (47)$$

For successive increases in area, the sequence of (45), (46), and (47) will permit a good approximation of two-dimensional, nonsteady wave motion by the one-dimensional analysis.

DISCUSSION

Henry M. Paynter[3]

The writer is extremely interested in the class of water-hammer problems treated by the authors and has outlined some alternative approaches in a recent paper.[4] In particular, this system can be estimated so rapidly, by applying "Green's Law," that some mention would seem inescapable.

In terms of (P, Q) variables where $Q = AV$ = volume flow, the specific acoustic impedance for the variable section pipe would be written:

$$Z(s) = \rho c/A(s)$$
$$Z = \rho c/a$$

Applying a Green's Law correction to this situation would suggest,

$$P(s)/P \cong \sqrt{Z(s)/Z} = \sqrt{a/A(s)}$$

Since the function $A(s)/a$ has been plotted in Figs. 4 and 5 of the paper, the writer wishes to contribute Fig. 8 and Table 1 of this discussion to suggest that the excellent fit to the authors' curve is worth consideration and comment. Certainly this result is obtained in a minute fraction of the time required for the authors' method of Appendix C.

Table 1

Station	Area ratio	Green's law Pressure ratio
s	A/a	$P/P_0 = \sqrt{a/A}$
0	2.0	0.71
1	3.5	0.53
2	12.0	0.29
3	18.0	0.24
4	19.0	0.23
5	16.0	0.25

[3] Associate Professor of Mechanical Engineering, Massachusetts Institute of Technology, Cambridge, Mass. Mem. ASME.

[4] H. M. Paynter and F. D. Ezekiel, "Water Hammer in Nonuniform Pipes as an Example of Wave Propagation in Gradually Varying Media," TRANS. ASME, vol. 80, 1958, pp. 1585–1595.

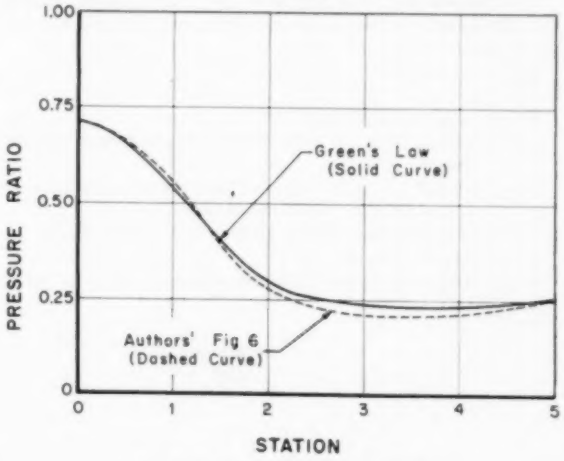

Fig. 8 Green's law pressure estimate

R. M. Rosser[5]

Considering the simplifying assumptions as stated by the authors, we are in accord with the report. However, we would like to point out the error introduced into the calculation of pressure pulse decay time (τ_0) by the authors' applying open-ended pipe boundary conditions, as stated in the report under "Explanation of Model Used in the Analysis."

When the results of the Armour Research Foundation's study were first submitted to The Babcock & Wilcox Company, we were of the opinion that pressure pulse decay time would be determined only by pipe friction and reactor plenum entrance and exit losses. Our calculations indicated that the pressure pulse would decay to 36.7 per cent of its initial value in approximately 30 seconds. Messrs. Lieberman and Brown calculate $\tau_D = 171.5$ sec, considering pipe friction only, and τ_D = less than one minute, when entrance and exit losses are added.

Since actual water-hammer test results indicate pressure pulse decay times of a few tenths of a second, it is apparent that considerably more decaying force is present than the simplifying assumptions allow. An open-ended pipe is equivalent to an infinitely large reactor plenum with no internals. In this case the plenum pressure would never be affected by pressure pulses within the pipe.

With the introduction of the actual finite plenum, a portion of the pipe pressure pulse is transmitted into the reactor as shown by Messrs. Lieberman and Brown's Fig. 6, which indicates a plenum pressure of 25 per cent of the pipe pressure, two pipe diameters from the opening. This plenum pressure increase retards the flow of water out of the pipe as the overpressurized pipe starts to relieve. Therefore the water does not attain the original extinguished velocity in the opposite direction and the reflected negative wave is 75 per cent of the initial positive wave.

On each round trip of the pressure wave there is an additional decay as the reactor absorbs a portion of the pipeline energy. The exact pressure history within the plenum would be difficult to determine because of internal wave reflections, energy absorption by the structure, and pressure relieving upward through the core section.

To illustrate the damping action of a finite plenum, assume that the pressure pulse is attenuated an equal fraction on each round trip.

Let:

P_i = initial pressure pulse
η = fraction of initial pulse which is reflected back into the pipe
n = number of round trips required for pressure pulse to reach 36.7 per cent of initial value
L = length of pipe between check valve and reactor, ft
c = velocity of sound, fps
τ_D = decay time to reach 36.7 per cent of initial value, sec

Then

$$P_i(\eta)^n = 0.367\,P_i$$
$$\eta^n = 0.367$$

and

$$\tau_D = \frac{4L}{c}\,n$$

when

$$\eta = 0.75,\ L = 60,\ \text{and}\ c = 5000$$
$$0.75^n = 0.367$$
$$n = 3.48,\ \text{say, 4 roundtrips}$$

$$\tau_D = \frac{4 \times 60}{5000}\,(4) = 0.19\ \text{sec}$$

Decay times of this order of magnitude occurred consistently during the testing of the Shippingport plant by Brewer Engineering Laboratory. These results are presented by report No. AECU-3854, TIS, Oak Ridge, Tenn., February, 1958, under the title "Water Hammer Tests PWR Land Reactor."

W. T. Rouleau[6]

It appears that this paper is concerned with the conditions of both laminar and turbulent flows in the pipe; Fig. 2 is for a constant frictional resistance F, implying laminar flow, and the hypothetical example is worked out for a constant friction factor f, which implies turbulent flow. However, the exponential time decay factor $\exp(-Ft/2\rho)$, derived in Appendix B, is valid only for laminar flow, in which F is constant. The constancy of F is a necessary condition for Equation (16) to be true, and this equation is basic to the derivation.

Although Equation (9) relates F to the friction factor f this relation does not introduce any generality. If the flow is turbulent then F is not constant but a function of the flow velocity U, and the time-decay factor is not readily apparent from the resulting nonlinear version of Equation (17). Thus some justification is necessary before the exponential time decay can be applied to the hypothetical example, or to any other turbulent flow situation.

E. B. Strowger[7]

This paper presents the solution of a timely but complicated problem and shows how to establish limits for the water-hammer pressures in a reactor supplied with water by coolant pumps. It may be of interest to point out some of the assumptions made by the authors to simplify the mathematics involved and to show that the basic water-hammer relations all stem from the original five Allievi equations.[8] These equations, in terms of the nomenclature used, may be stated as follows:

Allievi Equation I

$$\frac{\partial P}{\partial x} = \frac{W}{g}\left(\frac{\partial U}{\partial t} - U\frac{\partial U}{\partial t}\right) = \rho\left(\frac{\partial U}{\partial t} - U\frac{\partial U}{\partial t}\right)$$

Allievi Equation II

$$\frac{\partial U}{\partial x} = \left(\frac{1}{K} + \frac{D}{bE}\right)\frac{\partial P}{\partial t}$$

Allievi Equation III

$$\frac{1}{c^2} = \frac{W}{g}\left(\frac{1}{K} + \frac{D}{bE}\right) = \rho\left(\frac{1}{K} + \frac{D}{bE}\right)$$

Allievi Equation IV

$$\left\{\begin{array}{l} \dfrac{\partial U}{\partial t} = \dfrac{1}{\rho}\dfrac{\partial P}{\partial x} \\ \dfrac{\partial U}{\partial x} = \dfrac{1}{\rho c^2}\dfrac{\partial P}{\partial t} \end{array}\right\}$$

Allievi Equation V

---

[5] The Babcock & Wilcox Company, Atomic Energy Division, Lynchburg, Va.

[6] Assistant Professor of Mechanical Engineering, Carnegie Institute of Technology, Schenley Park, Pittsburgh, Pa. Assoc. Mem. ASME.

[7] System Project Engineer, Hydro Stations, Niagara Mohawk Paper Corporation, Buffalo, N. Y. Mem. ASME.

[8] Derivation of the Allievi Equations, Discussion No. 5, of ASME Symposium on Water Hammer, 1933.

$$\left\{\begin{aligned} \frac{P_t}{W} &= \frac{P_0}{W} + F\left(t - \frac{x}{c}\right) + f\left(t + \frac{x}{c}\right) \\ U_n &= U_0 - \frac{g}{c}\left[F\left(t - \frac{x}{c}\right) - f\left(t + \frac{x}{c}\right)\right] \end{aligned}\right\}$$

Where $F(t - x/c)$ represents the variable pressure height of the direct water-hammer wave and $f(t + x/c)$ represents the variable pressure height of the indirect water-hammer wave.

Equation (1) may be derived from Allievi's Equation I, if we remember that mass density ρ is equal to W/g and that in this particular application ∂U is negative when ∂P is positive.

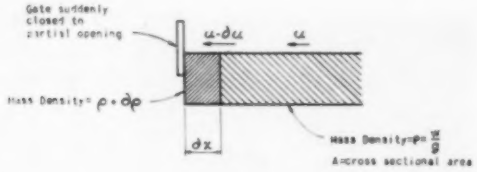

Fig. 9

For arriving at equation (48) reference is made to Fig. 9, which shows the condition upstream from a valve after an increment of closure has taken place. The increase in mass in the column of length ∂x is $\partial\rho \cdot \partial x \cdot A$. This equals the incremental mass entering the length ∂x, i.e., $-\partial t \cdot \partial(U\rho A)$ or $-\partial t \cdot A \cdot \partial(U\rho)$. From this

$$\frac{\partial \rho}{\partial t} + \frac{\partial (U\rho)}{\partial x} = 0 \tag{48}$$

Equation (49), expressing conservation of mass may also be obtained from Allievi's Equation I, as follows:

$$-\frac{\partial P}{\partial x} = \rho\left(\frac{\partial U}{\partial t} + U\frac{\partial U}{\partial x}\right) = \rho\frac{\partial U}{\partial t} + \rho U\frac{\partial U}{\partial x}$$

or

$$\frac{\partial U}{\partial t} + U\frac{\partial U}{\partial x} = -\frac{1}{\rho}\frac{\partial P}{\partial x}$$

Taking friction into account and assuming it varies linearly with velocity in order to get a solution

$$\frac{\partial U}{\partial t} + U\frac{\partial U}{\partial x} = \frac{1}{\rho}\frac{\partial P}{\partial x} - \frac{FU}{\rho} \tag{49}$$

Equation (50) may be derived from Allievi's Equation III, by considering an isentropic condition, i.e., the pipe wall is thick and does not stretch appreciably and no work is thus done on it. Under this condition $\frac{D}{bE}$ becomes negligible and the equation becomes

$$\frac{1}{c^2} = \frac{W}{g}\frac{1}{K} \quad \text{or} \quad c^2 = \frac{gK}{W} = \frac{K}{\rho}$$

But K = volume modulus of water $= \dfrac{\partial P}{\partial V}\Big/ V$ where V represents volume. The change in density $\partial\rho$ is equal to $\dfrac{\partial V}{V} \cdot \rho$ so that

$$K = \frac{\partial P/\partial \rho}{\rho}$$

and

$$c^2 = \frac{\partial P/\partial \rho}{\rho} \cdot \frac{1}{\rho} = \frac{\partial P}{\partial \rho}$$

We may then write

$$\partial P = c^2 \partial \rho$$

or

$$\frac{\partial P}{\partial t} = c^2\frac{\partial P}{\partial t} \tag{50}$$

The assumption that the stretch of the walls is negligible is probably justified on the basis that both the pipes and the reactor vessel are very heavy in construction considering their diameters and that the error involved causes the pressure rise to err on the high side.

An approximate solution[9] of the problem is suggested by the following equation:

$$P \text{ (in psi)} = \frac{Q\int_0^T dt}{\int_0^L \left(\frac{1}{K} + \frac{D}{Eb}\right) A\,dl} = \frac{QT}{\int_0^L \left(\frac{1}{K} + \frac{D}{Eb}\right) A\,dl}$$

where Q is discharge in cfs. For the pipe under consideration $\frac{D}{Eb}$

[9] Paynter and Ezekiel, "Water Hammer in Nonuniform Pipes as an Example of Wave Propagation in Gradually Varying Media," and Discussion by E. B. Strowger, TRANS. ASME, vol. 80, 1958, pp. 1585–1595.

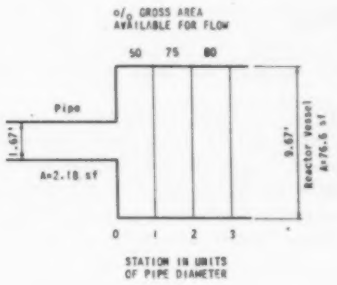

Fig. 10

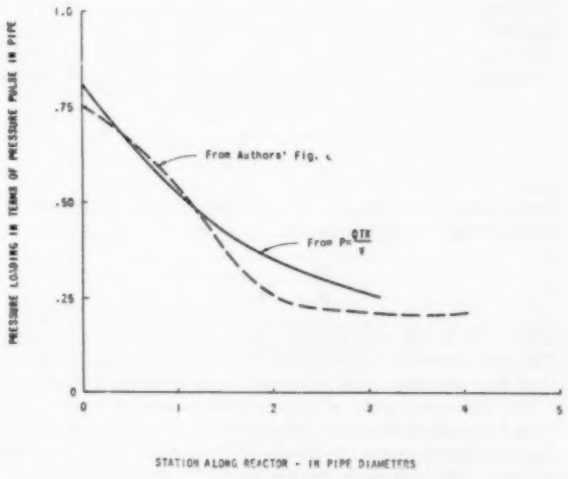

Fig. 11

is negligible so that

$$P = \frac{QTK}{\int_0^L A\,dl} = \frac{QTK}{V}$$

where V is the total volume. By examining the derivation of this equation in the reference cited, it is seen that T is the elapsed time of travel of the direct wave from the check valve and V is the total volume of the water passage beginning at the check valve. Assuming the dimensions and simplified layout of Fig. 10 to be approximately equivalent to the authors' problem the pressure rise may be calculated as shown by Table 2.

Table 2

$T = \frac{L}{4675}$, $P = 1{,}470{,}000 \times \frac{T}{V}$

Station	V, cu ft	L, ft	T, sec	P, psi	%
End of 20-in. pipe	131	60	....	189(Note 1)	100
1.67 ft in reactor	195	61.7	0.0132	100	53
3.33 ft in reactor	291	63.3	0.0135	69	36
5.00 ft in reactor	393	65.0	0.0139	52	27

$Q = 5$ cfs, $K = 294{,}000$ psi, and $QK = 1{,}470{,}000$.

(Note 1) $\frac{cU}{g} = \frac{4675 \times 3}{32.2} = 435$ ft or 189 psi.

Fig. 11 shows the calculated pressure rise as compared with the authors' result shown in Fig. 6. The agreement is good particularly considering the necessity to multiply the pressures presented by a factor ranging from 1 to 2, because of wave reflections.

Authors' Closure

The authors would like to thank Messrs. Paynter, Rosser, Rouleau, and Strowger for their comments concerning our paper.

Professor Paynter's plot of "Green's Law" closely matches the authors' graphical plot of the estimated water-hammer wave pulse transmitted through a pipe of changing cross-sectional area. The close match can be explained by demonstrating that Professor Paynter's solution, $P/P_0 = \sqrt{A_0/A}$, can be obtained from the authors' Equations (47) and (33)

$$(P_4 - P_5) - (P_1 - P_2) = -(P_1 - P_2)\left(\frac{A - a}{a + A}\right)$$

Note that $(P_4 - P_5)$ is the transmitted pressure jump at the area A, that $(P_1 - P_2)$ is the incident pressure jump at the area a, and that $(A - a)$ is the change in area. The limit of this finite difference equation, where the area-change and pressure-change go to zero, results in the differential equation:

$$\frac{dP}{P} = -\frac{dA}{2A}$$

Integration, where the pipe exit pressure and area are P_0 and A_0, results in the following solution

$$\frac{P}{P_0} = \sqrt{\frac{A_0}{A}}$$

This result is the same as that obtained by Professor Paynter. The authors are indebted to Professor Paynter for suggesting that their final equation could be integrated in this simple form.

Mr. Strowger's plot, of the estimated water-hammer wave pulse transmitted through a pipe of changing cross-sectional area, does not closely match the results of Professor Paynter or of the authors. This difference can be shown by examination of Mr. Strowger's expression for the transmitted pressure pulse P:

$$P = \frac{QTK}{V}$$

The various terms may be replaced by the following expressions:

$$K = C^2\rho$$
$$T = L/C$$
$$Q = A_0U_0$$
$$P_0 = \rho CU_0$$

Hence,

$$\frac{P}{P_0} = \frac{A_0}{V/L}$$

Strowger's equation could be better discussed by applying it to the simple problem sketched here:

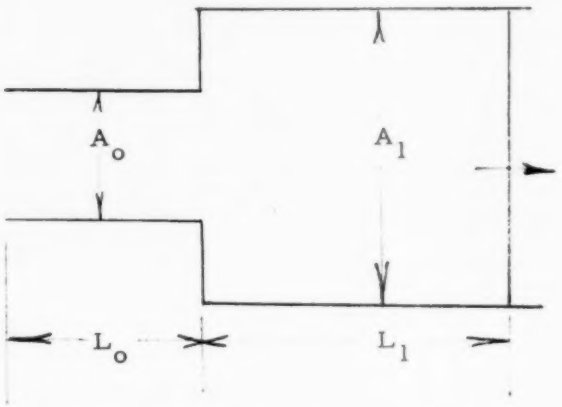

For the preceding sketch, Strowger's approximation becomes

$$\frac{P_1}{P_0} = \frac{A_0}{\left(\frac{A_0L_0 + A_1L_1}{L_1 + L_0}\right)} = \frac{V_0}{V_1}\left(\frac{L_1}{L_0} + 1\right)$$

$$= \frac{1}{1 + \left(\frac{\frac{L_1}{L_0}}{1 + \frac{L_1}{L_0}}\right)\left(\frac{A_1}{A_0} - 1\right)}$$

In the special case of $L_1/L_0 \gg 1$

$$\frac{P_1}{P_0} = \frac{A_0}{A_1} \quad \text{(Strowger)}$$

$$\frac{P_1}{P_0} = \sqrt{\frac{A_0}{A_1}} \quad \text{(Paynter)}$$

In the special cases of $L_1/L_0 = 1$

i All $\frac{A_0}{A_1}$

$$\frac{P_1}{P_0} = 2\frac{A_0}{A_1} \quad \text{(Strowger)}$$

$$\frac{P_1}{P_0} = \sqrt{\frac{A_0}{A_1}} \quad \text{(Paynter)}$$

ii Only $\frac{A_1 - A_0}{A_0} \ll 1$

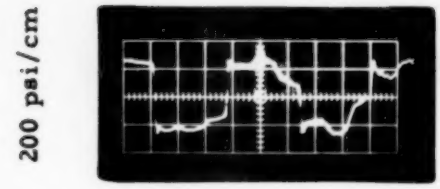

Fig. 12(a)

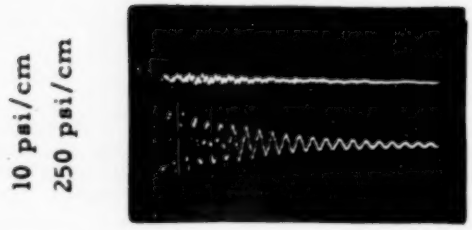

Fig. 12(b)

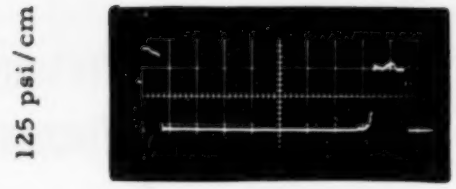

Fig. 13(a)

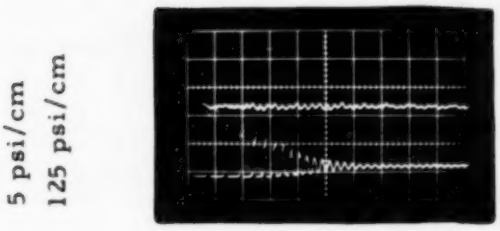

Fig. 13(b)

$$\frac{P_1}{P_0} = \frac{1}{1 + \frac{1}{2}\left(\frac{A_1 - A_0}{A_0}\right)} \approx \sqrt{\frac{A_0}{A_1}} \quad \text{(Strowger)}$$

$$\frac{P_1}{P_0} = \sqrt{\frac{A_0}{A_1}} \quad \text{(Paynter)}$$

In the special case of $L_1/L_0 \ll 1$

$$\frac{P_1}{P_0} = \frac{V_0}{V_1} \quad \text{(Strowger)}$$

$$\frac{P_1}{P_0} = \sqrt{\frac{A_0}{A_1}} \quad \text{(Paynter)}$$

Thus it may be concluded that there are certain problem in which Mr. Strowger's approximation may closely match Professor Paynter's and the authors' approximation, but, in general, Mr. Strowger's prediction would yield lower pressure values for a diverging duct. However, in all cases the results would have to be multiplied by a factor of one or two depending on whether the reflecting structure were oriented side-on or face-on to the incident wave.

We would like to thank Mr. Rosser for pointing out a technique for obtaining a reasonable estimate of the decay time when the pipe wall frictional effects and entrance-and-exit losses were not the dominant decaying mechanisms. Rather, it was more important to attribute a finite value to the impedance for the pipe boundary condition at the reservoir entrance, and this impedance could be established from the computed pressure-distance history in the plenum. The effects of a finite impedance at a free surface, of water column undergoing water hammer, were noted in the recent tests at the Armour Research Foundation.

Fig. 12(a) shows the wave form of the individual pressure pulse at the end where $\Delta U = 0$, while Fig. 12(b) shows the same oscillations on a longer time scale where it can be seen that the oscillations became small in less than 0.20 second for the class of water hammer where ρUC did not exceed the plenum chamber pressurization level. Figs. 13(a and b) are similar to Figs. 12(a and b), except that, in this class of water hammers ρUC did exceed the plenum chamber pressurization level, but the oscillations again damped in less than 0.20 second. Thus the weight of experimental evidence shows the importance of the error introduced by applying open-ended pipe boundary conditions to even those systems which have large reservoirs.

Professor Rouleau has objected to the extension of laminar flow frictional coefficients to the turbulent flow regime. To include it otherwise results in a nonlinear equation which is not so readily solvable. Since the purpose of this analysis was to determine the magnitude of the decay time for the pressure oscillations and not the exact form of the decay, one cannot seriously object to an overestimate of the pipe frictional effects. Especially, as Mr. Rosser and the authors showed, the finite impedance effects were 150 times more dominant than the entrance and exit loss effects, where the latter effects were in turn 6 times more dominant than the pipe friction effects.

In summary, the authors' treatment of water-hammer waves by steady-flow algebraic equations between wave fronts and by the "jump condition" equations across wave fronts has been found to meet the predictions of Green's Law for this particular type of unsteady flow. It is suggested that this approach be understood and utilized for other more complicated problems.

Pressure Surges in Pipelines Carrying Viscous Liquids

W. T. ROULEAU
Assistant Professor,
Mechanical Engineering Department,
Carnegie Institute of Technology,
Pittsburgh, Pa. Assoc. Mem. ASME

An analytical solution which includes frictional effects is developed for the pressure occurring in a pipeline when Poiseuille flow is stopped by the sudden closure of a valve. Limitations and deficiencies of past solutions of the same problem have been overcome in the present analysis. It is shown that for most pipelines of practical interest the pressure is given by the sum of four traveling waves multiplied by a time-decaying exponential; evaluation is easily accomplished with a few simple slide-rule calculations. The computed pressures are shown to compare closely with experimental measurements.

Introduction

One class of important surge problems is that in which the flow is initially steady and laminar (Poiseuille flow) and a valve downstream from a constant pressure source is suddenly closed. These problems arise, for instance, in gravity oil lines. In the past, the calculation of pressures in such lines has usually been accomplished graphically with the friction assumed to be lumped at a finite number of points, as explained in Reference [1].[1]

Several analytical solutions for this class of problems have been published, but they are not wholly satisfactory. The earliest is by Wood [2]; however it gives only "surge pressure" not actual pressure. Another is by Ludwig [3]; but it is good only for the first pressure surge because a semi-infinite pipe is assumed. The analysis applies only during the interval from valve closure to when the pressure wave front reaches the constant pressure source. An improved analysis was made by Binnie [4]; he considers a finite-length line and is thus able to account for wave reflections. However, his analysis, which is based on Heaviside's operational methods, leads to a general solution in terms of a complicated inversion integral involving Bessel functions, which is presently not tabulated. To obtain useful results he was forced to make some rather drastic approximations, and consequently his final solution is valid only for short times after valve closure.

In this paper the problem is solved by means of the separation of variables. The assumptions are those employed by Wood, Ludwig, Binnie, and in the graphical method; i.e., the liquid and pipe are each homogeneous and elastic, the velocity is uniform over any cross section, and the frictional resistance is constant, equal to that in Poiseuille flow. A general solution, valid for all time, is found in the form of an infinite trigonometric series, which can easily be summed by a modern digital computer. But remarkable simplification exists for most practical problems: The general solution reduces to the sum of four traveling waves multiplied by a time-decaying exponential. Thus, not only can the phenomenon be easily visualized, but the pressure distribution in the pipe can be readily computed for any time after closure with only a few simple slide-rule calculations.

Analysis

The physical situation to be analyzed is depicted in Fig. 1. The pipe, of length L, is assumed to be homogeneous and elastic, with a constant circular cross section in the unstressed state and a uniform wall thickness. One end is attached to a source of slightly compressible fluid maintained at a constant pressure p_0; the other end terminates in a valve. The velocity of the fluid is assumed uniform over any cross section. For $t' < 0$ the fluid is flowing with a velocity U, the Reynolds number being such that the pressure gradient is proportional to the velocity (Poiseuille flow). At $t' = 0$ the valve is suddenly closed. It is desired to de-

[1] Numbers in brackets designate References at end of paper.

Contributed by the Water Hammer Subcommittee of the Hydraulic Division and presented at the Gas Turbine Power & Hydraulic Conference, Houston, Texas, March 6–9, 1960, of The American Society of Mechanical Engineers.

Note: Statements and opinions advanced in papers are to be understood as individual expressions of their authors and not those of the Society. Manuscript received at ASME Headquarters, October 13, 1959. Paper No. 60—Hyd-5.

Nomenclature

A = cross-sectional area of pipe, ft²
b = thickness of pipe wall, ft
c = $\sqrt{K_1/\rho}$, Equation (16), ft/sec
$C_1 \ldots C_{12}$, C_{3n}, C_{4n} = integration constants
D = pipe inside diameter, ft
e = base of natural logarithms
E = modulus of elasticity of pipe material, lb/ft²
$f(x - t)$ = traveling wave, Equation (35)
g = acceleration of gravity, ft/sec²
$g(x + t)$ = traveling wave, Equation (36)
$h(x - t)$ = traveling wave, Equation (37)
H = elevation of pipe inlet above z-datum, ft
i = $\sqrt{-1}$
$j(x + t)$ = traveling wave, Equation (38)
k = $LR/\sqrt{K_1\rho}$, Equation (17)
K = bulk compression modulus of liquid, lb/ft²
K_1 = over-all bulk compression modulus of liquid and pipe, Equation (5), lb/ft²
L = length of pipe, ft
m_1, m_2 = positive integers
n = index, assumes the value of all positive integers
p = absolute fluid pressure, lb/ft²
p_1 = absolute initial fluid pressure at x', lb/ft²
p_0 = absolute pressure at inlet end of pipe, constant, lb/ft²
P = $p + \rho gz$, Equation (3), lb/ft²

(Continued on next page)

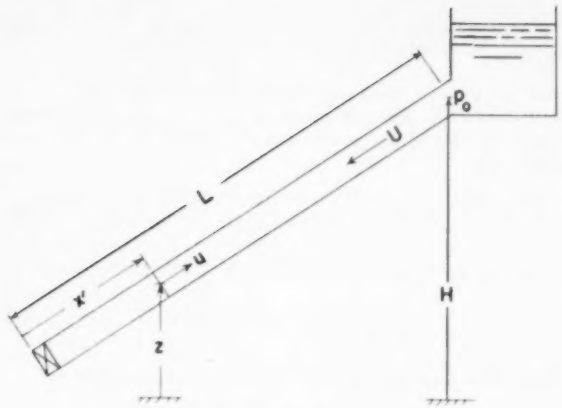

Fig. 1 Physical model and co-ordinate system

termine the pressure in the pipe as a function of time and position.

Following Joukowsky [5], Parmakian [6], and Binder [7], the governing equations, based on momentum and continuity considerations, are

$$\frac{\partial P}{\partial x'} = -\rho \frac{\partial u}{\partial t'} - Ru \tag{1}$$

$$\frac{\partial u}{\partial x'} = -\frac{1}{K_1} \frac{\partial P}{\partial t'} \tag{2}$$

where x' is measured upstream from the valve, t' is time measured from valve closure, u is the velocity in the x' direction, R the frictional resistance coefficient, K_1 the over-all modulus of elasticity for the fluid and the pipe, ρ the density of the fluid, and

$$P = p + \rho g z, \tag{3}$$

where p is the absolute fluid pressure, $\mathbf{g}$ the acceleration of gravity, and z the elevation above an arbitrary datum. The derivation is given in the Appendix.

In terms of fundamental parameters:

$$R = \frac{32\mu}{D^2}, \tag{4}$$

$$\frac{1}{K_1} = \frac{1}{K} + \frac{D}{bE}, \tag{5}$$

where μ is the coefficient of viscosity, D is pipe diameter, K is the bulk compression modulus of the fluid, b is pipe-wall thickness, and E is the modulus of elasticity of the pipe material.

If we let η' be the displacement of a fluid cross section from its position at $t' = 0$ we obtain

$$u = \frac{\partial \eta'}{\partial t'}. \tag{6}$$

With this equivalent for u Equation (2) becomes

$$\frac{\partial^2 \eta'}{\partial x' \partial t'} = -\frac{1}{K_1} \frac{\partial P}{\partial t'}. \tag{7}$$

Equation (7) is integrated to give

$$P(x', t') - P(x', 0) = -K_1 \left[\frac{\partial \eta'}{\partial x'}(x', t') - \frac{\partial \eta'}{\partial x'}(x', 0) \right]. \tag{8}$$

We have

$$\frac{\partial \eta'}{\partial x'}(x', 0) = 0 \qquad 0 < x' \leq L \tag{9}$$

and

$$P(x', 0) = P_0 + RU(x - L) \qquad 0 < x' \leq L \tag{10}$$

where

$$P_0 = P(L, 0) = p_0 + \rho g H, \tag{11}$$

H being the elevation of the pipe inlet above the z-datum. Equations (9) and (10) are substituted into Equation (8) which is then differentiated with respect to x'. This result and Equation (6) differentiated with respect to time are used with Equation (1) to obtain the following equation, which has only η' as the dependent variable:

$$RU - K_1 \frac{\partial^2 \eta'}{\partial x'^2} = -\rho \frac{\partial^2 \eta'}{\partial t'^2} - R \frac{\partial \eta'}{\partial t'}. \tag{12}$$

A further simplification is made with a new variable $\bar{\eta}$, defined by

$$\bar{\eta} = -\frac{RU}{2K_1} x'^2 + \frac{RU}{K_1} L x' + \eta'. \tag{13}$$

When $\bar{\eta}$ is introduced into Equation (12) there results

$$K_1 \frac{\partial^2 \bar{\eta}}{\partial x'^2} = \rho \frac{\partial^2 \bar{\eta}}{\partial t'^2} + R \frac{\partial \bar{\eta}}{\partial t'}. \tag{14}$$

It is now convenient to change to the dimensionless variables

Nomenclature

P_0 = $p_0 + \rho g H$, Equation (11), lb/ft²
R = frictional resistance coefficient, Equation (4), lb sec/ft³
t' = time, measured from valve closure, sec
t = ct'/L, dimensionless time, Equations (15)
T = function of time
u = fluid velocity in x' direction, ft/sec
U = initial mean velocity in pipe, ft/sec
x' = distance along pipe, measured from valve, ft
x = x'/L, dimensionless distance, Equations (15)
X = function of x
z = elevation above arbitrary datum, ft
α = $k/2$, Equation (60)
β = $\frac{1}{2}\sqrt{k^2 - 4\gamma^2}$, Equation (61)
β_n = $\frac{1}{2}\sqrt{k^2 - [(2n-1)\pi]^2}$, Equation (25)
γ = separation constant
γ_n = $(2n-1)\pi/2$, Equation (24)
η' = displacement of a fluid cross-section from its position at $t' = 0$, ft
$\bar{\eta}$ = $-\frac{RU}{2K_1} x'^2 + \frac{RU}{K_1} L x' + \eta'$, Equation (13)
η = $\bar{\eta}/L$, dimensionless displacement, Equations (15)
μ = coefficient of viscosity, slugs/ft sec
ν = μ/ρ, kinematic viscosity, ft²/sec
ξ = argument of traveling waves, Equation (41)
ρ = fluid density, slugs/ft³
ϕ = $\sin^{-1} dz/dx'$

$$\left.\begin{aligned} x &= \frac{x'}{L} \\ \eta &= \frac{\bar{\eta}}{L} \\ t &= \frac{ct'}{L}, \end{aligned}\right\} \tag{15}$$

where

$$c = \sqrt{\frac{K_1}{\rho}}, \tag{16}$$

and define the dimensionless parameter

$$k = \frac{LR}{\sqrt{K_1\rho}}. \tag{17}$$

Thus we obtain the dimensionless governing equation

$$\frac{\partial^2\eta}{\partial x^2} = k\,\frac{\partial\eta}{\partial t} + \frac{\partial^2\eta}{\partial t^2}. \tag{18}$$

The boundary conditions are:

$$\eta(0, t) = 0 \qquad 0 \le t \tag{19}$$

$$\frac{\partial\eta}{\partial x}(1, t) = 0 \qquad 0 \le t \tag{20}$$

$$\frac{\partial\eta}{\partial x}(x, 0) = \frac{RUL}{K_1}(1 - x) \qquad 0 < x \le 1 \tag{21}$$

$$\frac{\partial\eta}{\partial t}(x, 0) = -\frac{U}{c} \qquad 0 < x \le 1 \tag{22}$$

Equation (19) expresses the fact that the displacement of the fluid at the valve position is zero after the valve is closed. Equation (20) expresses constancy of pressure at the fluid source. Equation (21) results from the initial Poiseuille pressure distribution. Equation (22) states that the fluid is initially flowing with a uniform velocity U in the negative x' direction.

The solution of Equation (18) satisfying the boundary conditions [Equations (19), (20), (21), (22)] may be found by the method of separation of variables. It is

$$\eta = \frac{2U}{c}\,e^{-\frac{kt}{2}}\left\{\sum_{n=1,2,3,\ldots}^{n<\frac{1}{2}\left(\frac{k}{\pi}+1\right)}\left[\left(\frac{k^2}{2\gamma_n^2}-1\right)\left(\frac{\sinh\beta_n t}{\beta_n}\right) + \frac{k}{\gamma_n^2}\cosh\beta_n t\right]\frac{\sinh\gamma_n x}{\gamma_n} + \text{, only if } \frac{1}{2}\left(\frac{k}{\pi}+1\right) \text{ is an integer,}\right.$$

$$\left.\left(t+\frac{4}{k}\right)\frac{\sin\frac{k}{2}x}{\frac{k}{2}} + \sum_{n>\frac{1}{2}\left(\frac{k}{\pi}+1\right)}^{\infty}\left[\left(\frac{k^2}{2\gamma_n^2}-1\right)\left(\frac{\sin i\beta_n t}{i\beta_n}\right) + \frac{k}{\gamma_n^2}\cos i\beta_n t\right]\frac{\sin\gamma_n x}{\gamma_n}\right\}, \tag{23}$$

in which

$$\gamma_n = \frac{(2n-1)\pi}{2}, \tag{24}$$

$$\beta_n = \frac{1}{2}\sqrt{k^2 - [(2n-1)\pi]^2}, \tag{25}$$

and $i = \sqrt{-1}$. The details are shown in the Appendix.

What we are primarily interested in is the pressure; this is found in terms of $\partial\eta/\partial x$ by using Equations (8), (9), (10), and (15). It is

$$P - P_0 = -K_1\,\frac{\partial\eta}{\partial x}(x, t), \tag{26}$$

or, in dimensionless form, with Equation (16),

$$\frac{P - P_0}{U\sqrt{K_1\rho}} = -\frac{c}{U}\,\frac{\partial\eta}{\partial x}(x, t). \tag{27}$$

Thus, from Equation (23), we obtain the pressure equation

$$\frac{P - P_0}{U\sqrt{K_1\rho}} = -2e^{-\frac{kt}{2}}\left\{\sum_{n=1,2,3,\ldots}^{n<\frac{1}{2}\left(\frac{k}{\pi}+1\right)}\left[\left(\frac{k^2}{2\gamma_n^2}-1\right)\left(\frac{\sinh\beta_n t}{\beta_n}\right) + \frac{k}{\gamma_n^2}\cosh\beta_n t\right]\cos\gamma_n x + \text{, only if } \frac{1}{2}\left(\frac{k}{\pi}+1\right) \text{ is an integer,}\right.$$

$$\left.\left(t+\frac{4}{k}\right)\cos\frac{k}{2}x + \sum_{n>\frac{1}{2}\left(\frac{k}{\pi}+1\right)}^{\infty}\left[\left(\frac{k^2}{2\gamma_n^2}-1\right)\left(\frac{\sin i\beta_n t}{i\beta_n}\right) + \frac{k}{\gamma_n^2}\cos i\beta_n t\right]\cos\gamma_n x\right\}. \tag{28}$$

Equation (28) can be readily summed by digital computer. However, for most practical problems involving long lines it will be found that

$$k^2 \ll \pi^2, \tag{29}$$

with the consequence that

$$i\beta_n \doteq \gamma_n = \frac{(2n-1)\pi}{2}. \tag{30}$$

Thus the displacement Equation (23) and the pressure Equation (28) reduce to the greatly simplified forms:

$$\eta = -\frac{2U}{c}\,e^{-\frac{kt}{2}}\sum_{n=1,2,3,\ldots}^{\infty}\left(\frac{\sin\gamma_n t}{\gamma_n} - k\,\frac{\cos\gamma_n t}{\gamma_n^2}\right)\frac{\sin\gamma_n x}{\gamma_n} \tag{31}$$

$$\frac{P - P_0}{U\sqrt{K_1\rho}} = 2e^{-\frac{kt}{2}}\sum_{n=1,2,3,\ldots}^{\infty}\left(\frac{\sin\gamma_n t\cos\gamma_n x}{\gamma_n} - k\,\frac{\cos\gamma_n t\cos\gamma_n x}{\gamma_n^2}\right). \tag{32}$$

With the aid of trigonometric identities and Equation (16) we may rewrite Equation (32) in the form

$$\frac{P - P_0}{U\rho c} = e^{-\frac{kt}{2}}\left\{\frac{2}{\pi}\sum_{n=1,2,3,\ldots}^{\infty}\frac{\sin\frac{(2n-1)\pi}{2}(x+t)}{(2n-1)} - \frac{2}{\pi}\sum_{n=1,2,3,\ldots}^{\infty}\frac{\sin\frac{(2n-1)\pi}{2}(x-t)}{(2n-1)}\right.$$

$$- k \frac{4}{\pi^2} \sum_{n=1,2,3,\ldots}^{\infty} \frac{\cos \frac{(2n-1)\pi}{2}(x+t)}{(2n-1)^2} - k \frac{4}{\pi^2} \sum_{n=1,2,3,\ldots}^{\infty} \frac{\cos \frac{(2n-1)\pi}{2}(x-t)}{(2n-1)^2} \Bigg\}, \quad (33)$$

in which each of the four summations is a Fourier series representation of a traveling wave, and c is now the wave velocity.

By summing each of the series we obtain a remarkably simple equation for the pressure, in terms of traveling waves:

$$\frac{P - P_0}{U\rho c} = e^{-\frac{kt}{2}} \{f(x-t) + g(x+t) + k[h(x-t) + j(x+t)]\}, \quad (34)$$

where

$$f(x-t) = -\frac{2}{\pi} \sum_{n=1,2,3,\ldots}^{\infty} \frac{\sin \frac{(2n-1)\pi}{2}(x-t)}{(2n-1)} = \begin{cases} -1/2 & 0 < (x-t) < 2 \\ 1/2 & -2 < (x-t) < 0 \end{cases} \quad (35)$$

$$g(x+t) = \frac{2}{\pi} \sum_{n=1,2,3,\ldots}^{\infty} \frac{\sin \frac{(2n-1)\pi}{2}(x+t)}{(2n-1)} = \begin{cases} 1/2 & 0 < (x+t) < 2 \\ -1/2 & -2 < (x+t) < 0 \end{cases} \quad (36)$$

$$h(x-t) = -\frac{4}{\pi^2} \sum_{n=1,2,3,\ldots}^{\infty} \frac{\cos \frac{(2n-1)\pi}{2}(x-t)}{(2n-1)^2} = \begin{cases} -1/2[1-(x-t)] & 0 \le (x-t) \le 2 \\ -1/2[1+(x-t)] & -2 \le (x-t) \le 0 \end{cases} \quad (37)$$

$$j(x+t) = -\frac{4}{\pi^2} \sum_{n=1,2,3,\ldots}^{\infty} \frac{\cos \frac{(2n-1)\pi}{2}(x+t)}{(2n-1)^2} = \begin{cases} -1/2[1-(x+t)] & 0 \le (x+t) \le 2 \\ -1/2[1+(x+t)] & -2 \le (x+t) \le 0 \end{cases} \quad (38)$$

The functions f, g, h, j have a period of 4; thus if the arguments $(x+t)$ or $(x-t)$ should lie outside of the defined range

$$-2 < \begin{matrix}(x+t)\\(x-t)\end{matrix} < 2$$

it is only necessary to replace the arguments wherever they occur by

$$\left.\begin{matrix}(x+t) - 4m_1 \\ (x-t) + 4m_2\end{matrix}\right\} \quad (39)$$

where m_1 and m_2 are positive integers so chosen that

$$\left.\begin{matrix}-2 < (x+t) - 4m_1 < 2 \\ -2 < (x-t) + 4m_2 < 2.\end{matrix}\right\} \quad (40)$$

For example, if $x = 1/2$, $t = 2$, then

$$f(x-t) = f(1/2 - 2) = f(-3/2) = 1/2$$

$$g(x+t) = g(1/2 + 2 - 4) = g(-3/2) = -1/2$$

$$h(x-t) = h(1/2 - 2) = h(-3/2) = -1/2[1 + (-3/2)] = 1/4$$

$$j(x+t) = j(1/2 + 2) = j(1/2 + 2 - 4) = j(-3/2) = -1/2[1 + (-3/2)] = 1/4,$$

and the pressure is

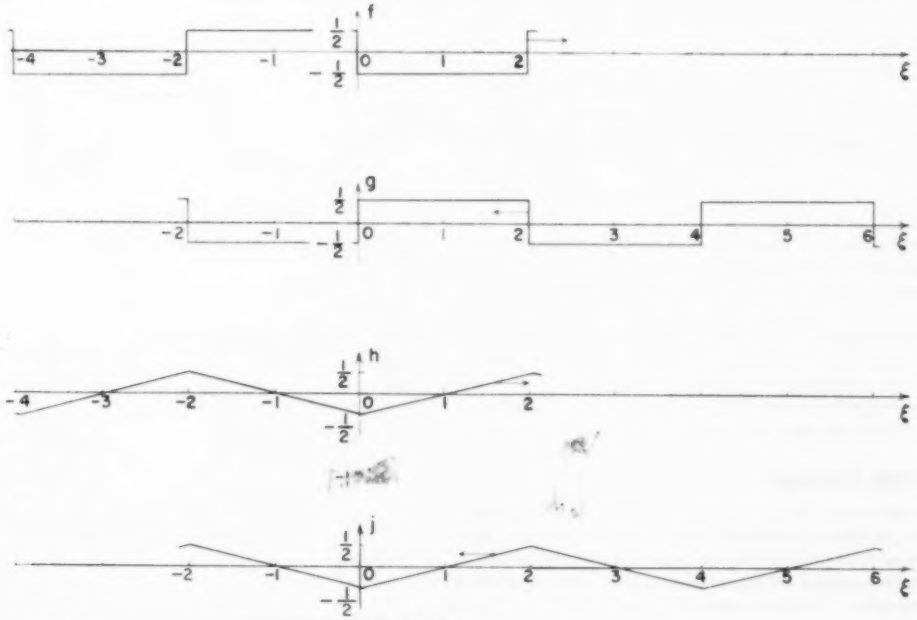

Fig. 2 Traveling waves

$$\frac{P - P_0}{U\rho c} = e^{-k}\{1/2 - 1/2 + k[1/4 + 1/4]\} = \frac{k}{2}\, e^{-k}.$$

The four traveling waves, defined by Equations (35), (36), (37), (38), are shown graphically in Fig. 2; the argument is ξ, where

$$\left.\begin{aligned} &\xi = (x - t) \qquad \text{for the } f \text{ and } h \text{ waves,} \\ &\text{and} \\ &\xi = (x + t) \qquad \text{for the } g \text{ and } j \text{ waves.} \end{aligned}\right\} \tag{41}$$

The wave velocity c in Equation (34) may be measured directly or computed from Equation (16), depending on circumstances. It should be noted that $\sqrt{K_1/\rho}$ in Equation (28) is not the velocity of the pressure waves and thus cannot be measured directly but must be computed.

Comparison With Earlier Work

It is of interest to compare our results with those of Binnie. Our traveling wave solution is limited only by the magnitude of k, whereas Binnie's approximation has no restriction on k but is limited to short times. He obtains the following relation for pressure at $x = 0$ and $0 \leq t \leq 2$ (his notation is here changed to correspond with ours):

$$\frac{P - P_0}{U\rho c} = \left[\frac{15}{4} - e^{-\frac{kt}{2}}\left(\frac{11}{4} + \frac{7}{8}\,kt + \frac{5}{32}\,k^2t^2 + \frac{1}{64}\,k^3t^3 + \frac{1}{1024}\,k^4t^4\right) - k\right], \tag{42}$$

which becomes, upon expanding the exponential term,

$$\frac{P - P_0}{U\rho c} = 1 - k + \frac{kt}{2} - \frac{1}{16}\,k^2t^2 + \frac{1}{96}\,k^3t^3 - \frac{5}{3072}\,k^4t^4. \tag{43}$$

Our solution for this time interval is

$$\frac{P - P_0}{U\rho c} = e^{-\frac{kt}{2}}\,[1 - k(1 - t)], \tag{44}$$

which can be expanded to give

$$\frac{P - P_0}{U\rho c} = 1 - k + \frac{kt}{2} + O(k^2t). \tag{45}$$

Thus, we observe that the two solutions agree to the first order in friction effects.

Results

For reasonable accuracy, Equation (34) should not be used for $k > 1$; for large k the more cumbersome Equation (28) is necessary. However, k's large enough to require Equation (28) are seldom encountered in practice. For example, a combination of typical parameters gives $k = 0.0892$ (References [4 and 8]). The pressure distribution in the pipe at various times after valve closure is given by Equation (34) and shown in Fig. 3.

Fig. 4 shows the pressure variation at the valve for $k = 0.0892$, also obtained from Equation (34).

Comparison With Experiment

Test #23 of Reference [8] was designed to fulfill the initial flow and boundary conditions considered in the present analysis. In this test crude oil flowed by the action of gravity through a 4-in. nominal diameter pipeline equipped with a quick-closing valve and pressure recorder. The pertinent specifications are:

Pipe length, L: 2232 ft

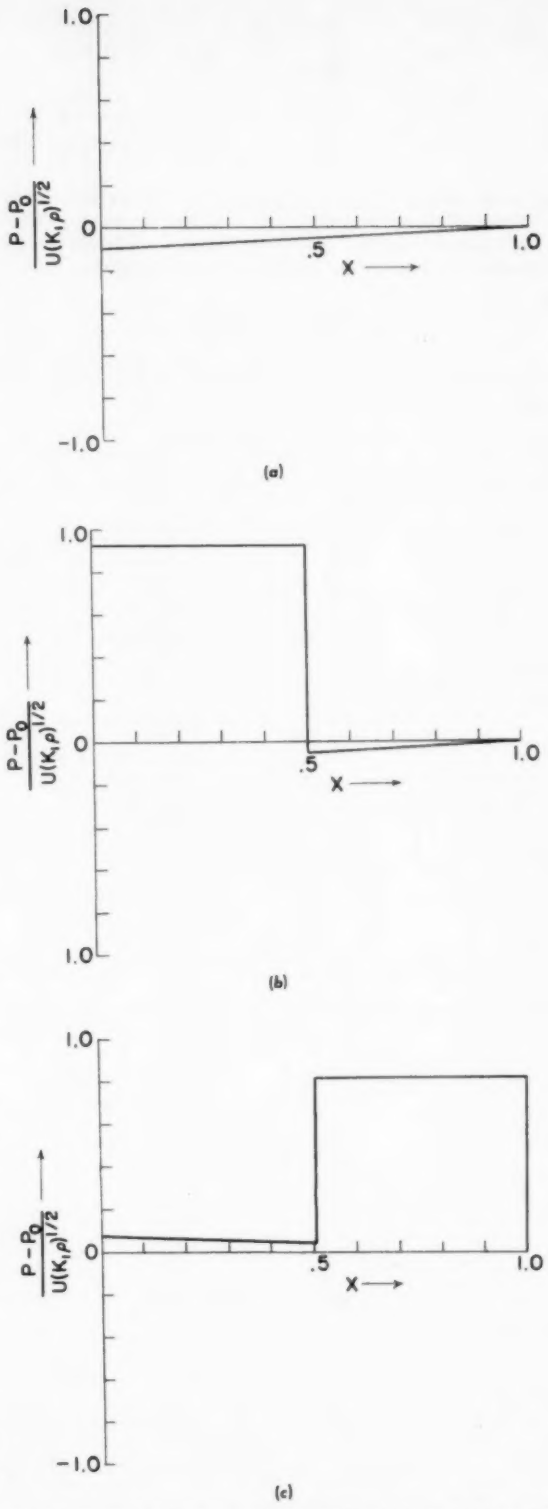

Fig. 3 Pressure distribution for $k = 0.0892$ at: (a) $t = 0$, (b) $t = 1/2$, (c) $t = 5\ 1/2$

Kinematic viscosity, ν:	5.26×10^{-4} ft²/sec
Density, ρ:	1.75 slugs/ft³
Wave velocity, c:	4010 ft/sec
Initial velocity, U:	1.03 ft/sec
k, Equation (17):	0.0892

The actual pressure at the valve, traced from a reproduction of the recorder chart, is shown in Fig. 5. Superimposed in Fig. 5(*a*) is the pressure obtained from Equation (34), for $c = 4010$ ft/sec. It is evident that the period of the computed pressure is slightly too short. However, some doubt exists about the value of c, because of the presence of vapor or gas in the line. In Reference [8], deviations from a graphical analysis are attributed to this effect.

Qualitatively, the vapors and gases introduce a "cushioning" effect that tends to smooth out discontinuities and reduce the wave velocity. Such a smoothing out is quite evident in the actual pressure wave. For comparison the pressure has been calculated for a 10 per cent lower wave velocity, $c = 3610$ ft/sec, shown in Fig. 5(*b*). The period of the fluctuations is in much closer agreement, but the pressure for the first surge is about 6 per cent low. However, considering the nonlinearities introduced by the vapors and gases in the line there is quite fair agreement between the observed and calculated pressures.

References

1 R. W. Angus, "Waterhammer in Pipes, Including Those Supplied by Centrifugal Pumps: Graphical Treatment," Bulletin 152, University of Toronto Press, Toronto, Canada, 1938.

2 F. M. Wood, "The Application of Heaviside's Operational Calculus to the Solution of Problems in Waterhammer," TRANS. ASME, vol. 59, Hyd-59-15, 1937, pp. 707–713.

3 M. Ludwig, "Attenuation of Surges in Long Pipe Lines," ASME Paper No. 50—SA-26, 1950.

4 A. M. Binnie, "The Effect of Friction on Surges in Long Pipelines," *Quarterly Journal of Mechanics and Applied Mathematics*, vol. IV, pt. 3, 1951, pp. 330–343.

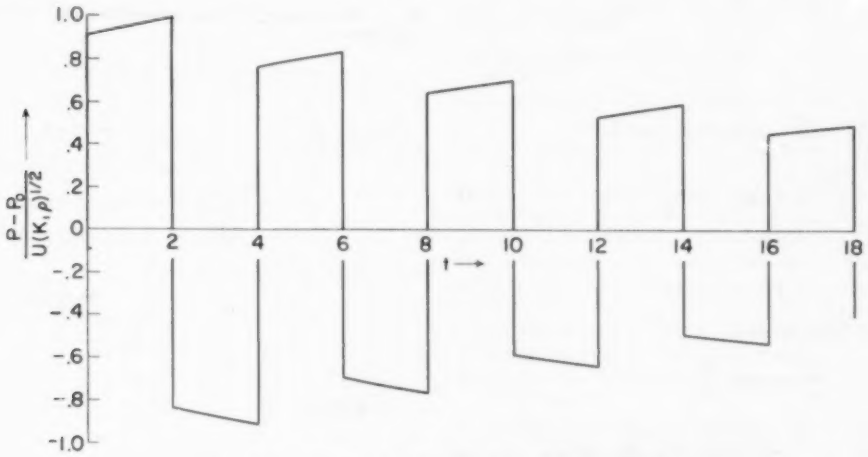

Fig. 4 Pressure variation at the valve ($x = 0$) for $k = 0.0892$

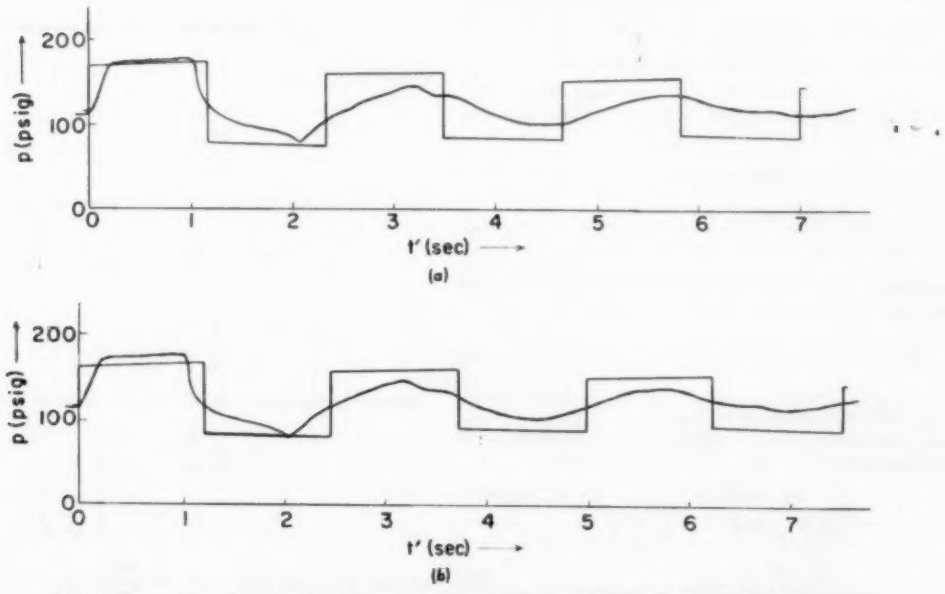

Fig. 5 Comparison of predicted and actual pressures: (a) $c = 4010$ ft/sec; (b) $c = 3610$ ft/sec

5 N. Joukowsky, "Waterhammer," translated by Miss O. Simin, *Proceedings of the American Water Works Association*, vol. 24, 1904, pp. 365–368.
6 J. Parmakian, "Waterhammer Analysis," Prentice-Hall, Inc., New York, N. Y., 1955.
7 C. B. Schuder and R. C. Binder, "The Response of Pneumatic Transmission Lines to Step Inputs," TRANS. ASME, Series D, JOURNAL OF BASIC ENGINEERING, vol. 81, 1959, pp. 578–584.
8 J. E. Green, "Pressure-Surge Tests on Oil Pipe Lines," *Proceedings of the American Petroleum Institute*, vol. 29, Sec. 5, 1949, p. 44.

APPENDIX A

Derivation of Equations

Consider, as a free body, an element of fluid, length $\Delta x'$ and cross-sectional area A, taken from the pipe (Fig. 6). Applying the Law of Conservation of Momentum to this element we obtain

$$pA - \left(p + \frac{\partial p}{\partial x'}\,\Delta x'\right) A - RuA\Delta x' - (\mathbf{g}\rho \sin \phi)A\Delta x' = \rho A \Delta x' \frac{\partial u}{\partial t'}. \quad (46)$$

But $\sin \phi = \dfrac{dz}{dx'}$; thus Equation (46) becomes

$$-\frac{\partial}{\partial x'}(p + \rho \mathbf{g} z) = \rho \frac{\partial u}{\partial t'} + Ru. \quad (47)$$

Let

$$P = p + \rho \mathbf{g} z \quad (3)$$

and substitute in Equation (47):

$$\frac{\partial P}{\partial x'} = -\rho \frac{\partial u}{\partial t'} - Ru. \quad (1)$$

Next consider an element of fluid of length $\Delta x'$ in a pipe of uniform area A (Fig. 7*a*). If the pressure on the element is changed from p_1 to p, the density of the element changes from ρ to $\rho + \delta\rho$, the cross-sectional area of the pipe changes from A to $A + \delta A$, and the length of the element from $\Delta x'$ to $\Delta x' + \dfrac{\partial \eta'}{\partial x'}\Delta x'$ (Fig. 7*b*). By the Law of Conservation of Matter we have

$$\rho A \Delta x' = (\rho + \delta\rho)(A + \delta A)\left(\Delta x' + \frac{\partial \eta'}{\partial x'}\Delta x'\right). \quad (48)$$

Neglecting higher order terms we obtain

$$\frac{\delta\rho}{\rho} + \frac{\delta A}{A} + \frac{\partial \eta'}{\partial x'} = 0. \quad (49)$$

For a slightly compressible fluid, pressure and density changes are related by

$$\frac{\delta p}{\delta \rho} = \frac{K}{\rho}, \quad (50)$$

where K = bulk compression modulus.

A change in pressure $(p - p_1)$ changes the pipes diameter D by δD, which is given by

$$\delta D = \frac{(D + b)(D)}{2bE}(p - p_1) \doteq \frac{D^2}{2bE}(p - p_1) \quad (51)$$

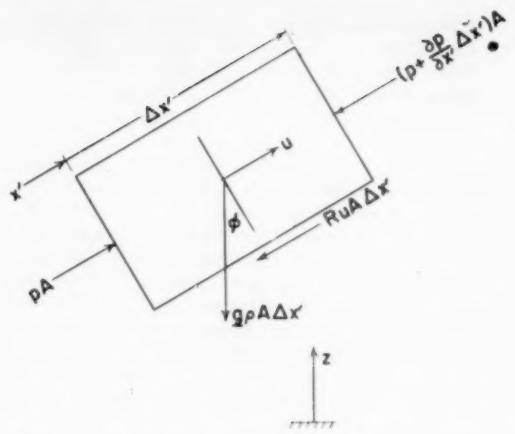

Fig. 6 Fluid element, showing external forces having a component along the x'-axis

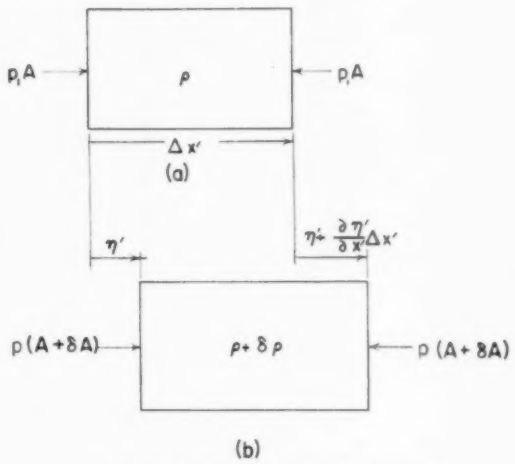

Fig. 7 Fluid element, showing displacement

(Reference [6], p. 12).

Thus

$$\frac{\delta A}{A} \doteq \frac{D}{bE}(p - p_1). \quad (52)$$

Using Equations (50) and (52) with Equation (49) gives

$$-(p - p_1)\left(\frac{1}{K} + \frac{D}{bE}\right) = \frac{\partial \eta'}{\partial x'}, \quad (53)$$

or

$$-\frac{1}{K_1}(p - p_1) = \frac{\partial \eta'}{\partial x'}. \quad (54)$$

Differentiating Equation (54) with respect to time we obtain

$$-\frac{1}{K_1}\frac{\partial p}{\partial t'} = \frac{\partial^2 \eta'}{\partial t' \partial x'} = \frac{\partial}{\partial x'}\left(\frac{\partial \eta'}{\partial t'}\right) = \frac{\partial u}{\partial x'}, \quad (55)$$

or

$$\frac{\partial u}{\partial x'} = -\frac{1}{K_1}\frac{\partial P}{\partial t'}. \tag{2}$$

APPENDIX B

Solution of Differential Equation

We have

$$\frac{\partial^2 \eta}{\partial x^2} = k\frac{\partial \eta}{\partial t} + \frac{\partial^2 \eta}{\partial t^2}. \tag{18}$$

Assume a solution of the form

$$\eta = X(x)T(t), \tag{56}$$

where X and T are functions of x and t, respectively. Inserting this solution into Equation (18) gives us two total differential equations

$$X'' + \gamma^2 X = 0 \tag{57}$$

$$T'' + kT' + \gamma^2 T = 0, \tag{58}$$

where γ^2 is real.

Solving Equations (57) and (58) for X and T and combining according to Equation (56) we obtain

$$\eta = c_1 e^{(-\alpha+\beta)t}\cos \gamma x + c_2 e^{(-\alpha-\beta)t}\cos \gamma x + c_3 e^{(-\alpha+\beta)t}\sin \gamma x + c_4 e^{(-\alpha-\beta)t}\sin \gamma x + c_5 + c_6 x + c_7 e^{-2\alpha t} + c_8 x e^{-2\alpha t}, \tag{59}$$

where

$$\alpha = \frac{k}{2} \tag{60}$$

and

$$\beta = {}^1/_2\sqrt{k^2 - 4\gamma^2}. \tag{61}$$

Consider Equation (59) and apply the boundary conditions, Equations (19) to (22):

With Equation (19) we have

$$0 = c_1 e^{(-\alpha+\beta)t} + c_2 e^{(-\alpha-\beta)t} + c_5 + c_7 e^{-2\alpha t}. \tag{62}$$

$$\therefore c_1 = c_2 = c_5 = c_7 = 0.$$

Applying Equation (20) gives

$$0 = c_3\gamma e^{(-\alpha+\beta)t}\cos \gamma + c_4\gamma e^{(-\alpha-\beta)t}\cos \gamma + c_6 + c_8 e^{-2\alpha t} \tag{63}$$

$$\therefore c_6 = c_8 = 0,$$

$$\gamma = \gamma_n = \frac{(2n-1)\pi}{2}; \quad n = 1, 2, 3, \ldots \tag{64}$$

Now we have

$$\eta = \sum_{n=1,2,3,\ldots}^{\infty} (C_{3n}e^{(-\alpha+\beta_n)t} + c_{4n}e^{(-\alpha-\beta_n)t})\sin \gamma_n x, \tag{65}$$

where

$$\beta_n = {}^1/_2\sqrt{k^2 - [(2n-1)\pi]^2}. \tag{25}$$

We obtain C_{3n} and C_{4n} by using Equations (20) and (21), and the theory of Fourier series:

$$C_{3n} = \frac{(\beta_n + \alpha)\left(\frac{RUL}{\gamma_n^2 K_1}\right) - \frac{U}{\gamma_n c}}{\beta_n}, \tag{66}$$

$$C_{4n} = \frac{(\beta_n - \alpha)\left(\frac{RUL}{\gamma_n^2 K_1}\right) + \frac{U}{\gamma_n c}}{\beta_n} \tag{67}$$

By inserting these values of C_{3n} and C_{4n} in Equation (65) and rearranging, we obtain Equation (23).

In Equation (23), if ${}^1/_2(k/\pi + 1)$ should be an integer, β_n is then zero for $n = {}^1/_2(k/\pi + 1)$ and this term in the sum is indeterminate. The term is easily evaluated by using L'Hospital's rule, as has been carried out in Equation (23).

DISCUSSION

Henry M. Paynter[2]

Professor Rouleau's sound treatment here of elastic wave propagation with viscous shear—a situation identical with the electrical engineer's R-L-C transmission line—presents a singular and novel contribution in pointing out the benefit of considering behavior as the damping effects became small compared to the elastic surges. He has analytically arrived at a simplified solution corresponding to the long-used technique—at least in electrical science—of superposing the (damped) surges on top of a time-varying gradeline due to the loss variation from mean flow in the pipe. His f and g functions correspond to the nondissipative water-hammer terms and the h and j functions represent the space-mean-flow-resistance effects. The decrement factor, of course, represents the dissipation of available stored energy.

When this solution is viewed in these terms, the results have very broad significance and the expressions can be still further simplified, particularly for pressure conditions at the valve.

The author's result may be obtained in a rather direct fashion from the original equations by considering the *impedance* operator of the pipeline looking into the pipe from the downstream end. Omitting the negative sign, this is found to be (for *any* transmission system whatsoever!)

$$Z_i = Z_c \tanh \gamma L$$

where Z_c and γL are evaluated for this case as:

$$Z_c = \rho c\sqrt{1 + (k/D)}$$

$$\gamma L = (L/c)D\sqrt{1 + (k/D)}$$

with notation similar to the author's except that $D \equiv d/dt$.

For values of $k \to 0$, Z_c and γL may be expanded in the approximate relations

$$Z_c \leqq \rho c[1 + (k/2D)] = Z_0[1 + (k/2D)]$$

$$\gamma L \leqq (L/c)D[1 + (k/2D)] = TD[1 + (k/2D)]$$

where the substitutions $Z_0 = \rho c$ and $T = L/c$ give the simplifications at the right. Now the terminal impedance becomes:

$$Z_i/Z_0 = [1 + (k/2D)]\tanh (TD[1 + (k/2D)])$$

or, with $k' = kT$

$$Z_i/Z_0 = \tanh (TD + k'/2) + k'\frac{\tanh (TD + k/2)}{2TD}$$

[2] Associate Professor of Mechanical Engineering, Massachusetts Institute of Technology, Cambridge, Mass. Mem. ASME.

The term on the right-hand side corresponds very nearly to the operational form of Professor Rouleau's Eq. (34) and suggests a number of practical computing procedures.

For example, the dissipation term may be handled by lumping one half of the total resistance at the reservoir-end of the pipe. The gradient change may then be evaluated by time integrating the resultant wave-pressure-time curve $P_0(t)$ scaling the result by the factor k^x, and adding this term to $P_0(t)$ to obtain:

$$P(t) = P_0(t) + k^x \int^t P_0(t)dt$$

This result would be valid not only for step flow change but also for any kind of closure condition and is very easy to instrument as part of an analog or digital computing procedure. The writer suspects that a very simple modification will also permit comparable ease of computing gradient change for quadratic or other nonlinear distributed resistance.

Professor Rouleau has not modified his solutions of Fig. 5 to allow for the evident finite closure time of the valve. While *part* of the discrepancy between observed and computed results may be attributed to this cause, a careful calculation and analysis leads to the conclusion that it is *dispersion* and not *dissipation* which is producing the rapid damping of the higher frequencies.

The writer has for some years been handling this problem by a simple modification of Allievi's equation. In place of the usual relation

$$U(t) + U(t - 2T) - 2U_0 = V(t - 2T) - V(t)$$

or, when $U_0 = 0$:

$$U(t) + V(t) = V(t - 2T) - U(t - 2T)$$

the writer substitutes the expression:

$$U(t) + V(t) = \sum_k c_k [V(t - 2T_k) - U(t - 2T_k)]$$

with the following conditions and definitions:

$U(t)$ = measure of pressure

$V(t)$ = measure of flow

$T = L/a$ = wave travel time

c_k = weighting coefficient ≥ 0

$\sum_k c_k = 1$: normalizing condition

T_k = component delay

$\sum_k c_k T_k = T$: normalizing condition

This technique can account for any time or frequency dependent (or anomalous) dispersion and may be matched accurately to any experimental data such as Fig. 5 of the paper.

Author's Closure

The author wishes to thank Professor Paynter for his stimulating discussion and extension of the results presented in the paper. It is interesting to note that his operational solution is valid for $k \to 0$, whereas the requirement for the traveling wave solution is only that $k^2 << \pi^2$, or $k < 0.3$ for a very good approximation. This is not as severe a condition and is usually true in practical problems. But for the limiting case of $k \to 0$ his methods have the enviable advantage of encompassing any arbitrary mode of valve closure.

The author agrees that the finite time of valve closure is not primarily responsible for the discrepancy between the observed and computed results. Professor Paynter's explanation on the basis of dispersion seems quite reasonable. During the experiment it was observed that the bulk compression modulus K of the crude oil had a significant time dependence, which was attributed to vaporization of certain fractions of the crude oil and to gases going into and out of solution. Professor Paynter himself has shown in a recent paper[3] that a time-dependent bulk compression modulus leads to dispersion, resulting in a smoothing of the pressure fluctuations, as was observed.

[3] F. D. Ezekiel and H. M. Paynter, "Firmoviscous and Anelastic Properties of Fluids and Their Effects on the Propagation of Compression Waves," ASME Paper No. 59—Hyd-19, 1959.

FRIEDRICH O. RINGLEB
Naval Air Material Center,
Naval Air Engineering Facility,
Philadelphia, Pa.

Two-Dimensional Flow With Standing Vortexes in Ducts and Diffusers

The conditions for the equilibrium of two vortexes in a two-dimensional flow through a duct or diffuser are derived. Potential-flow considerations and a few basic results from viscous-flow theory are used for the discussion of the role of cusps as separation control and trapping devices for standing vortexes. The investigations are applied to cusp diffusers especially with regard to the wind tunnel of the James Forrestal Research Center of Princeton University.

THE problem of creating standing vortexes in a flow and of their application to separation control are dealt with. It is well known that separation of a flow usually is connected with the formation of vortexes which are carried downstream by the flow, leading to a transient-flow process within the otherwise steady flow. It is also known that behind a separation point a standing vortex can form with the effect that the vortex transport in the downstream direction is at least reduced. For instance, in the case of a rectangular cutout of a wall a flow along the wall passes the cutout in general with little disturbance, producing within the cutout a standing vortex which acts like a roller bearing for the flow along the wall [1].[1] Also in the case of a rectangular step in a wall, standing vortexes can form on the downstream side of the step causing the separating flow to reattach to the wall on the downstream side, a case which has been discussed recently by I. Tani [2]. However, in both cases the flow velocity along the wall will decrease in the flow direction before reaching the cutout or step. This will result in an increase in thickness of the boundary layer and an increased transport of it into the free stream at the point of separation.

In nature a standing vortex is created on the downstream side of snow cornices at high mountain edges. Here the snow cornice forms itself on the downstream side of a mountain edge when the snow-carrying wind passes over it, representing a natural separation-control device. The cornice has a sharp edge almost like a cusp so that the flow velocity increases up to this cusp. Behind the cusp a rounded cavity forms in which the standing vortex is situated. On the downstream wall a stagnation point of the reattaching flow is indicated by an accumulation of snow, Fig. 1. The characteristic features of this natural separation-control device have been discussed by the author of the present paper [3, 4]. It is the subject of a detailed study in a recent publication [5].

The author also proposed in 1951 to use such a natural-separation control device instead of a badly separating 12-deg diffuser of the wind tunnel of the James Forrestal Research Center (Princeton University). C. D. Perkins and D. C. Hazen have reported the success of this short cusp diffuser [6, 7]. Though the results of the author's snow-cornice studies have been used for the construction of this approximately two-dimensional diffuser, it had not been exactly computed, mainly because the theory in the case of a duct with two cusps was not available at that time and seemed to present considerable mathematical difficulties.

It is the purpose of the present paper to provide such theory in a general form including curved two-dimensional ducts and to apply it to a shape which is approximately the same as that of the Princeton cusp diffuser.

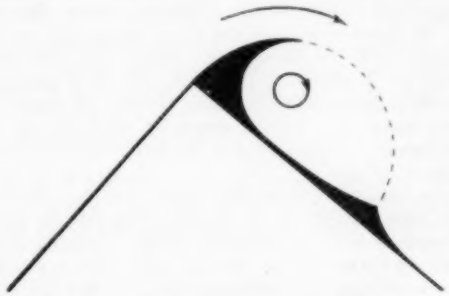

Fig. 1 Scheme of flow over a snow cornice

[1] Numbers in brackets designate References at end of paper.

Contributed by the Hydraulic Division and presented at the Gas Turbine Power and Hydraulic Conference, Houston, Tex., March 6–9, 1960, of THE AMERICAN SOCIETY OF MECHANICAL ENGINEERS.

NOTE: Statements and opinions advanced in papers are to be understood as individual expressions of their authors and not those of the Society. Manuscript received at ASME Headquarters, January 18, 1960. Paper No. 60—Hyd-16.

Nomenclature

t = time
x, y = rectangular co-ordinates in plane of two-dimensional duct or diffuser
$z = x + iy$ = complex co-ordinate in the x, y-plane
ξ, η = rectangular co-ordinates in plane into which flow area is transformed by conformal mapping
$\zeta = \xi + i\eta$ = complex co-ordinate in the ξ, η-plane
r, φ = polar co-ordinates in the ζ-plane
χ = complex potential function
ϕ = velocity potential
ψ = stream function
u, v = velocity components of flow in the z-plane
w = absolute value of velocity
θ = angle between x-axis and velocity vector of flow
Q = strength of a source
Γ = strength of a vortex (circulation)
C_Q, C_Γ = dimensionless coefficients

Subscripts denote special points or values. In particular ζ_0 and z_0 denote the position of a vortex in the ζ-plane or z-plane, respectively.

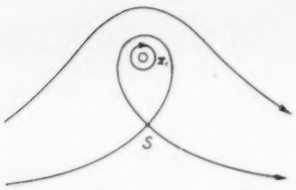

Fig. 2 Single vortex in parallel flow

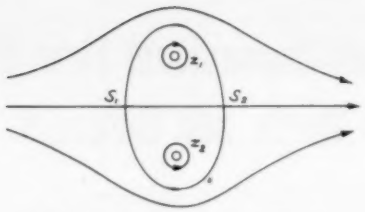

Fig. 3 Two vortexes in parallel flow

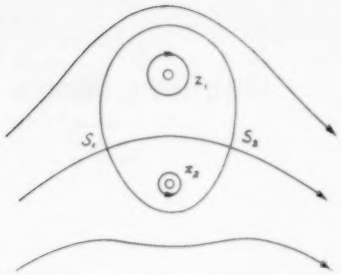

Fig. 4 Two vortexes in a curved flow, one being the image of the other with respect to the streamline S_1S_2 which does not enclose them

Formulation of the Problem

Consider a two-dimensional potential-flow vortex superimposed by a parallel flow, Fig. 2. One of the streamlines contains a stagnation point S. The same streamline encloses a finite area in which the center z_1 of the vortex is situated. Actually such vortex is known to move with the velocity w_0 of the parallel flow.

Further, two vortexes of equal strength are considered, turning in opposite directions, superposed symmetrically by a parallel flow; the resulting flow picture is that of Fig. 3, assuming that the vortexes are sufficiently close together. If one of these vortexes were removed the flow would change to the former case. In general these two vortexes will move too in the direction of the parallel flow though not with its velocity. However, there is the possibility that the center of one of the two vortexes is located in the stagnation point of the flow which the other vortex forms with the parallel flow. Owing to the symmetry the center of the second vortex is also located in the stagnation point which the first vortex forms when superposed with the parallel flow. In this case the two vortexes will not move. They are said to be in equilibrium. The flow picture now shows two stagnation points S_1 and S_2 situated on a streamline which encloses both vortexes. They are also situated on a second streamline which is a straight line. If this straight line is considered as a solid wall and it is assumed that the two vortexes are in equilibrium there is a flow in the upper half plane for which a standing vortex theoretically exists. However, in practice, this is not the case due to viscous properties of the flow; namely, the velocity along the wall approaching the stagnation point S_1 from the left is permanently decreasing toward zero and, therefore, the flow will separate from the wall before reaching the stagnation point S_1. In a free stream, however, without a wall the two vortexes will exist in equilibrium.

Finally, consider a flow passing over a curved wall superposing a vortex near the wall, Fig. 4. It is assumed that the wall is an ideal boundary without friction for the flow. In order that this boundary be a streamline on the other side, a proper second flow parallel to the boundary containing a proper vortex has to be assumed, forming an image of the first flow at the curved boundary. The picture of the total flow will be similar to the former example except that the straight streamline is now distorted (by conformal mapping) into a curved streamline. Thus there are two stagnation points, S_1 and S_2, on the ideal boundary and a second streamline containing the two stagnation points and enclosing the two vortexes. Again the two vortexes will move unless each one is situated in the stagnation point which the other vortex forms with the flow parallel to the wall. In this case the vortexes are in equilibrium. If the wall is a real one with continuous curvature, the velocity of the flow along the wall again will decrease toward zero when approaching the stagnation point S_1, and will separate before reaching this point. Thus a real flow with a standing vortex will not exist in this case.

If, however, the straight streamline in Fig. 3 is distorted by conformal mapping in such a way that at the point S_1 a cusp (a corner with the angle 2π within the flow area) is formed, the stagnation point S_1 will disappear and the streamline S_1S_2 enclosing the vortex, will leave the cusp smoothly with the same tangent. In this case the velocity at S_1 has a finite value different from zero and for proper shapes the flow velocity will increase toward this value when the flow approaches S_1. In this case the existence of a standing vortex in a real flow is possible. There is, however, the open question as to whether or not the equilibrium of the vortex is a stable one.

In the present paper a two-dimensional, in-general curved duct extending from infinity to infinity is dealt with. It is assumed that a flow within this duct has a source at one of the infinite points and a sink at the other one and that in general two standing vortexes exist within two cusp cavities. Under these assumptions the conditions for finite-flow velocities at the two cusps (Kutta-Joukowski conditions) and for the equilibrium of the vortexes will be derived. The results will also include the case of one vortex as a special case. The case of a symmetrical duct will be considered in particular. These conditions will be derived for any kind of mapping function and, therefore, for any kind of duct. However, it will first be shown how proper mapping functions can be obtained in a simple and elementary way.

Analytical Construction of Two-Dimensional Ducts and Diffusers

According to Riemann's theorem, for any simply connected area A with more than one boundary point a one to one conformal map exists which transforms this area into a half plane. Rectangular co-ordinates in this half plane are denoted by ξ and $\eta > 0$ and by x, y rectangular co-ordinates in the plane of the area A. The conformal map of the half plane into the area A is then given by a function

$$z = f(\zeta)$$

where (1)

$$z = x + iy, \qquad \zeta = \xi + i\eta.$$

$f(\zeta)$ is a regular analytical function in the half plane $\eta > 0$ with the condition $f'(\zeta) \neq 0$.

The simplest duct is obtained by mapping the upper ζ-half plane with

$$z = \ln \zeta - i\frac{\pi}{2}. \tag{2}$$

It consists of a duct bounded by two parallel straight lines with the distance π; for instance, $y = -\pi/2$ and $y = \pi/2$.

The function

$$z = \int \frac{(\zeta + i)^{\alpha+\beta}}{\zeta^{\alpha+1}} d\zeta \tag{3}$$

$\alpha, \beta \geqq 0$ yields a duct whose walls enclose the angle $\alpha\pi$ at the infinite point corresponding to $\zeta = 0$ and the angle $\beta\pi$ at the infinite point corresponding to $\zeta = \infty$. For instance, in the case $\alpha = 1, \beta = 0$, the function (3) takes the form

$$z = \ln \zeta - \frac{i}{\zeta} - i\,\frac{\pi}{2} \tag{4}$$

where the constant of integration has been determined so that the duct has the x-axis as axis of symmetry, Fig. 5. The flow area is the rounded outlet from a tank into a parallel duct.

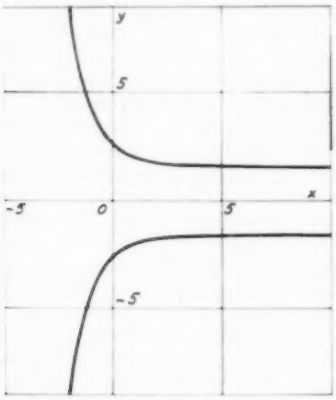

Fig. 5 Inlet from a tank into a parallel channel with known elementary potential flow

A duct[2] with parallel walls but different widths at the two infinite points is represented by the function

$$z = -\ln\left((\zeta + i)^{\alpha} - i^{\alpha}\right) + i\alpha\pi. \tag{5}$$

To $\zeta = \infty$ corresponds the width $\alpha\pi$ and to $\zeta = 0$ the width π. Fig. 6 shows the case $\alpha = 1/2$.

Ducts of much more general character can be obtained by transforming those easily computable ducts once or repeatedly by a function of the form

$$Z = z + \frac{\gamma_1}{z - c_1} + \frac{\gamma_2}{z - c_2} \tag{6}$$

[2] This and the preceding example for the construction of ducts or diffusers with known potential flow without vortexes has been mentioned here because some authors had difficulty with this problem and used rather unrealistic approximations which did not even result in simpler computations. The shapes contained in equation (3), especially those for $\alpha = 1$, are shapes commonly used for diffuser studies.

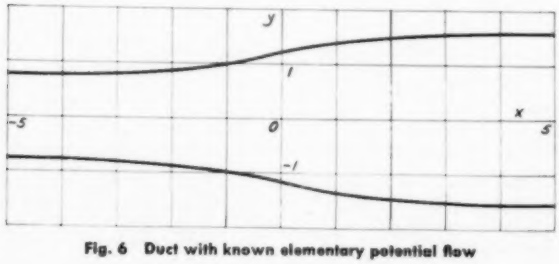

Fig. 6 Duct with known elementary potential flow

where the poles c_1 and c_2 are situated outside the duct to be transformed and the coefficients γ_1 and γ_2 are in general complex numbers.

A transformation of the form

$$Z = z + \frac{\gamma}{z - c} \tag{7}$$

can be constructed without difficulty. It is the same well-known transformation which is applied for the construction of a Joukowski-profile in aerodynamics. The more general transformation (6) is the arithmetical mean value of two of such transformations

$$Z = \frac{1}{2}\left(z + \frac{2\gamma_1}{z - c_1} + z + \frac{2\gamma_2}{z - c_2}\right)$$

and, therefore, can be constructed without difficulty too. The resulting duct will be in general an unsymmetrical one. In order to transform a duct situated symmetrically to the x-axis into a symmetrical one by a function of the type (6) the constants γ_2 and c_2 have to have the conjugate complex values of γ_1 and c_1, respectively. The transformation therefore has the form

$$Z = z + \frac{\gamma}{z - c} + \frac{\bar{\gamma}}{z - \bar{c}} \tag{8}$$

in the symmetrical case.

The transformation (6) has four points determined by $\frac{dZ}{dz} = 0$, where the angles within the z-plane are doubled. If the poles c_1 and c_2 have been chosen and if two of these four points, z_1, z_2 are prescribed on the boundary of the duct the constants γ_1 and γ_2 are determined by the equations

$$1 - \frac{\gamma_1}{(z_1 - c_1)^2} - \frac{\gamma_2}{(z_1 - c_2)^2} = 0,$$

$$1 - \frac{\gamma_1}{(z_2 - c_1)^2} - \frac{\gamma_2}{(z_2 - c_2)^2} = 0. \tag{9}$$

The transformed duct has then two cusps on its boundary. Fig. 7[3] shows the construction of a cusp diffuser by application of a transformation (8) to a parallel duct of width π. By repeated applica-

[3] For points z whose distance of $\bar{c}$ is large, the term $\frac{\bar{\gamma}}{z - \bar{c}}$ in equation (8) can be omitted. The same is the case with the term $\frac{\gamma}{z - c}$ if $|z - c|$ is large. In both cases the transformation (8) is then approximately a Kutta-Joukowski transformation. Fig. 7 has been obtained in this way.

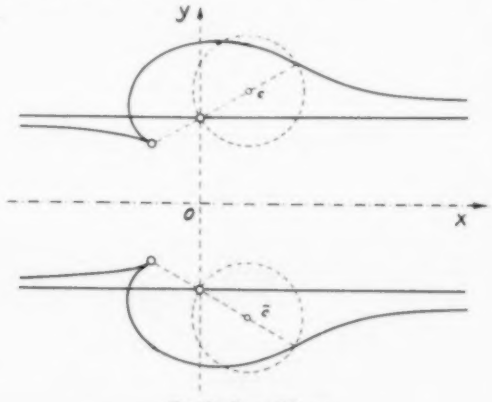

Fig. 7 Cusp diffuser

tion of transformations of the type (8) the shape of this cusp diffuser can be changed and approximated to a desired form. This method is related to an earlier mapping procedure developed by the author (see Bieberbach, Reference [8]).

Determinination of Equilibrium Conditions for Standing Vortexes

The mapping function

$$z = f(\zeta)$$

has been normalized so that $\zeta = 0$ corresponded to one of the infinite points of the duct and $\zeta = \infty$ to the other infinite point. A flow in the ζ-plane with a source or sink at $\zeta = 0$ and a sink or source, respectively, at $\zeta = \infty$ therefore corresponds to a potential flow of an incompressible medium through the duct, flowing from the first infinite point to the second infinite point without further singularities. Because the duct-flow area corresponds to the upper ζ-half plane the strength of the source for the duct is half the strength of that for the total ζ-plane. Thus the flow is given by the complex potential function

$$\chi = \frac{2Q}{2\pi} \ln \zeta \tag{10}$$

and its velocity vector $we^{-i\vartheta}$ in the z-plane by

$$\frac{w}{w_0} e^{-i\vartheta} = \frac{d\chi}{dz} = \frac{2C_Q}{\zeta} \frac{1}{f'(\zeta)} \tag{11}$$

where w_0 is any constant velocity value and

$$C_Q = \frac{Q}{2\pi w_0} \tag{12}$$

a dimensionless coefficient. Here Q denotes the strength of the source or sink determining the flow in the duct. Q is positive in the case of a source at $\zeta = 0$ and negative in the case of a sink. Setting $\zeta = re^{i\varphi}$, the streamlines are given by

$$\frac{\psi}{w_0} = 2C_Q\varphi = \text{const.} \tag{13}$$

Now the case will be studied where, in addition to the flow given by (10), two vortexes are contained in the flow area. Their positions in the upper half plane, Fig. 8, are assumed to be ζ_1 and ζ_2, their circulations Γ_1 and Γ_2. Symmetrical vortexes with the circulations $-\Gamma_1$ and $-\Gamma_2$ have to be assumed in the points $\bar{\zeta}_1$ and $\bar{\zeta}_2$, the conjugate complex values of ζ_1 and ζ_2. Two circulation coefficients are introduced

$$C_{\Gamma_1} = \frac{\Gamma_1}{2\pi w_0}, \qquad C_{\Gamma_2} = \frac{\Gamma_2}{2\pi w_0} \tag{14}$$

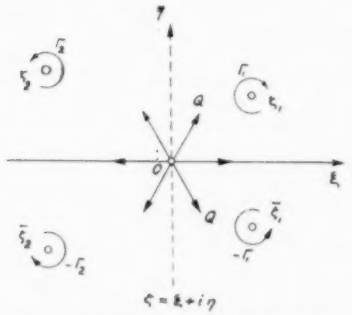

Fig. 8 Flow singularities within the ζ-plane

in analogy to the coefficient C_Q. The complex potential function—instead of (10)—is then given by

$$\frac{\chi}{w_0} = 2C_Q \ln \zeta + iC_{\Gamma_1} \ln \frac{\zeta - \zeta_1}{\zeta - \bar{\zeta}_1} + iC_{\Gamma_2} \ln \frac{\zeta - \zeta_2}{\zeta - \bar{\zeta}_2} \tag{15}$$

because $\frac{\Gamma}{2\pi} \ln (\zeta - \zeta_0)$ is the complex potential function of a vortex with the strength (circulation) Γ and the center ζ_0 in the ζ-plane. The strength of a source or vortex is not changed by conformal mapping. The function χ, therefore, also represents the flow in the duct of the z-plane with vortexes of the same strength if ζ is considered as a function of z.

In general the two vortexes $z_1 = f(\zeta_1)$ and $z_2 = f(\zeta_2)$ will move with the flow. The velocity of a vortex, say z_1, is determined by the velocity of the flow at the point z_1 if the vortex at z_1 but not its images with respect to the boundaries of the flow area are removed. In general the function $z = f(\zeta)$ will not be a single-valued function of ζ but will map a Riemann surface carpeting the ζ-plane into a Riemann surface carpeting the z-plane. The duct area A contained in the Riemann surface of the z-plane will correspond to a certain single sheet of the Riemann surface carpeting the upper ζ-half plane. In order to determine the velocity of the vortex z_1 within A this vortex has to be removed from its position within the Riemann surface. In order to do this the Riemann surface carpeting the ζ-plane must be mapped into a single sheeted τ-plane so that ζ becomes a single valued function of τ. Then also z is a single-valued function of τ. In other words ζ and z are represented by single-valued functions of a parameter τ (a variable of uniformization, Reference [8]). To the vortex z_1 to be removed from the Riemann surface covering the z-plane corresponds τ_1 in the τ-plane. After removal of the vortex τ_1 the flow is represented by the complex potential function χ_1 where

$$\frac{\chi_1}{w_0} = \frac{\chi}{w_0} - iC_{\Gamma_1} \ln (\tau - \tau_1) \tag{16}$$

Correspondingly the motion of the vortex in z_2 is determined by the complex potential function χ_2 where

$$\frac{\chi_2}{w_0} = \frac{\chi}{w_0} - iC_{\Gamma_2} \ln (\tau - \tau_2) \tag{17}$$

The velocity components of the flows represented by χ_1 and χ_2 within the ζ-plane are obtained by differentiation of χ_1 and χ_2 with respect to ζ. Denoting these velocity components by u_1, v_1 and u_2, v_2 one obtains

$$\frac{u_1 - iv_1}{w_0} = \frac{2C_Q}{\zeta} + iC_{\Gamma_1}\left(\frac{1}{\zeta - \zeta_1} - \frac{1}{\zeta - \bar{\zeta}_1} - \frac{\varphi'(\zeta)}{\varphi(\zeta) - \varphi(\zeta_1)}\right) + iC_{\Gamma_2}\left(\frac{1}{\zeta - \zeta_2} - \frac{1}{\zeta - \bar{\zeta}_2}\right) \tag{18}$$

and

$$\frac{u_2 - iv_2}{w_0} = \frac{2C_Q}{\zeta} + iC_{\Gamma_1}\left(\frac{1}{\zeta - \zeta_1} - \frac{1}{\zeta - \bar{\zeta}_1}\right) + iC_{\Gamma_2}\left(\frac{1}{\zeta - \zeta_2} - \frac{1}{\zeta - \bar{\zeta}_2} - \frac{\varphi'(\zeta)}{\varphi(\zeta) - \varphi(\zeta_2)}\right) \tag{19}$$

where

$$\tau = \varphi(\zeta) \tag{20}$$

is the variable of uniformization and ζ_1, ζ_2 correspond to the positions of the vortexes. The velocity components for the z-plane are obtained by multiplying the right sides of equations (18) and (19) by $1/f'(\zeta)$.

The necessary and sufficient conditions that the vortexes at z_1 and z_2 are standing vortexes are $u_1 = v_1 = 0$ for $\zeta = \zeta_1$ and $u_2 = v_2 = 0$ for $\zeta = \zeta_2$. Then

$$\lim_{\zeta \to \zeta_1} \left(\frac{1}{\zeta - \zeta_1} - \frac{\varphi'(\zeta)}{\varphi(\zeta) - \varphi(\zeta_1)} \right) = -\frac{1}{2} \frac{\varphi''(\zeta_1)}{\varphi'(\zeta_1)} \tag{21}$$

and there is a corresponding formula for $\zeta \to \zeta_2$ (see Appendix 1).

Therefore the necessary and sufficient conditions for the equilibrium of both vortexes are

$$\frac{2C_Q}{\zeta_1} - iC_{\Gamma_1} \left(\frac{1}{\zeta_1 - \bar{\zeta}_1} + \frac{1}{2} \frac{\varphi''(\zeta_1)}{\varphi'(\zeta_1)} \right) + iC_{\Gamma_2} \left(\frac{1}{\zeta_1 - \zeta_2} - \frac{1}{\zeta_1 - \bar{\zeta}_2} \right) = 0, \tag{22}$$

$$\frac{2C_Q}{\zeta_2} + iC_{\Gamma_1} \left(\frac{1}{\zeta_2 - \zeta_1} - \frac{1}{\zeta_2 - \bar{\zeta}_1} \right) - iC_{\Gamma_2} \left(\frac{1}{\zeta_2 - \bar{\zeta}_2} + \frac{1}{2} \frac{\varphi''(\zeta_2)}{\varphi'(\zeta_2)} \right) = 0. \tag{23}$$

In the case of a symmetrical duct with a symmetrical flow the mapping function $z = f(\zeta)$ is symmetrical with respect to the η-axis. Also $\tau = \varphi(\zeta)$ is symmetrical to the η-axis and, therefore,

$$\varphi(-\bar{\zeta}) = \overline{\varphi(\zeta)} \tag{24}$$

where the bar indicates the conjugate complex value. It can be shown (see Appendix 2) that in this case

$$\frac{\varphi''(-\bar{\zeta})}{\varphi'(-\bar{\zeta})} = -\overline{\left(\frac{\varphi''(\zeta)}{\varphi'(\zeta)} \right)} \tag{25}$$

In the symmetrical case

$$\zeta_2 = -\bar{\zeta}_1, \qquad \bar{\zeta}_2 = -\zeta_1 = -\zeta_0 \tag{26}$$

and

$$C_{\Gamma_2} = -C_{\Gamma_1} = -C_\Gamma \tag{27}$$

Separating $\zeta_0 = \xi_0 + i\eta_0$ the result obtained is that:

In the case of a symmetrical duct with a symmetrical flow the condition for the equilibrium of the two vortexes is

$$\frac{\varphi''(\zeta_0)}{\varphi'(\zeta_0)} = \left(1 - 4i \frac{C_Q}{C_\Gamma} \right) \frac{1}{\zeta_0} + \frac{i}{\eta_0} - \frac{1}{\xi_0}. \tag{28}$$

Conditions for Finite Velocities at Cusps

The velocity of the flow in the duct has the components u, v to be obtained from the complex potential function χ, formula (15), by differentiation with respect to ζ. Thus

$$\frac{u - iv}{w_0} = \frac{w}{w_0} e^{-i\vartheta} = \frac{1}{w_0} \frac{d\chi}{dz} = \frac{1}{w_0} \frac{d\chi}{d\zeta} \frac{1}{f'(\zeta)} \tag{29}$$

whereby

$$\frac{1}{w_0} \frac{d\chi}{d\zeta} = \frac{2C_Q}{\zeta} + iC_{\Gamma_1} \left(\frac{1}{\zeta - \zeta_1} - \frac{1}{\zeta - \bar{\zeta}_1} \right) + iC_{\Gamma_2} \left(\frac{1}{\zeta - \zeta_2} - \frac{1}{\zeta - \bar{\zeta}_2} \right) \tag{30}$$

The latter expression represents the velocity components (made dimensionless by division with w_0) for the flow within the ζ-plane. If this expression is set equal to zero an algebraic equation of the fourth order is obtained in ζ with four real solutions $\zeta_{s_n} (n = 1, 2, 3, 4)$ representing stagnation points of this flow on the real ζ-axis. To these stagnation points correspond stagnation points in the z-plane on the boundaries of the duct unless there is $f'(\zeta) = 0$ as has been explained in Section 1. According to this discussion two of these stagnation points will be eliminated, say z_{s_3} and z_{s_4}, by incorporating cusps at their place so that a streamline leaves each cusp with finite velocity ($\neq 0$) and forms a stagnation point at the wall behind each cusp.

The conditions for finite velocities ($\neq 0$) at the cusps corresponding to ζ_{s_3}, ζ_{s_4} are, therefore

$$\frac{2C_Q}{\zeta_{s_n}} + iC_{\Gamma_1} \left(\frac{1}{\zeta_{s_n} - \zeta_1} - \frac{1}{\zeta_{s_n} - \bar{\zeta}_1} \right) + iC_{\Gamma_2} \left(\frac{1}{\zeta_{s_n} - \zeta_2} - \frac{1}{\zeta_{s_n} - \bar{\zeta}_2} \right) = 0 \tag{31}$$

$$(n = 1, 2)$$

and

$$f'(\zeta_{s_1}) = 0, \qquad f'(\zeta_{s_2}) = 0. \tag{32}$$

These conditions are called Kutta-Joukowski conditions in analogy to the conditions which exist for a flow at the sharp trailing edge of an airfoil profile.

In the symmetrical case

$$\zeta_1 = -\bar{\zeta}_1, \qquad \bar{\zeta}_2 = -\zeta_1 = -\zeta_0,$$

$$C_{\Gamma_1} = C_\Gamma, \qquad C_{\Gamma_2} = -C_\Gamma, \qquad f(-\bar{\zeta}) = f(\zeta).$$

Without limitation of the generality it is assumed that the points in the ζ-plane corresponding to the cusps are

$$\zeta_{s_1} = 1, \qquad \zeta_{s_2} = -1.$$

Then the conditions (31) and (32) are reduced to

$$\frac{C_Q}{C_\Gamma} = \frac{4\xi_0\eta_0}{(1 + \xi_0^2 + \eta_0^2)^2 - 4\xi_0^2} \tag{33}$$

and

$$f'(\pm 1) = 0. \tag{34}$$

(33) and (34) are the Ku ta-Joukowski conditions in the symmetrical case.

For any duct and flow satisfying the derived conditions the velocity distribution can be computed within the duct and on its boundaries by formulas (29) and (30). This concludes the general theory as outlined at the beginning of the paper.

Application to Cusp Diffusers

By application of a transformation of the type (8) to a parallel duct, cusp diffusers as shown in Fig. 7 can be constructed. The equilibrium conditions for standing vortexes in this particular case of diffusers will now be studied. The transformation (8)

$$Z = z + \frac{\gamma}{z - c} + \frac{\bar{\gamma}}{z - \bar{c}}$$

is a single-valued function of z. The function (2)

$$z = \ln \zeta - i \frac{\pi}{2}$$

however, is multivalued. Therefore a variable τ has to be determined so that ζ and z are single-valued functions of τ. Such variable is $\tau = z$ itself because then

$$\zeta = ie^\tau, \qquad Z = \tau + \frac{\gamma}{\tau - c} + \frac{\bar{\gamma}}{\tau - \bar{c}} \tag{35}$$

are both single-valued functions of τ. Thus

$$\tau = \varphi(\zeta) = \ln \zeta - i\,\frac{\pi}{2} \tag{36}$$

and the equilibrium condition (28) takes the form

$$\frac{\varphi''(\zeta_0)}{\varphi'(\zeta_0)} = -\frac{1}{\zeta_0} = \left(1 - 4i\,\frac{C_Q}{C_\Gamma}\right)\frac{1}{\zeta_0} + \frac{i}{\eta_0} - \frac{1}{\xi_0} \tag{37}$$

from which

$$\frac{C_Q}{C_\Gamma} = \frac{1}{4}\,\frac{\xi_0^2 - \eta_0^2}{\xi_0\eta_0}$$

follows. The in-general complex condition (28), therefore, reduces in this case to a real condition.

If $\zeta = \pm 1$ are the points within the ζ-plane which correspond to the cusps within the z plane Eq. (33) is also valid, namely

$$\frac{C_Q}{C_\Gamma} = \frac{4\xi_0\eta_0}{(1 + \xi_0^2 + \eta_0^2)^2 - 4\xi_0^2}. \tag{38}$$

For ξ_0, η_0, polar co-ordinates are used

$$\xi_0 = r_0 \cos \varphi_0, \qquad \eta_0 = r_0 \sin \varphi_0 \tag{39}$$

to obtain from (37)

$$\frac{C_Q}{C_\Gamma} = \frac{1}{2}\,\operatorname{ctg} 2\varphi_0 \tag{40}$$

and from (38)

$$\frac{C_Q}{C_\Gamma} = \frac{\sin 2\varphi_0}{\frac{1}{2}\left(r_0^2 + \frac{1}{r_0^2}\right) - \cos 2\varphi_0}. \tag{41}$$

Fig. 9 shows the relation between ξ_0 and η_0.

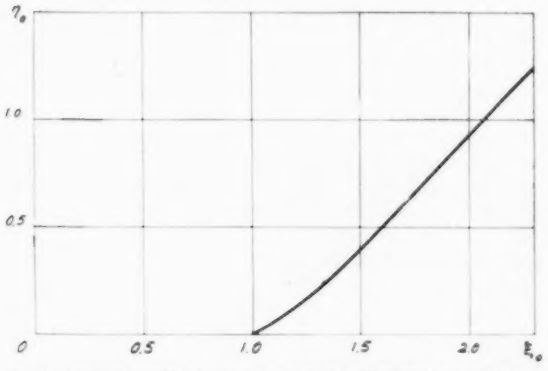

Fig. 9 Locus of equilibrium positions of standing vortexes within the ζ plane

Fig. 10 shows the locus of vortexes in equilibrium in the case of the cusp diffuser of Fig. 7. By repeated application of transformations of the type (8) this duct can approximately be deformed into the shape shown in Fig. 11 representing the expanding part of the Princeton cusp diffuser. If transformations of the type (8) are repeatedly applied to the parallel duct the resulting transformation is represented by a rational and, therefore, single-valued function within the plane of this duct. Therefore, again $\tau = \ln \zeta - i(\pi/2)$ is a proper variable of uniformization, and the locus of equilibrium positions of the vortexes within the ζ-plane is the same as before. This locus is transformed by each transformation of the type (8) into the locus of equilibrium positions for the resulting duct.

The Princeton cusp diffuser proved to be a workable diffuser in a case where all conventional and other unconventional designs failed, Ref. [7]. In particular, it reduced the turbulence of the wind tunnel, which made its operation unsafe without the cusp diffuser, to such a degree that a completely smooth flow was obtained, beside a pressure recovery of about 78 per cent. In Fig. 11 the locus of equilibrium positions of the standing vortexes for various $\frac{C_Q}{C_\Gamma}$ values is plotted as well as the measured vortex center which is situated on this curve. For this position the computed velocity of the flow at the cusp has a maximum.

Stability Considerations

The existence of an equilibrium position does not mean that a vortex in such position must be stable. A stability analysis based on potential-flow theory only would have to make use of the essential condition that the flow has a finite velocity at a cusp. Actually, however, a disturbance can and usually will result in the formation of a new vortex at the cusp, a process which is based on viscous-flow properties. Therefore stability considerations based on potential-flow theory only cannot be expected to lead to sufficiently accurate results. In the present paper, which deals with potential-flow theory only, such stability theory will, therefore, be omitted.

However, relating to the investigations of the preceding section, it might be worth while to note the role which the ratio $\frac{C_Q}{C_\Gamma} = \frac{Q}{\Gamma}$ plays in uniquely determining the equilibrium position.

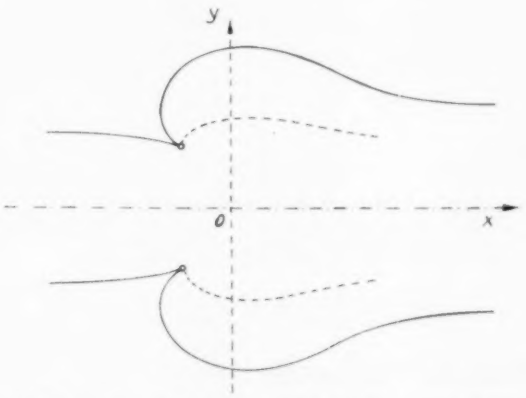

Fig. 10 Locus of equilibrium positions within the cusp diffuser

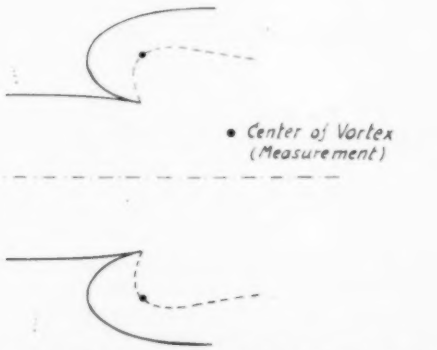

Fig. 11 Cusp diffuser of the James Forrestal Research Center of Princeton University

If it is assumed that a standing vortex within a closed-flow area is driven by shear forces from the outside flow [2] it seems to be reasonable that the mass flow in the duct influences the circulation of the standing vortex and, therefore, its position. Thus C_Q/C_T can be considered as a measure for the driving force involved. More detailed theoretical and experimental investigations on the stability of standing vortexes will be published later.

Conclusion

On the basis of potential-flow theory using a few results from viscous-flow theory, the conditions for a flow in a two-dimensional duct containing two standing vortexes have been derived. The use of cusps as separation-control devices and as trapping devices for standing vortexes has been explained as a logical consequence of the analytical study of the problem. It has been shown how proper shapes of ducts or diffusers, for which standing vortexes exist according to the theory, can be computed on the basis of the derived conditions. The investigation has been applied to a cusp diffuser which closely approximates the one used effectively in the wind tunnel of the James Forrestal Research Center of Princeton University.

References

1 A. Roshko, "Some Measurements of Flow in a Rectangular Cutout," NACA Tech. Note No. 3488, 1955.

2 I. Tani, "Experimental Investigation of Flow Separation Over a Step," in "Boundary Layer Research," Springer Verlag, 1958.

3 F. O. Ringleb, "Theory and Application of Flow Over a Cusp," Aero. Engrg. Lab. Rept. No. 192, Princeton University, 1952.

4 F. O. Ringleb, "Flow Control by Generation of Standing Vortices and the Cusp Effect," Research Bulletin, the James Forrestal Research Center, Princeton University, Rept. No. 317, 1955.

5 F. O. Ringleb, "Separation Control by Trapped Vortices," in "Boundary-Layer Control Principles and Applications," edited by V. Lachmann, Pergamon Press, London, England (in preparation).

6 D. C. Hazen, R. F. Lehnert, T. E. Sweeney, and F. O. Ringleb, "Preliminary Report on Circulation Control by Means of Trailing-Edge Suction and the Cusp Effect," Princeton University, Aero. Engrg. Rept. No. 234, 1953.

7 C. D. Perkins and D. C. Hazen, "Some Recent Advances in Boundary-Layer and Circulation Control," Fourth Anglo-American Aeronautical Conference, London, England, 1953.

8 L. Bieberbach, "Einführung in die konforme Abbildung," Walter de Gruyter, Berlin, Germany, 1956. English edition: "Conformal Mapping," Chelsea Publishing Company, New York, N. Y., 1953.

APPENDIX 1

Expansion of the expression

$$L(\zeta) = \frac{1}{\zeta - \zeta_1} - \frac{\varphi'(\zeta)}{\varphi(\zeta) - \varphi(\zeta_1)}$$

$$L(\zeta) = \left[\frac{\varphi''(\zeta_1)}{\varphi'(\zeta_1)}\left(\frac{1}{2!} - \frac{1}{1!}\right) + \frac{\varphi'''(\zeta_1)}{\varphi'(\zeta_1)}\left(\frac{1}{3!} - \frac{1}{2!}\right)(\zeta - \zeta_1) + \dots\right]$$
$$\cdot\left[1 + \frac{1}{2!}\frac{\varphi''(\zeta_1)}{\varphi'(\zeta_1)}(\zeta - \zeta_1) + \frac{1}{3!}\frac{\varphi'''(\zeta_1)}{\varphi'(\zeta_1)}(\zeta - \zeta_1)^2 + \dots\right]$$
$$= \frac{\varphi''(\zeta_1)}{\varphi'(\zeta_1)}\left(\frac{1}{2!} - \frac{1}{1!}\right) + \left(\frac{\varphi'''(\zeta_1)}{\varphi'(\zeta_1)}\left(\frac{1}{3!} - \frac{1}{2!}\right) - \frac{1}{2!}\left(\frac{1}{2!} - \frac{1}{1!}\right)\left(\frac{\varphi''(\zeta_1)}{\varphi'(\zeta_1)}\right)^2\right)(\zeta - \zeta_1) + \dots$$

Therefore

$$L(\zeta) = -\frac{1}{2}\frac{\varphi''(\zeta_1)}{\varphi'(\zeta_1)} + \left[\frac{1}{4}\left(\frac{\varphi''(\zeta_1)}{\varphi'(\zeta_1)}\right)^2 - \frac{1}{3}\frac{\varphi'''(\zeta_1)}{\varphi'(\zeta_1)}\right](\zeta - \zeta_1) + \dots$$

APPENDIX 2

Relations for functions which are symmetrical to the imaginary axis:

$$f(-\bar{\zeta}) = \bar{f}(\zeta).$$

This can be written because of

$$f = h(\xi, \eta) + ik(\xi, \eta), \qquad \zeta = \xi + i\eta, \qquad -\bar{\zeta} = -\xi + i\eta$$

in the form

$$h(-\xi, \eta) + ik(-\xi, \eta) = h(\xi, \eta) - ik(\xi, \eta)$$

Thus

$$h(-\xi, \eta) = h(\xi, \eta),$$
$$k(-\xi, \eta) = -k(\xi, \eta)$$

Therefore

$$h, \frac{\partial^2 h}{\partial \xi^2}$$

are even functions of ξ,

$$\frac{\partial h}{\partial \xi}, \frac{\partial^3 h}{\partial \xi^3}$$

odd functions of ξ,

$$k, \frac{\partial^2 k}{\partial \xi^2}$$

odd functions of ξ,

$$\frac{\partial k}{\partial \xi}, \frac{\partial^3 k}{\partial \xi^3}$$

even functions of ξ. Thus

$$f'(-\bar{\zeta}) = \left(\frac{\partial h}{\partial \xi}\right)_{-\xi,\eta} + i\left(\frac{\partial k}{\partial \xi}\right)_{-\xi,\eta} = -\frac{\partial h}{\partial \xi} + i\frac{\partial k}{\partial \xi},$$
$$f'(-\bar{\zeta}) = -\bar{f}'(\zeta),$$

$$f''(-\bar{\zeta}) = \left(\frac{\partial^2 h}{\partial \xi^2}\right)_{-\xi,\eta} + i\left(\frac{\partial^2 k}{\partial \xi^2}\right)_{-\xi,\eta} = \frac{\partial^2 h}{\partial \xi^2} - i\frac{\partial^2 k}{\partial \xi^2},$$
$$f''(-\bar{\zeta}) = \bar{f}''(\zeta),$$

$$f'''(-\bar{\zeta}) = \left(\frac{\partial^3 h}{\partial \xi^3}\right)_{-\xi,\eta} + i\left(\frac{\partial^3 k}{\partial \xi^3}\right)_{-\xi,\eta} = -\frac{\partial^3 h}{\partial \xi^3} + i\frac{\partial^3 k}{\partial \xi^3},$$
$$f'''(-\bar{\zeta}) = -\bar{f}'''(\zeta)$$

DISCUSSION

Jules L. Dussourd[4]

Another clever application of a standing vortex resides in the so-called "tangential fan." In this application, use is made, as in the author's paper, of an artificially induced stationary vortex, by fitting a short flow passage with a cusplike protuberance, in such a manner as to redistribute the flow in a desirable pattern. The comparison stops here however; the eddy in this case is not used as a fluid roller bearing or an anti-separation device, but rather as a means of establishing a certain distribution of flow velocity and flow direction.

In the tangential fan, a vortex is superimposed upon the source flow created by the squirrel cage-type rotor. The combination flow enters the rotor from one side in a radial tangential direction inward from the outer periphery and leaves in a radial tangential direction outward at the other side. Thus, the flow runs across the rotor rather than traveling radially out. Both at the entrance and exit there exist a strong velocity and absolute angle gradient, so designed as to properly match with the rotor blades. The advantages claimed for this type of operation are numerous. At low Reynolds numbers, say 10,000 (small rotors and low velocities), the efficiency is several times the efficiency of equivalent radial or axial fans. This is mainly attributed to the fact that the bulk of the flow goes through a small percentage of the periphery and operates at a much higher Reynolds number. The fan is unusually quiet (30 db lower than equivalent axial fan), mainly because the rotational tip speeds are low (7 to 9 per cent of equivalent axial machine). The direction of both mean entering and mean leaving flows is convenient for a large majority of installations. Installations consist mainly of household appliances, such as indoor heating fans, exhaust fans, driers, etc., and industrial appliances such as vacuum cleaners, conveyers, mixing equipment, etc.

As in Dr. Ringleb's diffuser, successful operation resides in the proper shaping and locating of the cusp that induces the vortex.

[4] AiResearch Manufacturing Company of Arizona, a division of The Garrett Corporation, Phoenix, Ariz.

Author's Closure

The author wishes to thank Mr. Jules L. Dussourd for his valuable contribution. The "tangential fan" is not just another practical application of a standing vortex. It is of particular interest because in this case a standing vortex is effectively stabilized by superposition with a source-sink flow. It has been observed that, in cases where it is difficult to stabilize the two-dimensional "roller bearing" flow between two parallel walls, stability can be created by weak suction in direction of the vortex center line through one or both of the walls where the vortex ends. This result can be explained as a boundary-layer control effect where the disturbing influence of the wall boundary layer on the vortex is removed by suction. However, in this case too the source-sink flow, superposed on the vortex by the suction process, might produce the stabilizing effect. There are other observations and possible applications of standing vortexes. A considerable number of them have been mentioned or suggested during the general discussion of this paper. The author is greatly indebted to all contributors and intends to return to the subject in a more detailed publication

G. M. WOOD
Mem. ASME

J. S. MURPHY
Assoc. Mem. ASME

J. FARQUHAR
CANEL Project,
Pratt & Whitney Aircraft,
Middletown, Conn.

An Experimental Study of Cavitation in a Mixed Flow Pump Impeller

A mixed flow impeller design was tested with six, five, and four vanes in a closed water loop to study the effects of cavitation on hydraulic performance and the results were compared with the work of other investigators. Two idealized flow models for incipient cavitation were derived to illustrate limits of cavitation design. It was found that both vane blockage and solidity effects are important when designing for optimum cavitation performance. Data showing incidence and speed effects plus the tip static pressure profiles in cavitating and noncavitating flow are also presented.

Introduction

CAVITATION occurs in a hydraulic system when the static pressure at any point in the fluid is lowered sufficiently to permit the liquid to rupture and form vapor filled cavities. Many experimenters have reported that initial or incipient cavitation usually takes place at a point where the local static pressure becomes equal to the vapor pressure [1, 3].[1] This experimental evidence is contrary to the known high rupture strength of pure liquids which would require a considerable decrease in pressure below the vapor pressure to rupture and form cavities. However, the concept of cavities forming about nuclei [1, 4, 7] offers a plausible explanation of why the theoretical underpressure is not realized in ordinary hydraulic systems.

Assuming that cavitation begins as soon as the local static pressure is equal to vapor pressure, it is convenient to use a parameter known as net positive suction head, NPSH, when correlating data from hydraulic machinery tests and is defined by the following equation:

$$\text{NPSH} = H_s + C_m^2/2g - H_v \qquad (1)$$

[1] Numbers in brackets designate References at end of paper.

Contributed by the Hydraulic Division and presented at the Gas Turbine Power & Hydraulic Conference, Houston, Texas, March 6–9, 1960, of THE AMERICAN SOCIETY OF MECHANICAL ENGINEERS.

NOTE: Statements and opinions advanced in papers are to be understood as individual expressions of their authors and not those of the Society. Manuscript received at ASME Headquarters, November 30, 1959. Paper No. 60—Hyd-7.

For pump tests, NPSH is usually determined at a reference station immediately upstream of the impeller vanes. This parameter gives the total head above vapor head which exists at the reference station for a given degree of cavitation in the pump. Although it may be assumed that the NPSH requirements for all liquids would be the same at the incipient point, Stepanoff [11] and Salemann [12] have shown the importance of including thermodynamic effects when correlating cavitation performance beyond the incipient stage.

A second cavitation correlating parameter which has been widely adopted in pump testing is suction specific speed N_{ss}. This parameter was first advanced by G. F. Wislicenus, R. M. Watson, and I. J. Karassik [6] and is defined as:

$$N_{ss} = \frac{N\sqrt{Q}}{(\text{NPSH})^{3/4}} \qquad (2)$$

Suction specific speed requires qualification with regard to the degree of cavitation existing at the point of evaluation. The NPSH value is usually selected at some definite percentage drop-off in the noncavitating head rise generated by the pump when operating at constant values of speed N and flow rate Q.

The mechanics of cavitation has been well described in the literature [4, 7, 8]. In flowing systems, cavitation is known to be a cyclic process wherein the cavities form at some point in the stream, grow in accordance with the laws of fluid dynamics and thermodynamics, and collapse violently, as in water hammer, when they are transported to regions of higher static pressure. Cavitation is objectionable in hydraulic systems for the following

Nomenclature

B_v = blockage coefficient = $\frac{t/\sin\beta^\circ}{2\pi r/z}$, dimensionless
C_m = meridional velocity, ft/sec
D = dimensional constant = $\frac{30\sqrt{448.8}\,(2g)^{3/4}}{\sqrt{\pi}}$
g = gravitational constant, ft/sec^2
H_s = static head, ft
H_t = total head, ft
H_v = head of vapor, ft
K = cavitation index = $\frac{\text{NPSH}}{C_m^2/2g}$, dimensionless
N = impeller rotative speed, rpm
N_{ss} = suction specific speed = $\frac{N\sqrt{Q}}{(\text{NPSH})^{3/4}}$
NPSH = net positive suction head = $H_s + C_m^2/2g - H_v$, ft
P_s = static pressure, psig
P_t = total pressure, psig
Q = flow rate, gpm
r = radial distance from impeller axis, in.
S = meridional tip streamline distance from impeller inlet, in.
S_t = total tip meridional streamline distance from impeller inlet, in.
T = torque, in-lb
t = impeller vane thickness, in.
u = impeller wheel speed, ft/sec
z = number of impeller vanes
β = relative flow angle, degrees
β° = vane angle, degrees
ψ = cavitation coefficient = $\frac{\text{NPSH}}{u^2/2g}$, dimensionless
ϕ = flow coefficient = C_m/u, dimensionless

Subscripts

0 = reference station upstream of impeller
1 = reference station inside vane row at impeller inlet
2 = Kiel probe station in impeller discharge
i = incipient cavitation condition
nc = noncavitating

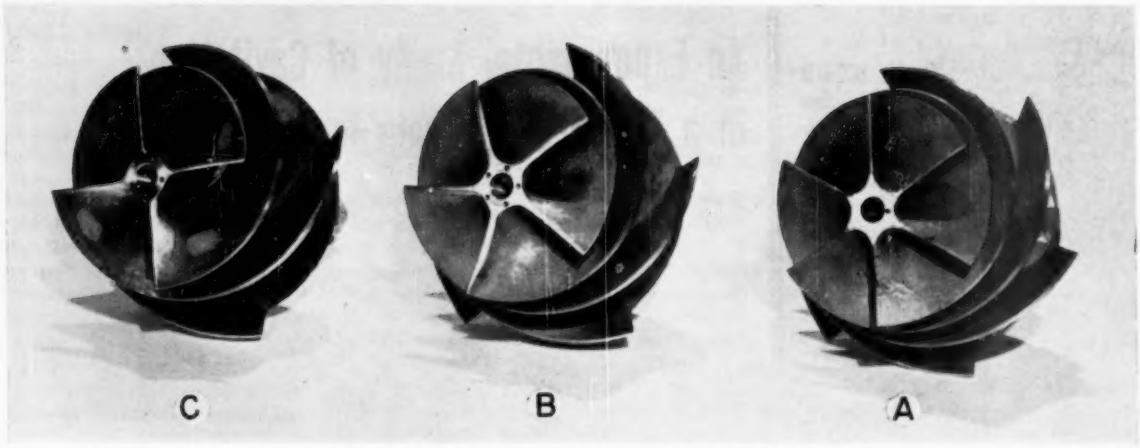

Fig. 1 Three versions of the mixed flow impeller tested

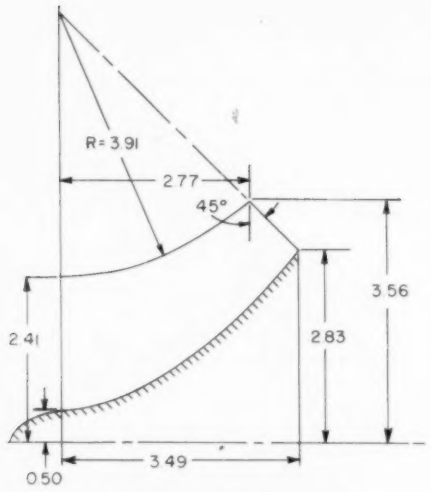

Fig. 2 Elevation view of the impeller

reasons: (*a*) Loss of hydraulic performance, (*b*) undesirable noise and vibration, and (*c*) damage to hydraulic equipment when the pitting action produced by the collapsing cavities reaches sufficient intensity to damage the structures of the system.

This paper is concerned with the hydraulic performance changes due to cavitation in the testing of a mixed flow pump impeller in a closed water loop. The basic design was tested with six, five, and four vanes to obtain specific data on the effects of varying the vane blockage and solidity of the rotating cascade. The data were correlated at the incipient cavitation point and the results compared with those obtained earlier by Gongwer [9]. An incipient cavitation index parameter K_i and a flow coefficient ϕ were used in the correlations and are defined as follows:

$$K_i = \frac{\text{NPSH}_i}{C_m^2/2g} \tag{3}$$

$$\phi = C_m/u \tag{4}$$

Impeller tip static pressure profiles were recorded in cavitating and noncavitating flow and the results qualitatively compared with those of H. Rouse and J. S. McNown [10] on water tunnel tests of symmetrical head forms at the no incidence condition.

Description of Test Impellers

The six, five, and four-vaned versions of the basic impeller design are shown in Fig. 1. For purposes of ready identification, these impellers are designated A, B, and C, respectively. The meridional profile of the impeller design is presented in Fig. 2 and the pertinent dimensions are indicated therein. This was an unshrouded, mixed flow design with an axial vane inlet and an inlet hub nose section of low hub-tip ratio. The impeller tip meridional profile was described by a circular arc with an inlet tangent of zero degrees and a discharge tangent of forty-five degrees with respect to the impeller axis of rotation. The design speed was 4920 rpm at a flow rate of 1500 gpm. The inlet tip running clearance was established at 0.030 in.

The detailed hydraulic design was based upon the stream filament technique reported by Hamrick, et al. [5]. This general method of analysis was programmed on an IBM-704 computer to expedite the design procedures. The studies completed to date by this method have all indicated the importance of including the vane blockage when analyzing the static pressure distribution. Exclusion of the vane blockage will invariably result in considerable error in the prediction of the minimum value of static pressure in the rotating vane passages, especially at the low vane angle settings.

The impellers were type-316 stainless steel investment castings. The impeller vanes and the hub section were individually produced in wax and manually joined to produce the final waxes for casting. This method of fabrication simplified the procurement of impellers with various numbers of vanes. The surface finish of the impellers in the "as-cast" condition was approximately 50 rms and no further finishing of the vane or hub surfaces was performed. Machining of the impeller tip contour and attachment details was completed prior to final inspection. The values of the vane angle and vane thickness used in the impeller analysis and in the correlation of the test results were those determined by detailed mechanical inspection. A summary of the impeller vane inlet geometry for the inlet tip half of the three test impellers is presented in Table 1.

Description of the Water Loop

A schematic of the test loop used for the impeller tests is shown in Fig. 3. The system was a closed water loop designed specifically for impeller performance testing. The impeller discharged into a vaneless conical diffuser section and then into a

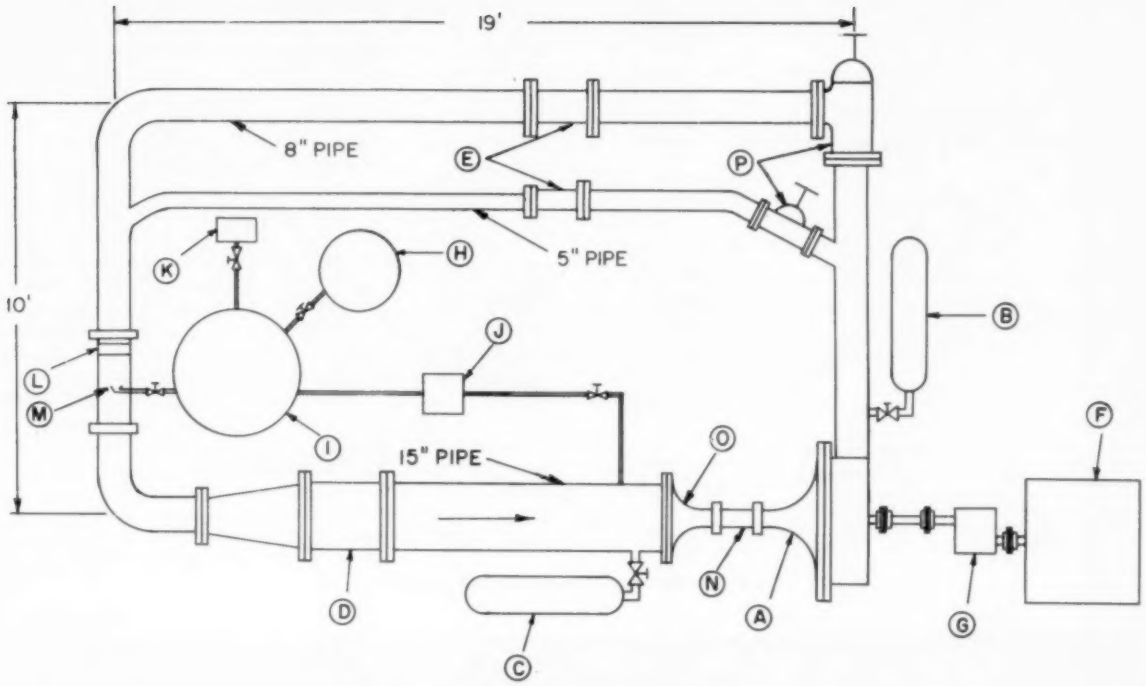

Fig. 3 Schematic view of the test loop

A	Impeller housing	F	D-C drive motor	L	Vortex generator
B	Discharge pressure accumulator	G	Gear box	M	Pick-up tube
C	Inlet pressure accumulator	H	Demineralizer	N	Transparent section
D	Heat exchanger	I	Degasser tank	O	Inlet flow nozzle
E	Flow meters	J	Fill pump	P	Throttle valves
		K	Vacuum pump		

Table 1 Impeller vane inlet geometry

Design values:

S/S_t	β_{tip}*, deg	β_{hub}*, deg	t_{tip}, in.	t_{hub}, in.
0	16.6	66.2	0.060	0.120
0.1	16.7	64.4	0.090	0.152
0.2	17.0	59.4	0.108	0.180
0.3	17.3	52.9	0.118	0.204
0.4	17.6	46.3	0.123	0.224
0.5	18.1	42.1	0.125	0.240

Inspection values:

	Impeller A	Impeller B	Impeller C
β_{tip}* at S/S_t = 0	18.3 ± 0.7	17.4 ± 0.5	17.0 ± 0.5

Maximum vane thickness deviation = $^{+0.020}_{-0.000}$

collector. This arrangement provided a uniform discharge circumferential static pressure distribution over a wide range of flows. An elevation view of the impeller installed in the vaneless diffuser with the associated instrumentation is shown in Fig. 4. The impeller housing, inlet plenum chamber, and inlet pipe with the instrumentation is shown in a photograph in Fig. 5. The system permitted either inlet or discharge pressure control of the test section through the use of air pressure regulation of hydraulic accumulators which were mounted on the impeller inlet and discharge pipe sections of the loop. The air and water within the accumulators were separated by an expandable rubber bag. The loop was provided with two parallel legs for accurate flow measurement over different flow ranges. Each leg contained a throttle valve and flowmeter. The flowmeters were calibrated prior to installation to insure accurate flow measurement. The 5-in. flow tube pressure differential was read on a 10-in. inclined mercury manometer while the larger 8-in. flow tube pressure differential was read on a mercury U-tube manometer. The inlet total pressure was measured by a pressure tap located at the center line of the inlet plenum chamber on an 8-in. compound Bourdon tube gage. The inlet pressure gage had a range of from −15 to 85 psi graduated in $^1/_4$-psi increments. Discharge total pressure was measured in the vaneless diffuser section by six manifolded shielded Kiel probes set at the midstream of the diffuser section. These probes were oriented at a 45-deg angle to the tangential plane to minimize incidence effects. They were read on an 8-in. Bourdon tube gage which had a range of from 0 to 375 psi and was graduated in $^1/_2$-psi increments. Static pressure measurements were taken by 13 static pressure taps located along the tip of the impeller and were read by a Bourdon tube gage similar to those described. An 8-in. Bourdon tube gage connected to the inlet plenum chamber at the impeller center line was used as a reference zero for all gages. The zero of all gages was checked daily prior to testing. The temperature of the water was measured by a thermocouple immersed in the inlet plenum chamber. The water temperature was maintained at a constant value of 100 F for almost all test points by an automatically regulated shell and tube type heat exchanger.

Traverse equipment was mounted immediately upstream of the impeller as shown in Fig. 5. The traverse gear, in conjunction

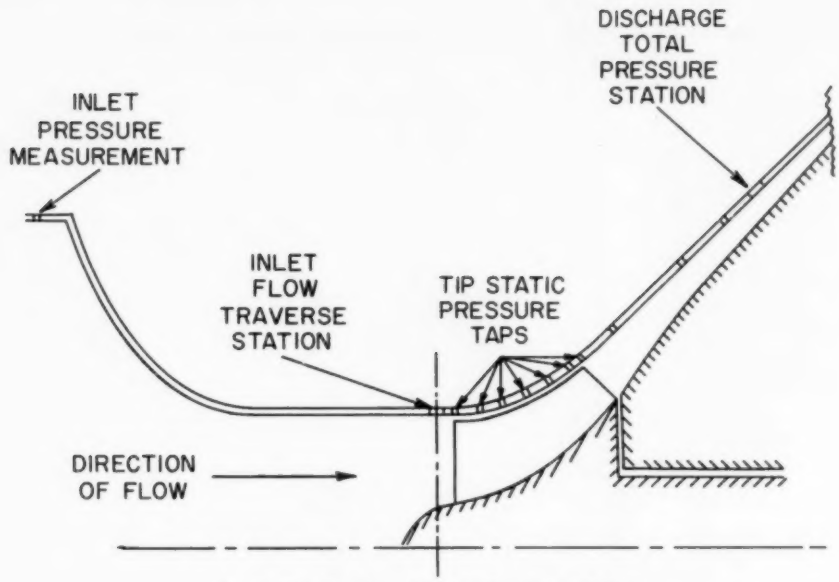

Fig. 4 Elevation view of the impeller test installation

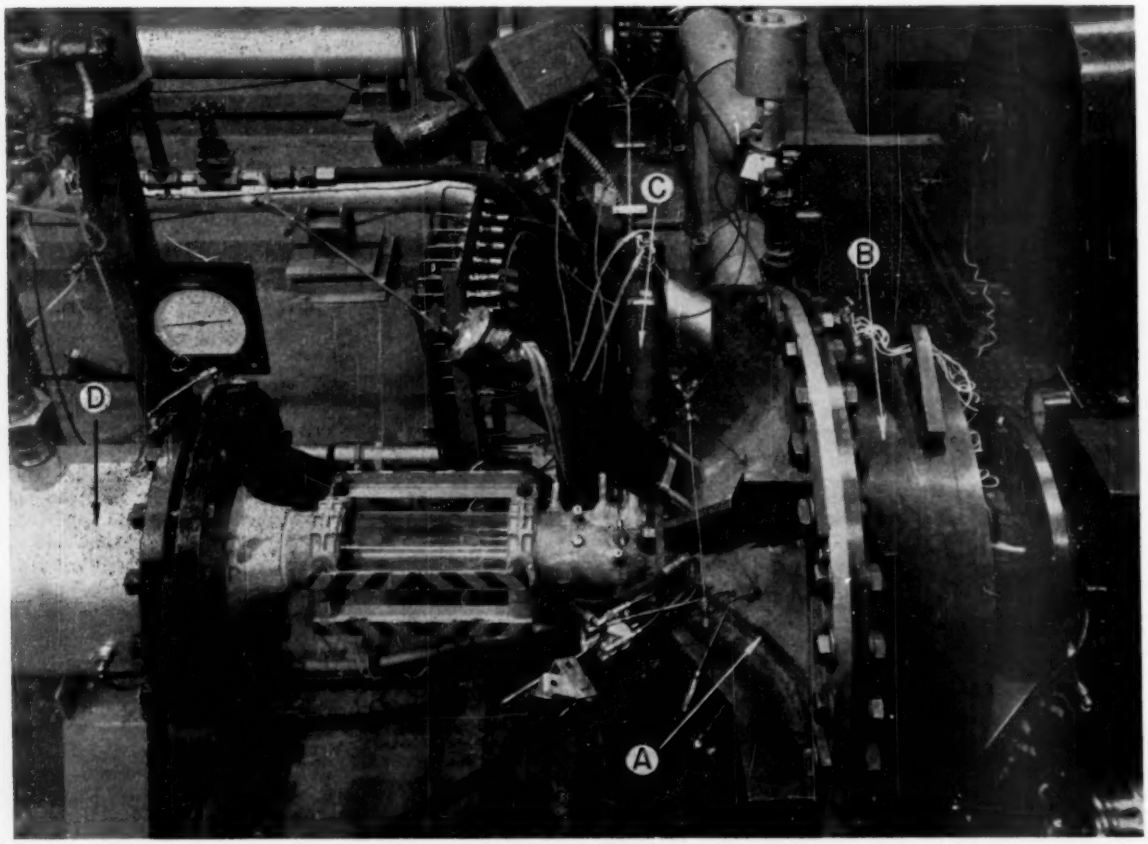

Fig. 5 Impeller test rig

A Impeller housing
B Collector
C Inlet traverse gear
D Inlet plenum chamber

with a balancing control, was used to radially and angularly position a yaw probe into the stream.

A degassing and demineralizing system was used to purify the water used in the test loop. The water entering the loop was first passed through an ion exchange demineralizer, then to a degasser tank. The degasser tank contained a steam heating coil and a vacuum pump connection. A small pump was provided to pump the degassed water from the tank into the test loop. A stationary vaned vortex generator with a pickup tube located three pipe diameters downstream, was used to remove the remaining entrained and dissolved gas in the water prior to testing. The pickup tube discharged into the degasser tank.

A 250 hp d-c motor coupled to a 2.33/1 step up gear box served as the drive unit. Speed was measured by a direct reading tachometer which took a signal from a tachometer generator mounted on the drive motor. The speed was checked several times during the testing by a photoelectric pickup which utilized a disk alternately painted black and white mounted on the drive motor shaft. The photoelectric pickup output was read on an E-PUT meter. These checks found the speed to be within 0.3 per cent of that read by the tachometer. The torque was read on a self balancing potentiometer graduated in 10-inch-pound increments. The torque meter was checked several times during testing by inserting a known resistance across the bridge circuit and reading the output on the potentiometer.

Test Procedure

The test loop was filled with water through the degassing and demineralizing system. In the degasser tank the water was heated by steam in a vacuum to remove the dissolved gas in the water and then pumped into the loop. After the system had been filled with water, it was circulated at a low flow rate with the discharge pressure so controlled that the impeller inlet pressure was maintained at about 5 psia. The water passed through the stationary vaned vortex generator which separated any remaining gas from the water. A mixture of gas and water was sucked out of the loop through the pickup tube to the degasser tank. The water carryover was pumped from the degasser tank back to the loop. This procedure resulted in a dissolved gas content of less than 3 ppm. The dissolved gas content of the water was measured by a gas analyzer prior to the start of testing.

The cavitation tests were performed by maintaining the flow and speed constant and recording the torque, inlet pressure, discharge total pressure, and water temperature. Pressure control was maintained by the discharge or inlet accumulator depending upon whether the lowest attainable inlet pressure was below atmospheric pressure or above.

Flow traverses of the inlet to the impeller were made with the flow and speed held constant and with the impeller operating in a noncavitating condition. A yaw probe was used to measure the stream total pressure and flow angle at radial increments across the inlet pipe. The inlet flow nozzle total pressure loss characteristics were evaluated from the traverse data and were found to be negligible in the flow range of interest.

The tip static pressure measurements were recorded individually at each test point by a manifolded valving arrangement at the control panel. Frequent purging of the gage lines was performed to insure that gas entrainment did not occur.

Test Results

Inlet traverse data were obtained using impeller A with a fixed throttle valve setting to give flows of 750, 1500, and 1980 gpm corresponding to impeller rotational speeds of 2460, 4920, and 6500 rpm. Fig. 6 is a graph of the meridional velocity C_m divided by the maximum velocity $C_{m\,max}$ as a function of radial distance

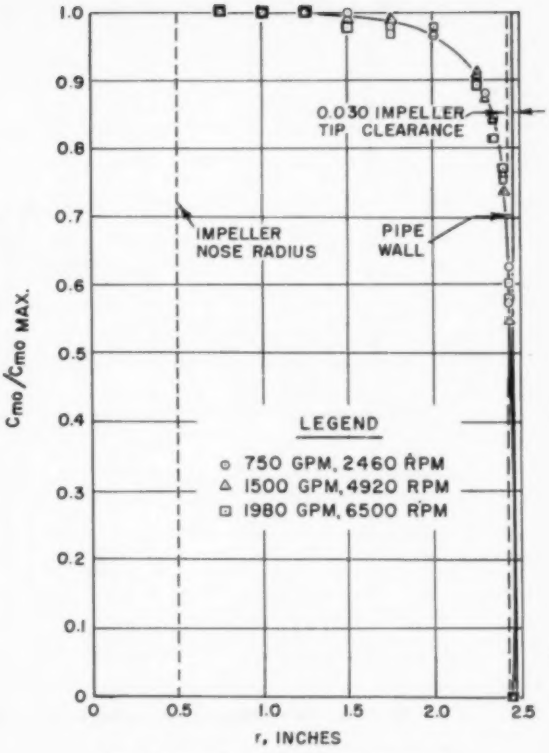

Fig. 6 Inlet velocity distribution—impeller A

from the impeller axis r. The values of C_m were computed from yaw probe total pressure and flow angle measurements and the wall static pressure at the inlet pipe radial traverse location shown in Fig. 4. The average measured swirl angle of the flow in the inlet region did not exceed two degrees from the meridional direction, and at most stations was under one degree.

In Fig. 7, typical cavitation data obtained for impeller A are shown. The total head generated by the impeller when operating in cavitation divided by the noncavitating head, $(H_{\mathcal{D}} - H_{\mathcal{S}})/(H_{\mathcal{D}} - H_{\mathcal{S}})_{nc}$, and the corresponding torque divided by the noncavitating torque values, T/T_{nc}, are plotted against NPSH for a series of cavitation tests at an impeller speed of 4920 rpm and flows from 1000 to 1900 gpm.

The net positive suction head values at cavitation inception, $NPSH_i$, were taken to be at the point where the impeller head rise first departed from the constant noncavitating value. The torque measurement proved to be a useful cross-check on the incipient cavitation point, although it was not generally as positive an identification as the head drop off determination.

The $NPSH_i$ values were determined in cavitation tests of impellers A, B, and C for flows of 450 to 1100 gpm at a speed of 2460 rpm and for flows of 1000 to 2300 gpm at 4920 rpm. For impellers A and B, $NPSH_i$ was also determined for flows of 1000 to 2240 gpm at a speed of 6500 rpm. These values of $NPSH_i$ were used to determine the cavitation index K_i as a function of the flow coefficient ϕ in accordance with the definitions given by equations (3) and (4), respectively. The results are plotted in Figs. 12, 13, and 14. These data points were converted to suction specific speed N_{ss} by substituting the proper speed N, flow Q, and $NPSH_i$ values in equation (2), and the results are plotted against the flow coefficient ϕ in Figs. 15, 16, and 17.

Curves of tip static pressure P_s are plotted against the ratio of

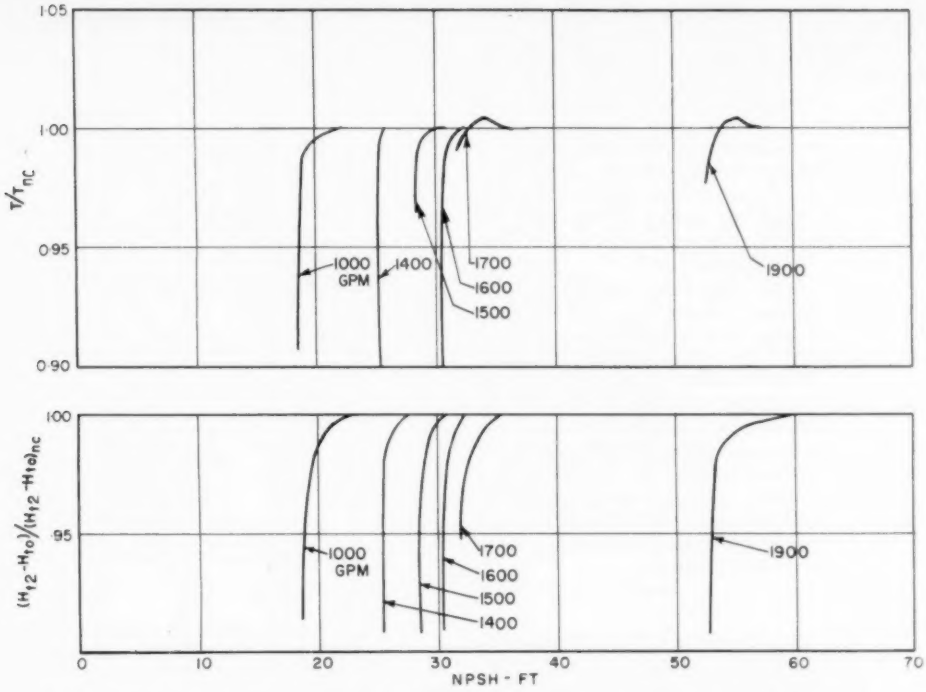

Fig. 7 Typical cavitating to noncavitating head and torque ratios versus NPSH—impeller A at 4920 rpm

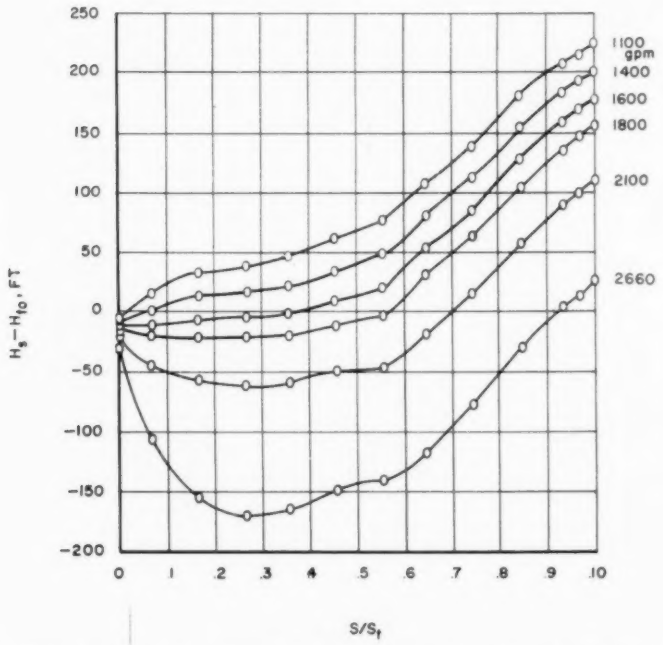

Fig. 8 Noncavitating tip static pressure distribution for various flows—impeller A at 4920 rpm

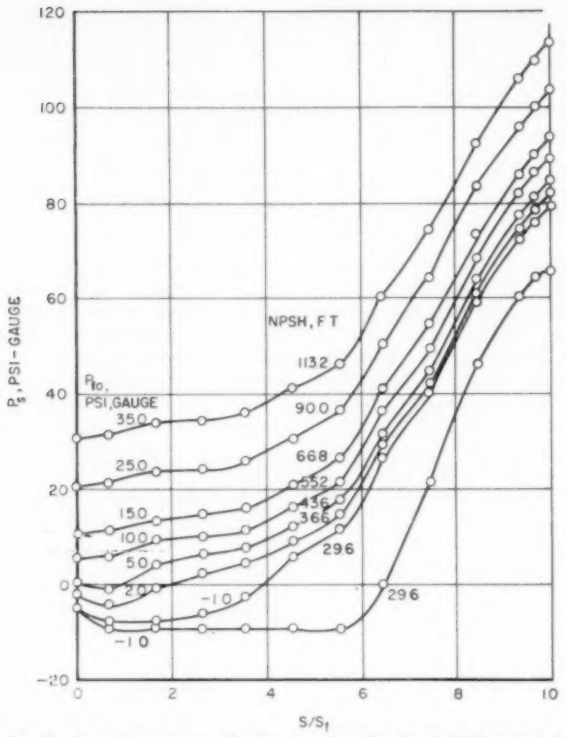

Fig. 9 Tip static pressure distribution—impeller A at 4920 rpm and 1500 gpm

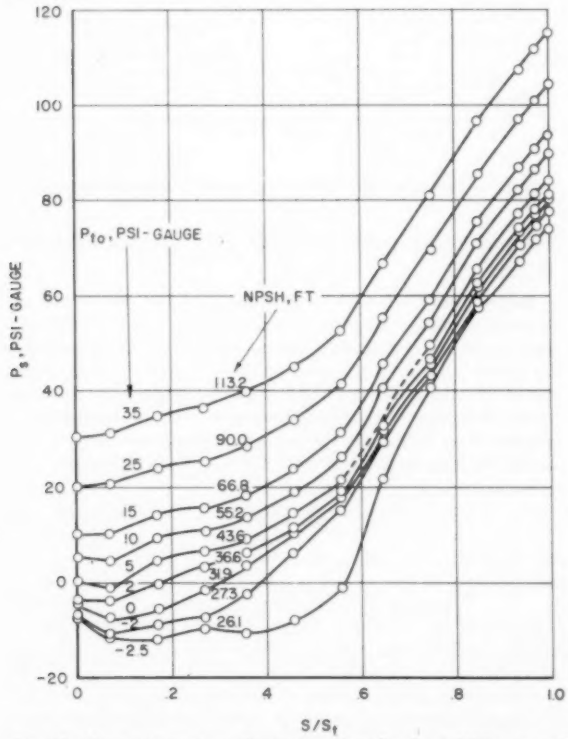

Fig. 10 Tip static pressure distribution—impeller B at 4920 rpm and 1500 gpm

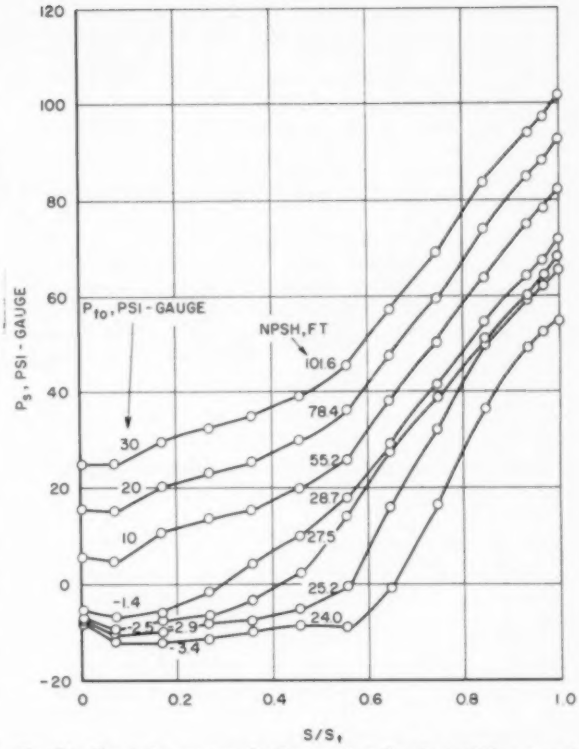

Fig. 11 Tip static pressure distribution—impeller C at 4920 rpm and 1500 gpm

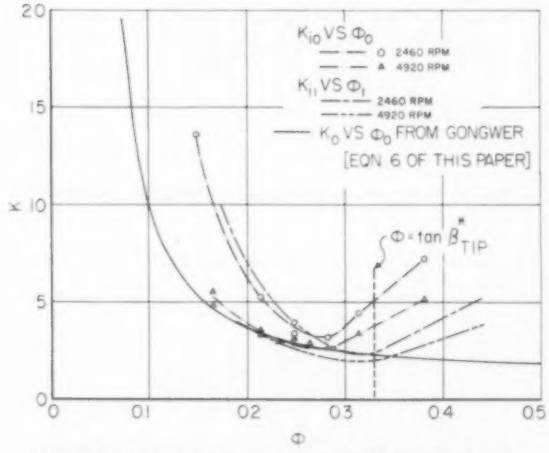

Fig. 12 Cavitation index versus flow coefficient—impeller A

the impeller tip streamline meridional distances from the inlet to the total meridional distance, S/S_t, for progressively lower inlet pressures. Figs. 9, 10, and 11 are for impellers A, B, and C, respectively, and correspond to an impeller speed of 4920 rpm and a flow rate of 1500 gpm.

For impeller A, the effect of varying incidence on the noncavitating tip static pressure distribution is shown in Fig. 8 where the static head minus inlet total head, $H_s - H_{s0}$, is plotted as a function of S/S_t for flows from 1100 to 2600 gpm at a constant impeller speed of 4920 rpm.

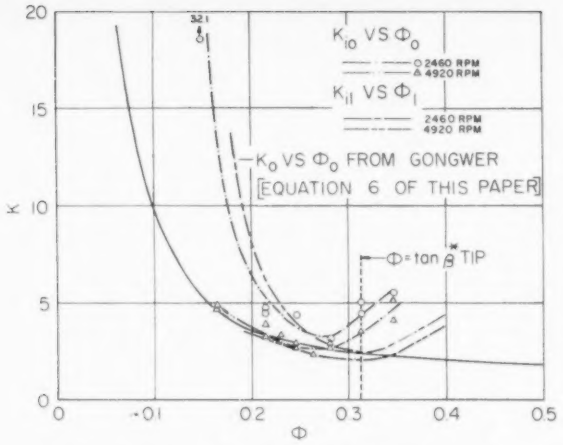

Fig. 13 Cavitation index versus flow coefficient—impeller B

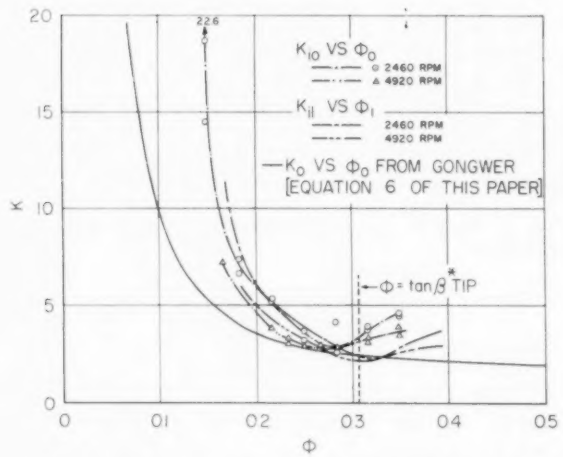

Fig. 14 Cavitation index versus flow coefficient—impeller C

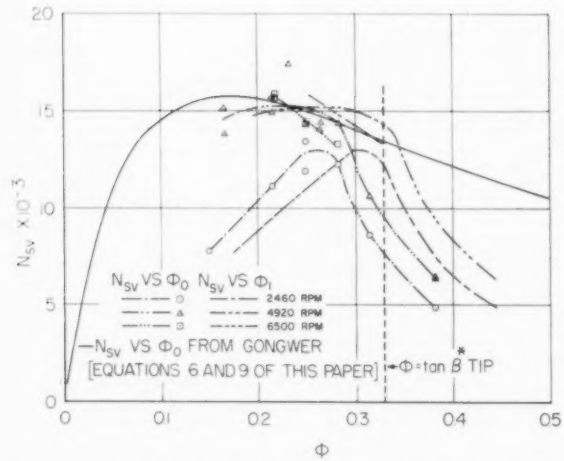

Fig. 15 Suction specific speed versus flow coefficient—impeller A

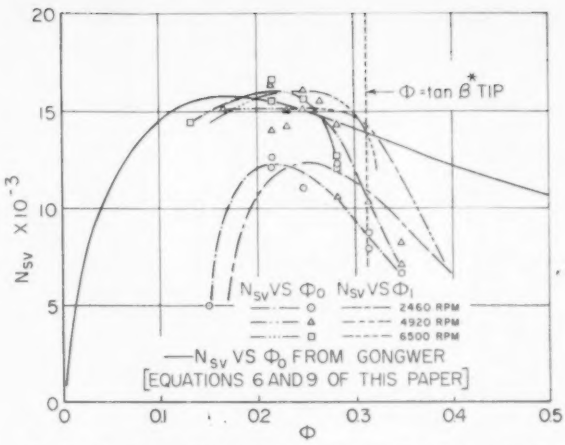

Fig. 16 Suction specific speed versus flow coefficient—impeller B

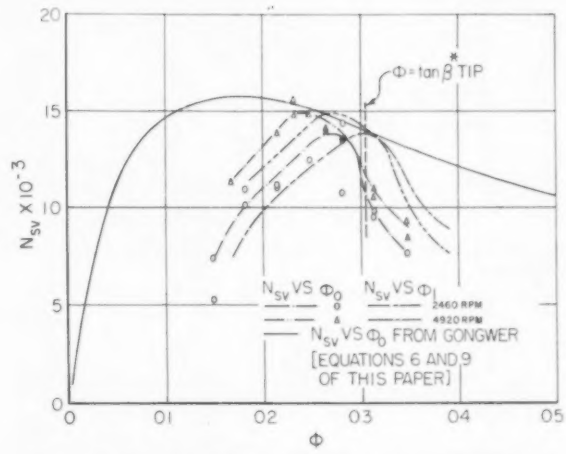

Fig. 17 Suction specific speed versus flow coefficient—impeller C

Gongwer's Correlation Compared With Two Idealized Flow Models

Before proceeding with a comparison of the test results obtained with those reported earlier by C. A. Gongwer [9], it is appropriate to briefly review the principal concepts developed in his paper. G. F. Wislicenus, in his discussion of this paper, stated that the three coefficients used by Gongwer can be shown by the methods of dimensional analysis to be the only independent dimensionless coefficients which can be formed out of the variables Q, NPSH, N, and r. These coefficients, in the terminology of the current study, are:

$$K = \frac{\text{NPSH}}{C_m^2/2g} \tag{3}$$

$$\phi = \frac{C_m}{u} \tag{4}$$

$$\psi = \frac{\text{NPSH}}{u^2/2g} \tag{5}$$

Equations (3) and (4), as noted in the Introduction, were used to correlate the cavitation data of the three impellers currently tested. The alternate correlation of ψ as a function of ϕ did not

offer any specific advantage over the K versus ϕ correlation and was therefore dropped in this study. The most significant part of the experimental correlation achieved by Gongwer was his trial and error fitting of an empirical curve through the data points of several different impellers at the no incidence condition and at the breakoff point in cavitation on the K_0 versus ϕ_0 plot. The equation of this empirical curve is:

$$K_0 = 1.4 + 0.085\left(1 + \frac{1}{\phi_0^3}\right) \tag{6}$$

This curve is shown plotted in Figs. 12, 13, and 14 for a direct comparison with the results of this study. The breakoff point was defined on the NPSH versus head rise cavitation plots, conducted at constant speed and flow rate, as where the head rise became equal to zero. Gongwer noted that the NPSH value at the breakoff point at zero incidence was only slightly lower than the NPSH value at the incipient cavitation point, indicating a very sharp breakoff in the head rise versus NPSH cavitation curve at this condition. On either side of this point, the apparent effect of incidence was to yield a more gradual breakoff in these cavitation curves. This observation will be referred to again in the discussion of results.

In a manner similar to that demonstrated by Gongwer, it is straightforward to translate this prediction curve on the K_0 versus ϕ_0 plot to a N_{ss} versus ϕ_0 plot. To illustrate, first write the suction specific speed equation as:

$$N_{ss} = \frac{N\sqrt{Q}}{(\text{NPSH})^{3/4}} \tag{2}$$

Now, the variables in equation (2) may be rewritten:

$$\left.\begin{aligned} N &= \frac{360\,u}{\pi r} \\ Q &= 448.8\,\frac{\pi r^2}{144}\,C_{m0} \\ \text{NPSH} &= K_0\,\frac{C_{m0}^2}{2g} \end{aligned}\right\} \tag{7}$$

Substituting the values of equation (7) into equation (2):

$$N_{ss} = \left[\frac{30\sqrt{448.8}\,(2g)^{3/4}}{\sqrt{\pi}}\right]\frac{1}{(K_0)^{3/4}\,\dfrac{C_{m0}}{u}} \tag{8}$$

Designating the constant within the brackets as D and substituting equation (4), equation (8) may be rewritten as:

$$N_{ss} = \frac{D}{(K_0)^{3/4}\,\phi_0} \tag{9}$$

Since from Gongwer's correlation K_0 is an established function of ϕ_0, the N_{ss} versus ϕ_0 plot may be readily determined and is presented in Figs. 15, 16, and 17 for comparison with the current test results.

At this point, it is of interest to consider two idealized flow models in the inlets of centrifugal pumps and to compare these with the empirical correlation derived by Gongwer.

The first model is represented by the ideal case where the incipient cavitation point is reached when the NPSH_i value becomes equal to the dynamic head existing at the eye of the impeller, $C_{m0}^2/2g$, corresponding to a one-dimensional flow and excluding all blockage. In Fig. 19, this is shown as a horizontal line of $K_0 = 1$. Substituting a value of $K_0 = 1$ into equation (9) yields:

$$N_{ssi} = \frac{D}{\phi_0} \tag{10}$$

This equation of an equilateral hyperbola is plotted in Fig. 20 and would predict values of N_{ss} approaching infinity as ϕ_0 approaches zero. On the other hand, this flow model illustrates the fact that it is certainly not possible to achieve very high values of suction specific speed at the higher range of ϕ_0 values since this flow model represents the idealized upper limits of N_{ss} in pump design.

The second flow model to be considered is one including a typical vane blockage effect. Again, assuming a one-dimensional flow pattern and an axial inlet section to simplify the geometry, it is possible to compute a vane blockage effect based upon the cascade shown in Fig. 18. A blockage coefficient B_v may be defined as:

$$B_v = \frac{t/\sin\beta^*}{2\pi r/z} \tag{11}$$

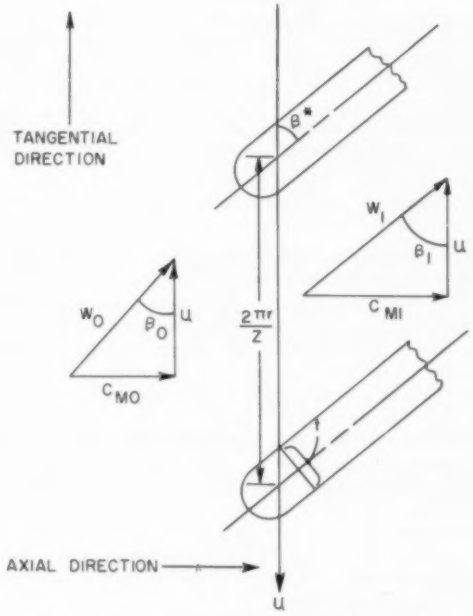

Fig. 18 Inlet vane geometry and velocity triangles

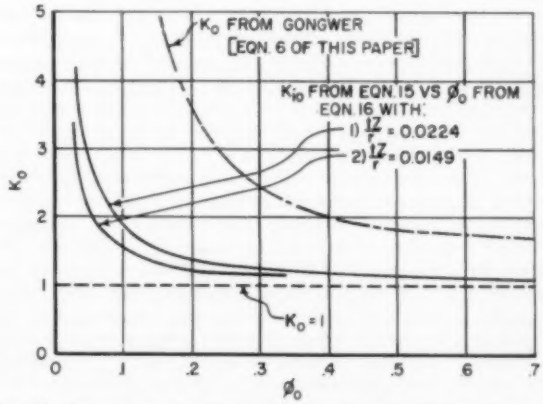

Fig. 19 Comparison of cavitation index versus flow coefficient for two idealized flow models and empirical curve from Gongwer

This model corresponds to the results of a vane blockage study reported earlier by J. D. Stanitz [2]. Now, due to the vane blockage, the meridional velocity is accelerated in passing from the upstream station to the station inside the vane row in accordance with the following equation:

$$C_{m1} = \frac{C_{m0}}{(1 - B_v)} \tag{12}$$

Assuming that the total head remains constant in the inlet region, the incipient $NPSH_i$ value would be:

$$NPSH_i = C_{m1}^2/2g = \frac{1}{(1 - B_v)^2} C_{m0}^2/2g \tag{13}$$

Dividing both sides of equation (13) by $C_{m0}^2/2g$ and substituting from equation (3):

$$K_i = \frac{1}{(1 - B_v)^2} \tag{14}$$

Equation (14) may be rewritten:

$$K_i = \frac{1}{[1 - (tz/r)(1/2\pi)(1/\sin \beta^*)]^2} \tag{15}$$

Now, for no incidence, $\tan \beta^* = C_{m1}/u$ so that ϕ_0 may be evaluated by the following equation:

$$\phi_0 = \frac{C_{m0}}{u} = \frac{C_{m1}}{u}(1 - B_v) = \tan \beta^*(1 - B_v) \tag{16}$$

These equations are shown plotted for $tz/r = 0.0224$ and $tz/r = 0.0149$ in Fig. 19 for the cases corresponding to Impellers A and C of this study, respectively. Equation (15) is also transcribed by the use of equation (9) for these two cases to produce the plot of N_{svi} versus ϕ_0 shown in Fig. 20. These two cases illustrate the importance of considering vane blockage, especially at the low values of ϕ_0 corresponding to low vane angle settings. In the ϕ_0 range under investigation, this idealized flow model would predict that Impeller C would be significantly better in cavitation performance than Impeller A. Also, this model would predict that the cavitation performance of Impeller B would lie between that for Impeller A and Impeller C. It is also to be noted that this idealized blockage flow model only crudely approximates the experimental trend derived by Gongwer and yields very optimistic prediction values of cavitation performance for the vane configurations tested.

Discussion of Test Results

The curves shown in Figs. 12, 13, and 14 were derived from the experimental results of Impellers A, B, and C, respectively, at the incipient cavitation point using the correlating parameters K_{i0} and ϕ_0 at the various speeds tested. These results were replotted on Figs. 15, 16, and 17 as N_{sv} versus ϕ using equation (9). A speed effect was noted for all three versions of the impeller design tested at speeds of 2460 and 4920 rpm which resulted in lower values of suction specific speed at corresponding ϕ values at the lower speed. A possible explanation is that the residence time for the cavitation bubbles in the cavitation zone is longer at the lower speed and this encourages more rapid bubble growth. However, a comparison of the data at 4920 and 6500 rpm on Impellers A and B did not reveal a distinct speed effect which suggests an upper limit to these phenomena. In general, it is to be noted that the results of these tests at the higher speeds indicate a superior cavitation performance over Gongwer's correlation. Impeller B showed improved performance over Impeller A which was in accord with the concept of reduced vane blockage effects. However, Impeller C, with the minimum blockage effect, did not result in the best cavitation performance. This raises the possibility that the reduced solidity of this impeller was more significant than the vane blockage in this limiting case. Referring to Figs. 2 and 18, the solidity is defined as the ratio of the total tip meridional streamline distance S_t to the vane gap $2\pi r/z$. For the fixed meridional profiles of the impellers tested, the solidity is thus directly proportional to the number of vanes.

The curves identified as ϕ_1 in Figs. 12 through 17 were derived from the curves designated ϕ_0 by substituting the meridional velocity inside the vane row C_{m1} for the upstream value C_{m0}. The velocity C_{m1} is greater than C_{m0} due to the blockage effect of the vanes. The method of evaluating vane blockage is shown in Fig. 18. An average value of blockage based upon the hub and tip sections was computed as shown in the Appendix. For the one dimensional flow considered, the values of C_{m1} were determined by continuity using the unblocked flow area. The significance of using the flow conditions inside the row are seen in Figs. 12, 13, and 14 where the minimum values for the curves designated ϕ_1 coincide quite closely to the measured vane angle for each impeller as denoted by the vertical broken lines. This correlation verifies that blockage effects must be considered when designing for no incidence.

A study of Figs. 9, 10, and 11 shows some very interesting similarities in the tip static pressure profiles in cavitating flow. It is noted that the point of very rapid pressure rise, as indicated by the lowest curve in each figure, occurs at about the same value of $S/S_t = 0.55$ which is just inside the "working" section of the impeller. The rapid static pressure rise characteristic at the point of collapse of the cavitation "bubble" was reported by H. Rouse

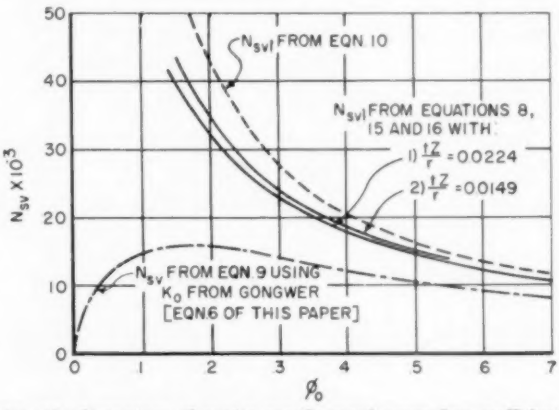

Fig. 20 Comparison of suction specific speed versus flow coefficient for two idealized flow models and empirical curve from Gongwer

and J. S. McNown [10] on water tunnel studies on symmetrical head forms at the no incidence condition. If the analogy to this study is valid, it may be assumed that the cavitation only begins to have a drastic effect on performance when the "bubble" progresses to the "working section." Another interesting observation made on these tip static pressure profile plots was that the first perceptible change of slope occurred near the leading edge at a total inlet pressure in the vicinity of 10 psig. This local effect might well be the true incipient cavitation point, but was not measurable in the head drop off characteristics.

The observation that the minimum difference between the NPSH values at the incipient and breakoff cavitation points occurs at the no incidence point is qualitatively verified by the plots shown in Fig. 7. The more gradual breakoff in the cavitation curves on either side of this point indicates that possibly the effect of incidence is to disperse or retard the progress of the cavitation bubble into the working section of the impeller.

Fig. 8 shows the effect of varying incidence on the tip static pressure profiles in noncavitating flow. At the lowest flow rate, the effect of a stall in the tip section is noted by the high inlet static pressure. In this flow regime, the flow patterns are undoubtedly very complicated.

From the meridional inlet velocity profile plot shown in Fig. 6, it is concluded that the velocity profiles were not shifting in the eye of impeller.

Conclusions

Several general conclusions may be drawn from this study of cavitation in a mixed flow centrifugal pump impeller.

1 For optimum incipient cavitation performance, the vane blockage effects should be kept at a minimum consistent with solidity limits in the inlet vane row of centrifugal impellers. This is especially important in the high suction specific speed range corresponding to low inlet vane angle settings.

2 The incipient cavitation index K_i was found to be very sensitive to incidence effects. The minimum value of K_i occurred at the no incidence condition. To avoid incidence effects, the inlet vane angle settings must be adjusted for the vane blockage effect.

3 It would appear that a more accurate empirical correlation curve could be derived by working with flow conditions inside the vane row rather than upstream as used by Gongwer. By using C_{mi} rather than C_{m0}, the effects of varying vane blockage could be eliminated when correlating the results of a wide range of impeller designs.

4 A qualitative conclusion reached during this study is that the solidity of the inlet vane row is of first-order significance. Impeller C did not live up to expectations on the basis of reduced vane blockage effects. This suggests that the reduced solidity of this design had a decided effect on the incipient cavitation condition.

5 A speed effect was found in the cavitation data for the three impellers tested. The suction specific speed was lower over the flow range tested at 2460 rpm as compared to that at 4920 rpm. The data agreed quite closely, however, at speeds of 4920 rpm and 6500 rpm. This may be due to the longer residence time existing in the cavitation zone at the lower speed, although this effect appears to have a definite upper limit.

6 A study of the tip static pressure profiles in cavitation reveals that the point of cavitation collapse, which is associated with the rapid static pressure rise, occurs at about the same station in the vane passage at the breakoff point on the cavitation curves for the three impellers tested. This implies that cavitation will only begin to have a drastic effect on performance when the cavitation bubble has migrated into the "working" section of the impeller.

7 The results of this study concur with those of Gongwer in that the NPSH values associated with the incipient and breakoff points are the closest to each other at the no incidence condition. A possible explanation for this is that the effect of incidence is to disperse or retard the migration of the cavitation bubble into the working section of the impeller.

8 A study of the tip static pressure profile plots consistently revealed a local drop in pressure at the leading edge of the vanes at intermediate pressure levels from those which were identified as cavitating and noncavitating flow on the basis of a change in the developed head rise. This local effect may well be the true incipient cavitation condition for the impellers tested.

Acknowledgments

The authors wish to express their appreciation to G. E Beardsley, Jr., and R. W. Kelly for guidance and encouragement. Thanks are extended to S. A. Smith and J. Johnson for aid in the preparation of the manuscript and to J. V. Altieri for assistance in obtaining test data.

References

1 R. T. Knapp, "Cavitation and Nuclei," TRANS. ASME, vol. 80, 1958, pp. 1315–1324.

2 J. D. Stanitz, "Effect of Blade-Thickness Taper on Axial-Velocity Distribution at the Leading Edge of an Entrance Rotor-Blade Row With Axial Inlet, and the Influence of This Distribution on Alinement of the Rotor Blade Angle for Zero Angle of Attack," NACA TN 2986, August, 1953.

3 J. W. Daily, "Cavitation Characteristics and Infinite-Aspect-Ratio Characteristics of a Hydrofoil Section," TRANS. ASME, vol. 71, 1949, pp. 269–284.

4 P. Eisenberg, "A Critical Review of Recent Progress in Cavitation Research," Proceedings of the Symposium on Cavitation in Hydrodynamics, held at the National Physical Laboratory, Teddington, England, Sept. 14–17, 1955.

5 J. T. Hamrick, A. Ginsburg, and W. M. Osborn, "Method of Analysis for Compressible Flow Through Mixed-Flow Centrifugal Impellers of Arbitrary Design," NACA Report 1082.

6 G. F. Wislicenus, R. M. Watson, and I. J. Karassik, "Cavitation Characteristics of Centrifugal Pumps Described by Similarity Considerations," TRANS. ASME, vol. 61, 1939, pp. 17–24.

7 P. Eisenberg, "Mechanism and Prevention of Cavitation," David Taylor Model Basin Report 712.

8 R. T. Knapp and A. Hollander, "Laboratory Investigation of the Mechanism of Cavitation," TRANS. ASME, vol. 70, 1948, pp. 419–435.

9 C. A. Gongwer, "A Theory of Cavitation Flow in Centrifugal Pump-Impellers," TRANS. ASME, vol. 63, 1941, pp. 29–40.

10 H. Rouse and J. S. McNown, "Cavitation and Pressure Distribution, Head Forms at Zero Angle of Yaw," Iowa University Bulletin 32, 1948.

11 H. A. Stahl and A. J. Stepanoff, "Thermodynamics Aspects of Cavitation in Centrifugal Pumps," TRANS. ASME, vol. 78, 1956, pp. 1691–1693.

12 V. Salemann, "Cavitation and NPSH Requirements of Various Liquids," TRANS. ASME, Series D, JOURNAL OF BASIC ENGINEERING, vol. 81, 1959, pp. 167–180.

APPENDIX

Evaluation of Inlet Blockage for Impellers Tested

Referring to Fig. 18, it is seen that the frontal thickness component of an impeller vane section presented to the axial inlet flow is:

$$t/\sin \beta^*$$

Using the design vane thickness value and the mean β^* angle from inspection (see Table 1) the frontal thickness for the tip is:

$$0.060/\sin 17.5^\circ = 0.200 \text{ in.}$$

Using design values, the frontal thickness component for the hub is:

$$0.120/\sin 66.2^\circ = 0.131 \text{ in.}$$

Each vane presents a trapezoidal area to the inlet flow, the trapezoid having bases of 0.200 and 0.131 in. and a height (see Fig. 2) of:

$$r_{tip} - r_{hub} = 2.41 - 0.50 = 1.91 \text{ in.}$$

The area of each vane is

$$(1.91/2)(0.200 + 0.131) = 0.316 \text{ in.}^2$$

The hub nose area is

$$\pi(0.50)^2 = 0.785 \text{ in.}^2$$

The area available for flow at the "o" station in the 4.89 in. diameter inlet pipe is 18.8 in.^{2} The formula for the area available for the flow immediately inside the impeller vane inlet section is:

Area = pipe area − hub nose area − (area per vane)(no. of vanes)

This is the area at reference station 1. The meridional velocity is inversely proportional to the area, therefore:

$$C_{m1}/C_{m0} = \text{area}_0/\text{area}_1 = 18.8/\text{area}_1$$

When this expression is combined with equation (12) the blockage coefficient B_v may be found as:

$$B_v = 1 - 1/(18.8/\text{area}_1)$$

For impeller A:

$\text{Area}_1 = 18.8 - 0.785 - (0.316)(6) = 16.1$ in.^{2}

$B_v = 0.143$

For impeller B:

$\text{Area}_1 = 18.8 - 0.785 - (0.316)(5) = 16.4$ in.^{2}

$B_v = 0.131$

For impeller C:

$\text{Area}_1 = 18.8 - 0.785 - (0.316)(4) = 16.7$ in.^{2}

$B_v = 0.109$

DISCUSSION

J. W. Holl[2]

The authors are to be congratulated on so fine a paper. I was particularly glad to see the presence of a velocity scale effect. This has been frequently observed in cavitation work on submerged bodies at Penn State and Cal Tech. In general these tests indicate that the cavitation number at inception increases with an increase in velocity. I wonder whether the authors have observed any difference between the pressure at which cavitation disappears and the pressure at which it first appears.

[2] Associate Professor of Mechanical Engineering, University of Nebraska, Lincoln, Nebr.

Authors' Closure

It has been gratifying to learn that the existence of the velocity scale effect agrees with the observations of other investigators. In the Nomenclature of this paper, the cavitation index K was observed to decrease with an increase in velocity at a constant value of the flow coefficient ϕ which yielded a higher value of the suction specific speed N_{ss}. The data presented by Mr. V. Salemann at the Cavitation Symposium of this conference agreed with the speed effect noted above. Also, during the open discussion of this paper, Mr. M. J. Hartmann commented that he had observed a similar trend in his tests of an axial flow pump. It is important to point out, however, that the true incipient cavitation point most probably occurred at higher values of the cavitation index than as determined by the first detectable change of the output head with decreasing NPSH. The observations of the tip static pressure distributions, as shown in Figs. 9, 10, and 11 of this paper, are cited in support of this conclusion.

In reply to Professor Holl's question, the "incipient cavitation" and "desinent cavitation," as defined in his paper at this meeting, would necessitate visual observation of these points on the rotating impeller vanes. Although this was not attempted on these tests, the authors certainly agree that such information would be of great interest.

An Effect of Air Content on the Occurrence of Cavitation[1]

J. W. HOLL[2]
Assistant Professor of Engineering Research,
Ordnance Research Laboratory,
The Pennsylvania State University,
University Park, Pa.

The simultaneous occurrence of vaporous and gaseous cavitation on hydrofoils is considered. The experimental results show that gaseous cavitation occurs at much higher ambient pressures than that for the vaporous cavitation resulting in desinent-cavitation numbers twice the minimum-pressure coefficient of the hydrofoil. The analysis indicates that the difference between the desinent-cavitation number for the gaseous cavitation and that for the vaporous cavitation is proportional to the dissolved air content and inversely proportional to the square of the velocity.

Introduction

THE EFFECT of air content on cavitation is of classical interest. This is particularly true for that state which lies between no cavitation and a limited amount. Like many other aspects of cavitation, this phenomenon is not well understood. It is not the intent of this paper to discuss the influence of air content in a general sense, but rather a particular case is considered.

The case considered is that of the simultaneous occurrence of vaporous and gaseous cavitation on hydrofoils. An analysis of this phenomenon based on the static equilibrium law for a spherical bubble has led to most encouraging results.

The experiments were conducted in the 4.5 × 20-in. Water Tunnel at the Ordnance Research Laboratory of the Pennsylvania State University. The results of this program were reported by Calehuff and Wislicenus [1][3] in 1956. However, it has only been recently [2] that the true meaning of these results was ascertained.

Flow Regimes

Cavitating flows are commonly described by the cavitation number

$$\sigma = \frac{P - P_v}{\frac{1}{2}\rho V^2} \tag{1}$$

where P is the free-stream or ambient pressure, P_v the vapor pressure at the bulk temperature of the liquid, ρ the mass density, and V the free-stream velocity.

Cavitation experiments are usually conducted by holding the velocity constant and varying the free-stream static pressure. In so doing various regimes of flow are observed; the "noncavitating flow" regime occurs at sufficiently large values of P that there is no evidence of cavitation bubbles whereas the "cavity flow" regime occurs at sufficiently small values of P that profuse cavitation is observed. Between these two states lies the regime of "limited cavitation" where a very small number of cavitation bubbles is in evidence.

Limited cavitation may be attained by lowering the pressure from the noncavitating flow regime and observing the first appearance of cavitation or by first establishing a cavity flow and raising the pressure to determine the disappearance of cavitation. The former is commonly called "incipient cavitation" and the latter is here defined as "desinent cavitation."

For incipient cavitation there will correspond a particular value of P called the "inception pressure" P_i, whereas for desinent cavitation there is the "desinence pressure" P_d. From these definitions there follows the incipient-cavitation number σ_i and desinent-cavitation number σ_d given by

$$\sigma_i = \frac{P_i - P_v}{\frac{1}{2}\rho V^2} \tag{2}$$

and

$$\sigma_d = \frac{P_d - P_v}{\frac{1}{2}\rho V^2} \tag{3}$$

Experiments indicate [3] that the desinence pressure is greater than or equal to the inception pressure. The difference between P_d and P_i is often called "cavitation hysteresis" [3]. In terms of the cavitation number, incipient and desinent cavitation are related by the expression

[1] This work was supported by the Bureau of Ordnance and Bureau of Ships of the Department of the Navy under contract NOrd 16597 and by the Office of Naval Research of the Department of the Navy under contract NR 062-139.

[2] As of September 1, 1959, Associate Professor of Mechanical Engineering, University of Nebraska, Lincoln, Nebraska.

[3] Numbers in brackets designate References at end of paper.

Contributed by the Hydraulic Division and presented at the Gas Turbine Power & Hydraulic Conference, Houston, Texas, March 6–9, 1960, of THE AMERICAN SOCIETY OF MECHANICAL ENGINEERS.

NOTE: Statements and opinions advanced in papers are to be understood as individual expressions of their authors and not those of the Society. Manuscript received at ASME Headquarters, November 30, 1959. Paper No. 60—Hyd-8.

Nomenclature

C_p = pressure coefficient
$C_{p\min}$ = minimum-pressure coefficient
P = free-stream static pressure
P_a = partial pressure of air in bubble
P_d = free-stream static pressure at the state of desinent cavitation
P_e = liquid pressure external to bubble
P_i = free-stream static pressure at the state of incipient cavitation
$P_{\min}$ = minimum pressure in the fluid
P_v = vapor pressure
r = bubble radius
s = surface tension
V = free-stream velocity
α = dissolved air content
β = Henry's law constant
ρ = mass density of liquid
σ = cavitation number
σ_d = desinent-cavitation number
σ_i = incipient-cavitation number

$$\sigma_d \geq \sigma_i. \tag{4}$$

Thus, for a given flow condition, σ_d appears to be the upper limit for σ_i. Furthermore, incipient cavitation is random in nature whereas desinent cavitation is repeatable. Because of the repeatable nature of the desinent state, many laboratories determine the regime of limited cavitation by this means. However, it has been the practice to call the state so determined incipient cavitation rather than desinent cavitation as introduced in this paper.

It must be emphasized that the distinction between incipient and desinent cavitation may be only a matter of definition in some cases. However, following a suggestion by M. Strasberg of the David Taylor Model Basin the author felt it was proper at this point to distinguish between the two in an attempt to end any confusion in terminology which has arisen.

Laws of Cavitation

In order to clearly bring out the problem to be considered it is necessary to distinguish between two broad types of cavitation. Vaporous cavitation is the sudden expansion of a vapor bubble due to vaporization of the liquid at the bubble wall whereas gaseous cavitation is the relatively slow expansion of a gas bubble due to diffusion.

Cavitation may be expected to occur at the point of minimum pressure in the fluid. For a bluff body the minimum pressure $P_{\min}$ occurs in the vortexes of the wake flow. On the other hand, for a streamlined body such as the hydrofoils considered in this paper, the minimum pressure occurs on the surface of the body. In any case, one can define a minimum-pressure coefficient

$$C_{P\min} = \frac{P - P_{\min}}{{}^1/_2\rho V^2}. \tag{5}$$

The minimum-pressure coefficient is taken as a measure of the minimum pressure in the noncavitating-flow regime.

It is usually assumed that the minimum pressure is equal to vapor pressure at the state of desinent vaporous cavitation. It is also assumed that the small vapor bubbles do not alter materially the pressure field from that obtained for the noncavitating-flow regime. From these assumptions it is evident that

$$\sigma_d = C_{P\min}. \tag{6}$$

Equation (6) is a statement of the fundamental theory of desinent vaporous cavitation and it states that the desinent-cavitation number is equal to the minimum-pressure coefficient for the noncavitating-flow regime.[4]

The fundamental theory of desinent vaporous cavitation has proved to be correct in many instances. Nevertheless, systematic cavitation tests in recent years on submerged bodies have indicated that because of so-called "scale effects" the minimum pressure is often less than vapor pressure at the state of desinent cavitation [4]. Therefore the general relation for vaporous cavitation is

$$\sigma_d \leq C_{P\min}. \tag{7}$$

In contrast to vaporous cavitation, gaseous cavitation can occur at pressures greater than vapor pressure provided the initial bubble radii are great enough [5]. Thus for fairly large bubbles gaseous cavitation is such that

$$\sigma_d > C_{P\min}. \tag{8}$$

[4] In the fundamental theory, no distinction is made between incipient and desinent cavitation. Thus Equation (6) is also a statement of the fundamental theory of incipient vaporous cavitation since $\sigma_i = \sigma_d$.

Experiments

In 1954 a program was initiated at the Ordnance Research Laboratory to study desinent cavitation on hydrofoils [1]. This program was very essential because of the dearth of information on two-dimensional bodies in contrast to the extensive experimental information on three-dimensional bodies [4].[5] The only extensive tests on hydrofoils available at that time were those conducted by Parkin on a family of 12 per cent thick symmetrical Joukowski hydrofoils [6, 7].

Several families of hydrofoils were employed in the ORL tests. The chord lengths of these models varied from two to five inches. However, it will be necessary to consider only two of the families in order to bring forth the point of this paper. These are the NACA 16012 and 0.5 caliber hydrofoils, the details of which are shown in Fig. 1. The span of all hydrofoils was 4.5 in. so that the models spanned the entire width of the water tunnel test section.

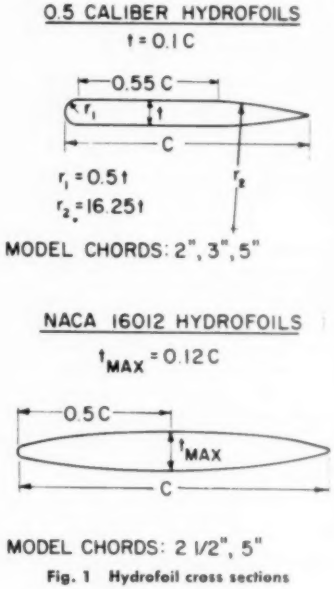

Fig. 1 Hydrofoil cross sections

The hydrofoils were tested at angles of attack from 0 to 3 deg at water velocities from 30 to 70 fps. The water temperature was about 75 F for most of the tests and the dissolved air content of the water, α, varied from 6 to 17 PPM.[6]

The 0.5 caliber hydrofoils were the first to be employed in the test program. Subsequently, the NACA 16012 hydrofoils were tested. A very striking phenomenon common to all the hydrofoils stood out among all other characteristics. It was observed that two types of desinent cavitation could be determined. As the pressure was increased causing the cavitation to disappear, a pressure was reached where the cavitation disappeared uniformly across the span. This was referred to as areal cavitation. However, it was observed that several cavitation bubbles still clung to the surface and continued to do so up to very high ambient pressures. These spots of cavitation were manifest on the 0.5 caliber hydrofoils and on the NACA 16012 hydrofoils at angles of attack above the critical angle.[7]

[5] A reanalysis of available tests on two and three-dimensional bodies has been made by the author in Appendix A of Reference [2].

[6] PPM = Moles of air per million moles of water.

[7] The critical angle of attack is that angle at which the change of $C_{p\min}$ with angle becomes very large. For angles above the critical one, the point of minimum pressure shifts forward close to the leading edge. The critical angle for the NACA 16012 hydrofoils is 1.5 deg from reference [8].

Examples of this phenomenon are shown in Figs. 2 through 4. Two sets of cavitation data are shown in each figure. The lower set of cavitation data shown by the black circles corresponds to the areal cavitation whereas the crosses denote the spots of cavitation. Referring to the data for the NACA hydrofoils, Figs. 2 and 3, it is seen that the areal cavitation obeys Equation (7) whereas the cavitation spots agree with Equation (8). Furthermore, it is seen that at the lower velocities the desinent-cavitation number corresponding to the cavitation spots is twice the minimum-pressure coefficient. The theoretical values of the minimum-pressure coefficient were determined from reference [8]. The data for the 0.5 caliber hydrofoils, Fig. 4, are similar to that for the NACA hydrofoils. The minimum-pressure coefficient was not determined for the 0.5 caliber hydrofoils.

Since large values of σ_d indicate that a body is quite susceptible to cavitation it was very necessary to determine the origin of the cavitation spots. As shown in recent papers [2, 9], surface irregularities can cause local reductions in pressure and thereby give desinent-cavitation numbers greater than the minimum-pressure coefficient based on the mean surface pressure. To test this hypothesis, a roughened hydrofoil was tested and the occurrence of cavitation spots appeared to be accentuated. Furthermore, the spots did not occur at angles of attack less than the critical angle for the NACA hydrofoils. This was attributed to the fact that at such angles the minimum pressure point is closer to the midchord where the boundary layer is thicker. This would tend to decrease the effect of a surface irregularity since it would be buried in the boundary layer [2, 9]. On the other hand, at angles greater than the critical one, the minimum pressure point was near the leading edge where the boundary layer was very thin and therefore the effect of surface irregularities would be more important. Because of this reasoning Calehuff and Wislicenus

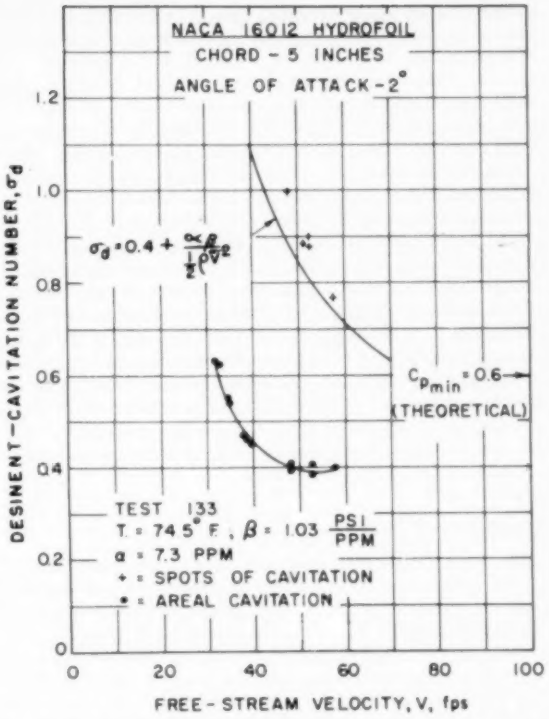
NACA 16012 HYDROFOIL
CHORD - 5 INCHES
ANGLE OF ATTACK - 2°
$\sigma_d = 0.4 + \frac{\alpha\beta}{\frac{1}{2}\rho V^2}$
$C_{p_{min}} = 0.6$
(THEORETICAL)
TEST 133
T = 74.5° F, β = 1.03 PSI/PPM
a = 7.3 PPM
+ = SPOTS OF CAVITATION
• = AREAL CAVITATION
DESINENT-CAVITATION NUMBER, σ_d
FREE-STREAM VELOCITY, V, fps

Fig. 3 Two types of cavitation on a 5-in. NACA 16012 hydrofoil

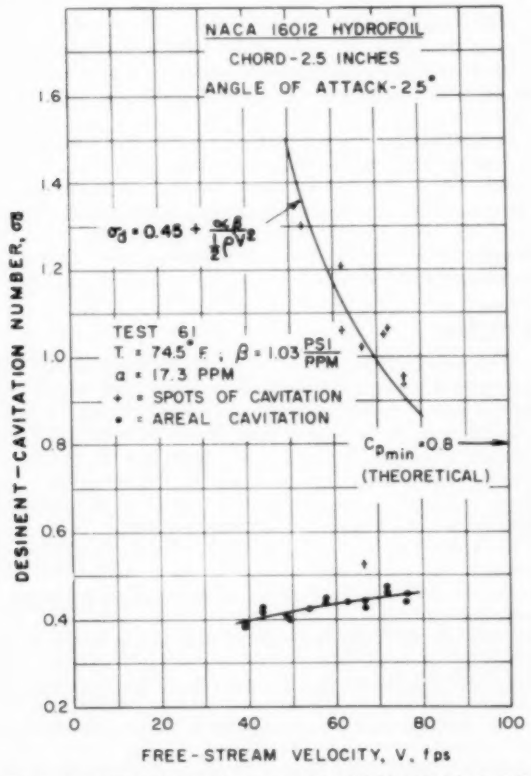
NACA 16012 HYDROFOIL
CHORD - 2.5 INCHES
ANGLE OF ATTACK - 2.5°
$\sigma_d = 0.45 + \frac{\alpha\beta}{\frac{1}{2}\rho V^2}$
TEST 61
T = 74.5° F, β = 1.03 PSI/PPM
a = 17.3 PPM
+ = SPOTS OF CAVITATION
• = AREAL CAVITATION
$C_{p_{min}} = 0.8$
(THEORETICAL)
DESINENT-CAVITATION NUMBER, σ_d
FREE-STREAM VELOCITY, V, fps

Fig. 2 Two types of cavitation on a 2.5-in. NACA 16012 hydrofoil

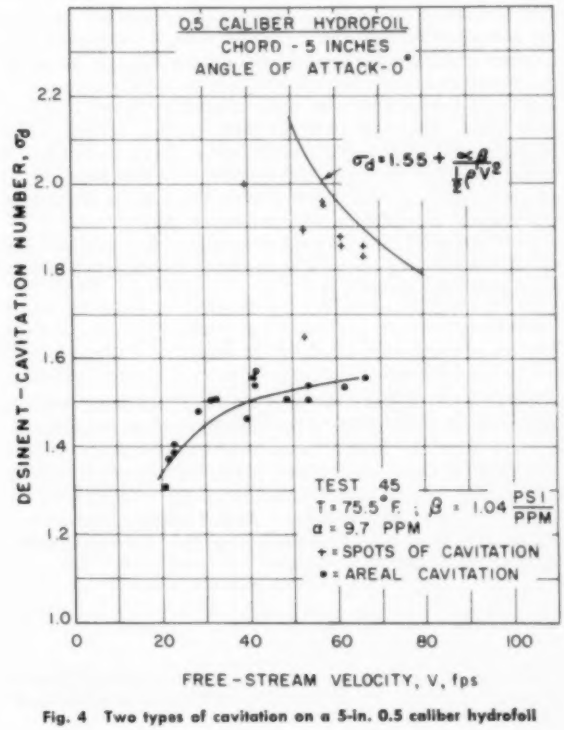
0.5 CALIBER HYDROFOIL
CHORD - 5 INCHES
ANGLE OF ATTACK - 0°
$\sigma_d = 1.55 + \frac{\alpha\beta}{\frac{1}{2}\rho V^2}$
TEST 45
T = 75.5° F, β = 1.04 PSI/PPM
a = 9.7 PPM
+ = SPOTS OF CAVITATION
• = AREAL CAVITATION
DESINENT-CAVITATION NUMBER, σ_d
FREE-STREAM VELOCITY, V, fps

Fig. 4 Two types of cavitation on a 5-in. 0.5 caliber hydrofoil

in their analysis of the hydrofoil tests [1] tentatively concluded that surface irregularities were the cause of spots of cavitation.

Certainly the conclusions of Calehuff and Wislicenus were plausible. However, the explanation was not complete. One would expect the surface irregularities to become progressively more important as the velocity is increased since a roughness would protrude further into the boundary layer at higher velocities than at low velocities. Thus one would expect the desinent-cavitation number of the cavitation spots to be a monotonically increasing function of the velocity. The results of references [2 and 9] which were not available at the time of Calehuff and Wislicenus' work confirm this reasoning. Referring to Figs. 2 through 4 it is seen, however, that the desinent-cavitation number for the cavitation spots is a monotonically decreasing function of the velocity. At the suggestion of G. F. Wislicenus[8] the author investigated this matter further. As described in the previous section, gaseous cavitation can occur at liquid pressures greater than vapor pressure. This could then be a cause for observed value of σ_d being greater than $C_{p_{min}}$. The reanalysis of these tests given in the following section shows that the spots of cavitation were, in fact, gaseous cavitation.

Analysis

The clear glassy appearance of the cavitation spots suggested to the author that they may have been gaseous rather than vaporous cavitation. Furthermore, when one considers the procedure employed in the tests this possibility is even more apparent. In the initial portion of the test cycle, when cavitation was well established, the pressure was very low and gas bubbles were formed by air coming out of the solution. As the pressure was increased, the vaporous cavitation disappeared leaving the gas bubbles. Since the gas bubbles were stabilized on the surface, one must postulate a mechanism for such a phenomenon. One explanation may be that surface irregularities acted as traps for air bubbles. Another explanation may be that bubbles were stabilized on the surface in the adverse pressure gradient following the minimum pressure point. Under these circumstances, the pressure gradient force apparently balances the drag, adhesion, and buoyancy forces. Bubbles stabilized in the adverse gradient of a hemispherical nose have been reported by Parkin and Kermeen [10]. Hence the fact that these bubbles occurred on the NACA hydrofoils at angles of attack above the critical angle and on the 0.5 caliber hydrofoils both of which have very predominant adverse pressure gradients, points to the possible role of the pressure gradient in stabilizing bubbles on the surface.

To clearly show that the spots of cavitation were gaseous cavitation, the following theory is presented. The static equilibrium equation for the bubble is [11]

$$P_a + P_v = P_s + \frac{2s}{r} \tag{9}$$

where P_a is the partial pressure of the air, P_s the liquid pressure on the outside of the bubble, s the surface tension, and r the bubble radius. When the bubble becomes saturated with air, the air pressure is $\alpha\beta$ where α is the dissolved air content and β Henry's law constant. Under these conditions an upper limit to the external pressure P_s is determined. At this pressure, surface tension reacts to cause the bubble to dissolve [12]. For the saturated condition, Equation (9) becomes

$$\alpha\beta + P_v = P_s + \frac{2s}{r} \tag{10}$$

Solving Equation (10) for P_s and multiplying the result by minus one gives

$$-P_v = -P_s + \alpha\beta - \frac{2s}{r} \tag{11}$$

Adding the free-stream static pressure at desinence P_d to both sides of Equation (11) and dividing the result by $\frac{1}{2}\rho V^2$ results in

$$\frac{P_d - P_v}{\frac{1}{2}\rho V^2} = \frac{P_d - P_s}{\frac{1}{2}\rho V^2} + \frac{\alpha\beta}{\frac{1}{2}\rho V^2} - \frac{2s/r}{\frac{1}{2}\rho V^2} \tag{12}$$

The term on the left-hand side of equation (12) is the desinent cavitation number σ_d by definition. The first term on the right-hand side of the equation is some pressure coefficient C_p. Employing σ_d and C_p in Equation (12) yields

$$\sigma_d = C_p + \frac{\alpha\beta}{\frac{1}{2}\rho V^2} - \frac{2s/r}{\frac{1}{2}\rho V^2} \tag{13}$$

The visual observation of cavitation indicated that the bubble radius r was approximately 0.01 in. Hence the last term on the right-hand side of Equation (13) is small and can be neglected.[9] Then Equation (13) reduces to

$$\sigma_d = C_p + \frac{\alpha\beta}{\frac{1}{2}\rho V^2} \tag{14}$$

The air content and Henry's law constant were determined from the test data. However, the pressure coefficient C_p is somewhat indefinite. The bubbles were probably stabilized in the adverse pressure gradient downstream from the minimum pressure point. Thus C_p is less than $C_{p_{min}}$. It will be assumed that C_p is approximately equal to σ_d for the areal cavitation at the highest velocity.

The results of this analysis are shown by the solid curves in Figs. 2 through 4. The agreement between this simple equilibrium theory and the measured values is most remarkable.[10] It definitely shows that the spots of cavitation were gaseous cavitation.

It should be pointed out that the increase in cavitation numbers at low velocities similar to that of the gaseous cavitation is occasionally observed in cavitation research. For example, see the data for the $\frac{1}{4}$-in. diameter hemispherical nose in reference [4]. Also note that the lower set of data in Fig. 3 has this characteristic. Possibly all these phenomenon are related and may be due to gas effects.

Discussion

Before bringing this paper to a close the author would like to discuss several points of interest. It is not known whether the gaseous spots of cavitation would adhere to the surface for a very wide range of air contents. Tests should be conducted to investigate this point. In addition, it may be that the existence of the cavitation spots is dependent upon the test procedure. Thus the spots of cavitation may be peculiar to desinent cavitation and therefore would not appear in incipient cavitation.

The theoretical curve agrees very well with the data by the assumption that the pressure coefficient corresponding to the location of the bubble on the surface, C_p, was equa to the desinent-cavitation number σ_d of the areal vaporous cavitation. Was this merely a fortuitous assumption? Or does it have physical significance in regard to the occurrence of vaporous cavitation? One might hypothesize that the most likely place for vaporous

[8] Director of the Garfield Thomas Water Tunnel of the Ordnance Research Laboratory and Professor of Aeronautical Engineering at the Pennsylvania State University.

[9] At 70 F for $r = 0.01$ in., the quantity $4s/r\rho$ is equal to 12.34 ft^3/sec.^{2}

[10] These results suggest that h hydrofoil might be used as an indirect means of measuring the dissolved air content.

cavitation to occur is where the time available for growth is a maximum. Under these circumstances, the vaporous cavitation would occur where the bubbles are stabilized on the body. There would be no so-called "time effects" in this case. Scale effects caused by changes in the length and/or velocity of the system would probably be due to shifts of the point of stabilization on the body since the force balance on the bubble must be influenced by the state of the boundary layer. In this case σ_d would always be less than $C_{p_{min}}$ since cavitation would be initiated in a region where the pressure is greater than at the minimum pressure point. Also, if this hypothesis is true then scale effects may be appreciably different depending upon whether a body has a flat pressure distribution such as an NACA 16012 at 0 deg angle of attack or a sharp pressure distribution such as a hemispherical-nosed body of revolution. In the former case, there may not be a point of stabilization on the body since the adverse pressure gradient is very small. At 0 deg angle of attack during the tests of the NACA 16012 hydrofoils there was no evidence of stabilized bubbles for all bubbles appeared to be traveling with the fluid. There is some evidence, see Appendix A of reference [2], indicating that there are different types of scale effects depending on the type of pressure distribution.

Tests should be conducted to determine C_p. This could probably be accomplished by visual observation of the location of the stabilized gas bubbles on the body. The pressure coefficient could then be found from the pressure distribution corresponding to the observed location of the bubble. Possibly an average value of C_p taken over a length equal to the bubble diameter would have to be used. Following this, high-speed motion pictures of the bubble growth process should be made along the lines of those conducted by Parkin and Kermeen [10].

Conclusions

The major conclusions of this investigation are as follows:

1 The difference between the desinent-cavitation number for the gaseous cavitation and that for the vaporous cavitation is directly proportional to the dissolved air content and inversely proportional to the square of the velocity.

2 Gaseous cavitation can occur at very high ambient pressures resulting in desinent-cavitation numbers which are several times the minimum-pressure coefficient of the body.

3 To minimize the effects of air content and thus avoid possible confusion of vaporous and gaseous cavitation, tests should be conducted at low dissolved air contents and high velocities.

4 It is not known whether the gaseous spots of cavitation would adhere to the surface for a very wide range of dissolved air contents. Furthermore, it is possible that the spots of gaseous cavitation are peculiar to desinent cavitation and therefore would not appear in incipient cavitation.

5 Perhaps the occasionally observed increase of σ_d at low velocities encountered in cavitation experiments is due to gas effects.

6 It may be that bubbles stabilized on the surface in the region of the adverse pressure gradient are also a source for vaporous cavitation. To investigate this point it is recommended that high-speed photographic studies be made of the bubble growth process.

Acknowledgments

The author wishes to express his appreciation of the many helpful suggestions of Dr. George F. Wislicenus. Appreciation is offered collectively to the numerous members of the faculty and staff of The Pennsylvania State University who contributed to this investigation. The investigation was conducted at the Ordnance Research Laboratory of The Pennsylvania State University and was sponsored by the Bureau of Ordnance and the Bureau of Ships of the Department of the Navy under contract NOrd 16597 and by the Office of Naval Research of the Department of the Navy under contract NR 062-139.

References

1 G. L. Calehuff and G. F. Wislicenus, "ORL Investigations of Scale Effects on Hydrofoil Cavitation," TM 19.4212-03, Ordnance Research Laboratory, The Pennsylvania State University, February, 1956.

2 J. W. Holl, "The Effect of Surface Irregularities on Incipient Cavitation," PhD dissertation or TM 5.3410-03, Ordnance Research Laboratory, The Pennsylvania State University, June, 1958.

3 R. W. Kermeen, "Some Observations of Cavitation on Hemispherical Head Models," Report E-35.1, Hydrodynamics Laboratory, California Institute of Technology.

4 B. R. Parkin and J. W. Holl, "Incipient-Cavitation Scaling Experiments for Hemispherical and 1.5 Caliber Ogive-Nosed Bodies," Report NOrd 7958-264, Ordnance Research Laboratory, The Pennsylvania State University, May, 1954.

5 M. Strasberg, "The Influence of Air-Filled Nuclei on Cavitation Inception," Report 1078, David Taylor Model Basin, August, 1956.

6 Blaine R. Parkin, "Scale Effects in Cavitating Flow," PhD dissertation, California Institute of Technology, 1952.

7 R. W. Kermeen, J. T. McGraw, and B. R. Parkin, "Mechanism of Cavitation Inception and the Related Scale-Effects Problem," ASME Paper No. 54—Mex-1, March, 1954.

8 Ira H. Abbott, Albert E. vanDoenhoff, and Louis S. Stivers, Jr., "Summary of Airfoil Data," NACA Report 824, 1945.

9 J. W. Holl, "The Inception of Cavitation on Isolated Surface Irregularities," TRANS. ASME, Series D, JOURNAL OF BASIC ENGINEERING, vol. 82, 1960, pp. 169–183.

10 B. R. Parkin and R. W. Kermeen, "Incipient Cavitation and Boundary Layer Interaction on a Streamlined Body," Report E35.2, Hydrodynamics Laboratory, California Institute of Technology, December, 1953.

11 F. G. Blake, Jr., "The Onset of Cavitation in Liquids," TM No. 12, Acoustics Research Laboratory, Harvard University, September 2, 1949.

12 P. S. Epstein and M. S. Plesset, "On the Stability of Gas Bubbles in Liquid-Gas Solutions," *Journal of Chemistry and Physics*, vol. 18, 1950, p. 1505.

DISCUSSION

Blaine R. Parkin[11]

Professor Holl's clear and concise discussion of his observations on the occurrence of cavitation is certainly of interest to all who have tried to unravel the fundamental physical relationships which must apply to these phenomena. Moreover, his suggestions for further research deserve serious consideration.

There are a number of points suggested by Dr. Holl's paper which I hope he will kindly amplify. For example, as long as the effects of surface tension are negligible it would seem that Eq. (14) should be valid for cavitation spots of any shape. I am prompted to inquire therefore if the spots were actually spherical bubbles. Could they have been glassy flattened cavities attached to the body? It is noted in the text that spots of cavitation were generally found in regions of adverse pressure gradient on the profiles. Is this also true of the areal cavitation? Was the chordwise location of the spots of cavitation related in any way to the position of the areal cavitation? At a constant value of σ do the spots of cavitation show any changes with time or is this strictly a steady phenomenon? Has it been possible to estimate even crudely any influence of boundary layer dimensions upon characteristic sizes of the two types of cavitation? Do you believe that the trend of σ_d versus V for the areal cavitation in Fig. 3 might be due to air nuclei effects of the sort studied by Ripken?[12] Is

[11] Physics Division, The RAND Corporation, Santa Monica, Calif.

[12] J. F. Ripken, "A Study of the Influence of Gas Nuclei on Cavitation Scale Effects in Water-Tunnel Tests," Project Report No. 58, St. Anthony Falls Hydraulics Laboratory, University of Minnesota, February, 1958. [ASTIA No. AD202626.]

there any difference in noise level produced by spots of cavitation and by areal cavitation?

I should like to conclude this inquisition by thanking Dr. Holl for preparing his stimulating paper.

Author's Closure

The author welcomes the discussion presented by Dr. Parkin and will attempt to be brief in answering the many questions. The bubbles observed on the surface of the hydrofoils were nearly spherical in shape and were not the glassy flattened cavities typical of the nearly desinent state of vaporous cavitation.

The analysis of these tests was carried out some five years after the tests were made. At the time the tests were conducted the role of diffusion in causing the spots of cavitation and the possible role of the adverse pressure gradient in stabilizing these bubbles was not realized. Thus accurate measurements as to the location of the various types of cavitation and other quantitative and qualitative information were not obtained. All that can be said is that the analysis seems to be the most logical when it is assumed that both the gaseous and vaporous cavitation occurred in the adverse pressure gradient. No extensive tests were conducted at constant σ to determine the nature of spot growth, but presumably the process was nearly a steady state phenomenon.

A crude estimate of the effect of boundary layer dimensions on the sizes of the various types of cavitation has not been made and at the time of the tests very little acoustic data were obtained. However, the vaporous cavitation would produce a much higher noise level than that of the gaseous cavitation.

The anomalous trend of σ_d versus V for the areal cavitation in Fig. 3 may be due to air nuclei effects of the type studied by Ripken since his data are quite similar in form to that in Fig. 3. However, the role of cavitation nuclei is still in doubt and awaits the concrete proof offered by a photographic record of growth from a nuclei of known size and origin.

T. W. VAN DER LINGEN
Senior Research Officer,
National Mechanical Engineering
Research Institute, Council for
Scientific and Industrial Research,
Pretoria, South Africa

A Jet Pump Design Theory

A compressible flow jet pump theory is evolved which can be more easily interpreted for design purposes than existing theories. It consists of a one-dimensional analysis based on the momentum equation and on complete mixing, used in conjunction with an over-all pressure recovery factor which is found experimentally.

Tests on a small jet pump are described and from the results it is shown that the over-all pressure recovery factor can be related to a single parameter in the analysis for all operating conditions of each general pump configuration.

In this way a general method for the correlation of results and for the design of jet pumps is established.

Introduction

Although most aspects of jet pump operation have been successfully analyzed, a general theory, which is easily interpreted for design purposes, has not yet been formulated. It is the purpose of this paper to attempt such a formulation.

The analysis presented here covers jet pumps operating on compressible fluids. In Appendix 2 it is also extended to incompressible fluids, but it is not applicable to jet pumps operating on vapors, for which more roundabout methods are required. The analysis is one-dimensional and is based on the momentum theory. It determines the delivery pressure of the pump, assuming that the quantities of induced and inducing fluid as well as their stagnation conditions are known. The results for the case of constant area mixing in the pump may be obtained directly, and for constant pressure mixing by an iterative method. For other cases, an approximate solution may be found by making assumptions for the pressures obtaining during the mixing process. For gases, the effect of overpressure in the inducing flow, caused by underexpansion, is taken into account, and parameters are used from which the limiting flow rate, set by the critical flow conditions, is evident.

The analysis takes into account losses due to mixing and to a normal shock in the mixing section, if one is present. To account for friction and other losses an over-all pressure recovery factor is introduced. This is related to the flow ratio after mixing, which is a parameter found in the analysis. The relation is determined experimentally by a series of tests made on different configurations of a variable geometry jet pump. These experiments and results are described briefly. A full record is available in reference [1].[1] The results indicate that for each general pump configuration one correlating curve applies to all operating conditions. In this way a comprehensive theory is established, from which the delivery pressure of a pump under any operating conditions in practice may be determined once its pressure recovery factor curve has been established or assumed. The capacity may also be estimated.

The analysis is presented first for a parallel-walled air-to-air jet pump with parallel injection of the two jets. It is then extended to a parallel-walled pump with angular injection and finally to the general case of a pump with nonparallel walls. A formula for over-all efficiency is stated. In the Appendixes consideration is given to incompressible fluids and to gases of different properties.

In the light of the present analysis a discussion of the analytical work of certain previous authors is given in section 7, after the nomenclature has been established. In this discussion the need for a more general and simple jet pump theory, which is fully correlated with experiment, is brought out, and the advantages of the present approach in these respects are made clear.

[For preliminary design estimates, the curves (Fig. 2) given for a parallel-walled jet pump with sonic injection will be found

Contributed by the Fluid Mechanics Subcommittee of the Hydraulic Division and presented at the Gas Turbine Power & Hydraulic Conferences, Houston, Texas, March 6–9, 1960, of The American Society of Mechanical Engineers.

Note: Statements and opinions advanced in papers are to be understood as individual expressions of their authors and not those of the Society. Manuscript received at ASME Headquarters, March 17, 1958. Paper No. 60—Hyd-6.

[1] Numbers in brackets designate References at end of paper.

Nomenclature

A = cross-sectional area of flow
B = nondimensional constant in equation for mixing distance (determined experimentally)
C_k = critical mass ratio of inducing air to delivery air

$$C_k = \frac{M_p}{M_p + M_{ik}} = \frac{K}{K+1}$$

C_v = specific heat at constant volume
C_p = specific heat at constant pressure
C_i = coefficient of discharge of inducing air nozzle M_p/M_{ik}
D = diameter
D_h = hydraulic mean diameter
e = base of Napierian logarithm
f = a function
F = pressure recovery factor, P_d^*/P_d
I = thrust ratio $= \dfrac{PA + MV}{P_1 A}$
J = momentum ratio $= \dfrac{MV}{P_1 A}$
K = induction ratio $= \dfrac{M_p}{M_{ik}}$
L = mixing distance
L_1 = length of mixing section
M = mass flow rate
$\mathbf{M}$ = Mach number $= \sqrt{\dfrac{\rho V^2}{\gamma P}}$
N_R = Reynolds number $= \dfrac{\rho V D_h}{\mu}$
P = absolute pressure
R = mass flow ratio, defined as the ratio of the mass flow rate to the critical mass flow rate for the same stagnation conditions and flow area M/M_k
$\mathbf{R}$ = gas constant $= \dfrac{P}{\rho T}$
S = entropy
T = absolute temperature
V = velocity of flow

(Continued on next page)

useful. A suitable pressure recovery factor may be assumed by reference to the experimental curves (Fig. 8). An example of a supersonic jet pump calculation including its over-all efficiency has been included in the discussion appearing in section 7.]

Analysis

1 Theory of the Parallel-Walled Air to Air Jet Pump With Parallel Injection. Configuration A.

The configuration of this pump is shown in Fig. 1(A). It is assumed that flow from a to s, from c to p, and from v to d is adiabatic and isentropic, and that between p–s and v there is no wall friction and no heat transfer across the walls. Stagnation conditions are supposed to hold at a, c, and d. p and s refer to conditions at the outlets of the inducing and induced air orifices and it is assumed that mixing is complete at v.

The theory is developed in terms of nondimensional parameters which are defined for adiabatic and isentropic gas flow such as exists between a and s, c and p, and v and d. If stagnation conditions (corresponding to a, c, and d) are indicated by suffix 1 the definitions of the parameters are as follows

$$\text{Flow ratio } R = \frac{M}{M_k} \tag{1}$$

$$\text{Thrust ratio } I = \frac{PA + MV}{P_1 A} \tag{2}$$

$$\text{Momentum ratio } J = \frac{MV}{P_1 A} \tag{3}$$

The critical flow condition for a gas flowing isentropically from given stagnation conditions occurs when the mass flow per unit area is a maximum. Such conditions are represented by subscript k.

The critical mass flow M_k for a gas is derived in textbooks on gas dynamics such as reference [2]. In terms of stagnation conditions and flow area, it may be written as:

$$M_k = A\sqrt{P_0\rho_0}\sqrt{\gamma\left(\frac{2}{\gamma+1}\right)^{\frac{\gamma+1}{\gamma-1}}}\left(\frac{P_1}{P_0}\right)\sqrt{\frac{T_0}{T_1}} \tag{4}$$

In this equation suffix 0 represents arbitrary standard conditions of temperature and pressure.

In reference [2] it is shown that, for a given value of specific heat ratio γ, the foregoing ratios and the ratio of static to stagnation pressure P/P_1 are functions of Mach number M only. They may therefore be found from gas tables (References [2 and 3]).[2]

Finally, a pumping parameter defined by the induction ratio

$$K = \frac{M_p}{M_{sk}} \tag{5}$$

is used in the analysis.

K and R_s represent the mass flows of the inducing and induced jets, respectively, divided by the critical or maximum mass flow in the induced jet. The flow ratio after mixing, $R_v = M_v/M_{sk}$ specifies conditions in the diffuser and is the principal determinant of the over-all pressure recovery factor as will be shown in section 12.

In order to find the stagnation pressure P_d and flow ratio after mixing, R_v, for given values of R_s and K and given stagnation conditions in the inducing and induced jets, we solve the equations of conservation of energy, mass, and momentum.

Energy Equation: By noting that the flow in the jet pump from points a and c to point d is adiabatic in the sense that there is heat transfer only between the two gas streams and no heat transfer to external sources or sinks, the relation for mass-energy mixing may be derived

$$M_p\frac{\gamma}{\gamma-1}RT_c + M_s\frac{\gamma}{\gamma-1}RT_a = (M_p + M_s)\frac{\gamma}{\gamma-1}RT_d$$

The introduction of the functions R and K defined in equations (1) and (5), yields

$$\frac{T_d}{T_a} = \frac{K\frac{T_c}{T_a} + R_s}{K + R_s} \tag{6}$$

Equation (6) specifies the temperature at d in terms of the tem-

[2] In terms of the symbols used in references [2 and 3], these functions may be expressed as follows:

$$R = 1\Big/\frac{A}{A^*}$$

$$I = I_k\frac{F}{F^*}\Big/\frac{A}{A^*}$$

$$\frac{I}{R} = I_k\frac{F}{F^*}$$

($I_k^* = 1.268$ for $\gamma = 1.4$)

Nomenclature

Y = mixing section area adjacent to inducing flow outlet (Fig. 1B)
W = available energy per unit mass of gas
γ = specific heat ratio of a gas
η = over-all efficiency
μ = absolute viscosity
ψ = half angle of taper of restricting needle
ψ_1 = half angle of divergence of diffuser

Subscripts and Superscripts

0 = standard conditions of pressure and temperature
1 = stagnation conditions in isentropic adiabatic flow, corresponding to conditions at a, c, and d in the pump for the flows at s, p, and v, respectively
* = practical or test value
a = induced air stagnation conditions
b = conditions of temperature and pressure in the surroundings of a gas
c = inducing air stagnation conditions
d = delivery air stagnation conditions
k = critical conditions of flow, when the maximum mass flow rate for the corresponding stagnation conditions and flow area is attained
m = maximum value attained experimentally
p = flow conditions at outlet of inducing air nozzle
s = flow conditions at outlet of induced air nozzle
t = flow conditions at throat of inducing air nozzle (for convergent nozzles $t = p$)
v = flow conditions at the point where the gases are fully mixed
v_1 = flow conditions in the diffuser throat

A = induced fluid properties
C = inducing fluid properties
D = delivery (mixed) fluid properties
M = maximum value attainable according to analysis

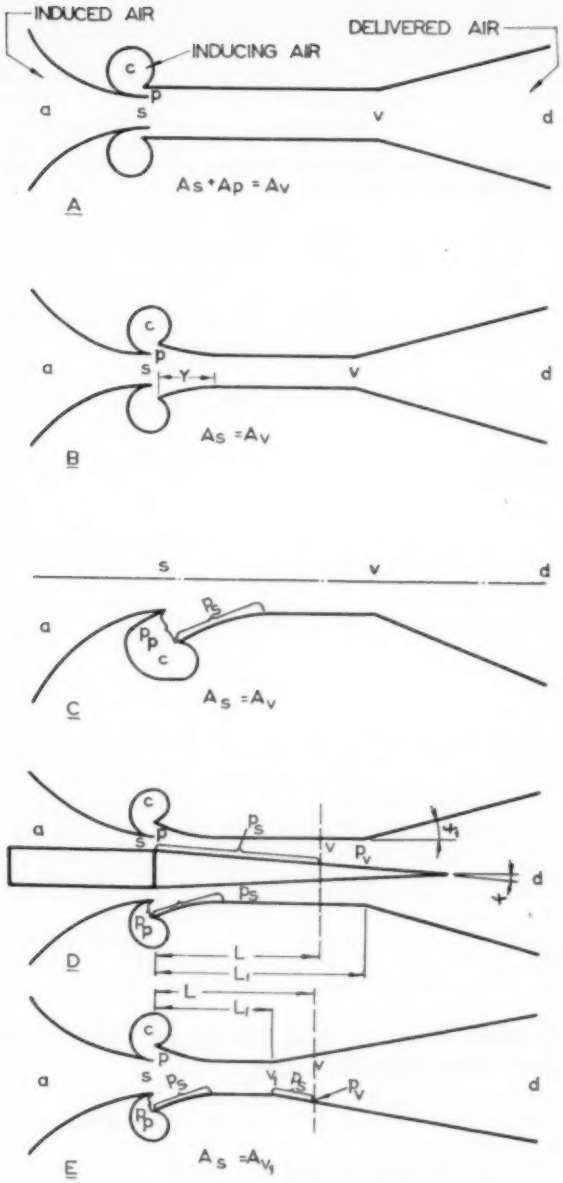

Fig. 1 Jet pump configurations

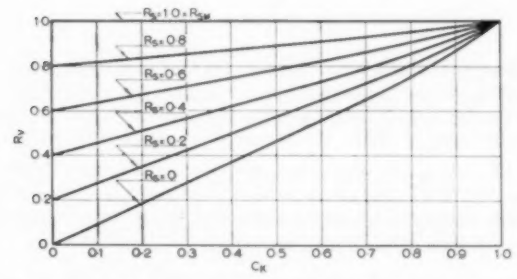

peratures at a and c and the parameters R_s and K. From this it is seen that if

$$T_c/T_a = 1, \text{ then } T_d/T_a = 1.$$

Mass Equation: The definitions in equations (1) and (5) together with the equation for conservation of mass

$$M_v = M_p + M_s$$

yield the relation

$$R_v = \frac{M_v}{M_{vk}} = \frac{M_p + M_s}{M_{vk}} = (K + R_s)\frac{M_{sk}}{M_{vk}}.$$

Applying equation (4) for critical mass flow to points s and v

$$\frac{M_{sk}}{M_{vk}} = \frac{A_s}{A_v}\frac{P_a}{P_d}\sqrt{\frac{T_d}{T_a}}$$

which may be substituted in the previous relation to give, after transposition:

$$\frac{P_d}{P_a} = \left(\frac{K + R_s}{R_v}\right)\frac{A_s}{A_v}\sqrt{\frac{T_d}{T_a}} \tag{7}$$

This equation specifies the pressure at d in terms of the flow ratio at v.

Momentum Equation: The momentum equation is

$$P_pA_p + M_pV_p + P_sA_s + M_sV_s = P_vA_v + M_vV_v$$

which in terms of thrust ratio defined in equation (2) becomes

$$P_cA_pI_p + P_aA_sI_s = P_dA_vI_v$$

We may derive A_p/A_s in terms of parameters defined by equations (1) and (5) by the application of equation (4) for critical flow at s and p, thus

$$\frac{K}{R_p} = \frac{M_{pk}}{M_{sk}} = \frac{A_p}{A_s}\frac{P_c}{P_a}\sqrt{\frac{T_c}{T_a}} \tag{8}$$

This is substituted in the momentum equation divided by P_aA_v to obtain

$$\frac{P_c}{P_a}\left(\frac{K}{R_p}\frac{P_a}{P_c}\sqrt{\frac{T_c}{T_a}}\right)I_p + I_s = \frac{P_d}{P_a}\frac{A_v}{A_s}I_v \tag{9}$$

This equation gives a relation between the pressure at d and the thrust ratio at v.

Area Equation: The condition of parallel walls gives in this case relation

$$A_v = A_p + A_s$$

which, when divided by A_s and after substitution of A_p/A_s from equation (8), becomes

$$\frac{A_v}{A_s} = \frac{K}{R_p}\frac{P_a}{P_c}\sqrt{\frac{T_c}{T_a}} + 1 \tag{10}$$

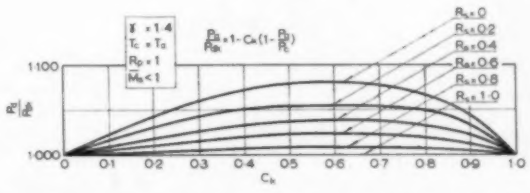

Fig. 2 Flow ratio R_v and stagnation pressure P_d after mixing for jet pump configuration A versus induced flow ratio R_s and critical mass ratio C_k of inducing air to total air

Solution: Flow Ratio: Since I_v and R_v are both functions of P_v/P_d only, and since A_v/A_s and T_d/T_a are known in terms of equations (10) and (6), we now have two equations (7) and (9) for two unknowns P_d/P_a and P_v/P_d.

We solve by substituting for P_d/P_a from equation (7) in equation (9), and substituting T_d/T_a from equation (6), to obtain:

$$\frac{R_v}{I_v} = \frac{(K + R_s)\sqrt{K\frac{T_c}{T_a} + R_s}}{\frac{K}{R_p}\sqrt{\frac{T_c}{T_a}}\,I_p + I_s} \tag{11}$$

In this form the equation corresponds to equations (22) and (27). In this simplified case it may, however, be written in the form

$$\frac{I_v}{R_v} = \frac{\frac{K}{R_s}\sqrt{\frac{T_c}{T_a}}\,\frac{I_p}{R_p} + \frac{I_s}{R_s}}{\left(\frac{K}{R_s} + 1\right)\sqrt{\frac{\frac{K}{R_s}\frac{T_c}{T_a} + 1}{\frac{K}{R_s} + 1}}}$$

which is more convenient for calculations from gas tables.

Equation (11) is used to determine R_v/I_v. The corresponding value of R_v is found from gas tables.

Pressure: After substitution of the relations for T_d/T_a and A_v/A_s in equations (6) and (10), equation (7) becomes:

$$\frac{P_d}{P_a} = \frac{K + R_s}{R_v}\,\frac{1}{1 + \frac{K}{R_p}\frac{P_a}{P_c}\sqrt{\frac{T_c}{T_a}}}\sqrt{\frac{K\frac{T_c}{T_a} + R_s}{K + R_s}} \tag{12}$$

Equation (12) together with the value of R_v derived from equation (11) gives the stagnation pressure after mixing.

There are two values of R_v and P_d/P_a corresponding to supersonic and subsonic flow, for each value of R_v/I_v. For the case where the mixed flow is initially supersonic, the maximum delivery pressure is attained when the normal shock has been forced back to the throat of the diffuser. The assumptions made about the flow between p-s and v also apply across a normal shock, so that in this case both solutions apply and they represent conditions before and after the normal shock. The expansion of the inducing stream during mixing may block the flow area for the induced stream and thereby decrease the capacity of the pump, but this does not affect the validity of the momentum equation, provided the correct mass flow rates are used.

These two equations, therefore, give the supersonic and subsonic flow ratios (or Mach numbers) and the stagnation pressures after complete mixing of the two flows.

Particular Cases: For certain particular cases the general equations (11) and (12) simplify considerably, as follows:

For sonic injection, $R_p = 1$, and equal stagnation temperatures $T_c = T_a$:

$$\frac{R_v}{I_v} = \frac{K + R_s}{KI_k + I_s} \tag{13}$$

and

$$\frac{P_d}{P_a} = \left(\frac{K + R_s}{R_v}\right)\left(\frac{1}{1 + K\frac{P_a}{P_c}}\right) \tag{14}$$

If, in addition, the induced flow is critical

$$R_s = 1 \text{ and } I_s = I_k,$$

then

$$\frac{R_v}{I_v} = \frac{K + 1}{(K + 1)I_k} = \frac{1}{I_k} = \frac{R_k}{I_k},$$

so that this pump configuration in theory chokes simultaneously at the throat v and the inlet s, and

$$R_s = R_v = 1 \tag{15}$$

Equation (12) or (14) then becomes:

$$\frac{P_{dk}}{P_a} = \frac{K + 1}{1 + K\frac{P_a}{P_c}} \tag{16}$$

For greater ease of calculation this is written in the form

$$\frac{P_a}{P_{dk}} = 1 - C_k\left(1 - \frac{P_a}{P_c}\right) \tag{17}$$

where

$$C_k = \frac{M_p}{M_p + M_{sk}} = \frac{K}{1 + K} \tag{18}$$

Equations (14) and (16) may be combined to yield:

$$\frac{P_d}{P_{dk}} = \frac{K + R_s}{(K + 1)R_v} \tag{19}$$

According to equation (13) R_v/I_v, and therefore R_v, are functions of K and R_s only and not of P_a/P_c. By equation (19) P_d/P_{dk} is then also a function of K and R_s only.

Graphs of R_v and P_d/P_{dk} as functions of $C_k = K/(1 + K)$ and R_s, for sonic inducing flow and subsonic induced flow, are given in Fig. 2. These may be used in conjunction with equation (17) to give flow ratios and stagnation pressures for these cases.

The maximum induced air flow ratio $R_{sM} = 1$ is attained when $R_v = 1$ and represents the theoretical limit to the pump capacity. Calculations made by using the graph and equation (17) indicate that the critical condition when the pump operates at full capacity is the most efficient operating condition.

2 Parallel-Walled Jet Pump With Angular Injection, With Overpressure Neglected. Configuration B.

This configuration is shown in Fig. 1(B). The induced stream flows in a parallel mixing section and the inducing stream flows in from the sides, at a small angle to the axis of symmetry.

For this case the energy and mass equations (6) and (7) remain valid. Instead of area equation (10) we have

$$\frac{A_v}{A_s} = 1 \tag{20}$$

Momentum Equation: In this case the area of the annular jet is outside the parallel section, and if we apply the momentum law across the parallel section only, and assume cosines of small angles equal to unity, the momentum equation (9) becomes

$$M_pV_p + P_vA_s + M_sV_s = P_vA_v + M_vV_v$$

which, on application of the definitions (2) and (3) for I and J, and equation (8) for A_p/A_s, reduces to:

$$\frac{K}{R_p}\sqrt{\frac{T_c}{T_a}}\,J_p + I_s = \frac{P_d}{P_a}\,I_v \tag{21}$$

This equation assumes that the velocity of the inducing fluid is unchanged between the point where it leaves the annular orifice and where it enters the parallel stream. This will only be true if the pressure in the mouth of the inducing orifice is balanced by the pressure on the curved wall opposite it. However, for sonic and supersonic flow the pressure ratio across the inducing orifice is determined by its shape, and for higher stagnation pressures the pressure P_p will exceed the pressure P_s and the pressure on the wall. Such overpressure in the inducing jet is neglected in this equation.

Solution: Solving as in section 1, the final equations are

$$\frac{R_v}{I_v} = \frac{(K + R_s)\sqrt{K\frac{T_c}{T_a} + R_s}}{\frac{K}{R_p}\sqrt{\frac{T_c}{T_a}}J_p + I_s} \tag{22}$$

$$\frac{P_d}{P_a} = \frac{K + R_s}{R_v}\sqrt{\frac{K\frac{T_c}{T_a} + R_s}{K + R_s}} \tag{23}$$

Particular Case: For the particular case of sonic injection and equal stagnation temperatures, where $Rp = 1$ and $T_c = T_a$

$$\frac{R_v}{I_v} = \frac{K + R_s}{KJ_k + I_s} \tag{24}$$

$$\frac{P_d}{P_a} = \frac{K + R_s}{R_v} \tag{25}$$

R_v and P_d/P_a are therefore functions of K and R_s only and not of P_a/P_c.

The maximum induced flow ratio R_{sM} is smaller than the critical value $R_k = 1$ due to choking of the mixed flow at v.

Note: The momentum equation assumed here did not apply in the practical case tested, where a well-faired inducing jet channel was used. Graphs for this case are omitted, but the result is discussed in section 12.

3 Parallel-Walled Jet Pump With Angular Injection, and Overpressure Accounted For. Configuration C.

For cases in which there is overpressure in the inducing jet ($P_p > P_s$) the momentum equation in section 2 implies that over the area marked Y in Fig. 1(B) the pressure is equal to P_p. As the pressure near this point in the pump must be P_s in order to induce the secondary flow, the equations may be rederived assuming pressure P_s to hold on the curved portion of the wall as indicated in Fig. 1(C).

The equations in section 4 for the general case apply also to this case when $A_p/A_s = 1$ is substituted. It is, however, not necessary to estimate the mixing distance for this case and the theory consequently gives a more accurate estimate.

4 General Case of Jet Pumps With Parallel and Nonparallel Walls. Configurations D and E.

The previous analysis may be extended to the case of the jet pumps with nonparallel walls represented by configurations D and E in Fig. 1, by assuming a distance after which mixing is completed, and approximating the pressure on the walls up to this point by the unmixed induced flow pressure P_s. If the solution so derived shows a considerable difference between P_s and P_v, a closer approximation to the true solution may be found by using the value of P_v so derived to estimate the average pressure between the inlet and the point where the flows are fully mixed. The angle between inducing and induced flow is again assumed to be small.

In this case the energy and mass equations (6) and (7) apply as before, but the value of A_v/A_s must be assumed, using turbulent mixing theory and the known configuration of the pump to determine the mixing distance.

For the pump configurations tested experimentally, it is assumed that, when mixing takes place, the inducing part of the mixed flow will tend to take up a volume corresponding to its share of the total mass flow, i.e., $K/(K + R_s)$. The assumptions are then made that the other part $R_s/(K + R_s)$ of the volume must be covered by diffusion, and that the volume covered is proportional to the forward movement L and the expansion ratio D_v/D_s.

The formula for mixing distance derived on this basis is $L/D_s = B[R_v/(K + R_s)]$ where B is a constant.

This formula conforms qualitatively to experimental and analytical results obtained on jets in free air (References [4, 5, 6]). The correlation of results described in section 12 has been slightly improved by the use of this formula with the value of $B = 9.25$.

Momentum Equation: With the assumptions given and assuming the cosine of small angles equal to one, the momentum equation (9) becomes:

$$P_pA_p - P_sA_p + M_pV_p + P_cA_s + M_sV_s + P_s(A_v - A_s) = P_vA_v + M_vV_v$$

Using definition (2) for I, and equation (8) for A_p/A_s, and dividing by P_aA_s this becomes:

$$\frac{P_c}{P_a}\left(\frac{K}{R_p}\frac{P_a}{P_c}\sqrt{\frac{T_c}{T_a}}\right)I_p - \left(\frac{K}{R_p}\frac{P_a}{P_c}\sqrt{\frac{T_c}{T_a}}\right)\frac{P_s}{P_a} + I_s + \frac{P_s}{P_a}\left(\frac{A_v}{A_s} - 1\right) = \frac{P_d}{P_a}\frac{A_v}{A_s}I_v \tag{26}$$

Solution: Solving as in section 1, the final equations are:

$$\frac{R_v}{I_v} = \frac{(K + R_s)\sqrt{K\frac{T_c}{T_a} + R_s}}{\frac{K}{R_p}\sqrt{\frac{T_c}{T_a}}I_p - \frac{K}{R_p}\frac{P_a}{P_c}\sqrt{\frac{T_c}{T_a}}\frac{P_s}{P_a} + I_s + \frac{P_s}{P_a}\left(\frac{A_v}{A_s} - 1\right)} \tag{27}$$

$$\frac{P_d}{P_a} = \frac{K + R_s}{R_v}\frac{A_s}{A_v}\sqrt{\frac{K\frac{T_c}{T_a} + R_s}{K + R_s}} \tag{28}$$

Particular Cases: When $R_p = 1$ and $T_c = T_a$ the choking condition may be found as follows:

If the pump chokes at s, $R_{sM} = 1$.

If the pump chokes at v, $R_{vM} = 1$ and $I_v = I_k$ so that equation (27) becomes:

$$\frac{1}{I_s} = \frac{K + R_s}{KI_b - \left(K\frac{P_a}{P_c}\right)\frac{P_s}{P_a} + I_s + \frac{P_s}{P_a}\left(\frac{A_v}{A_s} - 1\right)}$$

which reduces to

$$K\frac{P_a}{P_c} - \left(\frac{A_v}{A_s} - 1\right) = Z_s \tag{29}$$

where

$$Z_s = \frac{I_s - I_b R_s}{\frac{P_s}{P_a}} \tag{30}$$

A plot of $K\frac{P_a}{P_c} - \left(\frac{A_v}{A_s} - 1\right)$ against R_{sM} for subsonic induced flows is given in Fig. 3. This applies only when the flow chokes at v after mixing.

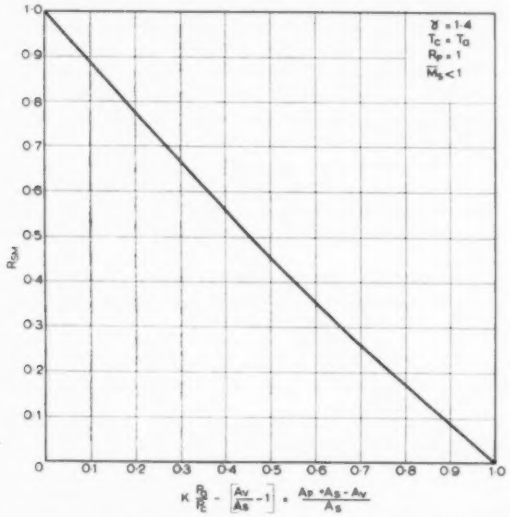

Fig. 3 Maximum induced flow ratio R_{sM} for the general pump configuration C, D, E versus the difference in area ratios at the inducing and choking points

If, for configuration E in Fig. 1, the pump chokes at v_1, where mixing is still incomplete, the maximum flow ratio R_{sM} may be approximated by substituting A_v/A_s in equation (29) and Fig. 3, thereby neglecting the effect of mixing. The result obtained in section 1 for sonic injection, where choking occurred simultaneously for the mixed and unmixed conditions, justifies this approximation to a certain extent, although the conditions are different.

Choking will occur at the point which gives the lowest value of R_{sM} provided the induced flow is subsonic.

Conclusion: The general theory presented in this section may be made to yield the results for configurations A and C in Fig. 1, by substituting

$$\frac{A_v}{A_s} = \frac{K}{R_p}\frac{P_a}{P_c}\sqrt{\frac{T_a}{T_s}} + 1$$

and $A_v/A_s = 1$, respectively.

The theory is extended to the case of different gases in the inducing and induced flows and to the incompressible case in the Appendixes.

5 The Relationship Between Over-All Pressure Recovery Factor and Flow Ratio in the Diffuser Throat

The foregoing analysis allows for mixing losses and for the loss across a normal shock in the mixing section if required. Friction and all other losses must, however, be accounted for by an over-all pressure recovery factor defined by

$$F = \frac{P_d^*}{P_d},$$

where P_d^* refers to delivery pressures obtained in a practical pump.

We consider first the divergent flow in the subsonic diffuser, which we assume to be adiabatic.

For isentropic flow,

$$P_d/P_v = \left(1 + \frac{\gamma - 1}{2\gamma}\frac{\rho_v V_v^2}{P_v}\right)^{\frac{\gamma}{\gamma-1}}$$

If, however, a portion k of the kinetic energy at the throat is lost, the delivery pressure will be

$$\frac{P_d^*}{P_v} = \left[1 + \frac{\gamma - 1}{2\gamma}(1 - k)\frac{\rho_v V_v^2}{P_v}\right]^{\frac{\gamma}{\gamma-1}}$$

which leads to the relation

$$\frac{P_d^*}{P_d} = \frac{P_v}{P_d}\left[1 + (1 - k)\left\{\left(\frac{P_v}{P_d}\right)^{\frac{1-\gamma}{\gamma}} - 1\right\}\right]^{\frac{\gamma}{\gamma-1}} \tag{31}$$

Thus the pressure recovery factor of the diffuser is a function of pressure ratio P_v/P_d only. For fixed γ, P_v/P_d and $\mathbf{M}_v$ are related only to the flow ratio R_v. Hence the pressure recovery factor will be a function of the flow ratio R_v only, provided k is a constant or a function of Mach number.

Both inducing and induced flows are present in the diffuser, which probably represents the principal source of loss in the pump. As pressure recovery factor in the diffuser is apparently a function of the flow ratio R_v, we now assume that, for the pump as a whole, the pressure recovery factor is a function of the flow ratio at the diffuser throat.

$$P_d^*/P_d = f(R_v) \tag{32}$$

The correlation of practical results on this basis is described in section 12, and the results are shown in Fig. 8.

6 Efficiency

Although the previous analysis together with the pressure recovery factor makes a comparison of different jet pumps possible, it is still of interest to find the true over-all efficiency of the pump. We may define the efficiency in terms of available work as follows:

$$\eta = \frac{\text{energy available as work in the delivered air}}{\text{energy available as work in the inducing and induced air}} \tag{33}$$

If suffix b denotes the fluid under the conditions of temperature and pressure of its surroundings, the energy W, available in a fluid supplied at constant pressure and at a negligible velocity, is the sum of its available internal energy, $C_v(T - T_b)$, the work continuously being done by some agency to supply it at this pressure $P/\rho - P_b/\rho_b$ and the heat energy $T_b(S_b - S)$, which it can draw in from its surroundings and convert to work due to its

entropy. By substituting for the pressure-volume terms and for the entropy, the available energy per unit mass of a gas becomes:

$$W = C_p(T - T_b) + \mathbf{R}T_b\left(\log_e P/P_b - \frac{\gamma}{\gamma - 1}\log_e \frac{T}{T_b}\right) \quad (34)$$

The efficiency equation for the jet pump is then

$$\eta = \frac{(K + R_s)\left[C_p(T_d - T_b) + \mathbf{R}T_b\left(\log_e P_d/P_b - \frac{\gamma}{\gamma - 1}\log_e \frac{T_d}{T_b}\right)\right]}{K\left[C_p(T_c - T_b) + \mathbf{R}T_b\left(\log_e P_c/P_b - \frac{\gamma}{\gamma - 1}\log_e \frac{T_c}{T_b}\right)\right] + R_s\left[C_p(T_a - T_b) + \mathbf{R}T_b\left(\log_e \frac{P_a}{P_b} - \frac{\gamma}{\gamma - 1}\log_e \frac{T_a}{T_b}\right)\right]} \quad (35)$$

For a jet pump inducing air from atmosphere, with atmospheric stagnation temperature in the inducing stream and with over-all adiabatic (but not isentropic) operation so that $T_a = T_s = T_d = T_b$, the efficiency equation simplifies to

$$\eta = \frac{(K + R_s)\log_e P_d/P_a}{K \log_e P_c/P_a}.$$

With the pressure recovery factor taken into account, the true efficiency is

$$\eta^* = \frac{(K + R_s)\log_e \frac{P_d^*}{P_a}}{K \log_e P_c/P_a}$$

$$= \frac{K + R_s}{K \log_e P_c/P_a}(\log_e P_d/P_a - \log_e P_d/P_d^*)$$

This form of the efficiency formula permits the loss in efficiency due to shock and mixing losses, and that due to friction lossses to be estimated separately and added together to give the total loss in efficiency.

7 Comparison With Previous Analyses

Notable work on the performance of jet pumps operating on compressible fluids has been done by Bailey and Wood [7], Flügel [8], Kastner and Spooner [9], Keenan, Neumann, and Lustwerk [10], and Irving [11]. Bailey and Wood presented their results in an empirical form without attempting to establish a comprehensive theory for its correlation. The analytical work of the other authors will be briefly recounted and discussed in the light of the present analysis.

Flügel was the first author to apply the momentum theory to jet pump calculations. In his paper he first made calculations based on the then established method of using the energy equation only. He proceeded to point out the advantages of the momentum equation and derived a wide range of results for compressible and incompressible fluids using this equation. He also discussed the mixing theory for different configurations. Neither the results based on the momentum theory nor that based on mixing theory are, however, applicable to compressible fluid pumps with overpressure in the inducing jet ($P_p > P_s$). His momentum equation ([2], equation 22) corresponded to equation (21) of the present analysis, with a friction term added. Discharge coefficients for the inducing and induced air jets and an independent diffuser efficiency were employed instead of an over-all pressure recovery factor. The method assumed that the pressures P_a, P_c, and P_d were known and that the ratio of inducing to induced air K/R_s had to be determined. The optimum value of P_s was found from a graph and K/R_s was based on this value. Constant pressure mixing and constant area mixing were both considered and the calculations were done partly with a generalized equation of state and partly by the use of total heat-entropy charts.

Flügel's theory is less general than the present theory since it cannot deal with overpressure in the inducing jet. It is also more difficult to apply because of the need for total heat-entropy charts and several loss factors. It can, however, be used for vapors, whereas the simpler form of the present theory cannot. In cases where the ratio of inducing to induced air is unknown, rather than the delivery pressure, it may give a quicker answer, especially for incompressible fluids. The diffuser efficiency to be used should, however, be modified to allow for the special inlet conditions obtained in the jet pump.

Kastner and Spooner gave a solution for the case of constant pressure mixing in terms of specially constructed total heat-entropy charts. For constant area mixing, a numerical solution was given which applied to large area ratios. Finally a solution was given for the case where there was no induced flow, i.e., a calculation of the terminal vacuum. This corresponds to the case where $R_s = 0$ and consequently $I_s = 1$ and $P_s/P_a = 1$, so that the general formulas in the present analysis may be easily simplified to give the corresponding results.

In the work of Keenan, Neumann, and Lustwerk, analyses were given of constant pressure as well as constant area mixing, using the parameters of mass ratio $M_s/M_p = R_s/K$, area ratio $A_v/A_t = A_v/(R_pA_p)$, and Mach number. Equations were derived for the Mach number after mixing, $\mathbf{M}_v$. This represents the full solution for the constant pressure case, since P_v is known to be equal to P_s, and P_d may therefore be determined. Unfortunately an equation for P_v in the constant area case is not stated.

The results for the constant pressure case may be obtained from the present general theory in section 4, but only by trial and error, assuming a fixed A_v value and varying A_s, until the value of P_v obtained from the result is equal to P_s. However, as P_v approaches P_s the theory will give better results, as the approximation involved in assuming the pressure in the mixing section equal to P_s is diminished.

The superiority of constant pressure mixing over constant area mixing, found by Keenan, et al., may be due to the type of diffuser assumed, rather than an inherent advantage of the method of mixing. This will be illustrated by analyzing the example quoted by them. The example is that of a jet pump operating at a pressure ratio P_c/P_a of 100, with $T_c = T_a$ and $R_s/K = 0.27$.

For constant pressure mixing at the best mixing pressure for $P_v/P_a = 0.89$, the stagnation pressure in the diffuser throat is $P_d/P_a = 11.02$ at a Mach number of $\mathbf{M}_v = 2.29$ which, after a normal shock and isentropic subsonic diffusion, becomes $P_d/P_a = 6.47$. The value of A_v/A_s corresponding to this operating condition is $A_v/A_s = 0.587$.

Using the simple equation (16) for sonic inducing and induced flows in a parallel jet pump, we obtain the delivery pressure $P_d/P_a = 4.54$. We may decide by intuition, however, that the best result with constant area mixing will be obtained when the induced jet area is a minimum and the inducing jet area is a maximum. This corresponds to the condition that $R_s = 1$ and $P_s/P_a = 0.528$, and $P_p/P_c = 0.00528$, giving full supersonic expansion of the inducing jet and R_p a minimum. From tables then, $R_p = 0.0804$, $I_p = 0.1336$, $I_p/R_p = 1.661$.

Substitution of these quantities in equation (11) gives $I_v/R_v = 1.578$. The values of $\mathbf{M}_v$ and R_v corresponding to this are 3.09

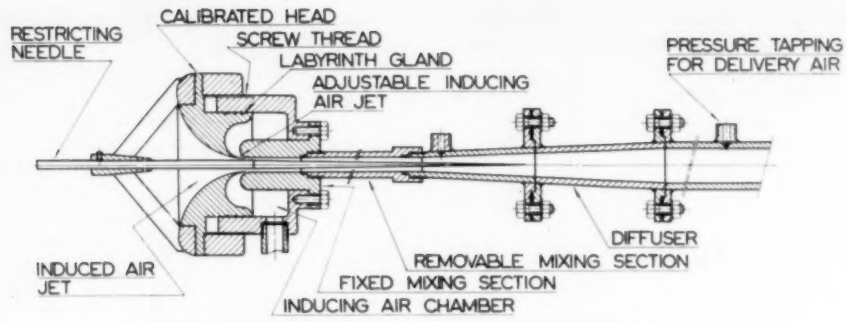

LAY-OUT OF JET PUMP WITH ADJUSTABLE ORIFICES

4(a)

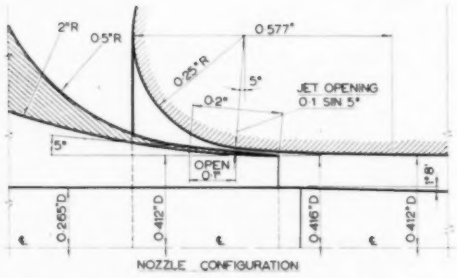

Fig. 4 Design details of the jet pump used in the tests

and 0.217 in the supersonic case, and 0.470 and 0.713 in the subsonic case. Substitution of R_v in equation (11) gives stagnation pressures of $P_d/P_a = 14.85$ and $P_d/P_a = 4.52$ before and after the shock. If isentropic supersonic diffusion could be maintained, followed by a normal shock at $M_v = 2.29$, as in the case of constant pressure mixing, a delivery pressure ratio $P_d/P_a = 8.72$ would be obtained, which is higher than for constant pressure mixing. The over-all efficiency for a pressure recovery factor of unity is 59.7 per cent as compared to 51.5 per cent. On these grounds constant area mixing is superior for this case. Unless a supersonic diffuser is used, however, nothing is gained by full expansion of the inducing jet.

The graph of pressure recovery factor by these authors in Fig. 12 of reference [4] appears to confirm the assumption that pressure recovery factor is a function of mass flow ratio after mixing, R_v.

A theoretical approach similar to that followed in the present analysis was adopted by Irving for use in the calculation of induction wind tunnels. The equations were developed in terms of mass ratio R_s/K, area ratio

$$\frac{A_p}{A_s} = \frac{K}{R_p}\,\frac{P_a}{P_c}\sqrt{\frac{T_c}{T_a}}$$

and Mach number, and use was made of the functions

$$N_1 = \left(\frac{2}{\gamma+1}\right)^{\frac{\gamma+1}{2(\gamma-1)}} R_s$$

$$N_2 = \left(\frac{2}{\gamma+1}\right)^{\frac{\gamma+1}{2(\gamma-1)}} R_p$$

and $L_1 = I_s$, $L_3 = I_p$.[3]

The use of the area ratio parameter is not favored in the present analysis because the area ratio is subject to limitations imposed by the critical flow condition, and cannot therefore be varied at will.[3] Furthermore, in the case of a narrow inducing air jet, where considerable boundary layer builds up, it is the quantity of induced air, rather than the area of the jet, which determines the output of the pump; so that an analysis in terms of parameter K is more easily applied to the practical case, as may be verified by reference to section 12.

Experiment

8 The Jet Pump

In order to test the surmise that the pressure recovery factor is a function of the flow ratio after mixing, a special jet pump was designed and tested. A configuration resembling Fig. 1(A) as

[3] The solution of the mass, energy, and momentum equations corresponded to equation (11) of the present analysis. It should be noted, however, that there is an error in equation (5) of reference [5], due to inversion of the factor $(N_3/L_3)^2$. In corrected form this equation should read:

$$\frac{M_5^2\left(1+\frac{\gamma-1}{2}M_5^2\right)}{(1+\gamma M_5^2)^2} = \left(\frac{N_2}{L_3}\right)^2 \frac{\left[\frac{N_1}{N_3}+\sigma\frac{\rho_4}{\rho_0}\left(\frac{a_4}{a_0}\right)^3\right]\left[\frac{N_1}{N_2}+\frac{\rho_4}{\rho_0}\left(\frac{a_4}{a_0}\right)\right]}{\left[\frac{L_1}{L_3}+\frac{\rho_4}{\rho_0}\left(\frac{a_4}{a_0}\right)^2\right]^2}$$

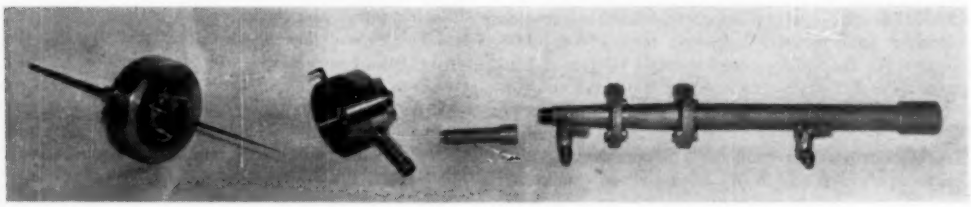

Fig. 5 Photograph of the dismantled jet pump

closely as possible was attempted, but with adjustable inducing and induced jet areas and a removable mixing section. The result was a pump corresponding to configurations C, D, or E of Fig. 1 for which the theory had to be modified. Although it is not essential from a theoretical point of view, an annular inducing jet was preferred to a central jet, because it may be expected to provide more rapid mixing and a better velocity distribution in the diffuser. A design drawing of the pump and an enlarged section of the nozzle configuration is shown in Fig. 4. Fig. 5 is a photograph of the dismantled pump.

9 Experimental Setup

To establish the pump characteristics, the stagnation conditions and the quantity of inducing air, induced air, and delivery air had to be determined. The pump was, therefore, set up as shown in Fig. 6.

The inducing air was lead via a rubber hose and throttle valve to a water trap. It then entered an orifice meter, passed straight into the stagnation chamber of the pump and issued through the inducing nozzle into the mixing section. The pressure drop from before the orifice to the stagnation chamber on the pump was small and was estimated by calculation.

The quantity of induced air was established by subtracting the mass flow rate of inducing air from that of the delivery air, and stagnation conditions were determined by periodic readings of atmospheric temperature and pressure at the test site.

The pressure of the mixed flow was measured just beyond the diffuser throat and six diameters beyond the diffuser in the delivery pipe, it then passed through a throttle valve to an orifice meter followed by the outlet. This orifice was calibrated against the inducing air orifice by closing off the induced air nozzle.

10 Description of Tests

Four series of tests (numbered 0, 1, 2, 3) were carried out on different configurations of the jet pump. The first series was performed on the pump with extended mixing section and without restricting needle in the inducing orifice. For the second series the needle was inserted fully. The tests were repeated for the third and fourth series without the extension in the mixing section. Each series comprised 25 tests with fixed inducing air pressures and jet areas. In each test, sets of readings were obtained at about ten delivery pressures, ranging from the point at which the pump just blows back to the minimum delivery pressure that could be reached.

The improved performance predicted theoretically, when the restricting needle was inserted in the induced air jet nozzle at low induced air flows, was observed during the tests.

11 Results

Form: The results were plotted in the form of graphs of delivery static gage pressure against standard volume of air delivered for each test, with the quantity of inducing air marked on each graph. Graphs for the same nominal inducing air pressure but different including nozzle openings were grouped together as in Fig. 7. These graphs may be consulted in reference [1].

The graphs indicated that the quantity of air delivered in each test increased with reduced delivery pressure until a choking point was reached, after which no further increase was possible. In some cases, however, the induction was not sufficiently strong to bring about the choking condition for positive delivery gage pressure. This may be explained by the surmise that the pressure recovery factors in these instances were so low that they canceled the theoretical pressure gain under choking conditions.

Accuracy: The position of points on the characteristics finally derived show that, with a few exceptions, the accuracy for any one test is of the order of 0.05 psi or 10 standard cfh which represents maximum random error of 0.18 and 0.3 per cent in the readings of delivery air pressure and quantity.

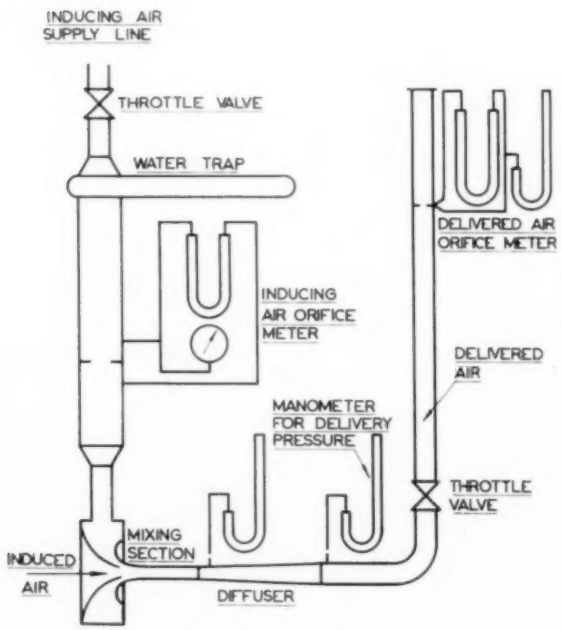

Fig. 6 Experimental setup

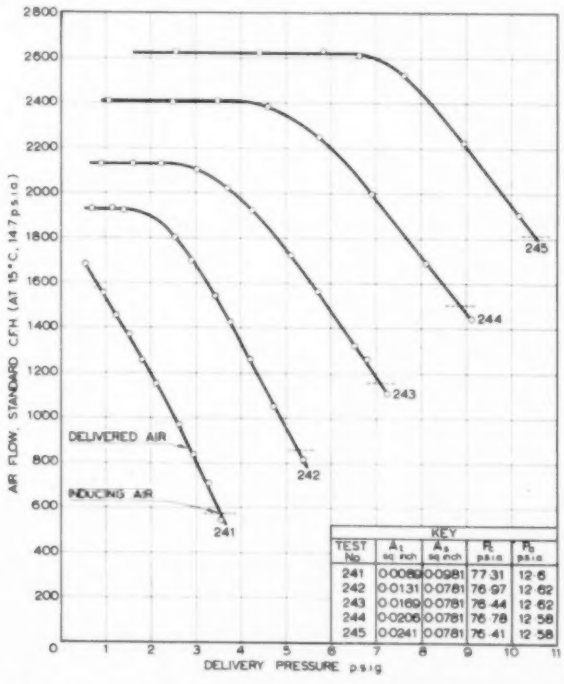

Fig. 7 Specimen test characteristics for jet pump (configuration E at nominal inducing pressure of 65 psig and five induced jet openings)

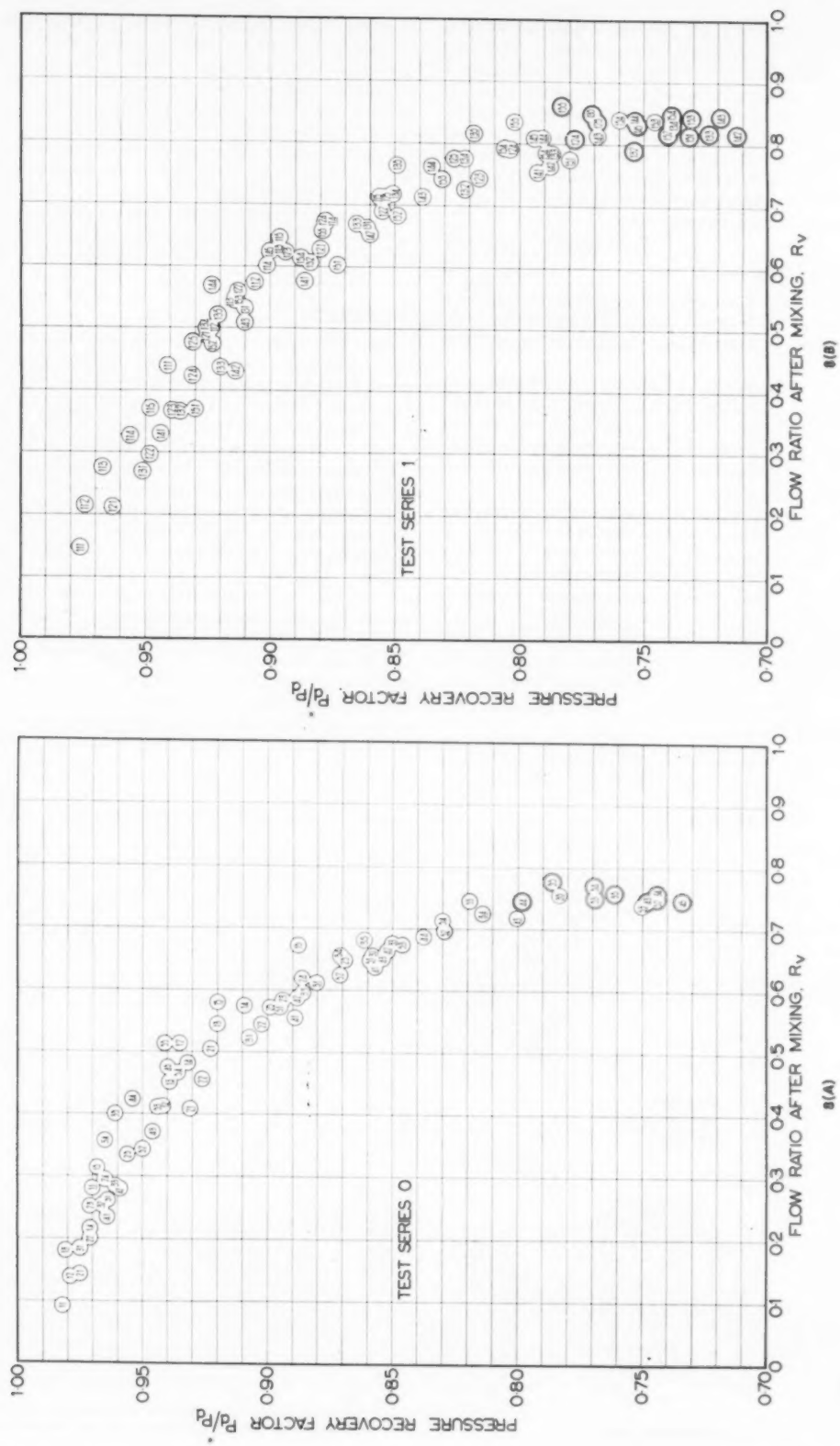
TEST SERIES 1
PRESSURE RECOVERY FACTOR P_d/P_d
FLOW RATIO AFTER MIXING, R_v
8(B)
TEST SERIES 0
PRESSURE RECOVERY FACTOR P_d/P_d
FLOW RATIO AFTER MIXING, R_v
8(A)

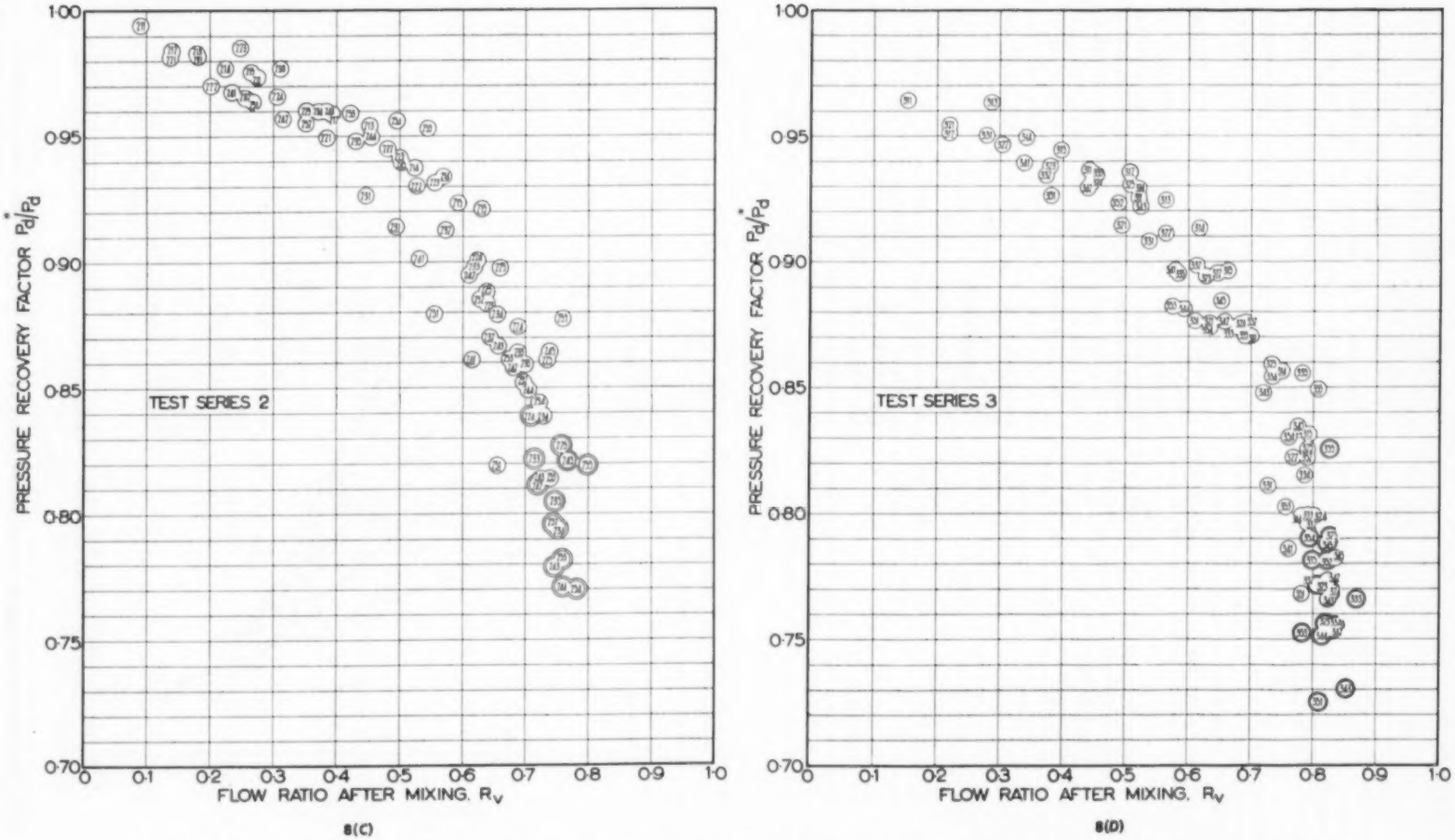

Fig. 8 Correlation of test results with general jet pump theory by plots of pressure recovery factor against flow ratio after mixing, for different configurations (see text)

12 Correlation of Results With Theory

Attempts were made to correlate the experimental results in section 11 with the analysis presented in earlier sections. A satisfactory correlation could not be achieved when using the theory for configuration A. In configuration B, where the overpressure in the inducing jet is neglected, the maximum delivery pressure predicted by the analysis was exceeded in the experiments.

The test results indicated that the assumption for configuration C, where the overpressure in the inducing jet exerted its full influence on the momentum equation, in spite of being outside the parallel section, yielded much closer agreement with experimental results. This is of importance, as overpressure is commonly neglected in similar cases (cf. reference [2], p. 220).

It was necessary, therefore, to compare the results with the more involved theories for configurations C, D, and E. The comparison was made by plotting the pressure recovery factor against the theoretical flow ratio after mixing.

In applying the theory, K and R_s were determined by dividing the experimental values of M_p and M_s by the calculated value of M_{sk}, based on the induced nozzle area and atmospheric pressure and temperature. As the shape and area of the inducing nozzle were difficult to specify exactly, sonic injection of inducing air was assumed, i.e., supersonic expansion of the inducing air was neglected. Equal stagnation temperatures were assumed. The theoretical delivery pressure P_d and flow ratio R_v were thus found from equations (27) and (28) with $R_p = 1$, $T_c = T_a$, and A_v/A_s determined as indicated in section 4.

The comparison of practice with theory on this basis is shown in the four graphs in Fig. 8. Inspection of these graphs shows that for test series 0 (configuration C), a mean line may be drawn through the points so that only 30 per cent of the points will be more than $^1/_2$ per cent off the mean, and only one point will be more than 3 per cent off the mean. At a delivery pressure of 2 psia one half per cent represents 0.1 psi which is of the same order as the scatter on the original pump characteristics, Fig. 7. Among the points lying off the mean, there seems to be a tendency for higher inducing flows to lead to higher pressure recovery factor and vice versa.

For test series 1, 2, and 3 (configurations D and E), where the approximations to pressures in the mixing distance apply, the scatter is greater and the tendency for high and low inducing air quantities to give high and low recovery factors, respectively, is more marked.

The graphs show that, for a given pump configuration, choking tends to occur at a more or less constant value of diffuser flow ratio R_v. The curves are very similar for the different pump configurations, the main difference being in the theoretical value of R_v attainable at choking. R_{vm} is considerably increased for tests where the restricting needle is included, so that a divergent mixing section is formed. The presence or absence of the parallel extension to the mixing section appears to have very little effect.

The discharge coefficient of the inducing orifice was also calculated and is plotted in Fig. 9. This coefficient is not a function of Reynolds number only as the alteration in shape of the nozzle leads to relatively high wall friction at small openings. This graph is given only as a guide for design calculations.

13 Conclusions

The agreement between theory and experiment justifies the use in practice of the assumption that pressure recovery factor is a function of the theoretical flow ratio after mixing. By assuming a suitable form of this relation, jet pump performance may be predicted by the foregoing theory. Once the curve is established for a particular pump, its performance over a wide range of operating conditions may be obtained with good accuracy.

The basic assumptions of the theory, including the applicability of the momentum equation assumed in section 3 are confirmed by the good correlation of points for test series 0. The correlation of points in the other three test series shows that the approximations made in the general theory lead to useful estimates under practical conditions.

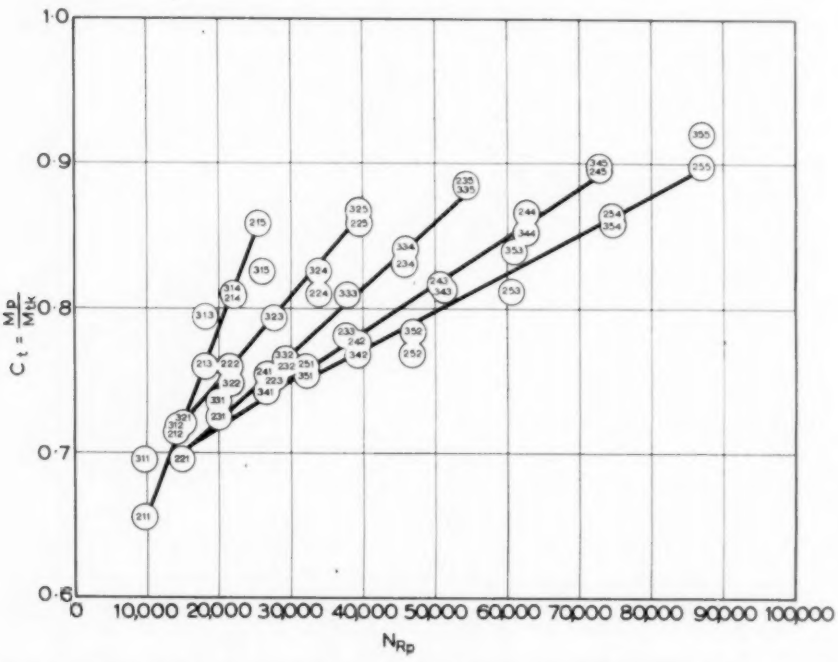

Fig. 9 Coefficient of discharge C_f of inducing air nozzle against theoretical Reynolds number at throat

In practice, the pump efficiency is lower than that predicted by theory, firstly due to the inability of the pump to operate at the maximum theoretical value of R_s (which is the most efficient condition) and secondly due to the pressure recovery factor at a given R_s value being lower than unity. The relative importance of these effects may be estimated by the efficiency formula in section 6, according to which efficiency losses are additive.

In general the test results obtained confirm the theory and indicate that it forms a sound basis for the design and analysis of jet pumps of this type.

Acknowledgments

This paper is published by permission of the South African Council for Scientific and Industrial Research. Thanks are due to Messrs. C. Cronje and J. A. Uyterlinden, who assisted with the experiments and calculations, and Mr. F. Zulch, who prepared the drawings and graphs appearing in this paper

References

1 T. W. van der Lingen, "A Jet Pump Design Theory, Based on Experiments With a Small Jet Pump," Internal Report, South African Council for Scientific and Industrial Research, 1960 (in Afrikaans).

2 A. H. Shapiro, "Compressible Fluid Flow," vol. 1, The Ronald Press Company, New York, N. Y., pp. 82–86 and Table B2.

3 J. H. Keenan and J. Kaye, "Gas Tables," Table 30, John Wiley & Sons, Inc., New York, N. Y., 1948.

4 A. J. A. Roux, "Investigation Into the Flow of Elastic Fluids Through Nozzles and Orifices and the Entraining Action of the Issuing Stream," thesis submitted for the degree of Doctor of Science at the Faculty of Engineering, University of the Witwatersrand, Johannesburg, South Africa, October, 1943.

5 H. B. Squire and J. Trouncer, "Round Jets in a General Stream," Great Britain, Aeronautical Research Council, R and M 1974, January, 1944.

6 M. D. Rousso and L. E. Boughmann, "Spreading Characteristics of a Jet Expanding From Choked Nozzles at Mach 1.91," NACA TN 3836, December, 1956.

7 A. Bailey and S. A. Wood, "An Investigation of the Principles of the Air Ejector," Technical Report of the Aeronautical Research Committee R and M 1945, Great Britain, 1933–34.

8 Gustav Flügel, "The Design of Jet Pumps," VDI Forschungsheft 395, English Translation, NACA TM 982, March-April, 1939.

9 L. J. Kastner and J. R. Spooner: "An Investigation of the Performance and Design of the Air Ejector Employing Low-Pressure Air as the Driving Fluid," *Proceedings, I.Mech.E.*, vol. 162, 1950, p. 155.

10 J. H. Keenan, E. P. Neumann, and F. Lustwerk, "An Investigation of Ejector Design by Analysis and Experiment," *Journal of Applied Mechanics*, vol. 17, TRANS. ASME, vol. 72, 1950.

11 F. G. Irving, "Note on the Theory of the Constant-Area Mixing of Compressible Flows as Applied to High-Speed Wind Tunnel Design," *Aeronautical Quarterly*, vol. 4, 1953, p. 165.

APPENDIX 1

Extension of General Theory to Case of Pump Operating With Two Different Gases

The theory of section 4 in the test may be fairly easily extended to pumps operating with different gases in the inducing and induced streams by calculating the properties of the mixture at c and slightly elaborating the equations.

Gas properties after mixing: If we note that K and R_s are respectively equal to M_p and M_s divided by the factor M_{sl}, we may use Dalton's Law[4] and Boyle's Law to prove that under standard conditions the two gases will have the same volume in the mixed and unmixed conditions and that

$$\frac{K + R_s}{\rho_{0D}} = \frac{K}{\rho_{0C}} + \frac{R_s}{\rho_{0A}}$$

or

$$\frac{\rho_{0A}}{\rho_{0D}} = \frac{K\dfrac{\rho_{0A}}{\rho_{0C}} + R_s}{K + R_s} \tag{36}$$

Since the same quantity of heat is required to raise the temperature of the mixture at constant pressure as is required for the individual gases, no loss of energy being involved in subsequent mixing, it follows that

$$KC_{PC} + R_sC_{PA} = (K + R_s)C_{PD}$$

which, on division by $(K + R_s)C_{PA}$ and substitution of $C_P = \dfrac{\gamma}{\gamma - 1}\mathbf{R}$, yields

$$\left(\frac{\gamma_D}{\gamma_D - 1}\Big/\frac{\gamma_A}{\gamma_A - 1}\right)\frac{\mathbf{R}_D}{\mathbf{R}_A} = \frac{K\left(\dfrac{\gamma_C}{\gamma_C - 1}\Big/\dfrac{\gamma_A}{\gamma_A - 1}\right)\dfrac{\mathbf{R}_C}{\mathbf{R}_A} + R_s}{K + R_s} \tag{37}$$

But by Avogadro's Law[5]

$$\rho_0 \propto H$$

where H is the molecular weight of the gas, and, as $\mathbf{R}H$ is a universal gas constant:

$$\mathbf{R} \propto \frac{1}{H} \propto \frac{1}{\rho_0} \tag{38}$$

Equation (37) therefore becomes

$$\left(\frac{\gamma_D}{\gamma_D - 1}\Big/\frac{\gamma_A}{\gamma_A - 1}\right)\frac{\rho_{0A}}{\rho_{0D}} = \frac{K\left(\dfrac{\gamma_C}{\gamma_C - 1}\Big/\dfrac{\gamma_A}{\gamma_A - 1}\right)\dfrac{\rho_{0A}}{\rho_{0C}} + R_s}{K + R_s}$$

which, on substitution for ρ_{0A}/ρ_{0D} from equation (36), reduces to

$$\left(\frac{\gamma_D}{\gamma_D - 1}\Big/\frac{\gamma_A}{\gamma_A - 1}\right) = \frac{K\left(\dfrac{\gamma_C}{\gamma_C - 1}\Big/\dfrac{\gamma_A}{\gamma_A - 1}\right)\dfrac{\rho_{0A}}{\rho_{0C}} + R_s}{K\dfrac{\rho_{0A}}{\rho_{0C}} + R_s} \tag{39}$$

Equations (36) and (39) give the density and specific heat ratio of the mixed gases.

Energy equation: The energy equation (6) now becomes:

$$K\frac{\gamma_C}{\gamma_C - 1}\mathbf{R}_CT_c + R_s\frac{\gamma_A}{\gamma_A - 1}\mathbf{R}_AT_A = \left(K\frac{\gamma_C}{\gamma_C - 1}\mathbf{R}_C + R_s\frac{\gamma_A}{\gamma_A - 1}\mathbf{R}_A\right)T_d = (K + R_s)\frac{\gamma_D}{\gamma_D - 1}\mathbf{R}_DT_d$$

on substitution of equation (37).

Using the previous relations (37) and (38), we may rewrite this equation in the form

$$\frac{T_d}{T_a} = \frac{K\left(\dfrac{\gamma_C}{\gamma_C - 1}\Big/\dfrac{\gamma_A}{\gamma_A - 1}\right)\dfrac{\rho_{0A}}{\rho_{0C}}T_c/T_a + R_s}{K\left(\dfrac{\gamma_C}{\gamma_C - 1}\Big/\dfrac{\gamma_A}{\gamma_A - 1}\right)\dfrac{\rho_{0A}}{\rho_{0C}} + R_s} \tag{40}$$

and, as before, if $T_c/T_a = 1$, then $T_d/T_a = 1$.

[4] In a volume filled by a mixture of gases, each gas exerts its own partial pressure independently of the others.

[5] Equal volumes of different gases at the same pressure and temperature contain the same number of molecules.

Solution: Reference to equation (4) for critical mass flow will indicate that the final equations for this case are modified by the factors $\frac{\rho_{0A}}{\rho_{0C}}\frac{\phi_A}{\phi_C}$ and $\frac{\rho_{0A}}{\rho_{0D}}\frac{\phi_A}{\phi_D}$ as follows:

$$\frac{R_v}{I_v} = \frac{(K+R_s)\sqrt{\frac{\rho_{0A}}{\rho_{0D}}\frac{\phi_A}{\phi_D}}\sqrt{T_d/T_s}}{\frac{K}{R_p}\sqrt{\frac{\rho_{0A}}{\rho_{0C}}\frac{\phi_A}{\phi_C}}\sqrt{T_c/T_s}I_p - \frac{K}{R_p}\frac{P_s}{P_s}\sqrt{\frac{\rho_{0A}}{\rho_{0C}}\frac{\phi_A}{\phi_C}}\sqrt{T_c/T_s}\frac{P_s}{P_s} + I_s + \frac{P_s}{P_s}\left(\frac{A_v}{A_s}-1\right)} \tag{41}$$

$$P_d/P_s = \frac{K+R_s}{R_v}\frac{A_s}{A_v}\sqrt{\frac{\rho_{0A}}{\rho_{0D}}\frac{\phi_A}{\phi_D}}\sqrt{\frac{T_d}{T_s}} \tag{42}$$

where

$$\phi = \gamma\left(\frac{2}{\gamma+1}\right)^{\frac{\gamma+1}{\gamma-1}} \tag{43}$$

The appropriate values of γ should be used for the functions I and R at different points.

APPENDIX 2

Modification of General Theory for Incompressible Flow

Basic Functions: In this case, for isentropic flow we may derive the relation

$$\frac{\rho V^2}{P} = 2\left(\frac{P_1}{P}-1\right) \tag{44}$$

The critical condition of maximum mass flow occurs when $P = 0$, so that the basic functions are

$$M_k = A\sqrt{2P_1\rho}$$

$$R = \frac{M}{M_k} = \left(1-\frac{P}{P_1}\right)^{1/2}$$

$$I = \left(2-\frac{P}{P_1}\right)$$

$$I_k = 2$$

$$J = \left(2-2\frac{P}{P_1}\right)$$

$$J_k = 2$$

The following significant relations exist between these functions:

$$J = 2R^2$$

$$I = 1+R^2$$

$$P/P_1 = 1-R^2$$

Since $P_p = P_s$:

$$R_p^2 = 1-(1-R_s^2)P_s/P_s$$

and finally

$$\frac{K}{R_p} = \frac{A_p}{A_s}\sqrt{\frac{P_s}{P_s}\frac{\rho_C}{\rho_A}}$$

Mixture Properties: Equation (36): If the volume of the mixture is the same as that of the unmixed fluids

$$\frac{\rho_A}{\rho_D} = \frac{K(\rho_A/\rho_C)+R_s}{K+R_s}$$

Mass equation (7):

$$R_v = (K+R_s)\frac{M_{sk}}{M_{vk}}$$

$$= (K+R_s)\frac{A_s}{A_v}\sqrt{P_s/P_d}\sqrt{\frac{K(\rho_A/\rho_C)+R_s}{K+R_s}}$$

so that

$$P_d/P_s = \left(\frac{K+R_s}{R_v}\right)^2\left(\frac{A_s}{A_v}\right)^2\frac{K(\rho_A/\rho_C)+R_s}{K+R_s}$$

Momentum equation (26): Since $P_p = P_s$ and friction is assumed to be absent between $p-s$ and v, the momentum equation becomes:

$$\frac{P_c}{P_s}\frac{K}{R_p}\sqrt{\frac{P_s}{P_c}\frac{\rho_A}{\rho_C}}J_p + I_s + \frac{P_s}{P_s}\left(\frac{A_v}{A_s}-1\right) = \frac{P_d}{P_s}\frac{A_v}{A_s}I_v$$

Solution: The equations may be solved as for the compressible case, and the relations between functions substituted to yield the final relations:

$$R_v^2 = \frac{(K+R_s)^2\left(\frac{A_s}{A_v}\right)\left(\frac{K\left(\frac{\rho_A}{\rho_C}\right)+R_s}{K+R_s}\right)}{2K\sqrt{\frac{\rho_A}{\rho_C}}\sqrt{\frac{P_c}{P_s}-(1-R_s^2)}+(1+R_s^2)+(1-R_s^2)\left(\frac{A_v}{A_s}-1\right)-(K+R_s)^2\left(\frac{A_s}{A_v}\right)\frac{K\frac{\rho_A}{\rho_C}+R_s}{K+R_s}} \tag{45}$$

$$P_d/P_s = \frac{A_s}{A_v}\left\{2K\sqrt{\frac{\rho_A}{\rho_C}}\sqrt{\frac{P_c}{P_s}-(1-R_s^2)}+(1+R_s^2)+(1-R_s^2)\left(\frac{A_v}{A_s}-1\right)-(K+R_s)^2\frac{A_s}{A_v}\frac{K\rho_A/\rho_C+R_s}{K+R_s}\right\} \tag{46}$$

These equations are considerably simplified if $\rho_A = \rho_C$ and $A_v = A_s$, as may be found by substitution.

Pressure Efficiency: As $(\rho_v V_v^2/P_v)$ and R_v are again functions of P_v/P_d only, the arguments used in the compressible case to show that P_d^*/P_d is a function of R_v are again applicable.

Accelerations and Mean Trajectories in Turbulent Channel Flow

S. IRMAY
Professor of Civil (Hydraulic) Engineering, Israel Institute of Technology, Haifa, Israel; and Visiting Professor, Stanford University, Stanford, Calif.

The author shows that even in steady uniform turbulent channel flow there exist on the average mean accelerations and forces acting on fluid particles. These are computed from the flow equations and Laufer's data. There exist both normal and axial mean accelerations, the latter highly negative (15g and more) in the dissipative "transition" layer near the wall, elsewhere constant. There most river bed-load and dune sand movement occurs. Mixing and sediment transportation are explained dynamically. Mean shear is shown to exist mainly in the dissipative layer. Mean turbulent trajectories are defined.

1 Introduction

FLOW OF WATER in conduits at the usual Reynolds numbers (Re) *is turbulent:* Any flow parameter B fluctuates rapidly and irregularly round its *mean* $\bar{B}$, the *fluctuation* B' being:

$$B' = B - \bar{B} \tag{1}$$

We observe mainly the *mean flow* [4, 5],[1] described by the mean parameters.

A simple example is steady uniform flow near the axis of a wide open rectangular channel of depth h and constant slope J. It is mathematically equivalent to the lower half of a steady uniform flow in a two-dimensional channel between two smooth parallel walls (mutual distance $2h$) under a constant hydraulic gradient J. Laufer [17] has published detailed experimental data on such flows.

Our knowledge of turbulent flow is meager, as it requires a statistical description. The first such study was done by Reynolds [22], and later developed by Taylor [25], Batchelor [3] in England; von Karman [14] in U. S. A.; Obukhov [20], Kolmogoroff [15] in USSR; Friedmann and Keller [8], Heisenberg [10] in Germany, and many others. They investigated *isotropic* and *homogeneous turbulence,* i.e., a mean flow with parameters invariant under rotation, reflexion, or translation of the co-ordinate system. The results found some application in meteorology, not in hydraulic engineering, where turbulence is inhomogeneous and nonisotropic. So engineers prefer a phenomenological and semiempirical description based on heuristic concepts, such as Boussinesq's eddy viscosity [4, 5], Prandtl's momentum transfer and mixing length hypothesis, etc. These theories were successfully applied to the study of spatial distribution of the mean velocity in channel and pipe flow, and to mixing phenomena. No great success is reported in curved flow or in sediment transportation. Recently Townsend [26] studied the turbulent shear flow.

In what follows the author uses Reynolds' approach and Laufer's empirical data [17, 18] and, analyzing mean accelerations, shows that some new insight in turbulent flow is thus obtained.

[1] Numbers in brackets designate References at end of paper.

Contributed by the Fluid Mechanics Subcommittee of the Hydraulic Division and presented at the Gas Turbine Power & Hydraulic Conference, Houston, Texas, March 6–9, 1960, of THE AMERICAN SOCIETY OF MECHANICAL ENGINEERS.

NOTE: Statements and opinions advanced in papers are to be understood as individual expressions of their authors and not those of the Society. Manuscript received at ASME Headquarters, October 8, 1959. Paper No. 60—Hyd-3.

2 Reynolds' Equations and Stresses

In a Cartesian orthogonal system of reference $Oxyz$, the components of the vector of instantaneous velocity are, u, v, w in the directions x, y, z; p = pressure; ρ = const. fluid density; ν = kinematic viscosity; Z = vertical elevation above a horizontal datum; P = combined pressure and gravity function:

$$P = p/\rho + gZ \tag{2}$$

At every instant by *continuity:*

$$u_x + v_y + w_z = 0 \tag{3}$$

the subscripts $x, \ldots$ representing partial derivations. Reynolds assumed that the *Navier-Stokes* equations of motion of a viscous fluid are valid in small even in turbulent flow:

Nomenclature

A = coefficient
a_1 = axial acceleration
a_2 = transversal acceleration
a_3 = normal acceleration
B = coefficient; any flow property
d = thickness of laminar sublayer
$\dot{E}$ = rate of energy dissipation
e_1 = thickness of first zone ($\bar{a}_1 < 0$)
e_3 = thickness of third zone ($\bar{a}_3 > 0$)
g = gravity acceleration
h = half channel width
J = hydraulic gradient; channel slope
M = $(-\bar{a}_1)_{max}$
P = $p/\rho + gZ$
p = fluid pressure
Re = $h\bar{u}_{max}/\nu$ = Reynolds number
t = time
u = axial velocity
$\bar{u}_{max}$ = axial velocity on axis
u_τ = $(ghJ)^{1/2}$ = shear velocity
v = transversal velocity
w = normal velocity
x = Cartesian axial co-ordinate
y = Cartesian transversal co-ordinate
Z = vertical elevation above datum
z = Cartesian normal co-ordinate
δ = du_τ/ν
ϵ_1 = e_1u_τ/ν
ϵ_3 = e_3u_τ/ν
η = hu_τ/ν
ζ = zu_τ/ν
μ = dynamic viscosity
ν = kinematic viscosity
ν' = eddy viscosity
ρ = density
τ = shear
$\bar{(\ )}$ = mean (in time)
$(\ )'$ = fluctuation
$(\ )_a$ = ∂/∂_a
$(\ )_0$ = initial data

$$
\left.
\begin{aligned}
a_1 &= du/dt = u_t + (u^2)_x + (uv)_y + (uw)_z \\
&\quad = -P_x + \nu(u_{xx} + u_{yy} + u_{zz}) \\
a_2 &= dv/dt = v_t + (uv)_x + (v^2)_y + (vw)_z \\
&\quad = -P_y + \nu\nabla^2 v \\
a_3 &= dw/dt = w_t + (uw)_x + (vw)_y + (w^2)_z \\
&\quad = -P_z + \nu\nabla^2 w
\end{aligned}
\right\} \quad (4)
$$

By averaging (4), each instantaneous linear parameter is replaced by its mean, and each quadratic parameter by two means:

$$\overline{uw} = \bar{u}\bar{w} + \overline{u'w'};\ \overline{w^2} = (\bar{w})^2 + \overline{w'^2} \quad (5)$$

$\overline{u'w'}$, $\overline{w'^2}$, and so forth, are central second moments, components of the symmetrical *tensor* of *correlation* of the velocity fluctuations, of rank 2. When multiplied by $(-\rho)$, they are components of a symmetrical tensor of rank 2 with the dimensions of a stress. They are improperly called *Reynolds' stress* or *turbulent stress:* $-\rho\overline{u'w'}$ is the *turbulent "shear"* and $-\rho\overline{w'^2}$ the turbulent *"pressure."* A true instantaneous shear is, e.g.,

$$\tau = \mu(u_z + w_x) \quad (6)$$

and the true mean shear

$$\bar{\tau} = \mu(\bar{u}_z + \bar{w}_x) \quad (7)$$

and not

$$\mu(\bar{u}_z + \bar{w}_x) - \rho\overline{u'w'} \quad (8)$$

Except in the vicinity of the wall, the Reynolds stresses are many thousands times larger than the mean stresses.

3 Two-Dimensional Channel Flow

Reynolds' method is applied to steady uniform mean flow in a two-dimensional channel (Fig. 1). The origin O of the Cartesian orthogonal system of reference is chosen on the channel bottom, x is in the direction of mean flow, y transversally, z normally to the bottom:

$$\bar{v} = \bar{w} = 0 \quad (9)$$

All t, x, y derivatives vanish, because of the type of flow, except for:

$$-\bar{P}_x = gJ \quad (10)$$

Equations (4) become:

$$\bar{a}_1 = (\overline{u'w'})_z = gJ + \nu\bar{u}_{zz} \quad (11_1)$$

$$\bar{a}_2 = (\overline{v'w'})_z = -\bar{P}_y \quad (11_2)$$

$$\bar{a}_3 = (\overline{w'^2})_z = -\bar{P}_z \quad (11_3)$$

Because of the nonslip condition at the solid boundary, we have everywhere:

$$\overline{v'w'} = 0 \quad \text{and} \quad \bar{a}_2 = 0 \quad (12)$$

The remaining two equations (11_1), (11_3) do not suffice to determine completely the four unknown functions of z:

$$\bar{u},\ \overline{u'w'},\ \overline{w'^2},\ \bar{P} \quad (13)$$

In order to overcome this difficulty Prandtl [21] developed the concept of *boundary layer*. The turbulent flow is divided into two zones:

(*a*) A thin layer next to the wall, called the *laminar sublayer*, where the fluctuations are small and the mean velocity gradient is very high. Its thickness d (in nondimensional units δ) is estimated along smooth walls to be of the order:

$$\delta \equiv du_\tau/\nu = 3 \text{ to } 13 \quad (14)$$

u_τ is the *shear velocity*

$$u_\tau = (ghJ)^{1/2} \quad (15)$$

In this zone very nearly:

$$\bar{u}/u_\tau \sim zu_\tau/\nu \equiv \zeta \quad (16)$$

For a water channel of $h = 100$ cm, $J = 0.001$, $u_\tau = 10$ cm/s, $d = 0.003$ to 0.013 cm.

(*b*) Most of the flow of thickness $(h\text{-}d)$ is the *turbulent zone*. Here at a distance z (in nondimensional units ζ) such that:

$$\zeta \equiv zu_\tau/\nu > 30 \quad (17)$$

we have the semiempirical relationship:

$$\bar{u}/u_\tau = A \ln zu_\tau/\nu + B = A \ln \zeta + B \quad (18)$$

with the exception of the channel axis and its vicinity. Laufer [17] gives $B = 5.5$ and $A = 3$ (though 2.9 seems to fit his data better).

Between the two zones:

$$3 < \zeta < 30 \quad (19)$$

and on the basis of the mean velocity diagram, there seems to

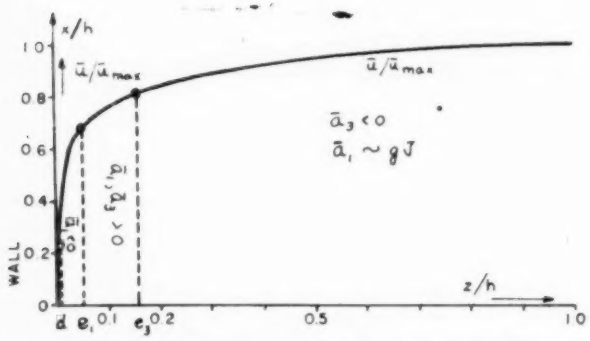

Fig. 1 Distribution of velocities $u/\bar{u}_{max}$ versus distance from wall z/h at Re = 30800

d/h = 0.003 end of boundary layer
e_1/h = 0.05 end of zone of negative $\bar{a}_1$

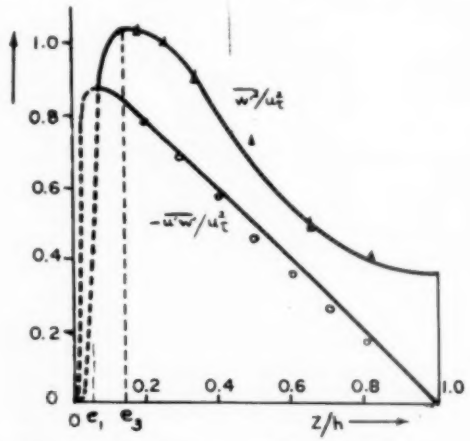

Fig. 2 Distribution of correlations — $\overline{u'w'}/u_\tau^2$ and $\overline{w'^2}/u_\tau^2$ versus distance from wall z/h at Re = 30800. Extrapolated data in interrupted lines.

exist a gradual unclearly defined turbulent transition. It will be shown later that this is really part of a distinct and clearly defined third zone.

Laufer [17] measured the flow data in a flat smooth channel of aspect ratios 12:1 with air flowing at Re = 12300 to 61600. Figs. 1 and 2 give $\bar{u}$; $\overline{u'w'}$; $\overline{w'^2}$ as functions of z (or rather the nondimensional $\bar{u}/\bar{u}_{max}$; $\overline{u'w'}/u_\tau^2$; $\overline{w'^2}/u_\tau^2$ as functions of z/h) corresponding to:

Reynolds number $\mathrm{Re} \equiv h\bar{u}_{max}/\nu = 30800$
half channel width $h = 6.35$ cm
in nondimensional units $\eta \equiv hu_\tau/\nu = 1180$
kinematic air viscosity (computed from Re) $\nu = 0.155$ cm²/s
maximum speed on channel axis $\bar{u}_{max} = 750$ cm/s
hydraulic gradient acceleration (computed) $gJ = 131$ cm/s²
shear velocity (computed) $u_\tau = 28.8$ cm/s

4 Mean Accelerations

Surprisingly enough equations (11_1) and (11_2) show that the axial ($\bar{a}_1$) and normal ($\bar{a}_2$) components of the mean acceleration do not vanish in steady uniform linear channel flow. This is due to the fact that instantaneous acceleration is a Lagrangian, hence nonlinear, rate of change of the velocity, as an observer accompanies each fluid particle in its complicated and tortuous path. Another stationary observer situated at the fixed point (x, y, z) (Eulerian point of view) takes the mean of the instantaneous accelerations of all the particles passing him successively. This mean defines the *mean acceleration* at a point.

The mean accelerations were computed by the author and Mrs. Geffen in her MSc thesis [11, 12, 13, 9], on the basis of Laufer's data [17] for Re = 30800, using Figs. 1 and 2. The results are shown in Figs. 3, 4, and 5. Because of the difficulties of a double differentiation, the numerical computations were carried out by the method of differences, by parabolic approximation, and by a graphical method developed by the author [11], based on drawing tangents and measuring radii of curvature of the $\bar{u}(z)$ curve. Each resulting curve was then smoothed out. The resulting points are shown by small circles or triangles, and seem to lie on quite smooth curves.

(a) The *axial component* $\bar{a}_1$ is computed by the two equations (11_1) from the $\bar{u}(z)$ and $\overline{u'w'}(z)$ curves to check each other. Throughout the turbulent zone $\bar{u}$ varies very slowly and the viscous term $\nu\bar{u}_{zz}$ may be neglected with respect to the constant hydraulic gradient acceleration gJ. There very nearly

$$\bar{a}_1 \sim gJ \tag{20}$$

When the wall is approached, but yet within the regular turbulent zone with the logarithmic law (18) still valid, the viscous negative term increases rapidly in absolute value, and there very nearly:

$$\bar{a}_1 \sim gJ - A\nu u_\tau/z^2 \tag{21}$$

$\bar{a}_1$ vanishes at the point:

$$z = e_1 = (A\nu u_\tau/gJ)^{1/2} = (Ah/u_\tau)^{1/2} \tag{22}$$

or in nondimensional units:

$$\epsilon_1 \equiv e_1 u_\tau/\nu = (A \cdot hu_\tau/\nu)^{1/2} \equiv (A\eta)^{1/2} \tag{23}$$

In our case:

$$\epsilon_1 \sim 60;\ e_1/h \sim 0.05;\ e_1 \sim 0.32 \text{ cm} \tag{24}$$

Nearer to the wall $\bar{a}_1$ becomes negative and at $z/h \sim 0.0045$ it reaches the enormous value of $-15g$. Then it falls rapidly to become vanishingly small at

$$z/h \sim 0.003 \quad \text{or} \quad \zeta \sim 3.5 \tag{25}$$

Comparison of (25) with (14) shows that this is the assumed (lower) limit of the thickness of the laminar sublayer. This laminar sublayer may now be defined more precisely as the zone of vanishing axial accelerations, with a thickness $\delta = 3$ to 3.5.[2]

Then:
$$d/h \sim 0.003; \quad d \sim 0.02 \text{ cm} \tag{26}$$

Equation (23) may now be rewritten

$$e_1 \sim (dh)^{1/2} \quad \text{or} \quad \epsilon_1 \sim (\delta\eta)^{1/2} \tag{27}$$

The thickness of the zone of negative axial accelerations is the geometrical mean between those of the laminar sublayer and of the total flow.

Integrating the first equation (11_1) between $z = 0$ and h, we obtain:

$$\int_{z=0}^{h} \bar{a}_1 dz = \overline{u'w'}\Big|_{z=0}^{h} = \overline{u'w'}(h) \tag{28}$$

as $\overline{u'w'} = 0$ at the bottom. By symmetry it vanishes also on the axis, so the value of the integral is 0. This means that the area of the positive portion in Fig. 3(a) is equal to that of the negative portion.

In other words, though there exists at each point a mean acceleration, on the average throughout the channel cross section there is no acceleration, as befits uniform flow. This fact gives a rough estimate of the maximum negative acceleration $M = (-\bar{a}_1)_{max}$.

The area of the positive portion of Fig. 3(a) may be computed from (21), which is valid there, and from (23):

$$\int_{z=e_1}^{h} \bar{a}_1 dz = gJ(h - e_1) - A\nu u_\tau(1/e_1 - 1/h)$$

The area of the negative portion is very roughly $M(e_1 - d)/3$ assuming it to consist roughly of an ordinary parabolic triangular segment of base $(e_1 - d)$ and height M. Equating the two, we obtain an estimate $M/g \sim 7.5$ as against $M/g \sim 14$ by numerical or graphical computation. The order of magnitude is the same.

A similar analysis applied to Laufer's data at Re = 61600 gives:

$\bar{u}_{max} = 1500$ cm/s; $u_\tau = 55.3$ cm/s
$gJ = 483$ cm/s²; $\eta = hu_\tau/\nu = 2260$
$e_1/h = 0.037$; $\epsilon_1 = e_1 u_\tau/\nu \sim 82$
$M/g \sim 80$

The higher the Reynolds number, the smaller the zone of negative accelerations, and the higher the maximum.

(b) The *normal component* $\bar{a}_2$ is computed by (11_2) on the basis of the $\overline{w'^2}(z)$ curve alone. At the wall ($z = 0$) both $\overline{w'^2}$ and $\bar{a}_2 = (\overline{w'^2})_z$ vanish. $\bar{a}_2$ vanishes also on the axis ($z = h$) and at some intermediate point $z = e_2$ such that:

$$e_2/h \sim 0.155; \quad \epsilon_2 = e_2 u_\tau/\nu \sim 183; \quad e_2 \sim 1.0 \text{ cm} \tag{29}$$

Closer to the wall $\bar{a}_2$ is positive, i.e., directed upward:

$$z < e_2 = 0.155h; \quad \zeta < \epsilon_2 = 183; \quad \bar{a}_2 > 0 \tag{30}$$

with a maximum approximately:

$$\bar{a}_{2max} \sim 2g \quad \text{at} \quad z/h \sim 0.05 \quad \text{or} \quad \zeta \sim 60 \tag{31}$$

[2] At the wall $\overline{u'w'}$ and $\bar{a}_1 = (\overline{u'w'})_z = \overline{u'w_z'} + \overline{w'u_z'} = 0$ as the velocity fluctuations vanish there. By (11_1)

$$\bar{u}_{zz} = -gJ/\nu = -u_\tau^2/h\nu$$

and a Taylor development in the laminar sublayer would start with the terms: $\bar{u}/u_\tau = zu_\tau/\nu - z^2u_\tau/2h\nu + \ldots = \zeta - \zeta^2/2\eta + \ldots$ The quadratic term is less than 1/800 of the linear term even at the end of the laminar sublayer ($\zeta = \delta \sim 3$).

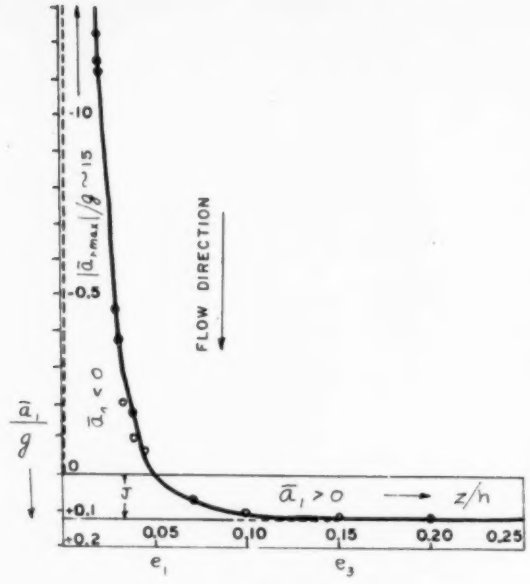

Fig. 3(a)

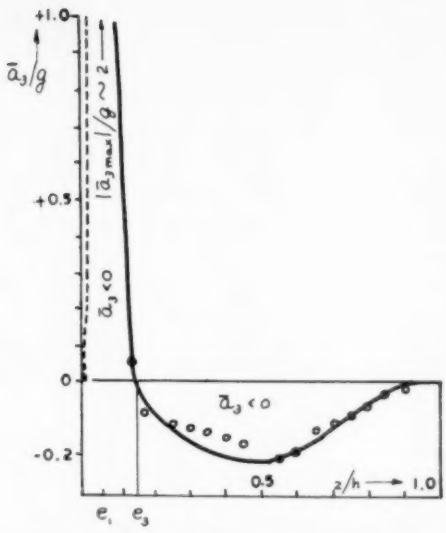

Fig. 4 Distribution of normal mean accelerations $\bar{a}_3/g$ versus z/h at Re = 30800

$(\bar{a}_3/g)_{max} \sim 2$ at $z/h \sim 0.05$
$\bar{a}_3/g = 0$ at $e_3/h \sim 0.155$
$(-\bar{a}_3/g)_{max} \sim 0.2$ at $z/h \sim 0.55$

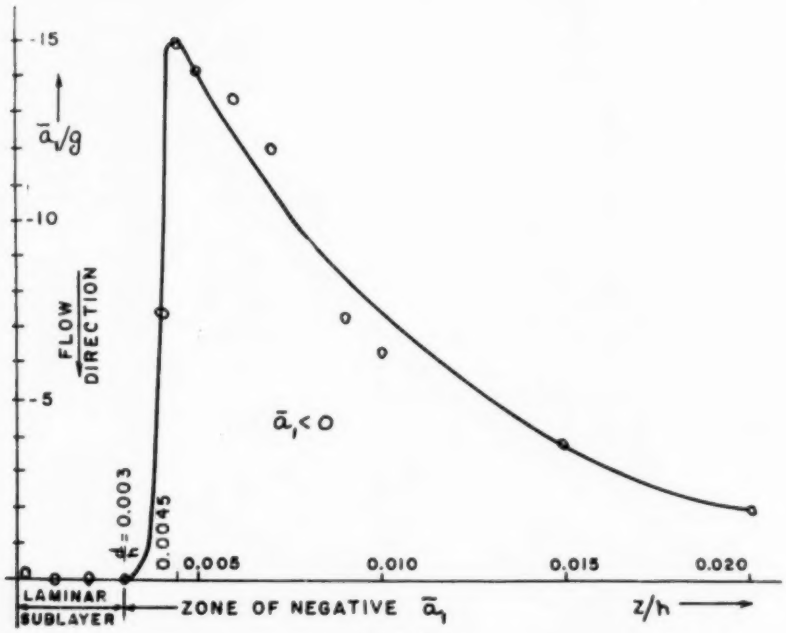

Fig. 3(b)

Fig. 3 Distribution of axial mean accelerations $\bar{a}_1/g$ versus distance from wall z/h at Re = 30800

$(-\bar{a}_1/g)_{max} \sim 15$ at $z/h \sim 0.045$
$\bar{a}_1/g = 0$ at $e_1/h = 0.05$
$(\bar{a}_1/g)$ asympt. $= J = 0.134$

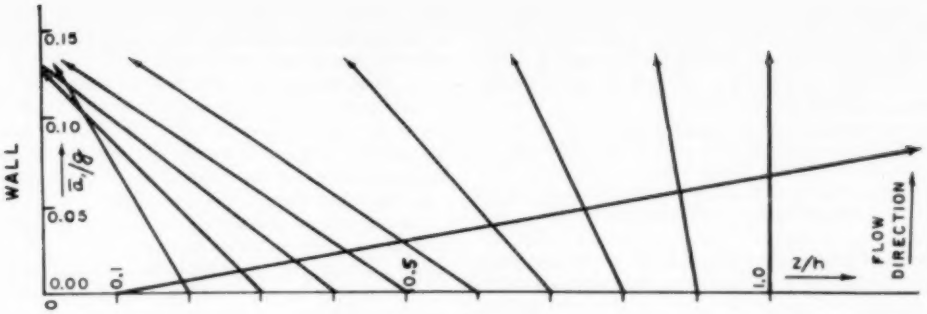

(a)

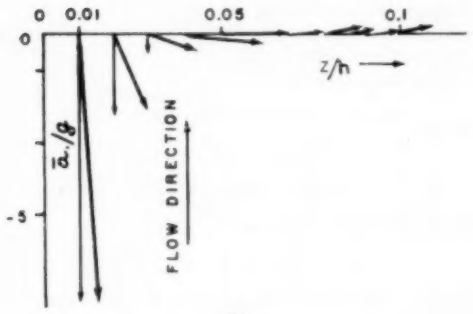

(b)

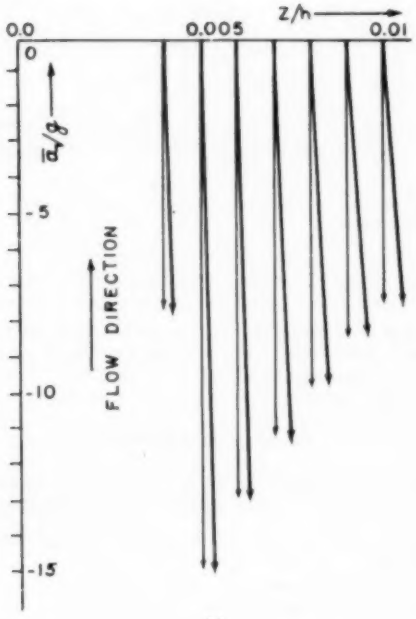

(c)

Fig. 5 Spatial distribution of vectors of mean acceleration $\bar{a}/g$ at Re = 30800
5(a) — scale 1 ($\bar{a}/g$ → 25 cm
5(b) & 5(c) — scale → 1 cm

Further away $\bar{a}_3$ is negative, i.e., directed toward the bottom:

$$z > e_3 = 0.155h; \qquad \zeta > \epsilon_3 = 183; \qquad \bar{a}_3 < 0 \tag{32}$$

with the maximum of its absolute value at about half depth:

$$(-\bar{a}_4)_{max} \sim 0.2g \qquad \text{at} \qquad z/h \sim 0.55 \tag{33}$$

These maxima are much smaller than those of $\bar{a}_1$

$$(-\bar{a}_1)_{max} \sim 14g$$

At Re = 61600 the data do not suffice, yet it is clear from [17] that:

$$e_4/h < 0.07; \qquad \epsilon_3 \equiv e_3 u_\tau/\nu < 160 \tag{34}$$

As $e_1/h = 0.037$ and $\epsilon_1 = 82$, we see that the range between ϵ_1 and ϵ_2 is much smaller than at Re = 30800 ($\epsilon_1 = 60$; $\epsilon_2 = 183$). Integration of (11_3) between $z = 0$ and h and Fig. 4 show that the area of the positive portion is much larger than that of the negative one.

(c) *Vector field of mean accelerations.* Fig. 5 shows the distribution of the acceleration vector throughout the channel, with the vicinity of the wall given in more detail.

This vector rotates rapidly in the turbulent zone: It is directed against the flow in the zone of negative accelerations, upward at $z = e_1$, in the direction of flow at $z = e_3$, turns another 35 deg toward the wall at about half depth, then resumes the flow direction on the axis ($z = h$). The absolute value of the rotating acceleration in the zone of negative accelerations is much higher than warranted by the axial components alone.

5. Interpretation and Applications

What is the meaning of these mean accelerations? When multiplied by the mass of a fluid particle, they give the mean external force acting on these particles.

The flow has then to be subdivided into three essentially different zones:

(a) *Zone I—laminar sublayer* of thickness d such that $\delta = du_\tau/\nu = 3$ to 3.5. There are practically no external forces acting on the particle. Assuming that a small solid particle of similar density is subjected to the same forces, such a particle (clay or silt size) will not be acted upon by forces. This is confirmed by observation.

(b) *Zone II—negative accelerations* of thickness $e_1 \sim (dh)^{1/2}$.

In it each particle is subjected to a retarding force against the flow, to a lifting force, and to a couple tending to rotate it forward. In the water channel assumed in Section 3(*a*) we have $e_1 \sim 0.5$ cm, which is the order of magnitude of the zone of most intensive bed load transportation by rotation [27].

In atmospheric phenomena, assuming a wind [19] of: $h = 300\text{m}$; $\bar{u} = 10\text{m/sec}$; $u_\tau = 0.2\text{m/sec}$; $\nu \sim 0.15\ \text{cm}^2/\text{sec}$; by (14) and (23):

$$d \sim 0.02\ \text{cm}; \qquad e_1 \sim 25\ \text{cm}.$$

This is the order of magnitude of the zone of saltation in dune transportation [1] and seat of most microclimate phenomena.

A curious implication results for particles of a size slightly larger than the thickness d of the sublaminar layer: Such particles are found in the most abrupt part of the negative $\bar{a}_1$ curve [Fig. $3(b)_1$], and the couple tends to rotate them backward. Further experimental data may test out this conclusion.

The existence of a zone of high turbulence near the wall has been confirmed by Schubauer [24].

(*c*) *Zone III—positive accelerations* of thickness $h - e_1 \sim h$. This is the zone of suspended load. In it each particle is subjected to a constant force in the direction of flow, which may explain the observed fact that floats move faster than the surrounding liquid. It is acted upon also by a lift force in the lower half depth, and by a force directed downward in the upper half, which may explain the intensity of turbulent vertical mixing. A couple acts only if the particle is asymmetrical, which may explain why such particles rotate little [7].

This zone may be said to consist of two subzones, the uplift zone and the downpush zone. This is borne out by the examination of Boussinesq's *eddy viscosity* ν' defined by:

$$\nu J(h - z) = \rho(\nu + \nu')\bar{u}_z \tag{35}$$

As very approximately (18) holds in zones II and III:

$$\nu'/\nu = (\eta/A)(1 - z/h)\cdot z/h \tag{36}$$

This expression is maximum at $z/h = 0.5$, as is the case with the vertical $\bar{a}_3$ (Fig. 4).

(*d*) *Rough walls and rough flow.* All the following results obtained in the turbulent zones II and III on the basis of Laufer's data for smooth flow, hold also for rough walls and rough flow. The reason is that equation (18) is still valid with the same value of A [23, 27] though with a different value of B. Zone I loses its physical meaning, as it is disrupted by roughnesses, which invade part of zone II.

(*e*) *Relationship to Reynolds' stresses.* In channel flow the mean body forces $\rho\bar{a}_1$ and $\rho\bar{a}_3$ are related to the Reynolds' stresses by the formulas:

$$\left.\begin{aligned} \rho\bar{a}_1 &= -(-\rho\overline{u'w'})_z \\ \rho\bar{a}_3 &= -(-\rho\overline{w'^2})_z \end{aligned}\right\} \tag{37}$$

which are somewhat similar to the formula relating gravity forces to hydrostatic pressure:

$$\rho g = -p_z \tag{38}$$

For curved flow equations (37) are not valid. No direct relationship can then be found between the mean body forces and the Reynolds' stresses.

(*f*) *Energy dissipation.* From the standpoint of mean shear forces $\bar{\tau}$ and energy dissipation rate $\bar{E}$, the flow may be divided into two portions: A lower portion with high $\bar{\tau}$ and $\bar{E}$, which consists of zones I and II; and an upper portion with very small $\bar{\tau}$ and $\bar{E}$, consisting of zone III. This is confirmed by [2, 24, 28]. Landau and Lifshitz call the upper portion "potential flow," as the shearless fluid behaves like an ideal fluid [16], though probably "rotational flow" would be a better name.

(*g*) *Mean trajectories.* The true trajectories of fluid particles in turbulent flow are very complicated and disorderly, yet they are not completely random. As $\overline{u'^2} \neq \overline{v'^2} \neq \overline{w'^2}$ and vary with z, the correlation tensor is neither isotropic nor homogeneous. It has been found that the distribution of velocities is not normal (Gaussian), but skewed (Townsend [26]).

Yet the concept of mean accelerations developed here enables us to define a certain "*mean trajectory*" as the trajectory of a fictitious particle that has acceleration components $\bar{a}_1(z)$, $\bar{a}_2(z)$, $\bar{a}_3(z)$, as defined by (11) and Figs. 3 and 4. These are not true trajectories, for they do not obey the continuity equation (in its Lagrange form), nor do they represent exactly the tracers or streaks formed by injecting continuously radioactive tracers, which spread out as blobs or clouds. Yet they are characteristics of a given turbulent flow and well defined for each starting point (x_0, y_0, z_0) and initial velocity (u_0, v_0, w_0).

Its differential equations are:

$$d^2x/dt^2 = \bar{a}_1(z) = (\overline{u'w'})_z = gJ + \nu\bar{u}_{zz} \tag{39}$$

$$d^2y/dt^2 = \bar{a}_2(z) = 0 \tag{40}$$

$$d^2z/dt^2 = \bar{a}_3(z) = (\overline{w'^2})_z \tag{41}$$

Double integration of (40) gives:

$$y = y_0 + v_0 t \tag{42}$$

This explains rapid transversal mixing in turbulent flow. Equation (41) gives:

$$2d^2z/dt^2 = d[(dz/dt)^2]/dz = (\overline{w'^2})_z$$

and by integration the vertical velocity is obtained:

$$w = dz/dt = w_0 \pm [2\overline{w'^2}(z)]^{1/2} \tag{43}$$

As at the wall $\overline{w'^2} = 0$, and it seems plausible to assume that there $w = 0$, the most probable initial condition is $w_0 = 0$, and

$$w = dz/dt = \pm[2\overline{w'^2}]^{1/2} \tag{44}$$

Integrating again:

$$t = \pm \int_{z=z_0}^{z} [2\overline{w'^2}]^{-1/2}\, dz \tag{45}$$

As the integrand varies little with z in the turbulent zone III, t is practically a linear function of z. This has been confirmed by observation of smoke plumes in air [6].

Introducing (44) in (39):

$$d^2x/dz^2 = \bar{a}_1(z)/2\overline{w'^2}(z) \tag{46}$$

By numerical integration one obtains the "mean trajectories" shown in Fig. 6(*a*) for different initial (or final) conditions:

Trajectory *a*:	$z/h = 0.1$;	$w_0 = -[2\overline{w'^2}(z)]^{1/2}$;	$u_0 = \bar{u}(z_0)$
Trajectory *b*:	0.1;	+	
Trajectory *c*:	0.003;	−	
Trajectory *d*:	0.003;	+	

Fig. 6(*b*) shows the portions of trajectories *c*, *d* at the walls, as computed by Geffen in her MSc thesis [9]. For convenience, *c'*, *d'* represent the neighborhood of the wall ($z/h = 2$). Except at the wall, the lines are almost straight lines, as borne out by observations [6]. It is only in the near vicinity of the wall that the lines curve out strongly. It is noteworthy that trajectory *d* moves against the flow to a distance exceeding $3h$. This implies some turbulent mixing upstream of an injection point.

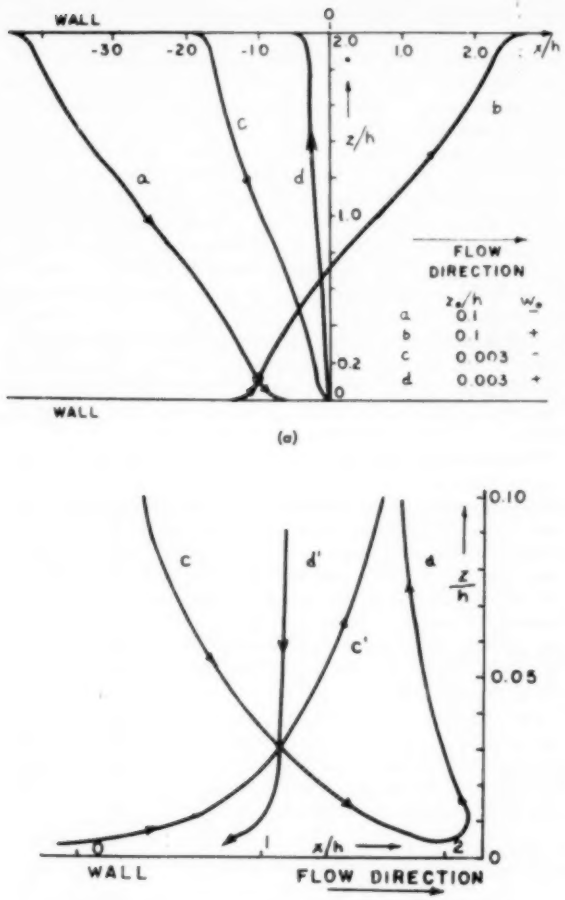

Fig. 6 Turbulent mean trajectories at different initial conditions

The individual trajectories of fluid particles are very complicated, in a way like those of molecules in the kinetic theory of gases. It is in general impossible to follow each trajectory because of the inertia of the recording instruments or their interference with the flow. This renders the individual trajectory an "inobservable" and requires a statistical approach.

The flow parameters are random or stochastic variables. The randomness is not complete due to the guiding action of, and adherence to, the solid boundaries and to the restrictions by continuity and the Navier-Stokes equations of motion.

It is possible to consider a fluid particle at a given point (x_0, y_0, z_0) and instant (t_0) as having a random velocity (u_0, v_0, w_0) with a certain probability distribution. A plausible assumption is:

$$u_0 = \bar{u}(z_0) + k_1 \sqrt{\overline{u'^2(z_0)}} \tag{47}$$

$$v_0 = k_2 \sqrt{\overline{v'^2(z_0)}} \tag{48}$$

$$w_0 = k_3 \sqrt{\overline{w'^2(z_0)}} \tag{49}$$

$$-\sqrt{2} \leqq k_1, k_2, k_3 \leqq +\sqrt{2} \tag{50}$$

(47) means that a fluctuation (positive or negative) is superimposed on the mean axial velocity $\bar{u}$; (48), (49) represent mere fluctuations in the y, z directions. Here k_1, k_2, k_3 are random variables obeying an unknown probability distribution (e.g., a uniform one). (The coefficient $\sqrt{2}$ may be justified considering a harmonic oscillation $U = U_m \sin \text{ft}$, $\overline{U^2} = U_m^2/2$, $U_m = \sqrt{2\overline{U^2}}$.) This means that a fluid particle situated at (t_0, x_0, y_0, z_0) will be situated after a time Δt at $(t_1 = t_0 + \Delta t;\ x_1 = x_0 + u_0\Delta t;\ y_1 = y_0 + v_0\Delta t;\ z_1 = z_0 + w_0\Delta t)$. This end point may be anywhere in a certain portion of space, which introduces an indeterminacy. One might consider the injection of a radioactive tracer and study its consequent distribution throughout the flow.

After the time Δt the fluid is situated at (t_1, x_1, y_1, z_1). As we cannot follow it individually, it loses there its identity, and one has to start again with $\bar{u}_1 = \bar{u}(z_1) + k_1\sqrt{2\overline{u'^2}(z_1)}$, etc. This is some kind of a Markoff process (see, e.g., A. Blanc-Lapierre and R. Fortet, "Théorie des Fonctions Aléatoires," Masson et Cie, Paris, France, 1953).

The mean trajectories introduced in our paper are not true trajectories, but an idealization: These are the trajectories of particles of similar mass if they could maintain their individuality throughout their life. As they meander in an orderly fashion they may serve to describe the turbulent channel flow.

(*h*) *Circular pipe flow.* Qualitatively similar results are obtained in circular pipes.

Briefly we might say that any turbulent channel or pipe flow comprises two distinct types of flow:

Dissipative zones near the wall with high shear values and dissipation rates. The mean accelerations and forces acting on fluid particles vanish in the laminar sublayer, but increase steeply, reaching 15*g* and more in the so-called "transition" layer, and are directed upstream and somewhat toward the axis. Mixing and sediment transportation by rolling and saltation are very strong.

A *nondissipative* zone throughout most of the turbulent flow, with very small shears and dissipation rates. It behaves almost like an ideal fluid in rotational flow. The mean accelerations and forces vary gradually, their axial components directed downstream and equal to those of a body falling along a slope equal to the energy gradient S. The normal components are directed toward the axis near the wall and toward the walls in most of the turbulent core.

References

1 Bagnold, "The Physics of Blown Sands and Desert Dunes," Methuen, London, England, 1941.

2 B. A. Bakhmeteff and W. Allen, "The Mechanism of Energy Loss in Fluid Friction," *Trans. ASCE*, vol. 3, 1946, pp. 1043–1102.

3 G. K. Batchelor, "The Theory of Homogeneous Turbulence," Cambridge University Press, Cambridge, England, 1953.

4 J. Boussinesq, "Essai sur la Théorie des Eaux Courantes," *Mémoires présentés par l'Academie des Sciences, Paris*, vol. 23, no. 1, 1877, pp. 1–680.

5 J. Boussinesq, "Théorie de l'Ecoulement Tourbillonnant," *Mémoires présentés par Divers Savants*, vol. 23, 1877.

6 B. Davidson, oral communication, 1959.

7 H. A. Einstein, oral communication, 1958.

8 A. A. Friedmann and L. W. Keller, "Differentialgleichungen für die turbulente Bewegung einer kompressiblen Flüssigkeit," Proceedings, First International Congress on Applied Mechanics, Delft, The Netherlands, 1924.

9 N. Geffen, "Kinematic Description of Turbulent Flow in a Two-Dimensional Channel" (in Hebrew), MSc thesis, Israel Institute of Technology, Haifa, Israel, 1958.

10 W. Heisenberg, "Zur statistischen Theorie der Turbulenz," *Zeitschrift für Physik*, vol. 124, 1938, p. 628.

11 S. Irmay, "On the Mean Acceleration of Particles in Turbulent Incompressible Flow," mimeographed lecture, Israel Institute of Technology, Haifa, Israel, 1955.

12 S. Irmay, "On Three Layers in Turbulent Flow," abstract, *Bulletin, Research Council of Israel*, vol. 6C, no. 1, 1957, p. 71.

13 S. Irmay, "On the Mean Acceleration of Fluid Particles in Turbulent Flow" (Second Note), abstract, *Bulletin, Research Council of Israel*, vol. 6C, no. 1, 1957, p. 90.

14 Th. von Karman, "The Fundamentals of the Statistical Theory of Turbulence," *Journal of Aeronautical Sciences*, vol. 4, 1937, pp. 134–138.
15 A. N. Kolmogoroff, "The Local Structure of Turbulence in an Incompressible Viscous Fluid at Very Large Reynolds Numbers" (in Russian), *Proceedings, Academy of Sciences, USSR*, vol. 30, 1941, no. 4, p. 299.
16 L. D. Landau and E. M. Lifshitz, "Mechanics of Continuous Media" (in Russian), Gossudarstvyennoye Izdatelstvo Tekhnicheskoy-Teoreticheskoy Literaturi, Moscow, USSR, 1953.
17 J. Laufer, "Investigation of Turbulent Flow in a Two-Dimensional Channel," NACA Report 1053, 1951.
18 J. Laufer, "The Structure of Turbulence in Fully Developed Pipe Flow," NACA Report 1174, 1954.
19 H. E. Lettau and B. Davidson, "Exploring the Atmosphere's First Mile," 2 volumes, Pergamon Press, 1957.
20 A. M. Obukhov, "Statistical Description of Continuous Fields" (in Russian), *Proc. Geophys. Inst. Acad. Sci. USSR*, no. 24, vol. 151, 1954, p. 3.
21 L. Prandtl, "Über Flüssigkeitsbewegung bei sehr kleiner Reibung," Verhandlungen, Third International Mathematical Congress, Heidelberg, Germany, 1904.
22 O. Reynolds, "On the Dynamical Theory of Incompressible Viscous Fluids and the Determination of the Criterion," *Philosophical Transactions of the Royal Society*, vol. 186, series A, 1895, p. 123.
23 H. Schlichting, "Grenzschicht-Theorie," Braun, Karlsruhe, Germany, 1931.
24 G. B. Schubauer, "Turbulent Process as Observed in Boundary Layer and Pipe," *Journal of Applied Physics*, vol. 25, no. 2, 1954, pp. 188–196.
25 G. I. Taylor, "The Statistical Theory of Turbulence," *Proceedings, Royal Society*, vol. 151, series A, 1935, p. 421.
26 A. A. Townsend, "The Structure of Turbulent Shear Flow," Cambridge University Press, Cambridge, England, 1956.
27 V. Velikanov, "Dynamics of Water Courses" (in Russian), Gidrometeorologicheskoye Izdatelstvo, Leningrad, USSR, 1949.
28 H. Reichardt, "Die Energieversorgung der Wandturbulenz," *Zeitschrift für Angewandte Mathematik und Mechanik*, vol. 33, no. 10/11, 1953, pp. 336–345.

DISCUSSION

J. W. Delleur[3]

The author is to be congratulated for a lucid analysis of turbulent flow in open channels. The writer wishes to comment on an attempt to observe the turbulent mean trajectories which led to some conclusions on secondary flows in open channels.

The general layout of the laboratory equipment used is shown in Fig. 7. The horizontal smooth brass open channel is 15 ft $7^1/_2$ in. long and $13^{11}/_{16}$ in. wide. It is part of a closed circuit formed by the reservoir, the pump, the constant head tank, the entrance section which precedes the channel, the exit channel with its measuring weir, and the volumetric tank. The entrance section included a metal deflecting plate, a $3^1/_2$-in. gravel baffle, and two 15-mesh copper wire screens. The transition between the entrance section and the channel consisted of quarter ellipses with semiaxes of 12 and 7 in. for the walls and 15 and 9 in. for the bottom. A camera mounted on a carriage moving along the channel made it possible to take movies of the particles in the flow. A wire grid suspended from the carriage and kept as close as possible to the free surface provided a traveling frame of reference. This made it possible to measure from the photographs the displacement of the particles with respect to the traveling frame of reference between consecutive film exposures. The position of the frame of reference could be measured from stationary marks located 6 inches apart along the flume wall.

The turbulent mean trajectories were investigated by means of marked particles. Three types of particles were used: paper, benzoic acid tablets, and a mixture of carbon tetrachloride and paraffin oil. Small pieces of paper of triangular, square, and semicircular shapes floated on the free surface and were used to show the flow pattern at the surface. Small benzoic acid tablets were used to visualize the flow pattern close to the bottom. These tablets are white and show well on the photographs; their specific gravity is slightly above one so that they remain close to the bottom without dragging along it. They are about half the size of an aspirin tablet. Both the paper particles or the benzoic acid tablets were dropped simultaneously into the fluid from a ruler placed across the flume at the upstream end. A colored mixture of paraffin oil and carbon tetrachloride with specific gravity of 1.0 provided a means for injecting immissible drops. They were introduced in the fluid by means of a hypodermic pitot tube. They were intended to visualize the flow pattern at intermediate depths, but it was found that they were extremely difficult to use because of the large change of density with very small change in temperature.

The particles were introduced at the upstream end of the channel and their paths were photographed with the movie camera moving along the channel at a speed approximately equal to the average flow velocity. A total of 28 tests were run as shown in Table 1. A typical photograph is shown in Fig. 8.

The film strips were then observed in a microfilm viewer, and the positions of a few particles were observed every five or ten frames depending on the camera speed. The positions were then plotted to obtain the trajectories shown in Fig. 9, which correspond to flow visualizations at the free surface and at the bottom, respectively. The general flow pattern near the bottom of the channel is seen to be from the center line outward and toward the center line near the free surface. These currents are probably accompanied by a downward flow at the center and an upward draft along the sides, forming a secondary flow consisting of two spirals.

For the first 16 test runs the depth to width ratios were approximately $^1/_{12}$ and $^1/_6$, and the flow may be assumed to be approximately two-dimensional. This fact will be used to simplify the general Reynolds equations of motion. The Reynolds equation in the transversal direction is:

$$v_t + (uv)_x + (v^2)_y + (vw)_z = -P_y - \nu\nabla^2 v - \left(\overline{u'v'}\right)_x - \left(\overline{v'v'}\right)_y - \left(\overline{v'w'}\right)_z \quad (51)$$

Table 1 Traced particles experiments

Run no.	Particle	Depth of flow at entrance, ft	Camera frames per sec
1	Paper	0.218	24
2	...	0.218	24
3	Oil	0.218	24
4	Oil	0.218	24
5	Benzoic	0.218	24
6	Lycopodium	0.218	24
7	Aluminum turnings	0.218	24
8	Paper	0.118	24
9	Benzoic	0.118	24
10	Oil	0.118	24
11	Paper	0.218	24
12	Benzoic	0.218	24
13	Oil	0.218	24
14	Paper	0.218	64
15	Benzoic	0.218	64
16	Oil	0.218	64
17	Paper	0.399	24
18	Benzoic	0.399	24
19	Oil	0.399	64
20	Paper	0.399	64
21	Benzoic	0.399	64
22	Aluminum turnings	0.399	24
23	Paper	0.439	24
24	Benzoic	0.439	24
25	Oil	0.439	24
26	Benzoic	0.439	64
27	Paper	0.439	64
28	Oil	0.439	24

[3] Associate Professor of Hydraulic Engineering, School of Civil Engineering, Purdue University, Lafayette, Ind. Assoc. Mem. ASME.

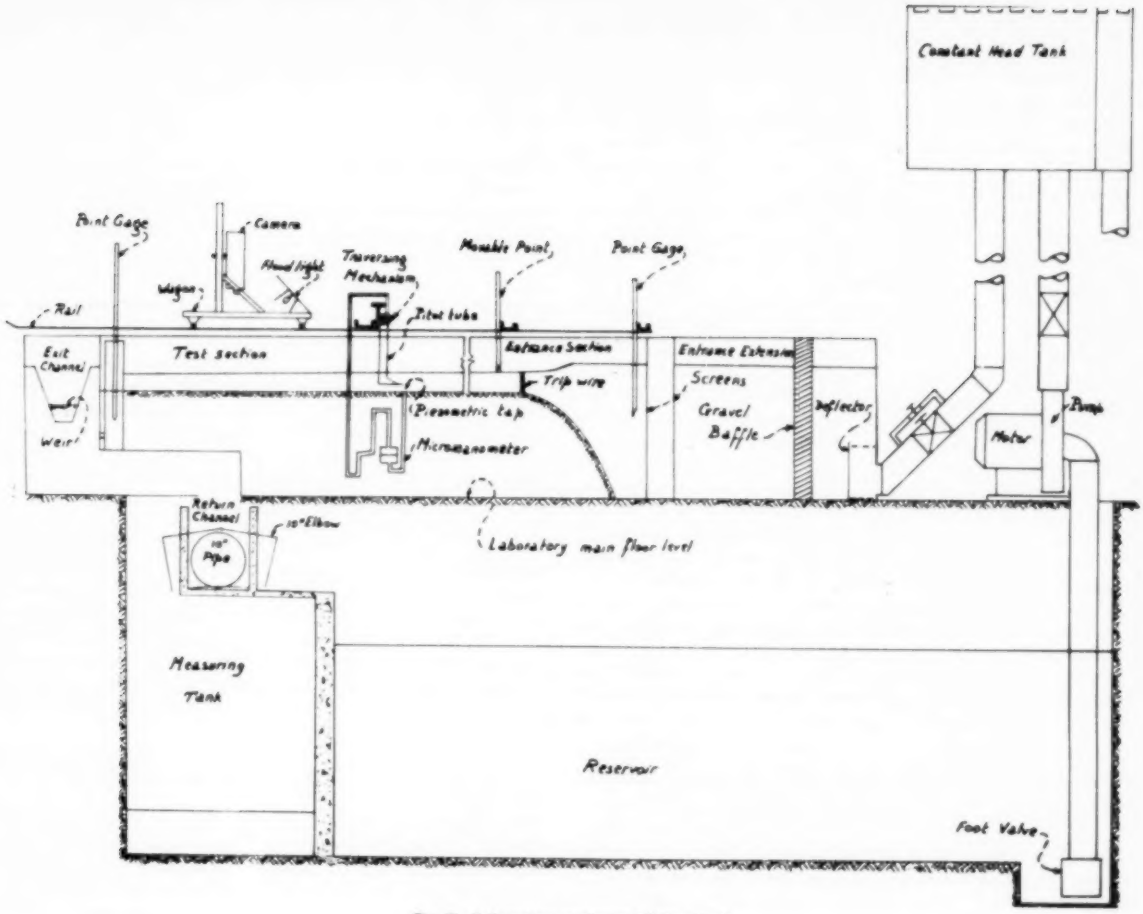

Fig. 7 Laboratory equipment (elevation)

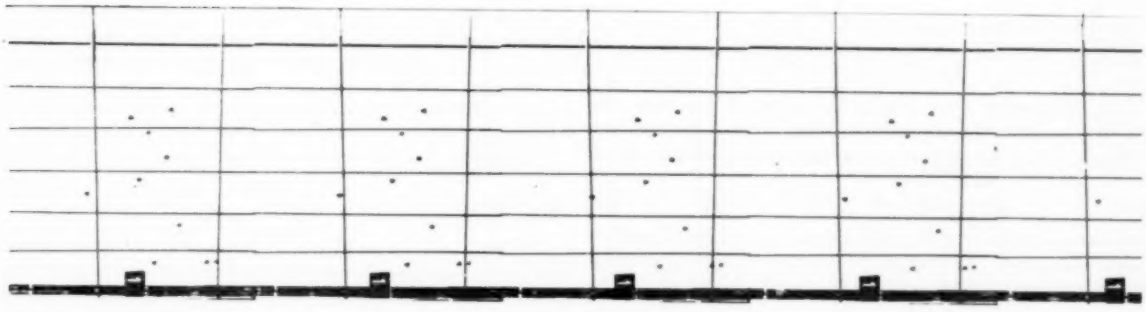

Fig. 8

A number of terms may be dropped by means of the following simplifying assumption for the mean flow: (*a*) The flow is steady; (*b*) the flow is nearly two-dimensional so that the convective acceleration in the y-direction is negligible; (*c*) the laminar shear stresses are negligible compared to the corresponding turbulent stresses in the y-direction. With these assumptions, equation (51) reduces to:

$$0 = \frac{1}{\rho}\left[\left(-\rho\,\overline{u'v'}\right)_x - \left(p + \overline{v'v'}\right)_y - \left(\rho\overline{v'w'}\right)_z\right] \qquad (52)$$

Consider next the turbulent terms. Laufer's experiments [17] show that in a two-dimensional air duct $\overline{u'u'}$, $\overline{u'v'}$, $\overline{u'w'}$, etc., are of the same order of magnitude. Since the flow is nearly two-dimensional, the shear stresses in the y-direction should be

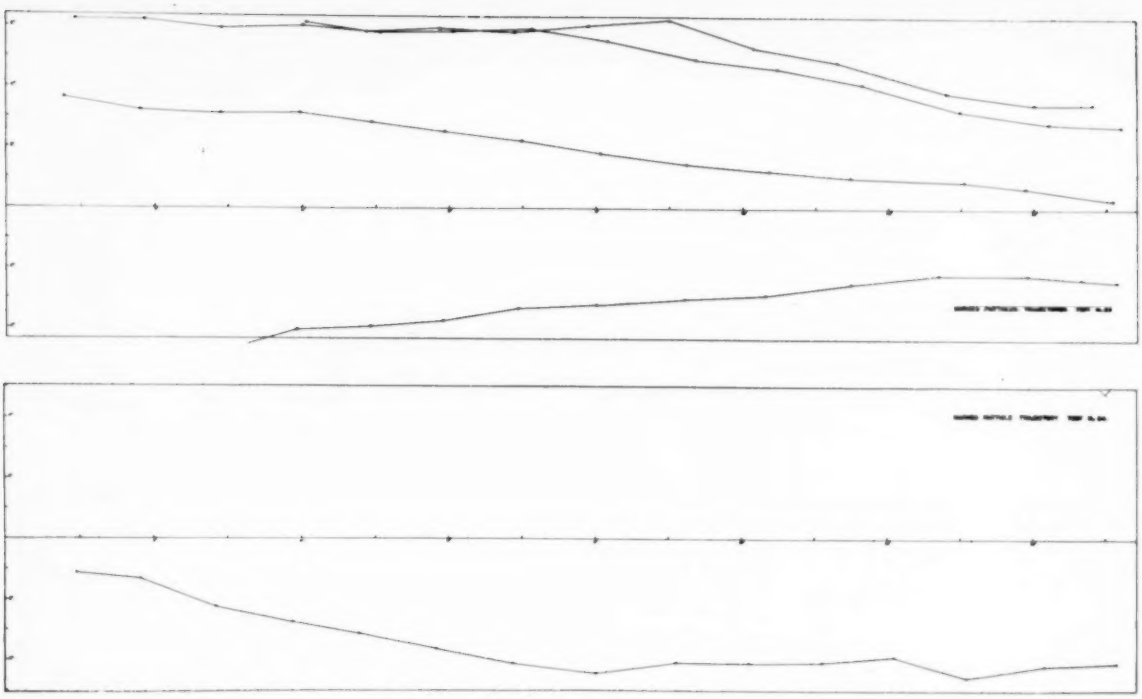

Fig. 9

negligible compared to those in the x and z-directions. However, by using Prandtl's [21] argument that the derivatives with respect to x and y are negligible compared to the derivatives with respect to z, it follows that taking a derivative with respect to z increases the order of magnitude of the term, and hence the term $\rho\overline{(v'w')}_z$ should be retained. With these assumptions (52) reduces to:

$$\overline{(v'v')}_y + \overline{(v'w')}_z = -\frac{1}{\rho} p_y \tag{53}$$

which may be integrated in the y-direction to give

$$\int_0^{b/2} \overline{(v'w')}_z \, dy = \overline{v'v'}, \tag{54}$$

since the pressure is constant in the horizontal direction. Referring to Laufer's experiments it may be seen that $\overline{(v'v')}^{1/2}/\sqrt{\tau_0/\rho} = 1.75$ throughout most of the boundary layer. Hence

$$\int_0^{b/2} \overline{(v'w')}_z \, dy = 3.06\tau_0 = 0(\tau_0) \tag{55}$$

In other words, the turbulent shear stress in the y-direction is not everywhere zero. Townsend [26] (p. 259) arrived at a similar conclusion for a finite plate in a wind tunnel. In that case

$$\int_0^{\infty} \overline{(v'w')}_z \, dy = 2.2\tau_0$$

If it is assumed, with Townsend, that this shear stress varies linearly from 0 at the center line to a maximum at the edge of the bottom, this stress gradient would produce a secondary flow in the boundary layer from the center line outward as it has been shown experimentally to exist. This flow would require a compensating flow from outside the boundary layer along the center line. This finally results in a double spiral, with flow downward at the center line, upward along the side, and from the side to the center line.

This theoretical confirmation of the visual observations led to study of the over-all spiral flow pattern.[4] It was assumed that three-dimensional flow consisted of two spirals with constant angular velocity, and the tangential velocity was taken as ω. This situation was analyzed by the Reynolds equations in cylindrical co-ordinates. By means of simplifying assumptions similar to those used in the foregoing, and a more sophisticated description of the turbulent field it was shown again that the helical motion and the turbulence of the flow were interrelated.

Experiments prove the existence of secondary motion in straight rectangular open channels and exhibit the turbulent mean trajectories. The analysis shows that the secondary motion and the turbulent stresses are related and hence turbulence is associated with the mechanism of the secondary flow.

S. J. Kline[5]

Professor Irmay's calculations of the longitudinal accelerations, a_1, show very clearly the large magnitude of the so-called Reynolds' stresses. These effects arise from the fact that on the average higher speed particles are being decelerated near the wall, and slow speed particles accelerated in the outer flow.

The strong deceleration appears to occur primarily in what is usually called the buffer layer in the English literature. This is

[4] J. W. Delleur and D. S. McManus, "Secondary Flow in Straight Open Channels," Proceedings Sixth Midwestern Conference on Fluid Mechanics, University of Texas, September, 1959.

[5] Associate Professor, Mechanical Engineering, Stanford University, Calif. Mem. ASME.

in definite agreement with the model proposed by the writer and Mr. P. W. Runstadler before the Society in 1958.[6]

Unfortunately, John Laufer's results which form the empirical basis for Professor Irmay's calculations do not extend close enough to the wall to illuminate what happens in the so-called laminar sublayer which is the region of greatest interest in connection with the unstable model which gives rise to the fluctuations. Professor Irmay remarks that the accelerations become vanishingly small in this region, but in view of the visual model studies this is questionable, and the writer would be very much interested in any justification which Professor Irmay can give for this remark.

A. A. Townsend[7]

I have read Professor Irmay's paper with interest and I agree with him that the consideration of mean particle accelerations is a novel and informative approach to the consideration of turbulent flow in pipes and channels. In particular, it seems to have possibilities for the description of transport of sediment and suspended matter. My only specific comment refers to the suggestion that the existence of positive accelerations in the fully turbulent part of the flow (Zone III) is sufficient to explain the observation that floating material moves faster than the surrounding liquid. In a paper shortly to be published in the *Journal of Fluid Mechanics*, T. H. Ellison shows that the mean velocity at the surface of an open channel is noticeably greater than the "surface velocity" found by extrapolating velocity measurements in the body of the liquid. The effect depends on the restriction of vertical turbulent movements by the free surface, equivalent to a decrease of the eddy viscosity to zero as the surface is approached.

Author's Closure

1 In answer to Professor Kline, John Laufer's results are insufficient for the exact computation of the accelerations near the wall. Yet they show an unmistakable decreasing trend toward the walls. On the other hand, theoretical considerations lead to the conclusion that the accelerations vanish at the wall, as the velocity fluctuations u', v', w' vanish there:

$$\bar{a}_1 = \overline{(u'w')_z} = \overline{u'w'}_z + \overline{w'u'}_z = 0 \quad \text{at} \quad z = 0$$

[In the text the subscript z, which stands for partial derivation, has been erroneously replaced by 2 (see note 2, referring to the text before formula 26).]
Also:

$$\bar{a}_3 = \overline{(w'^2)_z} = \overline{2w'w'_z} = 0 \quad \text{at} \quad z = 0$$

If u', v', w' may be expanded into a Taylor series in the neighborhood of the wall, continuity shows that:

$$u' = Az + \ldots$$
$$v' = Bz + \ldots$$
$$w' = Cz^2 + \ldots$$

so that

$$\bar{a}_1 = \overline{(u'w')_z} = Dz^2 + \ldots$$

$$\bar{a}_3 = \overline{(w'^2)_z} = Ez^3 + \ldots$$

A, B, C, D, E are functions of x, y.

The acceleration components are therefore vanishingly small in the vicinity of the wall.

2 In the transition from the sublaminar layer to the turbulent zone, the acceleration is very large. This indicates high curvature of the individual trajectories passing there. In spite of the very high value of the negative longitudinal component it is not a deceleration, for the individual trajectories are spatially twisted curves, and not straight lines. The best interpretation is to consider them as average resultant forces acting on fluid particles passing at a given point.

3 Turbulent flow is sometimes approximated by a potential flow of a fluid core gliding upon a viscous skin at the walls. Yet the flow of the core is essentially rotational, as curl $\bar{\mathbf{V}}$ vanishes only on the channel axis. On the other hand, inspection of Fig. 3(*a*) shows that for $z > 0.1h$ we have curl $\bar{\mathbf{a}} = 0$. Or ideal fluids in a conservative field obey the equation curl $\mathbf{a} = 0$. One may therefore generalize and conclude that turbulent flow behaves rather like a rotational ideal fluid which glides upon a viscous skin, the rotation being constantly supplied by this skin. The skin has large values of shear and rate of dissipation. Viscosity effects seem thus to extend far outside the laminar sublayer.

4 It is quite remarkable that similar results are obtained for any flow with rapid velocity fluctuations, even if these fluctuations are regularly spaced pulsations round the spatially-averaged motion. This is a kinematic flow property, independent of compressibility, viscosity, or electromagnetic effects, and even of the particular rheological equation obeyed by the fluid.

5 In answer to Dr. A. A. Townsend's discussion, the author has not asserted that the existence of positive accelerations in the fully turbulent part of flow (Zone III) is *sufficient* to explain the observation that floating material moves faster than the surrounding material; but only that it "*may* explain" it. He agrees with Professor Townsend that it is quite possible that another cause may give a better interpretation and is eager to read Mr. T. H. Ellison's paper on the subject.

6 The experiments described by Professor Delleur here and in the Delleur-McManus papers are very interesting. They refer to the formation of a double spiral, a fact observed by many authors in straight channels both in the laboratory and in rivers (e.g., M. A. Velikanov, "Dynamics of Water Courses," in Russian, *Gidrometeor. Izdat.*, Leningrad, 1949, p. 385, who reproduces

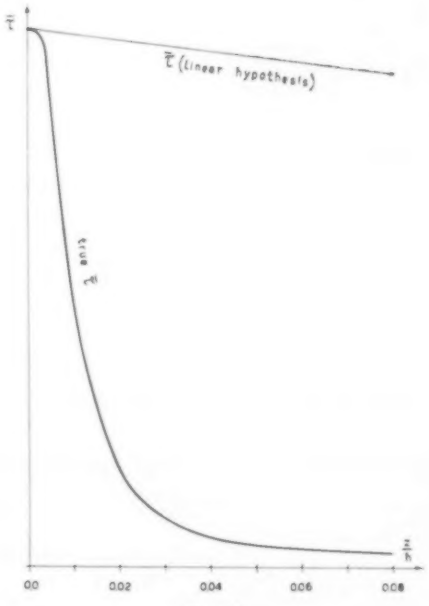

Fig. 10

[6] S. J. Kline and P. W. Runstadler, "Some Preliminary Results of Visual Studies of the Wall Layers of the Turbulent Boundary Layer," *Journal of Applied Mechanics*, vol. 26, TRANS. ASME, Series E, vol. 81, 1959, p. 166.

[7] Emmanuel College, Cambridge, England.

data published by A. I. Lossiyevski in 1934). There is no doubt that the spirals are somehow related to turbulence, though A. Einstein (*Construction and Industry*, Jan./Feb., 1927, Tel-Aviv) believes that the Coriolis acceleration due to the rotation of the earth is the main cause of the spiralling motion. The author's mean trajectories cannot be observed, as they are mathematical fictions, though they are characteristic for a given turbulent flow.

7 The author would be interested to know how equation (54) has been reached, as h (of the author's paper) represents half of the channel width in the direction of the Oz-axis, whereas the integration in (54) is with respect to y.

8 The author would like to stress another important conclusion, though mentioned in section 2 and 5(f) of the original paper. The diagram of the mean shear stress $\bar{\tau}$ is not a straight line as is usually believed on the basis of the erroneous assumption that there are no mean accelerations. The true mean shear is given by (7) which reduces in the case of two-dimensional channel flow to $\bar{\tau} = \mu\bar{u}_z$. The diagram of $\bar{\tau}$ versus z is shown in Fig. 10. Except for the near vicinity of the wall, the shear is very small: It is 10 per cent of its maximum value at the wall at $z/h = 0.027$; 5 per cent at $z/h = 0.045$; 2 per cent at $z/h = 0.10$; 1 per cent at $z/h = 0.25$, yet it is surprising how far from the wall the effect of viscosity extends.

F. DALLENBACH[1]
Assistant to the Chief Engineer,
AiResearch Manufacturing Company
of Arizona, Phoenix, Ariz.

N. VAN LE
Research Scientist, The
Garrett Corporation,
Los Angeles, Calif.

Supersonic Diffuser for Radial and Mixed Flow Compressors

Presentation is made for the design concepts of a novel diffuser that handles supersonic flow at the exit of radial and mixed flow compressors. The guide vanes incorporating a V shape at the inlet are shown to offer potentialities of a shock free deceleration of the supersonic flow. Optimum diffusion of a high-speed flow is considered. The results are applied to the design of two sets of guide vanes for the diffusing system. The experimental evaluation of these guide vanes confirms the original conceptual thinking, with a highest diffuser performance of 0.792 at an inlet Mach number of 1.3. Effect of the blade loading and of the subsonic inlet Mach number on the guide vanes are presented. Actual performance of the diffuser in a compressor of a gas turbine is discussed.

Introduction

In high-speed radial and mixed flow compressors, the flow leaving the impeller reaches supersonic values. The designer is confronted with the problem of recovering, with the maximum efficiency, the kinetic energy of this high-speed flow through a diffusing system.

Present approach to handle diffuser with a supersonic inlet flow consists in using a vaneless space usually with parallel walls, to allow the supersonic flow to decelerate to a subsonic state [1].[2] Further diffusion is achieved in a set of guide vanes; the inlet Mach number of these vanes is one of the main parameters of performance. Typical of this approach is found in Reference [2] which presents an inlet Mach number of 1.15 for the diffusing system; the guide vanes operate at inlet Mach number of 0.86.

As the inlet Mach number becomes higher with high-speed compressors or with compressor operating in high molecular weight gases, this conventional diffusing system of vaneless space and guide vanes presents deficiencies in performance as well as in physical characteristics. The long vaneless space required for the shock free diffusion of a high inlet Mach number has been found to be the source of back flow into the impeller [1]. The nonuniform velocity profile at the impeller exit develops in the vaneless space into a full three-dimensional flow pattern, creating a variation in incidence along the leading edges of the guide vanes.

A solution to this problem of supersonic flow diffusion is to bypass it, using a rotating diffuser where the relative flow is subsonic. Other suggestions have been to design configurations that give diffusion through a normal shock located in the diffuser channel. Besides the problem of starting the flow, the possibility of boundary-layer shock wave interaction may introduce separation downstream in the diffuser channel.

The object of this paper is to present an approach to the solution of this problem, the design concepts and the results of an experimental set of diffusers on a stationary test rig as well as on a compressor.

Design Concepts

Qualitative Theory of a Shock-Free Deceleration of a Supersonic Flow. The underlying idea of a shock-free deceleration of a radially symmetrical supersonic flow field consists in introducing a set of guide vanes with the leading edges slanted to accommodate a V shape as shown on Fig. 1. The flow is assumed to be uniform and supersonic along the inlet. On the cone of symmetry OG, the flow can be considered to be of a two-dimensional nature, and deceleration takes place as in a compressible free vortex. No

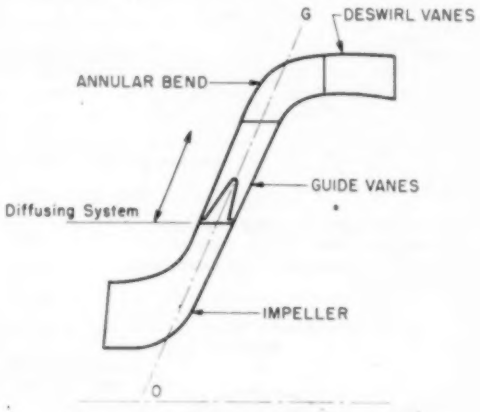

Fig. 1 The components of a diffusing system

[1] Formerly, Chief of Aerodynamics, AiResearch Manufacturing Company of Arizona.

[2] Numbers in brackets designate References at end of paper.

Contributed by the Hydraulic Division and presented at the Gas Turbine Power & Hydraulic Conference, Houston, Texas, March 6–9, 1960, of The American Society of Mechanical Engineers.

Note: Statements and opinions advanced in papers are to be understood as individual expressions of their authors and not those of the Society. Manuscript received at ASME Headquarters, October 8, 1959. Paper No. 60—Hyd-11.

Nomenclature

V, C = velocity
r = radius
θ = momentum thickness
δ^* = displacement thickness
H = shape parameter = δ^*/θ
m = meridional distance
Z = blade number
t = blade tangential thickness
D = diameter
p = static pressure
η_D = diffuser efficiency

Subscripts
e = exit
i = inlet
u = tangential
s = suction
p = pressure

shock occurs so long as the radial component of the Mach number is less than 1.0 [1]. The Mach lines corresponding to such a flow encompass the upstream and downstream flow pattern, the limiting line being imaginary circles (Fig. 2). When the radial component of the Mach number is supersonic, the extended Mach lines cover only the upstream region of the flow. The physical interpretation of these considerations is that, for a subsonic radial Mach number component, any disturbance downstream can be transmitted upstream, allowing the flow to adjust itself to avoid any discontinuity. Such a situation is not possible in Fig. 2(*b*); a circular shock occurs by reason of symmetry. Thus, when the supersonic flow on surface OG (Fig. 3) has a subsonic radial Mach number component, disturbance from any point downstream is transmitted upstream, particularly from point 3 where deceleration has been carried far enough so that the flow is subsonic. The problems involved in this paper deal with the supersonic flow having a subsonic radial component.

Consider surface b-b, Fig. 3(*a*), which does not present any feature of symmetry as does surface OG. The supersonic flow meets the leading edge of the guide vanes at point S. The extended Mach cone has traces in the meridional plane as shown. Downstream of point S, at a subsonic flow such as point 4, any disturbance is propagated upstream to point 1 via points 3 and 2. A shock free region at S is thought to be possible because of this very adjustment of the flow.

If the Mach number at S is relatively high, such that the traces of the extended Mach cone are shown in Fig. 3(*b*) propagation of any downstream subsonic disturbance such as point 4 to any upstream point such as point 1 is not possible (Fig. 3*b*).

It appears that, to avoid any possibility of shock formation on the leading edges, these edges are to be slanted from the farthest upstream point to be within all the Mach cones. Still, the danger of a head shock is imminent at the farthest upstream point of the wedge. Due to the existence of the neighboring free vortex field [plane OG, Fig. 3(*a*)] it is thought that the intensity of these shocks may be attenuated.

Thus, in using guide vanes to diffuse the supersonic flow with a subsonic radial component, the conceptual design is

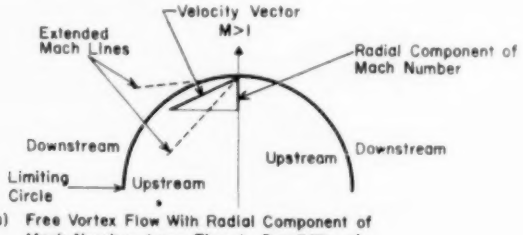

(a) Free Vortex Flow With Radial Component of Mach Number Less Than I. Possibility of Disturbance Propagation From Downstream To Upstream

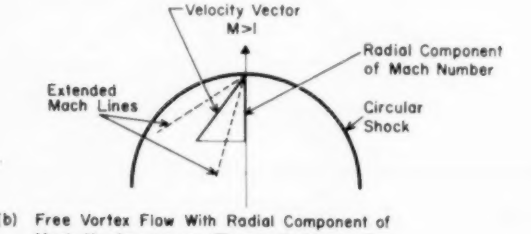

(b) Free Vortex Flow With Radial Component of Mach Number Larger Than I. No Means For Disturbance To Propagate From Downstream To Upstream Producing Discontinuity or Circular Shock.

Fig. 2 Diffusion in a supersonic free vortex

(*a*) To provide a liberal region of free vortex diffusion to carry downstream subsonic disturbance to any point in the supersonic flow region.

(*b*) To associate with this flow region guide vanes slanted as previously discussed.

On this basis a V-shape is introduced in the design of the guide vanes. Obviously, this design concept cannot stand in the case of flow with supersonic radial component, for upstream propagation of subsonic disturbance is not possible.

Optimum Diffusion of a High-Speed Flow. The problem of efficiently recovering the kinetic energy of a high speed flow is often made difficult because of the requirements at the exit of the diffusion systems. In gas turbine combustors for instance, a low Mach number is desirable; swirls are not tolerated. Since the inlet Mach number is inherently high in high-speed flow compressors, and since the exit Mach number is fixed at the desired level, it is common that these diffusing systems are required to handle a considerable diffusion ratio between inlet and exit. The problem arises as to the existence of any optimum diffusion ratio handled in any set of guide vanes conventionally designed, to yield the maximum recovery of the kinetic energy.

Since the flow in the channel of the diffuser guide vane is often accompanied by detrimental crossflow [3], it is thought that the ideal performance of such a channel would be that of conical diffuser which presents a symmetrical flow pattern. On this basis, an upper limit to the diffusion ratio would be obtained if study is to be made using conical diffusers. The optimum value would be the one at which separation takes place. The problem of optimum diffusion ratio in the channel of the guide vane diffuser is transferred to that of the velocity ratio at which separation is imminent in a conical diffuser.

To arrive at a solution, growth of the compressible turbulent boundary layer in these diffusers is calculated with a method specially developed for the purpose [4]. The maximum deceleration obtained from various boundary layer characteristics at the inlet to these conical diffusers are shown on Fig. 4. For reasonably good velocity profile entering the guide vanes, an estimate places the momentum thickness $(\theta/D)_i$ and the shape parameter H_i in the following range:

$$(\theta/D)_i = 0.01 - 0.08$$
$$H_i = 1.33 - 1.40$$

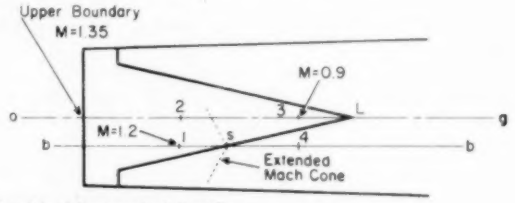

(a) Possible Adjustment of the Flow Between Points 1 and 4 No Discontinuity or Shock

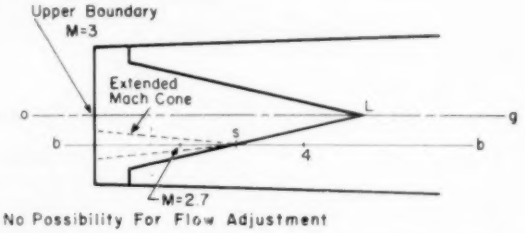

(b) No Possibility For Flow Adjustment

Fig. 3 A shock-free deceleration of guide vanes operating in a supersonic flow

Fig. 4, then, shows that the optimum value of the velocity ratio is of the order of 2:1. With unfavorable velocity profiles generally associated with low performance impellers (larger values of $(\theta/D)_i$ and H_i) it is hopeless to achieve any decent performance in diffusers designed on a conventional basis.

Design of the Supersonic Diffusing System. The concepts presented previously on the shock free deceleration of a supersonic flow using guide vanes with slanted leading edges and the limiting deceleration of the flow entering a set of guide vanes are now applied to the design of the supersonic diffusing system of the compressor of an experimental gas turbine.

Uniform conditions at the inlet to the diffuser are:

Mach number $\mathbf{M} = 1.132$, Flow angle $\beta = 64.7$ deg

A maximum performance is desired.

Preliminary investigations, made on the basis of one-dimensional calculations, led to the following components (Fig. 1):

1 A semivaneless space incorporating the extended guide vanes with a V-shape.

2 A set of guide vanes. The incident flow on the surface of symmetry (Point L of Fig. 3) is maintained at a subsonic level. The diffusion of the flow in the guide vanes (V_{inlet}/V_{exit}) is of the order of 1.85:1, with a resulting exit Mach number of 0.47.

3 An annular elbow, presenting a transition between the previous set of guide vanes and the next stage of diffusion. This bend design is adopted to decrease the over-all diameter of the compressor.

4 A set of "deswirl vanes" which represent an additional diffusing stage, bringing the flow to a lower Mach number level and reducing all the exit swirls.

Based on empirical loss data, the diffuser efficiency η_D is estimated to be 72.1 per cent, where η_D is defined as:

$$\eta_D = \frac{\left(\frac{p_e}{p_i}\right)^{\frac{k-1}{k}} - 1}{\frac{k-1}{2}\,\mathbf{M}_i^2} \qquad (1)$$

Calculation of the semivaneless space was made on the basis of a radially symmetrical flow using the numerical integration of Reference [5], which takes into account the viscous effect, the divergence of the meridional shape, the clogging of the flow area due to the blade thickness, and nonuniformity in velocity profiles. A major assumption in this application is that the contribution of the vanes to change the flow momentum is small. In other words, there is a small loading on these parts of the blades. The results (Fig. 5) show the variation of the flow angle along the radius, on the mean surface OG. For comparative purposes, the flow angle of a pure two-dimensional free vortex is also presented. The mean flow, located on the surface of symmetry of the diffusing system, enters the guide vanes at a selected Mach number of 0.917.

Design of the guide vanes was based on a quasi-three-dimensional calculation. For simplicity in manufacturing, constant thickness blades are used. In addition, the blades are to be normal to the surface of symmetry defined by the generatrix OG (Fig. 1). Thus, the blade is completely defined by the blade angle β on the surface of symmetry OG. For practical reasons, aiming at the intuition of the designer, the design problem is transformed into an analysis one.

A meridional shape of the guide vanes is selected. Manufacturing considerations generally dictate this choice. From this shape and the experimental values accounting for nonuniformity in velocity profiles and viscous effect, the one-dimensional velocity along the diffuser passage can be determined for a series of blade angle β distribution. This velocity distribution is then assumed to be that of the mean of the channel in a two-dimensional cascade located on the surface of symmetry OG. Channel theory (Appendix) is then applied to determine the blade loading for this cascade. The distribution that gives a satisfactory blade loading is selected.

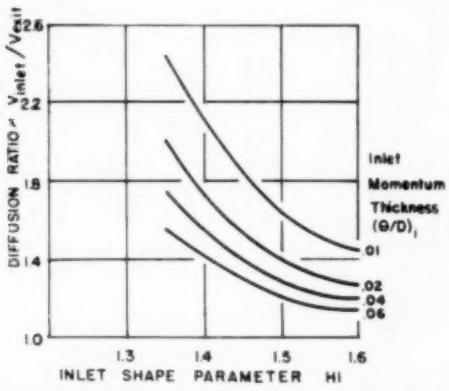

Fig. 4 Influence of the inlet boundary-layer conditions on optimum diffusion ratio

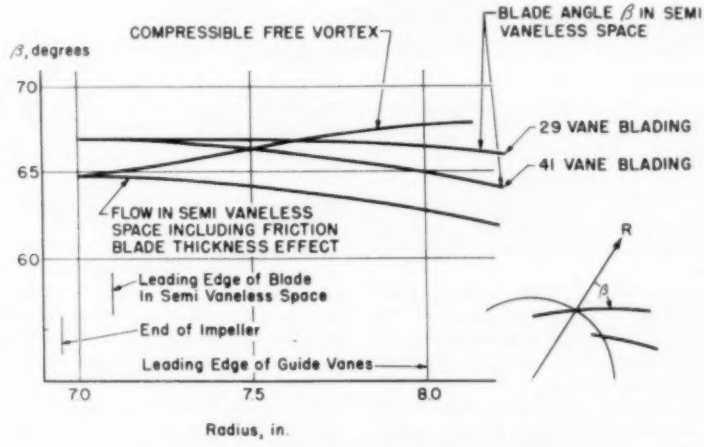

Fig. 5 Flow and blade angle in semivaneless space

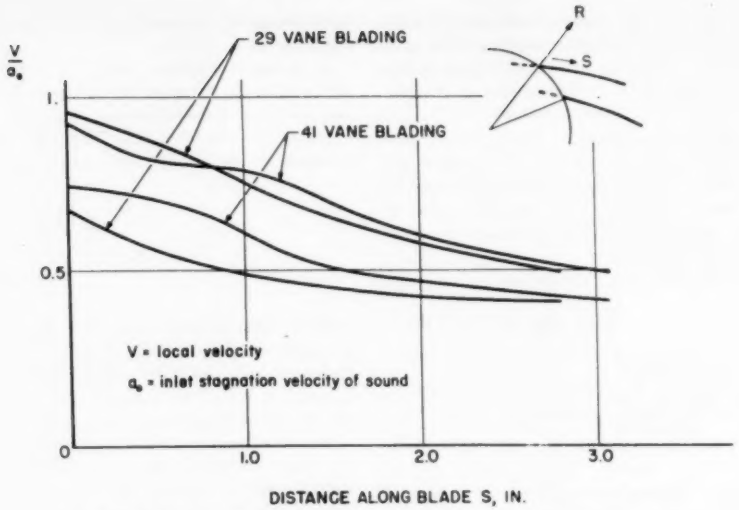

Fig. 6 Velocity distribution along the blade section of guide vanes

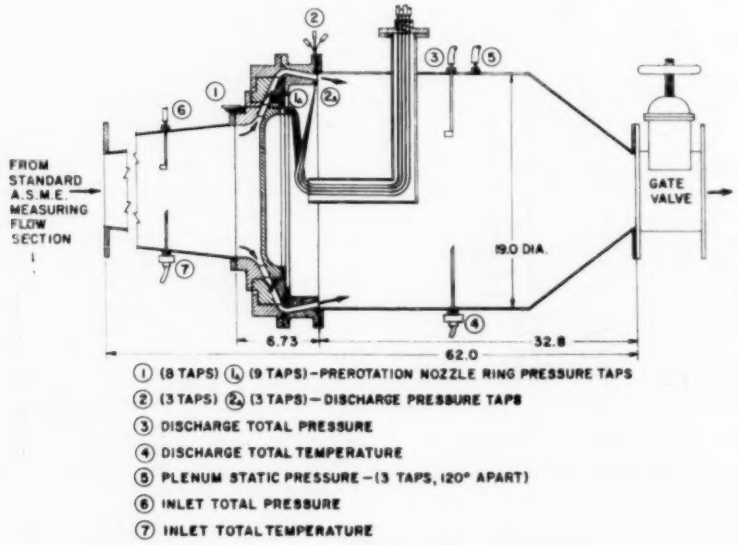
FROM STANDARD A.S.M.E. MEASURING FLOW SECTION
GATE VALVE
19.0 DIA.
6.73
32.8
62.0
① (8 TAPS) 1a (9 TAPS)—PREROTATION NOZZLE RING PRESSURE TAPS
② (3 TAPS) 2a (3 TAPS)—DISCHARGE PRESSURE TAPS
③ DISCHARGE TOTAL PRESSURE
④ DISCHARGE TOTAL TEMPERATURE
⑤ PLENUM STATIC PRESSURE—(3 TAPS, 120° APART)
⑥ INLET TOTAL PRESSURE
⑦ INLET TOTAL TEMPERATURE

Fig. 7 Diffuser test rig

Design calculations were carried out for two sets of blades (Fig. 6). One set has 41 blades characterized by a small diffusion from inlet to throat passage. The other set has 29 blades; this latter is considered to be an improvement over the 41-blade set, because of a higher diffusion at the inlet. In designing the 41-blade set, effort was made to avoid local supersonic flow. A daring approach was taken in the 29-blade set, allowing a small local supersonic flow at the inlet.

Design of the tongue or extended parts of the blade was made from consideration of the incidence at the guide vane inlet. The authors believe that a negative incidence is beneficial to the diffusing system. A negative incidence of -2 deg is shown on Fig. 5 for the beginning portion of the tongue.

To give a small loading to the tongue, its blade angle is supposed to differ little from the flow angle given by the vaneless space calculation. To avoid any sharp transition between the beginning portion of the tongue and that of the guide vanes, the deviation $\beta_{\text{blade}} - \beta_{\text{flow}}$ is maintained the same all along the tongue, with a resulting design shown on Fig. 5.

Performance of the Diffusing System on a Stationary Test Rig

Experimental Test Rig. A test rig was set up to determine the performance of the diffusing system as designed. Fig. 7 shows a drawing of the rig. Air flows through the nozzles designed to give the proper flow angle at the inlet to the diffuser. The inlet pressure and temperature were controlled so that the Reynolds number in the diffuser passage is the same as that in the final compressor. Static pressure taps are located on both sides of the nozzle, along a mean streamline of the nozzle passage. Total pressure probes are located at the nozzle inlet.

Determination of the inlet conditions to the diffuser is based on

$$\eta_D = \frac{\left(\frac{P_2}{P_1}\right)^{\frac{K-1}{K}} - 1}{\frac{K-1}{2} M^2}$$

WHERE:

P_2 = DISCHARGE TOTAL PRESSURE

P_1 = DIFFUSER INLET STATIC PRESSURE

$K = 1.400$

$M^2 = \eta_n M_{th}^2 \left[1 + (1-\eta_n)\frac{K-1}{2} M_{th}^2\right]$

η_n = PREROTATION NOZZLE COEFFICIENT (ASSUMED CONSTANT) = 0.940

$M_{th} = f(P_s/P_0)$

P = PREROTATION NOZZLE INLET TOTAL PRESSURE

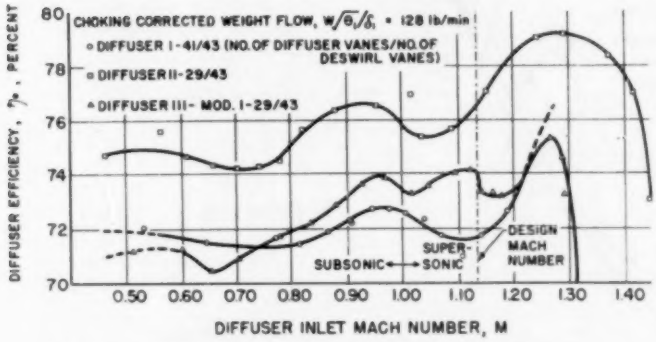

Fig. 8 Performance of supersonic diffusing system on stationary test

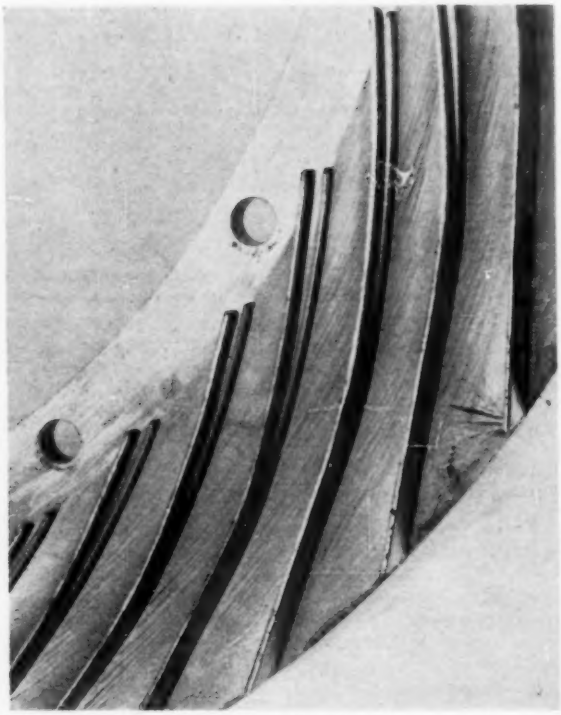

Fig. 9 Guide vanes

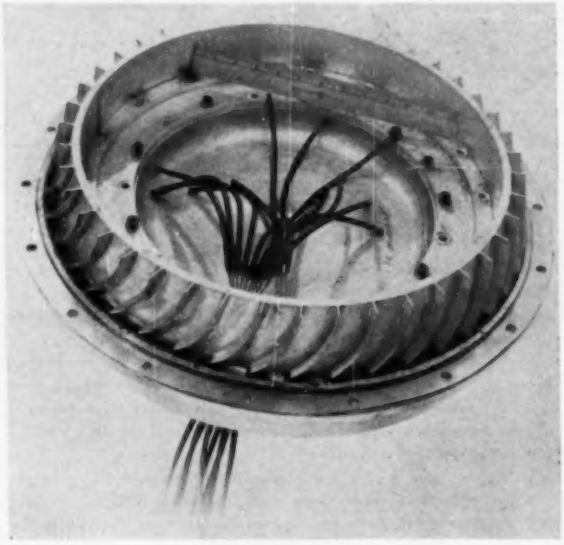

Fig. 10 Deswirl vanes

the static pressure readings, the total pressure at the nozzle inlet, and an assumed nozzle loss coefficient.

Experimental Results. The efficiency of the diffuser is defined by equation (1). The values obtained for the two calculated sets of blades which use the same deswirl vanes are shown in Fig. 8.

The first test was made with the 41-blade set. The results indicate that the desired performance of 0.721 at $M = 1.132$ is closely reached. In addition, at higher Mach numbers it shows better performance, which tends to confirm the design philosophy toward a higher blade loading applied to the 29-blade set. These preliminary results were so encouraging as to call for the immediate fabrication and evaluation of the 29-blade set. Fig. 8 indicates that the smaller number of blades shows considerable improvement in performance as anticipated. The highest efficiency is reached at:

$$M = 1.30 \qquad \eta_D = 0.792$$

Fig. 9 shows these vanes, and traces of dirt deposited during the evaluation program. No accumulation due to secondary flow losses and shock wave formation is seen. Fig. 10 presents the deswirl vanes used during the experimental program.

In an attempt to increase the blade loading, the vanes of the 29-blade set were moved forward, to a point where the incident

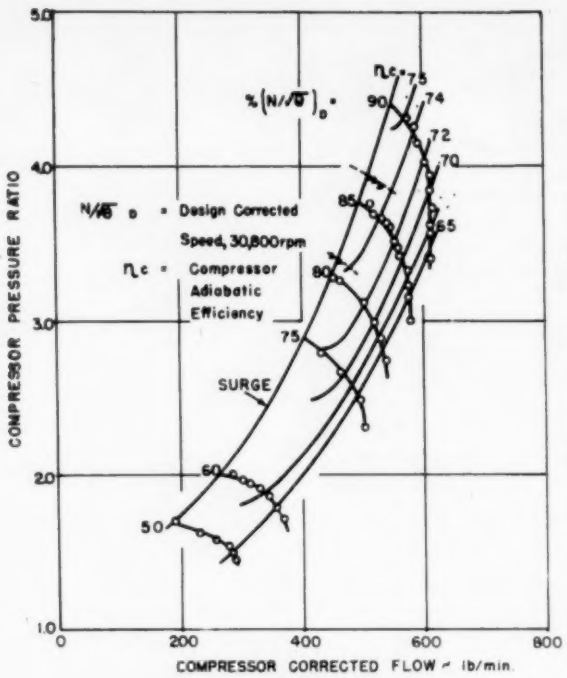

Fig. 11 Compressor performance

Mach number would be 1.0. The free space in the V shape is reduced. Performance of the modified diffuser (Fig. 8) indicates some deterioration. In addition, instability was noticed during the runs.

The Diffusing System in an Experimental Compressor

The experimental compressor [6] of which this diffusing system is a component was designed to give a pressure ratio of 5.2:1 operating with a supersonic relative Mach number of 1.24 at the shroud of the inducer inlet.

Test of the first prototype has produced the compressor map shown on Fig. 11. Due to cancellation of the experimental program, no data were available for the design speed; no instrumentation program was instituted to determine the performance of the components of the compressor.

At 90 per cent design speed, the Mach number entering the diffusing system is slightly above 1. If the diffuser performs with the impeller in the same way as in stationary test, from the compressor efficiency of 0.75 (90 per cent speed line, Fig. 11) calculation indicates an impeller efficiency of the order of 0.86, the inducer shroud relative Mach number being above 1.1. As this impeller performance is an upper limit of present data on supersonic centrifugal compressors [7] the conclusion is made that for this particular case the diffusing system yields practically the same results in both the stationary and compressor test.

Conclusion

Design of the diffusing system that incorporates a set of 29 guide vanes with a V-shape at the inlet was considered as having met the objectives of handling the supersonic flow at the exit of centrifugal impeller.

1 Under stationary test, an efficiency of 79 per cent was achieved for the diffusing system operating with an inlet Mach number of 1.3 behind stationary nozzles.

2 A centrifugal compressor made up by a supersonic impeller and the diffusing system under study was shown to operate at 4.3 pressure ratio with an efficiency of 75 per cent.

Further fundamental work has to be carried out to offer an explanation for this performance. Schlieren study will help in clarifying the existence of weak oblique shocks as some would think. Other studies have to be made to establish the effects of the vortexes generated along the edges of the V, on supersonic flow diffusion, and also the contribution of these edges to break-off the wakes of the flow at the impeller exit to allow a more uniform entering profile of supersonic flow, known to be advantageous [8].

Contributing to the team that designed high-speed radial and mixed flow compressors at AiResearch, from which this novel diffuser was evolved, were Dr. E. M. Knoernschild[3] and Dr. H. P. Eichenberger.[4] The accurate experimental evaluation was the valuable work of Mr. A. C. Ackerman.[5]

References

1 C. R. Faulders, "Experimental and Theoretical Study of Vaneless Diffuser Flow With Supersonic Entry," Gas Turbine Laboratory, Massachusetts Institute of Technology, Cambridge, Mass., June, 1952.

2 B. Eckert, "Axial und Radial Kompressoren," Springer-Verlag, Germany, 1953, p. 393.

3 C. R. Faulders, "An Aerodynamic Investigation of Vaned Diffusers for Centrifugal Compressors," Gas Turbine Laboratory, Massachusetts Institute of Technology, Cambridge, Mass., January, 1954.

4 J. E. Coppage, F. Dallenbach, H. P. Eichenberger, G. E. Hlavka, E. M. Knoernschild, and N. Van Le, "Study of Supersonic Radial Compressors for Refrigeration and Pressurization Systems," WADC TR 55-257.

5 J. D. Stanitz, "One-Dimensional Compressor Flow in Vaneless Diffusers of Radial and Mixed Flow Centrifugal Compressors, Including Effects of Friction, Heat Transfer, and Area Change," NACA TN 2610, January, 1952.

6 E. J. Hettlinger, "Design and Development Summary, Gas Turbine Compressor and Power Unit," Model GTCP185-1, AiResearch Manufacturing Company of Arizona, Phoenix, Arizona, AiResearch Report GT-5400-R, June, 1956. Contract AF 33 (038)-29533.

7 J. L. Dussourd, N. Van Le, and D. E. Lewis, "Aerodynamic Criteria for Optimum Design of Mixed Flow Impellers Experimental Results for Impellers I and IB," WADC TN 58-88.

8 V. D. Agosta and A. Martellucci, "An Investigation on Diffusion in a Supersonic Compressor Stator Passage in the Presence of Rotor Blade Wake and Hub and Shroud Boundary Layer," Polytechnic Institute of Brooklyn, PIBAL Report No. 394.

APPENDIX

Calculation of the Velocity Distribution Along the Blade Surface at the Mean Section of the Guide Vanes

The physical dimensions of the guide vanes (thickness, blade angle β, height of the blading) are assumed to be known. The velocity C along the middle of the blade channel is calculated on a one-dimensional flow basis. In the blade channel, over a distance Δm (Fig. 12) the torque acting on the blade is equal to the change in angular momentum of the flow between Δm or:

$$(\Delta p)(\Delta m)hr = \rho hr\, \Delta\varphi\, C \cos\beta \frac{\partial}{\partial m} rC_u (\Delta m) \qquad (2)$$

$$\Delta\varphi = \frac{2\pi}{z} - t/r$$

The velocity in the channel is assumed to vary linearly between suction and pressure side of the blade giving

$$2C = C_s + C_p; \quad \Delta C = C_s - C_p \qquad (3)$$

[3] AiResearch Manufacturing Company, Los Angeles, Calif.
[4] Thompson Products, Inc., Cleveland, Ohio.
[5] Marquardt Aircraft Company, Van Nuys, Calif.

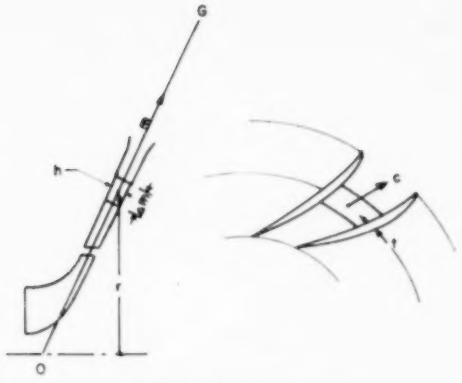

Fig. 12 Guide vane geometry

Introducing Bernoulli's equation between suction and pressure yields

$$\Delta P = {}^1/_2\rho(C_s^2 - C_p^2)$$

Elimination of ΔP and C from (2) gives:

$$\frac{\Delta C}{\Delta \varphi} = \cos\beta \frac{\partial}{\partial m} rC_u \tag{4}$$

$$C_u = C \sin\beta$$

Calculation of ΔC follows from determination of the slope of the curve rC_u versus m. The velocity C_s, C_p are then given by (4) and (3).

DISCUSSION

C. R. Faulders[6]

The authors are to be commended for arriving at a diffuser design, incorporating an innovation in leading edge configuration, with which efficiencies approaching 80 per cent can be realized in spite of inlet Mach numbers in the low supersonic region. Equally interesting is the indication that performance measured with a steady inlet flow is representative of the performance that can be obtained with the same diffuser when the inlet flow is supplied by a rotating impeller. By extending the diffuser vanes upstream and largely eliminating the vaneless preliminary section the over-all radius ratio can, in principle, be reduced. At the same time, as the authors mention, some of the losses associated with a vaneless diffuser can be eliminated. There are some advantages to leaving a vaneless preliminary, however, even if the supersonic Mach numbers can be handled. The noise produced by the interaction of the periodic flow pattern leaving the impeller and the diffuser vanes may be objectionable in some cases, and the performance of the vaned diffuser may suffer from the large variations in angle of attack corresponding to this periodic flow. In this regard the writer would be interested in knowing the number of impeller blades in the experimental compressor used by the authors.

The discussion of the authors regarding the use of a subsonic radial component of Mach number appears to require some clarification. There are actually two distinct types of disturbances in a supersonic vortex flow that can produce shocks unless the proper precautions are taken. The first type of disturbance is one that is axisymmetric, where the flow adjustment involves a change in the radial component of the Mach number only. Thus, with a supersonic radial component of Mach number, a circular shock will appear at some radius governed by the back pressure in order that the flow will diffuse toward the back pressure instead of continuing to accelerate to lower and lower pressures. With a subsonic radial Mach number, however, the flow can adjust to such things as a change in back pressure or an axisymmetric decrease in the axial width without shocks. The other type of disturbance is a local one where a nonuniform distribution of the tangential component of velocity around a circle is required. The latter situation arises at the leading edge of a diffuser vane, or along the vane surface, and here the local Mach number and the blade geometry determine whether shocks will appear. The case for leading edge sweepback to prevent shocks is properly stated by the authors. The principle of sweepback would also apply, however, if the radial component of Mach number were supersonic, the only criterion for a subsonic leading edge being a subsonic Mach number normal to the leading edge.

Although the vaned diffuser was designed for an incidence of −2 degrees and a Mach number at the inlet of 1.132, maximum efficiency was obtained at a Mach number of 1.30. Assuming a Prandtl-Meyer expansion at the nozzle exit, the decrease in the angle β corresponding to this increase in Mach number would be about 4 degrees, and the incidence angle at Mach number 1.30 would be −6 degrees. Although negative incidence is useful in decreasing blade curvature in order to reduce secondary flow, it would seem that a higher blade loading on the forward part of the blade would result in higher pressure ratio without significant loss of efficiency. Further data showing the effect of Mach number at constant incidence would be of interest.

The solidity, or chord-to-pitch ratio, of the vaned diffuser when mapped onto a rectangular plane by conformal transformation was computed by the writer for the two configurations tested by the authors. An approximate expression given in Reference [3] was used for this purpose, giving solidities of 3.0 for the 41-blade diffuser and 2.1 for the design with 29 blades. As rectangular cascade tests generally indicate the optimum solidity to lie between 1.5 and 2.0, the improvement in performance with the fewer blades is not surprising. If 41 blades can be tolerated on the basis of the interaction of the periodic flow from the impeller with the vaned diffuser, it should be possible to decrease the solidity and reduce the over-all radius ratio of the compressor.

Authors' Closure

The comments of Dr. Faulders have contributed to enlarging the understanding of the phenomenon presented in the paper.

The problem of noise as mentioned by the discusser was not encountered by the authors on the stationary test rig as well as on the actual experimental compressor. The number of impeller blades (18), that of the diffuser (29 and 41), and the operating speed were such that no aerodynamic excitation could take place.

In arriving at the design concept presented in the paper, the authors have insisted on the axisymmetric free space with a subsonic radial component of Mach number. This is to allow for any adjustment of the disturbance due to nonuniform distribution of the tangential component of the velocity as mentioned by the discusser. Due to the three-dimensional aspect of the problem, the authors do not think that successful operation of the diffuser would be feasible with a supersonic radial component of Mach number in the free space as contended by the discusser who argues on the basis of two-dimensional swept-back wing principle. The discusser rightly points out the effect of the incidence on the performance of the guide vanes obtained from the stationary test rig. Regretfully, not enough experimentation was performed to clarify this effect. It is also fortunate that the solidity used in this experimental work approaches closely the best one as determined by the discusser's experience. If a larger solidity was used, it is due to the introduction of a conservatism by the authors in this exploratory work.

[6] Aero-Space Laboratories, Missile Division, North American Aviation, Inc., Downey, Calif. Assoc. Mem. ASME.

Technical Briefs

This section consists of contributions of 750 words or less (about 2½ double-spaced typewritten pages, including figures). Technical Briefs will be reviewed and approved by the specific division's reviewing committee prior to publication. After approval such contributions will be published as soon as possible, normally in the next issue of the Journal.

Elastic Orifices for Gas Bearings[1]

JOHN H. LAUB[2]

EXTERNALLY pressurized gas bearings usually operate either with flow restriction by means of fixed-diameter orifices or by inherent regulation, in which case the annular entrance area from the inlet to the gap acts as a restrictor of the gas flow. If a fixed-diameter orifice is used, the mass flow rate G through the orifice can be expressed as:

$$G = C_D \phi A_2 [2\rho_{PL}(P_{PL} - P_0)]^{1/2} \tag{1}$$

where C_D denotes the orifice coefficient, P_{PL} the absolute pressure of the gas upstream of the orifice (i.e., in the plenum), P_0 the absolute pressure downstream, ρ_{PL} the density of the gas at pressure P_{PL}, A_2 the orifice area, and

$$\phi = \left[r^{2/K} \left(\frac{K}{K-1} \right) \left(\frac{1 - r^{\frac{K-1}{K}}}{1 - r} \right) \left(\frac{1 - \left(\frac{A_2}{A_1} \right)^2}{1 - \left(\frac{A_2}{A_1} \right)^2 r^{2/K}} \right) \right]^{1/2}$$

where $r = P_0/P_{PL}$, A_1 is the area of the flow upstream, and $K = C_p/C_v$, the ratio of the specific heats of the gas at constant pressure C_p to that at constant volume C_v.

Values of ϕ are plotted as a function of r in Fig. 1 for two values of K, i.e., $K = 1.4$ and $K = 1.3$, covering the range of K for air between very low and very high temperatures (approximately −200 to 1800 deg C). The ratio $(A_2/A_1)^2$ can be neglected, compared to 1, since the area A_2 of the orifice is very small compared with the upstream area.

The flow rate Q increases with increasing pressure differential $P_{PL} - P_0$ until the critical pressure ratio $r_{cr} = P_{0cr}/P_{PL}$ is reached, which for air with $K = 1.4$ is 52.8 per cent. The velocity of the gas then becomes sonic and does not increase further with increasing pressure differential $P_{PL} - P_0$. The orifice operates in the choked condition with no further increase of the flow rate with increasing pressure differential. This is shown by Fig. 2, in which measurements of the air flow rate Q_{fi} through a fixed

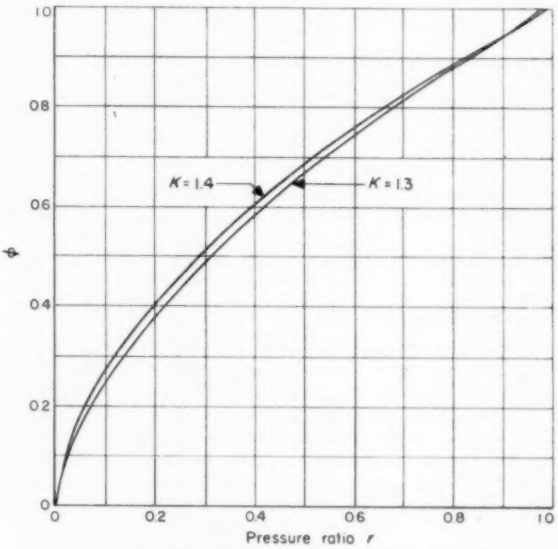

Fig. 1 Plot of ϕ as a function of r for two values of K

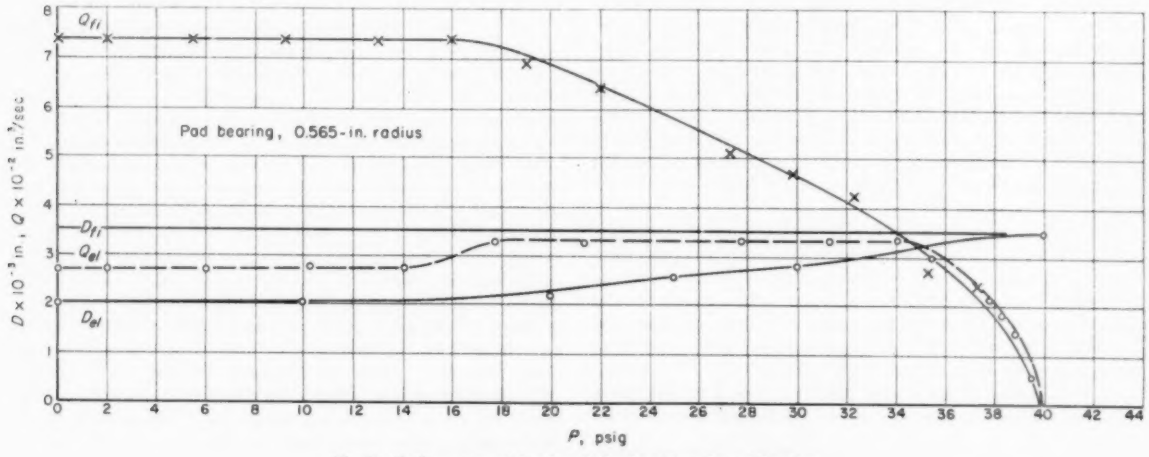

Fig. 2 Performance of fixed and elastic orifices in pad bearing

[1] This paper presents the results of one phase of research carried out at the Jet Propulsion Laboratory, California Institute of Technology, under Contract No. NASw-6, sponsored by the National Aeronautics and Space Administration.

[2] Jet Propulsion Laboratory, California Institute of Technology, Pasadena, Calif.

Contributed by the Lubrication Division of THE AMERICAN SOCIETY OF MECHANICAL ENGINEERS. Manuscript received at ASME Headquarters, May 31, 1960.

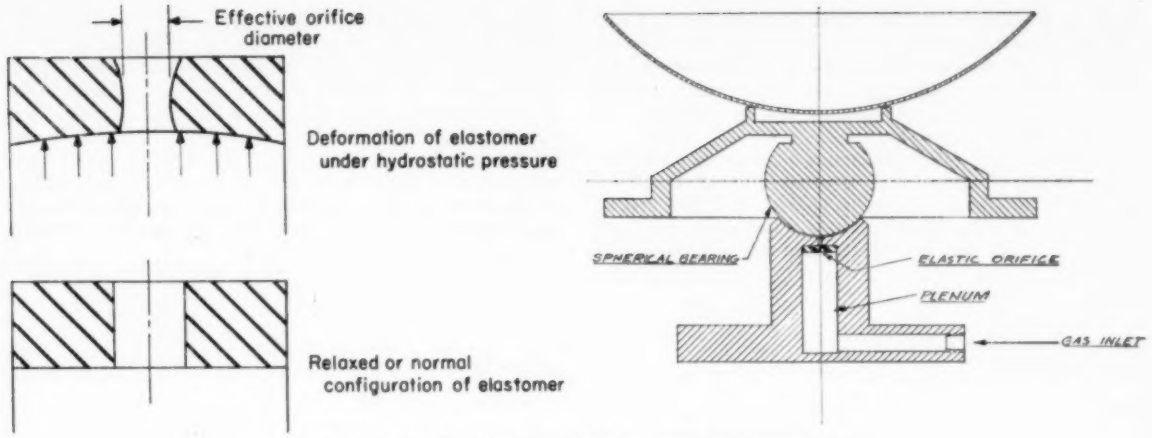

Fig. 3 Configuration of elastic orifice whose area is pressure-sensitive

orifice of 3.5-mil diameter in a pad bearing are plotted as a function of $P_{PL} - P_0$, with P_{PL} held constant at 40 psig.

In a gas bearing it is desirable to keep the gas consumption to a minimum, not only for reasons of economy but also in order to stay within the laminar flow regime in the gap and to avoid shock waves and negative pressure profiles with attendant impairment or loss of load-carrying capacity. Hence orifices with a small, fixed diameter of a few mils are often used. The lower limit of the orifice diameter is determined by mechanical considerations, such as the size of dust particles which may be carried along by the gas stream and must be prevented from clogging the orifices.

In most applications, a bearing with a high spring rate or stiffness is required. This is particularly true of gimbal axis bearings in gyros or similar inertial instruments in which the mass shift under accelerating forces must be held to a minimum. It has been shown[3] that the gap h varies with the $^1/_3$-power of the ratio of the flow rate Q and $(P_0^2 - P_1^2)$, where P_1 is the exhaust pressure. It is evident, therefore, that a fixed-diameter orifice is not conducive to high stiffness since the flow rate Q is constant below and decreases above the critical pressure. The stiffness can obviously be improved if the flow rate increases with increasing pressure or remains at least constant over as wide a pressure range as possible. (The ideal case would be Q proportional to $P_0^2 - P_1^2$, resulting in a constant gap h, i.e., infinite stiffness.)

These considerations led to the concept of an elastic orifice, i.e., an orifice whose area does not remain constant but decreases with increasing differential between upstream and downstream pressure. An orifice with a variable, pressure-sensitive area may consist, for instance, of a circular disk of silicone rubber or some other elastomer, as shown in Fig. 3. The orifice opening was made by molding the elastomer around a pin of 3.5-mil diameter and withdrawing the pin after the material had set. If the pressure differential across this orifice is zero, the elastomer will not be stressed and the orifice diameter in this *relaxed* state is 3.5 mil. If, however, a pressure difference between the upstream and the downstream area occurs, the material will be elastically deformed and the diameter of the opening will decrease. This is shown in Fig. 4, in which measured flow rates Q_{e1} through this orifice are plotted when the upstream pressure is varied between 8 psig and 48 psig and the downstream pressure is held constant at atmospheric pressure. Also shown is the diameter D of the orifice opening, which was calculated from the flow rate and Expression (1). It will be noted that the effective diameter of this orifice shrinks from 3.5 mil in the relaxed condition to 2.5 mil under a differential pressure of 48 psig; the corre-

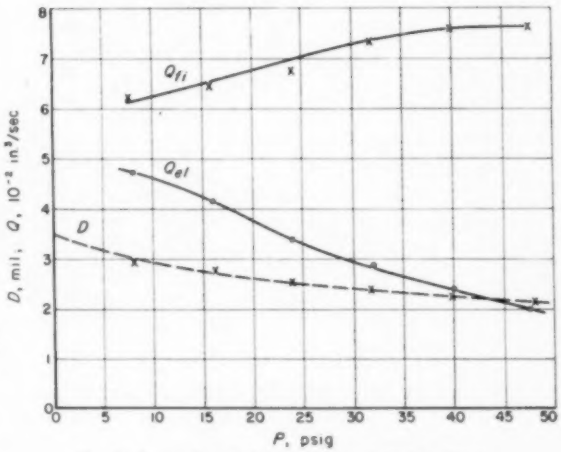

Fig. 4 Comparison between fixed and elastic orifices

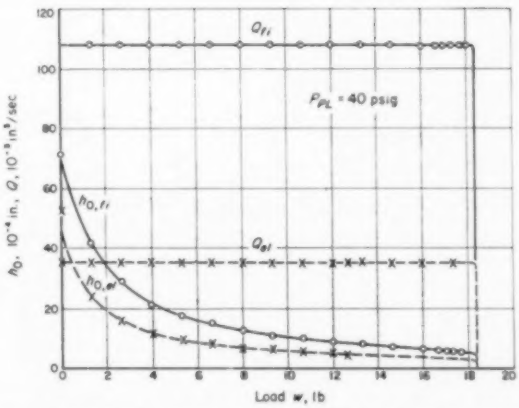

Fig. 5 Comparison between fixed and elastic orifices in recessed spherical bearing

[3] John H. Laub, "Hydrostatic Gas Bearings," TRANS. ASME, Series D, JOURNAL OF BASIC ENGINEERING, vol. 82, 1960, pp. 276–286.

sponding shrinkage of the orifice area is approximately 2 to 1. It is interesting to compare this with the performance of an orifice with a fixed diameter of 3.5 mil for which flow measurements made under the same conditions are also entered in Fig. 4 (Curve Q_{fi}). The flow rate Q_{fi} increases, whereas Q_{ei} decreases with increasing differential pressure.

The performance of the elastic orifice in a pad bearing of 1-in.^{2} area at 40 psig plenum pressure is compared in Fig. 2 with that of an orifice of a fixed diameter of 3.5 mil. It is seen that the gas flow through the elastic orifice is considerably lower over most of the range than through the fixed orifice; if the latter is run in the choked condition (which is common bearing practice) it consumes over 2.6 times as much air as the elastic orifice.

Similar results were obtained from tests on a hemispherical bearing, which are plotted in Fig. 5. The gas consumption Q_{ei} of the bearing with the elastic orifice is only 31.5 per cent of that with the fixed orifice at the same load. This means that a gas-lubricated instrument with elastic orifice in a space vehicle can travel three times further with the same initial supply of gas. At the same time, the stiffness of the bearing is substantially improved over a wide range of loads, as can be seen from the slope dh/dw of the $h_0 = f(w)$ curves in Fig. 5.

Journal of BASIC ENGINEERING

Information for Authors

• Manuscripts should be submitted in final form to the Editor. Each manuscript must be accompanied by a statement that it has not been published elsewhere nor has it been submitted for publication elsewhere. A paper which would occupy more than 8 pages of the Journal may be returned to the author for abridgment.

• The author should state his business connection, the title of his position, and his mailing address. A short abstract (50 to 100 words) should be included on the first page immediately preceding the introductory paragraph of the paper.

Three copies of the manuscript are required. One of these must be a carefully prepared printer's copy, typed in double spacing, on one side of the page only, with wide margins, on $8^1/_2$ by 11-in. opaque white paper. Mimeographed manuscripts, if prepared with exceptional care, can be accepted provided they are completely edited.

• As far as possible, all mathematical expressions should be typewritten. Greek letters and other symbols not available on the typewriter should be carefully inserted in ink. Care should be taken to distinguish between capital and lowercase letter, between zero (0) and the letter (*O*), between the numeral (1) and the letter (*l*), etc. A letter representing a vector cannot be printed with an arrow above or below it. The letter should be underscored with a single wavy line, wherever it appears in the text, to designate boldface type.

• A list of symbols carefully marked for the use of the editor (thus: κ, Greek l.c. kappa), if it has not been included in the body of the paper, should accompany the manuscript on a separate page.

• Before preparing a manuscript the author should study printed articles in the Journal, with special attention to the form and style of mathematical expressions, tables, footnotes, references, and abstract. Numbers that identify mathematical expressions should be enclosed in parentheses. Numbers that identify references at the end of the paper should be enclosed in brackets. Care should be taken to arrange all tables and mathematical expressions in such a way that they will fit into a single column when set in type. Equations that might extend beyond the width of one column (fractions that should not be broken or long expressions enclosed in parentheses) should be rephrased to go on two or more lines within column width. Fractional powers are preferred to root signs and should always be used in more elaborate formulas. The solidus should be used instead of the horizontal line for fractions wherever possible.

• A normal paper should not exceed 8 pages in the Journal. It is about 8000 words or 20 double-spaced typewritten pages exclusive of drawings. A Technical Brief should not exceed 750 words or about one page in the Journal inclusive of drawings.

• Originals and two copies of figures must accompany the manuscript. Line drawings should not be larger than $8^1/_2 \times 11$ in. and should be planned for reduction to column width. Lettering should be large enough to be clearly legible when the illustration is reduced. The originals of line drawings must be in India ink on white or pale blue tracing paper or tracing cloth. Photographs of equipment or test specimens must be glossy prints and should be used sparingly. Captions for figures should be typed double-spaced and included as the last page of the manuscript. The figure number and author's name should be written in the margin or on the back of each illustration.

• Titles of papers should be brief.

• Authors can obtain copies of the ASME Manual MS-4, "An ASME Paper," from the Editor and are urged to do so before drafting their papers in final form.

• Papers published in Journals of the Transactions of the ASME must be presented at a Meeting, either in person or by title.

• An author is entitled to 25 preprints free of charge (in the case of two authors, 15 each; three or more authors, 10 each). Larger quantities of preprints or reprints can be ordered from Editorial Department, The American Society of Mechanical Engineers, 29 West 39th Street, New York 18, N. Y. Quotations will be sent on request.

Please address all communications to:

Editor, ASME,

29 West 39th Street,

New York 18, N. Y.

ASME Publications Committee

ASME METALS ENGINEERING HANDBOOK

complete in four volumes, offers you a modern compilation of metals engineering data and methods, assembled from many sources and related directly to your design needs.

METALS ENGINEERING—DESIGN

Metals properties and other general criteria serve only as starting points in this volume. It gives you much more detail pertinent to special design problems—shows you how to test to see how a material will work for a specific purpose . . . how to determine performance of parts in your design . . . how to strengthen metal parts according to the uses that you need them for . . . how to design for production to keep costs down. Facts you get represent current practices in handling fatigue, corrosion, non-destructive testing, elasticity, etc.

Published 1953 405 pages 560 illustrations $10.00

METALS ENGINEERING—PROCESSES

In this volume you will find detailed data on the various processes by which metals are converted into finished products. Composed of a wealth of practical, day-to-day engineering helps, the book covers such areas as: heat treatment of steel, all forms of casting, hot and cold working, powder metallurgy, welding, machining, and electroforming. For each of the manufacturing methods there is a compilation of the basic physical characteristics to be considered, and the general advantages and limitations usually encountered.

Published 1958 458 pages 512 illustrations $13.50

ENGINEERING TABLES

This volume places in your hands a ready source of design information to save you from losing time in searching out specialized publications, periodicals, and miscellaneous data sheets. In 15 sections, this volume conveniently groups and arranges together those tables which apply to the design of specific parts. It covers such subjects as bar stock and shafting; bearings; spur, helical, herringbone, bevel, and worm gears; cylindrical fits; keys and keyseating; bolts, counter bores, screw threads; nuts, washers, wrench openings; serrations and splines; springs; aircraft and mechanical tubing; pipe, pipe threads and fittings; electrical motors; graphical symbols; gaskets; packings.

Published 1956 692 pages 560 tables $12.00

METALS PROPERTIES

The specific information a designer must have about the properties of the metals with which he must work is assembled for your convenience in this book. For more than 500 metals it tabulates working data on the metallurgical, physical, fabrication, and mechanical properties of metals—such typical data as chemical composition, industrial uses, draw temperatures, tensile strength, yield point, Rockwell "C" core hardness, hot working temperature, coefficient of thermal expansion, end-quench hardenability, etc.

Published 1954 445 pages 531 illustrations $11.00

20% discount to ASME members

THE AMERICAN SOCIETY OF MECHANICAL ENGINEERS

29 W. 39th St. New York 18, N. Y.

CURRENT PERIODICAL SERIES

PUBLICATION NO.: 1192

TITLE: JOURNAL OF BASIC ENGINEERING (Series D of the ASME Trans.)

VOLUME: 83 ISSUES: 1 - 4

DATE March - December, 1961

This publication is reproduced by agreement with the publisher. Extensive duplication or resale without permission is prohibited.

University Microfilms, Ann Arbor, Michigan,